ISMRM British & Irish Chapter Annual Meeting 2024

11th - 13th September

Monica Partridge Building
University of Nottingham
United Kingdom

50+ Years of MRI

Abstract Book

ISMRM | British & Irish CHAPTER

University of Nottingham
UK | CHINA | MALAYSIA

Message from the Organisers

Welcome to the 2024 Annual Meeting of the British and Irish Chapter of the ISMRM (BIC-ISMRM) which is being held at the University of Nottingham from 11th to 13th September.

The theme of this year's BIC-ISMRM meeting is *50+ years of MRI*, in part recognising Nottingham's long association with the development and application of magnetic resonance imaging and spectroscopy (MRI/S). This association began with the publication of Peter Mansfield's first paper on NMR imaging in 1973 and has encompassed the invention of slice selection, echo planar imaging and active magnetic shielding, as well as the development of the UK's first 3T and 7T scanners, and current plans for establishing a UK national facility for ultra-high field (11.7T) human MRI scanning.

The first day of the meeting comprises a Workshop on Beyond ^{1}H: Xing up MRI/S. This will focus on how to implement and exploit X-nuclei MRI/S on clinical and pre-clinical systems. There will be invited presentations, a poster session and talks from vendors. After the workshop there will also be an optional tour of the nearby Sir Peter Mansfield Imaging Centre.

The main BIC-ISMRM meeting takes place on Thursday and Friday and will include a mix of presentations of invited and proffered papers, as well as poster sessions, and an opportunity to meet with commercial exhibitors.

A fantastic set of speakers, including Nicolas Boulant (University of Paris-Saclay), Eleftheria Panagiotaki (UCL), Rhodri Cusack (Trinity College Dublin) and Mary McLean (University of Cambridge), have agreed to deliver invited lectures at the meeting, and we are delighted that past-ISMRM President, Professor Derek Jones (University of Cardiff), will deliver this year's flagship Bill Moore Lecture.

Introduction

We were very pleased to receive more than a hundred abstract submissions, many from PhD students and other trainees. These form the basis of 30 short talks and 83, one-minute power pitch presentations (each linked to a subsequent poster presentation) which will form the core of the meeting.

The conference dinner will be held in Cavendish Hall on Thursday evening from 19.30 and there will be a PubhD public engagement event at the Barley Twist in Nottingham City Centre on Wednesday evening.

We have tried to keep the costs for attending the meeting as low as possible to make it accessible and are happy that more than 170 delegates have registered to attend, including radiographers, technologists, scientists and medics from all career stages. We hope you all enjoy participating in the conference and hearing about the exciting recent developments in our field.

We would like to thank all our sponsors whose support has made the meeting possible.

Richard Bowtell (on behalf of the Local Organising Committee)

Sponsors

We are very grateful to the sponsors of this meeting

Gold Sponsors

GOLD STANDARD PHANTOMS

PHILIPS

GE HealthCare

SIEMENS Healthineers

Silver Sponsors

Xiel.

MR SHIM

skope

NVISION

MR SOLUTIONS

Bronze Sponsors

MR CoilTech

Quantified Imaging

IXICO

Workshop Sponsors

BRUKER

RAPID Biomedical

Introduction

Local Organising Committee

Dorothee Auer

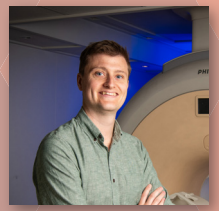

Adam Berrington

Nic Blockley

Richard Bowtell

Michael Chappell

Carolyn Costigan

Robert Dineen

Susan Francis

Paul Glover

Penny Gowland

Paul Morgan

Galina Pavlovskaya

Stefanie Thust

Getting Around

University Park Campus

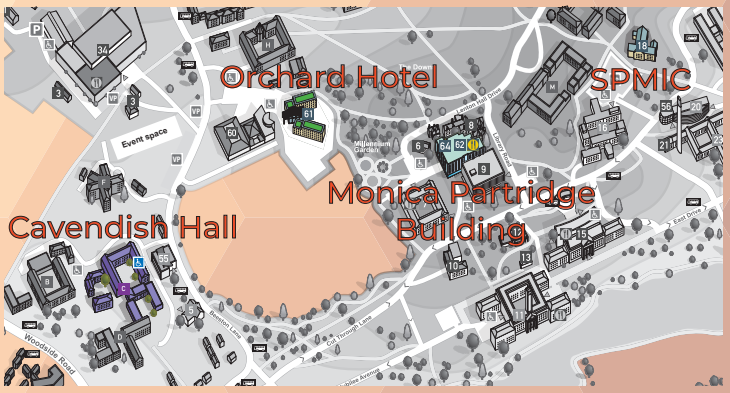

Google Maps Links

Cavendish Hall
Orchard Hotel
Monica Partridge Building
SPMIC

Monica Partridge Building

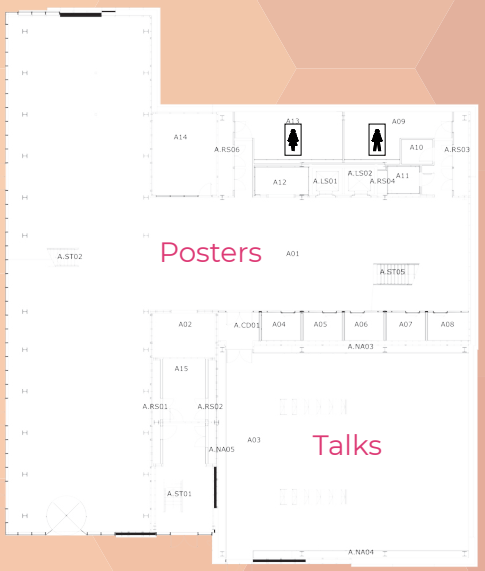

Wednesday 11th September

Beyond ^{1}H: Xing up MRI/S

12:00 - 12:45	Registration and Lunch
12:45 - 15:00	Invited Lectures Methods/Applications of Hyperpolarised Gas MRI Jim Wild (University of Sheffield) Making Metabolic Measurements with ^{13}C Damian Tyler (University of Oxford) Getting the Best Out of ^{31}P Chris Rodgers (University of Cambridge) Use of ^{23}Na Claidoa Gandini Wheeler Kingshott (UCL) Offbeat Nuclei with Upbeat Uses: Multinuclar MR in Clinical Research Pete Thelwall (Newcastle University) *Chairs: Stephen Bawden and Sue Francis (Nottingham)*
15:00 - 15:45	Refreshment Break: Posters and Exhibits
15:45 - 17:15	Vendor Presentations and Discussion Arnaud Comment (GE Healthcare), Matthew Clemence (Philips Healthcare), Willy Gsell (Bruker Biospin), Robin Heidemann (Siemens Healthineers) *Chairs: Richard Bowtell and Galina Pavlovskaya (Nottingham)*
17:15 - 18:00	Optional Tour of the SPMIC
19:30 - 21:30	PubhD Public Engagement Event Barley Twist, Nottingham City Centre, NG1 7FE

Thursday 12th September

09:00 - 09:30	Registration
09:30 - 09:45	Welcome
09:45 - 10:15	Invited Speaker: Nicholas Boulant (Neurospin) The Iseult 11.7T human MRI project: from first ideas to first in vivo images *Chair: Richard Bowtell (Nottingham)*
10:15 - 10:40	Power Pitch Session 1: Posters 1 - 20 *Chair: Olivier Mougin (Nottingham)*
10:40 - 11:15	Refreshment Break, Posters 1 - 20 & Exhibits
11:15 - 12:15	Proffered Talks Session 1 High Field MRI *Chair: Sydney Williams (Glasgow)* T1: Diffusion MRI acquisition methods for post mortem imaging at 10.5T Ben Tendler (University of Oxford) T2: High resolution diffusion MRI tractography at 10.5T in the in-vivo & ex-vivo NHP brain. Stam Sotiropoulos (University of Nottingham) T3: The 7T implant problem: participant exclusion rates in ultra-high field MRI. C. John Evans (Cardiff University) T4: Deuterium Metabolic Imaging (DMI) results at 7T following [$^2H_2$] and [$^2H_7$] glucose ingestion. Daniel Cocking (University of Nottingham)

	T5: Investigating Magnetic Field Correlation (MFC) sensitivity to demyelination and axonal loss using numerical simulations. Lewis Kitchingman (Cardiff University)
12:15 - 13:15	Lunch, Posters & Exhibits
13:15 - 13:45	Invited Speaker: Eleftheria (Laura) Panagiotaki (UCL) Non-invasive prostate microstructure estimation with Diffusion MRI *Chair: Steffi Thust (Nottingham)*
13:45 - 14:45	Proffered Talks Session 2 Preclinical and Cancer *Chair: Steffi Thust (Nottingham)* T6: Whole-brain imaging in rats using MRI and 3D microscopy: A cross-scale, multi-modal approach. Jenna Hanmer (University of Nottingham) T7: ^{1}H MR spectroscopy to evaluate the effects of a glycolysis inhibitor and temozolomide treatment in a mouse model of glioblastoma. Tareq Alrashidi (University of Liverpool) T8: Multiparametric ^{1}H/^{23}Na MRI for analysing the ionic microenvironment within preclinical breast tumour models. Alina Lavinia Capatina (University of York) T9: Lipid composition in the breasts of BRCA1/2 genetic mutation carriers via chemical shift-encoded imaging. Sai Man Cheung , (University of Newcastle)

	T10: Investigating prostate cancer using QSM in vivo. Laxmi Muralidharan (UCL)
14:45 - 15:10	Power Pitch Session 2: Posters 21 - 41 *Chair: Charlotte Buchanan (Nottingham)*
15:10 - 15:40	Refreshment Break, Posters 21 - 41
15:45 - 16:45	Proffered Talks Session 3 Contrast and Microstructure *Chair: Paul Morgan (Nottingham)* T11: Soma And Neurite Density Imaging (SANDI) is sensitive to changes in glial morphology induced by systemic inflammation. Mara Cercignani (Cardiff University) T12: Cross-species standardised subcortical tractography. Stephania Assimopoulos. (University of Nottingham) T13: The effects of maternal iron levels on the early development of white matter microstructure in the superior longitudinal fasciculus. Katie Smith (Cardiff University). T14: Comparison of susceptibility source separation methods without R_2. Patrick Fuchs (UCL) T15: Constrained model-based relaxation parameter mapping using balanced steady state free precession. Zimu Huo (University of Cambridge)

16:45 - 17:30	Bill Moore Lecture: Derek Jones (Cardif University) From Meteorology to Tractology: Forecasting a New Path in Neuroscience *Chair: Penny Gowland (Nottingham)*
19:30	Conference Dinner: Cavendish Hall

Friday 13th September

09:00 - 09:30	Invited Speaker: Rhodri Cusack (TCD) Measuring Cognitive Neurodevelopment in Infants with Awake fMRI *Chair: Gareth Barker (KCL)*
09:30 - 10:30	Proffered Talks Session 4 Quantitative Neuroimaging *Chair: Gareth Barker (KCL)* T16: Associations between Cerebrovascular Reactivity Delay and progression of Small Vessel Disease Features. Keelin N. Ridge, (University of Edinburgh) T17: Haematocrit-corrected QSM + qBOLD reveals globally elevated brain oxygen extraction fraction in sickle cell anaemia. Mitchel Lee (UCL) T18: Enhancing brain activity mapping through multi-modal data fusion and explainable machine learning. Jiri Benacek (Cardiff University) T19: Evidence for direct control of neurovascular function by circulating platelets in healthy older adults. Gabriella Rossetti, (Manchester Metropolitan University) T20: Age-trajectories of higher-order diffusion properties of major brain metabolites in cerebral and cerebellar gray matter using dMRS. Eirini Messaritaki (Cardiff University)

10:30 - 10:55	Power Pitch Sessions 3: Posters 42 - 62 *Chair: Nic Blockley (Nottingham)*
10:55 - 11:30	Refreshment Break, Posters 42 - 62
11:30 - 12:30	Proffered Talks Session 5 Respiratory and MSK *Chair: Pete Thelwall (Newcastle)* T21: Investigating gravitational influence on normal lung function using PREFUL MRI on an open scanner. Arthur Harrison (University of Nottingham) T22: Quantification of gas trapping in cystic fibrosis using residual volume (RV) lung ^{1}H-MRI. Amy V Simmons (University of Sheffield) T23: Dynamic ^{19}F-MRI of pulmonary ventilation in lung transplant recipients with and without chronic lung allograft dysfunction. Mary Neal (Newcastle University) T24: Unlocking Muscle Fatigue: Insights from multi-parametric ^{1}H, ^{23}Na & ^{31}P MRI in exercise-induced muscle damage and inflammation. Fabio Zambolin, (Manchester Metropolitan University) T25: Shoulder MRI Arthrograms – Is saline an intra-articular option? Charlotte Swain (Nottingham University Hospital)
12:30 - 13:15	Lunch, Posters & Exhibits
13:15 - 13:45	BIC ISMRM Annual General Meeting

13:45 - 14:15	Invited Speaker: Mary Mclean (University of Cambridge) Metabolic Multinuclear MR *Chair: Rob Dineen (Nottingham)*
14:15 - 14:55	Gold Sponsor Presentations *Chair: Adam Berrington (Nottingham)*
14:55 - 15:20	Power Pitch Session 4: Posters 63 - 83 *Chair: Eleanor Cox (Nottingham)*
15:20 - 15:55	Refreshment Break, Posters 63 - 83
15:55 - 16:55	Proffered Talks Session 6 Body MRI *Chair: Sue Francis (Nottingham)* T26: Placental contractions in low, high and extremely high-risk pregnancies. Amy Turnbull (University of Nottingham) T27: Towards accurate, reproducible PDFF quantification using a 3D dual-echo Dixon body composition sequence. Yifei Jin (Perspectum) T28: Multiparametric MRI and MRS to study changes across the Surgical Journey in Bariatric Patients with Type 2 diabetes or Prediabetes. Abi Spicer (University of Nottingham) T29: Rapid 3D gastrointestinal motility imaging using a stack-of-spirals sequence and compressed sensing reconstruction. Rebecca Baker (UCL)

	T30: The application of functional renal MRI to improve assessment of chronic kidney disease (AFiRM) Study. Charlotte Buchanan (University of Nottingham)
16:55 - 17:00	Awards and Close

Sponsors and Exhibitors

Bruker BioSpin GmbH & Co KG
Dassault Systèmes
GE Healthcare
Gold Standard Phantoms
IXICO
MR CoilTech Limited
MR Shim
MR Solutions
NVision Imaging Technologies GmbH
Philips Healthcare
Quantified Imaging
RAPID Biomedical GmbH
Siemens Healthineers
Skope
Xiel Ltd

Contents

Navigating This Document

Clicking on a talk/session in the programme will move the PDF to that abstract. Clicking the text in the footer will move the PDF to the start of the programme.

This PDF also has bookmarks for easy navigation.

Invited Speaker Biographies

In order of the talks in the program schedule

Jim Wild

Methods/Applications of Hyperpolarised Gas MRI

Learning Outcomes

- Understanding of the technical challenges of imaging a hyperpolarised non proton signal from a gas
- Understanding of the aspects of lung function and structure that can be measured with HP gas MRI
- Overview of clinical applications

My research is the physics and engineering and clinical applications of hyperpolarised gas (^{3}He and ^{129}Xe) and proton MRI in the lungs and pulmonary vasculature. Physics and engineering projects include:

- Rapid acquisition methods for imaging of inhaled hyperpolarised gases using compressed sensing, steady state free precession and parallel imaging.
- Techniques for simultaneous imaging of ^{1}H, ^{3}He and ^{129}Xe in the lungs.
- RF coil hardware engineering for ^{3}He and ^{129}Xe lung MRI.
- ^{3}He and ^{129}Xe MRI at different magnetic field strengths.
- Spin exchange optical pumping physics for polarisation of ^{3}He and ^{129}Xe.
- Measuring and modelling gas flow and diffusion in the lungs; physiological models of alveolar geometry and gas exchange.
- Measuring dissolved phase xenon in the brain and kidneys

These technical developments have made a clinical impact. Our research has demonstrated the role of these pulmonary MRI methods in Asthma, COPD, Cystic Fibrosis, Interstitial Lung Disease, Lung cancer and Pulmonary Hypertension. We have performed the first clinical studies in the UK with hyperpolarised ^{3}He and ^{129}Xe gas MRI. Using hyperpolarised gas and proton lung MRI as markers we are evaluating novel pulmonary therapies in collaboration with pharmaceutical companies.

Damian Tyler

Talk Title: Making Metabolic Measurements with ^{13}C

Learning Outcomes

- Understand the different approaches used to generate hyperpolarized 13C tracers for metabolic measurements
- With a focus on Dissolution Dynamic Nuclear Polarisation (d-DNP), understand the challenges involved in the generation of metabolic tracers for clinical studies
- Appreciate the different approaches used in the acquisition of hyperpolarized 13C metabolic images.

Damian is currently the Director of MR Physics at the Oxford Centre for Clinical Magnetic Resonance Research (OCMR) and a Fellow in Medicine at Somerville College, Oxford. He has been based in Oxford since 2001 and has more than 20 years experience in the development and application of Magnetic Resonance Imaging and Spectroscopy (MRI/MRS). Damian gained his MSci in Medical Physics in 1998 and his doctorate in 2001, both from the University of Nottingham. He is an associate member of the Cardiac Metabolism Research Group (CMRG) and leads the Oxford Metabolic Imaging Group. Damian's research in Oxford has been based on the study of cardiac structure, function and metabolism in normal and diseased hearts using MRI/MRS. This has included developing techniques using high spatial and temporal resolution CINE imaging to assess heart function and localized phosphorus and carbon spectroscopy to monitor and investigate abnormalities of metabolism. He was awarded British Heart Foundation Intermediate and Senior Research Fellowships to develop the technique of Dynamic Nuclear Polarization (DNP) for application to the study of cardiac metabolism in the human heart. A fundamental limitation of magnetic resonance is its low sensitivity, but the recently developed technique of DNP provides a practical method to gain up to 10,000-fold increases in sensitivity in molecules with an in vivo stability of approximately one minute. This has enabled visualization of 13C-labelled cellular metabolites in vivo and, more importantly, their enzymatic transformation into other species. This is an important development that could revolutionize spectroscopy using MR.

Chris Rodgers

Talk title: Getting the best of ^{31}P

Learning Outcomes

- Understand the main application areas for human phosphorus-31 MRS.
- Understand the benefits of ultra-high fields and optimised RF coil designs for phosphorus-31 MRS.
- Be aware of a variety of pulse sequences that are used to measure different aspects of metabolism by phosphorus-31 MRS.

I studied Chemistry MChem at Oxford and continued for a DPhil in Physical Chemistry. My DPhil thesis was entitled "Magnetic Field Effects in Chemical Systems", supervised by Peter Hore and Christiane Timmel. This included the first in vitro demonstration of a chemical magnetic compass such as is thought to drive the magnetic directional sense of migratory birds. I then moved into MRI, working on 3T cardiac phosphorus spectroscopy with Stefan Neubauer at Oxford. In 2012, I was awarded a Sir Henry Dale Fellowship to develop 7T cardiac phosphorus spectroscopy. In 2017, I moved to Cambridge to lead the 7T MRI physics program there. I lead the UK arm of the MITI EU project imaging metabolism across the whole heart using a novel dipole phosphorus coil. My lab have a growing interest in parallel transmit neuroimaging: we have introduced new algorithms for pulse design, and implemented them for BOLD EPI, diffusion and turbo spin echo imaging. In collaboration with Dr Thomas Cope, we have shown that parallel transmit 7T MRI changes clinical management in more than 50% of patients with drug-resistant focal epilepsy whose prior 3T MRI and PET scans were inconclusive.

Claudia Gandini Wheeler-Kingshott

Talk title: Use of ^{23}Na

Learning Outcomes

- Understand the importance of sodium homeostasis for brain function and the challenges of sodium ions concentration quantification using MRI;
- Understand the pulse-sequence requirements for measuring ^{23}Na signal using MRI;
- Understand the future directions for ^{23}Na imaging at 3T and higher field strengths.

Claudia A. M. Gandini Wheeler-Kingshott, PhD is professor of Magnetic resonance physics at UCL (UK) where she works since 1999. Her main interest is in developing imaging biomarkers for assessing brain diseases, and in particular multiple sclerosis. Claudia has been working on sodium imaging of the brain for more than 15 years, focusing on optimising methods for sodium concentration quantification in tissue in vivo, both in the brain and in the spinal cord. Claudia also has an appointment at the University of Pavia (Italy) where she works in a multidisciplinary team developing brain digital twin technology, using MRI to personalise computational realistic models of brain dynamics.

Pete Thelwall

Talk title: Offbeat Nuclei with Upbeat Uses: Multinuclear MR in Clinical Research

Learning Outcomes

- Understand that multinuclear MRI enables quantitative measurement of key physiological and metabolic processes
- Learn that the challenges in multinuclear MR are the lower sensitivities and spin densities compared to 1H nuclei in body tissues
- Be aware that advanced MR technologies that are well established in conventional 1H-MRI (RF coil arrays, scan acceleration) are less well integrated for multinuclear MR, but can bring substantial advances in scan capabilities.
- Understand that simple spectroscopic MR methods can bring advantages over imaging for key physiological measurements

Pete Thelwall is Professor of Magnetic Resonance Physics and Director of the Centre for In Vivo Imaging at Newcastle University. He leads an interdisciplinary research team with a remit to develop novel MR methodologies and apply them to clinical research. He studied at Nottingham and Cambridge, and was a postdoc at the University of Florida before taking an academic post at Newcastle University. His current research studies use ^{7}Li, ^{13}C, ^{23}Na, ^{19}F, ^{31}P, and ^{35}Cl magnetic resonance in patient studies to quantify function and dysfunction of physiological and biochemical processes, and to monitor the distribution and effects of pharmacological agents and treatment strategies.

Nicolas Boulant

Talk title: The Iseult 11.7T human MRI project: from first ideas to first in vivo images

Learning Outcomes

- What was the most severe obstacle to overcome was in the commissioning of the 11.7T MRI scanner?
- What were the main challenges for successfully acquiring human in vivo first images at 11.7T?

I got a PhD in nuclear science and engineering in 2005 at MIT, Cambridge, USA. The subject of my thesis was the control of quantum open systems using liquid state NMR quantum computing. I then did a two-year post-doc on solid state quantum computing at CEA (Atomic Energy Commission) located in Saclay, France. I swicthed to a more applied discipline in 2007 by starting working on MRI at ultra-high field at NeuroSpin, still at CEA Saclay. During the 2007-2020 period, the main topic of my research was parallel transmission for brain imaging at 7T. I became head of the Iseult 11.7T project in 2018. I have led the scientific, safety, regulatory and organisational efforts to test, commission and exploit the CEA unique whole-body 11.7T scanner since. I am deputy editor at Magnetic Resonance in Medicine (since 2020) and I serve as an external scientific advisor for Skope MRT and the Dutch 14T initiative.

Eleftheria (Laura) Panagiotaki

Talk title: Non-invasive prostate microstructure estimation with Diffusion MRI

Learning Outcomes

- How can we infer tissue indices with diffusion MRI.
- What are the key differences between ADC and VERDICT.
- How can we validate imaging methods.

Dr. Eletheria (Laura) Panagiotaki is an Associate Professor at the Centre for Medical Image Computing and the Department of Computer Science at UCL. She leads the Computational Cancer Microstructure Imaging group (Cami). Laura studied Mathematics at the University of Crete, and did a Masters in Vision, Imaging, and Virtual Environments at UCL. She then pursued a PhD in medical imaging at UCL, focusing on developing brain models of diffusion MRI. Near the end of her PhD, she successfully secured funding from EPSRC's Doctoral Prize scheme to extend her research to cancer pathology, and later received an EPSRC Early Career Fellowship. Recently, she has taken on the role of training lead for the new CDT tech4health UCL/Ulster.
Laura's research primarily focuses on the computational modeling of quantitative MRI and validation techniques to develop and clinically translate new non-invasive biomarkers for cancer (see also EP/R006032/1). She developed the VERDICT-MRI analysis technique, one of the first non-invasive microstructure imaging methods for cancer. Together with her UCL colleagues, she is working towards the clinical translation of VERDICT, with the first clinical trial (INNOVATE PCUK ~ 365 patients; ClinicalTrials.gov identifier NCT0268927114 - concluded) and an ongoing trial funded by CRUK (~420 patients).

Derek Jones

Talk title: From Meterology to Tractology: Forecasting a New Path in Neuroscience

Learning Outcomes

- To be able to explain the benefits of stronger gradients for characterisation of tissue microstructure;
- To be aware of the possibilities for microstructural MRI on portable, low field MRI systems

Prof Derek K Jones is an MRI physicist and is Director of the Cardiff University Brain Research Imaging Centre (CUBRIC). Before moving to Cardiff, he worked at Kings College London, and the National Institutes of Health, Maryland.

He has held various external positions including Programme Chair of the International Society for Magnetic Resonance in Medicine (ISMRM) annual scientific meeting, Programme Chair for the European Society for Magnetic Resonance in Medicine and Biology (ESMRMB), Deputy Editor for Magnetic Resonance in Medicine, and is immediate Past-President of the ISMRM.

Derek has 30 years' experience in microstructural imaging and has more than 230 research papers on all aspects of the microstructural MRI pipeline. He now divides his time between focusing on micro-structural imaging with the ultra-strong gradients of the Connectom scanner and helping to democratise MRI in LMICs with low field.

But most important of all, is that Derek is a graduate of the University of Nottingham where he first encountered MRI in the Sir Peter Mansfield Imaging Centre!

Rhodri Cusack

Talk title: Measuring Cognitive Neurodevelopment in Infants with Awake fMRI

Learning Outcomes

- Describe state-of-the-art methods for awake infant fMRI
- Describe application of fMRI and deep neural networks to characterise developing brain
- Present a new model of the development of visual categories in humans

Rhodri Cusack is the Thomas Mitchell Professor of Cognitive Neuroscience at Trinity College Dublin, and Director of the Trinity College Institute of Neuroscience. His team studies how the brain and mind develop in infants using neuroimaging and online testing. The goals are to understand healthy development and to provide tools for earlier diagnosis in the neonatal intensive care unit.

Rhodri studied physics at Pembroke College, Cambridge, and then obtained a PhD in psychology from the University of Birmingham. He was then a postdoctoral fellow and subsequently group leader at the MRC Cognition and Brain Sciences Unit in Cambridge, and then an Associate Professor at the Brain and Mind Institute of the University of Western Ontario. He joined Trinity College in 2017.

His research has been funded by the ERC, SFI, IRC, MRC, Wellcome Trust, BBSRC, EPSRC, CIHR, and NSERC. He has 136 peer-reviewed publications.

Learn more about our team and its research at www.cusacklab.org

Biographies

Mary Mclean

Talk Title: Metabolic Multinuclear MR

Learning Outcomes

- What causes the low sensitivity in imaging of carbon and deuterium, and how is it addressed differently for the two nuclei?
- What are some metabolic processes that can be measured using carbon and deuterium?
- What are some possible clinical applications of these techniques in the future?

Mary McLean is a Principal Research Associate in the University of Cambridge Department of Radiology and leads their postgraduate programme. Her main expertise is in clinical MR spectroscopy, following a PhD in Biochemistry with Peter Morris. Most of her career has focused on diagnosis and monitoring of cancers and neurological conditions. She is on the Governance Board of ISMRM and formerly served on the Executive Committee of the British and Irish Chapter, where she was founding editor of the newsletter Positive Spin.

Proffered Talk Abstracts

In order of the talks in the program schedule

Published 03/09/2024

Diffusion MRI acquisition methods for post-mortem imaging at 10.5 T

Benjamin C. Tendler[1], Wenchuan Wu[1], Shaun Warrington[2], Edward J. Auerbach[3], Hamza Farooq[3], Steen Moeller[3], Pramod Pisharady[3], Christophe Lenglet[3], Sarah Heilbronner[3,4], Essa Yacoub[3], Kamil Ugurbil[3], Saad Jbabdi[1], Stamatios N. Sotiropoulos[2], Karla L. Miller*[1], Jan Zimmermann*[3,5] (*Equal Contribution)

[1]Wellcome Centre for Integrative Neuroimaging, FMRIB, Nuffield Department of Clinical Neurosciences, University of Oxford, Oxford, UK; [2]Sir Peter Mansfield Imaging Centre, School of Medicine, University of Nottingham, UK; [3]Centre for Magnetic Resonance Research, University of Minnesota-Twin Cities, MN, USA; [4]Baylor College of Medicine, TX, USA, [5]Department of Neuroscience, University of Minnesota, MN, USA.

Introduction: Post-mortem imaging on ultra-high field (UHF) MRI scanners aims to leverage the benefits of increased signal amplitude and long scan times to acquire exemplary datasets for detailed anatomical investigations. When considering a conventional diffusion-weighted spin-echo (DW-SE) sequence with an EPI readout, short T_2 and increased B_0 inhomogeneity at UHF can lead to images with (1) reduced SNR, (2) T_2*-blurring and (3) geometric distortions. These challenges are exacerbated for post-mortem tissue, which has reduced T_2 and diffusion coefficient versus in vivo.

In this work, we investigate sequences for post-mortem diffusion imaging on a 10.5 T wide-bore scanner with a conventional gradient set (G_{Max} = 70 mT/m). Specifically, we perform a theoretical SNR comparison of the (1) DW-SE, (2) diffusion-weighted stimulated-echo[1] (DW-STE) and (3) diffusion-weighted steady-state free precession[2] (DW-SSFP) sequence. Based on our findings, we acquire DW-SSFP data in a post-mortem macaque brain at 0.4 mm isotropic resolution. We demonstrate that DW-SSFP achieves distortion-free, high-resolution post-mortem diffusion MRI data at 10.5 T.

Theory: Figure 1 depicts the diffusion-encoding modules of the DW-SE, DW-STE and DW-SSFP sequences. The DW-STE[1] sequence replaces the 180˚ pulse with two 90˚ pulses separated by a "mixing time", during which the magnetization is stored longitudinally. Long mixing times increase the b-value whilst only incurring T_1 signal loss, making this an attractive possibility for short T_2 tissues. However, DW-STE signal-forming mechanisms result in a 2x signal reduction versus DW-SE. Long mixing times also necessitate an EPI readout, incurring the same T_2^*-blurring and distortion challenges as DW-SE.

DW-SSFP[2] contains only a single diffusion-encoding gradient per TR. By using very short TRs (20 - 40 ms), transverse magnetization persists over multiple repetitions and forms effective diffusion gradient pairs. The resulting signal is a combination of diffusion-weighted spin and stimulated echoes. DW-SSFP achieves high-SNR efficiency and strong diffusion-weighting in post-mortem tissue[3], with improved SNR at 7T versus 3T[4]. Its short TR is compatible with a single-line readout for distortion-free imaging.

SNR efficiency is a measure as the relative signal per unit time, defined as $S \cdot \rho^{1/2}$ (S = signal level, ρ = fraction of TR spent acquiring signal)[3]. Based on experimental estimates of T_1 & T_2 in a post-mortem macaque brain at 10.5 T, Figure 2 displays the optimised SNR-efficiency predictions of the DW-SE, DW-STE & DW-SSFP sequence. We identify that the DW-SSFP sequence achieves increased or similar levels

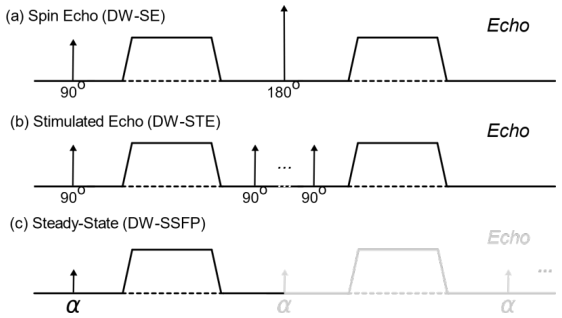

Figure 1: Diffusion encoding of the (a) Diffusion-weighted spin-echo (DW-SE), (b) Diffusion-weighted stimulated echo (DW-STE), (c) Diffusion-weighted steady-state free precession (DW-SSFP) sequence.

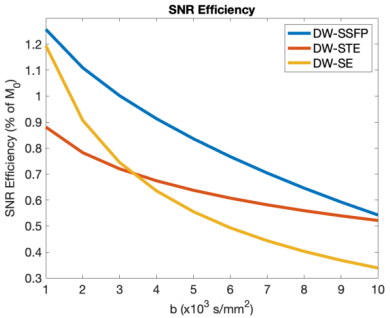

Figure 2: Optimised SNR efficiency estimates for the DW-SE (yellow), DW-STE (red) and DW-SSFP (blue) sequence for estimated T_1 & T_2 values (1350 & 28 ms) in a post-mortem macaque brain at 10.5 T. DW-SSFP predicts increased SNR efficiency across the investigated regime. Simulations performed assuming diffusivity = $2{\cdot}10^{-4}$ mm^2/s, T_2^* = 14 ms and T_{dead} = 5 ms (i.e. time dedicated to other pulses[3]).

of SNR efficiency across the b-value range, whilst also having the benefit of very low image distortion.

Methods: Data were acquired in a fixed post-mortem macaque brain on a Siemens 10.5T scanner (CMRR, University of Minnesota) (G_{Max} = 70 mT/m, G_{Slew} = 200 T/m/s). To avoid gradient duty cycle limitations, SNR-efficiency optimisations were performed setting G_{max} = 52 mT/m. From the optimisations, DW-SSFP data were acquired at 0.4 mm (isotropic) with an effective b-value[3] of 3040 s/mm^2 & 5430 s/mm^2 (alongside b_0-equivalent): G = 7.4/34.7/52 mT/m, δ = 10.6 ms, q = 3.2/15/22.5 mm^{-1}, TR = 21 ms, TE = 16 ms, $\alpha = 14^o$, 121 directions, 13.5 minutes/direction, single-line readout. Data were reconstructed offline, denoised (NORDIC[5]), and processed with a Tensor model incorporating the DW-SSFP signal equation[6].

Results & Discussion: Acquired DW-SSFP data displays strong diffusion contrast (Figure 3). Principal diffusion direction maps (Figure 4) demonstrate high-SNR diffusivity estimates across the brain, without geometric distortion. DW-SSFP may offer considerable benefits for the challenging imaging environment of post-mortem tissue at 10.5 T, notably when restricted to conventional gradient sets.

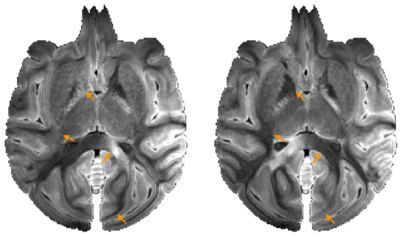

Figure 3: Image contrast of two b = 5430 s/mm^2 volumes. Arrows highlight some key differences.

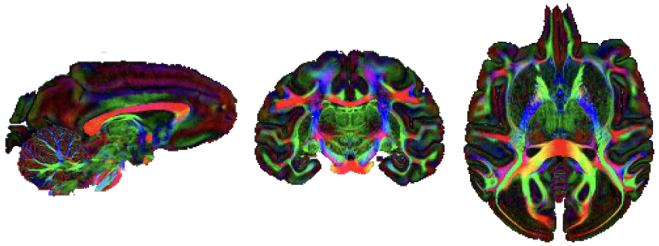

Figure 4: Principal diffusion direction (modulated by FA) in a post-mortem macaque brain (0.4 mm isotropic resolution).

Acknowledgements: This work is supported by NIH (Grant UM1NS132207) and the Center for Mesoscale Connectomics. BCT is supported by a Wellcome Fellowship [222829/Z/21/Z]. WW is supported by the Royal Academy of Engineering (RF\201819\18\92).

References: [1] Merboldt KD, et al., *JMR* (1985); [2] Merboldt KD, et al., *JMR* (1989); [3] Miller KL, et al., *NeuroImage* (2012); [4] Foxley S, et al., *NeuroImage* (2014); [5] Moeller S, et al., *NeuroImage* (2021). [6] Freed et al., *J. Chem. Phys.* (2001).

High Resolution Diffusion MRI Tractography at 10.5T in the in-vivo & ex-vivo NHP brain

Shaun Warrington[1], Benjamin C. Tendler[2], Hamza Farooq[3], Steen Moeller[3], Pramod Pisharady[3], Wenchuan Wu[2], Edward J. Auerbach[3], Sarah Heilbronner[3,4], Essa Yacoub[3], Kamil Ugurbil[3], Christophe Lenglet[3], Karla Miller[2], Saad Jbabdi[2], Jan Zimmermann[3,5], Stamatios N. Sotiropoulos[1]

[1]Sir Peter Mansfield Imaging Centre, School of Medicine, University of Nottingham, UK. [2]Wellcome Centre for Integrative Neuroimaging, FMRIB, Nuffield Department of Clinical Neurosciences, University of Oxford, UK. [3]Centre for Magnetic Resonance Research, University of Minnesota-Twin Cities, MN, USA. [4]Baylor College of Medicine, TX, USA. [5]Department of Neuroscience, University of Minnesota, MN, USA.

Introduction: A key challenge in diffusion MRI (dMRI) is resolving complex white matter (WM) fibre architecture and WM bundles through relatively low spatial resolution data. To push the limits of spatial resolution, one approach is to take advantage of the greater baseline signal available when scanning at high and ultra-high field[1,2]. However, high-field MRI has its own set of challenges[3]. In this work, we present a high resolution dMRI dataset for the non-human primate (macaque) brain obtained using an ultra-high field 10.5T whole-body human MRI scanner. We propose in-vivo and ex-vivo acquisition protocols for pushing resolution towards the mesoscale using an ultra-high field scanner and showcase exemplar tractography reconstructions.

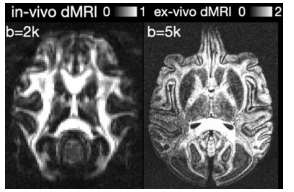

Figure 1 – Angular contrast-to-noise ratio (CNR) maps for highest b-shell of in-vivo and ex-vivo data.

Methods: We acquired dMRI data of the macaque in-vivo and ex-vivo using the MAGNETOM (Siemens, Erlangen) 10.5T scanner at the CMRR, University of Minnesota, fitted with SC72D gradients (70 mT/m, 200 T/m/s slew rate). Data were acquired using custom-made coils for in-vivo and ex-vivo scans (32-channels receive). In-vivo acquisitions from an anesthetized macaque used a PGSE-EPI sequence at an isotropic resolution of 0.75mm (TE=67ms, TR=6.55s) with two shells (b=1000, 2000 s/mm^2), with 4 repeats of 116 volumes (464 volumes in total), including 36 b=0 volumes (scan time=50 mins). Ex-vivo data were acquired using a diffusion-weighted steady-state free precession (DW-SSFP) protocol[4,5] (TE=16ms, TR=21ms, flip angle=14^o, single-line readout) with an isotropic spatial resolution of 0.4mm, two q values (150 & 225 cm^{-1} equivalent[6] to b=3,040 & 5,430 s/mm^2) and 121 volumes, including 6 b=0 equivalent volumes (scan time=~28hrs). Data were reconstructed offline, denoised in the complex domain using NORDIC[7] and preprocessed using the following steps: Susceptibility-induced off-resonance fieldmap estimation; Eddy-current, motion and susceptibility artifact correction[8]; QC metric estimation[9] (SNR, angular CNR, outliers); Tensor estimation using the lower shell; Fiber orientation estimation (up to 3) using parametric spherical deconvolution and a stick response kernel[10]; Non-linear registration to standard NMT[11] macaque space[12]; Standardised tractography using landmark-based protocols in NMT space (XTRACT)[13,14]. For the DW-SSFP data, the first two distortion correction steps were skipped, as data were distortion-free. A rigid-body transform of all volumes to the first was instead used to account for drifting.

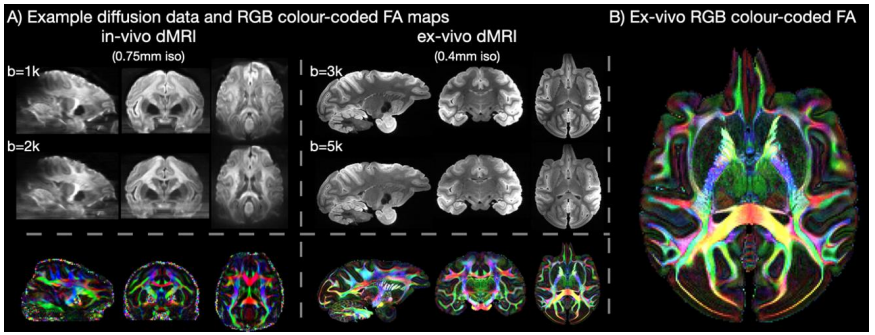

Figure 2 – A) Example pre-processed dMRI data from the in-vivo (left) and ex-vivo (right) acquisitions. Top rows: the average across all volumes for each diffusion-weighted shell. Bottom row: the RGB color-coded principle diffusion direction map derived from DTI, modulated by FA. B) A higher magnification version of the ex-vivo RGB-color coded FA map.

Results and Discussion: Figure 1 presents angular CNR maps for the highest acquired shells, indicating high diffusion and uniform contrast, both in-vivo and ex-vivo. Figure 2 examples the preprocessed diffusion data from the in-vivo and ex-vivo scans. Top and middle rows show averaged volumes across respective b-shells, while bottom row shows DTI RGB-color coded maps. The reported spatial resolutions demonstrate feasibility to scan are amongst the highest reported to date for the macaque brain, both in-vivo and ex-vivo, and are

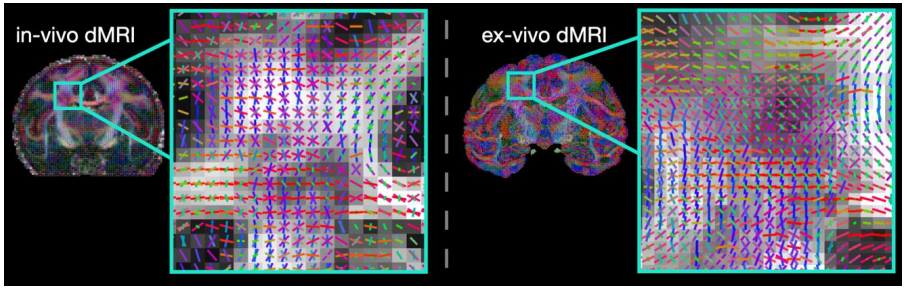

Figure 3 – Estimated fibre orientations (up to 3 fibres per voxel), overlaid on FA maps for in-vivo (left) and ex-vivo (right).

achieved at high b-values with a conventional gradient insert. Figure 3 shows estimated crossing-fibres in the centrum semiovale, revealing sensitivity to detect 3-way crossings at very high resolution. WM tracts using XTRACT were reconstructed in each case. Figure 4 shows a set of tracts used

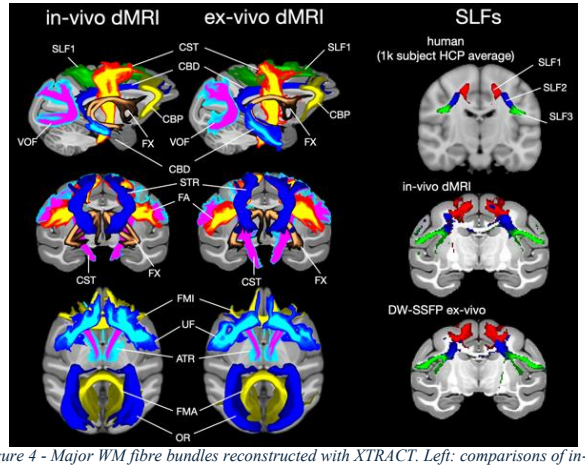

Figure 4 - Major WM fibre bundles reconstructed with XTRACT. Left: comparisons of in-vivo and ex-vivo tracts used to assess overall performance. Right: coronal slices of the SLFs for the in-vivo and ex-vivo data, with an average tract HCP atlas shown for reference.

to assess overall tractography performance, revealing high overall correspondence between in-vivo and ex-vivo data. XTRACT was also used to reconstruct the superior longitudinal fasciculi (SLFs I/II/III) that mediate fronto-parietal connections. Figure 4 (right) shows a coronal slice through the SLFs and a comparison to SLFs in the human brain (HCP tract atlas, 1k subjects, 1.25mm isotropic resolution). Finally, we constructed a whole-brain tract density image (TDI) using the ex-vivo data and probabilistic tractography. This is shown in Figure 5, where the spatial distribution of streamlines has been RGB colour-coded by principal fibre orientation and binned into 0.2mm isotropic voxels.

Acknowledgements: This work is supported by NIH (Grant UM1NS132207) and the Center for Mesoscale Connectomics. SW and SNS are supported by ERC (101000969). BCT is supported by a Sir Henry Wellcome Postdoctoral Fellowship (Wellcome Trust) [222829/Z/21/Z].

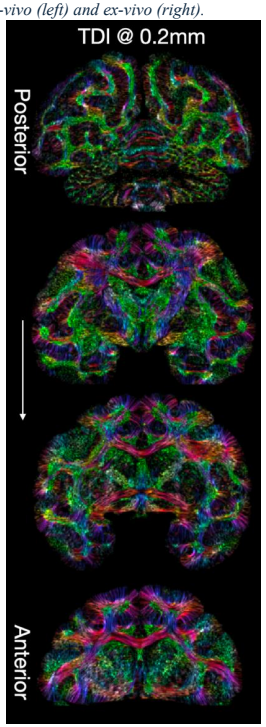

Figure 5 – Coronal views of probabilistic TDI at 0.2mm.

Proffered Talks Session 1

References

1. Vu, A. T. *et al.* High resolution whole brain diffusion imaging at 7T for the Human Connectome Project. *NeuroImage* **122**, 318–331 (2015).
2. Grier, M. D. *et al.* Ultra-high field (10.5T) diffusion-weighted MRI of the macaque brain. *NeuroImage* **255**, 119200 (2022).
3. Nilsson, M. Chapter 20 - Diffusion MRI at ultra-high field strengths. in *Advances in Magnetic Resonance Technology and Applications* (eds. Markenroth Bloch, K., Guye, M. & Poser, B. A.) vol. 10 321–331 (Academic Press, 2023).
4. McNab, J. A. & Miller, K. L. Steady-state diffusion-weighted imaging: theory, acquisition and analysis. *NMR Biomed.* **23**, 781–793 (2010).
5. Tendler, B. C. *et al.* Diffusion MRI methods for post-mortem imaging at 10.5 T. in (2024).
6. Miller, K. L., McNab, J. A., Jbabdi, S. & Douaud, G. Diffusion tractography of post-mortem human brains: Optimization and comparison of spin echo and steady-state free precession techniques. *NeuroImage* (2012) doi:10.1016/j.neuroimage.2011.09.054.
7. Moeller, S. *et al.* NOise reduction with DIstribution Corrected (NORDIC) PCA in dMRI with complex-valued parameter-free locally low-rank processing. *NeuroImage* **226**, 117539 (2021).
8. Andersson, J. L. R. & Sotiropoulos, S. N. An integrated approach to correction for off-resonance effects and subject movement in diffusion MR imaging. *NeuroImage* **125**, 1063–1078 (2016).
9. Bastiani, M. *et al.* Automated quality control for within and between studies diffusion MRI data using a non-parametric framework for movement and distortion correction. *NeuroImage* **184**, 801–812 (2019).
10. Jbabdi, S., Sotiropoulos, S. N., Savio, A. M., Graña, M. & Behrens, T. E. Model-based analysis of multishell diffusion MR data for tractography: How to get over fitting problems. *Magn. Reson. Med.* **68**, 1846–1855 (2012).
11. Seidlitz, J. *et al.* A population MRI brain template and analysis tools for the macaque. *NeuroImage* **170**, 121–131 (2018).
12. Andersson, J. L. R., Jenkinson, M. & Smith, S. M. Non-linear optimisation. FMRIB technical report TR07JA1. *Pr.* (2007) doi:10.1109/EMOBILITY.2010.5668100.
13. Warrington, S. *et al.* XTRACT - Standardised protocols for automated tractography in the human and macaque brain. *NeuroImage* **217**, 116923 (2020).
14. Assimopoulos, S. *et al.* Generalising XTRACT tractography protocols across common macaque brain templates. *Brain Struct. Funct.* (2024) doi:10.1007/s00429-024-02760-0.

The 7T Implant Problem: Participant Exclusion Rates in Ultra-High Field MRI

C. John Evans[1], Sarah Allwood-Spiers[2], Daniel Bates[3], Philippa Bridgen[4], Jon Campbell[5], Mara Cercignani[1], Andrew Cooper[6], Allison Cooper[1], Penny Gowland[6], Emre Kopanoglu[1], Victoria Lupson[7], Shaihan Malik[4], Jan Paul[6], Andrew Peters[6], Sebastian W. Rieger[5], Jonathan Zenilman[8], Aaron Hess[5]

[1]CUBRIC, Cardiff University, Cardiff, UK; [2]NHS Greater Glasgow & Clyde, Glasgow, UK; [3]Queen Square Institute of Neurology, UCL, London, UK; [4]King's College London, St. Thomas' Hospital, London, UK; [5]Wellcome Centre for Integrative Neuroimaging, University of Oxford, Oxford, UK; [6]Sir Peter Mansfield Imaging Centre, University of Nottingham, Nottingham, UK; [7]Wolfson Brain Imaging Centre, University of Cambridge, Cambridge, UK; [8]Division of Infectious Diseases, Johns Hopkins Bayview Medical Centre, Johns Hopkins University School of Medicine, Baltimore, USA

Introduction: The enhanced signal-to-noise of ultra-high field MRI systems has afforded numerous benefits for clinical imaging and research [1]. However, access to these methods is limited for individuals with medical implants, as only around 300 implants have been tested at 7T, compared to approximately 6000 at 3T or lower [2], particularly impacting clinical and older populations. The UK7T Safety Process Group, was formed from representatives of all member sites of the UK7T network (Cambridge, Cardiff, Glasgow, KCL, Nottingham, Oxford, UCL) to develop common practice and share information to widen the pool of individuals who could safety be scanned at 7T.

Methods: To evaluate current screening practice, questionnaires consisting of 73 common surgeries, medical and cosmetic procedures were sent to the UK7T sites. Sites' responses were categorised according to whether such participants would be 'Included', 'Uncertain' (additional information would be necessary) or 'Excluded' from imaging at 7T.

The 73 procedures were classified into fifteen implant classes. For example, the 'bone fixation' class contained twelve separate procedures/implants (cranial fixation plates, screws, sternal wiring, etc). Responses were combined to evaluate the proportion of procedures which would be excluded across all UK7T sites. The implant classes (and number of procedures) were: surgical clips (17), bone fixation (12), dental implants (9), other implants (9), surgery without implant (5), active implants (AIMD) (4), contraceptive implants (4), stents & filters (3), tattoos (3), breast implants (2), heart valves (1), joint replacement (1), ocular implants (1), shunts (1), surgical mesh (1). Note that, for example, all types of joint replacement were treated as a single procedure in the original questionnaire.

To evaluate the impact of these screening decisions, implant prevalence data were obtained from a study of the general population of Hungary [3], and from the source data of an investigation of inpatients at Johns Hopkins Hospital, USA [4]. The implant classes above had been chosen to match the available population data from these two sources. Population exclusion rates could thus be estimated for both patient and general populations by applying the proportion of the implant exclusions for a given implant class to the prevalence of that implant class within the general/patient populations.

Results:

The implant exclusion rates are shown in Fig. 1A. The highest implant exclusion rates were for shunts, active implants, heart valves and stents/filters which were all excluded in more than 75% of all procedures of these classes. The only implants which were excluded in fewer than 25% of all procedures were ocular implants and surgical mesh.

Data from combining the questionnaire data with the population implant prevalence data are shown in Fig 1B. Within the general population, the most common implants were bone fixation devices, ocular, contraceptive and dental implants [3]. Each of these has an implant exclusion rate <50%, resulting to a maximum population exclusion rate of 5.9% for bone fixation devices. For the patient populations [4], more than 5% of the population is excluded for each of active implants, bone fixation and stents/filters.

Proffered Talks Session 1

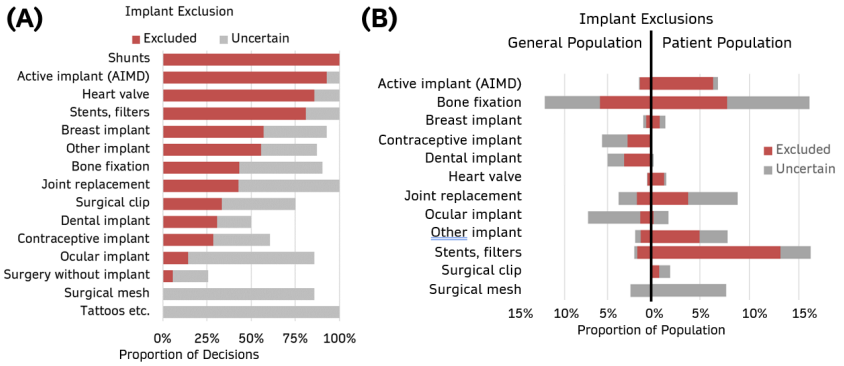

Fig. 1. (A) Proportion of decisions, across UK7T sites, which resulted in exclusion of a class of implant ('Excluded'), or a situation where additional information would be required to evaluate MR conditionality ('Uncertain'). **(B)** Implant exclusions expressed as a proportion of the general population (left) and the patient population (right).

The overall exclusion rates, across all implant classes, are tabulated in Table 1. For the general population, an estimated 19.4% of the population would be absolutely contraindicated, with a further 23.4% requiring further information to confirm MR conditionality. Thus, the remaining 57.2% would be cleared for scanning at 7T without any further information required.

	Excluded	**Uncertain**
General Population	19.4%	23.4%
Patient Population	39.5%	30.9%

Table 1. The overall implant exclusion rate for all implant classes shown in Fig 1.

Discussion: The estimated exclusion rate for a patient cohort is twice that of the general population, highlighting the potential challenges in scanning these cohorts. However, as we do not have equivalent data from other field strengths, we cannot draw inferences about the relative difficulty of screening at ultra-high field compared with 3T. This work assumes an equal distribution of procedures within the implant classes, which may not be accurate. In our experience, the potential for surgical clips results in a larger number of exclusions than this analysis indicates, perhaps due to the difference between the reported and potential presence of unreported clips. These data relate to research scanning, which will influence the risk-benefit decision making of the sites. Finally, the population data are sourced from two different countries (USA and Hungary) – the distribution of implants is likely to vary between countries.

Conclusions: This work has estimated the exclusion rates for participants and patients being scanned at the UK7T sites. It has highlighted the classes of implants for which an enhanced risk assessment framework would have most impact to increase the number of individuals with implants who have access to 7T. Safety testing of bone fixation implants, stents and filters could significantly reduce patient attrition rates at 7T.

References

[1] Burkett, B. J. *et al.*, "Clinical 7-T MRI for neuroradiology: strengths, weaknesses, and ongoing challenges" *Neuroradiology*, **63**, 167–177 (2021).

[2] Hoff, M. N. *et al.*, "Safety Considerations of 7-T MRI in Clinical Practice", *Radiology* **292**, 3, 509–518 (2019).

[3] Hölgyesi, Á., *et. al.* "Epidemiology and patients' self-reported knowledge of implantable medical devices", *PloS One*, 18(4), e0284577 (2023).

[4] Kuder, M. *et. al.*, "Prevalence of Implanted Medical Devices in Medicine Inpatients", *Journal of Patient Safety*, 14(3), 153–156 (2018).

Deuterium Metabolic Imaging (DMI) results at 7T following [$^2H_2$] and [$^2H_7$] glucose ingestion

Daniel J. Cocking[1,2], Robin A. Damion[1,3,4], Elizabeth Simpson[4], Dorothee P. Auer[1,3,4], and Richard Bowtell[1,2,4]

[1]Sir Peter Mansfield Imaging Centre, University of Nottingham.
[2]School of Physics and Astronomy, University of Nottingham.
[3]Mental Health& Clinical Neuroscience, School of Medicine, University of Nottingham.
[4]NIHR Nottingham Biomedical Research Centre/Nottingham Clinical Research Facilities, Queen's Medical Centre.

Introduction

Deuterium (^2H) metabolic imaging (DMI) using labelled glucose is a potentially advantageous method for mapping glucose metabolism in the human body [1,2]. Most DMI studies have employed doubly labelled glucose (glucose-D_2) [1-3], but fully labelled glucose (glucose-D_7) can also be used, providing higher deuterium concentrations in downstream metabolites. This yields a higher signal-to-noise ratio. Here we present a detailed comparison of 7T DMI measurements in the brain in 15 participants who ingested either glucose-D_7 or glucose-D_2.

Methods

Data was acquired on a 7T Philips Achieva scanner with a dual-tuned $^2H/^1H$ birdcage coil (Rapid Biomedical). Baseline scanning at natural abundance (NA) included a ^1H MPRAGE scan and a 3D ^2H chemical shift image (CSI) (NSA=6, T_{scan}=670 s, FOV=180x180x120 mm^3, TR=230 ms, TE=2.4 ms, 15 mm isotropic voxels). Participants then drank an aqueous solution of 0.75g/kg (body-weight) of glucose-D_2 or D_7. Followed by 4-5 repeats of the ^2H CSI scans. Eight participants ingested glucose-D_2 while seven ingested glucose-D_7.

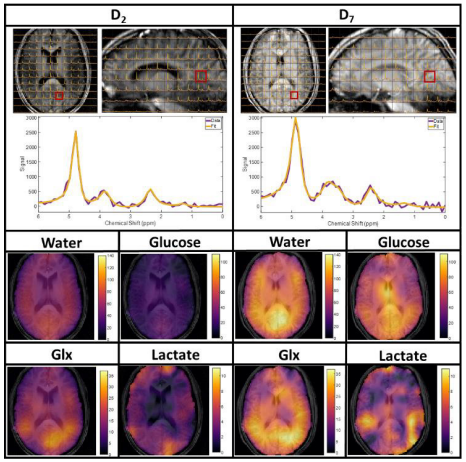

Figure 1. *3D CSI data from two participants after ingestion of D2 glucose (left) and D7 glucose (right). Spectra were fitted and then averaged over all scans acquired > 50 mins after ingestion, and overlaid on the MPRAGE image. Experimental data (purple) and fits (yellow) from highlighted voxels are shown along with amplitude metabolite maps.*

Each CSI dataset was denoised using a Tucker decomposition [4] with a core matrix size of [64 6 6 4] (1 spectral and 3 spatial dimensions). Spectra were then fitted using OXSA-AMARES [5] to model signals from water (HDO), glucose (Glc), glutamate and glutamine (Glx) and lactate (Lac). Each glucose label for each anomer [6] was fitted with a different Lorentzian peak (four/fourteen for glucose-d_2/-d_7). MPRAGE images were registered to the MNI-152 image using the FSL toolbox [7-9] masks were then created for the occipital and frontal lobes, and whole-brain. Complex amplitude maps were then averaged over the different masks to obtain metabolite signal values at each timepoint.

Results

Metabolite amplitude maps from CSI data of two subjects who ingested glucose-d_2 or glucose-d_7 (averaged over all CSI datasets acquired more than 50 minutes after ingestion) can be seen in Fig. 1.

The signal (normalised to NA HDO) averaged over all subjects who ingested glucose-d_2 (blue) or glucose-d_7 (pink) is shown in Fig. 2 for the different brain regions. The error-bars show the standard deviation over subjects.

Discussion

Figure 1 shows generally increased metabolite amplitudes in images and spectra arising from glucose-D_7 compared with glucose-D_2. These increased signal amplitudes for glucose-D_7 are more evident in the participant-averaged time-course plots (Fig. 2). At late time-points, the D7/D2 ratios for Glc, Glx and Lac are similar to values predicted using the ratio of the number of relevant ^2H labels: 7/2 for glucose, 3/2 for Glx, and Lac (corresponding to number of labels at the C1 and C6 sites of glucose) [10].

Conclusion

Glucose-D_7 ingestion produces significantly larger HDO and Glx signals compared to glucose-D_2. This allows more accurate spectral fitting and hence improved mapping of the signals from labelled metabolites. It was possible to track concentration changes in different regions in a reasonable scan time using DMI. This lays the ground for future studies that aim to use glucose-D7 ingestion followed by DMI to investigate *in vivo* metabolism in brain tumour patients. Thus far, data has been acquired successfully from one brain tumour patient.

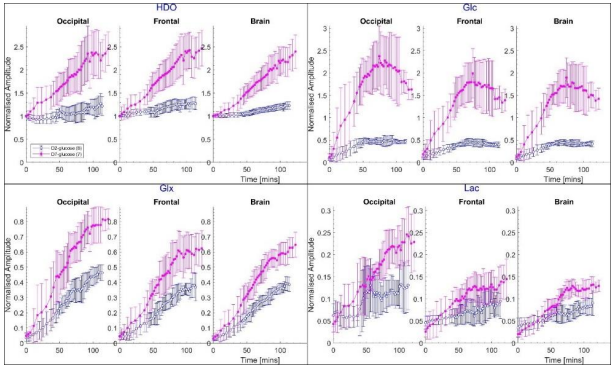

Figure 2. *Time-courses of metabolite signals for occipital lobe, frontal lobe, and the whole brain, averaged over participants who ingested D2-glucose (blue) or D7-glucose (pink). Values have been normalised by scaling with NA HDO signals. A running average was performed over data from all participants. Error bars represent the standard deviation over subjects.*

References

1. Lu M, Chen W, et al. Quantitative assessment of brain glucose metabolic rates using in vivo deuterium magnetic resonance spectroscopy. J Cereb Blood Flow Metab 2017;37(11):3518-3530.
2. De Feyter HM, de Graaf RA et al. Deuterium metabolic imaging (DMI) for MRI-based 3D mapping of metabolism in vivo. Science advances 2018;4(8):eaat7314.
3. de Graaf RA, De Feyter HM, et al. On the magnetic field dependence of deuterium metabolic imaging. NMR Biomed 2020;33(3):e4235.
4. Bader BW, Kolda TG. Efficient MATLAB Computations with Sparse and Factored Tensors. SIAM Journal on Scientific Computing 2007; 30: 205–231.
5. Purvis LAB, Rodgers CT, et al. OXSA: An open-source magnetic resonance spectroscopy analysis toolbox in MATLAB. Plos One 2017; 12(9):e0185356.
6. Mahar R, Merritt ME, et al. Deuterated water imaging of the rat brain following metabolism of [2H7] glucose. Magn Reson Med. 2021 Jun;85(6):3049-3059. doi: 10.1002/mrm.28700.
7. Smith SM. Fast robust automated brain extraction. Hum Brain Mapp 2002; 17: 143–155.
8. Jenkinson M, Brady M, et al. Improved Optimization for the Robust and Accurate Linear Registration and Motion Correction of Brain Images. Neuroimage 2002; 17: 825–841.
9. Andersson J, Jenkinson M, et al. FNIRT-FMRIB's non-linear image registration tool. In: Organization for Human Brain Mapping (OHBM). 2008.
10. de Graaf RA, Thomas MA, Behar KL, De Feyter HM. Characterisation of kinetic isotope effects and label-loss in deuterium-based isotopic labelling studies. ACS Chem. Neurosci. 2021;12: 234−243

Investigating Magnetic Field Correlation (MFC) Sensitivity to Demyelination and Axonal Loss using Numerical Simulations

Lewis Kitchingman[1], Maëliss Jallais[1], Kadir Şimşek[1], Emre Kopanoglu[1], Robert Turner[2], Marco Palombo[1,3]

[1]Cardiff University Brain Research Imaging Centre, Cardiff University, Cardiff, United Kingdom
[2]Max Planck Institute for Human Cognitive and Brain Sciences, Leipzig, Germany
[3]School of Computer Science & Informatics, Cardiff University, Cardiff, United Kingdom

Introduction: Myelin is a fundamental component of human nervous system function that facilitates saltatory conduction, increases action potential velocity, physically anchors axons and reduces crosstalk [1]. When myelin is compromised the consequences are severe, as for example in multiple sclerosis (MS), a chronic neurodegenerative disease involving central nervous system inflammation which causes demyelination and axonal loss [2,3]. While MRI is a valuable tool for diagnosing MS [4], conventional MRI techniques lack specificity to accurately quantify myelin changes [5,6], thus the development of more specific MRI techniques is needed [7]. Here, we focus on asymmetric spin echo (ASE) MRI acquisitions to encode susceptibility-induced contrast [8]. In particular, one technique that utilises ASE is magnetic field correlation (MFC) imaging, which quantifies the microscopic magnetic field inhomogeneities (MFIs), i.e. occurring on a length scale comparable to that of water diffusion. MFC has previously been used to quantify iron content within tissue [9,10], which is associated with oxidative stress [11], but has not been applied to myelin. Here, we use numerical simulations to assess the sensitivity of MFC to demyelination and axonal loss, and whether and to what extent it can characterize myelin status.

Methods: Using MATLAB, we constructed a 200 µm x 200 µm substrate model comprising approximately 7500 infinitely long axons (modelled as hollow cylinders) arranged orthogonally to an external magnetic field (B_0), along the x-axis with a strength of 7 Tesla (**Fig. 1A**). The focal coordinates for the fibres were placed using rejection sampling. Each cylinder's outer radius ranged from 0.5 µm to 3 µm, and was assigned a g-ratio value, randomly chosen from a Gaussian distribution, with a mean of 0.65 and standard deviation of 0.05, from which the corresponding axon radii, and hence myelin thickness, was derived. Axon density was controlled by changing the intra-axonal area fractions ranging from 1% to 25%. To simulate demyelination within the substrate, a subset of fibres was randomly selected to have their g-ratios set to 1 before recalculating the axon radii. This resulted in 3 compartments: axonal, myelin, and extracellular. The areas corresponding to the myelin compartment was allocated a magnetic susceptibility χ value of -0.08 ppm. The myelin-induced MFIs were calculated using Eqs. 1-3 in [12] to produce a spatial map of the Larmor frequency Φ (**Fig. 1B**). Using Monte Carlo methods, we simulated random walks of 20,000 particles diffusing for 100 ms within the extracellular compartment of the substrates. Each walk had a diffusion coefficient D_0 of 2 µm^2/ms, a time step of 0.1 ms and reflected on collision with myelin boundaries. For each trajectory, the frequencies Φ(**r**(t)) at the location **r** of each step position were recorded and used to calculate the MFC as $\gamma^2 K(t)$, where the temporal correlation function $K(|t|) = < B(0)\,B(t) >$ [9,10] was computed as $K(|t|) = \frac{<\phi(r(0))\phi(r(t))>}{\gamma^2}$, with <...> indicating the average over all the particle trajectories and γ indicating the proton gyro-magnetic ratio. The approximation $MFC(t) = MFC(0)\left(1+\frac{4D_0 t}{L^2}\right)^{-3/2}$, Eq. 18 in [9], was used to characterise $MFC(t)$ (**Fig. 1C**), and gave insight into the MFC's characteristic length (L) and temporal ($\tau = L^2/4D_0$) scales.

Results: By increasing demyelination within the substrate, we observed that the characteristic time τ decreased. This effect was mediated by axon density, suggesting both demyelination and axon density affect MFC (**Fig. 2**). We estimate τ ≈ 0.175 ms at 7T in myelinated substrates (axon area fraction ≈ 25.6%, demyelination = 0%). A 33% increase in demyelination in a substrate with the same axon density had a τ of ~0.437 ms. In substrates with an axon area fraction of 15.74%, a 33% increase in demyelination induced an increase in τ ≈ 0.333 ms, therefore this effect may be used as a novel marker for myelin status.

Conclusions: Our results indicate for the first time that MFC is sensitive to myelin in a measurable way

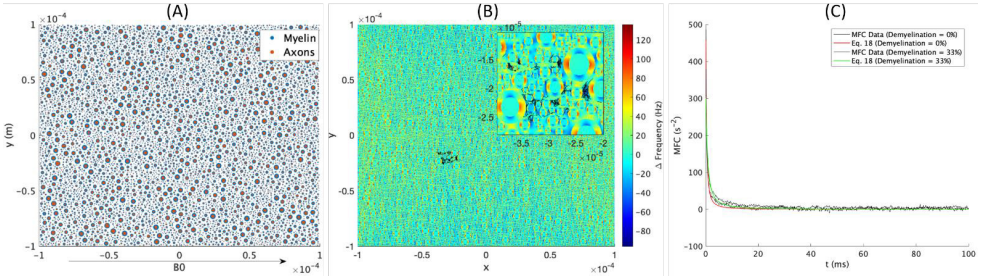

Fig. 1. (A) Schematic layout of a fully-myelinated substrate (aspect ratio is exaggerated for viewing purposes). Axons in red (n = 7601) are surrounded by myelin (blue), with a cellular area fraction (axons & myelin) of 60.35%. (B) **.** Larmor frequency shift map of the substrate, showing positive shifts (red) and negative shifts (blue) due to myelin. An example of a particle trajectory in the extracellular compartment is shown (black). (C) Temporal correlation decay as a function of time (black) for two substrates of same axon density (-21%) with two different levels of demyelination (0 and 33%), across a time scale of 100 ms. The approximation used to characterise MFC decay is fitted to the data (red and green). For demyelination = 0%: fitted MFC(t=0) = 577 s^{-2}, and τ = 0.35 ms ; for demyelination = 33%: fitted MFC(t=0) = 322 s^{-2}, and τ = 0.77 ms.

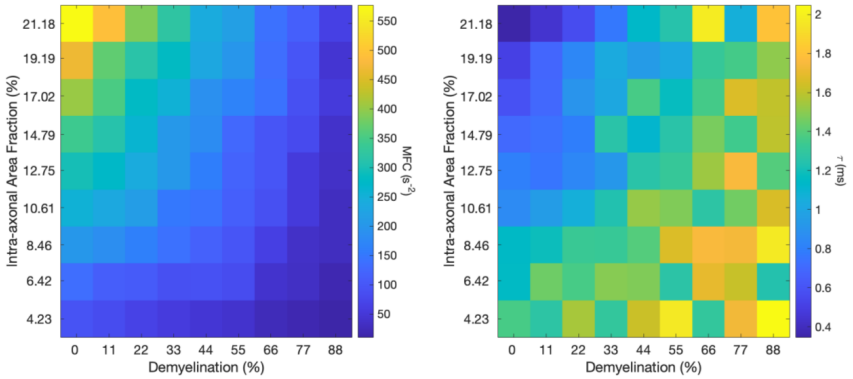

Fig. 2. Colour map showing the MFC (s^{-2}) (left) and the time constants (ms) (right) for varying percentages of demyelination and axon density.

at high field (B_0 = 7T), suggesting MFC as a novel approach to characterise myelin status in neurodegenerative diseases, e.g. MS.

Acknowledgements: This work was funded by UKRI BBSRC grant BB/X005089/1. MP, MJ and KS are funded by UKRI FLF MR/T020296/2.

References. [1] Turner, R. *Front Neural Circuits* (2019) [2] Lassmann, H., Brück, W., & Lucchinetti, C. F. *Brain Pathology* (2007) [3] Lassmann, H., Van Horssen, J., & Mahad, D. *Nature Reviews Neurology* (2012). [4] Hemond, C. C., & Bakshi, R. *Cold Spring Harbor perspectives in medicine* (2018).[5] van der Weijden, C. W., García, D. V., Borra, R. J., Thurner, P., Meilof, J. F., van Laar, P. J., & de Vries, E. F. *Neuroimage* (2021). [6] Lazari, A., & Lipp, I. *Neuroimage* (2021). [7] Elena, Z. A., & María, D. S. *World Journal of Neuroscience* (2013). [8] Stables, L. A., Kennan, R. P., & Gore, J. C. *Magnetic resonance in medicine* (1998). [9] Jensen, J. H., Chandra, R., Ramani, A., Lu, H., Johnson, G., Lee, S. P., & Helpern, J. A. *Magnetic Resonance in Medicine* (2006). [10] Jensen, J. H., Szulc, K., Hu, C., Ramani, A., Lu, H., Xuan, L., & Helpern, J. A. *Magnetic Resonance in Medicine: An Official Journal of the*

International Society for Magnetic Resonance in Medicine (2009). [11] Niedzielska, E., Smaga, I., Gawlik, M., Moniczewski, A., Stankowicz, P., Pera, J., & Filip, M. *Molecular neurobiology* (2016). [12] Chen, W. C., Foxley, S., & Miller, K. L. *Neuroimage* (2013).

Whole-brain imaging in rats using MRI and 3D microscopy: A cross-scale, multi-modal approach

Jenna Hanmer[1], M. Craig[1], M. Prior[1], J. Correia[2], M. Tachrount[3], J. Lerch[3], R.C. Trueman[4], P.S. Morgan[1], T.D. Farr[4], S.N. Sotiropoulos[1]

[1]Sir Peter Mansfield Imaging Centre, School of Medicine, University of Nottingham, UK. [2]Institute of Cardiovascular Sciences, University of Birmingham, UK. [3]Wellcome Centre for Integrative Neuroimaging (WIN), University of Oxford, UK. [4]School of Life Sciences, University of Nottingham, UK.

Introduction: Diffusion MRI (dMRI) is a powerful tool for non-invasive mapping of brain connectivity and microstructure. However, dMRI measures are indirect, noisy, and of low spatial resolution. In contrast, optical imaging of post-mortem brain tissue serves as a microstructural gold standard, which can be used to evaluate, interpret, and validate MRI contrasts [1]. Yet, mapping 2D microscopy onto 3D MRI poses many challenges. Fortunately, advances in tissue clearing [2] and light-sheet microscopy [3] enable optical imaging of intact rodent brains, thereby facilitating optimal MRI-microscopy comparisons in 3D. Whilst previous studies combined MRI and light-sheet microscopy in *mice* [4-6], our approach (Fig. 1) allows for MRI, whole-brain tissue clearing, white matter staining, and 3D microscopy of the much larger *rat* brain.

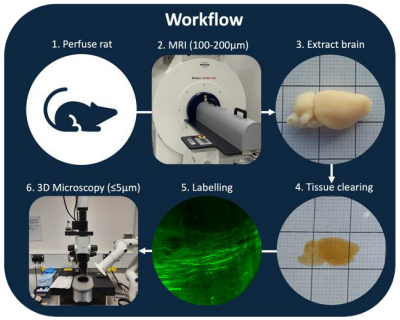

Fig. 1. *A cross-scale, multi-modal approach for whole brain imaging in rats*

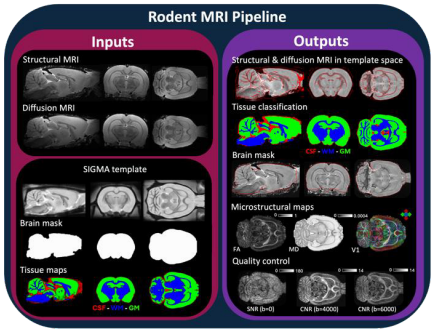

Fig. 2. *Automated pre-processing pipeline for structural and diffusion MRI of the rat brain*

Methods: To optimise *ex-vivo* MRI acquisition protocols for the rat brain, we perfused 5 male Sprague-Dawley rats (Charles River, UK), with (n=3) and without (n=2) gadolinium-based contrast agent (2mM Multihance). High-resolution MRI was performed on all samples using two preclinical scanners (7T Bruker BioSpec 70/30 or 70/20 USR) with differing hardware (transmit/receive volume coil or surface cryo-coil) and software (PV6 or PV360). We optimised acquisition protocols for multi-shell (200 µm isotropic, b=4000, 6000s/mm^2) 90-direction dMRI, using 2D- and 3D-EPI. A T2-weighted 3D-RARE structural scan (100µm) was also acquired. This dataset ensured that the pre-processing MRI pipeline (Fig. 2), which we developed, was generalisable to different acquisitions, data qualities, and large multi-site studies.

Rat brain hemispheres were optically cleared using a passive or active approach, with the AdipoClear+ [7] protocol and SmartBatch+ device [8-9] respectively. White matter was then stained using antibodies targeting myelin (CST #62596, Encor MCA-7G7) and neurofilament (Sigma AB1991, Encor MCA-9B12). Once the brain hemispheres were optically transparent, high resolution (≤5µm) volumetric imaging of sample autofluorescence (561nm) and antibody signal (640nm) was conducted using an UltraMicroscope II (LaVision Biotec) or BLAZE (Miltenyi Biotec) with ImspectorPro software (LaVision BioTec). As the rat brain is larger than the field of view for 3D microscopy, multiple tiles with ~30% overlap were required. The resulting image stacks were stitched together using FIJI and converted to nifti format to produce a high-resolution 3D image (10µm) of brain microstructure.

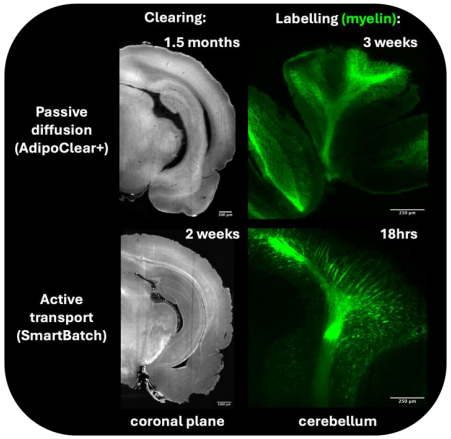

Fig. 3. *Active transport of detergent and antibodies with the SmartBatch+ device accelerates clearing and labelling, whilst also preserving sample size*

3D microscopy allowed us to observe specific microstructural features across the whole brain hemisphere and simplified registration to MRI. We found that even a simple affine transformation aligns MRI with 3D microscopy well (Fig. 4). Only marginal improvement was observed with a standard non-linear registration (ANTs) using the default parameters. This outcome contrasts with the complex framework required to align histology with MRI [10].

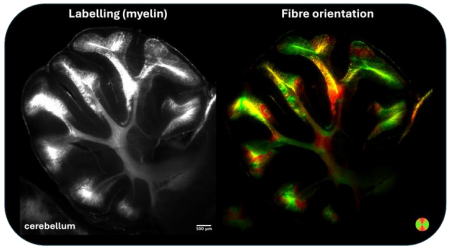

Fig. 5. *Myelin staining with the SmartBatch+ provides a ground-truth measure of neuronal fibre organisation at a microscopic sale.*

Results and Discussion: White matter staining, which is challenging to combine with tissue clearing, was achieved in the much larger rat brain (Fig. 3) using both passive and active approaches. The passive approach is simple but slow and results in shrinkage. In contrast, the active approach preserves sample size and is faster, but requires an electrophoretic device and expensive reagents. Additionally, we found both approaches to be compatible with gadolinium, which allows for shorter MRI acquisitions with improved SNR.

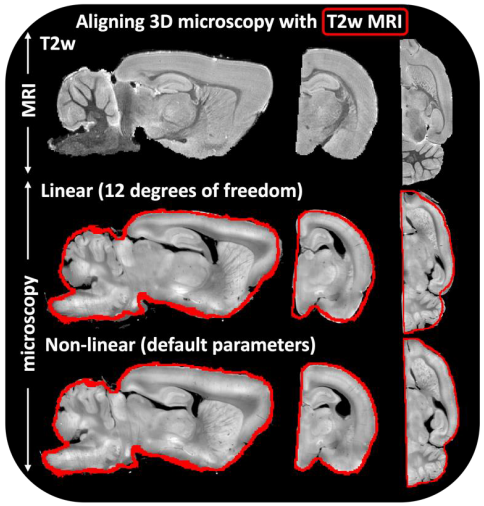

Fig. 4. *Aligning autofluorescence signal, after AdipoClear+, with the corresponding T2-weighted scan is relatively straightforward.*

Structure tensor analysis (which is being expanded to 3D) was used to estimate features, like fibre orientation, from microscopy (Fig. 5). These estimates will be compared with measures obtained non-invasively using dMRI.

Conclusion: By providing an end-to-end pipeline for integrating whole-brain 3D microscopy, white matter staining, and MRI in the same rat, this work paves the way for bridging microscopic information to a macroscopic resolution in larger brains, thereby improving our understanding of dMRI contrasts and the microstructural features they capture.

Acknowledgements: JH is supported by an MRC-funded studentship (grant MR/N013913/1). Special thanks to Kurt Schilling (Vanderbilt University) for his advice and support, and to Cristiana Tisca and Aurea Martins-Bach (University of Oxford) for their role in developing the acquisition protocols for *ex vivo* rodent MRI.

Proffered Talks Session 2

References

[1] A. Yendiki, M. Aggarwal, M. Axer, A.F.D. Howard, A. van Walsum, and S.N. Haber *NeuroImage,* **256**, 119146 (2022).
[2] H.R. Ueda, H. Dodt, P. Osten, M.N. Economo, J. Chandrashekar, and P.J. Keller *Neuron*, **106**, 369-387 (2020).
[3] J. Perens, and J. Hecksher-Sørensen *Front. Neurosci.*, **16**, 866884 (2022).
[4] E.H. Chang, M. Argyelan, M. Aggarwal, T.S. Chandon, K.H. Karlsgodt, S. Mori, and A. K. Malhotra *Data in Brief*, **10**, 438-443 (2017).
[5] M. Goubran, C. Leuze, B. Hsueh, M. Aswendt, L. Ye, Q. Tian, M.Y. Cheng, A. Crow, G.K. Steinberg, J.A. McNab, K. Deisseroth, and M. Zeineh *Nat. Commun.,* **10**, 5504 (2019).
[6] H.B. Stolp, G. Ball, P.W. So, J.D. Tournier, M. Jones, C. Thornton, and A. D. Edwards *Sci. Rep.*, **8**, 4011 (2018).
[7] A. Branch, D. Tward, A.C. Kolstad, V. Pulyadi, J.T. Vogelstein, Z. Wu and M.Gallagher *bioRxiv*, doi:10.1101/639674 (2021).
[8] K. Chung, J. Wallace, S.Y. Kim, S. Kalyanasundaram, A.S. Andalman, T.J. Davidson, J.J. Mirzabekov, K.A. Zalocusky, J.Mattis, A.K. Denisin, S. Pak, H. Bernstein, C.Ramakrishnan, L. Grosenick, V. Gradinaru and K. Deisseroth *Nature*, **497**, 332-337 (2013).
[9] S. Kim, J.H. Cho, E. Murray, N. Bakh, H. Choi, K. Ohn, L. Ruelas, A. Hubbert, M. McCue, S.L. Vassallo, P.J. Keller, and K. Chung *PNAS*, **112**(46): E6274-83 (2015).
[10] I.N. Husvar, M. Pallebage-Gamarallage, S. Bangerter-Christensen, H. Brooks, S. Fitzgibbon, S. Foxley, M. Hiemstra, A.F.D. Howard, S. Jbabdi, D.Z.L. Kor, A. Leonte, J. Mollink, A. Smart, Be.C. Tendler, M.R. Turner, O. Ansorge, K.L. Miller, and M. Jenkinson *NeuroImage,* **265**, 119792 (2023).

^{1}H MR spectroscopy to evaluate the effects of a glycolysis inhibitor and temozolomide treatment in a mouse model of glioblastoma

Tareq Alrashidi[a], Sourav Bhaduri[b], Elisabeth Non Gash[a], Mohesh Moothanchery[a], Christopher Ball[a], Stephen Pickup[d], Mahon L Maguire[a], Harish Poptani[a]

[a] Centre for Pre-Clinical Imaging Depart. University of Liverpool, Crown Street, Liverpool, L69 3BX
[b]Institute for Advancing Intelligence (IAI), TCG CREST, Kolkata, India
[c] Department of Radiology, University of Pennsylvania, Philadelphia, USA

Enhanced glycolysis is the most distinctive hallmark of cancer (Warburg effect)[1]. Lonidamine (LND) is a mitochondrial inhibitor that has a modest antineoplastic impact when used as a single agent[2]. However, when combined with temozolomide (TMZ), it results in a dramatic effect in melanomas[3]. TMZ is the standard of care chemotherapy and has increased the median overall survival in patients with Glioblastoma (GBM)[4]. Lonidamine results in selective tumour intracellular acidification, lactate accumulation and depletion of ATP production by inhibiting various metabolic pathways related to lactate production such as mitochondrial-bound hexokinase II, monocarboxylate transporters (MCTs) and the mitochondrial carrier pyruvate (MCP)[3,5,6]. A previous study reported the effect of LND and TMZ in a human melanoma xenograft grown subcutaneously using ^{31}P MRS and ^{1}H MRS with a selective Multiple Quantum Coherence pulse sequence (SelMQC)[7]. However, the combination of these drugs has not been tested in glioblastomas. The current study was thus performed to evaluate the synergistic effect of LND and TMZ using longitudinal MRS.

Methods: C57BL6 mice were injected intracranially with 2.5x10^{5} GL261 GBM cells in the right cortex. Once the tumours were observed on T2 weighted MRI (>2 mm in diameter), animals were treated for five consecutive days with a combination of intraperitoneal injection (i.p. 100mg/kg) of Lonidamine and 50mg/kg TMZ via oral gavage (n=5), while sham control animals received saline for the same period (n=15, i.p. injections). Imaging was performed on days 0 (baseline), 3 (during treatment), and 6 (end of treatment). Single voxel (2x2x2 mm^{3}) MR spectra were acquired from the tumour region using a PRESS sequence: TR = 2000 ms, TE1 = 9.13 ms and TE2= 7.37 ms, number of averages= 200, complex points = 2048 and spectral width =4401 Hz. Metabolite amplitude ratios (tCho/tCr, tCho/NAA and mI/tCr) were calculated using QUEST algorithm in jMRUI software. Lactate-edited spectroscopy was conducted using an ISIS-SelMQC[8]. The voxel position and dimensions were the same as for the PRESS spectrum. Sequence parameters were: TR=2000 ms, 16 averages (128 FIDs), 2048 points, 8012 Hz spectral width.

Results: A representative T2-weighted image of a mouse bearing the GL261 tumour with the MRS voxel placement displayed as an inset in Figure 1. A. Representative in vivo ^{1}H PRESS spectra from the tumour region of mice treated with saline (Fig. 1 B) and a combination of LND+TMZ (Fig. 1 C). Representative ^{1}H ISIS-SelMQC spectra are shown in Fig 1. D (day 0) and E (day 6) for the same mouse treated with LND+TMZ. No significant change in tumour volume (Fig. 2A) between the two animal groups was observed. However, there was a steady decrease in the tCho/NAA ratio in the treated animals while the saline controls demonstrated an increase in the tCho/NAA ratio in comparison to baseline. This resulted in a significant difference in the percentage change of tCho/NAA between the two groups at the end of treatment (p=0.04, Fig. 2B). The LND+TMZ group also demonstrated a significant decrease in Lip+Lac/tCr (p=0.01, Fig. 2C) and mI/tCr ratio (p=0.03, Fig. 2D) on day 6 compared to saline control. Lactate signal was clearly visible using ^{1}H ISIS-SelMQC before the initiation of treatment, however, it could not be detected at the end of the treatment (Fig. 1 D and E).

Discussion and Conclusion: In this preliminary study, we demonstrated a significant metabolic shift in tumours treated with LND+TMZ even though there were no differences in the tumour growth between treated and control animals. However, this could be due to the limited sample size since we only had two usable spectra from this group at the end of the treatment. A significant reduction in tCho/NAA suggests an arrest in cellular proliferation, as well as DNA damage-induced apoptosis by TMZ, triggered in cancer cells[3]. A significant reduction of Lip+Lac/tCr is probably due to a significant decrease in tumour lactate as evidenced by the ^{1}H ISIS-SelMQC. The disappearance of lactate signal indicates inhibition of lactic acid production and subsequent depletion of ATP, resulting in reduced tumor cell proliferation due to the synergistic effects of LND and TMZ[7]. However, as the tumours kept growing at a similar rate to controls, further studies are needed in a larger cohort as well as longer study points to evaluate whether the metabolic changes are only acute in nature or whether the therapeutic effect (reduction in volume) of the combined treatment with LND+TMZ happen much later, which would further indicate that metabolic changes are earlier marker of treatment response.

References

[1] Vander Heiden MG, Cantley LC, Thompson CB. Understanding the Warburg effect: the metabolic requirements of cell proliferation. *Science*. 2009;324(5930):1029-1033.
[2] Forster R, Campana A, D'Onofrio E, Henderson L, Mosesso P, Scorza Barcellona P. Lonidamine: a non-mutagenic antitumor agent. *Carcinogenesis*. 1990;11(9):1509-1515.
[3] Huang Y, Sun G, Sun X, et al. The Potential of Lonidamine in Combination with Chemotherapy and Physical Therapy in Cancer Treatment. *Cancers (Basel)*. 2020;12(11):3332.
[4] Ortiz R, Perazzoli G, Cabeza L, et al. Temozolomide: An Updated Overview of Resistance Mechanisms, Nanotechnology Advances and Clinical Applications. *Curr Neuropharmacol*. 2021;19(4):513-537. doi:10.2174.
[5] Nath K, Guo L, Nancolas B, et al. Mechanism of antineoplastic activity of lonidamine. *Biochim Biophys Acta*. 2016;1866(2):151-162. doi:10.1016.
[6] Cervantes-Madrid D, Romero Y, Dueñas-González A. Reviving Lonidamine and 6-Diazo-5-oxo-L-norleucine to Be Used in Combination for Metabolic Cancer Therapy. *Biomed Res Int*.2015:690492. doi:10.1155.
[7] Nath K, Nelson DS, Roman J, et al. Effect of Lonidamine on Systemic Therapy of DB-1 Human Melanoma Xenografts with Temozolomide. *Anticancer Res*. 2017;37(7)
[8] Nath K, Nelson DS, Ho AM, et al. (31) P and (1) H MRS of DB-1 melanoma xenografts: lonidamine selectively decreases tumor intracellular pH and energy status and sensitizes tumors to melphalan. *NMR Biomed*. 2013;26(1)

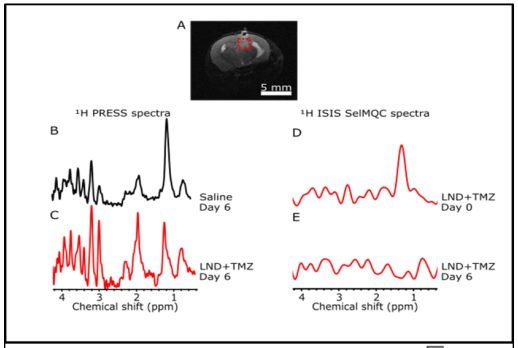

Fig. 1. A_E. ^{1}H PRESS spectra (B and C), voxel overlaid on T2 weighted image (A) comparing treatment response on day 6 in two different groups with GBM (Saline and LND+TMZ, respectively), showing Lip +Lac, NAA, Glx, tCr, tCho and mI peaks from the tumour. D, E, ^{1}H ISIS-SelMQC spectra of tumor region showing the effect of LND+TMZ on Lactate on day 6 (E) compared with baseline (D).

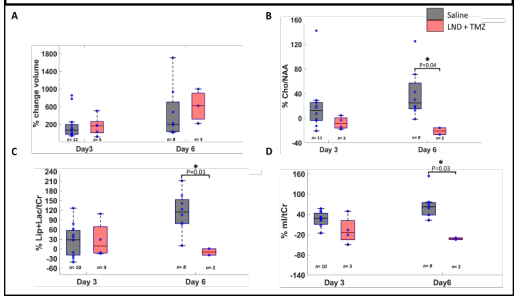

Fig. 2. A-D. Box plots comparing percentage change (with respect to baseline) in tumour volume and three amplitude ratios (tCho/NAA, Lip+Lac/tCr and mI/tCr) between saline and LND+TMZ groups. Asterisk indicate that the difference between groups reached a significance level of ≤ 0.05. n denotes the number of samples used for quantification.

Multiparametric $^{1}H/^{23}Na$ MRI for analysing the ionic microenvironment within preclinical breast tumour models.

Alina L. Capatina[1], Isaac Watson[1], Oliver Mundell[2], Aneurin J. Kennerley[2,3,4], William J. Brackenbury[1,2]

Affiliations

1. Department of Biology, University of York, York, UK. 2. York Biomedical Research Institute University of York, York, UK. 3. Department of Chemistry, University of York, York, UK 4. Manchester Metropolitan University, Manchester, UK

Background:

Breast cancer is the most common cancer in UK females, accounting for almost a third (30%) of all female cases. Around 11 500 patients die per year from breast cancer [1-3]. Studies have correlatd the more agressive, highly hypoxic subtypes, such as tripple negative breast cancer (TNBC), with increased intratuoral Na^+ levels thought to promote survival and methastasis [4-7]. This highlights an urgent need for new treatments that target ionic transporters within the breast tumour tissue. ^{23}Na MRI can be used to assess the efficacy of repurposed sodium-transport targeted drugs and conventional chemotherapies in limiting disease progression, by interfering with the local hypoxic microenvironment and metabolic adaptations required for cancer survival.

In this study, we describe the optimisation of multiparametric $^{1}H/^{23}Na$ MRI for analysing the breast cancer microenvironment in a preclinical orthotopic TNBC tumour model. We present data on Na^+ dynamics, tumour oxygenation and metabolic changes, and correlate those with disease progression. By investigating changes in Na^+ content and distribution within the tumour, as well as by evaluating changes in glucose content and tumour oxygenation, this study aims to research a potential correlation between the hypoxia-mediated tumour progression (via metabolic adaptation and oxygen deprivation) and Na^+ dynamics.

Methods:

We used an *in vivo* longitudinal (3 week) xenograft mouse model to investigate the breast tumour microenvironment and disease progression in response to Na^+ transport targeted drugs or chemotherapy. Ethical approval was granted by University of York Animal Welfare and Ethical Review Body, under the authority of the UK Home Office.

Data acquisition was perforemd using a 7T Bruker Biospec 70/30 USR AVANCE III, with a 12 channel RT-shim system (B-S30) and a preinstalled 660mT/m imaging gradient set (BGA12S). Imaging was carried out using a dual-tuned linear $^{1}H/^{23}Na$ transceiver coil (ID 35 mm, RAPID Biomedical GmbH).

Intratuomural Na^+ in female Rag2-/- γc-/- Balb/c and Rag2 -/- IL2rg -/- C57BL/6 and129 mix mice bearing orthotopic TNBC tumours (MDA-MB-231s) was imaged using a 2D gradient echo spiral out sequence.

The distribution of Na^+ between the intra and extracellular compartments was assessed using the Tm-DOTP exogenous paramagnetic polyanionic contrast agent injected i.p. 45 min prior to data acquistion, using a Chemical Shift Imaging (CSI) apparoach [8].

Variations in glucose levels within tumours were explored using a Chemical Exchange Saturation Transfer (CEST) MRI imaging sequence. Tumour oxygenation was evaluated using oxygen enhanced MRI following 3 cycles of consecutive exposure to medical grade air and 100% medical grade oxygen compressed gas.

Results:

We confirm elevation in the Na^+ concentration in xenograft breast tumours [5]. Our novel high resolution ^{23}Na imaging data highlights a heterogenous Na^+ distribution across the tumour. CEST confirms increased glucose concentration within tumour tissue. We observe limited response to gas challenges in the in tumour compared to counter-lateral muscle tissue (Figure 1). Additionally, we present the results of our CSI analysis to compartmentalise the ^{23}Na signals and elaborate on the limitations of Tm-DOTP i.p. administration for the purpose of mapping Na^+ distribution within the extra and intracellular spaces of the breast tumour.

Conclusion & Discussion:

Our data points towards an ionically dysregulated microenvironment characterised by Na^+ elevations, with limited oxygen delivery and subsequent glycolytic preference. Data suggest a hypoxic tumour microenvironment in control animals and variations in multiparametric measures are explored in response to different Na^+ channel inhibiting drugs and chemotherapy. We describe our approach on using MRI to evaluate multiple aspects of the tumour microenvironment and understand the connections between them. Future studies will use the developed methodology to explore response to metabolic regulators and hypoxia inhibitors/ stabilisers. Data will also be combined with post-mortem benchtop biology such as gene and protein expression studies, and immunohistochemistry.

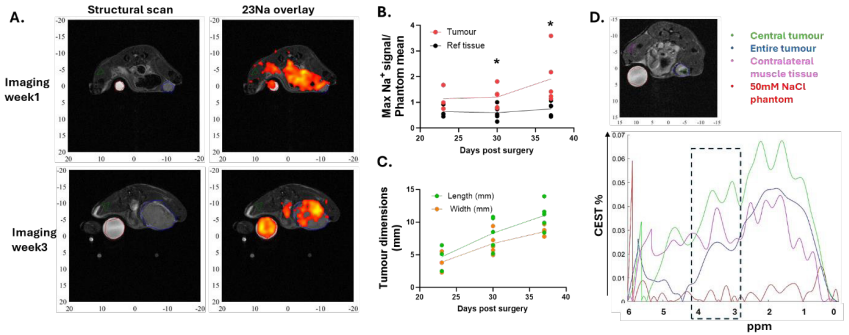

Figure 1. *^{23}Na and CEST MRI in preclinical breast tumours.* **A.** Representative scans and ^{23}Na signal overlay at imaging week 1 and 3, regions of interest correspond to the phantom (red), tumour (blue) and reference tissue (green); **B.** Changes in maximum ^{23}Na signal in tumour Vs control tissue over time, * $p<0.05$; **C.** Tumour dimensions at each imaging date; **D.** CEST results, the CEST z-spectra shows the intensity of glucose chemical shift (area between 3 and 4 ppm) in each region of interest [9].

Proffered Talks Session 2

References:

1. Bray, F., et al., *Global cancer statistics 2018: GLOBOCAN estimates of incidence and mortality worldwide for 36 cancers in 185 countries.* CA: A Cancer Journal for Clinicians, 2018. **68**(6): p. 394-424.
2. Santucci, C., et al., *European cancer mortality predictions for the year 2024 with focus on colorectal cancer.* Ann Oncol, 2024. **35**(3): p. 308-316.
3. Siegel, R.L., A.N. Giaquinto, and A. Jemal, *Cancer statistics, 2024.* CA: A Cancer Journal for Clinicians, 2024. **74**(1): p. 12-49.
4. Leslie, T.K., et al., *Sodium homeostasis in the tumour microenvironment.* Biochim Biophys Acta Rev Cancer, 2019. **1872**(2): p. 188304.
5. James, A.D., et al., *Sodium accumulation in breast cancer predicts malignancy and treatment response.* Br J Cancer, 2022. **127**(2): p. 337-349.
6. Ouwerkerk, R., et al., *Elevated tissue sodium concentration in malignant breast lesions detected with non-invasive 23Na MRI.* Breast Cancer Res Treat, 2007. **106**(2): p. 151-60.
7. Liu, L., et al., *Hypoxia-mediated activation of hypoxia-inducible factor-1α in triple-negative breast cancer: A review.* Medicine (Baltimore), 2023. **102**(43): p. e35493.
8. Khan, M.H., et al., *Imaging the transmembrane and transendothelial sodium gradients in gliomas.* Scientific Reports, 2021. **11**(1): p. 6710.
9. Stolz, M., et al., *Feasibility of precise and reliable glucose quantification in human whole blood samples by 1 tesla benchtop NMR.* NMR in Biomedicine, 2020. **33**(9): p. e4358.

Lipid composition in the breasts of BRCA1/2 genetic mutation carriers via chemical shift-encoded imaging

Sai Man Cheung[1,2], Kwok Shing Chan[2,3], Yazan Masannat[4], Senthil Ragupathy[5], Zosia Miedzybrodzka[2], Jiabao He[1,2]

[1]Newcastle Magnetic Resonance Centre, Translational and Clinical Research Institute, Faculty of Medical Sciences, Newcastle University
[2]Institute of Medical Sciences, University of Aberdeen
[3]Massachusetts General Hospital, Boston, United States of America
[4]Breast Unit, Broomfield Hospital, Mid and South Essex NHS Foundation Trust
[5]Department of Radiology, Aberdeen Royal Infirmary

Introduction: Breast cancer is a major and expanding health challenge, despite significant improvement in survival rate [1]. Genetic mutation carriers of BRCA1/2 have over 30% increased risk of developing breast cancer and receive annual DCE-MRI surveillance [2]. DCE-MRI contrast is sensitive to tumour angiogenesis, however detects malignancies that are well under development. Deregulation of lipid composition, including monounsaturated, polyunsaturated and saturated fatty acids (MUFA, PUFA and SFA), has been shown in the breast of BRCA1/2 carriers using single voxel spectral edited MR spectroscopy [3], and in the peri-tumoural region of the breast [4]. Novel chemical shift-encoded imaging (CSEI) allows rapid lipid composition mapping of the whole breast, and the spatial distribution may further distinguish the disease state. We therefore hypothesise that lipid composition in the breast of BRCA1/2 carriers show no difference from patients with breast cancer and healthy controls, and determine the repeatability of CSEI.

Methods: Twenty-one patients with invasive ductal carcinoma (age 31 – 55 years), 22 BRCA1/2 genetic mutation carriers (age 32 – 51 years) and 15 healthy controls (age 24 – 49 years) participated in the study. Patients with a tumour size larger than 1 cm on mammography and have not had hormonal therapy or chemotherapy were eligible. Participants with diabetes or on long-term medications that might alter lipid metabolism were excluded. The study was approved by the North West – Greater Manchester West Research Ethics Committee (ID: 19/NW/0225), and written informed consents were obtained from all the participants (Figure 1).

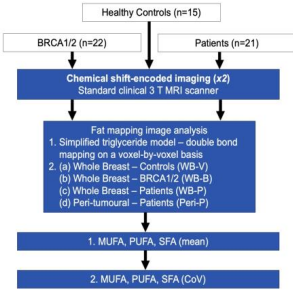

Figure 1. Study design.

CSEI All images were acquired on a 3 T whole-body clinical MRI scanner (Ingenia dStream, Philips Healthcare, Best, Netherlands). Lipid composition images were acquired from all participants using a 2D fast field echo sequence [5,6] with 16 echoes, initial echo time of 1.14 ms, echo spacing of 1.29 ms, repetition time of 60 ms, reconstruction pixel size of 2.0 × 2.0 mm^2 and slice thickness of 3.0 mm, with subsequent repeated acquisition.

Data Processing Image analysis was conducted in MATLAB (R2020a, MathWorks Inc., Natick, MA, USA). The maps of the number of double bonds in triglycerides were computed from raw data, before subsequent quantification of MUFA, PUFA and SFA as a fraction of the total lipids [5,6]. The delineation of tumour was conducted on the first echo of magnitude image, with reference to DCE-MRI images. The whole breast in BRCA1/2, patients and healthy controls, and the peri-tumoural region in patients were the four regions-of-interest. The whole breast was defined to contain only adipose and fibroglandular tissue in BRCA1/2 and healthy controls, and excluding the tumour in patients. The peri-tumoural region was defined as an annular ring of 16 mm (8 voxels) around the tumour. Adipose voxels with lipid signal below 60% of total signal were excluded from further analysis. The mean lipid composition from the regions-of-interest was subsequently computed.

Statistical Analysis All statistical analysis was performed in the *R* software (v4.3.1, *R* Foundation for Statistical Computing, Vienna, Austria). Wilcoxon signed rank paired tests were performed for

comparison of lipid composition in the whole breast and the peri-tumoural region in patients, with Wilcoxon rank sum tests performed between the whole breast of BRCA1/2, patients and healthy controls. The within-subject coefficient of variance (%wCoV) was calculated as: [standard deviation / mean] × 100%. A *p*-value < 0.01 was considered a statistically significant difference for 4-group comparisons, after Bonferroni correction.

Results: The participant demographics of the entire cohort are shown in Table 1.

BRCA1/2 and Patients There was no significant difference in mean MUFA, PUFA and SFA in the whole breast of BRCA1/2 against the whole breast nor the peri-tumoural region of patients (Figure 2).

BRCA1/2 and Controls There was a significantly higher mean MUFA (p<0.01) and lower mean SFA (p<0.01) in the whole breast of BRCA1/2 against the whole breast of healthy controls, although there was no significant difference in mean PUFA (Figure 2).

Patients There was a significantly lower MUFA (p<0.01) and higher SFA (p<0.01) in the peri-tumoural region compared to the whole breast, although no significant difference in PUFA (Figure 2).

Characteristic	Patients (n=21)	BRCA1/2 (n=22)	Healthy Controls (n=15)	p value
Age (year)	46.8 ± 9.6	46.6 ± 12.1	43.7 ± 7.2	NS
Body Mass Index (BMI)	25.3 ± 3.4	25.6 ± 3.8	23.8 ± 3.7	NS
Tumour size (mm)	20.8 ± 5.6	-	-	
Histology grade II III	 13 8	-	-	
Lymphovascular invasion Positive (+) Negative (-)	 5 16	-	-	
Oestrogen receptor status Positive (+) Negative (-)	 16 5	-	-	
Progesterone receptor status Positive (+) Negative (-)	 14 7	-	-	
HER2 status Positive (+) Negative (-)	 7 14	-	-	

NS – not significant, HER2 – human epidermal growth factor receptor 2.
Body mass index calculated as weight / height in metre squared (kg/m²).

Table 1. Cohort demographics.

Within-subject CoV The %wCoV in all the four regions-of-interest were below 10.0% (Figure 3).

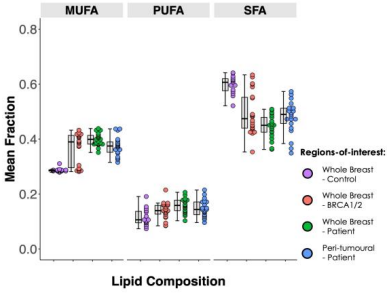

Figure 2. Difference in lipid composition.

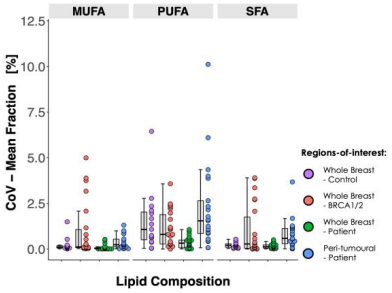

Figure 3. Repeatability in lipid composition.

Discussion: Deregulation of lipid composition in the breast of BRCA1/2 genetic mutation carriers resembled the diseased group, serving as potential precursor of breast cancer. There was a decrease in MUFA in the peri-tumoural region to support accelerated membrane synthesis for tumour growth [7], while an increase in SFA in the peri-tumoural region to avoid lipotoxicity and enhance chemoresistance [7]. CSEI has excellent repeatability in lipid composition mapping of the breast critical for effective disease monitoring.

Conclusions: Lipid composition in BRCA1/2 showed similarity to positive control, and lipid composition in the peri-tumoural region was altered due to tumour growth. CSEI has excellent repeatability for accurate measurement of lipid composition in the breast.

Acknowledgements: The authors would like to thank Dr Matthew Clemence (Philips Healthcare Clinical Science, UK) for clinical scientist support. The project was funded by Cancer Research UK (CRUK) and Friends of Aberdeen and North Centre for Haematology, Oncology and Radiotherapy (ANCHOR).

References:

[1] Pan H, Gray R, Braybrooke J, *et al*. *N Engl J Med.* **377**, 1836-1846 (2017).
[2] Malone KE, Begg CB, Haile RW, *et al*. *J Clin Oncol*. **28**, 2404-2410 (2010).
[3] Ramadan S, Arm J, Silcock J, *et al*. *Radiology*. **275**, 675-682 (2015).
[4] Chan KS, Cheung SM, Senn N, *et al*. *BMC Cancer*. **22**, 285 (2022).
[5] Bydder M, Girard O, Hamilton G. *Magn Reson Imaging*. **29**, 1041-1046 (2011).
[6] Peterson P, Månsson S. *Magn Reson Med.* **69**, 688-697 (2013).
[7] Broadfield LA, Pane AA, Talebi A, Swinnen JV, Fendt S. *Dev Cell*. **56**, 1363-1393 (2021).

Investigating Prostate Cancer Using QSM In Vivo

Laxmi Muralidharan[1], Manju Mathew[2], Adam Retter[2], Joey Clemente[2], Lucy Caselton[2], Sumandeep Kaur[2], Julia Markus[2] , Shonit Punwani[2], Karin Shmueli[1]
[1]Department of Medical Physics and Biomedical Engineering, University College London, UK
[2]Centre for Medical Imaging, University College London, UK

Introduction: Previous QSM studies in prostate cancer (PCa) have investigated the potential to detect intraprostatic calcifications to use as fiducial markers for radiotherapy[1] and post biopsy[2] but none have assessed subtle tissue susceptibility changes. Blood's susceptibility is directly proportional to its deoxygenation[3], and low oxygenation (hypoxia) is thought to occur early in the evolution of PCa and is linked to an aggressive phenotype[4]. All this underpins our aim to investigate whether QSM can help detect and classify cancerous lesions in the prostate.

Methods: 27 subjects undergoing PCa screening were recruited as part of a clinical study [5] and scanned on a 3T Philips Ingenia using a 4x4 channel receive coil array on the front with a 4x4 array in the table. All subjects were given Buscopan to reduce rectal gas and bowel motion. 7 patients had lesions and underwent prostatectomy (***surgical*** group), 8 patients had malignant lesions on biopsy and underwent other treatment (***non-surgical*** group) and 12 patients had radiologically negative MR results for prostate cancer (***control*** group).

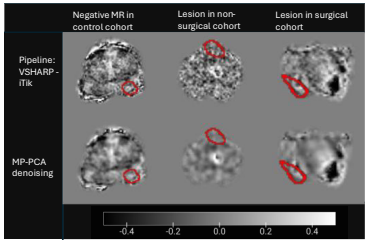

Fig.1: Susceptibility maps and ROI contours (red) with and without the MP-PCA denoising in noisy datasets in the different

Optimised 3D GRE parameters [6] included: FOV 420 x 320 x 128 mm, 1 mm isotropic resolution, 5 in-phase echoes: TE1 4.6 ms, ΔTE 6.9 ms, and SENSE factor 3. A QSM pipeline was optimized in 9 control subjects and applied to all subjects: The complex signal was de-noised using Marchenko-Pastur Principal Component Analysis (MP-PCA)[7]. Fig.1 demonstrates effective denoising in the susceptibility maps. Total field maps from a non-linear fit of the denoised complex data [8] underwent Laplacian unwrapping[9]. Background field removal was performed using VSHARP [10, 11] with a maximum kernel width of 25 mm and a whole prostate mask contoured (MIM software[12]) on the T2-weighted images acquired in the same session/different session (FOV 180x180x96.6 mm, reconstructed voxel size 0.375x0.375x3 mm) by an experienced radiologist and transformed into the QSM space using the global registration of T2w and echo-combined [13] magnitude GRE images (NiftyReg[14, 15]). Susceptibility calculation was performed using iterative Tikhonov regularization[16] with the default regularization parameter α=0.05. Cancerous **Lesion** ROIs in the surgical (9) and non-surgical (10) groups, and **negative MRI** ROIs in the control (14) and non-surgical (3) groups were obtained in a similar manner to the whole prostate contour. To minimize partial volume effects, ROI masks were eroded by 1 voxel using a spherical kernel. A t -test was performed to compare the ROI mean susceptibility values between lesions and negative MRI ROIs.

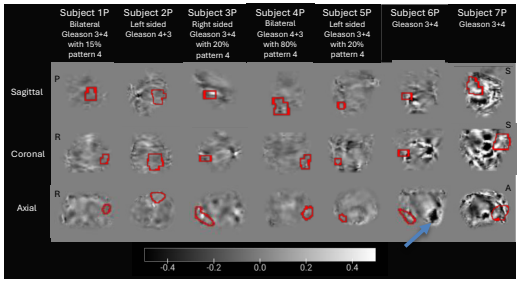

Fig.2: Susceptibility maps and **lesion** ROI contours (red) in the surgical cohort. The Gleason grade of the lesions for each subject is included. There are no salient lesion susceptibility

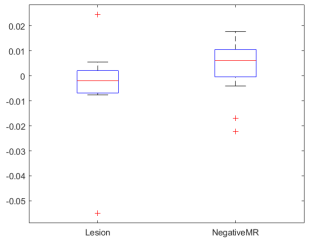

Fig. 3: Box plot of mean susceptibility values in cancerous **lesion** ROIs (surgical and non-surgical groups) and **negative MRI**

Results and Discussion: Diamagnetic regions (blue arrows), likely to be calcium-rich secretion residues, were observed in the prostates of several subjects (Fig. 2). Visually, there were no clear susceptibility differences in ROI susceptibilities between the groups. We found no significant difference in the mean susceptibility values (t(32)= -1.4620, p=0.16). Although we would hypothesize that hypoxia in cancerous lesions would lead to increased susceptibility, there seems to be a general trend of lower mean susceptibility values in the **lesions** compared to **negative MR**. These results could be attributed to prostate cancers' poor vasculature compared to other tumours such as renal carcinomas [17, 18].

Conclusions: An optimized high-resolution sequence and processing pipeline were used to obtain prostate susceptibility maps. We found no difference in the mean susceptibility values in the cancerous lesions compared to the negative MRI non-cancerous tissue. More data are being acquired to improve the statistical power of this preliminary study.

References

1. Kan, H., et al., *Delineation of prostatic calcification using quantitative susceptibility mapping: Spatial accuracy for magnetic resonance-only radiotherapy planning.* J Appl Clin Med Phys, 2021.
2. Straub, S., et al., *Potential of quantitative susceptibility mapping for detection of prostatic calcifications.* J Magn Reson Imaging, 2017. **45**(3): p. 889-898.
3. Jain, V., et al., *Investigating the magnetic susceptibility properties of fresh human blood for noninvasive oxygen saturation quantification.* Magn Reson Med, 2012. **68**(3): p. 863-7.
4. Fraga, A., et al., *Hypoxia and Prostate Cancer Aggressiveness: A Tale With Many Endings.* Clin Genitourin Cancer, 2015. **13**(4): p. 295-301.
5. Singh, S., et al., *Histo-MRI map study protocol: a prospective cohort study mapping MRI to histology for biomarker validation and prediction of prostate cancer.* BMJ Open, 2022. **12**(4): p. e059847.
6. Muralidharan L, M.M., Clemente J, Caselton L, Kaur S, Brizmohun M, Punwani S, Shmueli K *An Optimized High Resolution Acquisition and Processing Pipeline for QSM in the Prostate*. in *ISMRM & ISMRT Annual meeting* 2023. Toronto, Canada.
7. Does, M.D., et al., *Evaluation of principal component analysis image denoising on multi-exponential MRI relaxometry.* Magn Reson Med, 2019. **81**(6): p. 3503-3514.
8. Liu, T., et al., *Nonlinear formulation of the magnetic field to source relationship for robust quantitative susceptibility mapping.* Magn Reson Med, 2013. **69**(2): p. 467-76.
9. Schweser, F., et al., *Toward online reconstruction of quantitative susceptibility maps: superfast dipole inversion.* Magn Reson Med, 2013. **69**(6): p. 1582-94.
10. Schweser, F., et al., *Quantitative imaging of intrinsic magnetic tissue properties using MRI signal phase: an approach to in vivo brain iron metabolism?* Neuroimage, 2011. **54**(4): p. 2789-807.
11. Wu, B., et al., *Whole brain susceptibility mapping using compressed sensing.* Magn Reson Med, 2012. **67**(1): p. 137-47.
12. *MIM Software Inc.*; Available from: https://www.mimsoftware.com/.
13. Kundu, P., et al., *Multi-echo fMRI: A review of applications in fMRI denoising and analysis of BOLD signals.* Neuroimage, 2017. **154**: p. 59-80.
14. Computing, C.f.M.I. *NiftyReg*. 2019; Available from: http://cmictig.cs.ucl.ac.uk/wiki/index.php/NiftyReg.
15. Rueckert, D., et al., *Nonrigid registration using free-form deformations: application to breast MR images.* IEEE Trans Med Imaging, 1999. **18**(8): p. 712-21.
16. Karsa, A., S. Punwani, and K. Shmueli, *An optimized and highly repeatable MRI acquisition and processing pipeline for quantitative susceptibility mapping in the head-and-neck region.* Magn Reson Med, 2020. **84**(6): p. 3206-3222.
17. Zhang, K. and D.J. Waxman, *Impact of tumor vascularity on responsiveness to antiangiogenesis in a prostate cancer stem cell-derived tumor model.* Mol Cancer Ther, 2013. **12**(5): p. 787-98.
18. Eberhard, A., et al., *Heterogeneity of angiogenesis and blood vessel maturation in human tumors: implications for antiangiogenic tumor therapies.* Cancer Res, 2000. **60**(5): p. 1388-93.

Soma And Neurite Density Imaging (SANDI) is sensitive to changes in glial morphology induced by systemic inflammation

Mara Cercignani[1], Natalie Jones[1], Abiodun Olorunda[1], Sara Obudi[2], Maryam Afzali[1,3], Andrè Döring[4], Kadir Şimşek[1], James Coulson[5], Claire MacIver[1], Marco Palombo[1], Neil A Harrison[1]

[1]Cardiff University Brain Research Imaging Centre, Cardiff CF24 4HQ, Wales, UK
[2]School of Medicine, Cardiff University, Cardiff CF14 4YS, Wales, UK
[3]Leeds Institute of Cardiovascular and Metabolic Medicine, University of Leeds, Leeds, UK
[4]CIBM Center for Biomedical Imaging, EPFL CIBM-AIT, EPFL Lausanne, Lausanne, Switzerland
[5]Clinical Pharmacology, School of Medicine, Cardiff University, Cardiff CF14 4YS, Wales, UK

Introduction: Effects of systemic inflammation on the brain have been implicated in the etiology of mental illnesses and neurodegenerative diseases [1] and are thought to be mediated by actions on glial cells [2]. As inflammation-induced changes in glial function are coupled with changes in cell morphology (increase in cell body (soma) volume and retraction of processes) [3], it is plausible that diffusion-weighted (DW) MR techniques could be sensitive to these alterations. In line with this hypothesis, we have previously shown that the apparent diffusion coefficient (ADC) of choline, measured by DW MR spectroscopy, is increased after injection with low-dose lipopolysaccharide (LPS), a well-known method for inducing systemic inflammation [4]. DW MRI offers the advantage of providing whole-brain coverage and better spatial resolution than spectroscopy, albeit with less cellular specificity. Here, we investigate whether advanced multi-compartmental models of DW MRI, like Soma And Neurite Density Imaging (SANDI, [5]), may overcome this lack of specificity to provide a useful biomarker of neuroinflammation. We test this hypothesis by scanning healthy participants twice, once after administering intravenous LPS and once after placebo.

Methods: Thirteen healthy participants (M/F=7/6, mean age [range] = 28.8 [21-41] years) have been included to date. All were screened to exclude underlying neurological, immunological, cardiovascular or psychiatric condition, including substance misuse. All participants received an intravenous injection of either LPS (1 ng/Kg) prepared from Escherichia coli O:113 (U.S. Standard Reference Endotoxin, manufactured for the Clinical Center, NIH) or normal saline (placebo control) in random order in two separate study sessions. After injection, participants were kept under observation, with blood pressure and body temperature regularly monitored, and blood samples taken at baseline, 3½ and 6 hours post injection. After 4-hours, participants underwent an MRI scan on a 3T Siemens Connectom scanner including MPRAGE, DW-MRI and MRS (not presented here). The total duration was ~75 minutes, with a break in the middle. The DW sequence used to fit SANDI had: TE=65ms, δ=10ms, Δ=22ms, maximum b value=7500 smm^{-2}, 5-shells, 3-mm isotropic voxels. Data preprocessing included correction for Gibbs ringing, drift, motion, susceptibility and eddy-currents effects. SANDI was fitted using the SANDI Matlab Toolbox publicly available at: https://github.com/palombom/SANDI-Matlab-Toolbox-Latest-Release, yielding maps of soma and neurite density, soma radius, extra-cellular fraction (estimated as 1 minus soma and neurite signal fractions) and extra-cellular diffusivity. The b=0 images were affine registered to each participant's MPRAGE, which was then segmented and warped to MNI space. The 48 cortical regions of interest (ROIs) from the Harvard-Oxford Atlas were then mapped back to the native space of SANDI maps. Every ROI was masked with each participant's grey matter segment to minimize partial volume with CSF. The mean SANDI parameters were extracted for each ROI and compared within-subject using a paired sample t-test. False discovery rate (FDR, [6]) was used to control for multiple comparisons. We hypothesized that LPS would induce an increase in soma radius, and possibly soma density.

Results: SANDI maps were of good quality for all participants (Fig 1A). The only parameters to show an effect of LPS ($p<0.05$) were the extracellular diffusivity (D_e, decreased) and soma radius (R_{soma}, increased) in several ROIs. After FDR, D_e remained significantly reduced in the post-central gyrus (original p value 0.0001) and the superior parietal lobule (original p value 0.002), while R_{soma} remained significantly increased (original p value 0.0002; Cohen's d=1.01) in the anterior insula (Fig 1B).

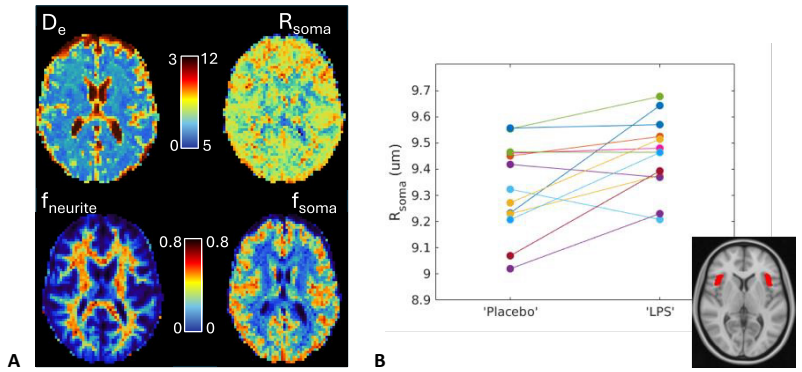

Fig. 1. A: SANDI maps obtained for one participant, D_e is measured in $\mu m^2/ms$, R_{soma} in μm; **B**: mean anterior insula soma radius (in μm) for every participant after placebo and LPS injection. The inset shows the location of the ROI (red) on the MNI template.

Discussion: These preliminary results support the hypothesis that DW MRI is sensitive to changes in glial cell morphology induced by systemic inflammation, when an advanced (SANDI) model of the signal is used. The finding of increased soma radius in the anterior insula is consistent with cell body swelling, and with the previous literature highlighting the central role of the insula in immune-brain communication [2]. Limitations of this work include the small sample size, and the coarse image resolution, which could result in partial volume effects. We are currently exploring approaches to mitigate this problem [7]. Further analyses of the associations between soma radius changes and immunological responses are currently on-going.

Conclusions: SANDI could provide a valuable non-invasive tool to measure the effects of systemic inflammation on the brain.

Acknowledgements: MP is supported by UKRI Future Leaders Fellowship (MR/T020296/2). MA was supported by Wellcome Trust Investigator Award (219536/Z/19/Z). We are grateful to the National Institute of Health Clinical Centre (NIHCC), Bethesda, Maryland, US for supplying the GMP grade LPS used in this study.

References

[1] Khandaker, G., Harrison, N., Bullmore, E., Dantzer, R. (Eds.), 2021. Textbook of Immunopsychiatry. Cambridge University Press. Doi: 10.1017/9781108539623.

[2] Critchley, H.D., Harrison, N.A. Visceral Influences on Brain and Behavior. Neuron, 2013;10.1016/j.neuron.2013.02.00

[3] Paolicelli, R.C., Sierra, A., Stevens. B., et al. Microglia states and nomenclature: A field at its crossroads. Neuron, 2022; 110:3458-3483. doi: 10.1016/j.neuron.2022.10.020.

[4] De Marco, R., Ronen, I., Branzoli, F., et al. Diffusion-weighted MR spectroscopy (DW-MRS) is sensitive to LPS-induced changes in human glial morphometry: A preliminary study Brain, Behavior, and Immunity, 2022; 99: 256-265. doi.org/10.1016/j.bbi.2021.10.005.

[5] Palombo, M., Ianus, A., Guerreri, M., et al. SANDI: A compartment-based model for non-invasive apparent soma and neurite imaging by diffusion MRI. Neuroimage, 2020; 215:116835. doi: 10.1016/j.neuroimage.2020.116835.

[6] Benjamini, Y., Hochberg, Y. Controlling the false discovery rate: A practical and powerful approach to multiple testing. J. R. Stat. Soc. Ser. B, 57 (1995), pp. 289-300

[7] Alexander DC, Zikic D, Ghosh A, et al. Image quality transfer and applications in diffusion MRI. Neuroimage, 2017;152:283-298. doi: 10.1016/j.neuroimage.2017.02.089.

Cross-species Standardised Subcortical Tractography

Stephania Assimopoulos[1], Shaun Warrington[1], Davide Folloni[2], Katherine L. Bryant[3,4], Sarah Heilbronner[5], Saad Jbabdi[4], Rogier B. Mars[4,6], Stamatios N. Sotiropoulos[1,4]

[1]Sir Peter Mansfield Imaging Centre, School of Medicine, University of Nottingham, UK.[2]Nash Family Department of Neuroscience and Friedman Brain Institute, Icahn School of Medicine at Mount Sinai, NY, USA.[3]Laboratoire de Psychologie Cognitive, Aix-Marseille Université, France.[4]Wellcome Centre for Integrative Neuroimaging (WIN-FMRIB), University of Oxford, UK. [5]Baylor College of Medicine, Texas, USA. [6]Donders Institute for Brain, Cognition & Behaviour, Radboud University, Nijmegen, Netherlands

Introduction: White matter (WM) bundles connecting cortical areas with subcortical nuclei are crucial for relaying and modulating cortical function (1,2). Their disruption is linked to abnormal function and pathology in neurodegenerative and mental health disorders (3,4). Diffusion MRI (dMRI) and tractography enable exploration and reconstruction of WM bundles (5,6), but their relative size, the complexity and associated bottlenecks, make their estimation challenging and sensitive to anatomical priors (7,8). Standardised tractography approaches (9,10) provide a way to overcome these challenges enabling reproducible and consistent bundle delineation. Previous efforts involved cortico-cortical connecting bundles, or tract reconstruction using subject-specific protocols (11). Here we build upon our previous work (9,12,13) introducing tractography protocols for delineating cortico-subcortical connections, between cortex and the amygdala, hippocampus, striatum and thalamus. Guided by chemical tracer literature in the macaque, we devised protocols for the macaque, and then extended to the human. We incorporated these protocols into a common space framework (13,14) and assessed their efficacy in predicting subcortical nuclei across species based on their connectivity patterns.

Methods: Tractography protocols for 7 subcortical bundles were defined using a standardised approach (9). They were first defined for the macaque brain and then transferred to the human using correspondingly defined landmarks. Each protocol included a unique combination of anatomically-defined masks, delineated in standard macaque space (F99), chosen based on literature descriptions of the tracts (eg. macaque tract-tracer studies). Protocols included the amygdalofugal tract (AMF), anterior commissure, sensorimotor and frontal cortico-striatal bundle (STB) / extreme capsule (EC), sensorimotor and frontal Muratoff Bundle (MB)/Subcallosal Fasciculus. Even if not a cortico-subcortical bundle, we included the extreme capsule (EmC) that runs close to the putamen connecting the insula and frontal cortices. These protocols were added to our standardised set of cross-species XTRACT protocols of mainly cortico-cortical bundles (9,12). Using dMRI data from 6 ex-vivo rhesus macaque brains (13) (available through PRIME-DE) and 50 unrelated HCP subjects (15) we performed tractography in human and macaque. We evaluated the new protocols in 2 ways. First, we assessed if the addition of subcortical bundles allowed identification of cross-species similarities of subcortical nuclei, based on their connectivity patterns to respective landmark bundles. KL-divergence was used as a measure of divergence as in (13,14). Then, we explored if including subcortical tracts increases predictability of cortical areas and translation of cortical maps across species. We used measured T1/T2 (myelin) maps for human and macaques and assessed if subcortical connections improve predictability of one from the other (12,13).

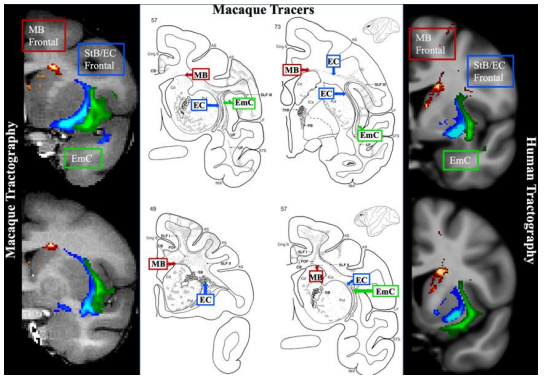

Figure 1 *Tractography and tracer results. MB: Muratoff bundle/Subcallosal fasciculus; StB/EC: Striatal bundle/external capsule; EmC: extreme capsule. Tracer image adapted from Schmahmann & Pandya, 2009.*

Proffered Talks Session 3

Results/Discussion: Fig.1 shows examples of tractography reconstructions relative to bundles identified by chemical tracing, and how their relative positions are preserved across macaques and humans (e.g. EmC is more lateral than the EC, MB is at the dorsal tip of the caudate). Fig.2 shows maximum intensity projections of the reconstructed tracts. Using the similarity of connectivity patterns of subcortical nuclei to WM tracts, we identified corresponding nuclei between humans and macaques (Fig.3) when considering subcortical tracts (blue dashed line, Fig.3A), compared to not using them (red dashed line). For instance, human putamen has more similar connectivity (lower divergence) to macaque putamen, with STBs contributing to their connectivity profile, compared e.g. to macaque hippocampus or thalamus that connect to other bundles. Similarly, we used the cross-species similarity of connectivity patterns throughout the cortex to translate cortical myelin maps. Our myelin map prediction was improved in both species when considering subcortical tracts (Fig. 4, r=0.8 vs 0.74).

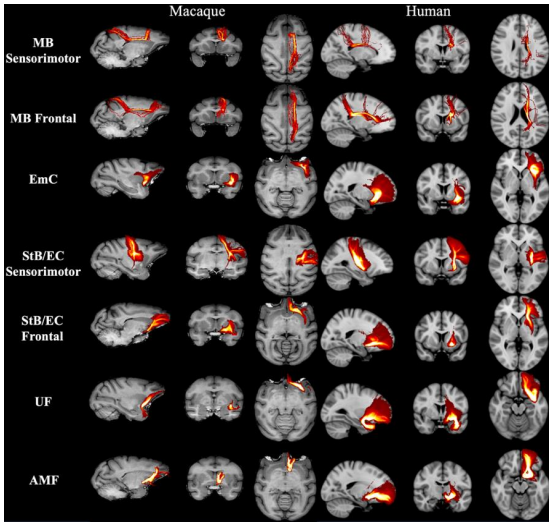

Figure 2. *Maximum intensity projections of the new subcortical bundles for macaques and humans. Averages of 6 animals and 50 human subjects.*

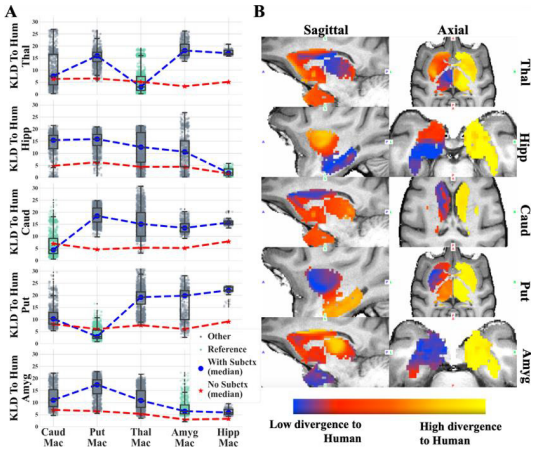

Figure 3. *KL divergence between corresponding human and macaque subcortical ROIs. (A) KL-Divergence values of macaque to human subcortical nuclei, when new subcortical tracts are included (blue dashed line) vs not (red dashed line). (B) KLD maps in the macaque for human nuclei (each row for a different human nucleus – left hemisphere).*

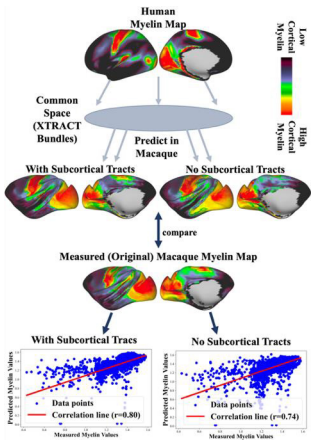

Figure 4. *Predicted macaque myelin maps from human ones, based on similarity of connectivitity patterns to WM tracts. Prediction is better with the addition of subcortical tracts.*

Acknowledgements: SA, SW and SNS are supported by an ERC Consolidator grant (101000969).

References

1. Haber SN. Corticostriatal circuitry. Dialogues Clin Neurosci. 2016 Mar 31;18(1):7–21.
2. Chumin EJ, Faskowitz J, Esfahlani FZ, Jo Y, Merritt H, Tanner J, et al. Cortico-subcortical interactions in overlapping communities of edge functional connectivity. NeuroImage. 2022 Apr;250:118971.
3. Heller AS. Cortical-Subcortical Interactions in Depression: From Animal Models to Human Psychopathology. Front Syst Neurosci [Internet]. 2016 Mar 7 [cited 2024 Jun 27];10. Available from: http://journal.frontiersin.org/Article/10.3389/fnsys.2016.00020/abstract
4. Weerasekera A, Ion-Mărgineanu A, Nolan GP, Mody M. Subcortical-cortical white matter connectivity in adults with autism spectrum disorder and schizophrenia patients. Psychiatry Res Neuroimaging. 2024 Jun;340:111806.
5. Jbabdi S, Sotiropoulos SN, Haber SN, Van Essen DC, Behrens TE. Measuring macroscopic brain connections in vivo. Nat Neurosci. 2015 Nov;18(11):1546–55.
6. Jbabdi S, Lehman JF, Haber SN, Behrens TE. Human and Monkey Ventral Prefrontal Fibers Use the Same Organizational Principles to Reach Their Targets: Tracing versus Tractography. J Neurosci. 2013 Feb 13;33(7):3190–201.
7. Catani M, Howard RJ, Pajevic S, Jones DK. Virtual in Vivo Interactive Dissection of White Matter Fasciculi in the Human Brain. NeuroImage. 2002 Sep;17(1):77–94.
8. Wakana S, Jiang H, Nagae-Poetscher LM, van Zijl PCM, Mori S. Fiber Tract–based Atlas of Human White Matter Anatomy. Radiology. 2004 Jan;230(1):77–87.
9. Warrington S, Bryant KL, Khrapitchev AA, Sallet J, Charquero-Ballester M, Douaud G, et al. XTRACT - Standardised protocols for automated tractography in the human and macaque brain. NeuroImage. 2020 Aug;217:116923.
10. de Schotten MT, Dell'Acqua F, Forkel SJ, Simmons A, Vergani F, Murphy DGM, et al. A lateralized brain network for visuospatial attention. Nat Neurosci. 2011 Oct;14(10):1245–6.
11. Folloni D, Sallet J, Khrapitchev AA, Sibson N, Verhagen L, Mars RB. Dichotomous organization of amygdala/temporal-prefrontal bundles in both humans and monkeys. eLife. 2019 Nov 5;8:e47175.
12. Assimopoulos S, Warrington S, Bryant KL, Pszczolkowski S, Jbabdi S, Mars RB, et al. Generalising XTRACT tractography protocols across common macaque brain templates. Brain Struct Funct [Internet]. 2024 Feb 23 [cited 2024 Jun 27]; Available from: https://link.springer.com/10.1007/s00429-024-02760-0
13. Mars RB, Sotiropoulos SN, Passingham RE, Sallet J, Verhagen L, Khrapitchev AA, et al. Whole brain comparative anatomy using connectivity blueprints. eLife. 2018;7:1–15.
14. Warrington S, Thompson E, Bastiani M, Dubois J, Baxter L, Slater R, et al. Concurrent mapping of brain ontogeny and phylogeny within a common space: Standardized tractography and applications. Sci Adv. 2022 Oct 21;8(42):eabq2022.
15. Van Essen DC, Smith SM, Barch DM, Behrens TEJ, Yacoub E, Ugurbil K. The WU-Minn Human Connectome Project: An overview. NeuroImage. 2013 Oct;80:62–79.

The effects of maternal iron levels on the early development of white matter microstructure in the superior longitudinal fasciculus

Katie Smith, Simone R. Williams, Jessica E. Ringshaw, Michal R. Zieff, Chloë A. Jacobs, Layla Bradford, Khula South Africa Data Collection Team, Derek K. Jones, Kirsty Donald*, Carolyn B. McNabb

*Corresponding author: kirsty.donald@uct.ac.za

Introduction: Iron deficiency is the most common nutritional deficiency worldwide (World Health Organisation, 2020; https://www.who.int/health-topics/anaemia), and is prevalent amongst pregnant women, posing significant risks to optimal brain development in their children. This micronutrient deficiency may cause effects on child neurodevelopment, leading to negative consequences on learning and performance in school. Even with the use of standard dietary management, iron deficiency may persist, with long-term impacts on brain development and behavioral outcomes. Research has identified poor cognitive and neurodevelopmental outcomes in children exposed to low maternal iron levels [1], with iron deficiency in early childhood associated with neurocognitive deficits in late adolescence [2].

A recent study investigating the effects of iron deficiency across childhood and adolescence revealed that lower haemaglobin concentration (an indicator for iron levels) was associated with worse cognitive performance and lower fractional anisotropy (an indicator of white matter integrity) in the superior longitudinal fasciculus (SLF) and uncinate fasciculus [3]. The SLF develops slowly throughout the first 2 years of life [4] and could be particularly susceptible to the impacts of low maternal iron levels. Evidence of the SLF's role in executive functioning [5], and its susceptibility to maternal iron deficiency suggests the SLF could provide a link between maternal iron deficiency and poor cognitive outcomes in children.

Methods: In this study, we explore a unique dataset comprising diffusion-weighted imaging (DWI) MRI scans from children in South Africa, where nutritional risk is high. Scans were collected in children at 3-months of age (N=17) and combined with exposure measures of maternal haemoglobin (Hb) and ferritin, as indicators of maternal iron levels. DWI acquisition parameters include a voxel size of 1.5mm^3, phase encoding directions (A>P and P>A), 104 diffusion directions per phase, repetition time (TR) of 3272ms, echo time (TE) of 101.2ms, and b-values ranging from 0 to 2000 s/mm^2.

The imaging data were preprocessed using multi-parametric principal component analysis (MPPCA [6]) for denoising and slice-wise outlier detection (SOLID [7]) on un-merged DWI data, susceptibility-induced distortion correction, eddy current, and motion correction [8], followed by multi-shell multi-tissue constrained spherical deconvolution [9]. Subsequent diffusion tensor imaging, tract segmentation and tractometry, including fractional anisotropy (FA), mean diffusivity (MD), and radial diffusivity (RD) analyses, were conducted. We used linear regression analysis in R to examine the relationship between iron deficiency (measured using maternal haemaglobin [Hb] and ferritin levels) and white matter microstructure (fractional anisotropy [FA], mean diffusivity [MD] and radial diffusivity [RD]).

Results: Results suggest that there is no significant correlation between maternal Hb levels and any mean DTI measures in the SLF at 3 months of age (FA: $F(1, 11) = 1.429$, $p = 0.257$, MD: $F(1, 11) = 0.182$, $p = 0.678$ and RD: $F(1, 11) = 0.250$, $p = 0.628$. Similarly, we show no significant correlation between maternal ferritin levels and all mean SLF DTI measures (FA: $F(1, 11) = 0.067$, $p = 0.801$, MD: $F(1, 11) = 0.008$, $p = 0.932$, RD: $F(1, 11) = 0.016$, $p = 0.902$).

Discussion: These findings suggest that, at 3-months, maternal iron (as measured by Hb and ferritin) does not have a measurable impact on the microstructure of white matter in the SLF of infants in this small group. These preliminary findings provide initial insights into the effects of maternal iron deficiency on white matter microstructure in the SLF, laying the foundation for examining longitudinal progression throughout early childhood, across additional timepoints and brain regions.

Acknowledgements:
The Khula Study is supported by funding from the Wellcome Leap 1kD programme (The First 1000 Days) [222076/Z/20/Z].

References:

[1] Georgieff MK. Maternal gestational iron status and infant haematological and neurodevelopmental outcomes. BJOG: An International Journal of Obstetrics and Gynaecology. 2023;130(Suppl 3):92–98. https://doi.org/10.1111/1471-0528.17612

[2] Lukowski AF, Koss M, Burden MJ, Jonides J, Nelson CA, Kaciroti N, et al. Iron deficiency in infancy and neurocognitive functioning at 19 years: evidence of long-term deficits in executive function and recognition memory. Nutritional Neuroscience. 2010;13(2):54–70. https://doi.org/10.1179/147683010X12611460763689

[3] Larsen B, Baller EB, Boucher AA, Calkins ME, Laney N, Moore TM, et al. Development of iron status measures during youth: associations with sex, neighborhood socioeconomic status, cognitive performance, and brain structure. The American Journal of Clinical Nutrition. 2023;118(1):121-131. https://doi.org/10.1016/j.ajcnut.2023.05.005

[4] Zhang J, Evans A, Hermoye L, Lee SK, Wakana S, Zhang W, et al. Evidence of slow maturation of the superior longitudinal fasciculus in early childhood by diffusion tensor imaging. NeuroImage. 2007;38(2):239-47. https://doi.org/10.1016/j.neuroimage.2007.07.033

[5] Ribeiro M, Yordanova YN, Noblet V, Herbet G, Ricard D. White matter tracts and executive functions: a review of causal and correlation evidence. Brain. 2024;147(2):352-371. https://doi.org/10.1093/brain/awad308

[6] Veraart J, Fieremans E, Novikov DS. Diffusion MRI noise mapping using random matrix theory. Magnetic Resonance in Medicine. 2016;76(5):1582-93.

[7] Sairanen V, Leemans A, Tax CM. Fast and accurate Slicewise OutLIer Detection (SOLID) with informed model estimation for diffusion MRI data. NeuroImage. 2018;181:331-46.

[8] Andersson JL, Skare S, Ashburner J. How to correct susceptibility distortions in spin-echo echo-planar images: application to diffusion tensor imaging. NeuroImage. 2003;20(2):870-88.

[9] Jeurissen B, Tournier JD, Dhollander T, Connelly A, Sijbers J. Multi-tissue constrained spherical deconvolution for improved analysis of multi-shell diffusion MRI data. NeuroImage. 2014;103:411-26.

Comparison of Susceptibility Source Separation Methods without R_2

Patrick S. Fuchs, Matthew T. Cherukara, Karin Shmueli
Department of Medical Physics and Biomedical Engineering, University College London

Introduction: Susceptibility source separation methods allow separation of diamagnetic (negative) and paramagnetic (positive) magnetic susceptibility sources co-located in a voxel. This is possible due to the distinct effects of susceptibility on the tissue relaxation rate (R_2') and on the magnetic field (ΔB). Sources of opposing sign cancel each other out in their contribution to the magnetic field inhomogeneity, but their contributions sum in shortening the relaxation rate.

The relationship between susceptibility and relaxation rate however is not straightforward. This means that, unless the transverse relaxation rate R_2 is mapped separately, to allow direct estimation of R_2' from the R_2^* relaxation rate, assumptions need to be made about the contribution of the susceptibility to R_2^*. In many clinical applications there may not be matched R_2 or spin-echo acquisitions. In these cases, there are currently four published algorithms that allow for an approximate separation of paramagnetic and diamagnetic sources. These are: the DECOMPOSE algorithm from Chen et al.[1], χ-separation and χ-sepnet by Shin et al.[2], and QSM-ARCS by Kan et al.[3]. Of these, all except for the most recently published QSM-ARCS are publicly available. In this abstract, we compared the available algorithms on a 12-echo and a 5-echo dataset to investigate how well their different approaches relate and highlight some potential caveats of the respective methods.

Methods: The methods were compared using two acquisitions with a different number of echoes. We acquired 3D-GRE using both 12 echoes and 5 echoes on a 3T Prisma system (Siemens AG, Erlangen, Germany) in a healthy volunteer with prior approval from our local ethics committee during a single scan session. The acquisition parameters were: 1 mm^3 isotropic resolution, 15° flip angle, 3-fold parallel imaging acceleration, with a 192×256×176 mm field of view. Echo times were (TE_{first}/ΔTE/TE_{last}) 2.03/1.59/30 and 5/7/38 ms with a bandwidth of 890 Hz/pix and 280 Hz/pix for the 12 and 5-echo acquisitions, respectively. For anatomical segmentation a T_1 weighted MPRAGE acquisition with 1 mm^3 isotropic resolution was acquired. Since χ-sepnet essentially incorporates a QSMnet[4]-like reconstruction in the separation algorithm and it has been shown that DECOMPOSE is sensitive to the dipole inversion algorithm choice[5] all data were processed using the pipeline provided with χ-sepnet: Laplacian based phase unwrapping[6], V-SHARP background field removal[7] using a mask generated with FMRIB's brain extraction tool[8] (BET), and QSMnet to compute input susceptibility maps. As χ-separation and χ-sepnet use a combined local field map input (as opposed to separate echoes for DECOMPOSE) the multi-echo phase was combined using non-linear fitting[9] from the MEDI Toolbox prior to the processing described above. To generate the proxy R_2' maps used in χ-separation and χ-sepnet, R_2^* maps were computed using ARLO[10]. Both algorithmic variations of χ-separation are included separately ("MEDI+0", and "iLSQR" based regularisation, these are not the input QSM methods). All algorithms were run with their default parameters.

To compare the maps several brain regions of interest were segmented. The thalamus, putamen, caudate, globus pallidus and substantia nigra were segmented using MRICloud[11], and the corpus callosum was segmented using FreeSurfer[12] on the T_1 image as it is optimal for white matter.

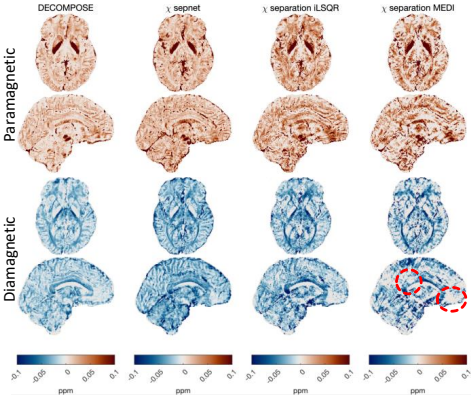

Figure 1 Axial and sagittal slices of the four different source separation algorithms (columns). Paramagnetic (positive) sources at the top, and diamagnetic (negative) sources at the bottom. Data are shown for the 5-echo acquisition. Red circles denote artifacts.

Results: Figure 1 shows a visual comparison of the outputs from the various methods. Figure 2 shows ROI comparisons for four primarily paramagnetic and two primarily diamagnetic regions of interest.

Discussion and Conclusions: Figure 1 shows that the MEDI based χ-separation algorithm suffers from artefacts (highlighted with red dashed circles), originating near the nasal cavity. Further, in the frontal lobe the separated maps look like thresholded bulk susceptibility maps (not shown). This results in no clear delineation of the substantia nigra which is corroborated in Figure 2 where the variance in the substantia nigra is much larger than the variance of any of the other approaches.

The other approaches yield similar visual results, with DECOMPOSE and χ-sepnet appearing least noisy, and χ-sepnet having a notably higher contrast in the diamagnetic component compared to DECOMPOSE. This contrast difference is not reflected in the ROI statistics in Figure 2 which suggest that χ-separation (especially the χ-separation iLSQR based method) yields better apparent separation, that is higher paramagnetic and more strongly diamagnetic (lower) mean values, when compared to the other approaches and the QSM. χ-separation does come with an increased variance, which corroborates the lower visual quality of these maps.

Without a ground truth it is not possible to compare the accuracy of the models. In terms of precision, χ-sepnet generally provides the lowest variance within these ROIs, likely due to its powerful machine-learning-based denoising. DECOMPOSE shows the lowest sensitivity to the number of echoes but takes much longer to compute (multiple hours) χ-sepnet is computationally the fastest, with χ-separation in between those.

Acknowledgements: PSF and KS are funded by European Research Council Consolidator Grant DiSCo MRI SFN 770939, MTC was supported by Cancer Research UK Multidisciplinary Award 24348.

References

[1] J. Chen, N.-J. Gong, K. T. Chaim, M. C. G. Otaduy, and C. Liu, *NeuroImage*, vol. 242, p. 118477, Nov. 2021.
[2] H.-G. Shin *et al.*, *NeuroImage*, vol. 240, p. 118371, Oct. 2021.
[3] H. Kan, Y. Uchida, S. Kawaguchi, H. Kasai, A. Hiwatashi, and Y. Ueki, *NeuroImage*, vol. 296, p. 120676, Aug. 2024.
[4] J. Yoon *et al.*, *NeuroImage*, vol. 179, pp. 199–206, Oct. 2018.
[5] P. Fuchs, J. Chen, O. C. Kiersnowski, R. Murdoch, C. Liu, and K. Shmueli, in *Joint Annual Meeting ISMRM-ESMRMB & ISMRT 32st Annual Meeting*, Toronto, Canada, 2023.
[6] D. Zhou, T. Liu, P. Spincemaille, and Y. Wang, *NMR Biomed.*, vol. 27, no. 3, pp. 312–319, Mar. 2014.
[7] W. Li, B. Wu, and C. Liu, *NeuroImage*, vol. 55, no. 4, pp. 1645–1656, Apr. 2011.
[8] S. M. Smith, *Hum. Brain Mapp.*, vol. 17, no. 3, pp. 143–155, Nov. 2002.
[9] T. Liu, C. Wisnieff, M. Lou, W. Chen, P. Spincemaille, and Y. Wang, *Magn. Reson. Med.*, vol. 69, no. 2, pp. 467–476, Feb. 2013.
[10] M. Pei *et al.*, *Magn. Reson. Med.*, vol. 73, no. 2, pp. 843–850, Feb. 2015.
[11] S. Mori *et al.*, *Comput. Sci. Eng.*, vol. 18, no. 5, pp. 21–35, Sep. 2016.
[12] Available: http://surfer.nmr.mgh.harvard.edu/

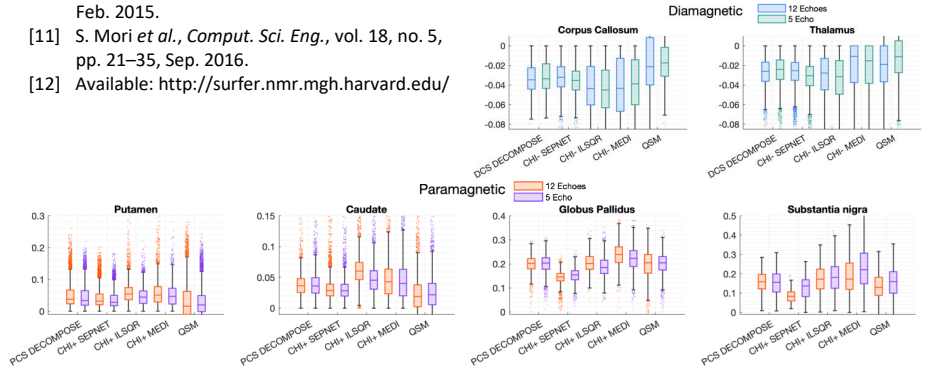

Figure 3 Box plots comparing model outputs for four paramagnetic and two diamagnetic deep brain structures. QSM denotes the input QSMNet reconstruction used in the χ-separation iLSQR and MEDI approaches. DCS: diamagnetic component susceptibility and PCS: paramagnetic component susceptibility.

Constrained Model-based Relaxation Parameter Mapping using Balanced Steady State Free Precession

Zimu Huo[1], Minghao Zhang[2], Yiyun Dong[3], Joshua Kaggie[1], Pete Lally[4], Neal Bangerter[5], Michael Hoff[6], Martin Graves[1]

1. Department of Radiology, University of Cambridge. 2. Wolfson Brain Imaging Centre, University of Cambridge. 3. Department of Physics, University of Washington. 4. Department of Bioengineering, Imperial College London. 5. Department of Electrical and Computer Engineering, Boise State University. 6. Radiology and Biomedical Imaging, University of California, San Francisco.

Introduction: In balanced steady state free precession (bSSFP), the real and imaginary components of the steady-state transverse magnetization form an ellipse across phase cycles on the complex plane. Quantitative parameters may be derived using analytical expressions based on the geometric properties of this ellipse using a method referred to as PLANET[1]. However, voxel-wise fitting is sensitive to additive noise, leading to inaccuracies.

We propose estimating relaxation parameters as a constrained nonlinear least square problem subject to data consistency costs in *k*-space to improve its noise robustness. Unlike traditional methods that extract quantitative relaxation parameters pixel by pixel, our approach leverages global information by jointly estimating T_1 and T_2 across the entire image and assessing reconstruction errors in k-space. Additionally, it supports flexible regularization options, such as total variation, which further mitigates noise sensitivity.

Theory: In this work, we aim to cast the parameter mapping as a constrained nonlinear optimization problem of the standard form:

$$\text{minimize } C(T_1, T_2, M_0, B) = (F \cdot M(T_1, T_2, M_0, B_0) - y)^2 + \lambda R(T_1, T_2, M_0, B_0) \text{ st: } p_i = 0, q_i < 0$$

Here, y signifies the collected data, F denotes the linear Fourier transform operator, and M is a nonlinear operator denoting the bSSFP steady state magnetization at TE. The goal is to jointly estimate the T_1, T_2, M_0, and B_0 maps that best align with the acquired *k*-space measurement y. p is an equality constraint and q is an inequality constraint on the parameter range. For example, T_1 and T_2 values should be non-negative, and T_1 is always greater than or equal to T_2 in biological tissues. R is an optional regularization function and λ is the regularization parameter. To accelerate the optimization, the analytical gradient and Hessian is provided to the optimization algorithm:

$$\partial C = (\Phi \cdot \partial M)^H \cdot (F \cdot M - y) = (\Phi \cdot J)^H (F \cdot M - y)$$

$$\partial^2 C = (\Phi \cdot J)^H \cdot (\Phi \cdot J) + (\Phi \cdot \nabla J)^H \cdot (F \cdot M - y)$$

J is the Jacobian matrix of the bSSFP steady state equation. $\Phi_{i,j}$ is the Fourier basis function and defined as $\Phi_{i,j} = F\delta_{i,j}$. The δ symbol denotes a 2D Kronecker delta function, resulting in a matrix with a 1 at position (i,j) and 0 elsewhere. Our approach is different by performing the parametric fitting in k-space, where voxel information is correlated through Fourier basis functions. Intuitively, If there exists an overestimated T_1 due to noise for a given voxel, this will propagate to k-space via the Fourier basis function and have a strong penalty in the data consistency cost.

Methods: To evaluate noise sensitivity, we perform a Monte Carlo simulation by randomly generating T_1, T_2, and M_0 on a 16 by 16 image patch. T_1 is generated from 100 ms to 3000 ms, T_2 ranges from 1 ms and is upper bounded by the generated T_1 value, and M_0 values range from 0 to 2. B_0 map is generated based on low frequency noise in k-space to create smooth and slowly varying modulations in the image domain. We used a flip angle of 30 degrees, TR of 10 ms, TE of 5 ms. We used conservatively high values of TR to yield a worst-case scenario for banding artifacts. We simulated various datasets of 6-10 phase cycles with an increment of 2. The Monte Carlo simulation is repeated 5000 times for each combination of SNR and phase cycles. In the second simulation, we apply total variation as the regularization term on the T_1 and T_2 maps to investigate its effects on a simulated uniform phantom. The optimization is implemented in MATLAB.

Figure 1. Noise Sensitivity Analysis. The conventional approach fits each pixel individually across the phasecycle dimension (e.g., fitting through 6 complex data points for 6 phase cycles). In contrast, our method simultaneously fits the entire image by utilizing the entire k-space data across all phase cycles.

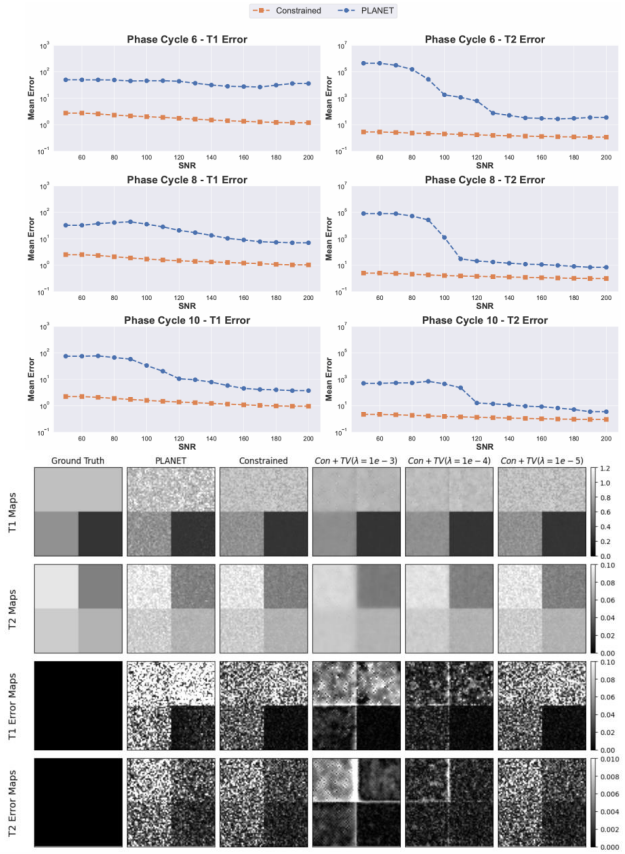

Figure 2. Effect of Total Variation. In this simulation, total variation leverages neighboring pixels to better inform the fitting process, further reducing noise sensitivity.

Results: In Figure 1, the constrained method consistently shows lower mean errors in T_1 and T_2 estimations across all SNR levels, outperforming the gold standard PLANET method. Figure 2 shows the effect of the total variation. This simulation serves as a proof of concept, illustrating that these regularization techniques can effectively guide the reconstruction process similar to what is observed in image optimization tasks.

Discussion: The proposed method can be extended to multiple coils for parallel imaging. A key advantage is its ability to jointly solve for parameter maps by leveraging information across phase cycles and coils, effectively utilizing data redundancy. One limitation is the assumption of an ideal single-component relaxation model. Factors like diffusion, multi-compartment, and magnetization transfer can cause deviation and the steady state equation used in this work cannot fully capture this complexity[2]. It is possible, at least partially, to include these secondary effects into the model. Future work will include phantom and in vivo acquisitions to validate the results.

Conclusions: The proposed constrained model-based fitting approach demonstrates robustness to noise across various phase cycles and SNR levels and outperforms the gold standard PLANET method. This is due to 1) jointly solving parameter maps over an image, 2) constraining the search space, and 3) allowing additional regularizations.

References [1] Y. Shcherbakova. MRM, vol. 81, no. 3, pp. 1534–1552, Oct. 2018 [2] K. Miller. MRM, vol. 63, no. 2, pp. 385–395, Jan. 2010

Proffered Talks Session 4

Associations between Cerebrovascular Reactivity Delay and progression of Small Vessel Disease Features

Keelin N. Ridge[1,2], Emilie Sleight[3,4], Michael S. Stringer[1,2], Una Clancy[1,2], Carmen Arteaga[1,2], Daniela Jaime Garcia[1,2], Maria C. Valdés-Hernández[1,2], Francesca M. Chappell[1,2], Fergus N. Doubal[1,2], Michael J. Thrippleton[1,2], Joanna M. Wardlaw[1,2], on behalf of the Mild Stroke Study 3 study group
[1]Centre for Clinical Brain Sciences, University of Edinburgh, United Kingdom
[2]UK Dementia Research Institute at the University of Edinburgh, United Kingdom
[3]Ecole Polytechnique Fédérale de Lausanne, Lausanne, Switzerland
[4]CIBM Centre d'Imagerie Biomedicale, Geneva, Switzerland

Introduction: Small vessel disease (SVD) is a brain microvasculature disorder that causes many strokes plus cognitive decline, gait problems and depression [1]. It is characterised by brain structural alterations visible on magnetic resonance imaging (MRI), including lacunes, microbleeds, perivascular spaces (PVS) and white matter hyperintensities (WMH) [2,3]. Advanced MRI techniques also highlight functional abnormalities in SVD [4], including impaired brain blood vessel response (cerebrovascular reactivity, CVR) [5–7] to a vasodilatory stimulus. CVR can be measured using blood-oxygen-level-dependent (BOLD) MRI during hypercapnic gas administration [6,8]. CVR magnitude, the vasodilation extent, predicts WMH and PVS burden [9,10], but few studies have assessed how CVR delay, the latency of response, relates to SVD progression [11]. This study aimed to investigate the one-year longitudinal relationships between tissue-specific CVR delay, SVD-related imaging features and stroke recurrence in mild stroke.

Methods: We recruited individuals presenting with lacunar or cortical mild ischaemic stroke in Mild Stroke Study 3 (MSS-3) [12]. Within three months of index stroke, we performed 3T BOLD-MRI (TR/TE=1550/30ms; isotropic resolution=2.5mm^3) with 6% carbon dioxide (CO_2)-enriched gas challenge, monitoring end-tidal CO_2 ($EtCO_2$) throughout, as previously described [6]. In the same visit, and at one-year follow-up, we acquired structural MRI data to determine PVS volumes in the basal ganglia (BG) and centrum semiovale (CSO), brain and WMH volumes, lacune and microbleed count according to STRIVE-1 criteria [2,3]. We also recorded new MRI lesions and stroke/transient ischaemic attack (TIA) recurrence between visits. We performed least-squares linear regression [6,12] with variable delay between the mean BOLD signal in regions-of-interest (ROI) and $EtCO_2$ to assess CVR delay in subcortical grey matter (SGM), normal appearing white matter (NAWM) and white matter hyperintensity (WMH) using established processing methods [6,12]. We calculated total PVS volume by summing BG and CSO PVS volumes. We normalised volumes to intracranial volume (ICV) or ROI volume (PVS only) and log-transformed to base-10 to ensure normality of residuals. Finally, we defined a *new ischaemic event* variable by combining new focal MRI ischaemic lesion and stroke/TIA recurrence.

We performed univariable and multivariable statistical analyses in R. For the imaging variables, we implemented linear regression between the follow-up imaging feature (outcome) and regional CVR delay (independent). We corrected univariable analyses for baseline imaging feature, and additionally corrected multivariable analyses for baseline age, sex, mean arterial pressure (MAP), smoking status (current vs. ever vs. never), normalised WMH volume and hypertension, hypercholesterolaemia and diabetes diagnoses. For new MRI lesion, stroke/TIA and ischaemic event, we performed binomial logistic regression. Univariable models were corrected for normalised baseline WMH volume and multivariable models were additionally corrected for age, sex, MAP and, to avoid overfitting, a score combining smoking, hypertension, hypercholesterolaemia and diabetes status.

Results: We recruited 208 participants for CVR-MRI: 180 were included in this analysis (15/11/2: no CVR/poor data quality/no follow-up). We show the standardised regression coefficients/odds ratios (β/OR) and 95% confidence intervals (95%CI) from the multivariable analyses in forest plots (Figs. 1-2). Patients with longer baseline WMH delays had lower one-year BG, CSO and total PVS burden (total PVS volume ~ WMH delay [$\log_{10}$(%ROI)/s×10^{-4}]: regression coefficient (B)=-7.46, 95%CI=[-14.3, -0.0631], p=0.032), but no significant change in WMH volume. SVD burden differed little with NAWM and SGM delay (WMH volume ~ NAWM delay [$\log_{10}$(%ICV)/s×10^{-4}]: B=4.27, 95%CI=[-4.73, 13.3], p=0.35). Patients with new MRI or clinical ischaemic events (n=34) generally had longer baseline CVR delay (new ischaemic event ~ NAWM delay: OR=2.26, 95CI%=[1.45, 3.71], p=0.00059).

Discussion: Longer baseline CVR delays in WMH precede lower PVS burden after one-year, while longer NAWM and SGM delays are associated with stroke/TIA recurrence and new MRI lesions, mirroring CVR magnitude findings [10]. Our study is the first to explore longitudinal associations between CVR delay and SVD features in mild stroke, utilising highly-phenotyped patients and reproducible CVR protocol. Limitations include that the least-squares linear regression method systematically overestimates delay when input contrast-to-noise ratio is low [12], typical of WMH BOLD data. Moreover, WMH delays may be influenced by partial volume effects when ROI volume is small. Since our region-wise approach assumes tissue-wide delay homogeneity, pathologically significant variations in delay may not be captured. Finally, about 20% of patients had new clinical/MRI ischaemic events, which may have limited statistical power.

Conclusions: We found some links between baseline regional CVR delay in mild stroke and one-year PVS burden, and new clinical/MRI ischaemic events. However, delay values used in this analysis may be biased by processing method, particularly WMH delays. More robust computation strategies optimised for patient data are needed to better understand the role of CVR delay in SVD progression.

References

[1]Wardlaw, et al. *Lancet Neurol.* **18**, 684-96 (2019); [2]Wardlaw, et al. *Lancet Neurol.* **12**, 822-38 (2013); [3]Duering, et al. *Lancet Neurol.* **22**, 602-18 (2023); [4]van den Brink, et al. *Int. J. Stroke* **18**, 28-35 (2023); [5]Sleight, et al. *Stroke.* **54**, 2776-84 (2023); [6]Thrippleton, et al. *Int. J. Stroke* **13**, 195-206 (2018); [7]Blair, et al. *Neurology.* **94**, 2258-69 (2020); [8]Sleight, et al. *Front. Physiol.* **12**, 643468 (2021); [9]Sam, et al. *Ann. Neurol.* **80**, 277-85 (2016); [10]Sleight, et al. *Under review*; [11]Atwi, et al. *NMR Biomed.* **32**, e4064 (2019); [12]Clancy, et al. *Eur. Stroke J.* **6**, 81-8 (2021); [13]Sleight, et al. *Front Physiol.* **14**, 1070233 (2023)

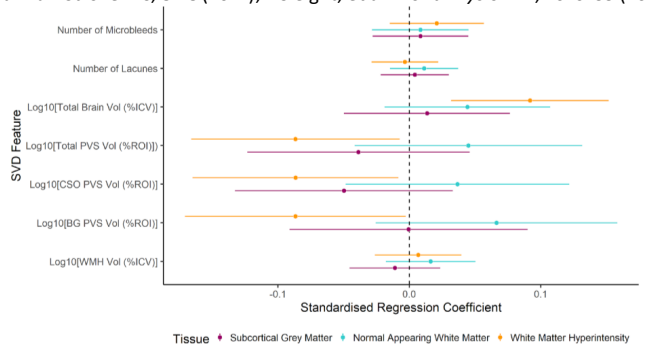

Fig. 1. β (dots) and 95%CI (horizontal lines) from multivariable linear regression between imaging markers and regional CVR delay. The vertical black line is at β = 0 (no association).

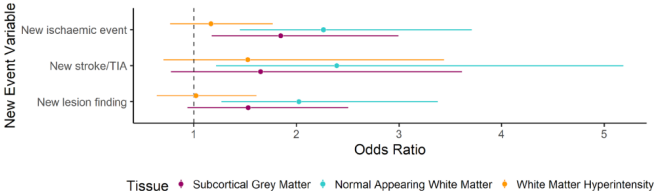

Fig. 2. OR (dots) and 95%CI (horizontal lines) from multivariable binomial logistic regression between new event variables and regional CVR delay. The vertical black line is at OR = 1 (no association).

Haematocrit-Corrected QSM + qBOLD Reveals Globally Elevated Brain Oxygen Extraction Fraction in Sickle Cell Anaemia

Mitchel Lee[1*], Isabelle Hawley[2*], Fenella Kirkham[2], Karin Shmueli[1]

*[1]Medical Physics and Biomedical Engineering, University College London, London, UK; [2]Developmental Neurosciences, Institute of Child Health, University College London, London, UK; *Joint First Authors*

Introduction: Sickle cell anaemia (SCA) is a genetic blood disorder characterized by abnormal sickle haemoglobin, which polymerizes in the deoxygenated state. Brain complications, such as stroke and cognitive deficits, occur secondary to microcirculatory obstruction, ischaemia, and inflammation [1]. A key marker of brain health is the cerebral metabolic rate of oxygen consumption ($CMRO_2$), determined by the product of cerebral blood flow (CBF), arterial oxygen content (CaO_2) and tissue oxygen extraction fraction (OEF) [2]. Autoregulatory mechanisms can lead to increases in CBF and/or OEF to maintain sufficient $CMRO_2$ levels for brain function in situations of reduced CaO_2 due to anaemia [3]. CBF increases are well documented in SCA [4], but studies of OEF in SCA show diverse results, primarily due to differences in calibration models used in T2-relaxation-under-spin-tagging (TRUST) methods [5,6].

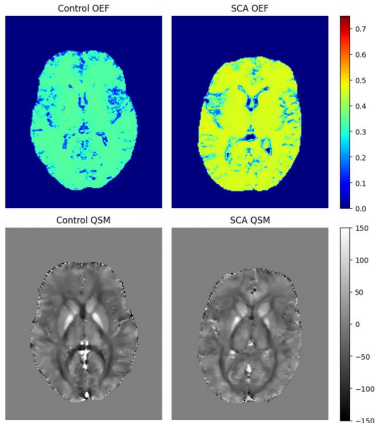

Figure 1: *Left: OEF map and QSM (ppb) in a representative control subject. Right: OEF map and QSM in a representative SCA patient*

QSM + qBOLD (QQ), a novel MRI technique for oxygen extraction fraction (OEF) mapping, models the contribution of paramagnetic deoxyhaemoglobin to both the phase (quantitative susceptibility mapping - QSM) and magnitude (quantitative blood-oxygen-level-dependent - qBOLD) information obtained from multi-echo gradient-echo (ME-GRE) sequences to estimate voxel-wise tissue OEF. This technique has been found to perform comparably to the gold standard [7]. An extension to the QQ method, QQ-CCTV [8], integrates temporal and tissue-type clustering with total variation regularization to enhance the signal-to-noise ratio (SNR).

This study used QQ-CCTV to investigate OEF changes in the brain in SCA, building on previous work with the paediatric subset of our cohort [9], and accounting for reduced haematocrit in SCA patients.

Methods: 90 SCA patients (18.0±9.9 years, 44 male) and 33 healthy age and race matched controls (18.9±10 years, 16 male) were imaged on a 3T Siemens Magnetom Prisma system with a 64-channel head RF coil. 3D ME-GRE images were acquired with parameters: TE_1 = 3ms, ΔTE = 4ms, 7 echoes, TR = 38ms, flip angle = 15°, resolution = 1.15 x 1.15 x 1.15 mm^3. T1-weighted MP-RAGE images were also acquired at 1 mm^3 resolution.

The QQ-CCTV algorithm was applied to estimate OEF maps and QSMs from the ME-GRE magnitude and phase data. QSMs were obtained using a MEDI toolbox pipeline, consisting of linear phase gradient correction, nonlinear field fitting, region-growing phase unwrapping, projection onto dipole fields (PDF) background field removal and CSF-referenced MEDI+0 dipole inversion [10]. The combined QSM and qBOLD cost function was then minimized to estimate venous blood oxygenation (Y_v), transverse relaxation rate (R_2), non-blood susceptibility (χ_{nb}), venous blood volume fraction (v) and initial signal intensity (S^0). OEF was estimated from Y_v as OEF = $1-Y_v/Y_a$, assuming arterial blood oxygenation (Y_a) to be 0.98 for both groups.

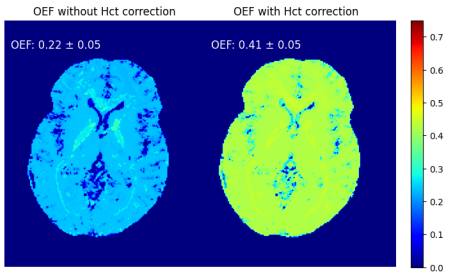

Figure 1: *Left: OEF map calculated in a 15-year-old female SCA patient using default haematocrit value (47%). Right: OEF map calculated in the same patient using measured venous haematocrit of 26%. The mean whole-brain OEFs (mean±sd) are shown beside each map.*

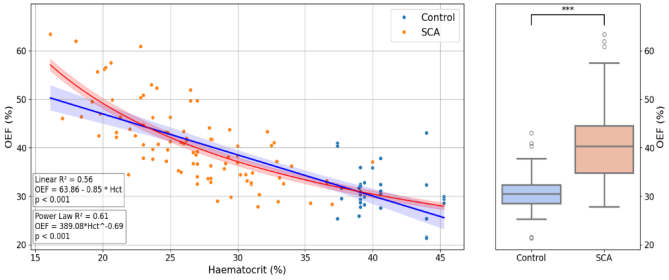

Figure 2: *Left: Whole-brain OEF as a function of Hct with fitted linear (blue) and power law (red) curves and 95% confidence intervals. Right: Box plot of whole brain OEF in SCA patients and controls, with (***) indicating statistical significance at p<0.001.*

For the SCA patients, venous haematocrit (Hct_v) was obtained from the closest blood test to the MRI scan. Measurements of Hct_v were not available for the controls in this study, so reference values were obtained from the literature [11]. Capillary haematocrit (Hct) was estimated as a constant fraction of Hct_v, taken to be Hct = 0.759 * Hct_v for both SCA patients and controls. We investigated the relationship between Hct_v and mean whole-brain OEF by linear regression and compared OEF values between patients and controls. Given OEF's expected inverse variation with Hct (OEF ∝ 1/Hct), a power law model was also fitted.

Results: SCA patients had significantly lower haemocrit (26.6±4.9%) than controls (40.4±2.5%). Example SCA and control OEF maps and QSMs are shown in Figure 1. An SCA OEF map with and without haematocrit correction is shown in Figure 2, showing increased OEF throughout the brain when Hct is considered. Figure 3 shows the relationship between mean whole-brain OEF and Hct, with fitted linear and power law curves and parameters. Both models identified a significant negative relationship between OEF and Hct, with the power law exponent estimated at -0.69±0.05. Whole-brain OEF in SCA (40.9±7.9%) was significantly higher than in controls (30.9±4.9%), as depicted in Figure 3.

Discussion and Conclusions: We found significantly elevated OEF throughout the brain in SCA, with whole brain OEF measures agreeing with previous results from ASE OEF mapping studies [12,13]. The inclusion of measured haematocrit in the QQ model resulted in large increases in OEF in the SCA patients (Fig. 2) compared to our previous work [9]. The deviation of the exponent of the fitted power law model (Fig. 3) from -1 suggests that other QQ parameter changes in SCA may influence the OEF-Hct relationship. Future research will further investigate these relationships and apply this method to a separate SCA study with control haematocrit measurements, addressing the current study's limitation of estimated control Hct.

References

[1] Rees, David C et al. *Lancet*, vol. 376,9757 (2010): 2018-31. **[2]** Rodgers, Zachary B et al. *Journal of cerebral blood flow and metabolism*, vol. 36,7 (2016): 1165-85. **[3]** Wood, John C. *Blood* 2019; 133 (22): 2356–2358. **[4]** Stotesbury, Hanne et al. *Expert review of hematology* vol. 14,5 (2021): 473-491. **[5]** Bush, Adam M et al. *Magnetic resonance in medicine* vol. 80,1 (2018): 294-303. **[6]** Murdoch, Russell et al. *Frontiers in physiology* vol. 13 913443. 29 Aug. 2022 **[7]** Cho, Junghun et al. *Journal of cerebral blood flow and metabolism* vol. 41,7 (2021): 1658-1668. **[8]** Cho, Junghun et al. *Magnetic resonance in medicine* vol. 86,5 (2021): 2635-2646. **[9]** Hawley, Isabelle et al. *Proceedings of the 18th International Child Neurology Congress* (2024) **[10]** Liu, Zhe et al. *Magnetic resonance in medicine* vol. 79,5 (2018): 2795-2803. **[11]** Castro, O L et al. *Public health reports* vol. 102,2 (1987): 232-7. **[12]** Fields, Melanie E et al. *Neurology* vol. 90,13 (2018): e1134-e1142. **[13]** Fields, Melanie E et al. *Annals of neurology* vol. 88,5 (2020): 995-1008.

Enhancing brain activity mapping through multi-modal data fusion and explainable machine learning.

Jiri Benacek[1], Krish Singh[1], Derek Jones[1], David Marshall[2,3], Simon Rushton[4], Marco Palombo[1,3]
[1] Cardiff University Brain Research Imaging Centre, Cardiff University, Cardiff, UK
[2] School of Computer Science and Informatics, Cardiff University, Cardiff, UK
[3] School of Engineering, Cardiff University, Cardiff, UK
[4] School of Psychology, Cardiff University, Cardiff, UK

Introduction: Functional magnetic resonance imaging (fMRI) and magnetoencephalography (MEG) each have unique strengths and limitations. MEG provides neuronal activation measurements of milli-second precision and closely reflects neuronal activation but it has low spatial resolution (SR) and insensitivity to subcortical signals [1]. fMRI provides finer SR and can map activation in subcortical areas, but does so indirectly through blood-oxygen-level-dependent signal (BOLD) [2,3]. Combining fMRI and MEG data can leverage their complementary traits, but disparities in their signals present challenges [4,5,2]. This work aims to provide a first step towards a more comprehensive understanding of the interplay of the two functional imaging approaches. We used multimodal data to determine whether MEG recordings can be predicted and spatially upsampled by fMRI data, utilizing explainable machine learning (eML).

Methods: 16 volunteers underwent both MEG and fMRI scans, watching a 20-minute movie sequence [6] edited to feature a broad range of stimuli. BOLD responses were acquired with a 3T scanner using echo-planar imaging with SR ($3mm^3$) and images were registered to common space at $2mm^3$ and $6mm^3$. High resolution anatomical scans were collected for each participant ($1mm^3$), using a fast-spoiled gradient echo sequence. MEG recordings were taken using a 275-channel MEG system and filtered into functionally-specific frequency bands: delta (δ; 1-4Hz), theta (θ; 4-8Hz), alpha (α; 8-13Hz), beta (β; 13-30Hz), low-gamma (low-γ; 40-60Hz), and various high-γ bands ranging from 60-149Hz. Data at each frequency band were source-localized using synthetic-aperture magnetometry, with SR to match that of the fMRI data. MEG time-series were de-spiked, high-pass filtered, and convolved with the canonical haemodynamic response function to match the BOLD response. Group-level Tensorial Independent Component Analysis (TICA) [7] was used to decompose a multivariate signal into 25 (MEG) and 30 (fMRI) independent spatial maps to capture granular, yet specific networks. A series of Extreme Gradient Boosted tree regressors [8] were trained to predict MEG components from downsampled fMRI signals, and the best-performing models were subsequently used for upsampling MEG's SR at voxel-level by inputting higher-resolution fMRI components. Results were evaluated in terms of explained variance (R^2), mean squared error (MSE), and structure similarity index (SSI) [9] against spatial maps upsampled using trilinear interpolation from FSL's 'applywarp' [10], and trained models were explained with SHapley Additive exPlanations (SHAP) [11].

Results: Correlations of all fMRI-MEG pairings showed large amount of significant inter-modal linear relationships (Tab. 1), with 77.41% interactions remaining significant after Bonferroni correction (Fig. 1).

MEG component	fMRI component	Correlation	Corrected P-Value
f100to120-8	7	0.50	p < .001
lowGamma-11	17	0.50	p < .001
f140to149-2	15	0.47	p < .001
f140to149-2	5	0.46	p < .001
lowGamma-10	15	0.45	p < .001
Delta-3	5	0.44	p < .001
f60to80-18	15	0.44	p < .001
f80to100-2	7	0.44	p < .001
lowGamma-18	7	0.43	p < .001
Theta-7	10	0.43	p < .001
f140to149-2	10	0.42	p < .001
Alpha-15	5	0.42	p < .001
f120to140-21	28	0.42	p < .001
f80to100-11	18	0.42	p < .001
Beta-3	5	0.41	p < .001
Beta-1	1	0.41	p < .001
f120to140-14	7	0.41	p < .001
f80to100-6	28	0.41	p < .001
lowGamma-23	28	0.41	p < .001
Theta-7	5	0.40	p < .001
f60to80-19	17	0.40	p < .001
Alpha-15	10	0.40	p < .001

Tab. 1. *Pearson correlation coefficients (cutoff r=0.4) for inter-modal pairs of components from different MEG bands, and fMRI*

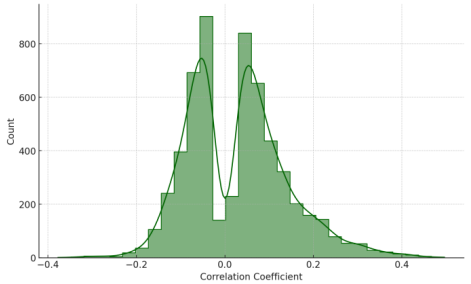

Fig. 1. *Histogram of correlation coefficients for all fMRI-MEG component pairings across bands*

Then, we pre-trained a model on $6mm^3$ data, using fMRI signals to predict each of the MEG components. This way, we modelled a component from low-γ (40-60Hz) band, positively (r=.43) correlated with early visual areas [12], here represented mainly by fMRI Component 7. After training, we inputted $2mm^3$ fMRI data and predicted MEG components in the upsampled $2mm^3$ SR. Figure 2a shows spatial maps and deviations between the maps at $6mm^3$ (MSE=.069; SSI=.87), and interpolated 2mm (MSE=.13; SSI=.80). Subfigures 2b and 2c show related SHAP feature importances, and top 4 predictors. The final model achieved R^2=.93 at 6mm, and R^2=.8 at 2mm.

Fig. 2. (a)*: Visualisation of component 18 from low-γ band (40-60Hz). From top: Original $6mm^3$ image, $6mm^3$ image predicted using fMRI input, Mean squared error map between original and predicted images, interpolated $2mm^3$ image, image resulting from fMRI-guided upsampling to 2mm, MSE between interpolated $2mm^3$ and predicted $2mm^3$.* ***(b)****: Shapley feature importances, quantifying the predictive power of the values used for modelling.* ***(c)*** *top 4 predictors for low-γ 18*

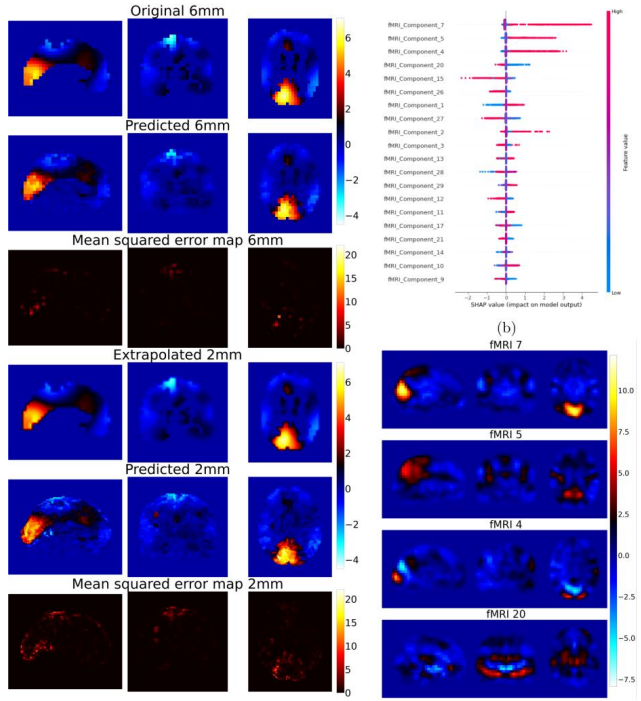

Discussion: The map upsampled using our model had high similarity to the interpolated image, and visual inspection showed higher specificity, as informed by fMRI. This data-guided approach provides an evidence-based alternative to purely algorithmic super-resolution of functional images. Additionally, the enhanced explainability of the models provided by SHAP values offers data-driven means of informing the electro-haemodynamic coupling discussion. However, the inter-modal relationships need to be interpreted with caution as predictivity alone does not necessarily reflect biological validity. Future efforts should focus not only on the overlapping relationships, but also on more thorough integration of their unique contributions by analysing all data streams in parallel, as well as targeted confirmatory evaluation of the formulated cross-modal functional relationships.

Conclusions: Our proof-of-concept model was able to exploit electro-neurovascular coupling between fMRI and MEG, with moderate inter-modal predictability. Using eML, we showed that it is possible to predict high-SR MEG signals using fMRI, with trained models providing additional data-driven insights into the strength and directionality of this relationship.

References

[1] A. Hillebrand and G. R. Barnes, "A quantitative assessment of the sensitivity of whole-head meg to activity in the adult human cortex," Neuroimage, vol. 16, no. 3, pp. 638–650, 2002.
[2] Z.-Q. Liu, G. Shafiei, S. Baillet, and B. Misic, "Spatially heterogeneous structure-function coupling in haemodynamic and electromagnetic brain networks," NeuroImage, vol. 278, p. 120276, 2023.
[3] D. Rangaprakash, R. L. Barry, and G. Deshpande, "The confound of hemodynamic response function variability in human resting-state functional mri studies," Frontiers in Neuroscience, vol. 17, p. 934138,2023.
[4] K. D. Singh, "Which "neural activity" do you mean? fmri, meg, oscillations and neurotransmitters," Neuroimage, vol. 62, no. 2, pp. 1121–1130, 2012.
[5] J. Daunizeau, H. Laufs, and K. J. Friston, "Eeg–fmri information fusion: biophysics and data analysis," EEG-fMRI: Physiological Basis, Technique, and Applications, pp. 511–526, 2010.
[6] M. G. Wilson, B. Broccoli, N. Purvis, R. Wade, and J. Logan, Skyfall. Sony Pictures Entertainment, 2012.
[7] C. F. Beckmann and S. M. Smith, "Tensorial extensions of independent component analysis for multi- subject fmri analysis," Neuroimage, vol. 25, no. 1, pp. 294–311, 2005.
[8] T. Chen and C. Guestrin, "Xgboost. a scalable tree boosting system. arxiv. 2016; 1603.02754 v3," 2023.
[9] Z. Wang, A. C. Bovik, H. R. Sheikh, and E. P. Simoncelli, "Image quality assessment: from error visibility to structural similarity," IEEE transactions on image processing, vol. 13, no. 4, pp. 600–612, 2004.
[10] M. Jenkinson, C. Beckmann, T. Behrens, M. Woolrich, and S. Smith, "Fsl," NeuroImage, vol. 62, no. 2, pp. 782–790, 2012.
[11] S. M. Lundberg and S.-I. Lee, "A unified approach to interpreting model predictions," in Advances in Neural Information Processing Systems 30 (I. Guyon, U. V. Luxburg, S. Bengio, H. Wallach, R. Fergus, S. Vishwanathan, and R. Garnett, eds.), pp. 4765–4774, Curran Associates, Inc., 2017.
[12] S. M. Smith, P. T. Fox, K. L. Miller, D. C. Glahn, P. M. Fox, C. E. Mackay, N. Filippini, K. E. Watkins, R. Toro, A. R. Laird, et al., "Correspondence of the brain's functional architecture during activation and rest," Proceedings of the national academy of sciences, vol. 106, no. 31, pp. 13040–13045, 2009.

Evidence for direct control of neurovascular function by circulating platelets in healthy older adults

Gabriella MK Rossetti*[1,2], Joanne L Dunster[3], Aamir Sohail[1], Brendan Williams[1], Kiera M Cox[3] Suzannah Rawlings[3], Elysia Jewett[1], Eleanor Benford[1], Julie A Lovegrove[3], Jonathan M Gibbins[3], Anastasia Christakou[1]

1.Centre for Integrative Neuroscience and Neurodynamics (CINN), University of Reading, UK

2.Department of Sport and Exercise Sciences, Manchester Metropolitan University, UK

3.Institute for Cardiovascular and Metabolic Research (ICMR), University of Reading, UK

Introduction: Platelets play a vital role in preventing haemorrhage through haemostasis, but complications arise when platelets become overly reactive, leading to pathophysiology such as athero-thrombosis. Elevated haemostatic markers are linked to dementia [1] and predict its onset in long-term studies [2]. Despite epidemiological evidence, the mechanism linking haemostasis with early brain pathophysiology remains unclear. Here, we aimed to determine whether a mechanistic association exists between platelet function and neurovascular function in healthy older adults.

Methods: Fifty-one healthy middle-aged and older adults (50-80 years) completed this cross-sectional study. We used a high throughput plate-based aggregation (PBA) assay and the Phenomic Analysis data analysis platform [3] to investigate the association between platelet reactivity and neurovascular function assessed by haemodynamic responses (HRF) to a visual stimulus. We incorporated experimental manipulations that targeted peripheral vascular reactivity (laser doppler imaging with iontophoresis of vasoactive agents) and cerebrovascular reactivity (hypercapnia, hypocapnia, resting cerebral blood flow) to determine whether any association could be attributed to systemic vascular effects, or direct interactions between platelets and the neurovascular unit.

Results: We show a direct association between platelet reactivity and neurovascular function that is independent of vascular reactivity and mechanistically specific. PBA differentiated neurovascular function in this general population sample (F=5.032, p=0.01). Higher platelet reactivity was associated with a shorter cerebral blood flow response to neural activity (HRF FWHM) in the visual cortex (r=-0.45, p=0.006, Fig. 1).

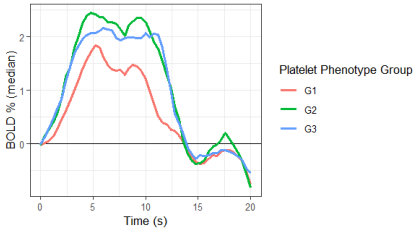

Fig 1. Platelet reactivity multiparameter phenotyping revealed associations with neurovascular function. Median haemodynamic response function (HRF) in the primary visual cortex (V1) for each platelet phenotype. Higher platelet reactivity (Group 1) was linked to shorter HRF full-width half maximum (FWHM) and smaller area under the curve (AUC).

Distinct platelet signalling mechanisms (Adenosine 5'-diphosphate [ADP], Collagen-Related Peptide [CRP], Thrombin Receptor Activator Peptide 6 [TRAP-6]) were directly associated with different physiological components of the haemodynamic response to neural (visual) stimulation (full-width half-maximum [FWHM], time to peak [TTP], area under the curve [AUC]). Platelet reactivity to ADP was selectively associated with HRF FWHM, while platelet reactivity to the collagen receptor agonist CRP was selectively associated with HRF TTP (Fig. 2). The association between platelet reactivity and neurovascular function was independent of systemic vascular function (mediating effect range -0.01-0.02; p≥0.39), suggesting platelet reactivity may directly affect neurovascular function (direct effect -0.44[-0.66;-0.22], p<0.001) (Fig. 3).

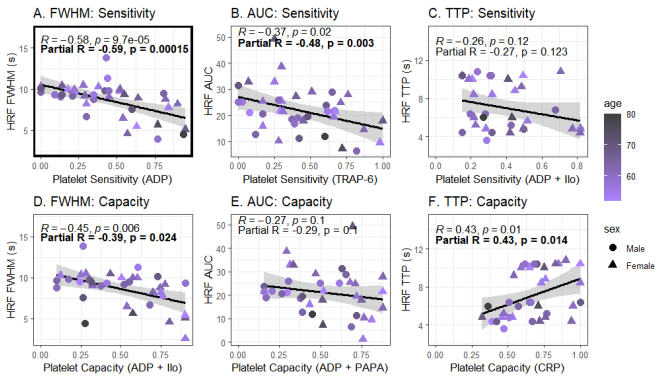

Fig 2. Platelet reactivity and neurovascular function relationships are mechanistically distinct. Different platelet signaling mechanisms (ADP, Collagen-Related Peptide, TRAP-6) were linked to various haemodynamic response components (FWHM, TTP, AUC) to visual stimulation. (A-F) show relationships between platelet reactivity measures (e.g., sensitivity to ADP, TRAP-6) and HRF parameters. Correlations accounting for age, sex, and BMI (partial R) were similar to the total correlations, indicating demographic variables did not affect the associations.

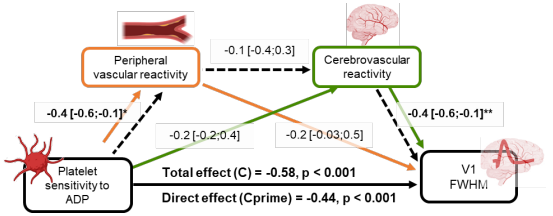

Fig 3. Systemic vascular function does not explain the platelet-neurovascular relationship: Serial mediation analyses. Eighteen models tested whether the association between platelet sensitivity to ADP and HRF FWHM, surviving FDR correction, was mediated by peripheral (M1) and cerebrovascular (M2) effects. No M1 and M2 combinations significantly explained the relationship between platelet sensitivity (ADP) and neurovascular response duration (HRF FWHM).

Discussion: This study is the first to directly link platelet reactivity with neurovascular function in humans. Individuals with higher platelet reactivity showed reduced haemodynamic responses to visual cortex activation, suggesting issues with vascular response matching energy demand in active brain regions, potentially contributing to neurodegeneration [4]. These findings align with previous research on altered neurovascular coupling in aging [5] and subjective cognitive decline [6].

Conclusions: This study challenges the belief that systemic vascular health alone determines neurovascular function, highlighting the role of circulating platelets. Understanding this link could advance our knowledge of early dementia pathophysiology and inform new therapeutic approaches.

References

[1] T.J. Quinn et al *J. Thromb. Haemost.* **9**, 1475–1482 (2011).
[2] J. Ramos-Cejudo et al *J. Am. Heart Assoc.* **11**, e023918 (2022).
[3] J. Dunster, J. et al *Blood Adv*. **5**, 4017–4030 (2021).
[4] B. V. Zlokovic *Nat. Rev. Neurosci.* **12**, 723–738 (2011).
[5] K. L. West et al *NeuroImage.* **188**, 198–207 (2019).
[6] L. Lu, G. Li, Z. Song, Z, Zhang and X. Tang *Neurosci. Inform.* **2**, 100093 (2022).

Age-trajectories of higher-order diffusion properties of major brain metabolites in cerebral and cerebellar gray matter using dMRS

Kadir Şimşek[1,2], Cécile Gallea[3,4], Guglielmo Genovese[6], Stephane Lehéricy[3,4], Francesca Branzoli[4,5], Marco Palombo[1,2] - *[1]Cardiff University Brain Research Imaging Centre (CUBRIC), School of Psychology, Cardiff University, Cardiff, United Kingdom; [2]School of Computer Science and Informatics, Cardiff University, Cardiff, United Kingdom; [3]Brain and Spine Institute - ICM, Team "Movement Investigations and Therapeutics", Paris, France; [4]INSERM U 1127, CNRS UMR 7225, Sorbonne University, Paris, France [5]Paris Brain Institute - ICM, Centre for Neuroimaging Research - CENIR, Paris, France;* [6]Center for Magnetic Resonance Research, Department of Radiology, University of Minnesota, Minneapolis, Minnesota, USA

Introduction: Healthy brain aging involves numerous functional and structural changes in the brain[1-5].

Diffusion-weighted MRS (dMRS) provides higher cell-type specificity[6–12], offering the opportunity to quantify alteration of both the cellular composition and microstructure with age. However, besides only a few works investigating brain metabolites changes in concentration[13,14] and apparent diffusion coefficient[15] in healthy aging, it is still unknown how other informative diffusion properties (e.g. apparent diffusional kurtosis) of brain metabolites change with aging. This work aims to provide the first normative age-trajectories of higher-order diffusion properties of major metabolites in the cerebral and cerebellar gray matter (GM) using dMRS.

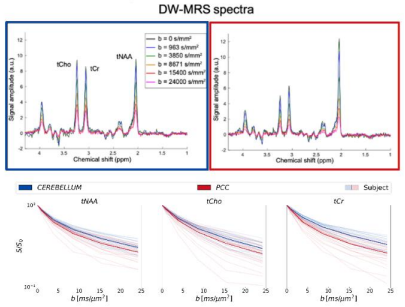

Fig.1:(Top) Exemplary DW-spectra after post processing, showing high spectral quality and SNR. (Bottom) diffusion signals obtained from LCModel fitting for all subjects (light) and cohort average signal (dark).

Methods: ***Data acquisition/processing****:* 25 healthy participants (age-range 25-80) were scanned on a 3T Siemens Prisma with 64-channel head coil, using a DW-semi-LASER (TE|TR = 125 ms |3 cardiac cycles)[16] in two region of interests (ROIs): cerebellum and posterior cingulate cortex (PCC). Metabolite DW-spectra (24 transients per b-value) were recorded with 6 b-values up to 24 ms/μm² (Δ=62.5 ms; δ=26.4 ms) using tetrahedral encoding. Post-processed spectra averaged[16] and then quantified using LCModel[17]. Signals at each b were direction-averaged and analyzed. ***Data analysis:*** We estimated kurtosis K by fitting the kurtosis representation[12,18] to the data up to b≤9 ms/μm² and the apparent intra-neurite axial diffusivity D_{intra} by fitting the astro-sticks model[12,19] to the data. In addition, we estimated intra-neurite apparent axial diffusivity D_{intra} and kurtosis K_{intra} by fitting to the data at all b-values a modified astro-sticks model that incorporates an effective intra-stick axial diffusivity defined as: $D_{eff}(D_{intra}, K_{intra}, b, \theta) = D_{intra}(1 - K_{intra} D_{intra} b cos^2\theta)$[11,20–22], where θ is the angle between the main axis of a given stick and the applied diffusion gradient. Here, K_{intra} quantifies non-Gaussian diffusion stemming from the spines and/or other hindering structures[20,21]. The numerical integration yields direction-averaged diffusion signal: $S/S_0 = \int_0^1 e^{-bD_{eff}cos^2\theta} d(cos\theta)$

Results: **Fig.1** illustrates diffusion signals for both ROIs. **Fig.2** reports that results of estimated model parameters for both ROIs. **Fig.3** depicts the normative age-trajectories of diffusion kurtosis and modified astro-stick model.

Discussion & Conclusion: Estimated metabolite K values in the PCC agree with literature[23–26]. Overall higher K and K_{intra} for tNAA agree with the expected higher spine density in cerebellum due to Purkinje cells and density packed granule cells [27]. Higher K and K_{intra} values for tCho in cerebellum are possibly due to the presence of highly-arborized Bergmann glia[28].

Overall, estimated apparent diffusivities do not present any significant changes with aging, in contrast to estimated mono-exponential ADCs in the literature[15], which might originate from different diffusion times and encoding scheme. The normative age-trajectories of metabolite diffusion properties reported here for the first time showing only significant increase in K_{intra} of tCho in PCC agree with literature[29], (which is not confounded by changes in the tissue composition).

This study offers previously unavailable normative age-trajectories of major brain metabolites diffusion properties in PCC and cerebellar GM. These provide benchmarks for identifying anomalies in the diffusion properties of major brain metabolites.

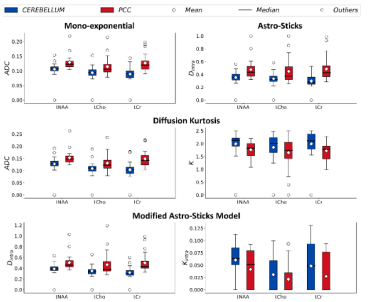

Fig.2: Estimated model parameters are shown in box-whiskers plot for all metabolites in both ROIs.

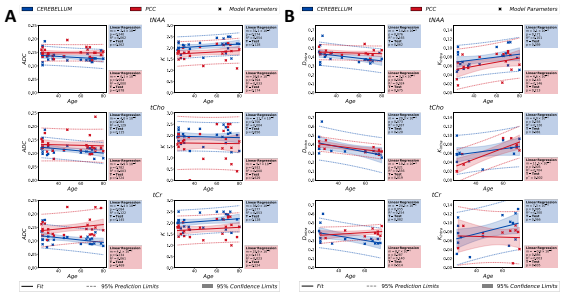

Fig.3: Age dependences of the estimated model parameters for kurtosis (ADC & K) in (A) and modified astro-stick model (D_{intra} & K_{intra}) in (B), obtained from studied metabolite signals, are depicted in the figure. For each brain region, a linear regression and an independent T-test are performed between two groups [age < 50 and age ≥ 50] to analyze statistical significance (p<0.00833) in the age-related variations of estimated parameters.*

Acknowledgements: *This work, KS and MP are supported by UKRI Future Leaders Fellowship (MR/T020296/2). This project has received funding d from Engineering and Physical Sciences Research Council (EPSRC EP/N018702/1). FB and CG acknowledge support from the programs 'Institut des neurosciences translationnelle' ANR-10-IAIHU-06 and 'Infrastructure d'avenir en Biologie Santé' ANR-11-INBS-0006. The authors would like to thank Dr. Edward J. Auerbach and Dr. Małgorzata Marjańska for providing us the dMRS sequence for the Siemens platform.*

References: 1. Feldman ML, et al. *Anat Embryol. 1975* 2. Benavides-Piccione R., etal. *Cerebral Cortex. 2013* 3. Segal M. *Nature Reviews Neuroscience 2005 4. Dickstein DL, et al. Neuroscience. 2013 5. Louis RJ, et al. Parkinsonism Relat Disord. 2014 6. Ronen Iet al. eMagRes 2015 7. Cao P et al. NMR Biomed. 2017 8. Palombo M, et al. Neuroimage. 2018 9. Vincent M, et al. Neuroimage. 2020 10. Palombo M, et al. PNAS. 2016 11. Palombo M, et al. MRM. 2017 12. Ligneul C, et al. MRM. 2023 13. Haga KK, et al. Neurobiol Aging. 2009 14. Cleeland C, et al. Neurosci Biobehav Rev. 2019 15. Deelchand DK, et al. Neurobiol Aging. 2020 16. Genovese G, et al. ISMRM, 2018 17. Provencher SW. MRM. 1993 18. Novikov DS, et al. MRM. 2018 19. Panagiotaki E, et al. Neuroimage. 2012 20. Sukstanskii AL, et al. J. Magn. Reson. 2008 21. Yablonskiy DA, et al. NMR Biomed. 2010 22. Palombo M, et al. Neuroimage. 2018 23. Ingo C, et al. Brain Struct Funct. 2018 24. Mougel E, et al. ISMRM 2022 25. Döring A, et al. ISMRM 2023 26. Genovese G, et al. NMR Biomed. 2021 27. Santamaria F, et al. Neuron. 2006 28. Sild M, et al. Neuroscientist. 2011 29. Mitoma H, et al. Cerebellum. 2020*

Proffered Talks Session 5

University of Nottingham
UK | CHINA | MALAYSIA

Investigating Gravitational Influence on Normal Lung Function Using PREFUL MRI on an Open Scanner

Arthur Harrison[1,2], Thomas Meersmann[1,2], Galina E Pavlovskaya[1,2], Penny Gowland[1,2], Jan A Paul[1,2], Rashed Sobhan[1,2], Amanda Goodwin[2], Olivier Mougin[1,2]

[1]Sir Peter Mansfield Imaging Centre, University of Nottingham, Nottingham, NG2 7RD, UK
[2]Nottingham NIHR Biomedical Research Centre, University of Nottingham, Nottingham, NG2 7RD, UK

Introduction:

Understanding the factors influencing local ventilation and perfusion within the lungs is of great importance for improving patient care. Initially attributed solely to gravity and compression of lung parenchyma, our insight into the determinants of lung function heterogeneity have evolved with improvements in imaging methodologies. Differences in ventilation and perfusion within gravitational planes have contributed to the theory that the geometry of vascular and airway trees also play a role in regional lung function.[1]

Phase Resolved Functional Lung (PREFUL) MRI[2] has been demonstrated to visualise dynamic lung function in health and disease. However, conventional MRI systems typically offer limited opportunity to investigate the effect of gravity on the lungs. In contrast, open MRI systems allow for a greater range of scanning positions beyond lying down in an enclosed space. This capability is valuable for exploring posture-dependent lung function, which could serve as a marker for lung disease and be crucial to support stratified treatment approaches.

Methods:

Twenty-one healthy volunteers (average age 21±2yrs.) were recruited with ethics approval from the University of Nottingham Medical School Ethics Committee. Subjects were scanned in three postures: Supine, Sitting and Upside-Down (Figure 1) whilst breathing normally and deeply. All experiments were carried out on a 0.5T Open MRI Scanner (Paramed, Italy) with a four channel receive body coil and a gradient system with a maximum power of 20mT/m and rise time 0.2ms. 200 dynamic images were captured at a rate of 2.6Hz using a 2D GRE protocol: TR/TE=5.7/1.2ms, FOV=32×32cm^2, matrix size=89×89, slice thickness=10mm.

PREFUL analysis was implemented in MATLAB-R2022b to reconstruct ventilation and perfusion maps. Ventilation and cardiac phase were determined for each frame using diaphragm position and aorta artery intensity respectively. Each image was registered to an intermediary inhalation position such that the lung parenchyma appears stationary throughout the time series. These images were used to reconstruct a single breath and single heartbeat consisting of 20 frames, interpolated onto an equidistant time series using a gaussian kernel (σ=0.05π). Changes in lung voxel intensity were used to attain local ventilation, perfusion, and respective time-to-peak information. Normalised variation along the vertical axes was fitted via weighted linear model to attain the rate of change, apex to base.

Results:

Fractional Ventilation

Whilst sitting, an increasing gradient of ventilation from the lung's apex to base was apparent. This gradient increased when the subjects took deep breaths. A similar effect, albeit to a lesser magnitude was observed when supine. However, when positioned upside-down, the gradient decreased substantially to near zero and was further reduced when breathing deeply.

Perfusion

When sitting, the base of the lung exhibited greater perfusion than the apex. This effect persisted whilst supine, though to a lesser degree. When upside-down this effect reversed, albeit with a reduced magnitude compared to the other postures.

Discussion:

The variation in fractional ventilation indicates that it depends both on gravity and physiological factors. If gravity were the sole mechanism, an inverse effect would be anticipated when participants were upside-down compared to seated. Instead, gravitational forces on inverted lungs appears to counter physiological effects to nullify most vertical variation. Furthermore, when the subjects were supine, the base of the lung continued to exhibit greater ventilation than the apex. As neither region experienced greater compressive forces than the other, this is likely attributed to physiology.

The observed variation in perfusion mirrored that of ventilation. Greater magnitude at the base of the lung whilst supine suggests physiological contributions. When sitting or upside-down the effect was amplified or reversed respectively possibly due to the change in hydrodynamic pressure and tissue density. The lower magnitude observed whilst upside-down and positive effect whilst supine suggests sustained influence from physiological factors.

Conclusion:

This work suggests that regional variation in lung function depends on both gravitational and physiological effects. The lungs appear to naturally ventilate and perfuse more at the base. This effect is amplified when upright and reduced (but not reversed) when upside-down.

References:

1) Glenny RW. Determinants of regional ventilation and blood flow in the lung. Intensive Care Med. 2009 Nov;35(11):1833-42. doi: 10.1007/s00134-009-1649-3. PMID: 19760203.

2) Voskrebenzev A, Gutberlet M, Klimeš F, Kaireit TF, Schönfeld C, Rotärmel A, Wacker F, Vogel-Claussen J. Feasibility of quantitative regional ventilation and perfusion mapping with phase-resolved functional lung (PREFUL) MRI in healthy volunteers and COPD, CTEPH, and CF patients. Magn Reson Med. 2018 Apr;79(4):2306-2314. doi: 10.1002/mrm.26893. Epub 2017 Aug 30. PMID: 28856715.

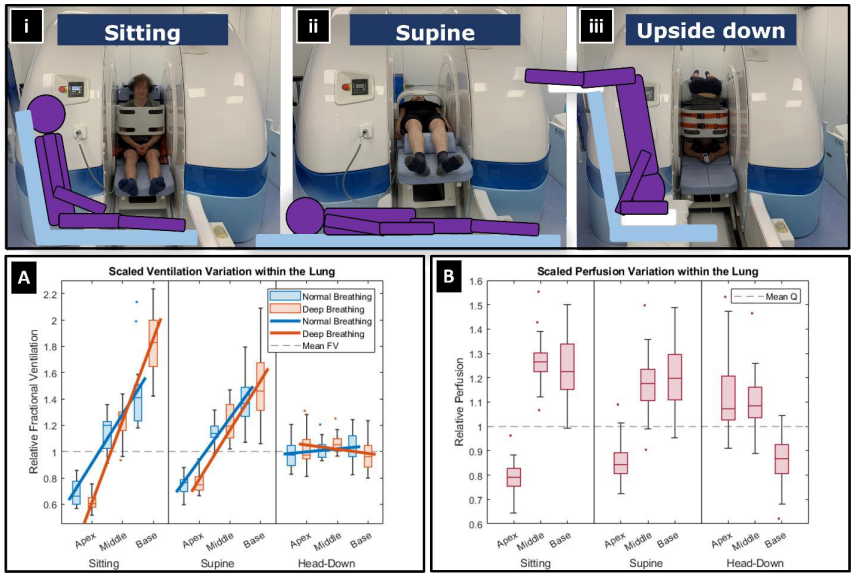

Figure 1: Images of a participant in each of the scanned positions: Sitting **(i)**, Supine **(ii)** and Upside-Down **(iii)** with corresponding diagrams of each posture. Normalised average fractional ventilation for each lung segment whilst in each position **(A)** whilst breading normally and deeply. Normalised average perfusion for each lung segment whilst in each position **(B)**.

Quantification of Gas Trapping in Cystic Fibrosis using Residual Volume (RV) Lung 1H-MRI

Amy V Simmons, Laurie J Smith, Zoe Somerville, Alberto M Biancardi, Neil J Stewart, Jim M Wild
POLARIS, Division of Clinical Medicine, Faculty of Health, The University of Sheffield

Introduction: Cystic Fibrosis (CF) is a genetic disorder primarily affecting the lungs and digestive system. Disease typically originates in smaller airways, causing obstruction and narrowing. This leads to gas trapping during exhalation, a key feature of early CF disease. Detecting and measuring early CF disease is crucial, as intervention can significantly improve long-term outcomes. Gas trapping is clinically assessed on a whole-lung basis using body plethysmography, which measures lung volume subdivisions, including the residual volume (RV), which is the volume of gas present in the lung after complete exhalation. CT is a sensitive imaging measure of gas trapping, however, it is infrequently used due to ionising radiation risks. Lung 1H-MRI using a 3D spoiled gradient echo (SPGR) sequence acquired at RV has been proposed as a non-ionising alternative for qualitatively imaging gas trapping [1], which appears as regions of low signal intensity (see Fig. 1). Hyperpolarised ^{129}Xe MRI ventilation defects are also commonly observed in CF patients [1]. This work aims to develop an image processing pipeline to automatically quantify gas trapping from widely available lung 1H-MRI techniques and compare this measure to pulmonary function tests (forced expiratory volume in one second; FEV1 z-score), direct measures of gas trapping (RV/total lung capacity; RV/TLC%) and ^{129}Xe ventilation MR metrics (Xe ventilation defect percentage; Xe VDP%).

Methods: A retrospective analysis was conducted on lung 1H-MRI images from 16 healthy children (median age 10.43 years, range 8.71-11.92 years, 56.3% male) and 27 individuals with CF (median age 16.90 years, range 6.40-47.50 years, 40.7% male). 14 CF patients had normal FEV1, defined as a z-score of > -1.64, the remaining 13 had abnormal FEV1. All MRI scans were performed on a 1.5T GE HDx scanner with an 8-channel thoracic receive array. Participants underwent a 3D SPGR 1H-MRI scan acquired at RV (breath-hold ~10 seconds, voxel size=3mm^3, TE=0.7ms, TR=1.8ms, FA=3°). CF patients underwent ^{129}Xe ventilation MRI as per [1] and pulmonary function tests (PFTs), including spirometry and body plethysmography. An N4 bias correction with parameters spline spacing = [150] and convergence = [85x85x85, 0.001] was empirically chosen to correct for anterior-posterior signal intensity variations and enhanced image contrast (see Fig. 1(b)) [2]. Lung segmentation was performed using an in-house deep-learning algorithm [3], with manual edits made in ITK-SNAP. A reference histogram was generated from the bias-corrected signal intensity distribution in segmented lung regions of all healthy patients. After exploring various threshold and binning methods, the mean-1.64SD of this histogram was selected as the gas trapping threshold. Signal intensities below this threshold were identified as gas trapping regions (Fig. 2). Applying this threshold to healthy and CF data, a gas trapping volume (GTV%) was computed as a percentage of total lung volume. Fig. 1(c) illustrates gas trapping regions identified in two example CF patients. A normal threshold was set as the maximum GTV% observed in healthy patients. In CF patients, GTV% values were compared to lung function metrics (FEV1 z-score and RV/TLC%) and ^{129}Xe ventilation MR metrics (Xe VDP%) using linear regression and Pearson's correlation. Differences in GTV% distribution for healthy and CF cohorts was calculated using a Mann-Whitney U-test.

Results and Discussion: Healthy volunteers had a median (range) GTV% of 9.98% (4.40-14.55%). CF patients had a median (range) GTV% of 18.27% (7.25-46.42%). The distribution of GTV% in healthy and CF patients is visualised in Fig. 3. The difference in median GTV% between the groups was highly significant ($p<0.001$). GTV% in CF patients correlated well with ^{129}Xe ventilation MRI metrics, Xe VDP% ($p<0.001$, $r = 0.800$), physiological measures of gas trapping, RV/TLC% ($p<0.001$, $r = 0.757$), and spirometry results, FEV1 z-score ($p<0.001$, $r = -0.762$) (see Fig. 4). 18/27 CF patients had a GTV% above the upper normal limit (14.6%), 6 of which had normal FEV1 z-scores, suggesting that GTV% may provide added value over spirometry measures in these cases. This approach also provides regional information on gas trapping distribution (see Fig. 1(c)), which body plethysmography cannot offer.

Conclusions: Gas trapping in CF can be qualitatively and quantitatively assessed from breath-hold residual volume 1H lung MRI. Our proposed metric of gas trapping volume correlates well to direct

measures of gas trapping, pulmonary function tests, and ^{129}Xe ventilation MRI. Our preliminary data shows evidence of abnormal GTV% in patients with CF with normal lung function.

References:

[1] L. J. Smith et al. 129Xe ventilation and 1H anatomical MRI to detect functional and structural abnormalities in sub-clinical cystic fibrosis lung disease [abstract]. In: ISMRM 2019.; 11-16 May; Montréal, QC Canada.
[2] J. G. Sled et al. (1998), A nonparametric method for automatic correction of intensity nonuniformity in MRI data. IEEE Trans. Med Imaging. 17(1):87-97. https://doi.org/10.1109/42.668698.
[3] J. R. Astley et al. (2023), Implementable Deep Learning for Multi-sequence Proton MRI Lung Segmentation: A Multi-center, Multi-vendor, and Multi-disease Study. J. Magn. Reson. Imaging. 58:1030-1044. https://doi.org/10.1002/jmri.28643

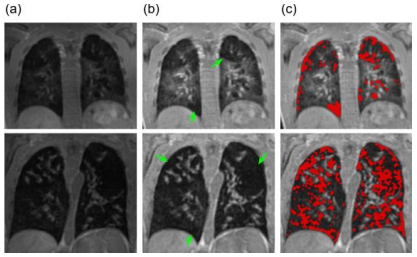

Fig. 1. *Impact of N4 bias field correction (parameters: spline spacing = [150] and convergence = [85x85x85, 0.001]) on 3D SPGR images acquired at RV. Posterior slices are shown before (a) and after (b) correction in 2 CF patients. Green arrows indicate areas of gas trapping. (c) shows areas of gas trapping as selected by the proposed automated approach.*

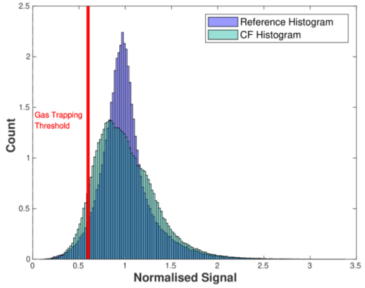

Fig. 2. *Derivation of gas trapping threshold from bias-corrected, normalised signal distribution derived from a healthy cohort. The gas trapping threshold is derived from the mean -1.64SD of the reference histogram (indicated by the red vertical line). A histogram from an example CF patient is shown for comparison (CF Histogram).*

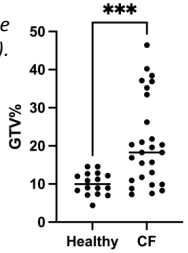

Fig. 3. *Box-whisker plot of the distribution of GTV% for the healthy and CF datasets (p<0.001).*

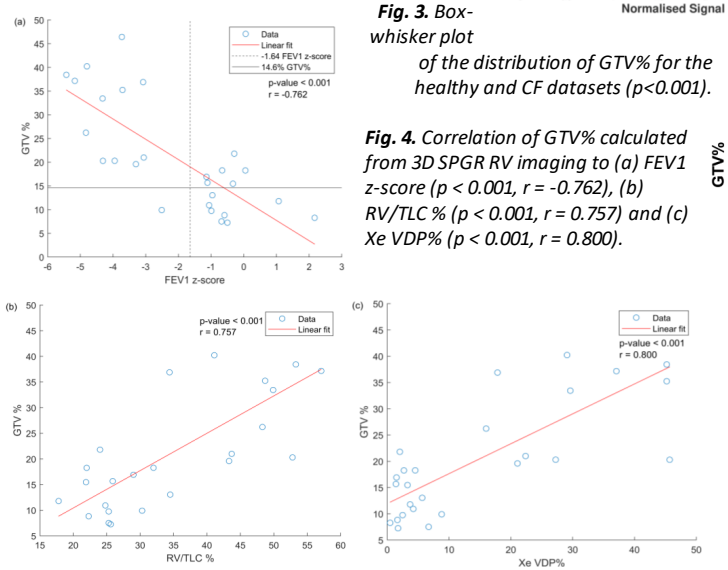

Fig. 4. *Correlation of GTV% calculated from 3D SPGR RV imaging to (a) FEV1 z-score (p < 0.001, r = -0.762), (b) RV/TLC % (p < 0.001, r = 0.757) and (c) Xe VDP% (p < 0.001, r = 0.800).*

Dynamic ^{19}F-MRI of pulmonary ventilation in lung transplant recipients with and without chronic lung allograft dysfunction

Mary A. Neal[1,2], Saskia Bos[2,3], Charlotte W. Holland[1,2], Kieren G. Hollingsworth[1], Gerard Meachery[3], Arun Nair[3], James L. Lordan[3], Andrew J. Fisher[2,3], Peter E. Thelwall[1,2]

1 - Newcastle Magnetic Resonance Centre, Newcastle University, Newcastle upon Tyne, UK
2 - Translational and Clinical Research Institute, Newcastle University, Newcastle upon Tyne, UK
3 - Institute of Transplantation, Newcastle upon Tyne Hospitals NHS Trust, Newcastle upon Tyne, UK

Background: Chronic lung allograft dysfunction (CLAD) encompasses all forms of chronic rejection after lung transplantation. Its two predominant phenotypes: bronchiolitis obliterans syndrome (BOS) and restrictive allograft syndrome (RAS), are characterised by airway and parenchymal fibrosis, respectively. CLAD occurs in approximately 50% of lung transplant recipients within five years of transplantation and is a substantial contributor to the ~50% 10-year post-transplant mortality rate [1]. Current diagnostic tools, such as spirometric-based tests and chest x-ray, are insensitive to early changes due to CLAD, or in the case of CT, bring increased exposure to ionising radiation. Dynamic fluorine-19 magnetic resonance imaging (^{19}F-MRI) of inhaled perfluoropropane (PFP) is an emerging technique used to directly image ventilation. Dynamic ^{19}F-MRI for assessment of ventilatory function over multiple inhalations has recently been tested in human studies of patients with cystic fibrosis and chronic obstructive pulmonary disease [2-4]. The aim of this feasibility study was to investigate whether multi-breath wash-in and washout ^{19}F-MRI of inhaled PFP can detect regional ventilatory dysfunction in lung transplant recipients with CLAD compared to stable allograft recipients.

Methods: Lung transplant recipients with and without CLAD were recruited, and attended a single study session. MR imaging was performed with a clinical MRI scanner (Philips Achieva 3T) interfaced to a dual-tuned ^{19}F/^{1}H transmit-receive birdcage torso coil (Rapid Biomedical GmbH). Participants were positioned supine. An anatomical chest image was acquired using a 3D ^{1}H spoiled gradient echo acquisition during a breath-hold at maximum inhalation. Multi-breath dynamic ^{19}F-MRI was then performed over up to fourteen 7.6-second dynamics: Participants deeply inhaled a 79% PFP/21% oxygen gas mixture and held their breath on alternate inspirations, wherein a 3D ^{19}F-MR imaging dynamic was performed (acquisition parameters: '3D-FFE', TE/TR=1.7/7.5 ms, flip angle=45°, field of view=400x320x250 mm^3, acquisition resolution=10x10x10 mm^3, acquisition bandwidth=500 Hz/pixel, compressed sensing acceleration factor=1.8, averages=3) [5]. After the 7th imaging dynamic, participants were supplied with room air under the same breathing protocol for the remaining 7 dynamics, permitting collection of PFP wash-out images.

Following 4D (3D dynamic) image segmentation, voxelwise wash-in and washout rates were calculated applying mono-exponential curve fitting to the wash-in and washout signal separately. The 'regional lung clearance index' (RLCI) was calculated as $RLCI_{in/out} = -ln\left(\frac{2.5}{100}\right)\tau_{in/out}$, where τ is the exponential recovery/decay time constant for signal wash-in/out, respectively. $RLCI_{in}$ therefore represents the number of breathing cycles required to increase the ^{19}F-MRI signal to 39/40^{ths} of the theoretical maximum signal and $RLCI_{out}$ is the number of breaths required to equivalently reduce the signal. Correlation between spirometric tests and whole-lung and regional (centre/periphery) RLCI measurements were analysed using the Pearson correlation coefficient. Significance of correlations were tested using Fisher z transformation. All averages are displayed as median (25th-75th percentile).

Results: Ten patients (median age: 54 (31-63); 7 male) were recruited to the study. Five participants had a diagnosis of BOS (three stage 1, one stage 2, one stage 3) and one of RAS (stage 1). Four stable lung transplant recipients (without any CLAD diagnosis) were also recruited.

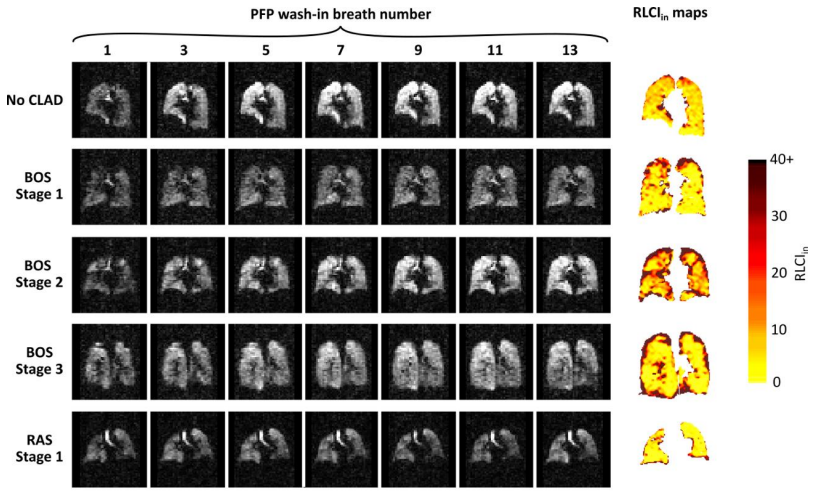

Fig. 1: *The central coronal slice through 3D ^{19}F-MRI images of inhaled PFP in five representative participants. Images were taken during consecutive breath holds to capture PFP gas wash-in. The corresponding central slice of the resultant 3D RLCI map is displayed in colour.*

PFP wash-in was visually homogeneous and rapid in stable patients and substantially more heterogeneous in CLAD (Fig.1). BOS patients exhibited a significant difference in RLCI$_{in}$ between central and peripheral lung regions (W = 30, p = 0.016) and a wider interquartile range of RLCI$_{in}$ compared with stable patients (no CLAD: 8.1, BOS: 21.3; W = 11, p = 0.032) (Fig. 2). Though the distribution of wash-in rates in the patient with RAS was visibly different to other groups (Fig.2), this could not be tested for significance due to the N=1 sample size. Similar findings were observed in PFP washout (RLCI$_{out}$) datasets. Spirometric tests negatively correlated with RLCI during wash-in, most strongly for the periphery (r = -0.844, p = 0.002), retaining significance after Bonferroni correction (p < 0.05).

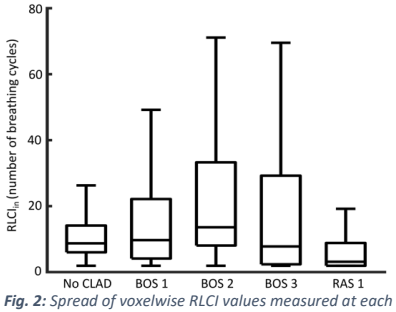

Fig. 2: *Spread of voxelwise RLCI values measured at each diagnostic stage.*

Discussion: Our study presents the first application of dynamic ^{19}F-MRI in lung transplant recipients with and without CLAD. We demonstrate that ^{19}F-MRI with a dynamic multiple breath-hold approach is feasible and well tolerated even in patients with more severe CLAD, and provides 3D visualisation and quantification of regional ventilation defects. This study identified statistically significant between-group differences in RLCI. Though apparent ventilation defects in RAS and BOS stage 1 patients were visible (Fig. 1), sub-group (diagnostic stage) statistical significance was not achieved, at least in-part due to the small study sample size. Future work should validate these findings in larger cohorts and longitudinal studies.

Conclusions: Dynamic ^{19}F-MRI identified quantifiable and significant differences in regional ventilation heterogeneity between patients with and without CLAD. ^{19}F-MRI presents a promising tool for early detection of regional ventilation defects in CLAD.

1. Chambers, D.C., et al. J Heart Lung Transplant, 2019. **38**(10): p. 1042-1055.
2. Goralski, J.L., et al. JCI Insight, 2020. **5**(2).
3. McCallister, A., et al. Magn Reson Med, 2021. **85**(2): p. 1028-1038.
4. Gutberlet, M., et al. Radiology, 2018. **286**(3): p. 1040-1051.
5. Neal, M.A., et al. Magnetic Resonance in Medicine, 2019. **82**(4): p. 1301–1311.

Unlocking Muscle Fatigue: Insights from Multi-Parametric ^{1}H, ^{23}Na & ^{31}P MRI in Exercise-Induced Muscle Damage and Inflammation

Fabio Zambolin[1,2], Susan Pinner[1,2], James McStravick[1,2], Fiona E. Smith[1,2], Aneurin J. Kennerley[1,2], Jamie Stewart McPhee[1,2].

[1] Department of Sport and Exercise Sciences. Manchester Metropolitan University, Manchester, UK
[2] Manchester metropolitan Institute of Sport. Manchester Metropolitan University, Manchester, UK

Corresponding author

Fabio Zambolin, PDRA.
Lecturer in Applied Physiology, Department of Sport and Exercise Sciences, Manchester Metropolitan University, Manchester, UK
99, Oxford Road. M15 6BH
e-mail: f.zambolin@mmu.ac.uk

ABSTRACT (750words)

Introduction: Skeletal muscle type III-IV nerve afferents orchestrate the cardiovascular responses to exercise [1,2], maintaining adequate blood flow and oxygen delivery to the exercising muscle [3]. However, muscle nerve afferents function can be altered in disease states [4], and following inflammation induced by uncustomed exercise (i.e., exercise induced muscle damage - EIMD) [5]. While previous research has shown similar or attenuated cardiovascular responses before and after EIMD [6-9] none of these studies accounted for the cofounding factors present following EIMD (i.e., changes in muscle oxygenation, metabolism, and weakness). Therefore, the aim of the present study was to investigate whether changes of muscle oxygenation and metabolism were associated with changes in cardiovascular responses to exercise and the muscle nerve afferents activity following EIMD. We hypothesised that changes in the muscle environment following EIMD alters the blood pressure response driven by muscle III-IV afferents. In turn the 'perception' of effort (RPE) would increase during exercise.

Methods: The study was approved by the local research ethics committee and 12 healthy males (age 25.2 ± 5.0 years) volunteered to take part and provided written, informed consent to participate. Assessments (questionnaire, MVC and MRI) were completed before and 48h after EIMD (Fig 1.). EIMD consisted of 40 min downhill running (DHR) at a 20% decline on a treadmill (H/P Cosmos Saturn 300/100). We recorded indicators of EIMD which included Maximal Voluntary Contraction (MVC), Soreness (VAS), and swelling measured from quadriceps cross sectional area (Qcsa). All MRI measures used a SIEMENS MAGNETOM 3T Vida system. Participants were in a feet first supine position with suitable RF coils placed over the thigh. 1H T_2 mapping confirmed muscle inflammation post EIMD. Muscle metabolism and oxygenation was measured at rest, during isometric knee extension and post-exercise cuff occlusion (PECO) with non-localized ^{31}P NMR spectroscopy and Blood Oxygenation Level Dependent measures, respectively. The latter was preceded and followed by ^{23}Na imaging to assess the ionic microenvironment of the muscle tissue (Fig 1). Measures of blood pressure (MAP) and heart rate (HR) were recorded throughout the MRI assessments with a non-invasive beat by beat device. All MRI related outcomes were analysed offline in MATLAB 2020a (The MathWorks, Natick) using software routines developed in-house on the middle portion of the *vastus lateralis* muscle. Paired t-test was used to analysed outcomes of neuromuscular function and soreness while a two-way repeated measures ANOVA was implemented to analyse significant effects of time (pre- vs post-EIMD), phase (rest, exercise, PECO, recovery) and interaction. Sidak post-hoc analysis was

implemented to assess changes between pre and post EIMD and the various phases of the exercise protocol. Statistical significance was set when p<0.05.

Results: The downhill running protocol had a significant effect on neuromuscular function and soreness 48h post-EIMD, showing a significant decrease in MVC torque (p<0.01) with increase in Qcsa (p<0.01) and VAS_{SQ} (p<0.01). RPE during exercise increased at 48 post-EIMD (p<0.01), (Fig 2). Moreover, significant increases in muscle T_2 were observed 48h post-EIMD (p<0.01) confirming related tissue inflammation. No significant changes were found for resting Na+ concentration post-EIMD (p=0.98) whilst changes in [ΔNa+] were found from rest to post sustained isometric contraction exercise between conditions (p<0.01). BOLD measures confirmed that muscle oxygenation significantly decreased post-EIMD while ^{31}P MRS showed significant increases in Pi/PCr, intracellular and extracellular Pi pre- to 48h post-EIMD. Interestingly, no changes w*in* ATPγ, PCr and pH from pre- to 48h post-EIMD were observed (Fig 3). No changes were found in MAP and HR from pre to post-EIMD. On the other hand, index of Metaboreflex sensitivity (Pi) changed significantly from pre- to post-EIMD, with no significant changes in Metaboreflex sensitivity for pH following EIMD (Fig 4).

Discussion: In line with previous investigations, we found a considerable loss in muscle force and soreness after EIMD (induced via downhill running). This correlated with MRI T_2 measures showing increased inflammation 48h later [10]. Damaged muscles showed an elevated Pi/PCr ratio during rest, exercise, PECO, and recovery [11], as well as decreased oxygenation during occlusion [12] and increased RPE during exercise [13]. Moreover, we found for the first time increases in delta sodium in damaged muscles that has been previously linked with muscle fatigability and weakness [14,15]. However, despite these peripheral perturbation, cardiovascular responses were unchanged from the non-damaged state, suggesting that muscle afferents did alter the cardiovascular responses to isometric exercise and PECO. These results show possible interference on oxygen delivery and blood flow during exercise that may in turn increase the metabolic demand following EIMD, resulting in extensive reduction in muscle oxygenation and consequent increase in exercise effort and muscle fatigability.

Conclusion: This study highlights the importance of an integrative multi-parametric MRI approach to study the physiological consequences underlying muscle inflammation following uncustomed exercise. This is crucial for advancing our understanding on the abnormal responses present in several medical conditions characterised by muscle weakness and fatigability. Our mechanistic study delivers an integrated protocol to track the impact of acute exercise bouts on recovery/rehabilitation in inflammatory conditions.

References:

1. McCloskey DI, Mitchell JH. Reflex cardiovascular and respiratory responses originating in exercising muscle. *The Journal of physiology.* 1972;224(1):173-186.
2. Goodwin GM, McCloskey DI, Mitchell JH. Cardiovascular and respiratory responses to changes in central command during isometric exercise at constant muscle tension. *The Journal of physiology.* 1972;226(1):173-190.
3. Amann M, Runnels S, Morgan DE, et al. On the contribution of group III and IV muscle afferents to the circulatory response to rhythmic exercise in humans. *The Journal of physiology.* 2011;589(Pt 15):3855-3866.
4. Vianna LC, Fisher JP. Reflex control of the cardiovascular system during exercise in disease. *Current opinion in physiology.* 2019;10:110-117.
5. Zambolin F, Giuriato G, Laginestra FG, et al. Effects of nociceptive and mechanosensitive afferents sensitization on central and peripheral hemodynamics following exercise-induced muscle damage. *Journal of Applied Physiology.* 2022;133(4):945-958.
6. Ray CA, Mahoney ET, Hume KM. Exercise-induced muscle injury augments forearm vascular resistance during leg exercise. *The American journal of physiology.* 1998;275(2):H443-447.
7. Miles MP, Li Y, Rinard JP, Clarkson PM, Williamson JW. Eccentric exercise augments the cardiovascular response to static exercise. *Med Sci Sports Exerc.* 1997;29(4):457-466.
8. Lee JB, Katerberg C, Bommarito J, Power GA, Millar PJ. Blood Pressure Responses to Post-Exercise Circulatory Occlusion Are Attenuated Following Exercise-Induced Muscle Weakness. *Med Sci Sports Exerc.* 2023.
9. Zambolin F, Peçanha T, Pinner S, Venturelli M, McPhee JS. Effects of exercise induced muscle damage on cardiovascular responses to isometric muscle contractions and post-exercise circulatory occlusion. *European Journal of Applied Physiology.* 2023.
10. Bontemps B, Vercruyssen F, Gruet M, Louis J. Downhill Running: What Are The Effects and How Can We Adapt? A Narrative Review. *Sports Medicine.* 2020;50(12):2083-2110.
11. Davies RC, Eston RG, Fulford J, Rowlands AV, Jones AM. Muscle damage alters the metabolic response to dynamic exercise in humans: a 31P-MRS study. *J Appl Physiol (1985).* 2011;111(3):782-790.
12. Larsen RG, Thomsen JM, Hirata RP, et al. Impaired microvascular reactivity after eccentric muscle contractions is not restored by acute ingestion of antioxidants or dietary nitrate. *Physiological reports.* 2019;7(13):e14162.
13. Clarkson PM, Newham DJ. Associations Between Muscle Soreness, Damage, and Fatigue. In: Gandevia SC, Enoka RM, McComas AJ, Stuart DG, Thomas CK, Pierce PA, eds. *Fatigue: Neural and Muscular Mechanisms.* Boston, MA: Springer US; 1995:457-469.
14. Gast LV, Baier LM, Meixner CR, et al. MRI of Potassium and Sodium Enables Comprehensive Analysis of Ion Perturbations in Skeletal Muscle Tissue After Eccentric Exercise. *Invest Radiol.* 2023;58(4):265-272.
15. Höger SA, Gast LV, Marty B, et al. Sodium and quantitative hydrogen parameter changes in muscle tissue after eccentric exercise and in delayed-onset muscle soreness assessed with magnetic resonance imaging. *NMR in biomedicine.* 2023;36(2):e4840.

Figures:

Preview Figure: 1 figure, no caption, legible at the width of a mobile smartphone (640x320)

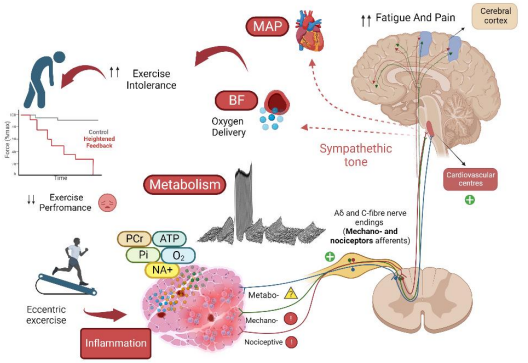

Proffered Talks Session 5

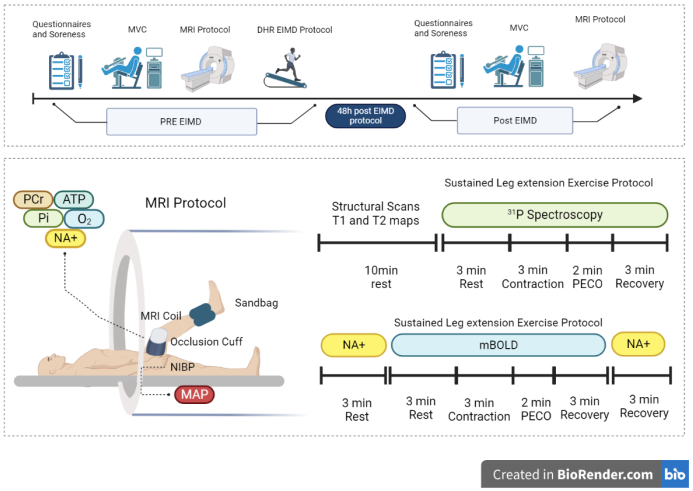

Figure 1. Design of the study, MRI protocol and timeline of each imaging acquisition sequences. Participant underwent preliminary questionnaire and soreness assessment followed by maximum voluntary contraction (MVC) and MRI. Thereafter, participant performed the downhill running (DHR). Two days later participants present in the lab and performed all baseline assessments. Multi-parametric MRI assessment was composed of structural scans (T_1 and T_2) sequences with recording of ^{31}P, ^{23}NA, and muscle oxygenation (mBOLD) during exercise and muscle occlusion (PECO). *Created with BioRender.com*

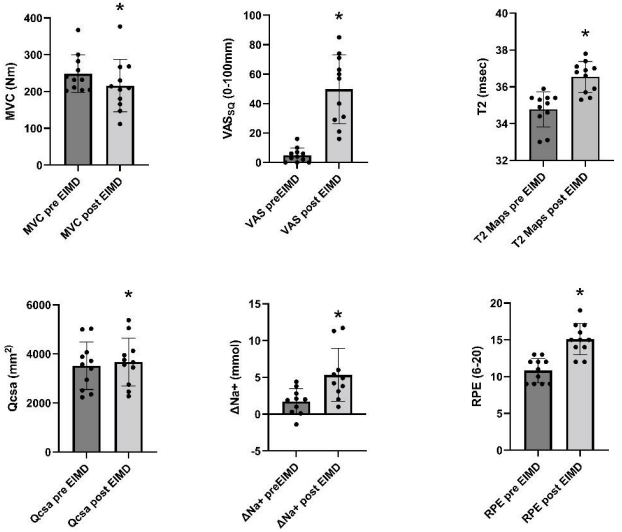

Figure 2. Changes in indicators of EIMD, before and after our EIMD (downhill running) protocol. MVC = Maximal voluntary Contraction; VAS_{SQ} = Visual Analog Scale for Soreness; T_2 =1H T_2 Map; Qcsa = Quadriceps Cross Sectional Area, ΔNa+ = Delta Sodium from rest to exercise; RPE = Rate of perceived exertion; Data are presented as mean ± SD, *p<0.05.

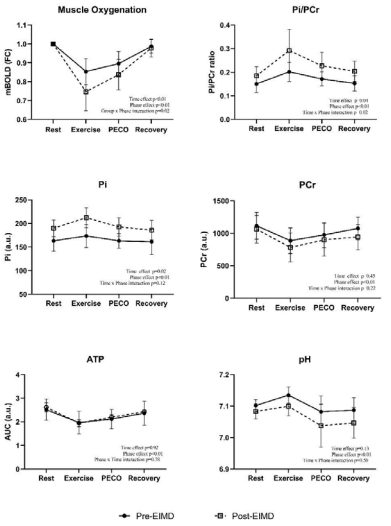

Figure 3. Changes in muscle metabolism and oxygenation before and 48h after EIMD. On the bottom right of each graph is reported the results from the statistical analysis and its respective p-values. Data are presented as mean ± SD.

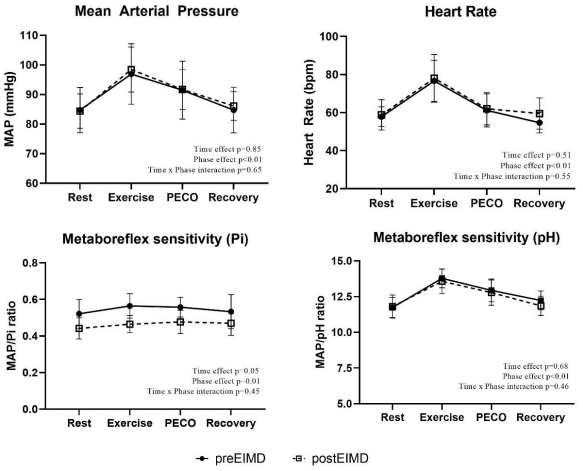

Figure 4. Changes in Cardiovascular responses and metaboreflex sensitivity before and 48h after EIMD. . On the bottom right of each graph is reported the results from the statistical analysis and its respective p values. Data are presented as mean ± SD.

Proffered Talks Session 5

Shoulder MRI Arthrograms – Is saline an intra-articular option?

Charlotte Swain[1], Rafal Panek[1,2], Iain Macleod[1]
[1] Nottingham University Hospitals, Nottingham, UK
[2]University of Nottingham, Nottingham, UK

Introduction: Shoulder arthrograms with intra-articular gadolinium-based contrast agents (GBCA) are considered the imaging option of choice for diagnosing labral tears and lesions[1,2]. Recent changes to the availability of GBCA licensed for intra-articular use mean an alternative imaging methodology has been sought[2,3]. While saline has been shown to be effective for hip arthrograms, there is limited evidence for its use in shoulders[4,5].

A new protocol was developed locally using saline (0.9% NaCl) rather than a GBCA (Magnevist, 2mmol/l in 15ml pre-filled syringe). The initial trial period included scan supervision by a Radiologist and MR Physicist followed by image review and protocol consensus by the local MSK Radiology Team. This review presents the new saline-specific protocol and examines the MRI report alongside the surgical report to ascertain the accuracy of using saline with the new saline-specific protocol compared to the conventional GBCA protocol.

Methods: A retrospective review of 10 patients was undertaken (5-GBCA/5-saline) comparing the effectiveness of intra-articular GBCA with saline for shoulder MR-arthrograms. Patients were randomly selected from a 1-year period (May 2023-May 2024), 6 months before and after the date of the protocol change. Inclusion criteria were: patient age over 18 years with a successful shoulder MRI arthrogram with GBCA/saline and subsequent surgery with available report. All images were acquired on a 1.5T Siemens MAGNETOM Sola with a dedicated 16 channel shoulder coil.

The original protocol utilised T1-weighted TSE GBCA enhanced imaging in axial and sagittal planes with fat saturation (FS) together with 3D PD FS (space) axial and coronal scans to provide adequate visualisation of the glenohumeral joint. The new protocol includes T2-weighted TSE in all three planes, 3D isotropic PD FS coronal (axial reconstruction) and T1-weighted non-FS TSE sagittal scan to visualise medial muscles. The new saline-only protocol utilised AI based acceleration software (Deep Resolve Boost and Deep Resolve Sharp, Siemens Healthcare).

The MRI arthrogram report was compared with the surgical report to compare accuracy of both imaging protocols. Agreement between the MRI report and surgical findings were compared using Fisher's exact test with p = 0.05 significance threshold.

Results: The quality of acquired images was found sufficient for diagnostic evaluation in all 10 patients. Differences between agreement of surgical reports and MRI reports at the time of scan are presented in Table 1 for both protocols.

Table 1. Agreement between surgical report and MRI findings at the time of scan

	Full agreement between MR and surgical report	Minor discrepancy between MR and surgical report
GBCA	2	3
Saline	4	1

All 10 cases showed utility of the MR arthrogram, identifying pathology that was best treated surgically. Minor discrepancies between imaged and surgical findings were found in 4 out of 10 patients. These included one false positive SLAP tear and overcall of tear locations in the GBCA group; whereas one false negative was seen in the saline group with labral deformity correctly identified but a small tear overlooked. The agreement with the surgical findings was comparable for both imaging protocols in the assessed patient group (p = 0.524).

Discussion: Our work presents the successful implementation of saline MRI arthrograms and the initial results suggest that the use of the new saline protocol is not inferior to the standard GBCA based imaging. This new method utilising saline showed fewer discrepancies with the surgical findings, which may relate to improved visualisation from an updated protocol rather than anything inherent in the contrast.

The use of GBCA has the potential for allergic reaction, possible nephrotoxicity, is associated with the development of nephrogenic systemic fibrosis, and the more recently recognised gadolinium deposition within the brain[6]. Whilst the chance for these effects is minimal, they must still be considered when deciding to perform any contrast enhanced MRI. The GBCA which is licenced for intra-articular use is classed as high risk for these complications due to their linear formulation and have therefore been withdrawn from intra-vascular use, prompting a similar approach to intra-articular use within many departments[2,3,6]. Saline is safe, readily available, inexpensive[7], and can be visualised within the joint space by MRI. Furthermore, costs can be variable but a pre-filled GBCA syringes is likely to cost in the region of 10 times as much as an ampoule of saline.

The main limitation of this study is the small number of patients analysed. Further review is required to ascertain the significance of these findings, with additional case reviews planned going forwards. It is also worth noting that all images included in this review were acquired on a 1.5T Siemens MAGNETOM Sola with the use of AI based acceleration software which enabled faster scan times, allowing for acquisition of additional sequences within the protocol and improved image quality, which may not be widely available. One disadvantage of the new protocol is a potential for flow artefacts in the vicinity of large vessels in T2-weighted sequences, which was addressed in our study using a combination of flow compensation and saturation bands.

Conclusion: This review presents a new saline-based MRI arthrogram protocol for the shoulder and demonstrates its suitability as an alternative for GBCA MR arthrography when comparing diagnostic value and agreement with surgical findings, whilst considering the reduced risk to the patient, increased availability and lower cost.

References

[1] Chang, E.Y.*et al.* SSR white paper: guidelines for utilization and performance of direct MR arthrography. *Skeletal Radiology 53*, 209–244 (2024). Available from: https://doi.org/10.1007/s00256-023-04420-6
[2] Kho, J., Azzopardi, C., Davies, A.M. et al. Direct MR arthrography of the shoulder: current practice in the UK. La Radiologica Medica125, 605–608 (2020). https://doi.org/10.1007/s11547-020-01144-8
[3] Medicines and Healthcare products Regulatory Agency. Drug Safety Update: volume 11 issue 5; December 2017: 1.
[4] Meier MK et al. Can gadolinium contrast agents be replaced with saline for direct MR arthrography of the hip? A pilot study with arthroscopic comparison. European radiology. 2023 Sep;33(9):6369-80.
[5] Tiegs-Heiden et al. Does gadolinium improve magnetic resonance arthrography of the hip beyond fluid distension alone? Clinical Radiology. 2020 Sep 1;75(9):713-e1.
[6] The Royal College of Radiologists. Guidance on gadolinium-based contrast agent administration to adult patients. BFCR (19)4 [Internet]. London; The Royal College of Radiologists. 2019
[7] Liu X, Lu M. Normal saline: Past, present, and future. Science progress. 2023 Apr;106(2):00368504231168821.

Proffered Talks Session 6

Placental contractions in low, high and extremely high risk pregnancies

Amy Turnbull[1], George Hutchinson[1], Louise Dewick[2], Ruizhe Li[3], Chris Bradley[1,4], Xin Chen[3], Grazziela Figueredo[3], Neele Dellschaft[1], Kate Walker[2], Nia Jones[2], Penny Gowland[1]
[1]Sir Peter Mansfield Imaging Centre, School of Physics and Astronomy, University of Nottingham, Nottingham, United Kingdom,
[2]School of Medicine, University of Nottingham, Nottingham, United Kingdom,
[3]School of Computer Science, University of Nottingham, Nottingham, United Kingdom,
[4]National Institute for Health Research, Biomedical Research Centre, Hospital NHS Trust and University of Nottingham, Nottingham, United Kingdom

Introduction: Placental contractions have recently been discovered to be distinct from uterine contractions using MRI and had been previously theorised in biological literature due to the contractile elements of anchoring villi [1,2]. Placental contractions have been characterised in low risk pregnancies but have previously not been investigated in compromised pregnancies [3]. These contractions have an impact on the haemodynamics in the placenta so differences in contractions may indicate underlying placental insufficiencies.

Methods: Ethics approval was obtained from a regional ethics committee and 37 pregnant participants were consented and scanned. 30 pregnancies were considered low risk, 3 were considered high risk and 4 extremely high risk using the NHS Saving Babies Lives Care Bundle Version 2 criteria.

Participants were scanned using a 3T Philips Ingenia, in a left lateral tilt. Dynamic MRI was acquired for between 10 and 30 minutes using respiratory triggered, multislice, single shot gradient echo EPI (TE 25ms, minimum TR 9s, voxel size 1.56x1.56x4 mm^3, Sense 3), with some series also including quantitative flow encoding.

Non flow encoded images were segmented using nnU-Net, a convolutional neural network trained on 44 volumes from 11 pregnancies, to create placental and uterine masks. Flow encoded images were segmented manually as the network was not trained for these images. Placental volume was estimated using a percentage change of a central, axial slice in which minimal fetal movement was observed. Placental contractions were identified visually from the dynamic MRI and the placental volume timecourse. Placental contractions were defined by contraction of the placental bed, reduction in placental volume and changes in the BOLD signal of the placenta. While placental contractions are independent of uterine contractions, they occurred simultaneously in some cases which are marked accordingly. The rate of placental contractions was determined by the number of contractions observed in the scan duration.

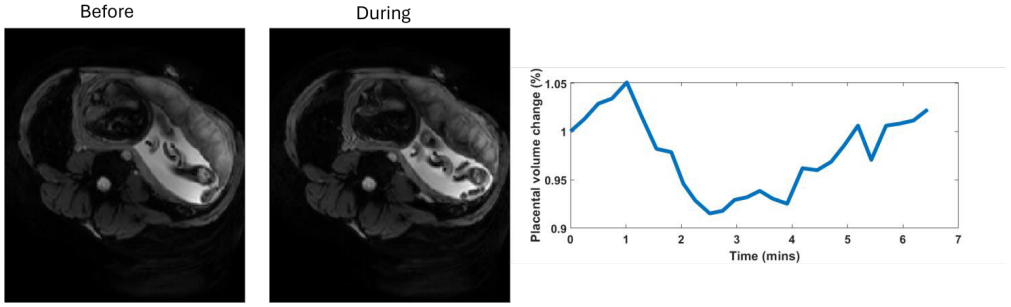

Fig. 1. An example of a placenta before and during a contraction and the corresponding change in placental volume.

Results: Placental contractions were observed in 33 out of 37 participants. and shown in figure 2A. There was no statistically significant trend with gestational age although the variability increased with gestational age.
Placental volume decrease is shown in figure 2B. Placental contractions and simultaneous placental and uterine contractions are plotted separately. Where individual participants had more than one contraction, the volume reduction is shown as the average volume change for that participant and the range. No significant trend was found with gestational age.

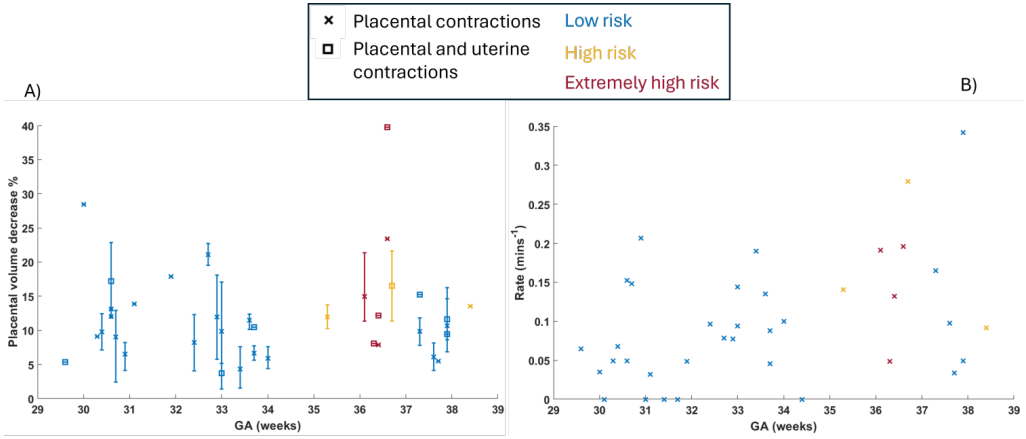

Fig. 2. A) Rate of placenta contractions across gestational age for low, high and extremely high risk pregnancies. B) Percentage of placental volume decrease during placental contractions and simultaneous placental and uterine contractions for low, high and extremely high risk pregnancies. Average is shown for participants with multiple contractions with the minimum and maximum shown as error bars.

Discussion: The higher risk groups showed no difference in the frequency or volume change of placental contractions. However the criteria for these categories is broad and therefore retrospective categorising based on pregnancy outcome may help to better distinguish placental function. This is part of an ongoing study and more data will be acquired from the higher risk groups as well as longitudinal information showing the progression of contractions across gestation.

Conclusions: Placental contractions have been characterised in high and extremely high risk pregnancies for the first time. The presence of contractions in the majority of participants across all risk groups indicates the necessity of these contractions and highlights the need to further understand their purpose.

Acknowledgements: This work is funded by the Wellcome Leap In Utero program.

References

[1] Dellschaft, N.S., Hutchinson, G., Shah, S., Jones, N.W., Bradley, C., Leach, L., Pratt., Bowtell, R., Gowland P., The haemodynamics of the umanplacental in utero, P PLOS Biology 18(5): e3000676, 2020.
[2] Kato, Y., Oyen, M.L., and Burton, G.J. Villous tree model with active contractions for estimating blood flow conditions in the human placenta.Open Biomed Eng J, 11, 36-48m 2017.
[3] Gowland, P., Turnbull, A., Hutchinson, G., Dewick, L., Li, R., Bradley, C., Chen, X., Figueredo, G., Stockwell, S., Ramesh, D., Dellschaft, N., Walker, K., & Jones, N. (2024). Characterising Placental Contractions. *ISMRM*.

Towards accurate, reproducible PDFF quantification using a 3D dual-echo Dixon body composition sequence: validation in phantoms

Yifei Jin[1], Markus Henningsson[1], Carolina Fernandes[1]
[1]Perspectum, Oxford, United Kingdom

Introduction: The dual-echo Dixon technique is commonly used for water-fat separation, its commercialised 3D Dixon sequence with inline water-fat separation is available on major vendors, including Siemens, GE and Philips. The separated fat signal facilitates quantification of fat volumes in areas of nearly pure fat such as visceral and subcutaneous fat, needed for body fat composition. However, the signal fat fraction (SFF) calculated from the scanner-derived water and fat images with conventional imaging parameters (flip angle α~10°, repetition time TR~4-8 msec) is T1-biased compared to proton density fat fraction (PDFF) sequences with small α and long TR [1]. Additionally, different echo times (TE) and fat model choice of the vendor introduce vendor-specific bias [2]. In this work, we propose a T1-bias correction followed by a simulation-based vendor-specific correction for more accurate and reproducible PDFF quantification using commercial 3D dual-echo Dixon sequences.

Theory: The different T1 of water ($T1_{water}$) and fat ($T1_{fat}$) result in different T1 weighting ($T1W_{component} = \frac{(1-e^{-TR/T1_{component}})\sin\alpha}{1-e^{-TR/T1_{component}}\cos\alpha}$) on the water and fat component signals, leads to biased SFF ($SFF = \frac{Fat \times T1W_{fat}}{Fat \times T1W_{fat} + Water \times T1W_{water}} \times 100\%$) relative to PDFF. With known $T1_{water}$, $T1_{fat}$, α and TR, a correction factor $f_{T1} = \frac{T1W_{water}}{T1W_{fat}}$ can be calculated and applied to the fat signal for T1-bias correction. The choice of fat model and TEs introduce bias due to the mismatch of the vendor-implemented signal model and the actual signal model. To address this, we simulated a dictionary to find the corresponding unbiased result of the biased SFF for each vendor. The combined water and fat signal at each TE were simulated for the full range of PDFF values (0-100%), assuming a 6-peak peanut oil fat model [3]. The biased SFF was then reconstructed from the simulated signals using the derived vendor-specific fat model and algorithm. By searching the closest simulated SFF value to the acquired SFF, the corresponding PDFF can be found.

Experiments: To evaluate the proposed T1-bias correction performance, experiments were performed on a 1.5T GE SIGNA Voyager system using a water/oil phantom (Model 450, Calimetrix), which has 5 PDFF vials (5%, 10%, 20%, 30%, 40%) and known T1 (1.5T/3T: $T1_{fat}$ = 294/307 msec, $T1_{water}$ = 635/607 msec). Data were acquired with Lava-Flex ($TE_{1,2}$ = 2.084, 4.468 msec, TR = 7 msec) using three different flip angles 5°, 10°, 15°. And then using α = 2°, TR = 15 msec to minimise the T1-bias (SFF_{pd}). The different flip angle datasets were T1-bias corrected and compared to the SFF_{pd}. The manufacture-specified magnetic resonance spectroscopy (MRS) PDFF was used as the ground truth PDFF.

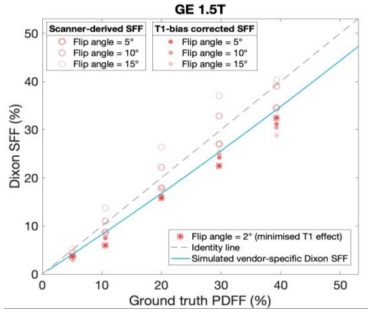

Fig. 1. The Dixon SFF is plotted against manufacture-specified MRS PDFF for each phantom vial. The simulated SFF is plotted against the known ground truth PDFF.

To evaluate dual-echo Dixon-derived PDFF reproducibility using the proposed T1-bias and vendor-specific correction, data from different vendors, field strengths and multiple sites were acquired using seventeen identical Calimetrix phantoms (Table 1). $T1_{water}$ and $T1_{fat}$ were assumed identical in all phantoms for a given field strength. The Dixon PDFF values after proposed correction were compared to manufacture-specified MRS-PDFF. Vials with water-fat swaps were excluded from the analysis.

Table 1. Number of experiments for each vendor and field strength (grey background), and protocol used in the multivendor experiment.

Vendor		GE	Siemens	Philips
Sequence name		Lava - Flex	VIBE - Dixon	Thrive - mDixon
Field strength	1.5 T	10 cases	10 cases	3 cases
		$TE_{1,2}$ = [2.08, 4.17] msec TR = [5.64 - 6.19] msec α = 15°	$TE_{1,2}$= [2.39, 4.77] msec TR = [6.69 - 7.47] msec α = [9°- 15°]	$TE_{1,2}$ = [1.71 - 1.81, 3.60 - 4.40] msec TR = [5.30 - 6.50] msec α = 10°
	3 T	10 cases	10 cases	7 cases
		$TE_{1,2}$ = [1.12, 2.23] msec TR = [3.62 – 3.78] msec α = 9°	$TE_{1,2}$ = [1.23, 2.46] msec TR = [3.87 – 3.97] msec α = 9°	$TE_{1,2}$ = [0.98 - 1.34, 1.98 - 3.00] msec TR = [3.20 - 4.80] msec α = [9°- 15°]

Results: The 40% PDFF vial value was excluded for eight GE 1.5T datasets because of the water-fat swaps. With T1-bias correction, the SFF acquired with different α and hence different amount of T1-bias were all corrected towards the SFF_{pd} (Fig. 1). However, the corrected values are still biased compared to ground truth due to remaining vendor-specific bias, which can be modelled by the SFF simulation shown in Fig. 1. With the full proposed correction, 95% limits of agreement (LoA) within ± 5% and 0.41% mean bias were achieved across all vendors and field strengths, which meet the QIBA 95% LoA and mean bias requirement for phantom PDFF bias [4] (Fig. 2).

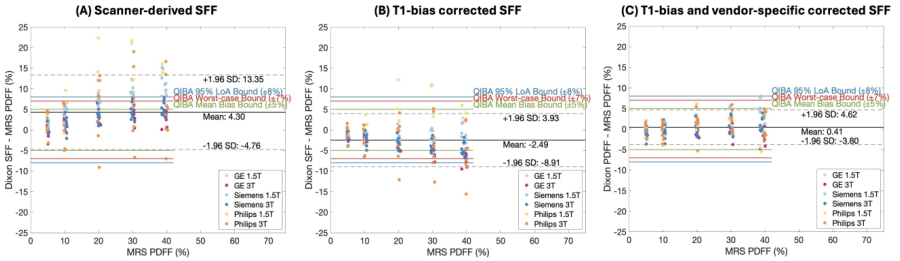

Fig. 2. Bland-Altman plots of Dixon SFF using MRS-PDFF as ground-truth, for scanner-derived SFF when no correction is applied (A), for T1-bias corrected SFF (B) and for T1-bias and vendor-specific corrected SFF (C). Data acquired at different vendors and field strength are plotted with different colour, and the QIBA requirement for 95% LoA, mean bias and worst-case bias [4] are also shown in the figure.

Conclusions: We proposed a bias correction method for commercialised 3D dual-echo Dixon sequences to achieve more reproducible and accurate PDFF quantification across scanners and field strengths. The proposed method was evaluated using water/oil phantom datasets from GE, Siemens and Philips scanner, at 1.5T and 3T. The corrected dual-echo Dixon-derived PDFF shows good agreement with the ground truth MRS-PDFF.

Limitations: The proposed method does not correct for noise and T2* bias, which are not major confounders in phantom experiments but will be important for in-vivo study. The correction was tested on multivendor datasets, however, limited data were available for Philips 1.5T and GE 1.5T at 40% PDFF value, as water-fat swapped vials were excluded. Also, the QIBA requirement for worst-case bias was not met, further investigation of the unsuccess cases is needed.

References

[1] CY Liu et al. *Magn Reson Med.* 58(2), 354-64 (2007)
[2] D Hernando et al. *Magn Reson Med.* 64(3), 811-822 (2010)
[3] A Triay Bagur et al. *Magn Reson Med*. 82(1), 460-475 (2019)
[4] QIBA Proton Density Fat Fraction Biomarker Committee, 2023. Quantitative Imaging Biomarkers Alliance, December 2023. Available at: https://qibawiki.rsna.org/index.php/Profiles

Multiparametric MRI and MRS to study changes across the Surgical Journey in Bariatric Patients with Type 2 diabetes or Prediabetes.

Abi Spicer[1], Rebekah Wilmington[2,3], Stephen Lloyd-Brown[4], Chris Bradley[1,5], Liz Simpson[5,6], Stephen Bawden[1,5], Gerry McCann[7], Guru Aithal[5], Penny Gowland[1,5], Iskandar Idris[2,3], and Susan T Francis[1,5]

[1]Sir Peter Mansfield Imaging Centre, University of Nottingham.

[2]Division of Medical Sciences and Graduate Entry Medicine, School of Medicine, University of Nottingham.

[3]Bariatric Metabolic Institute, University Hospitals of Derby and Burton NHS Foundation Trust.

[4]Intelligent Modelling and Analysis, School of Computer Science, University of Nottingham.

[5]David Greenfield Human Physiology Unit, MRC/ARUK Centre for Musculoskeletal Ageing Research, University of Nottingham School of Life Sciences, Queen's Medical Centre.

[6]National Institute for Health Research Biomedical Research Centre, Hospital NHS Trust and University of Nottingham.

[7]Department of Cardiovascular Sciences, University of Leicester and NIHR Leicester Biomedical Research Centre, Glenfield Hospital.

Introduction: Obesity rates are climbing, leading to a rise in related diseases such as Type-2 diabetes mellitus (T2D). Bariatric surgery is an effective strategy to induce sustained weight loss and diabetes remission. Before surgery, patients undergo a 2-week Very Low-Calorie Diet (VLCD), consuming ~800kcal a day, which has been independently shown to induce diabetes remission [1,2], either Roux-en-Y gastric bypass (RYGB) or sleeve gastrectomy (SG) is then performed. Whether diabetes remission occurs due to the VLCD or additional changes in insulin-sensitive tissues after surgery is unclear.

Aim: To collect multi-parametric ^{1}H MRI and MRS at four time points across bariatric patients surgical journey: baseline (before treatment), after a VLCD, 6-weeks post-surgery and 6-months post-surgery.

Methods: 17 participants (BMI≥35kg/m3, diagnosis of T2D or pre-diabetes, no history of liver cirrhosis) registered for bariatric surgery were recruited to have MRI scans at baseline, end of VLCD, and 6 weeks and months post-surgery, Fig.1. Of these participants, 6 had RYGB, and 11 had SG. To date, 16 participants have completed scans up to +6 weeks, with 12 having completed all 4 time points. Participants arrived fasted (≥8 hours) at 08:30 for a 3-hour mixed meal test followed by a 1-hour multiparametric MRI.

MR acquisition: MR measures were collected on a Phillips 3T Ingenia using a large FOV (450 x 450 mm) centred on the pancreas, including liver and spleen. Scans included a 6-point abdominal mDIXON to assess Fat Fraction (FF) and T_2*, MOLLI T_1 mapping (with physiologically simulated 60 bpm) and fat-suppressed (FS) SE-EPI T_1 mapping, GraSE T_2 mapping, B_0 and B_1 maps. Kidney T_2* and MOLLI T_1 scans were also acquired. Single voxel (20x20x20 mm) ^{1}H STEAM MRS of the liver was also collected with 4 TE's (15,30,45 and 80 ms), TR = 2500ms, BW = 2000Hz.

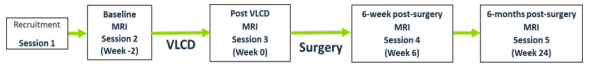

Figure 1 - Timeline of study

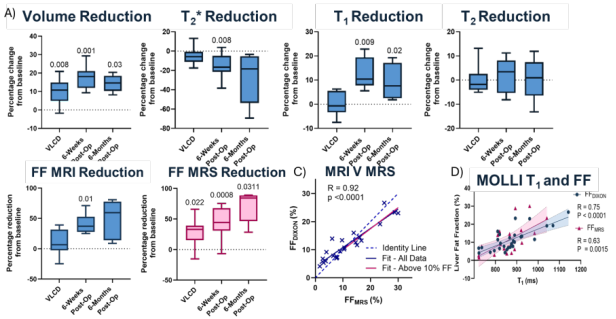

Figure 2 - Liver MRI (blue) and MRS (pink). A) Box plots of the percentage reduction from baseline. Significant p-values shown above box plots. (B) Comparison of MRS and MRI measured FF, identity line (dashed), full dataset fit (blue) and fit for FF_{MRS} > 10% shown in pink with R and p values. (D) Strong correlation of FF and MOLLI T_1 seen for all time points.

Analysis: Masks of the liver, spleen and Subcutaneous Adipose Tissue (SAT) were created from the mDIXON using a nnU-NET [3] previously trained on 40 adult participants' data. These masks were then used to compute liver and spleen volume, FF and T_2*, and SAT volume. Liver and spleen masks were re-sampled (FSL, fMRIB) and applied to the abdominal T_2 and T_1 MOLLI maps. Pancreas ROIs were manually drawn, and FF maps interrogated. Liver MRS data were analysed using MATLAB, spectra were phase corrected, peaks fitted, and FF corrected for T_2.

Results: To date, data from 9 participants has been analysed. Liver volume was significantly different from baseline at all subsequent time points (Fig. 2). Liver T_2* significantly increased at 6-weeks compared to baseline, and liver MOLLI T_1 reduced at 6-weeks and 6-months compared to baseline (Fig.2). At baseline, all participants had a fatty liver when measured by either MRI or MRS (> 6.4% FF [4]) with MRI and MRS measures of FF shown to correlate well (R=0.92, p<0.001), Fig.2. There was a significant reduction of liver FF from baseline to 6-weeks, and from the end of VLCD to 6-weeks (Fig.2). 7 of 9 patients had a fatty pancreas (> 6.2% FF [5]) (Fig. 3). SAT volume significantly reduced at 6-months compared to baseline. No significant reduction was observed in pancreatic FF or spleen measures (Fig. 3).

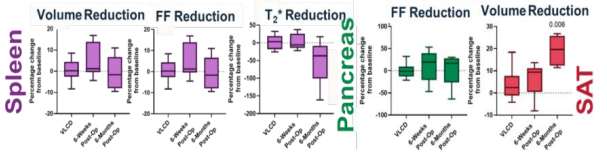

Figure 3 - Box plots of the percentage reduction from baseline of spleen (purple) volume, FF and T2, pancreas FF (green) and SAT (red). Significant p-values can be seen above their respective box plots.*

Discussion: This study's preliminary findings show liver changes associated with bariatric surgery. A bias is seen in lower values of FF (FF < 10%), with imaging overestimating compared to MRS. The reduction in liver MOLLI T1 is likely an effect of reduced FF and will be compared to FS SE-EPI T_1 mapping [6]. In future, we will also study the effect of bariatric surgery on pancreas T_2*, T_2 and T_1, as well as kidney T_2* and MOLLI T_1 kidney measures, and compare differences between the two types of surgery. The MRI measures will be related to blood measures of glucose, GLP-1, GIP, glucagon, C-peptide, ghrelin, insulin and bile acids.

Conclusion: MRI can detect a quantitative decrease of fatty infiltration within the liver after bariatric surgery and could be a valuable tool to monitor NAFLD/ NASH postoperatively.

Acknowledgements: The study was supported by funding from the NIHR BRC, with PhD funding to AS from the MRC DTP and to SLB from the EPSRC DTP.

References

[1] Juray S, Axen K V, Trasino SE, Martínez-Hervás S, González-Navarro H. Remission of Type 2 Diabetes with Very Low-Calorie Diets—A Narrative Review. Nutrients 2021, Vol 13, P 2086. 2021 Jun 18;13(6):2086.

[2] Steven S, Hollingsworth KG, Al-Mrabeh A, Avery L, Aribisala B, Caslake M, et al. Very Low-Calorie Diet and 6 Months of Weight Stability in Type 2 Diabetes: Pathophysiological Changes in Responders and Nonresponders. Diabetes Care [Internet]. 2016 May 1;39(5):808–15.

[3] Isensee F, Jaeger PF, Kohl SAA, Petersen J, Maier-Hein KH. nnU-Net: a self-configuring method for deep learning-based biomedical image segmentation. Nature Methods 2020 18:2. 2020;18(2):203–11.

[4] Tang A, Tan J, Sun M, Hamilton G, Bydder M, Wolfson T, et al. Nonalcoholic fatty liver disease: MR imaging of liver proton density fat fraction to assess hepatic steatosis. Radiology 2013 May 1 ;267(2):422–31.

[5] Singh RG, Yoon HD, Wu LM, Lu J, Plank LD, Petrov MS. Ectopic fat accumulation in the pancreas and its clinical relevance: A systematic review, meta-analysis, and meta-regression. Metabolism. 2017, 1;69:1–13.

[6] Mozes FE, Tunnicliffe EM, Pavlides M, Robson MD. Influence of fat on liver T1 measurements using modified Look–Locker inversion recovery (MOLLI) methods at 3T. JMRI, 2016;44(1):105–11

Rapid 3D gastrointestinal motility imaging using a stack-of-spirals sequence and compressed sensing reconstruction

Rebecca R. Baker[1,2], Vivek Muthurangu[2], Naomi Sakai[1], Chloe Dennis[1], Stuart Taylor[1], David Atkinson[1], Jennifer A. Steeden[2]
[1] Centre for Medical Imaging, University College London, London, UK
[2] Centre for Translational Cardiovascular Imaging, University College London, London, UK

Introduction

Impaired gastrointestinal (GI) function is a symptom in several diseases, such as irritable bowel syndrome, Crohn's disease and Parkinson's disease, and GI motility assessed using MRI has the potential to act as an imaging biomarker.[1] However, GI motility is often assessed using 2D MRI methods, which are unable to fully characterise the 3D, unpredictable and aperiodic motion of the GI tract. Furthermore, planning of the 2D slices requires skilled radiographers to ensure the correct anatomy is captured. Although previous studies have achieved 3D cine imaging of the stomach with temporal resolutions of 3-7 s,[2,3] this is insufficient to fully capture motion in the small bowel, which requires a temporal resolution of 1 s.[4] However, 3D cine imaging in the heart has been shown with temporal resolutions of 1.2 s.[5] Therefore, in this study we aimed to adapt methods used in cardiac imaging, to perform 3D motility imaging of the stomach and small bowel, with a temporal resolution of 1 s.

Methods

3D motility sequence: A 3D stack-of-spirals balanced steady-state free precession (bSSFP) sequence with fat saturation was developed. A variable density spiral strategy was used in kx-ky (readout duration = 3.0 ms), with 30 interleaves required to fill the centre 50% of kspace at each of the 96 kz partitions. To accelerate acquisition, kx-ky data was undersampled by a factor of 6 and kz was undersampled by a factor of 2. In addition, partial Fourier (75%) was applied along kz. kz partitions were acquired pseudo-randomly in the inner loop, while kx-ky spirals were acquired in the outer loop, ordered by the golden angle (Fig. 1). Fat saturation was performed at the start of each inner loop. Total acceleration factor was 16×, enabling acquisition of a 400×400×202 mm^3 volume with 2.1 mm^3 isotropic resolution approximately every 1 s.

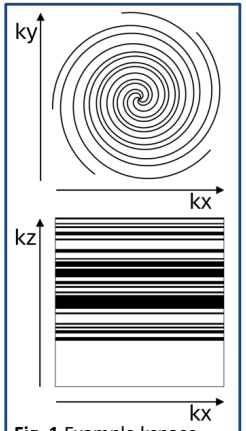

Fig. 1 Example kspace sampling. Variable density spirals acquired in kx-ky, and pseudo random partitions acquired in kz.

Image reconstruction: Undersampled data was reconstructed using compressed sensing (CS) with spatial and temporal total variation. Frames were reconstructed in batches of 10. To calculate coil sensitivities, the central 8 partitions from the first 8 frames were combined to provide a low resolution fully sampled kspace. Reconstruction was performed offline using Python and Tensorflow MRI.[6]

Imaging protocol: Imaging was performed on a 1.5 T MRI scanner (Avanto fit, Siemens Healthineers). Data was acquired in three patients with Parkinson's disease, following overnight fasting and withdrawal from medication. Patients were given 800 mL of 2% mannitol solution, which was consumed over 40 minutes prior to the scan. 3D motility images were acquired as described above. To assess stomach motility, 120 frames were acquired, resulting in a total acquisition time of 2 minutes. To assess small bowel motility, 20 frames were acquired, resulting in a total acquisition time of 20 s. Small bowel imaging was performed with a breath-hold.

Results

3D cine data was successfully acquired and reconstructed in the stomach and small bowel, with a temporal resolution of 1 s and isotropic spatial resolution of 2.1 mm^3. The CS reconstruction took approximately 1 minute/frame. Example images of the stomach and small bowel, in three orthogonal planes, are presented in Fig. 2. Good contrast is observed between the contents of the stomach/small bowel and surrounding tissue. A 3D rendering of the stomach and small bowel, performed in Osirix, are presented in Fig. 3.

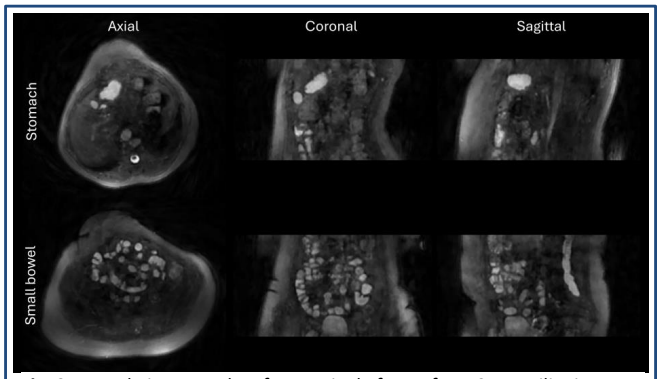

Fig. 2 Example images taken from a single frame from 3D motility images acquired in the stomach and small bowel.

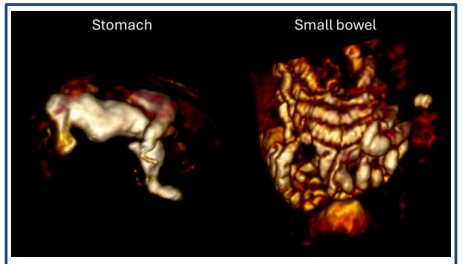

Fig. 3 3D rendering of the stomach and small bowel.

Discussion

In this study, we have provided proof of concept for a rapid 3D imaging method to assess GI motility, with images successfully acquired in the stomach and small bowel. By performing 3D motility imaging, it is possible to more accurately characterise the unpredictable motion of the GI tract, in comparison to 2D motility imaging. Furthermore, planning of the scan is easier to perform, thus negating the need for specialist training and reducing the overall time that patients are in the scanner.

The next step of the project is to perform motility analysis, which will be performed using GIQuant, validated software that can reliably measure GI motility in the stomach[7] and small bowel.[8] Using a bSSFP sequence provides good contrast between the fluid contents of the GI tract and surrounding tissue, which will ease segmentation of regions of interest when performing the analysis, whether done manually or using automated methods.

Conclusions

In conclusion, we have presented proof of concept of 3D motility imaging in the GI tract, with sufficiently short temporal resolution to capture motion of both the stomach and small bowel. This method may be used to better characterize GI motion than 2D imaging, and is much easier to plan, thus reducing overall time that patients are in the scanner.

References

[1] Oertel WH, Paule E, Hasemann T, et al. *Movement Disorders* **2024**;39:53–63. **[2]** Sclocco R, Nguyen C, Staley R, et al. *Neurogastroenterology & Motility* **2021**;33:e14146. **[3]** Lu K-H, Liu Z, Jaffey D, et al. *Neurogastroenterology & Motility* **2022**;34:e14239. **[4]** de Jonge CS, Gollifer RM, Nederveen AJ, et al. *BJR* **2018**;91:20170845. **[5]** Kowalik GT, Steeden JA, Atkinson D, et al. *MRM* **2019**;81:90–101. **[6]** Montalt-Tordera J, Steeden J, Muthurangu V. *Proceedings of the 31st Annual Meeting of ISMRM, London, UK* **2022**; p. 2769. **[7]** Menys A, Hoad C, Spiller R, et al. *Neurogastroenterology & Motility* **2019**;31:e13557. **[8]** Khalaf A, Nowak A, Menys A, et al. *Neurogastroenterology & Motility* **2019**;31:e13466.

Proffered Talks Session 6

The Application of FunctIonal Renal MRI to improve assessment of Chronic Kidney Disease (AFiRM) Study

Charlotte Buchanan[1], Alexander J Daniel[1], David Morris[2], Andrew Priest[3], Kevin Teh[4], David Thomas[5,6,7], Mark Gilthorpe[8], Philip Kalra[9], Iosif Mendichovszky[10], Steven Sourbron[4], Maarten Taal[11], Nicholas Selby[11], Susan Francis[1], on behalf of the AFiRM investigators.
[1]Sir Peter Mansfield Imaging Centre, University of Nottingham, UK
[2]Centre for Cardiovascular Science, University of Edinburgh, UK
[3]Department of Radiology, University of Cambridge, Cambridge, UK
[4]Department of Infection, Immunity and Cardiovascular Disease, University of Sheffield, UK
[5]Neuroradiological Academic Unit, University College London, UK
[6]Dementia Research Centre, , University College London, UK
[7]Wellcome Centre for Human Neuroimaging, University College London, UK
[8]Obesity Institute, Leeds Beckett University, UK
[9]Salford Royal NHS Foundation Trust, UK
[10]Department of Radiology, Addenbrooke's Hospital, Cambridge, UK
[11]Centre for Kidney Research and Innovation, University of Nottingham, UK

Introduction: The global burden of chronic kidney disease (CKD) is significant, affecting ~10% of the world's population. CKD can progress to kidney failure and increases cardiovascular risk. Better imaging methods to determine cause and prognosis are required. Renal multiparametric MRI provides whole kidney structural and functional measurements. The Application of Functional Renal MRI to improve assessment of Chronic Kidney Disease (AFiRM) study is a NIHR funded UK-wide multi-centre prospective cohort study to assess if multiparametric structural and functional renal MRI can deliver prognostic information and ultimately help guide treatment decisions.

Methods: AFiRM [1] is a multi-centre, prospective cohort study of patients with CKD from 10 UK centres, utilising the UKRIN-MAPS [2] multiparametric MRI protocol. Renal multiparametric MRI [3-8] is being collected at baseline and Year 2. Subjects are being scanned across GE, Philips and Siemens 3T MR scanners (1 GE site, 4 Philips sites, 5 Siemens sites) following quality assurance using the ISMRM/NIST phantom.

The MRI protocol (Fig. 1) comprises B_0 and B_1 mapping (for scanner characterization, correction of quantitative measures, and distortion correction), relaxometry measures of T_1 (both MOLLI and inversion recovery spin echo EPI), T_2 and T_2* mapping, Diffusion Weighted Imaging (DWI, multiple b-values and directions for an IVIM fit and estimation of fractional anisotropy (FA)) angiograms and phase contrast MRI (PC-MRI) of the renal arteries, magnetization transfer ratio (MTR) mapping, volumetric T_2- and T_1-weighted scans for estimation of total kidney volume (TKV) and cortex and medulla volume, mDIXON, and ASL perfusion scans.

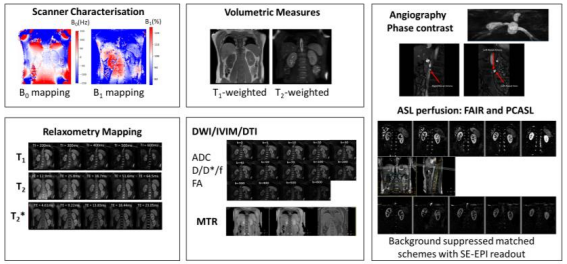

Fig 1: *The multiparametric UKRIN-MAPS protocol, comprising B0 and B_1 mapping, relaxometry (T1 MOLLI and Inversion recovery SE-EPI, ME-SE T2 and BOLD R_2*/T_2*), Diffusion Weighted Imaging, angiograms and phase contrast MRI, magnetization transfer ratio mapping, volumetric T_1- and T_2-weighted scans, mDIXON, and ASL perfusion scans.*

The analysis pipeline consists of machine learning based segmentation from the T_2-weighted (for total kidney [9]) and T_1-mapping (for cortex and medulla [10]) scans. B_0, B_1 and MTR maps are generated, BOLD R_2*/T_2*-mapping data is fit to an exponential model, T_2-mapping data is fit to both a simple exponential model and a StimFit model [11]. Distortion correction (FUGUE and TOP-UP) can be applied to SE-EPI-based data and model driven registration (MDR) is used to realign T_1 (MOLLI and SE-EPI), ASL and DWI data and quantitative maps subsequently generated.

Results: AFiRM has completed recruitment with baseline MRI scans on 421 participants with CKD across 10 UK centres on GE, Philips and Siemens 3T scanners at baseline, and has scanned ~100 Year 2 scans. Preliminary MRI analyses have been completed in 300 baseline datasets for estimation of TKV from T_2-weighted scans, B_0 and B_1 mapping, T_1 MOLLI and T_2* mapping as shown in Figure 2.

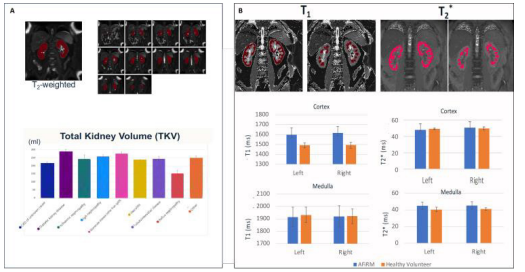

Fig 2: *Results of preliminary MRI analyses of 300 datasets from the AFiRM study showing A) Example T_2-weighted scan and u-Net masks, and TKV values separated by CKD aetiology. B) Example T_1 MOLLI and T_2* maps, u-Net cortex and medulla masks, and associated range T_1 and T_2* values in cortex and medulla in AFiRM patients and healthy volunteers.*

Discussion: The AFiRM study is a UK-wide large-scale multicentre clinical study of renal multiparametric MRI in people with CKD, applying the UKRIN-MAPS harmonised renal MRI protocol, data storage, and quality assurance and centralised analysis. Baseline recruitment to AFiRM completed in February 2024 and baseline results of measures in the full cohort are now being undertaken.

Conclusions: This study applies the UKRIN-MAPS multiparametric renal MRI protocol to understand changes in renal structure and function in CKD disease progression. This has the potential to transform the study of novel drugs for CKD progression, assessing changes earlier than traditional clinical measures.

Acknowledgements: This work was funded by the UKRIN-MAPS MRC Partnership grant (MR/R02264X/1) and the NIHR AFiRM project (NIHR128494).

References

[1] Application of Functional Renal MRI to improve assessment of chronic kidney disease (AFiRM) study website: https://www.uhdb.nhs.uk/afirm-study/
[2] UKRIN-MAPS (MRI Acquisition and Processing Standardisation) website: https://www.nottingham.ac.uk /research/groups/spmic/research/uk-renal-imaging-network/ukrin-maps.aspx
[3] Mendichovszky, I et al. Technical recommendations for clinical translation of renal MRI: a consensus project of the Cooperation in Science and Technology Action PARENCHIMA. Magn. Reson. Mater. Physics, Biol. Med. 2019, doi:10.1007/s10334-019-00784-w.
[4] Bane, O.; Mendichovszky, I. A.; Milani, B.; Dekkers, I. A.; Deux, J.-F.; Eckerbom, P.; Grenier, N.; Hall, M. E.; Inoue, T.; Laustsen, C.; Lerman, L. O.; Liu, C.; Morrell, G.; Pedersen, M.; Pruijm, M.; Sadowski, E. A.; Seeliger, E.; Sharma, K.; Thoeny, H. C.; Vermathen, P.; Wang, Z. J.; Serafin, Z.; Zhang, J. L.; Francis, S. T.; Sourbron, S.; Pohlmann, A.; Fain, S. B.; Prasad, P. V. Consen-sus-based technical recommendations for clinical translation of renal BOLD MRI. Magn. Reson. Mater. Physics, Biol. Med. 2019, doi:10.1007/s10334-019-00802-x.
[5] Dekkers, I. A.; Boer, A. de; Sharma, K.; Cox, E.; Lamb, H.; Buckley, D. L.; Bane, O.; Morris, D. M.; Prasad, P. V; Semple, S. I.; Gillis, K. A.; Hockings, P.; Buchanan, C.; Wolf, M.; Laustsen, C.; Leiner, T.; Haddock, B.; Hogenduin, J. M.; Pullens, P.; Sourbron, S.; Francis, S. Consensus-based technical recommendations for clinical translation of renal T1 and T2 mapping MRI. Magn. Reson. Mater. Physics, Biol. Med. 2019, doi:10.1007/s10334-019-00797-5.
[6] Fabio Nery et al. Consensus-based technical recommendations for clinical translation of renal ASL MRI. MAGMA 2020.
[7] Ljimani, A.et al. Consensus-based technical recom-mendations for clinical translation of renal diffusion-weighted MRI. Magn. Reson. Mater. Physics, Biol. Med. 2019, doi:10.1007/s10334-019-00790-y.
[8] Villa G, et al. Phase-contrast magnetic resonance imaging to assess renal perfusion: a systematic review and statement paper. MAGMA. 2020 Feb;33(1):3-21. doi: 10.1007/s10334-019-00772-0.
[9]Daniel AJ et al, Automated renal segmentation in healthy and chronic kidney disease subjects using a convolutional neural network, Magn. Reson. Med. Volume86, Issue2, 1125-113, 2021.
[10] Cox EC et al Automated Analysis of Kidney MRI data in the UK Biobank. 5th Renal MRI meeting Ghent, 2023.
[11] Li H et al, Improved Harmonization of Renal T2 Mapping Between Vendors using Stimulated Echo. ISMRM 2022

Poster Abstracts

In order of the power pitches in the program schedule

Published 03/09/2024

Ultra-low field Magnetic Resonance Imaging of the human forearm in the Earth's Magnetic Field of Dublin, Ireland.

Friedrich Wetterling[1,2,3], Conor Conway[1], Shane Hunt[1], Arun Bokde[2], and Anil Kokarem[1]
[1]Electronic and Electrical Engineering, Trinity College Dublin, Dublin, Ireland
[2]Trinity College Institute of Neuroscience (TCIN), Trinity College Dublin, Dublin, Ireland
[3]Trinity Centre for Biomedical Engineering (TCBE), Trinity College Dublin, Dublin, Ireland

Introduction: The aim of this work was to explore the limits and opportunities for ultra-low field Magnetic Resonance Imaging in the earth's magnetic field at 50µT (EF-MRI) in Dublin, Ireland. MRI normally requires high static magnetic fields (>0.5T) to polarise the hydrogen-1 nuclei in tissue and to maximise the available signal. Callaghan et al. developed EF-MRI for use in antarctica [1] before advancing the technology to commercialisation as an educational systems globally [2]. Nowadays those systems can be developed at low material cost of less than 200EUR [3, 4]. However, their use has not evolved much beyond scientific and educational exploration. Some universities reported student laboratories for undergraduates using the system in physics [5] and in chemistry [6]. Yet, other examples demonstrated the remaining signal challenges to work with this approach in practice [7].

Fig. 1. *the top image shows the location of the Medical Circuits and Systems laboratory (www.MediCAS-Lab.eu) hosted at the Electronics and Electrical engineering Department at Trinity College Dublin (TCD) in the city centre of Dublin, Ireland. The bottom picture shows the Magritek Earth's Field MRI system positioned for measurements of the forearm.*

Methods: All EF-MRI experiments were carried out on a system with an inner diameter of 80mm (Terranova, Magritek, Wellington, New Zealand, Figure 1) which provided approximately 21mT polarization magnetic field strength using 7A polarization current. The maximum gradient strength was 80µT/m. First-order shimming was achieved by supplying the three-axis gradient coil set with currents of up to 30mA. An autoshim algorithm was applied, employing a modified bisection approach to iterate towards the ideal shim by maximizing the peak height. The B_1-coil was tuned by 9.5nF to 2095Hz Larmor frequency. The Free Induction Decays (FIDs) (Tpol/TB1/Tdelay/Tacq/TR=1.5s/0.65ms/17ms/0.5s/3s, 8192 points) were processed offline using a routine written in MATLAB (Mathworks, Nattick, USA). *EF-MRI* of phantoms filled with tab water were conducted using a 2D filtered back projection sequence (Tpol/TB1/Tdelay/TE/TR=4s/0.7ms/17ms/100ms/8s, 32 projections, 64Hz bandwidth, and 64 samples, for 200x200mm FOV in z-direction and y-direction resulting in a nominal voxel resolution of 3mm x 3mm). The total imaging time was 4min16s. For the forearm the following parameters were reduced: TE to 50ms, Tpol to 1s, TR to 2s, TB1 to 0.66ms, and projections to 16 with 32 samples per projection. The total acquisition time was 32 seconds. Ten FIDs were collected for the forearm (Tpol/TB1/Tdelay/Tacq/TR=1.5s/0.6ms/17ms/0.5s/3s, 8192 points).

Results: Figure 2 shows the raw data captured for a single FID of the water bottle, the filtered result, and the full spectral extend of this signal showing substantial amount of 50-Hz related noise peaks. The resonance was conveniently positioned between the 2150Hz and 2250Hz harmonic noise peaks. Notably, the noise was substantially reduced from ~50µV to ~10µV root mean square through orienting the device 90degree rotated compared to the recommended position – requiring a slight tilt of the system itself. Figure 3 shows the FIDs for 100 recordings within 10 minutes. Expectedly, the noise peak was more stable at a mean and standard deviation of 2151.5±1.0Hz than the water resonance that showed larger variance at 2193.6±3.4Hz translating to a magnetic field strength of 51.52±0.08µT. Figure 4 shows images captured of the water bottle and structured water phantom. Figure 5 shows a spectrum captured of the human forearm and a corresponding first image. While some signal is visible compared to the noise image more work remains to be conducted to substantiate this method.

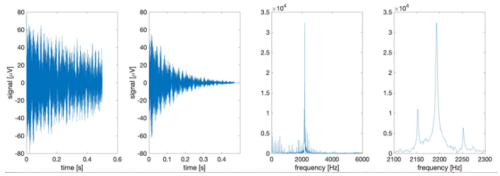

Fig. 2. Free Induction Decay (FID) recorded for a bottle filled with tab water (0.5l). The raw data recorded as a function of time is shown in the graph on the left. The filtered data using an exponential decay time constant at 150ms and 8 times zero filling is shown on the left central graph. The spectrum for that signal is shown in the right central graph demonstrating several harmonic peaks originating from 50 Hz noise. The right graph shows zoomed in spectrum to magnetic resonance of water at 51.4uT (2190Hz).

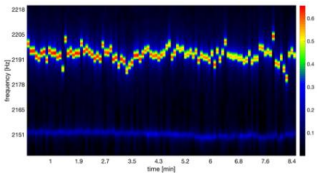

Fig. 3. 100 FIDs captured for water bottle and plotted as a function of time to explore the local magnetic field fluctuations. The mean and standard deviation of the resonance frequency was at 2193.6Hz±3.4 Hz while the 50Hz harmonic at 2150Hz was estimated to be 2151.5±1.0Hz.

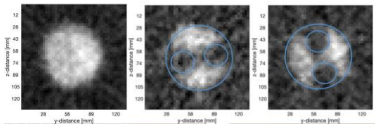

Fig. 4. cross-sectional image of water bottle with 75mm diameter captured using back-projection recording and resonance frequency correction (left). Images from phantom containing two air filled tubes horizontally (centre) and vertically arranged (right).

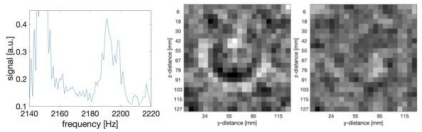

Fig. 5. Magnetic Resonance signal obtained from 10 FIDs for lower arm showing a resonance between 2180 and 2205Hz. Note harmonic of 50Hz at 2150Hz at a much higher magnitude (top). Magnetic Resonance Images obtained Image obtained for lower arm inside scanner (bottom, left) and corresponding noise image when the arm was removed (bottom, right).

Discussion: Imaging of water filled phantoms is easily achievable even in the city centre of Dublin, a major capital city in Europe. However, imaging of tissue remains challenging. The shortened relaxation times in tissue require adaptation of existing solutions. Future systems may facilitate shorter acquisition delays and faster repetition times. Currently, 20ms delay are required before the transmit coil ringdown is complete and before signal can be received and TRs must be twice the polarisation time to prevent overheating of the system. Cooling and more appropriate transmit-only receive-only resonator solutions may offer first innovation approaches to advance EF-MRI further. Sodium-23 MRI suffers from a comparable signal loss as EF-MRI achieving approximately 20 000 less signal than hydrogen-1 MRI, yet while whole body sodium MRI has been captured in 2012 [8], EF-MRI remains to be challenging. The use of SQUIDs and higher pre-polarisation may offer a viable avenue to boost signal for EF-MRI.

Conclusions: In conclusion, EF-MRI offers sufficient signal for MRI of water phantoms. Device positioning and calibration remains challenging and magnetic field variations require correction for imaging. Optimized resonator coils and sequences may offer a new avenue for EF-MRI in the future.

References

[1] P. T. Callaghan, C. D. Eccles, and J. D. Seymour, *Review of Scientific Instruments,* vol. 68, no. 11, pp. 4263-4270, 1997.

[2] M. E. Halse, A. Coy, R. Dykstra, C. Eccles, M. Hunter, R. Ward, and P. T. Callaghan, *J Magn Reson,* vol. 182, no. 1, pp. 75-83, Sep, 2006.

[3] C. A. Michal, *Measurement Science and Technology,* vol. 21, no. 10, pp. 105902, 2010/08/09, 2010.

[4] C. A. Michal, *Journal of Magnetic Resonance,* vol. 319, pp. 106800, 2020/10/01/, 2020.

[5] B. Kami Pars, D. Baudouin, L. Ryma, P.-Q. Marie, and D. Luc, *European Journal of Physics,* vol. 36, no. 3, pp. 035032, apr, 2015.

[6] P. Bergstrom Mann, S. Clark, S. T. Cahill, C. D. Campbell, M. T. Harris, S. Hibble, T. To, A. Worrall, and M. Stewart, *Journal of Chemical Education,* vol. 96, no. 10, pp. 2326-2332, 2019/10/08, 2019.

[7] L. Deshmukh, K. Bagree, and S. Sharma, *International Journal of Engineering Research and Applications,* vol. 07, pp. 26-30, 05/01, 2017.

[8] F. Wetterling, D. M. Corteville, R. Kalayciyan, A. Rennings, S. Konstandin, A. M. Nagel, H. Stark, and L. R. Schad, *Phys Med Biol,* vol. 57, no. 14, pp. 4555-67, Jul 21, 2012.

Tuneable Digital Phantoms for Grey Matter Modelling

1 Cardiff University Brain Research Imaging Centre (CUBRIC), School of Psychology, Cardiff University, Cardiff, United Kingdom. 2 School of Computer Science and Informatics, Cardiff University, Cardiff, United Kingdom. 3 École polytechnique fédérale de Lausanne, Lausanne, Switzerland. 4 Frankfurt Institute for Advanced Studies, Frankfurt am Main, Germany. 5 Ernst Stru¨ngmann Institute (ESI) for Neuroscience in cooperation with the Max Planck Society, Frankfurt am Main, Germany

Introduction: Numerical phantoms play an indispensable role in advancing and validating magnetic resonance imaging (MRI) techniques[1]. This is particularly true of diffusion MRI (dMRI), where the need arises for generating adjustable and microstructurally accurate representations of complex biological tissues. While considerable effort has been dedicated to developing numerical phantoms for brain white matter (WM)[2-4], the same tuneable phantoms capable of replicating the complexity of grey matter (GM) microstructure are lacking. In this work, we introduce *Contextual Cellular Growth* (ConCeG) as a solution to synthesize morphologically accurate GM tissue substrates, employing principles similar to the Contextual Fibre Growth (ConFiG) approach applied to WM[2].

Methods: To create realistic GM phantoms, it is essential to define the key morphological features required to faithfully replicate neural cells, including neurons and glia[5]. We categorized these attributes into three groups: structural, topological, and shape (Fig.1). Real neural cell reconstructions from open-access datasets such as neuromorpho.org[6] and the Allen brain atlas[7] were used to estimate distributions of these morphological features within the GM of the healthy adult mouse brain, utilising the TREES toolbox in MATLAB[8].

ConCeG is the algorithm introduced to synthesize realistic GM phantoms and it is implemented in Matlab. It takes as inputs: voxel size, the number of nodes, predefined morphological parameters (structural, topological, and shape, see Fig.1), and layer-specific density profiles for each cell type. The output consists of cells formatted in SWC[9] format. Similar to ConFiG[2], ConCeG relies on a network of connected nodes. The algorithm starts by distributing soma nodes within specified dimensions, following the user-defined cell density with respect to cortical depth. Additional nodes are randomly placed within the voxel space, creating a connected network for cellular projections. This network serves as a guide for cellular projections to navigate, considering biologically informed cost functions. The projections extend toward attractor points efficiently while avoiding nodes already occupied by existing projections or nodes that would lead to unrealistic projection shrinkage. ConCeG facilitates branching by employing the topological neuron synthesis approach[10]. As a projection grows, its path length increases, and the probability of branching is determined in relation to the birth lengths of remaining bars in the barcode. The branching probability increases as the path length approaches the birth length of another bar and satisfy the probability of branching given the current branch order. Newly initiated branches select angles from the angle distribution and pick attractor points that satisfies this angle in relation to the parent branch. Cellular growth occurs contextually, with the maximum node radius for nodes in the network updated at each growth step.

Results: Fig.2 demonstrates that ConCeG can recreate cellular structures accurately when cells are grown individually, preserving key morphological characteristics' distributions. Fig.3 shows that the same degree of accuracy can be achieved when cells are grown contextually.

Finally, in Fig.4 we illustrate ConCeG's flexibility and capabilities by synthesizing a column of the mouse visual cortex based on density profiles from the Allen brain atlas [11] and [12].

Discussion: Here, we have developed a highly versatile approach, ConCeG, which leverages real cellular data to create realistic digital phantoms of brain GM. These phantoms are ready to be incorporated into dMRI simulators, such as Camino[13], DiSimPy[14] and MCDS[15].

The current implementation of ConCeG enables the generation of large voxels within reasonable computational time (e.g. ~5 hours to generate a 100x100x1200 μm^3 voxel using a single CPU-thread). However, further developments are necessary to achieve dense cellular packing. In fact, the densest voxel we were able to generate thus far has a 54% intracellular volume fraction. Future work will focus on increasing ConCeG ability to achieve denser cellular packings (e.g. ~70%), implementing strategies such as post-growth optimization similar to ConFiG[2]and MEDUSA[4].

Power Pitch Session 1

Conclusion: Here we introduced ConCeG: a significant contribution to the field of neuroimaging and computational biology, enabling more accurate and insightful simulations of complex neural tissues.

Acknowledgements: Dr Palombo, myself, and this work is supported by UKRI Future Leaders Fellowship.

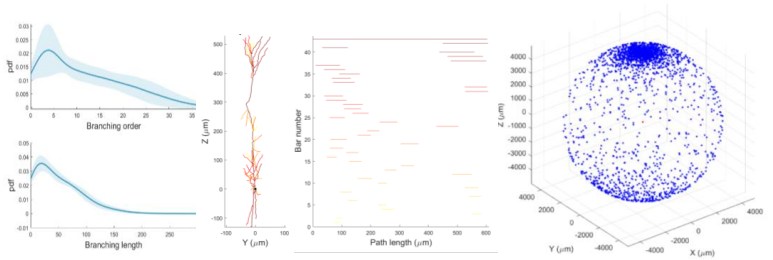

Figure 1: Morphological features for ConCeG. Structural: branch and order; Topological Persistence Barcode[16]: which encodes the start and end of each branch; Shape: shape is described by the distribution of terminal points onto a sphere.

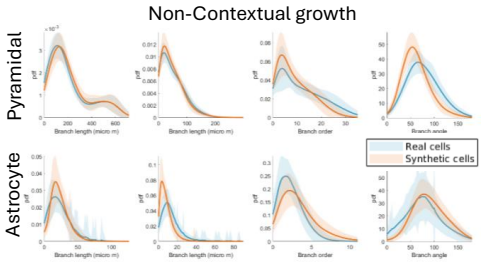

Figure 2: Comparison between real and non-contextually synthesised cells.

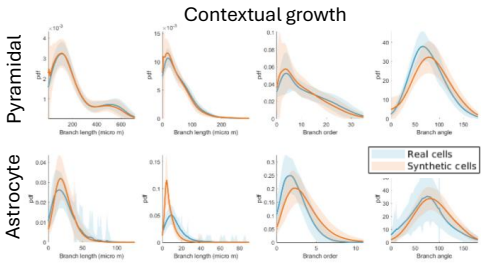

Figure 3: Comparison between real and contextually synthesised cells.

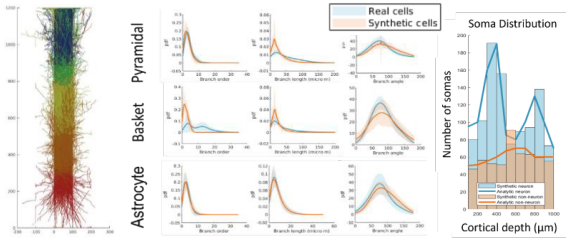

Figure 4: A column of synthesised mouse visual cortex, colours indicate the different cortical layers. Histogram of somas with respect depth for neurons and non-neurons overlaid with analytic al solutions given the real distribution [12].

References

[1]. Fieremans, E., et al. Neuroimage, 2018. [2]. Callaghan, R., et al. Neuroimage, 2020. [3]. Villarreal-Haro, J.L., et al. Front Neuroinform, 2023. [4]. Ginsburger, K., et al. Neuroimage, 2019. [5]. Zisis, E., et al. Cereb Cortex, 2021. [6]. Akram, M.A., et al. Sci Data, 2018. [7]. Atlas, D.M.B., Allen brain atlas. 2006. [8]. Cuntz, H., et al. PLoS Comput Biol, 2010. [9]. Cannon, R.C., et al. Journal of neuroscience methods, 1998. [10]. Kanari, L., et al. Cell Rep, 2022. [11]. Gouwens, N.W., et al. Nat Neurosci, 2019. [12]. Tsai, P.S., et al. J Neurosci, 2009. [13]. Alexander, D., et al. ISMRM. 2006. [14]. Kerkelä, L., et al. Journal of Open Source Software, 2020. [15]. Rafael-Patino, J., et al. Front Neuroinform, 2020. [16]. Kanari, L., et al. Neuroinformatics, 2018.

Simultaneous Structural and Functional Susceptibility and Conductivity Mapping Using a Rapid High-Resolution Multi-Echo EPI Acquisition

Jierong Luo[1], Oliver C. Kiersnowski[2], Patrick Fuchs[1], Jannette Nassar[1], Oriana V. Arsenov[1], Stephen Wastling[3,4] and Karin Shmueli[1]

[1]Department of Medical Physics and Biomedical Engineering, University College London (UCL), London, UK
[2]Azienda Ospedaliera Universitaria San Martino di Genova, Neuroradiology Unit, Genoa, Italy
[3]Neuroradiological Academic Unit, UCL Queen Square Institute of Neurology, UCL, London
[4]Lysholm Department of Neuroradiology, National Hospital for Neurology & Neurosurgery, London

Introduction: Quantitative susceptibility mapping (QSM), electrical conductivity mapping (EPT) and fMRI show promise in characterising neurodegenerative diseases [1–2], but each currently needs a separate ~5-minute acquisition. Using a highly accelerated multi-echo EPI acquisition, simultaneous structural and functional QSM and EPT can be achieved. Here we optimised a rapid (~6 minutes) and high-resolution (1.3 mm isotropic) multi-echo GRE-EPI acquisition, and processing pipelines, to provide simultaneous structural and functional MRI, QSM and EPT and characterized their temporal signal-to-noise ratios (tSNR).

Methods: Three healthy volunteers (HVs) were scanned on a 3T Prisma (Siemens, Erlangen, Germany) using a single-shot 2D GRE-EPI sequence [3], with 1.3 mm isotropic resolution, GRAPPA=4, MB=3, partial Fourier 6/8, TR=4034 ms, TEs =15.6, 41.6, 67.6 ms. Seventy volumes were acquired with a block design visual stimulus paradigm [4], in a total acquisition time of 6 min 15 s including reference scans.

To calculate QSM within each volume, a total field map was estimated from a non-linear fit [5] of MP-PCA denoised [6-7] complex data, followed by Laplacian unwrapping [8]. Background fields were removed using V-SHARP [9,10] and PDF [11], and dynamic distortion correction was applied to the local field map [12]. Susceptibility was calculated using non-linear total variation [13] with $\alpha=2.4\times10^{-4}$ and two-pass masking [14].

For EPT, the MR transceive phase (φ_0) was extrapolated from the multi-echo complex data and unwrapped as described previously [15], followed by correction of slice-to-slice inconsistencies [16]. To reduce noise and preserve anatomical structures, the conductivity was calculated as the surface integral of the φ_0 gradient estimated by weighted polynomial fitting within kernels based on tissue segmentations [17]. The temporal mean image over all volumes of the CNR-optimal echo-combined magnitude [18] was used for the fitting weights and segmentations using SPM12 [19].

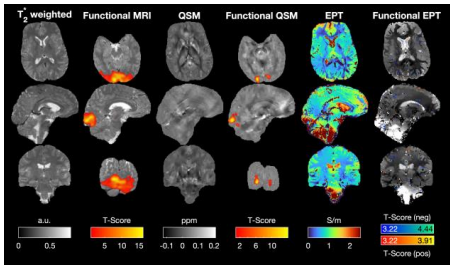

Fig. 1. Structural and functional contrasts calculated from the multi-echo 2D GRE-EPI acquisition in HV1. Whole-brain positive (red) and negative (blue) fEPT activations are projected on the median EPT image.

Final structural contrasts were calculated as the mean over all 70 volumes co-registered across the time series, and temporal SNR (tSNR) maps for the echo-combined magnitude, absolute QSM and EPT were also calculated as the temporal mean over the temporal standard deviation in each voxel. The structural EPT was calculated as the median of non-zero conductivity over all 70 volumes to minimise the effect of non-physiological conductivities. For functional analysis, the registered echo-combined magnitude MRI, QSM and EPT images were analysed using a standard SPM12 pipeline [20], with the default haemodynamic

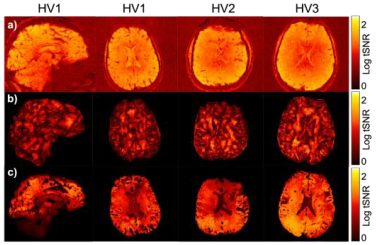

Fig. 2. Temporal SNR (tSNR) calculated for echo-combined magnitude (a), QSM (b) and EPT (c) time series in different subjects.

response function. To avoid bias introduced by preprocessing [21], no smoothing was applied to the EPT time series prior to the functional analysis.

Results and Discussion: Fig. 1 shows structural contrasts with regional susceptibility values and conductivity values in line with literature values at 3T [22, 23]. Temporal SNR maps (Fig.2) characterise the image quality across the time course, with the absolute QSM tSNR difficult to interpret and low EPT tSNR in the ventricles and cerebellum. Fig. 3 shows novel multi-echo fQSM activations that were weaker and less extensive than fMRI activations [24,25] and highly novel fEPT activations with large inter-subject variability [26, 27].

Conclusions: The highly accelerated multi-echo 2D GRE-EPI acquisition and processing pipelines we have developed provide high-quality simultaneous structural and functional QSM and EPT, together with conventional magnitude and fMRI. Multi-echo fQSM is more localised than fMRI and fEPT provides novel information and requires further optimisation.

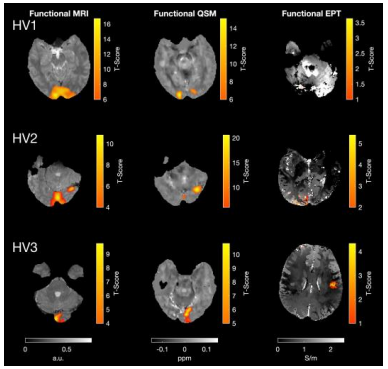

Fig. 3. Functional activations of fMRI, fQSM and fEPT in different subjects. Note only negative fEPT activations are shown here.

References

[1] Eskreis-Winkler S, et al. The clinical utility of QSM: disease diagnosis, medical management, and surgical planning. NMR Biomed 2017; 30(4). [2] Tha KK, et al. Noninvasive electrical conductivity measurement by MRI: a test of its validity and the electrical conductivity characteristics of glioma. Eur Radiol 2018; 28(1): 348-355. [3] Center for Magnetic Resonance Research Department of Radiology. Multi-Band Accelerated EPI Pulse Sequences. [4] Nassar J et al. Preliminary Functional Quantitative Susceptibility Mapping with Multi-Echo EPI. Proc Ann Meeting ISMRM 2023; 2533. [5] Liu T, et al. Nonlinear formulation of the magnetic field to source relationship for robust quantitative susceptibility mapping. Magn Reson Med 2013; 69(2):467-476. [6] Veraart J, et al. Denoising of diffusion MRI using random matrix theory. Neuroimage 2016; 142:394-406. [7] Doniza L, et al. MP-PCA Image Denoising Techniques for High Resolution Quantitative Susceptibility Mapping (QSM) of the Human Brain In Vivo. Proc Ann Meeting ISMRM 2023; 2948. [8] Schofield MA, Zhu Y. Fast phase unwrapping algorithm for interferometric applications. Opt Lett 2003;28(14):1194. [9] Wei H, et al. Joint 2D and 3D phase processing for quantitative susceptibility mapping: application to 2D echo-planar imaging. NMR Biomed 2017;30(4). [10] Li W, et al. Quantitative susceptibility mapping of human brain reflects spatial variation in tissue composition. Neuroimage. 2011; 55:1645-1656. [11] Liu T, et al. A novel background field removal method for MRI using projection onto dipole fields (PDF). NMR Biomed 2011;24(9):1129-1136. [12] Visser E, et al. Reference-free unwarping of EPI data using dynamic off-resonance correction with multiecho acquisition (DOCMA). Magn Reson Med 2012; 68(4):1247-1254. [13] Milovic C, et al. Fast nonlinear susceptibility inversion with variational regularization. Magn Reson Med 2018;80(2):814-821. [14] Karsa A, Shmueli K. A New, Simple two-pass masking approach for streaking artifact removal in any QSM pipeline. Proc Ann Meeting ISMRM 2023; 2462. [15] Luo J, et al. preliminary whole-brain functional electrical properties tomography using gradient-echo echo-planar imaging. Proc Ann Meeting ISMRM 2024; 3681. [16] Arsenov O V, et al. Artifact reduction for rapid phase-based EPT in the human brain in vivo using a multi-echo 2D EPI sequence. Proc Ann Meeting ISMRM 2024; 3675. [17] Karsa A, Shmueli K. New approaches for simultaneous noise suppression and edge preservation to achieve accurate quantitative conductivity mapping in noisy images. Proc Ann Meeting ISMRM 2021; 3774. [18] Poser B A, et al. BOLD contrast sensitivity enhancement and artifact reduction with multiecho EPI: parallel-acquired inhomogeneity-desensitized fMRI. Magn Reson Med 2006; 55: 1227–1235. [19] Ashburner J, Friston KJ. Unified segmentation. NeuroImage 2005; 26: 839-851. [20] Friston K J, et al. Statistical parametric maps in functional imaging: a general linear approach. Hum Brain Mapp 1995; 2: 189-210. [21] S. Mandija et al. The first MR electrical properties tomography (MR-EPT) reconstruction challenge: preliminary results of simulated data. Proc Ann Meeting ISMRM 2024; 182. [22] Kiersnowski O C, et al. Rapid high resolution integrated structural and functional susceptibility and conductivity mapping in the human brain. Proc Ann Meeting ISMRM 2024; 188. [23] Gabriel S, et al. the dielectric properties of biological tissues: II. Measurements in the frequency range 10 Hz to 20 GHz. 1996; 41. [24] Balla D Z, et al. Functional quantitative susceptibility mapping (fQSM). Neuroimage 2014; 100: 112-124. [25] Özbay P S, et al. Probing neuronal activation by functional quantitative susceptibility mapping under a visual paradigm: A group level comparison with BOLD fMRI and PET. Neuroimage 2016; 137: 52-60. [26] K. J. Jung, et al. Investigation of electrical conductivity changes during functional activity of the brain via phase-based MR-EPT: Preliminary observation. Proc Ann Meeting ISMRM 2023; 0922. [27] G. H. Jahng, et al. High-frequency conductivity signal changes measured with functional MREPT during visual stimulation. Proc Ann Meeting ISMRM 2023; 0923.

Adaptive Wavelet Noise Suppression

Teddy Zhao [1,2] [1]Cancer and Genomic Sci, Uni of Birmingham [2]Oncology, Birmingham Children's Hospital

Introduction Proton magnetic resonance spectroscopy (^{1}H-MRS) [1] can observe the *in vivo* metabolite profiles of brain tissue non-invasively. Spectral noise, one of the main challenges in clinical and scientific ^{1}H-MRS observation, leads to inaccurate metabolite concentration estimation, and it hardly be fully avoided by optimising physical sequences [2]. This abstract presents a novel computational method, naming adaptive wavelet noise suppression (AWNS), for suppressing spectral noise and evaluated its performance through simulated brain tissue ^{1}H-MRS [3].

Methods *Adaptive wavelet noise suppression* AWNS is a spectral processing method that combines the concepts of wavelet theory and data mining (Fig. 1A). Wavelet decomposition and reconstruction can remove spectral components based on their energy distribution, and the assignment of noise and noiseless components is often manually determined [4]. AWNS assesses all the possible wavelet variations and finally selects the outstanding spectrum according to quality-control parameters.

Evaluation AWNS was assessed by using simulated ^{1}H-MRS that was generated with VeSPA [5] and 1.5T/3T short-TE point-resolved spectroscopy (PRESS) or stimulated-echo acquisition mode (STEAM) (Fig. 1B). Metabolites that can be fitted with visibly minimal residual were used for simulating artificial normal brain, epilepsy and tumour spectra [3,6,7] and Gaussian white noise (fSNR 4—30). Spectra were quantified by using LCModel [8] and TARQUIN [9]. The metabolite ratio improvement was measured as $f = \left|\frac{\text{metab ratio of noise–suppressed MRS – metab ratio of noiseless MRS}}{\text{metab ratio of noisy MRS – metab ratio of noiseless MRS}}\right|$, and the metabolite ratio error was calculated as $e = \left|1 - \frac{\text{metabolite ratio of noise suppressed MRS or noisy MRS}}{\text{metabolite ratio of noieless MRS}}\right|$.

Results The source code and simulation examples are available at teddychao.github.io/awns.html. Totally 6 metabolites were used after fitting assessment, namely alanine, creatine, GABA, glutamate, glutamine, and NAA (Fig 1C). Simulated brain tissue includes frontal lobe for normal subjects, idiopathic generalised epilepsy, white matter (normal), meningioma, astrocytomas, anaplastic astrocytomas (example given in Figure 2), glioblastomas, and metastases for adults (1.5T, PRESS/STEAM), ependymomas, medulloblastomas and pilocytic astrocytomas for paediatrics (1.5T/3T, PRESS). Metabolite concentration error showed decreased after performing AWNS (mean f<1). Metabolites showed significantly more accurate (paired P<.05, Figure 3) in some tissues.

Discussion This study focuses on the noise issue in real-world ^{1}H-MRS by presenting computational analysis. Initially, the results showed spectral noise can affect the accuracy of metabolite concentration estimation since the metabolite ratios became inaccurate after adding noise and the fitting performance was impacted. Suppressing ^{1}H-MRS noise is challenging due to the complexity of ^{1}H-MRS line shape and the unpredictable level of spectra noise. There have been methods such as apodisation, principal component analysis and deep learning, yet they suffer from enlarged line width [2], signal leakage [10] and the dependence on training data [11] that are not always available due to the diverse clinical metabolite profiles. AWNS is designed to address these issues, where its dependence on quantification preserves signals from leakage and makes it free from dependence on any training data. Theoretically, AWNS learn from prior knowledge from the process of spectral quantification, so it can be adaptive based on the diverse noise in real-world MRS acquisition. Previous results indicated potential of AWNS for improving diagnosis [3], yet better diagnosis does not directly prove more accurate metabolite profiles. To do that, this study uses simulated ^{1}H-MRS where the ground truth is known and metabolites can be freely controlled, so that various human brain tissue profiles can be studied. It then assesses the performance of AWNS for suppressing the negative impact of manually added noise. As the result, the included metabolites can be more accurately determined in noise-suppressed ^{1}H-MRS than noisy ^{1}H-MRS. The study started from observing the metabolites that have basic line shapes that can be fitted with not much visible residual. Some other metabolites, such as *myo*-Inositol and choline, have not been included in this study, because the fitting of noiseless spectra for these metabolites is visibly much poorer in their single-metabolite spectra. The future work is to improve fitting for other important and challenging metabolites like choline, *myo*-Inositol, lactate, and taurine and to include other tissue profiles and field strength whereas available.

Conclusion Simulation suggests ^{1}H-MRS spectral noise can limit metabolite concentration accuracy and can be suppressed through computating for providing more accurate estimation. (700 words)

References [1] R.R. Ernst & W.A. Anderson *Rev. Sci. Instrum.* **37**, 93 (1966). [2] R. Kreis, et al. *NMR Biomed.* **34**, e4347 (2020). [3] T. Zhao, et al. *NMR Biomed.* **37**, e5129 (2024). [4] M. Stéphane, A wavelet tour of signal processing: The sparse way, Academic Press, Massachusetts, 2009. [5] B.J. Soher et al. *Magn. Reson. Med.* **90**, 823 (2023). [6] F.A. Howe et al. *Magn. Reson. Med.* **49**, 223 (2003). [7] R.J. Simister et al. *Neurology* **61**, 897 (2003). [8] S.W. Provencher *NMR Biomed.* 14, 260 (2001). [9] M. Wilson et al. *Magn. Reson. Med.* **65**, 1 (2011). [10] J. Mosso et al. *NeuroImage* **263**, 119634 (2022). [11] M Dziadosz et al. *Magn. Reson. Med*. **90**, 1749 (2023)

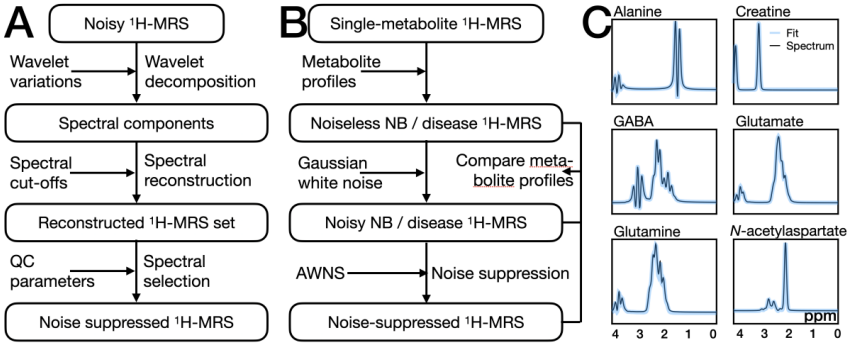

Fig. 1. Flowchart of the study and example data: **A**, AWNS pipeline; **B**, generating and analysing artificial normal or disease ^{1}H-MRS; **C**, 1.5 T artificial short-TE single-metabolite spectra (PRESS).

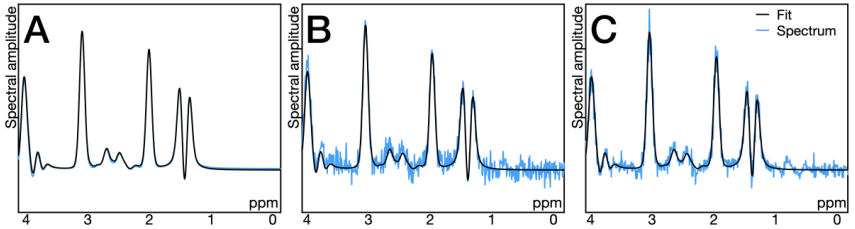

Fig. 2. Example of noise suppression performance on artificial ^{1}H-MRS that simulates anaplastic astrocytoma by using creatine, glutamate, glutamine, GABA, and NAA, including ^{1}H-MRS spectra as noiseless (A), noise-added (B, by adding GWN) and noise-suppressed (C, processed with AWNS).

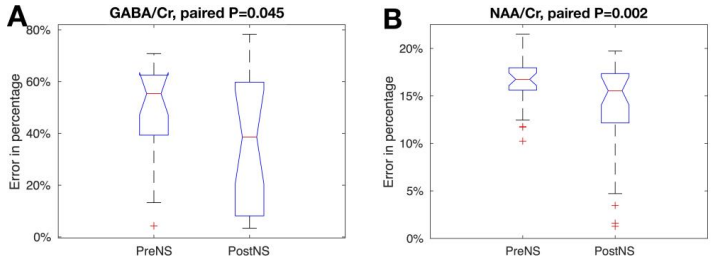

Fig. 3. Examples of metabolite concentration estimation error comparing pre and post noise suppression (preNS, postNS). Examples are given by GABA/Cr of frontal lobe in idiopathic (genetic) generalised epilepsy patients (A) and NAA/Cr of white matter in normal controls (B).

Magnetic Source Separation in the Head and Neck: Comparing Three Gradient Echo Methods

Matthew T. Cherukara,[1] Patrick Fuchs,[1] and Karin Shmueli[1]

[1]*Department of Medical Physics and Biomedical Engineering, University College London, London, UK*

Introduction: Quantitative susceptibility mapping (QSM) is an MRI technique that reconstructs tissue magnetic susceptibility (χ) distributions from the MRI signal phase. Recently, several methods have been proposed to quantify the relative contributions to bulk susceptibility of paramagnetic and diamagnetic compartments within each voxel [1-5]. Such techniques typically rely on the assumption that para- and diamagnetic sources interfere constructively in causing reversible R_2' decay, while interfering destructively in their effect on phase [2]. As such, many source-separation techniques require a spin-echo-based R_2 estimate or make simplifying assumptions about the relationship between R_2 and R_2^* [1,4]. The DECOMPOSE method for example fits multi-echo data to a three-pool model to estimate susceptibility sources without the need for R_2' [3]. These techniques have been used in the brain [5], but the head and neck (HN) region presents unique challenges including fat-water phase artefacts and greater air-tissue interfaces, flow effects, and physiological motion. In this study, we compared the results of susceptibility source separation using three publicly available methods applied to GRE data in the head and neck.

Methods: This analysis was applied retrospectively to four-echo GRE data acquired from ten healthy subjects using a 3T Achieva system (Philips, Netherlands). Acquisition parameters were: $TR = 22$ ms, $TE_1 = \Delta TE = 4.61$ ms, flip angle 12°, 1.25 mm isotropic resolution. QSMs were reconstructed using a standard pipeline, consisting of: MP-PCA denoising [6], non-linear complex fitting across echoes [7], SEGUE phase unwrapping [8], V-SHARP background field removal (with a 22mm kernel width) [9], and dipole inversion using Star QSM [10]. These results were used to calculate para- and diamagnetic maps using χ-separation (with iLSQR regularization) [2] and χ-sepnet. The same pipeline was applied to GRE data from each echo separately, and the resulting single-echo QSMs were used to estimate para- and diamagnetic signal compartments using DECOMPOSE [3].Regions of interest (ROIs) in the brain (thalamus, caudate nucleus, putamen, and globus pallidus) were segmented automatically from first-echo magnitude GRE images using FSL FIRST [11] and ROIs in HN (submandibular gland, parotid gland, and several lymph nodes) were obtained by manual segmentation checked by an experienced radiologist. Average values of paramagnetic and diamagnetic susceptibility were compared in each ROI.

Results: Fig. 1 shows a visual comparison of the source separation methods in a representative subject. Each method achieved source separation, although the contrast varies. χ-sepnet achieved clear muscle-fat contrast in the posterior neck (yellow and red arrows). DECOMPOSE produced more uniform values in the ROIs. Fig. 2 shows average values of component susceptibilities in each ROI.

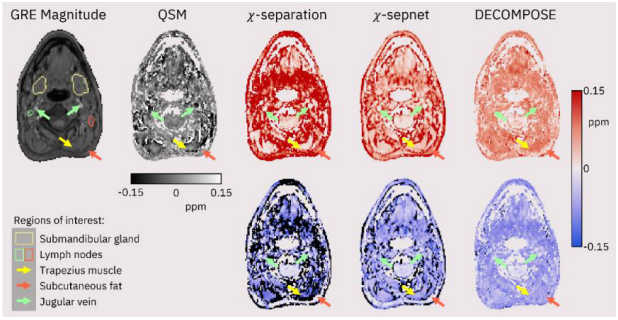

Fig. 1. Axial slice of the neck from one subject: GRE magnitude data (with ROIs outlined), Star QSM susceptibility map, and para- and diamagnetic susceptibility maps from three separation algorithms.

Discussion: The challenges of QSM in the neck are exemplified by the Star QSM results, where the submandibular gland has large χ variations, and in the posterior neck there are strong fat-water

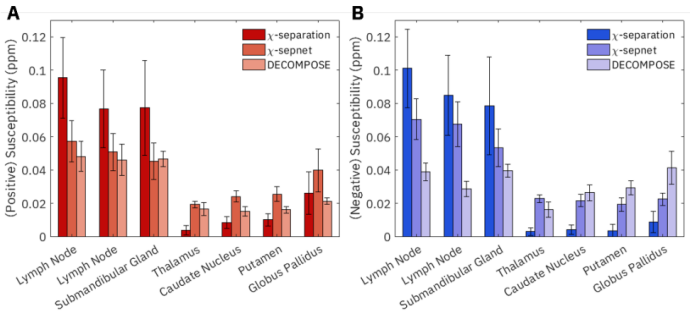

Figure 2. Mean paramagnetic (**A**) and diamagnetic (**B**) compartment susceptibilities in HN and brain ROIs. Error bars indicate standard deviation across 10 subjects.

effects at the muscle boundaries (Fig. 1, yellow & red arrows). These phenomena propagate into the para- and diamagnetic susceptibility maps produced by χ-separation, values are higher than other methods in the neck (probably driven by noise, Fig. 1 & 2) but lower in the brain (Fig. 2).

DECOMPOSE estimated paramagnetic χ components with lower variance than the other methods in all ROIs except the thalamus. Diamagnetic χ values from DECOMPOSE had lower variance in HN ROIs, but in deep-brain ROIs χ-sepnet produced the most consistent diamagnetic results. Across all ROIs, the total χ from DECOMPOSE was more diamagnetic than the results of other methods (not shown). Venous vessels such as the internal jugular veins (Figure 1, green arrows) have strong signal in the first-echo GRE magnitude and are expected to be strongly paramagnetic due to the presence of deoxyhemoglobin, but they are not obviously elevated in paramagnetic component maps, likely due to inflow effects.

There are several limitations to this study. The DECOMPOSE multi-compartment model ideally uses five echoes for fitting and is underdetermined with this four-echo dataset. χ-sepnet was trained on brain data at 1-mm resolution, and so may not perform optimally on these 1.25-mm-resolution data. Finally, there are no ground truth values available, nor comparable source-separated results in the literature, so it is necessary to rely on visual inspection and differences across subjects to compare these methods qualitatively.

Conclusions: This first study shows that susceptibility source separation using only GRE data is possible in the neck, but further work is needed to validate the resulting maps and regional values.

References

[1] Schweser F et al. (2011). "SEMI-TWInS: Simultaneous extraction of myelin and iron using a T_2^*-weighted imaging sequence," *Proc. ISMRM* 19, #120.
[2] Shin H et al. (2021). "χ-separation: Magnetic susceptibility source separation toward iron and myelin mapping in the brain," *NeuroImage*, 240: 118371.
[3] Chen J, Gong N, Chaim K T, Otaduy M C G, Liu C (2021) "Decompose quantitative susceptibility mapping (QSM) to sub-voxel diamagnetic and paramagnetic components based on gradient-echo MRI data," *NeuroImage*, 242: 118477.
[4] Dimov A V et al. (2022). "Susceptibility source separation from gradient echo data using magnitude decay modelling," *J. Neuroimaging*, 32(5), pp.852-859.
[5] Ji S et al. (2024). "Comparison between R2'-based and R2*-based χ-separation methods: A clinical evaluation in individuals with multiple sclerosis," *NMR Biomed.* May 2024, e.5167.
[6] Doniza L et al. (2023). "MP-PCA image denoising technique for high resolution quantitative susceptibility mapping (QSM) of the human brain in vivo," *Proc. ISMRM* 32, #2948.
[7] Liu T et al. (2013). "Nonlinear formulation of the magnetic field to source relationship for robust quantitative susceptibility mapping," *Magn. Reson. Med.* 69(6), pp.1581-1593.
[8] Karsa A, Shmueli K (2019). "SEGUE: A speedy region-growing algorithm for unwrapping estimated phase." *IEEE Trans. Med. Imaging* 38(6), pp.1347-1357.
[9] Wu B et al C (2011). "Whole brain susceptibility mapping using compressed sensing." *Magn. Reson. Med*. 24, pp.1129-1136.
[10] Wei H et al. (2015). "Streaking artifact reduction for quantitative susceptibility mapping of sources with large dynamic range." *NMR Biomed.* 28(10), pp.1294-1303.
[11] Patenaude B et al. (2011). "A Bayesian model of shape and appearance for subcortical brain," *NeuroImage* 56(3), pp.907-922.

ON-HARMONY 2.0: A comprehensive travelling-heads resource for multi-modal neuroimaging harmonisation

Andrea Torchi[1*], Shaun Warrington[1*], Olivier Mougin[2], Jon Campbell[3], Martin Craig[1], Asante Ntata[1], Fidel Alfaro-Almagro[3], Karla Miller[3], Mark Jenkinson[3], Paul S Morgan[1], Stamatios N Sotiropoulos[1]

[1]Sir Peter Mansfield Imaging Centre, School of Medicine, University of Nottingham, United Kingdom. [2]Sir Peter Mansfield Imaging Centre, School of Physics, University of Nottingham, United Kingdom. [3]Wellcome Centre for Integrative Neuroimaging, WIN-FMRIB, University of Oxford, UK. *Equal Contribution

Introduction: In studies that involve multiple MRI scanners, an important challenge that arises is the dependence of measured imaging features on scanner- and site- dependent factors that are not related to the scanned subject [1-3]. To tackle this problem, several approaches are possible; some of them involve attempting to harmonise as much as possible the acquisition protocols and the processing pipelines [4,5], including using vendor-agnostic sequences [6]; while others directly address the final parameters to try and regress out the non-biological differences [7,8]. In order to assess the nature of these confounding factors for neuroimaging studies, we ran a travelling heads study involving a group of healthy participants, scanned over different 3T MRI systems of several types and vendors across different sites. The Oxford-Nottingham Harmonisation (ON-HARMONY 2) study builds upon our previous work [9] and comprises one of the most comprehensive travelling heads resources with data from 20 subjects (9 subjects with multiple within-scanner repeats), each scanned in 6 3T scanners (Siemens, Philips and GE) and 5 modalities (T1w-MPRAGE, T2w-FLAIR, diffusion MRI, resting-state fMRI, SWI).

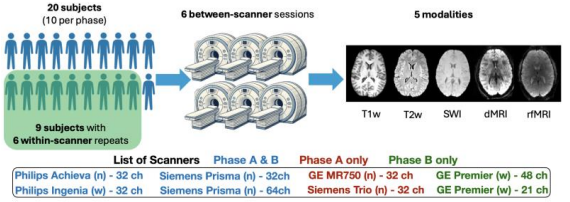

Figure 1. *Summary of the acquisition paradigm for subjects, scanners and modalities involved in each phase of the study (w: wide-bore, n: narrow-bore, ch: Number of head coil channels).*

Methods: The study ran in two phases (10 subjects per phase) (Figure 1). The first phase took 2 years to complete (median time difference (TD) between first and last rescan for a subject across scanners: 374 days), as interrupted by the COVID19 pandemic. The second phase was completed in less than 6 months (TD: 126 days). Phase A involved 3 Siemens, 2 Philips and 1 GE scanner, while Phase B had 2 scanners from each vendor (Figure 1). A better sex balance was maintained in Phase B (50% females vs 20% females in phase A). Acquisition protocols were aligned with the UK Biobank imaging study [10], however adjustments were made to respect best practices for each scanner/imaging site (therefore parameters were not simply nominally matched) [9]. Each participant was scanned in 6 different scanners, while 9 participants (4 in phase A, 5 in B) had in addition 6 within-scanner repeats (most of scanners had at least one participant with 6 within-scanner repeats). That way between-scanner and within-scanner variability for subjects could be characterised and compared to between-subject (i.e. biological) variability, which is typically the variance of interest. All data underwent quality control using MRIQC [11] and eddyQC [12] leading to image-quality metrics (IQMs) for 4 modalities. They were subsequently processed with a modified version [9] of the UK Biobank pipeline [13]. Hundreds of imaging-derived phenotypes (IDPs), i.e. multi-modal imaging features were derived for each session. That way, different pools of IDP and IQM variability could be compared.

Results and Discussion: Figure 2 demonstrates examples of the raw data, depicting a subset of the sessions acquired for each of the participants, across scanners (columns) and modalities (rows). We subsequently extracted IQMs to assess consistency of data quality across subjects and scanners for each imaging modality (Figure 3). In the top plots, each quality metric for each subject was z-scored across the six scanners. The z-scores were then averaged across the subjects. In the bottom plots, each IQM was z-scored across the ten subjects and then averaged across the scanners. The plots indicate that across both phases A and B there are no scanners/subjects that act as major outliers in terms of

Power Pitch Session 1

image quality. Subsequently, we assessed how the similarity of IDPs changes across different pools of variability (Figure 4). We represented each scan session in terms of the multi-modal imaging features we could extract and computed Spearman correlations across sessions for different IDP groups (subcortical volumes, brain tissue volumes, subcortical T2*, cortical parcel volumes, dMRI regional and tract-wise microstructure (FA, MD, MO, L1, L2, L3), rfMRI functional connectivity node amplitude and edges). Figure 4 shows the median correlation across IDP groups for session pairs belonging to three different pools (between-subject/same scanner, between-scanner/same subject and same-scanner/same-subject). It shows how biological variability (red) has hardly any overlap with scan-rescan variability of a subject (blue) as expected, however it overlaps quite substantially with between-scanner variability (green).

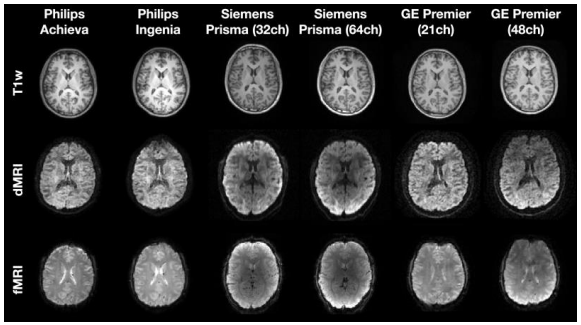

Figure 2. *Example of a subset of the acquired data for a single subject. Five different modalities (three shown here) and 6 scanners, located in five different imaging sites were obtained for all 20 participants. Data from Phase B scanners are shown.*

Conclusion: We have presented one of the most comprehensive harmonization resources for multi-modal neuroimaging, which we will use as a testbed to develop and explore both explicit and implicit harmonisation approaches [9].

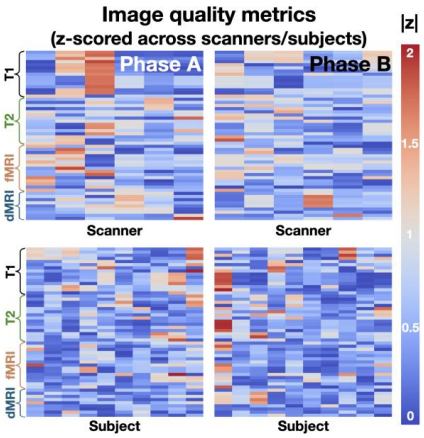

Figure 3*. IQMs of each session, averaged across each IDP group, then z-scored across subjects and averaged across scanners (upper row) or vice-versa (lower row) for each study phase.*

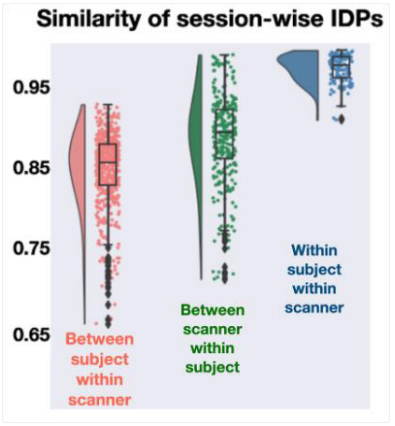

Figure 4*. Spearman correlation of session IDPs (calculated as the median across groups of the Spearman correlation of IDPs in the same group for each session). Violin plots show IDP similarities across the different categories.*

References

[1] Pinto MS, Paolella R, Billiet T, Van Dyck P, Guns PJ, Jeurissen B, Ribbens A, den Dekker AJ, Sijbers J. Harmonization of brain diffusion MRI: concepts and methods. Frontiers in Neuroscience. 2020 May 6;14:396.

[2] Friedman L, Stern H, Brown GG, Mathalon DH, Turner J, Glover GH, Gollub RL, Lauriello J, Lim KO, Cannon T, Greve DN. Test–retest and between-site reliability in a multicenter fMRI study. Human brain mapping. 2008 Aug;29(8):958-72

[3] Han X, Jovicich J, Salat D, van der Kouwe A, Quinn B, Czanner S, Busa E, Pacheco J, Albert M, Killiany R, Maguire P. Reliability of MRI-derived measurements of human cerebral cortical thickness: the effects of field strength, scanner upgrade and manufacturer. Neuroimage. 2006 Aug 1;32(1):180-94.

[4] Potvin O, Chouinard I, Dieumegarde L, Bartha R, Bellec P, Collins DL, Descoteaux M, Hoge R, Ramirez J, Scott CJ, Smith EE. The Canadian dementia imaging protocol: Harmonization validity for morphometry measurements. NeuroImage: Clinical. 2019 Jan 1;24:101943.

[5] Chen J, Ades-Aron B, Lee HH, Mehrin S, Pang M, Novikov DS, Veraart J, Fieremans E. Optimization and validation of the DESIGNER preprocessing pipeline for clinical diffusion MRI in white matter aging. Imaging Neuroscience. 2024 Apr 8;2:1-7.

[6] Layton KJ, Kroboth S, Jia F, Littin S, Yu H, Leupold J, Nielsen JF, Stöcker T, Zaitsev M. Pulseq: a rapid and hardware-independent pulse sequence prototyping framework. Magnetic resonance in medicine. 2017 Apr;77(4):1544-52.

[7] Fortin JP, Cullen N, Sheline YI, Taylor WD, Aselcioglu I, Cook PA, Adams P, Cooper C, Fava M, McGrath PJ, McInnis M. Harmonization of cortical thickness measurements across scanners and sites. Neuroimage. 2018 Feb 15;167:104-20.

[8] Mirzaalian H, Ning L, Savadjiev P, Pasternak O, Bouix S, Michailovich O, Grant G, Marx CE, Morey RA, Flashman LA, George MS. Inter-site and inter-scanner diffusion MRI data harmonization. NeuroImage. 2016 Jul 15;135:311-23.

[redacted]

[10] Miller KL, Alfaro-Almagro F, Bangerter NK, Thomas DL, Yacoub E, Xu J, Bartsch AJ, Jbabdi S, Sotiropoulos SN, Andersson JL, Griffanti L. Multimodal population brain imaging in the UK Biobank prospective epidemiological study. Nature neuroscience. 2016 Nov;19(11):1523-36.

[11] Esteban O, Birman D, Schaer M, Koyejo OO, Poldrack RA, Gorgolewski KJ. MRIQC: Advancing the automatic prediction of image quality in MRI from unseen sites. PloS one. 2017 Sep 25;12(9):e0184661.

[12] Bastiani M, Cottaar M, Fitzgibbon SP, Suri S, Alfaro-Almagro F, Sotiropoulos SN, Jbabdi S, Andersson JL. Automated quality control for within and between studies diffusion MRI data using a non-parametric framework for movement and distortion correction. Neuroimage. 2019 Jan 1;184:801-12.

[13] Alfaro-Almagro F, Jenkinson M, Bangerter NK, Andersson JL, Griffanti L, Douaud G, Sotiropoulos SN, Jbabdi S, Hernandez-Fernandez M, Vallee E, Vidaurre D. Image processing and Quality Control for the first 10,000 brain imaging datasets from UK Biobank. Neuroimage. 2018 Feb 1;166:400-24.

Assessing the influence of heart rate on MOLLI T_1 mapping in the UK Biobank

Margot Roeth, Martin Craig, Ali-Reza Mohammadi-Nejad, Dorothee Auer, Stamatios N Sotiropoulos, Eleanor Cox, Susan Francis

Sir Peter Mansfield Imaging Centre, University of Nottingham, Nottingham; and the DEMISTIFI consortium

Introduction: Organ fibrosis occurs in many conditions, including chronic kidney disease and liver cirrhosis. MRI can provide a non-invasive, quantitative assessment of fibrosis by performing longitudinal (T_1) mapping of the tissues. The UK Biobank (UKBB) [1] is a prospective population study which includes abdominal Shortened Modified-Look-Locker-Imaging (ShMOLLI) [2] T_1 mapping of the liver, pancreas and kidneys of participants with healthy organs and those with a primary disease, with abdominal data collected on 55K participants scanned to-date. In February 2021, dedicated kidney ShMOLLI MRI scans were added with data collected on ~7K participants. However, ShMOLLI T_1 mapping data is collected ECG-triggered, rather than with a fixed spacing. This work aims to simulate and correct the effect of heart rate on measured ShMOLLI T_1.

Methods:

Abdominal MRI data: UKBB Siemens 1.5T abdominal ShMOLLI 5(1)1(1)1 data (T_1 recovery curve in three epochs over 9 heartbeats using single-shot balanced steady-state free precession (bSSFP) acquisitions) with separate schemes used for the liver & pancreas, compared to the kidney. (Liver/pancreas: TE/TR = 1.93/4.8 ms, flip angle (FA) 35°, Field of View (FoV) 440mm, resolution 192, Trigger delay (TD) 50 ms, 1st ShMOLLI inversion time (TI) 170 ms, five increments of 50 ms; Kidney: TE/TR = 1.41/3.4 ms, FA 35°, FoV 384mm, resolution 256, TD 0 ms, 1st TI 156 ms, 5 increments of 50 ms; both collected with GRAPPA 2 and 24 reference lines).

Simulations: Simulations were performed in Python to solve the Bloch equations and iteratively simulate the ShMOLLI scheme for the liver/pancreas and kidney UKBB acquisitions. Simulations were performed at a FA of 35° , and a lower 30° FA to account for B_1 field inhomogeneities. The center k-space of the simulated signals was fit to estimate T_1* and corrected to give $T_{1measured} = (B/A-1)T_1$*. A range of tissue T_1 (0.4-2.0s) and heart rates (30-120bpm) were simulated, selected to cover the range of the data in the UKBB data. Measured and simulated T_1 values were compared to assess the impact of heart rate. The measured and simulated T_1 values were then used to create a look-up table (MATLAB) to correct the UKBB $T_{1\,measured}$ based on a participants' heart rate.

Analysis and correction of UKBB Data: Initial analysis compared the results of 500 healthy volunteer (HV) participants (no chronic/fibrotic disease) with 235 participants with disease [124 kidney (ICD10:I12-13,N08,11,14-18), 24 pancreas (ICD10:K85-86), 87 liver (ICD10:B18,22,K70-77)]. Automated segmentation of the data was performed using machine learning [3]. Measured T_1 values of participants' liver, pancreas, kidney cortex and kidney medulla were corrected using the look-up table and the uncorrected measures compared with corrected.

Results:

Simulations: Figure 1A shows the ShMOLLI simulated signals for the liver/pancreas scheme. Figure 1B shows for both liver/pancreas and kidney ShMOLLI schemes the greater dependency of measured T_1 on heart rate at higher T_1 values (kidney cortex and medulla) compared to organs with lower T_1 (liver and pancreas). Low heart rates (below 60bpm) led to an underestimation in measured T_1 across most of the simulated T_1 range (except at low T_1), while higher heart rates led to a overestimation of measured T_1. The kidney shMOLLI scan led to a greater distribution of measured T_1 with heart rate compared to the liver/pancreas shMOLLI.

Figure 2 shows measured UKBB for the 500 HV participants T_1 data versus heart rate before correction, in agreement with the simulation, a higher measured T_1 value with a higher heart rate is seen for the kidney medulla and liver ($P<0.0001$), whilst the kidney cortex and pancreas show no dependence. After applying the HR correction, the HV data shows no significance HR dependence in the medulla or pancreas, and the liver showed a reduced significance ($P<0.01$). Similar trends were observed for the disease participants.

Discussion: Simulations show that for UKBB kidney ShMOLLI data, heart rate will modulate the measured T_1 especially for the medulla which has a longer T_1. Using a look-up table the influence of HR on measured T_1 can be corrected. It should be noted that the measured ShMOLLI T_1 is also influenced by other factors such as B_1, and so here the look-up corrected assumed a 30° delivered flip angle for the ShMOLLI scheme to account for lower than 100% B_1 delivery. In future work the corrected T_1 values will be used to assess changes between HVs and disease groups in the assessment of fibrosis. As part of this work we will also correct for the influence of fat fraction (FF) (in the liver and pancreas), for which higher FF is known to increase ShMOLLI T_1 [4].

Acknowledgements

Data were provided by the UK Biobank under Project ID 43822. This study was supported by the DEMISTIFI Consortium.

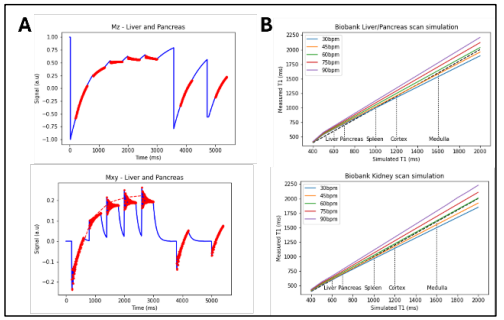

Figure 1: (A) Bloch simulation of UKBB ShMOLLI 5(1)1(1)1 liver and pancreas scheme for a simulated T_1 of 800ms showing the longitudinal (M_z) magnetisation (*top*) and transverse (M_{xy}) magnetisation (*bottom*) which is fit to estimate T_1*. (B) Measured T_1 versus simulated T_1 for a range of heart rates in BPM simulated for the liver/pancreas shMOLLI scheme (*top*) and the kidney ShMOLLI scheme (*bottom*). Note the dependence on HR, particularly at higher T_1 values found in the kidney.

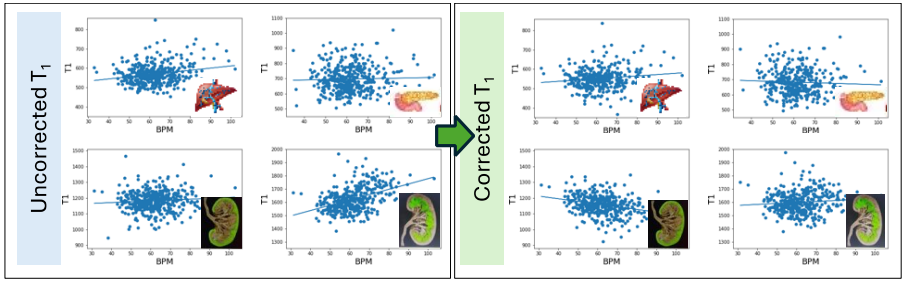

Figure 2: Plots of measured T_1 against BPM shown uncorrected and after correction using shMOLLI scheme look-up table. Results shown for HV data in the liver, pancreas and kidney cortex and medulla. Note the strong increase in measured T_1 (slope $P<0.0001$) with increasing BPM for medulla which is then corrected.

References

1. The UK Biobank imaging enhancement of 100,000 participants: rationale, data collection, management and future directions. Littlejohns TJ, Holliday J, Gibson LM *et al. Nat Commun* **11**, 2624 (2020).
2. Look-Locker inversion recovery (MOLLI) for high-resolution T1 mapping of the heart. Messroghli DR, Radjenovic A, Kozerke S, Higgins DM, Sivananthan MU, Ridgway JP. *Magn Reson Med*. 52 (2004)
3. Automated Analysis of the UK Biobank MRI data for the Assessment of Multi-organ Involvement in Disease. Cox E, Gong Z, Craig A, Mohammadi-Nejad AR, Aithal G, Stewart ID, Wain L, Jenkins G, Auer DP, Sotiropoulos SN, Chen X, Francis ST; on behalf of the DEMISTIFI Consortium. *ISMRM* 2024.
4. Influence of fat on liver T1 measurements using modified Look-Locker inversion recovery (MOLLI) methods at 3T. Mozes F, Tunnicliffe E, Pavlides M, Robson M. J Magn Reson Imaging 2016 Jul;44(1):105-11.

Optimization of a Silent ZTE Magnetization Transfer Ratio Sequence at 3T

Oliver Pinna[1], Gareth J. Barker[1], Tobias C. Wood[1]
[1]Centre for Neuroimaging Sciences, King's College London

Introduction: Previous research from our group has shown the feasibility of performing myelin-weighted acquisitions exploiting the MT effect [1]. Since then, substantial improvements have been made in the reconstruction and acquisition side of our ZTE data allowing us to push the reconstructed pixel size to 1mm isotropic. This abstract guides us through the optimization process and shows the latest results.

Methods: We used a 3T GE Premier scanner with a 48ch head coil. The sequence was a local implementation of 3D radial ZTE with curved k-space spokes and a generalized spiral trajectory with golden means rotation between segments [2]. Simulation of MTw and PDw signals following the method of [3] pointed us towards the choice of the lowest possible number of SPS to maximise the MT-weighting hence the contrast of myelinated tissue, see Fig. 1.

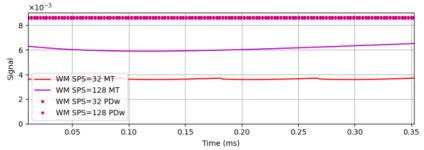

Fig. 1 MTw and PDw ZTE steady states in WM as a function of SPS.

We first acquired a base scan of a healthy volunteer with the MT-prepared ZTE with 32 spokes-per-segment (SPS). The scan resulted in artefacts impacting the image quality significantly. We hypothesized that the origin of these artefacts could be attributed to the refocusing of FIDs from previous spokes which we did not model. While we use RF-spoiling and obtain some spoiling from the readout gradients, it is possible that the overall phase induced by the gradients over a spherically symmetric acquisition of k-space can sum up to zero before the FID decays thus causing gradient echoes.

To test our hypothesis, we acquired data in a CALIBER phantom investigating configurations of 128, 64 and 32 SPS with a trajectory consisting of either half of our spherically symmetric k-space or the full k-space. If our hypothesis was correct, we expected to observe a reduction in the artefact when increasing the SPS or when acquiring half of the k-space due more T2* FID decay or unbalanced gradient moments respectively.

After verifying that the k-space trajectory was the main factor causing the artefact, we re-acquired brain MTw and PDw volumes with optimized scan settings and used them to compute the MTR.

The full optimized scan settings were Gaussian MT preparation pulse Δ=2.0kHz, τ_{MT}=7.68ms, α_{MT}=800°, SPS=32, α_{RO}=2°, τ_{RO}=16µs, BW=25kHz, TR=2.672ms, FOV=240mmx240mmx240mm. We used Riesling [4] to reconstruct the data with Total Generalized Variation (TGV) regularized least squares, λ=0.01.

Results: In line with our hypothesis, we observed a reduction in artefacts when increasing the number of SPS and an even more noticeable reduction when using the modified trajectory, see Fig 2.

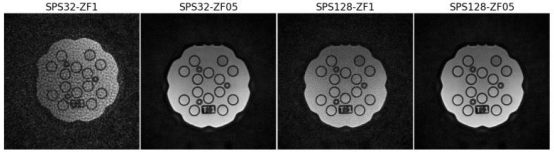

Fig 2. Artefact changes as a function of the sequence used (ZF1 = full k-space, ZF05 = half k-space). The first image was acquired on a separate day hence at a slightly different location. (please zoom in to appreciate image details)

The optimized brain scan showed reduced artefacts on a basic reconstruction which we were able to slightly improve using TGV regularization, see Fig. 3. The MTw scan shows a strong GM/WM contrast which can be noticed especially in the putamen, the cortex and the head of the caudate nuclei. The GM/WM contrast is also present in the MTR scan as to be expected. However, it is much less accentuated.

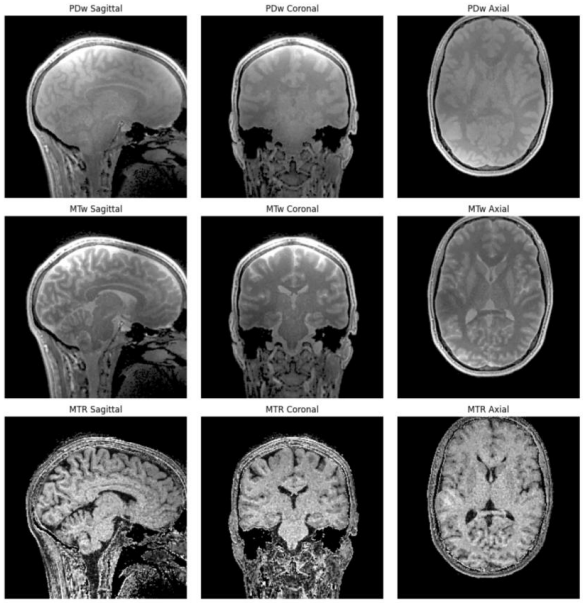

Fig. 3 Optimized silent-MTR mapping. (please zoom in to appreciate image details)

Discussion: This work showed an empirical correction to artefacts that were observed when using ZTE at a low number of SPS to optimally image the MTR. Compared to our previous work [2] we observed a promising increase in contrast and resolution in the MTw volume as to be expected from our optimization. However, the MTR map is yet to be improved. It would be desirable to model the refocusing effects using EPGs or isochromat simulations to optimally choose the k-space trajectory. This may help to reduce the grainy appearance of the reconstructions. Further work will investigate correcting the receive B1 inhomogeneity observed in the top part of the image. Lack of image registration may also be responsible for some of the grainy appearance of MTR and will be implemented soon.

Conclusions: We have shown that it is possible to reduce scan time while improving the contrast and resolution of silent MTw imaging using a low number of spokes per segment and optimized k-space trajectories. This may prove fruitful in a future attempt to optimize silent MTR acquisitions.

References

[1] R. W. Chan *et al*, *Magn. Reson. Med.*, vol. 61, no. 2, pp. 354–363 (2009).
[2] T. C. Wood *et al*, *Wellcome Open Research*, vol. 5, pp. 74 (2020).
[3] S. J. Malik *et al*, *Magn. Reson. Med.*, vol. 83, no. 3, pp. 935–949 (2020).
[4] T. Wood *et al*, 'spinicist/riesling: v0.11'. Zenodo, May 17, 2023. doi: 10.5281/zenodo.7944190.

Power Pitch Session 1

Pharmacokinetic Modelling of DCE-MRI for Differentiation Between True Tumor Progression and Pseudoprogression of Glioblastoma

Gabriela W Kostrzanowska[1], Sourav Bhaduri[1,2], Madhav K Madhusudhanan[1], Archith Rajan[3], Mahon L Maguire[1], Sanjeev Chawla[3], Harish Poptani[1]

[1]Centre for Preclinical Imaging, University of Liverpool, Liverpool, UK. [2]Institute for Advancing Intelligence (IAI), TCG CREST, Kolkata, India. [3]Department of Radiology, Perelman School of Medicine at the University of Pennsylvania, Philadelphia, PA, USA.

Introduction: Glioblastomas (GBMs), the most common malignant tumours of the central nervous system, carry a 5-year survival rate of <10%, and despite intensive treatment, reoccurrence is inevitable [1,2,3]. During post treatment follow up with MRI, up to 36% of patients present with the appearance of new lesions, termed pseudoprogression (PsP), that show enhanced T1-weighted MR image contrast, mimicking true progression (TP) [4]. TP and PsP are handled differently with PsP managed conservatively and TP with aggressive treatment strategies or enrolment in new trials. However, discriminating PsP from TP remains a diagnostic dilemma, with histology remaining the gold-standard despite biopsy carrying a risk of mortality [4]. Dynamic contrast-enhanced magnetic resonance imaging (DCE-MRI) has been suggested as a tool to differentiate between TP and PsP [5,6,], as it allows quantification of parameters related to tumour vascularity and permeability using different pharmacokinetic (PK) models. However, no consensus has been reached as to which PK model to use for the most accurate differentiation. This study aimed to evaluate the efficacy of different PK models of DCE-MRI in distinguishing TP from PsP in postoperative GBM patients.

Methods: This retrospective study included thirty-one patients clinically diagnosed with either TP (n=24) or PsP (n=7). Diagnosis was confirmed through histological examination or verified through radiological follow-up. DCE-MRI data for each patient was fitted to five PK models (Non-linear Tofts, Extended Tofts, Shutter-Speed, Two-Compartment Exchange (2CXM), and Three-Site Two-Exchange (3S2X) models) to generate parametric maps. The parameters K^{trans}, v_e, k_{ep}, v_p, F_p, and τ_i were extracted from the contrast enhancing areas.

Results: Representative images and parametric maps from a PsP and TP patient are shown in Figure 1. In general, the PsP group exhibited lower median K^{trans}, v_e, and k_{ep} values (Table 1). In the Shutter-speed and the 3S2X models, the PsP group demonstrated higher v_e values when compared to the TP group. The τ_i value was lower in PsP than TP in both the Shutter-Speed and 3S2X model, while v_p displayed variable trends across models, and F_p was lower in PsP. However, these differences did not reach statistical significance (p>0.05).

Table 1: Median values of DCE-MRI parameters from the enhancing region of TP and PsP patients derived using the various PK models.

	K^{trans} (min^{-1})		V_e (ml)		K_{ep} (min^{-1})		τi (s)		V_p (ml)		F_p (ml/min/100mg)	
	TP	PsP	TP	PsP	TP	PsP	TP	PsP	TP	PsP	TP	PsP
Non-linear Tofts	0.19	0.11	0.21	0.15	1.17	0.87	N.A.	N.A.	N.A.	N.A.	N.A.	N.A.
Extended Tofts	0.12	0.06	0.24	0.20	0.65	0.45	N.A.	N.A.	0.04	0.02	N.A.	N.A.
Shutter-Speed	0.22	0.15	0.28	0.28	0.94	0.75	0.22	0.15	N.A.	N.A.	N.A.	N.A.
2CXM	0.11	0.06	0.24	0.20	0.46	0.44	N.A.	N.A.	0.19	0.20	0.58	0.55
3S2X	0.34	0.23	0.42	0.42	0.88	0.94	0.43	0.38	0.35	0.35	N.A.	N.A.

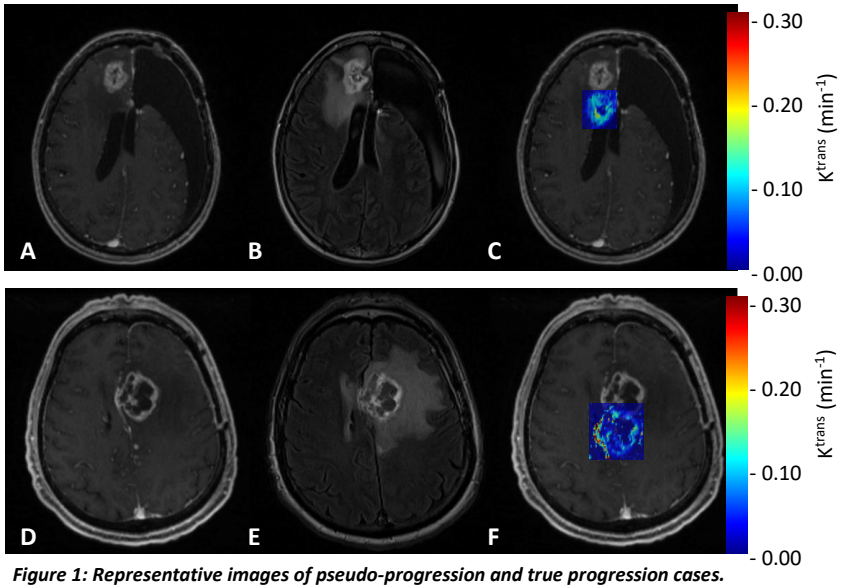

Figure 1: Representative images of pseudo-progression and true progression cases.
(A-C) Pseudoprogression: (A) Axial T1-weighted post-contrast image, (B) Axial T2-weighted FLAIR image, (C) T1-weighted image with overlay of parametric K^{trans} map on the lesion of interest.
(D-F) True progression case: (D) Axial T1-weighted post-contrast image, (E) Axial T2-weighted FLAIR image, (F) T1-weighted image with overlay of parametric K^{trans} map on the lesion of interest.

Discussion: The study highlights the complexity of using DCE-MRI-derived PK parameters to distinguish between TP and PsP in GBM. While no significant differences in parametric values were observed between the TP and PsP groups, the volume transfer constant K^{trans}, which measures tissue perfusion and vascular permeability, was generally lower in PsP than in TP, potentially reflecting TP's higher vascular permeability. Similarly, the rate constant k_{ep}, indicative of contrast agent transfer from the extracellular extravascular space to plasma, was also lower in PsP for all models. The extracellular volume fraction v_e was higher in PsP in some models potentially due to treatment-related edema. F_p, plasma flow, was higher in TP, while v_p, the plasma volume fraction, displayed variable trends across models. The intracellular water lifetime τ_i, which was hypothesized to be higher in PsP due to decreased metabolism in necrotic areas, was higher in TP for both the shutter speed and 3X2M models [7,8]. The absence of significant differences may be attributed to the small sample size and the lack of histological confirmation of diagnosis for all cases, underscoring the need for larger studies with histological confirmation which can provide more robust evidence to guide clinical decision-making and improve patient outcomes in the management of glioblastoma progression.

Conclusions: Although we observed trends in K^{trans}, k_{ep} and τ_i values in TP across various models, these differences were not statistically significant. Future studies with larger sample sizes and histological confirmation are needed for improving clinical decision-making in GBM management.

References

[1] Schaff, L.R. and Mellinghoff, I.K. (2023), JAMA, 329(7), p. 574. [2] Brown, N.F. et al. (2022), Cancers, 14(13), p. 3161. [3] Fekete, B. et al. (2023), Frontiers in Surgery, 10. [4] Young, J.S. et al. (2023), Journal of Neurosurgery, pp. 1–12. [5] Yun, T.J. et al. (2015), Radiology, 274(3), pp. 830–840. [6] Jing, H. et al. (2022), Contrast Media & Molecular Imaging, 2022, pp. 1–8. [7] Wang, W. et al. (2023), Acta Neuropathologica Communications, 11(1). [8] Yankeelov, T.E. et al. (2003), Mag Reson Med, 50(6), pp. 1151–1169.

Reproducibility of 3T MRI metrics across multi-site, multi-vendor settings for a mild Traumatic Brain Injury study

Ruwan Wanni Arachchige[1], Iman Idrees[2], Yidian Gao[3], Tara Ghafari[3], Alice Waitt[2,3], Sebastian Coleman[1], Jessikah Fildes[1], Dan Ford[1], Aliza Finch[3], Waheeda Hawa[2], Martin Craig[1], Lisa Hill[4], James L. Mitchell[4], Alexandra J. Sinclair[4], Samuel J.E. Lucas[3], Matthew J Brookes[1], Jan Novak[2], Martin Wilson[3], Andrew Bagshaw[3], Davinia Fernandez-Espejo[3], Karen J Mullinger[1], *on behalf of the UK mTBI Predict Consortium*

[1]Sir Peter Mansfield Imaging Centre, University of Nottingham, UK, [2]Institute of Health and Neurodevelopment, Aston University, UK, [3]Centre for Human Brain Health, University of Birmingham, UK, [4] Translational Brain Science, Institute of Metabolism and Systems Research, University of Birmingham, UK

Introduction: Traumatic brain injury (TBI) is a silent epidemic leading to 1.4M hospital visits every year in England and Wales, of which 85% are classed as mild (mTBI). ~30% of mTBI patients have disabling long-term sequelae impairing their ability to return to work, play or duty. Whilst conventional clinical MRI/CT scans of mTBI patients are mostly negative, advanced MRI measures show promise as biomarkers [1]. However, the reliability of these biomarkers is compromised when combining data acquired across different sites and scanners [2] – limiting clinical potential. To prepare for a multi-site, multi-vendor mTBI patient study, this work aims to minimise inherent variability by optimising the setup of MRI sequences across platforms to best match neuroimaging metrics to be used on patients.

Method: Three different 3T MRI scanners equipped with 32-channel head receive coils were utilised across three research facilities (Table 1). The optimised scans included: T1-weighted MPRAGE; multi-slice, multi-shell 2D-EPI Diffusion-Weighted Imaging (DWI); multislice 2D-EPI for functional MRI (fMRI); and pseudo Continuous Arterial Spin Labelling (pCASL), as detailed in Table 1. These imaging sequences were optimised by adjusting parameters to ensure high quality and consistent data across sites. Two multimodal data sets were acquired per site from a single healthy participant during separate visits. Standard neuroimaging tools were employed for preprocessing and analysis. Reproducibility and agreement between sites were assessed for the following metrics within anatomically relevant regions of interest (ROIs). Cortical thickness and subcortical volume were derived from FreeSurfer using the Desikan-Killiany-Tourville atlas and ASEG (62 cortical and 20 subcortical ROIs). Mean Fractional Anisotropy (FA) and Mean Diffusivity (MD) values were extracted using the diffusion toolbox (FDT) in FSL with the Johns Hopkins University white matter atlas (48 ROIs). Temporal signal-to-noise ratio (tSNR) for EPI scans was calculated using an in-house MATLAB script (frontal, cingulate, temporal, parietal, occipital grey matter ROIs). Additionally, Cerebral Blood Flow (CBF) was extracted using BASIL in FSL, with same ROIs as tSNR. Coefficient of variation (CoV) and linear regressions were calculated to assess systematic and random variability across data.

Manufacturer		Scanner Model	Bore Size (cm)	Gradient Performance	Software Version
1	Phillips	Ingenia 3T	70	45 mTm^{-1} 200$mTm^{-1}ms^{-1}$	R590
2	Siemens	Siemens PRISMA 3T	60	XR Gradients 80 mTm^{-1} 200$mTm^{-1}ms^{-1}$	VE11C
3	Siemens	MAGNETOM 3T PRISMA	60	XR Gradients 80 mTm^{-1} 200$mTm^{-1}ms^{-1}$	Syngo MR XA30

Modality	Site	Acquisition Time (min:sec)	Resolution (mm)	Matrix (mm)	Key Parameters
T1 (MPRAGE)	1	4:55	1.0x1.0x1.0	256x256x208	TR/TE = 8.1ms/3.7ms, α =8°
	2	4:54	1.0×1.0×1.0	256x256X208	TR/TE=2000ms/2.03ms, α = 8°
	3	4:54	1.0x1.0x1.0	256 x 256x208	TR/TE=2000ms/2.03ms, α = 8°
DWI	1	12:27	2.0x2.0x2.0	224x224x120	TR/TE = 6369ms/97ms, α = 90°, b=0; dir=5, b=1000; dir=50, b=2000; dir=50, MB=2, blip reversed b = 0, α = 78°
	2	6:32	2.0x2.0x2.0	224x224x120	TR/TE= 3600ms/ 92 ms, b=0; dir=6, b=1000; dir=50, b=2000; dir=50, MB=3, blip-reversed b = 0, α = 78°
	3	6:32	2.0x2.0x2.0	224x224x120	TR/TE =3600ms/ 92ms, b=0; dir=6, b=1000; dir=50, b=2000; dir=50, MB 3 blip-reversed = 0, α = 78°
EPI-fMRI	1	4:46	2.33x2.33x2.4	224x224x130	TR/TE=2000ms/40ms, MB=2, α = 85°
	2	4:48	2.3x2.3x2.4	224x224x144	TR/TE=2000ms/40ms, MB=4, α = 85°
	3	4:48	2.3x2.3x2.4	224x224x144	TR/TE=2000ms/40ms, MB=4, α = 85°
pCASL	1	6 .00	3.39X3.39X4.95	217x217x119	TR/TE = Variable with PLD, tag 1400, PLDs = 200:700:1200:1700:2200, 1 M0 Calibration, α = 90°
	2	5:27	3.4x3.4x5.0	217x217x119	TR/TE = 3580ms/19ms, tag = 1400 PLDs = 200:700:1200: 1700:2200, 1 M0 Calibration, α = 90°

MPRAGE = Magnetization Prepared Rapid Gradient Echo, TR = Repetition Time; TE = Echo Time; MB = multi-band acceleration factor; α = Flip Angle.

Table 1. *Summary of scanner information and acquisition parameters across all sites*

Results and Discussions: Tables 2 and 3 summarise the CoV and the outcomes of the linear regressions for the MRI metrics respectively. Measures from structural data show that cortical thickness, subcortical volumes, FA, and MD exhibit minimal variability, indicating high consistency across sessions and sites. In contrast, functional MRI measures showed relatively increased variability; however, both tSNR and CBF metrics achieved satisfactory reproducibility. The variablity in tSNR measures was highest in Site 2, this is driven by overall higher tSNR values in Session 2. However, Table 3 shows that there is still a strong relationship of tSNR values across ROIs for Site 2. CBF demonstrated low within-site variability but high between-site variability as indicated by both the CoV and R^2 values. Importantly, the variablity in the CBF data is in line or better than previous multi-vendor studies [3,4]. After motion correction was employed in the analysis, the observed within-site variability in the tSNR and CBF metrics suggests that some of this variability could be attributed to physiological changes between days as well as differences in sequences across sites. For CBF data, differences in end-tidal CO_2 between days for the subject may partially explain the differences in measured values. In addition, improvement in CBF reproducibility may be achieved by using novel ASL analysis pipelines such as Bayesian approaches developed by Quantified Imaging Ltd to harmonise metrics across vendors.

Biomarkers	Within Site CoV (%)			Between Site CoV (%)
	Site 1	Site 2	Site 3	
Cortical thickness	0.04	0.34	0.55	0.86
Subcortical volume	0.88	0.02	2.24	2.37
FA	0.25	0.42	0.59	3.24
MD	0.73	0.04	2.48	5.65
tSNR	1.95	10.21	1.44	5.69
CBF	0.61	1.36		12.18

Table 2. *Coefficient of variation of MRI metrics within-site (left side) and between-site (right side) calculated from an average of all relevant ROI measures. Majority of CoV values are below the threshold of 10% [5]. *pcASL data not available for Site 3.*

Biomarker	Within Site	Gradients	Intercept	R^2	Between Site	Gradients	Intercept	R^2
Cortical Thickness	Site1	0.93	0.18	0.96	Site 1 vs Site 2	1.06	-0.10	0.91
	Site2	0.93	0.20	0.97	Site 1 vs Site 3	1.07	-0.14	0.92
	Site3	1.06	-0.14	0.97	Site 2 vs Site 3	1.00	0.01	0.98
Subcortical Volume	Site1	0.97	43.57	1.00	Site 1 vs Site 2	1.07	-57.08	1.00
	Site2	0.98	51.49	1.00	Site 1 vs Site 3	1.03	-5.16	1.00
	Site3	0.94	69.61	0.99	Site 2 vs Site 3	0.96	52.61	1.00
FA	Site1	0.98	0.01	0.99	Site 1 vs Site 2	0.93	0.01	0.95
	Site2	1.00	0.00	0.99	Site 1 vs Site 3	0.92	0.01	0.95
	Site3	0.98	0.02	0.99	Site 2 vs Site 3	0.99	0.01	1.00
MD	Site1	0.98	0.00	0.97	Site 1 vs Site 2	0.93	0.00	0.82
	Site2	1.00	0.00	0.99	Site 1 vs Site 3	0.92	0.00	0.82
	Site3	1.03	0.00	0.94	Site 2 vs Site 3	0.98	0.00	0.99
tSNR	Site1	0.83	13.70	0.78	Site 1 vs Site 2	1.22	-14.30	0.87
	Site2	1.20	-3.95	0.96	Site 1 vs Site 3	1.19	-12.00	0.93
	Site3	1.01	1.42	0.96	Site 2 vs Site 3	0.93	7.12	0.96
CBF	Site1	0.64	19.00	0.82	Site 1 vs Site 2	0.94	15.25	0.74
	Site2	1.39	-23.25	0.87				

Table 3. *Linear Regression of MRI metrics across all relevant ROIs. Results within sites (left side of the table) and between sites (right side of table) are shown. *pcASL data not available for Site 3*

Conclusion and future work: This study successfully optimised MRI sequences for a multi-site mTBI study. For most of the MRI metrics assessed, the CoV was below the 10% threshold often targeted in MRI studies as biologically meaningful [5], with the highest consistency for structural measures, as expected [6]. The subsequent phase of this study will evaluate the variability of these MRI measures across sites using a cohort of 20 healthy controls and 20 patients. This evaluation will determine which MRI measures have adequate sensitivity and reliability to be used as biomarkers in the large-scale, longitudinal study, mTBI-PREDICT: a harmonised program of detailed clinical phenotyping of acute mTBI patients coupled with state-of-the-art multimodal biomarker evaluation to best predict outcomes in over 610 patients.

References [1] Kim SY, *et al*. Military-related mild traumatic brain injury: clinical characteristics, advanced neuroimaging, and molecular mechanisms. Transl Psychiatry. 2023 Aug 31;13(1):289. [2] Harris AD, *et al*. Harmonization of multi-scanner *in vivo* magnetic resonance spectroscopy: ENIGMA consortium task group considerations. Front Neurol. 2023 Jan 4; 13. [3] Wu B, *et al.* Intra- and interscanner reliability and reproducibility of 3D whole-brain pseudo-continuous arterial spin-labeling MR perfusion at 3T. J Magn Reson Imaging. 2014 Feb;39(2):402-9. [4] Mutsaerts HJ, et al. Multi-vendor reliability of arterial spin labeling perfusion MRI using a near-identical sequence: implications for multi-center studies. Neuroimage. 2015 Jun; 113:143-52. [5] Marenco S, *et al*. Regional distribution of measurement error in diffusion tensor imaging. Psychiatry Research: Neuroimaging, 2006,147(1). p. 69-78. [6] McGuire SA, *et al.* Reproducibility of quantitative structural and physiological MRI measurements. Brain Behav. 2017 Aug 2;7(9).

Are Physics Informed Neural Networks feasible for efficient spatiotemporal tracer kinetics?

Eve S. Shalom [1,2], Amirul Khan [3], Sven Van Loo [4], Steven P. Sourbron [1]
[1]Division of Clinical Medicine, School of Population and Health Sciences, University of Sheffield, UK
[2]School of Physics and Astronomy, University of Leeds, UK
[3]School of Civil Engineering, University of Leeds, UK
[4]Department of Applied Physics, Ghent University, Belgium

Introduction: Conventional tracer kinetics applies temporal models within single voxels and neglects local exchange between voxels. Spatiotemporal tracer kinetics [1] models the tracer transfer between and within voxels directly via continuum mechanics. This approach improves accuracy, removes inaccurate assumptions such as a global input function, and allows extraction of parameters that characterise spatial perfusion and flow patterns [2]. Spatiotemporal 1-compartment systems are readily identifiable, but extension to 2-compartment perfusion (hereinafter 2-compartment) systems yields degenerate solutions in some toy models [3]. Additionally, standard gradient descent requires long runtimes and is susceptible to local minima even in small systems [3]. Physics Informed Neural Networks (PINNs) [4] have shown promise in uncovering transport parameters from concentration data in both computational fluid dynamics [5] and conventional tracer kinetics [6]. The aim of this work is to determine whether PINNs can produce accurate solutions to spatiotemporal tracer kinetics systems. This could provide feasible analysis runtimes for 3D perfusion datasets with further development. Results are presented for a 1D and 2D 1-compartment model and a 1D 2-compartment model.

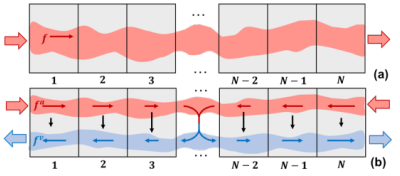

Fig 1: System layout for (a) 1-compartment and (b) 2-compartment models.

Table 1: Hyperparameter values.

Hyperparameter	Value (1C/2D1C/2CP)
Nodes	100/100/150
Hidden Layers	10
Training Iterations	7.5k/100k/250k
Learning Rate	0.001
Activation Function	Swish [7]

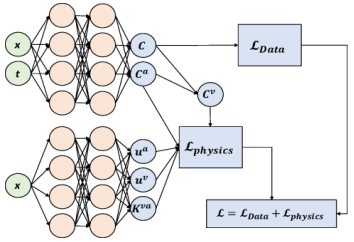

Fig 2: PINNs layout shown for 2-compartment.

Methods: *Theory:* A fluid dynamics approach was used, proposed in [1], which employs incompressibility, mass conservation and spatially variable transport coefficients to describe compartmental tracer evolution. Specifically, transport proceeds via convection between identical compartment types of neighbouring voxels and via perfusion exchange from arterial to venous compartments in the 2-compartment case.

Model: System layouts are illustrated in Fig 1. Interface velocities (u, u^a, u^v) and centred exchange terms (K^{va}) are defined. Influx at the arterial compartment boundaries were based on a population arterial input function [8], with no influx at the venous boundaries. A zero initial condition was used.

Simulations: A forward time and upwind advection discretization was used. Systems were 25.6x0.8cm (1D) or 25.6x25.6x0.8cm (2D) with voxel width 0.8cm and evolved to 80s. An internal time step of 0.2s was used with concentration measurements taken every 2s.

Inverse Approach: Parameters, P, are normalised, such that |P|≤1. The fitted concentration was optimised via a PINNs approach (Fig 2, Table 1) employing a least squares data fit and adherence to governing equations. For optimization in 1-compartment P={u}, for 2-compartment P={u^a, u^v, K^{va}}. Network weights were updated to minimise the data and physics loss terms via backpropagation using a full batch size.

Results: Spatial velocities are recovered with low error in 1-compartment systems for noiseless data in both 1D and 2D (Fig 3a/c) and noisy 1D data (Fig 3b). In the 2-compartment system, velocity parameters are accurately recovered at the system edges but around x=14cm the solution lowers in quality (Fig 4). In particular, the exchange term is not well captured, with consistently lower values than the ground truth at the system centre. Inclusion of measurement noise results in significantly erroneous 2-compartment parameters.

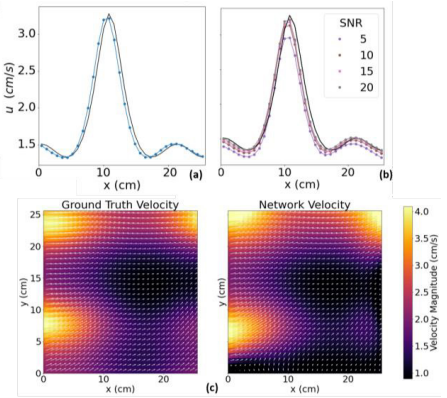

Fig 3: Parameter retrieval for 1-compartment 1D: noiseless (a) and noisy (b) data, and (c) 2D noiseless data. The black lines show ground truth parameters.

Discussion: Successful recovery of parameters for 1-compartment 1D and 2D systems illustrates PINNs approaches are appropriate for simple spatiotemporal systems. Particularly, the robust retrieval under increasing measurement noise in 1D and easy extension to 2D systems highlight the potential translation into realistic datasets. Hyperparameter tuning, such as batch size optimisation, could reduce runtimes. The PINNs approach for 2-compartment systems is highly susceptible to measurement noise and returns low accuracy exchange parameter values. Currently, boundary conditions are not enforced due to the general application of physics loss terms. Definition of appropriate boundary conditions could help better define these systems and may allow robust identification via a PINNs approach.

Conclusions: PINNs allow excellent parameter recovery in 1-compartment systems for the voxel interface velocities. Successful extension to 2D systems illustrates the potential for spatiotemporal applications of realistic scale via PINNs, with hyperparameter optimization proposed as future work. Within 2-compartment systems only the interface velocities were well reconstructed. Boundary conditions to better define these 2-compartment systems may improve parameter retrieval.

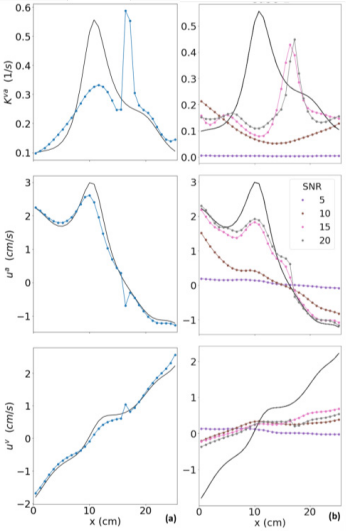

Fig 4: Parameter retrieval for: 2-compartment noiseless (a) and (b) noisy data. The black lines show ground truth parameters.

Acknowledgements: Funding from EPSRC-CASE PhD Studentship with Bayer AG at University of Leeds.

References: **[1]** Sourbron. 2014. *A tracer-kinetic field theory for medical imaging.* IEEE; 33(4):935-46. **[2]** Shalom et al. 2024. *Current status in spatiotemporal analysis of contrast-based perfusion MRI.* Magn Reson Med; 91(3):1136-48. **[3]** Shalom et al. 2024. *Identifiability of spatiotemporal tissue perfusion models*. Phys Med Biol; 69(11):115034. **[4]** Raissi et al. 2019. *Physics-informed neural networks: A deep learning framework for solving forward and inverse problems involving nonlinear partial differential equations.* J Comp Phys; 378:686-707. **[5]** Raissi et al. 2020. *Hidden fluid mechanics: Learning velocity and pressure fields from flow visualizations.* Science; 367:1026-30. **[6]** van Herten et al. 2022. *Physics-informed neural networks for myocardial perfusion MRI quantification.* Med Image Anal; 78:102399. **[7]** Ramachandran et al. 2017. *Searching for Activation Functions.* arXiv; 1710.05941. **[8]** Parker et al. 2006. *Experimentally-derived functional form for a population-averaged high temporal-resolution arterial input function for DCE-MRI.* Magn Reson Med; 56(5):993-1000.

Hierarchical-µGUIDE: Fast and Robust Bayesian Hierarchical Modelling using Deep Learning Simulation-Based Inference

Louis Rouillard[1], Demian Wassermann[1], Marco Palombo[2,3], Maëliss Jallais[2,3]

[1]Université Paris-Saclay, Inria, CEA, Palaiseau, 91120, France; [2]Cardiff University Brain Research Imaging Centre (CUBRIC), Cardiff University, Cardiff, United Kingdom; [3]School of Computer Science and Informatics, Cardiff University, Cardiff, United Kingdom

Introduction: Diffusion-weighted MRI is a promising imaging technique for characterizing brain microstructure in-vivo [1,2,3]. By fitting a biophysical model to the acquired diffusion signals, one can quantify histologically meaningful microstructural parameters within each voxel [1]. However, most approaches a) only provide the most likely parameter value without offering insights about their robustness and reliability, although crucial interpreting the results, and b) fit each voxel independently, without exploiting information redundancy across voxels. A recent approach, µGUIDE [4], based on Simulation-Based Inference (SBI) [5], estimates full posterior distributions and quantifies the uncertainty of the estimated tissue parameters [4,5,6]. µGUIDE circumvents the limitations of traditional Bayesian inference approaches (e.g. Markov-Chain-Monte-Carlo) by providing faster and more robust estimates of parameters posteriors in each voxel independently. However, the estimated voxel-independent posterior distributions can present large variance (i.e. high uncertainty) due to low signal-to-noise ratio (SNR). Resulting parameter maps can be noisy and obscure or misdiagnose pathologies. Here we introduce hierarchical-µGUIDE, a new method enhancing the fitting quality of microstructure parameters by combining information across voxels presenting a similar microstructure, hypothesising a hierarchical structure [7,8,9]. Similar voxels are grouped into parcels. The posterior distributions and the parcellation are jointly estimated from the observed data. Voxel parameters are estimated with higher precision, enhancing their clinical utility.

Methods: Hierarchical-µGUIDE: Hierarchical-µGUIDE relies on Bayesian inference, which takes as input a multi-shell diffusion-weighted signal for each voxel X^{vox}, and outputs the posterior distributions $p_{hier}(\theta^{vox}|X^{vox})$ of the microstructure parameters θ^{vox}, defined by a given biophysical model of the tissue [2,3]. Contrary to µGUIDE [4], voxels are not considered independently. Instead, we group voxels into L parcels of similar microstructure. Each parcel is associated with the average parameters θ^{parc}, and each voxel's microstructure θ^{vox} is assumed to be a perturbation of the parcel parameters it belongs to, with variability σ^{parc}. Using hierarchical-µGUIDE, we 1) learn a parcellation, and 2) reduce the uncertainty in each voxel's estimation by sharing information across voxels in the same parcel. Hierarchical-µGUIDE consists of two successive steps. First, using µGUIDE [4], we learn the independent posteriors $p_{ind}(\theta^{vox}|X^{vox})$, by training over a large synthetic dataset of microstructure-signal pairs, sampled from a simulator with a uniform prior $p_{ind}(\theta^{vox})$. Second, we hypothesise a hierarchical structure over the voxels [7,8,9] with prior $p_{hier}(\theta^{vox}, l^{vox}, \theta^{parc})$, that replaces the independent prior $p_{ind}(\theta^{vox})$. Using Plate Amortized Variational Inference (PAVI) [7], we start from the posteriors $p_{ind}(\theta^{vox}|X^{vox})$, and progressively regularise those into $p_{hier}(\theta^{vox}|X^{vox})$.

Exemplar application: As demonstrator, we applied hierarchical-µGUIDE to the Standard Model (SM) [3], a two-compartment model with five microstructural parameters: neurite signal fraction, intra-neurite diffusivity, orientation dispersion index, and parallel/perpendicular diffusivity within the extra-neurite space.

Training: SBI training was performed on 10^5 synthetic simulations computed using MISST [10] with random combinations of the model parameters, uniformly sampled from biologically plausible ranges. To match experimental data, Rician noise (SNR=30) was added to the simulated signals.

Experiment: MRI data: We applied hierarchical-µGUIDE to a participant with epilepsy. Data were acquired using a PGSE acquisition with b-value=[200,500,1200,2400]s/mm^2, respectively [20,20,30,61]diffusion encoding directions uniformly distributed, δ/Δ=7/24ms and TE/TR=76/3200ms.

Results: Fig.1 presents the results over simulated data, fitting the voxels using µGUIDE and Hierarchical-µGUIDE. Hierarchical-µGUIDE provides more accurate and precise parameter estimates. Fig.2 presents the SM parametric maps estimated using µGUIDE and Hierarchical-µGUIDE on a participant with epilepsy, alongside their uncertainty and parcellation. The sharper parametric maps and the parcellation highlight the lesion.

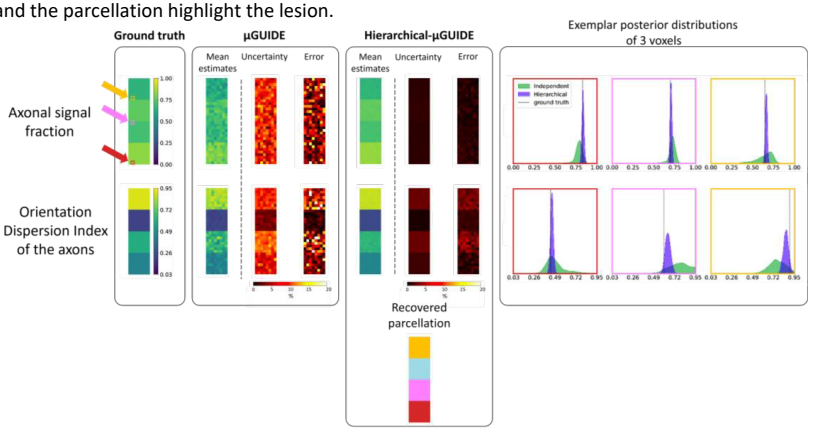

Fig. 1. Simulation results on a synthetic phantom with the SM, representing realistic white matter tissue configurations [11] using µGUIDE and Hierarchical-µGUIDE.

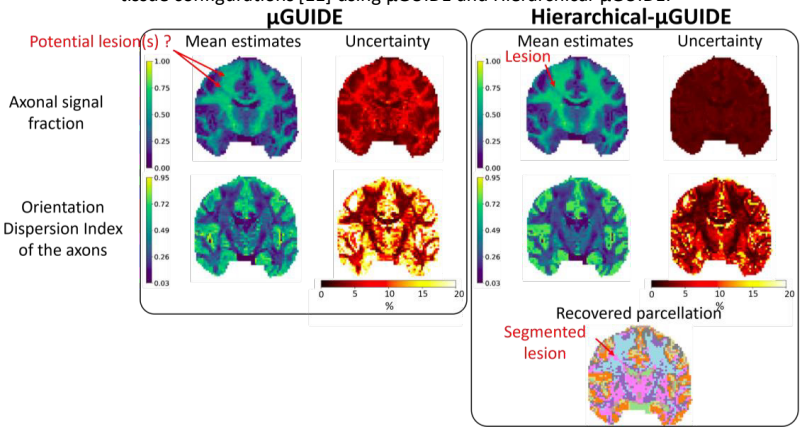

Fig. 2. Parametric maps of a participant with epilepsy using µGUIDE and Hierarchical-µGUIDE (L=8 parcels), with the SM. The lesion appears to be clearly segmented in the obtained parcellation.

Discussion: Hierarchical-µGUIDE yields faster posterior distribution estimates compared to existing hierarchical methods relying on MCMC[8,9], and returns a parcellation learnt from, not imposed on, the data. Its efficiency unlocks applications on large datasets, therefore gaining statistical power. Hierarchical-µGUIDE can seamlessly be applied to other biophysical models or hierarchical structures.

Conclusion: Hierarchical-µGUIDE improves the quality of tissue microstructure estimations by using a hierarchical Bayesian approach to efficiently estimate full posterior distributions along with a tissue parcellation. Hierarchical-µGUIDE reduces estimates uncertainty, while preserving tissue heterogeneity, allowing for pathology detection.

Acknowledgements: This work, MJ and MP are supported by UKRI Future Leaders Fellowship (MR/T020296/2). LR and DW are supported by the ERC-StG NeuroLang (ID:757672).

References: [1]Alexander et al., *NMR in Biomed* (2019) [2]Jelescu et al., *J Neurosci Methods* (2020) [3]Novikov et al., *NMR in Biomed* (2019) [4]Jallais et al., *arxiv* (2024) [5]Cranmer et al., *PNAS* (2020) [6]Jallais et al., *MELBA* (2022) [7]Rouillard et al., *TMLR* (2023) [8]Powell et al., *CDMRI* (2021) [9]Orton et al., *MRM* (2014) [10]Ianuş et al., *MRM* (2017) [11]Coelho et al., *NeuroImage* (2022)

Power Pitch Session 1

Automation of Small Bowel Water Content Evaluation using Machine Learning Image Segmentation Methods.

Stephen Lloyd-Brown[1], Caroline Hoad[2], Xin Chen[1]
[1]School of Computer Science, Faculty of Science, University of Nottingham, Nottingham.
[2]Sir Peter Mansfield Imaging Centre, University of Nottingham, Nottingham.

Introduction: Measurement of small bowel water content (SBWC) using MRI requires manual annotation of the small bowel [1]. For volumetric images this process can be extremely time consuming. For studies involving multiple participants over multiple sessions this process is even more protracted. Machine learning methods present an alternative annotation solution. We show that machine learning methods allow for a quicker way of determining SBWC in timeseries data, and we compare these results to manual annotation.
Methods: To form our training set, a set of 298 heavily T2 weighted TSE scans was compiled, taken from a variety of studies across four different scanners (two 1.5T, two 3T). The scans in the training set each had their small bowels manually labelled. These scans were fed to nnU-Net [2], a self-configuring variant of the popular image segmentation network U-Net [3]. nnU-Net was trained with hyperparameters which were automatically determined by the network. The network was trained using a single RTX 2060 TI, 15GB of RAM, and 4 CPU cores. Training was allowed to run for the full 1000 epochs, for a duration of 40 hours.
To test our model, data from a prior study [4], which investigated small bowel water content (SBWC) changes after ingestion of carbohydrates, were recompiled into a testing set. The full test set consisted of 58 participants, of which half were irritable bowel syndrome (IBS) patients, and half were healthy controls. They were scanned after ingesting one of three types of food, on three separate occasions, so that each participant has ingested each food once. The scans consisted of 7 scans taken at 60-minute intervals after ingestion, including one baseline scan before ingestion. Scans from the testing set were fed to the trained image segmentation model. Voxels identified as small bowel were deemed to contain entirely water. Total water content was therefore taken as the sum of small bowel voxels multiplied by voxel volume.
Results: Our results can be seen on the right-hand side of figure 1. For ease of comparison the results from the study by Major et al [4] are reproduced on the left-hand side of figure 1. There is clear agreement of trend behavior between the two methods for both IBS patients and healthy controls, with the relative responses between the different carbohydrates matching well between methods. There are differences in overall measured volume, especially at large volume. These differences are being investigated.

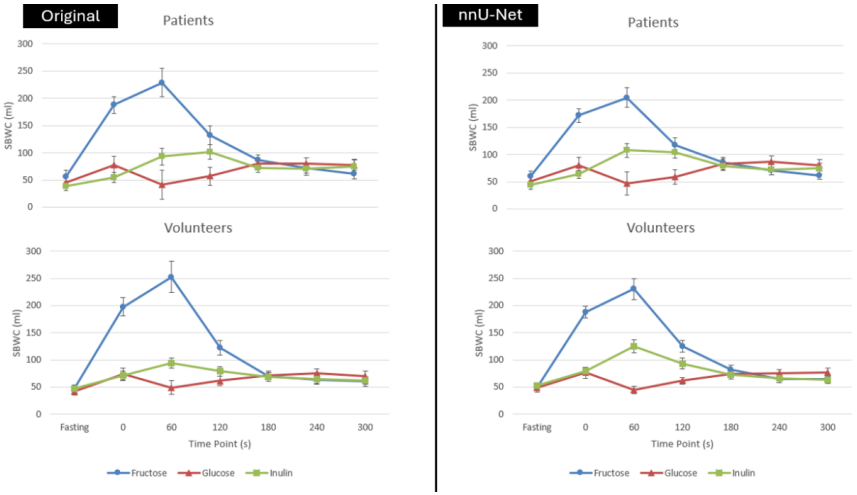

Fig. 1. Small bowel water content (SBWC) measured over time after ingestion of one of three food groups (glucose, fructose or Inulin). The left-hand side was produced by manual segmentation, and is reproduced from the work by Major et al [4]. The right-hand side was produced for this abstract using machine learning methods.

Discussion: The principal benefit of measuring SBWC in this way compared to traditional methods is the time difference. Manual annotation of the near thousand scans required to produce the generated figures took many months of work. Using the machine learning method described above, segmentation of all scans can be conducted in as little as 25 minutes. This is a colossal time save, even if training time is considered. The difference in overall volume is not ideal, however correction of erroneous masks is faster than segmentation from scratch. This significant decrease in annotation time opens the pathway to potential future clinical viability, which is currently not possible with manual annotation due to the time required.
Conclusions: We used nnU-Net, a popular state of the art image segmentation network, to reproduce manually analyzed results from literature. The time required to do this was significantly reduced from months to minutes. The trend of results was clearly reproduced, with some discrepancy of measurement at the larger volumes. The significance of this work is that the time decrease opens a pathway to clinical viability. Future work will target automatic methods to determine which datasets may need manual corrections following machine learning segmentation.
Acknowledgements: Stephen is funded by the Engineering and Physical Sciences Research Council. We thank the authors of Reference [4] for allowing their anonymised data to be shared for this work.

References

[1] Hoad, C. L., et al. "Non-invasive quantification of small bowel water content by MRI: a validation study." Physics in Medicine & Biology 52.23 (2007): 6909.
[2] Isensee, Fabian, et al. "nnU-Net: a self-configuring method for deep learning-based biomedical image segmentation." Nature methods 18.2 (2021): 203-211.
[3] Ronneberger, Olaf, Philipp Fischer, and Thomas Brox. "U-net: Convolutional networks for biomedical image segmentation." Medical image computing and computer-assisted intervention–MICCAI 2015: 18th international conference, Munich, Germany, , proceedings, part III 18. Springer International Publishing, 2015.
[4] Major, Giles, et al. "Colon hypersensitivity to distension, rather than excessive gas production, produces carbohydrate-related symptoms in individuals with irritable bowel syndrome." Gastroenterology 152.1 (2017): 124-133.

Assessment of Composite Pulses in Ultra-Low field MRI: application to TSE Imaging

Finn Aubrey Conboy[1], Samira Bouyagoub[1], Itamar Ronen[1], Ivor Simpson[2], Nick Dowell[1]
[1]Clinical Imaging Sciences Centre, Brighton and Sussex Medical School, Brighton, BN1 9RR
[2]School of Engineering and Informatics, University of Sussex, Brighton BN1 9QJ

Introduction

Ultra-low field (ULF) MRI offers increased accessibility, lower costs and greater mobility than high field scanners. However, imaging at ULF is typically characterized by poor signal to noise ratio (SNR) caused primarily by field strength and exacerbated by inhomogeneity in B_0 and B_1 fields.

Composite refocusing Radio Frequency (RF) pulses consist of a series of contiguous, or near-contiguous, pulses, each may have a different phase or flip angle. These have been shown to be less sensitive to common imperfections such as B_1 inhomogeneity and off-resonance and have demonstrated improved efficiency over conventional rectangular (i.e. single component) pulses [1].

Method

Table. 1: Refocusing pulses discussed in this work

Designation	Refocusing Pulse Components (flip angle$_{phase}$)	Compensation
Rectangular	$180^\circ_{0^\circ}$	None
LF	$90^\circ_{90^\circ}180^\circ_{0^\circ}90^\circ_{90^\circ}$	B_1 inhomogeneity
LT	$90^\circ_{135^\circ}270^\circ_{45^\circ}90^\circ_{135^\circ}$	Resonance offset
TPG	$180^\circ_{256^\circ}180^\circ_{52^\circ}180^\circ_{0^\circ}180^\circ_{128^\circ}180^\circ_{0^\circ}180^\circ_{232^\circ}180^\circ_{0^\circ}180^\circ_{308^\circ}180^\circ_{104^\circ}$	B_1 inhomogeneity (+ Resonance offset)

Data was acquired on a Multiwave MGNTQ scanner equipped with a 50mT Halbach permanent magnet array, solenoid head coil and Kea2 Magritek spectrometer [2,3]. Three composite refocusing pulses (Table. 1) [1], were implemented in a 1-dimensional spectra spin echo pulse sequence with acquisition parameters: TE=42ms, number of points=512, Dwell time=50µs, TR=15000ms, using a lactate solution phantom. LF and LT pulses compensate for off-resonance and B_1 inhomogeneity respectively, and TPG offering a degree of compensation for both.

To assess composite pulse performance in the presence of B_0 inhomogeneity, off-resonance conditions were created by modulating the centre-frequency of the spectra in increments of 0.5KHz in the range of ± 5kHz. To assess the effect of B_1 inhomogeneity, refocusing pulse amplitudes were modulated from the experimentally-determined optimum (B_{1opt}) for the rectangular refocusing pulse, from B_1/B_{1opt}=0.12 to B_1/B_{1opt}=1.05 in increments of B_1/B_{1opt}=0.025. The resulting spin echo signal intensity was used to assess the performance of the composite refocusing pulses compared to a rectangular pulse in both of the above experiments.

Performance of the composite refocusing pulses was then assessed in vivo (male, 26 years old). Brain images were acquired with a 3D Turbo Spin Echo sequence: ETL=4, TR=500ms, TE=20ms, averages=2, resolution=2.5mm x 2.5mm x 5mm, FOV 200mm, 8 mins per acquisition, using the composite refocusing pulses in Table 1. A B_0 map was acquired using a TSE B_0 acquisition with two readings taken with an echoshift of 1µs and 200µs, with the same acquisition parameters except for ETL 16 (as used for TSE imaging). Two regions-of-interest (ROIs) as shown in B_0 map were used to assess the performance of the composite pulses in the presence of high and low B_0 inhomogeneity (Fig. 2a), and 4 noise regions were taken (Fig. 2b) with the average of the standard deviation. SNR was then calculated for each ROI using: $SNR = \frac{0.66 \times mean\ signal}{average\ of\ noise\ region\ standard\ deviation}$

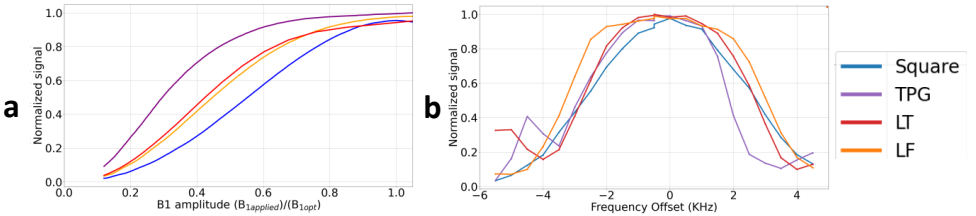

Fig. 1. Performance of rectangular (single-component) and composite refocusing pulses in a 1-dimensional spin-echo acquisition of phantom. (a) Normalized spin echo signal intensity across a range of B_1 scaling factors and (b) 0KHz being on-resonance.

Results and Discussion

The rectangular pulse showed greater sensitivity to B_1 inhomogeneity and off-resonance compared to composite refocusing pulses (Fig. 1). TPG showed most insensitivity to B_1 inhomogeneity (Fig 1a), while LT showed the most insensitivity to off-resonance effects in the range of ±1kHz (Fig 1b).

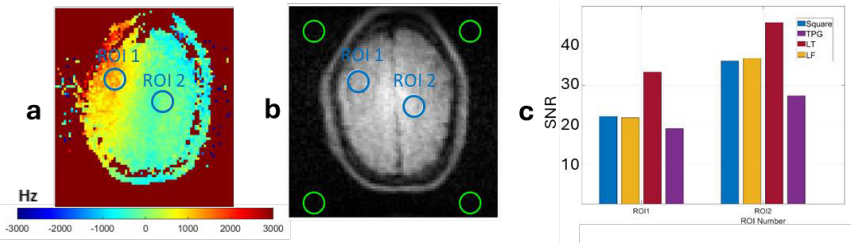

Fig. 2 (a) In vivo B_0 map with two ROIs in high (ROI1) and low (ROI2) off-resonance conditions. (b) The corresponding slice in the TSE image showing the noise ROIs (green circles). (c) Bar graph showing SNR of ROIs displayed in (a, b) with each refocussing pulse.

In vivo imaging showed significant B_0 inhomogeneity (Fig 2a); the average off-resonance frequency within ROI 1 and ROI 2 is 1288Hz and -98Hz respectively. The SNR for all refocusing pulses is lower in ROI 1 than ROI 2 (Fig 2c), likely due, in part, to off-resonance effects. LT, which is designed to compensate for off-resonance conditions, offers improvements in SNR in both regions and the effect is largest in the region of greatest off resonance. This is in keeping with the phantom study, where LT performed best in the range of ±1kHz (Fig. 1b).

Conclusions

This work shows that composite pulses that compensate for off-resonance effects boost SNR which is one of the limiting factors for image quality at this field strength. Overall, LT showed an improvement in SNR over other refocusing pulses for in vivo. This suggests that that B_0 inhomogeneity has the greater influence on SNR compared to B_1 inhomogeneity; however, this will need to be further investigated with a B_1 map to establish this.

References

[1] Odedra, S, Wimperis, S (2012). *Use of composite refocusing pulses to form spin echoes*. J. Magn. Reson. 214 (2012) 68-75.
[2] Meet MGNTQ. Available at: https://multiwave.ch
[3] O'Reilly T, Teeuwisse WM, Webb AG. *Three-dimensional MRI in a homogenous 27 cm diameter bore Halbach array magnet*. J Magn. Reson. (2019) Oct;307:106578.

Scalable spokes pTx pulses for 2D turbo-spin-echo imaging at 7T

Minghao Zhang[1], Christopher T. Rodgers[1]

1. Wolfson Brain Imaging Centre, University of Cambridge

Introduction

7T MRI gives excellent resolution and SNR but often suffers from regions of signal drop-out. The clinically important Turbo-spin-echo (TSE, RARE, FSE)[1] sequence is particularly affected because its repeated refocusing pulses allow any flip angle error to accumulate.

Parallel transmit (pTx) scans can improve image homogeneity, but a pTx TSE sequence must still satisfy Carr-Purcell-Meiboom-Gill (CPMG) conditions.[2] Recent studies have improved 2D TSE by phase-matching the excitation and refocusing pulses,[3] or by using direct-signal-control (DSC) to directly optimize the echo signals with dynamic RF shimming.[4] For 3D TSE, the scalable kT-point pulses were introduced by Eggenschwiler et al[5] and formally proven by Gras et al.[6] We introduce 2D scalable spokes pTx pulses for TSE.

Methods

Pulse design

It was proven[6] that the flip angle of a pulse scales well with the applied voltage if the RF waveform is symmetric about the centre of the pulse, and the gradient trajectory is antisymmetric. It also means that the 90° phase difference between excitation and refocusing pulses required by the CPMG condition can be satisfied with a single phase shift, which conventional magnitude least squares (MLS) pulse design can not assure.

For 2D imaging, each slice-selective subpulse is often approximated as a single packet of RF energy, and hence we propose the slice-selective gradient is exempt from this requirement. We create spokes pTx pulse forms that satisfy this symmetry condition (Figure 1). This reduces the number of degrees of freedom. The pulses also include a pre- and post- in-plane blips, which ensures that the middle spoke is in the centre of the transmit k-space.

Pulse optimizations were performed with a modified PPD code (Siemens). Spokes parameters were optimized with Bayesian Optimization of GrAdient Trajectory[7] (BOGAT) and a Tikhonov-regularized magnitude least squares RF optimizer.[8]

Simulation

Simulations were performed on a database of phantom and in vivo field maps from our Terra 7T MRI (Siemens) and 8Tx32Rx head coil (Nova) and the vendor-provided satTFL B_1^+ and dual-echo GRE B_0 mapping sequences.

To test the scalability, 3-spoke pulses with and without symmetry constraints were designed on a set of phantom fieldmaps for a 120° flip angle. The voltage was then scaled, and their performance computed with Bloch simulations.

To simulate the TSE performance, a 120° 3-spoke scalable pulse was designed for a set of in vivo field maps. The pulse was scaled to 90° and 180°, and a 90° phase shift was applied to the refocusing pulse. The TSE echo train was simulated with extended phase graph (EPG),[9] where each pulse was represented by an instantaneous rotation whose effect is calculated from Bloch simulation of the 3-spoke pulse. The EPG simulates 9 echoes with 12ms echo spacing, T1=1000ms, T2=100ms. The result is compared with conventional circularly polarized (CP) pulses, and with DSC-optimized RF shimming[4] TSE train.

Validation experiments

A 3-spoke scalable pTx pulse was designed as described above for a spherical agar phantom. To reduce SAR, VERSE was applied[10] without changing the spacing between the centres of subpulses. TSE images were acquired, first for a standard TSE train with 120° refocusing, TE=76ms, TR=5000ms, 0.9mm in-plane, echo spacing 12.8ms, 9 echoes per shot, GRAPPA 3. Further images were acquired with a hyperecho train[11] to further reduce SAR.

The 120°-refocusing TSE scan was repeated for one volunteer (with written consent) for hippocampus imaging.

Results

Figure 2 demonstrates that a scalable 3-spoke pulse scales better with voltage than unconstrained 3-spoke pulse as predicted by theory. Crucially, scaling maintains a more consistent phase pattern.

Figure 3 shows EPG simulations of the TSE echo train. The scalable 3-spoke pulse performed comparably with DSC optimization for the mean echo strengths, and showed better spatial homogeneity.

Figure 4 show the phantom TSE images acquired with the scalable pulses. The 3-spoke pulse images show better uniformity than CP images.

Discussions and Conclusion

We have demonstrated that 2D scalable spokes pTx pulse designs are well suited for CPMG TSE imaging. Simulations show that 3-spoke pulses outperform RF shimming, and only required the computational burden of 1 single pulse design (<10s) per optimization volume.

Fitting the duration of a 3-spoke pulse in TSE presents a significant SAR challenge. However, with VERSE conversion and the hyperecho train, we achieved an estimate of 50% slices per TR compared with CP acquisitions under the currently strict Nova 8Tx headcoil limit. Slice-by-slice design could improve this efficiency since different pulses are likely not limited by the same VOP.

The superior flip angle homogeneity is translated into more uniform images, validated in the phantom and in vivo experiments.

References

1. Hennig, J. et al. MRM 3, 823–833 (1986). 2. Meiboom, S. & Gill, D. Review of Scientific Instruments 29, 688–691 (1958). 3. Yetisir, F. et al. MRM 93, 87–96 (2022). 4. Sbrizzi, A. et al. MRM 77, 361–373 (2017). 5. Eggenschwiler, F. et al. MRM 71, 1478–1488 (2014). 6. Gras, V. et al. MRM 80, 53–65 (2018). 7. Zhang, M. & Rodgers, C. T. MRM 91, 2358–2373 (2024). 8. Setsompop, K. et al. MRM 59, 908 (2008). 9. Weigel, M. JMRI 41, 266–295 (2015). 10. Hargreaves, B. A. et al. MRM 52, 590–597 (2004). 11. Weigel, M. & Hennig, J. Zeitschrift für Medizinische Physik 18, 151–161 (2008).

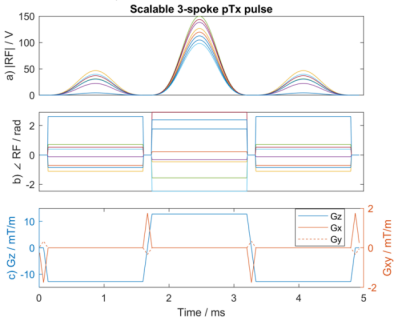

Figure 1 Form of an example scalable 3-spoke pTx pulse. The RF form is symmetric in time, and G_{xy} is antisymmetric.

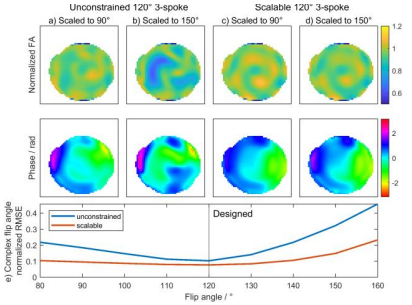

Figure 2 Scalability illustration with Bloch simulations. (a-b) show the behaviour of an unconstrained 3-spoke pulse designed without restrictions on the G_{xy} waveform symmetry. Scaling the voltage significantly changes the flip angle magnitude and phase patterns. Whereas (c-d) shows 3-spoke pulses where the Gxy waveform symmetry was constrained. These "scalable" pulses show better scaling properties under the same extent of voltage scaling. (e) compares the complex normalized RMSE between the two designs, where the target magnitude is the target flip angle, and target phase is the actual phase pattern of the designed pulse (the 120° pulse in this case).

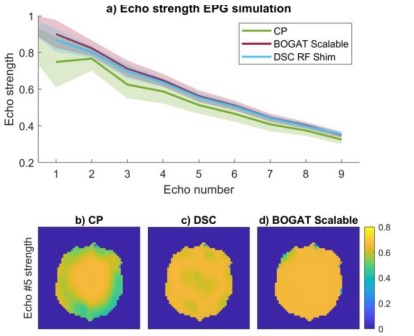

Figure 3 Turbo-spin-echo (TSE) echo strengths simulated by extended phase graph (EPG), comparing the performance between CP, direct signal control RF shimming optimization, and our scalable BOGAT 3-spoke pulses. (a) shows the mean and standard deviation of each echo across all voxels in a slice. (b-d) show the spatial variation of the echo magnitude at the center (5th) echo.

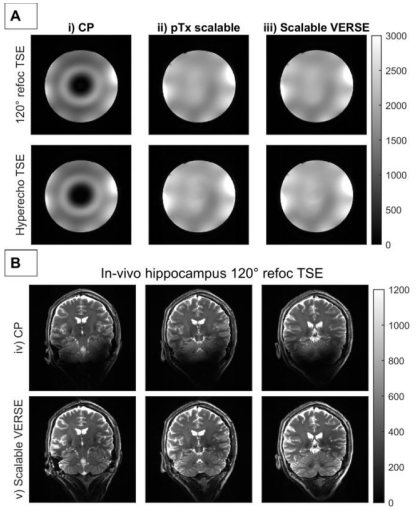

Figure 4 (A) Phantom TSE acquisitions with (i) CP, (ii) pTx scalable 3-spoke pulses designed with BOGAT, and (iii) the scalable pulse after VERSE conversion in phantom. Two types of echo trains were tested – a 120° constant refocusing train, and a variable flip angle hyperecho train. (B) In vivo comparison between (iv) CP and (v) VERSE scalable 3-spoke pulse, with 120° constant refocusing train shown in 3 slice positions. The scalable 3-spoke pulses show superior performance in both cases.

B_0 shimming using a multi-coil array for simultaneous regional and whole brain acquisition at 7T

Claire Lucas, Susan Francis, Adam Berrington
Sir Peter Mansfield Imaging Centre, School of Physics and Astronomy, University of Nottingham

Introduction: Single-voxel Magnetic Resonance Spectroscopy (MRS) has recently been combined with whole brain functional Magnetic Resonance Imaging (fMRI) to investigate simultaneous changes in neurochemicals and BOLD during tasks [1,2]. However, large B_0 inhomogeneities that arise at 7T cause MRS line-broadening and distortions in the imaging data. For interleaved fMRI-MRS approaches, higher order shimming on small volumes of interest (VOIs) can generate suboptimal B_0 field distributions outside of the VOI, resulting in poor water suppression in MRS and geometric distortions in MRI. Dynamic shimming using spherical harmonic shim coils can improve local and global B_0 homogeneity, but this is generally limited to updating linear shim terms only due to eddy current effects [3]. Multi-coil shim arrays offer the possibility to improve B_0 homogeneity at 7T, with fast switching, for simultaneous local and whole brain shimming [4].

A commercially available 24-channel coil array used in combination with a weighted shimming approach was simulated to assess the improvement in B_0 field homogeneity over a small MRS VOI and the whole brain.

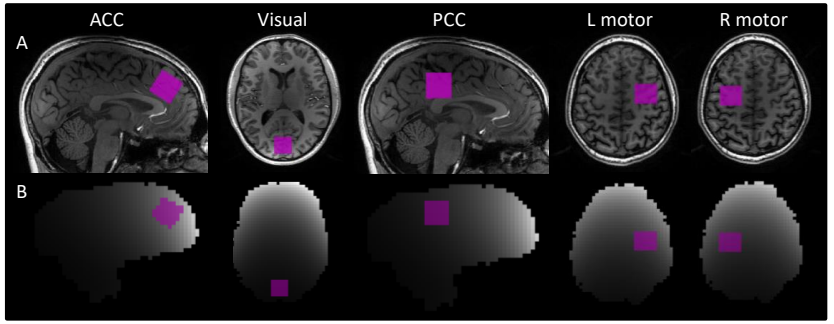

Fig. 1 – Location of anterior cingulate cortex, visual cortex, posterior cingulate cortex, and left/right motor cortex VOIs used for simulation, shown in (A) T1 weighted structural image and (B) map showing coverage of the multi-coil array within the brain, where bright areas indicate higher coverage.

Methods: A weighted algorithm for simultaneous shimming over two regions was developed in Python based on a previous approach [3], using B_0 field maps acquired in phantom (n=4) and *in vivo* (n=4). B_0 maps used for simulations were acquired on a Philips 7T Achieva system (Philips Healthcare, Netherlands) using a 32-channel Nova Medical head coil (Nova Medical, Massachusetts). B_0 distribution was optimised using a least squares algorithm, using spherical harmonic basis fields (n=9, up to second order) from the scanner's inbuilt shim system (S) and the individual currents (n=24) of the multi-coil array (M) (*Elara*, MR Shim GmbH, Germany) mounted onto the anterior of the head coil. Resulting B_0 fields were simulated for 3 shimming methods: individually (M or S) and together (M+S). The predicted effect of performing the shim optimisation for a 25x25x25mm^3 MRS VOI placed in various regions across the brain versus the whole brain was investigated using a weighting parameter, α, where for high values of α more weight is given to whole brain homogeneity. Simulations for the weighted shim were performed on 4 MRS VOIs placed in the anterior cingulate cortex (ACC), visual cortex, posterior cingulate cortex (PCC), and left/right motor cortex (Fig. 1A). A coil coverage map was produced using the sum-of-squares image of the coil bases (Fig. 1B), to visualise areas where the multi-coil array might be most effective.

Results & discussion: The algorithm successfully calculated optimum shim weights for the two regions using all 3 methods (M, S, and M+S). Within the MRS VOI, increasing α led to an increase in the standard deviation of B_0. The opposite was true for the whole brain (Fig. 2A). When shimming was strongly weighted towards either the MRS VOI or whole brain, M+S always predicted a lower standard deviation within the corresponding VOI. There were no instances in which using M alone would be beneficial compared to using S alone, so this prediction was not considered in further analysis. An intermediate weighting value of α (indicated in Fig. 2A) was used to characterise the relative benefit of M+S compared to S alone. This weighting predicted an improvement of whole brain homogeneity for a <1 Hz increase of in standard deviation in the MRS VOI, in all regions. The addition of the multi-coil array predicted varying levels of improvement in the MRS VOI when placed in different brain regions (Fig. 2B), with the MRS VOI in the ACC and left/right motor cortex showing a predicted improvement in homogeneity within these regions using M+S instead of S alone. In the visual cortex and PCC, the use of M+S does not predict an improvement. This is potentially because the position of the VOI is distant from the multi-coil array (Fig. 1B), so the shim is unlikely to improve with the additional use of M. In the whole brain, the use of M+S predicts a 15±4% improvement in standard deviation compared to S alone at this value of α.

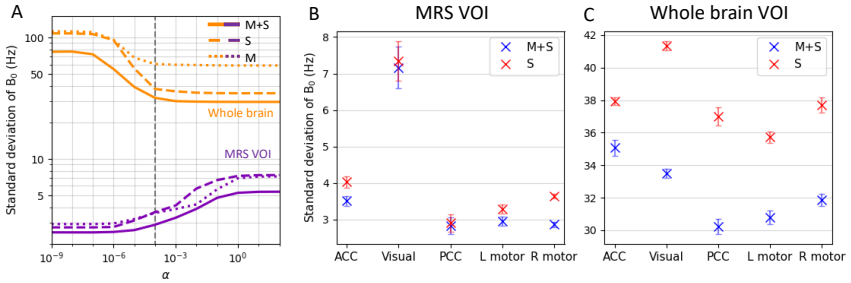

Fig. 2 – (A) Effect of α on predicted standard deviation of B_0 in an MRS VOI (right motor cortex, purple) and whole brain (orange), with shims predicted using the scanner spherical harmonics (S, dashed line), multi-coil array (M, dotted line), and both together (M+S, solid line). The grey dashed line shows α = 10^{-4}, used to compare standard deviation of B_0 within (B) MRS VOI and (C) whole brain, with the MRS VOI placed in different brain regions, comparing S and M+S configurations.

Conclusions: In future work, these predicted changes will be tested *in vivo*, using a static shimming approach comparing M, S, and M+S. Subsequently, a dynamic approach will be performed, applying a fixed value of the spherical harmonic terms and dynamically updating the shim applied with the multi-coil array to improve the field over the MRS VOI and whole brain. Dynamic shimming will then be integrated into an interleaved fMRI-MRS approach to simultaneously investigate haemodynamics and changes in metabolism.

References

[1] Ip, I. B., Berrington, A., Hess, A. T., Parker, A. J., Emir, U. E., & Bridge, H. (2017). Combined fMRI-MRS acquires simultaneous glutamate and BOLD-fMRI signals in the human brain. *NeuroImage*, *155*, 113–119.
[2] Schrantee, A., Najac, C., Jungerius, C., van der Zwaag, W., Jbabdi, S., Clarke, W. T., & Ronen, I. (2023). A 7T interleaved fMRS and fMRI study on visual contrast dependency in the human brain. *Imaging Neuroscience*, *1*, 1–15.
[3] Boer, V. O., Andersen, M., Lind, A., Lee, N. G., Marsman, A., & Petersen, E. T. (2020). MR spectroscopy using static higher order shimming with dynamic linear terms (HOS-DLT) for improved water suppression, interleaved MRS-fMRI, and navigator-based motion correction at 7T. *Magnetic Resonance in Medicine*, *84*(3), 1101–1112.
[4] Juchem, C., Nixon, T. W., McIntyre, S., Boer, V. O., Rothman, D. L., & de Graaf, R. A. (2011). Dynamic multi-coil shimming of the human brain at 7 T. *Journal of Magnetic Resonance*, *212*(2), 280–288.

Power Pitch Session 1

Investigation of Electromagnetic Interaction Between RF Coil & Graphene-based Electrophysiology Probes at 7 Tesla Preclinical MRI

Suchit Kumar[1], Samuel M. Flaherty[2], Alejandro Labastida-Ramírez[2], Anton Guimerà Brunet[3], Ben Dickie[4], Kostas Kostarelos[2], Rob C. Wykes[1,2], Louis Lemieux[1*]
[1]University College London Queen Square Institute of Neurology, London, UK
[2]Centre for Nanotechnology in Medicine & Division Neuroscience, University of Manchester, UK
[3]Centro de Investigación Biomédica en Red en Bioingeniería, Biomateriales y Nanomedicina (CIBER-BBN), Madrid, Spain
[4]Division of Informatics, Imaging and Data Sciences, University of Manchester, Manchester, UK

Introduction: New graphene-based electrophysiological recording technology (known as Graphene Solution-Gated Field-Effect Transistors, or gSGFET) [1], offers several advantages over existing electrodes. These advantages include a significantly reduced amount of metal that can interfere with MRI and high-fidelity DC-coupled brain signal recording in rodents [2]. There is interest in being able to perform MRI acquisitions in animals with such probes implanted, therefore the MR compatibility and safety of the graphene-based EEG probe need to be ensured. Here we report on computational simulations to assess the electromagnetic (EM) interaction and safety of the animals with these probe in the MRI environment, with the ultimate goal of achieving the highest possible level of MR compatibility.

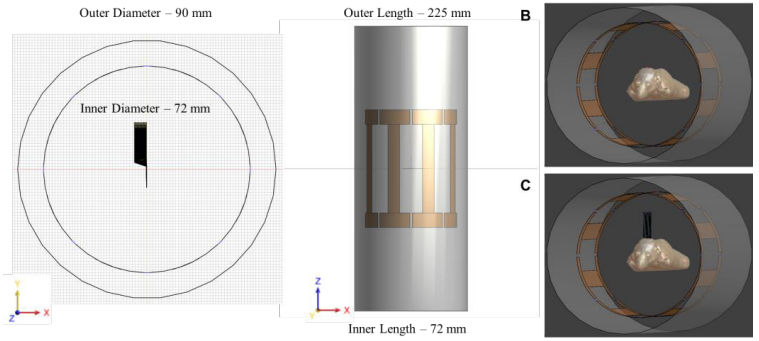

Fig. 1*. (A) Transmit highpass birdcage RF coil dimensions; (B) Configuration of rodent model placed in MRI RF coil without, and (C) with graphene-based EEG probe model as a brain implant.*

Methods: EM simulation analysis based on finite-difference time-domain (FDTD) method was performed using Sim4Life (V8.0, ZMT, Switzerland) in a 3D rodent model, which includes a total of 68 tissues [3, 4]. For RF transmission, quadrature birdcage RF coil is used which has the following specifications: coil diameter: 72mm, coil length: 72mm, shield diameter: 90 mm, shield length: 225mm, 8 rungs, each rung (width: 9.9mm) has a capacitor (14.2pF) placed on the end-rings (width: 11.5mm) (Fig.1A). Figure 1B shows the rodent model inside the transmit RF coils without and with EEG probe model implemented in this work.

The 3D model of graphene-based EEG probes was generated from 2D drawings (.dxf format) and exported to CAD (.stl format) via Autodesk Fusion 360 (California, USA). The simulations were performed on a Windows 11 PC (3.00GHz, 32GB RAM, 23GB GPU) as follows: 300MHz of gaussian excitation with bandwidth of 650MHz excited in two-port and results were combined in circular-polarized mode. The additional sub-gridding feature was used and obtained from ZMT for localized mesh refinement. Mean and peak specific absorption rate (SAR) averaged over 0.01g, 0.1g and 1g tissue-mass were calculated following IEC guidelines [5].

Results: The RF coil was tuned and matched to 300MHz using Sim4Life matching toolbox. Fig. 2 shows the B_1^+-field and E-field distributions in the rodent model, which clearly show that the graphene-based probes can increase the B_1^+ as well as E-field magnitudes by approximately 15-20 % in the vicinity of the probes. It is due to the induced current during transmission to the metal present in the layers of probes. Fig. 3 shows the SAR distributions in the rodent model, clearly shows the elevated SAR due to the probe. The mean mass-avg SAR (W/kg) values are 0.63 and 0.83 in the rodent model without and with probe, respectively. The peak mass-avg SAR (W/kg) values for 0.01g, 0.1g and 1g tissue mass are 2.49, 1.29, 0.82; and 5.9, 2.8, 1.6 in the rodent model without and with probe, respectively, and was localized in the skin. The computational time for a rodent with a probe is around 160 hours per port, while without a probe it is 1.5 hours per port on a single GPU. There is a computational power restriction on a single GPU that needs to be addressed, and cluster GPU implementation is required.

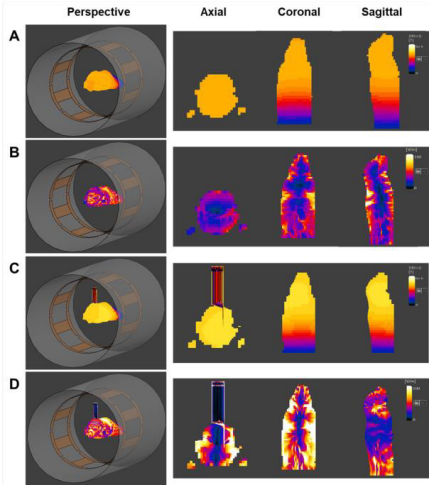

Fig. 2*. Simulated B_1^+-field distribution in rodent model (A) without, (C) with probe model; E-field distribution in rodent model (B) without, (D) with probe model.*

Discussion: The simulation results indicate that the graphene-based EEG probes increase the SAR deposition but remain within acceptable limits. There are no SAR limit guidelines for rodents, however the permissible mass-averaged SAR values for humans are 2W/kg for the whole body and 3.2W/kg for the head.

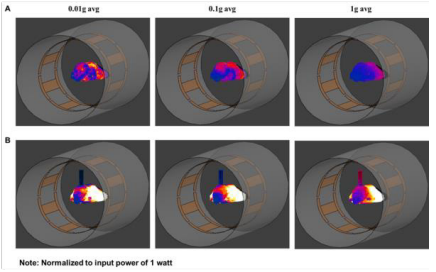

Fig. 3*. Simulated mass-avg SAR distribution in rodent model (A) without, (B) with EEG probe model for 0.01g, 0.1g and 1g tissue mass.*

Conclusions: This study successfully demonstrates the EM interaction of graphene-based EEG probes in an MRI environment. Through meticulous EM simulations, it was shown that graphene-based probes can affect RF transmission and increase SAR deposition while remaining within permissible limits, thus ensuring MR compatibility and safety. Further work is necessary to optimize computational efficiency, experimental verification using phantom, concurrent EEG-fMRI studies *in vivo* in chronically epileptic rodents and scale these probes for human application.

Acknowledgements: This project is funded by the EPSRC under grant no. EP/X013669/1. The authors are grateful for the support from Sim4life, ZMT for providing the science license.

References: [1] Bonaccini Calia, Andrea, et al. Nature Nanotechnology 17.3 (2022): 301-309. [2] Wykes, Rob C., et al. Clinical and Translational Medicine 12.7 (2022): 1-4. [3] Sim4Life, ZMT, <http://www.zurichmedtech.com>. [4] Kainz, Wolfgang, et al. Physics in Medicine & Biology 51.20 (2006): 5211. [5] International Electrotechnical Commission (IEC) (2022): IEC 60601-2-33.

Multi-split ring surface coil for gradient free volume localised sodium spectroscopy at 0.5T.

Kristina I Popova [1], Anna A Hurshkainen[1], Georgiy A Solomakha[2], Arthur Harrison[3], Thomas Meersmann[3,4], Galina E Pavlovskaya[3,4]
[1] School of Physics and Engineering, ITMO University, St. Petersburg, Russian Federation, [2]Department of High Field Magnetic Resonance, Max Plank Institute for Biological Cybernetics, Tuebingen, Germany, [3]Sir Peter Mansfield Imaging Centre, Medicine, University of Nottingham, [4]Nottingham NIHR Biomedical Research Centre, Nottingham.

Introduction. Low field (< 0.5T) has been acknowledged as an emerging technological development in the attempt to democratise MRI. Low field MRI scanners are affordable by low-income countries thus enabling higher quality healthcare currently hampered in these countries by MRI instrumentation costs. While low field MRI development has been mainly focussed on anatomical imaging using protons, our group explored sodium detection at 0.5T with the view of translation to sodium sensory technology. Availability of sodium sensors is highly anticipated in diabetes research as it enables departure from glucocentric views on diabetes aetiology. Exploration of sodium role in Diabetes can help in managing about 20% of Diabetes cases currently not responsive to available treatment [1].
However, sodium detection at 0.5T needs to be optimised to achieve sodium signal collection from clinically relevant ROI. To address this, we have simulated and built sodium surface coil that allows for collection of sodium signal from the dermis skin layer. We report relevant proof of principal data in phantoms studies.
Methods. RF-coil was designed as multi-split ring resonator (MSRR) [2] The RF-coil was numerically simulated using the CST Studio 2021 (Dassault Systèmes, Vélizy-Villacoublay, France) software using finite-element method in the frequency domain [3]. External dimensions of the resonator were chosen as 54 × 42 mm what correspond to desired field of view. The coil was tested at 0.5T Paramed open magnet using portable Kea2 console (Magritek, Germany) in phantoms.
Results. The resulting setup of RF-coil as MSRR is presented on Fig. 1A. In such system of ten coupled split-ring resonators, it is possible to excite ten eigenmodes at different frequencies. Numerically simulated frequency response of the reflection coefficient S_{11} of RF-coil is presented in Fig. 1B, which illustrates the tuning of the second order eigenmode to the Larmor frequency of ^{23}Na in a field of 0.5 T - 5.63 MHz. The graph of magnetic field profile (the dependence of the amplitude on the coordinate along the normal to the plane of RF-coil) in Figure 1C shows that magnetic field amplitude generated by single-loop coil several tens of times lower than the field of MSRR and is falling slightly along normal to the surface of the RF-coil. Calculated H-field map generated by a RF-coil at the Larmor frequency of ^{23}Na in the central cross section is presented in Figure 1D. Magnetic field magnitude values were normalized to the 1 W of the power accepted by the RF-coil.

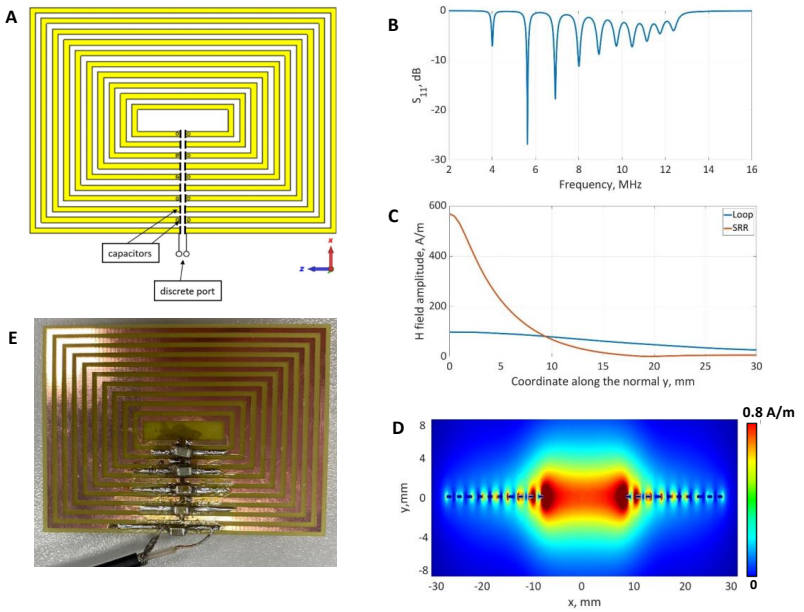

Figure 1 A, General view of RF-coil simulation model. B, Frequency dependence of the reflection coefficient on the discrete port of RF-coil. C, Calculated B_1^+ maps at the Larmor frequency of ^{23}Na plotted in the central cross section. D, The field profile for the second eigenmode. E. Manufactured RF-coil.

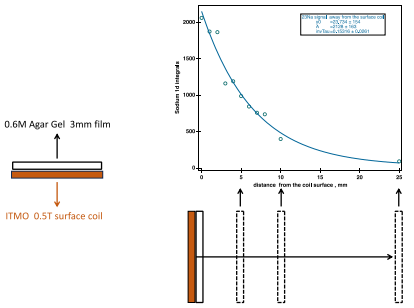

Figure 2. 0.6M Agar Gel 3mm film moved from the coil surface as shown in the bottom panel. ^{23}Na signal was recorded for each position. Signal decay away from the coil surface is exponential.

Sodium spectra acquired at 0.5T in 0.6M NaCl agar phantom are shown in Figure 2. As one can see the signal falls off exponentially as the spacing between the phantom and the coil surface increases, in line with simulation shown in Figure 1C.
Discussion. The coil behaviour is in line with theoretical predictions. Sodium signal from physiological 0.1M NaCl was collected within 10 min. Sodium signal collection using native Paramed console using this coil is currently under way to evaluate coil performance for in vivo

gradient free volume localised sodium spectroscopy.

Conclusion. Eigen mode coil design allows for sodium volume localised spectroscopy without the use of gradients thus enabling fast sodium signal collection for clinically relevant ROIs in the body.

References: [1] https://doi.org/10.1080/17446651.2022.2092094; [2] https://doi.org/10.1364/OE.17.005933; [3] https://archive.ismrm.org/2013/0231.html

Prospective 8Tx thoracic-lumbar spinal array at 7T MRI

Yiling Hu[1], Divya Baskaran[1], Belinda Ding[2], David A. Porter[1], Natasha Fullerton[3], Shajan Gunamony[1,4]
[1]Imaging Centre of Excellence, University of Glasgow, Glasgow, UK
[2]Siemens Healthcare Ltd., Frimley, UK
[3]Queen Elizabeth University Hospital, NHS Greater Glasgow and Clyde, UK
[4]MR CoilTech Limited, Glasgow, UK

Introduction: The appeal of 7T MRI's superior resolution compared to 1.5T and 3T is countered by increased radiofrequency (RF) field inhomogeneity and tissue power deposition associated with the higher resonant frequency of hydrogen at 7T [1]. Parallel transmission (pTx) is a method that splits the transmit coil into multiple independently-controlled channels to mitigate the above issues [2]. This abstract presents preliminary simulation results from a new pTx spinal array design with eight transmit elements for thoracic-lumbar spinal imaging, and compares it with an existing spinal array design similar to the one introduced by Kraff et al. [3].

Methods: Finite-difference time-domain (FDTD) EM simulations were performed in CST 2022 (CST Studio Suite, Dassault Systems, France). An eight-channel transmit array was modelled in CST with copper wire loops of width 100mm, length 135mm, and wire radius 1mm. The loops are arranged in a dual-column configuration, with nearest-neighboring elements overlap-decoupling and next-nearest-neighboring elements inductively decoupling (Fig. 1a). Elements are displaced by 4mm from their nearest neighbors in the *y*-direction (Fig. 1b). Each loop has fixed capacitors of 6.8 pF to 7.5 pF (in blue) and ports (in red) for matching, tuning, and decoupling circuits. A copper EM shield of 0.2mm thickness is placed 30mm from the coil (Fig. 1c). Scanner conditions were recreated using a 325mm radius copper bore and FR-4 coil housing. The right column (Tx5-8) has a 180° phase shift from the left column, as Kraff described in his paper [3]. B_1 simulations were performed on a phantom with tissue properties of muscle taken from digital voxel model Ella (ε = 55.032, σ = 0.9429S/m) with 1W power input per channel for a total of 8W input power. SAR simulations were performed on a 1mm resolution Duke digital voxel model loaded as shown in Fig. 1c, with a total input power of 1W. This array ("non-offset") was compared to a design similar to Kraff's ("offset") in Fig. 1d&e where the right column is shifted in the -*z*-direction by half of a loop length. The offset array used only overlap-decoupling and all elements sat on the same *xy*-plane, with jumper cables used to avoid contact.

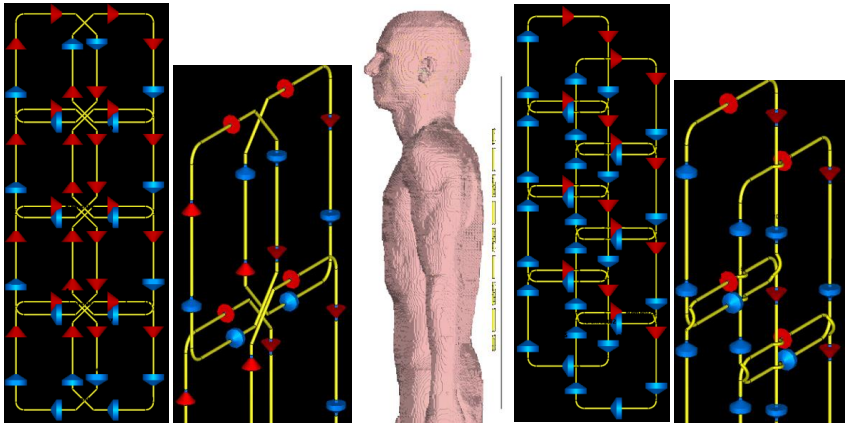

Fig. 1. Non-offset (a,b) and offset (d,e) coil layouts and Duke's positioning with respect to the coil and shield (in gray) (c).

Results: Optimal overlap dimensions for the non-offset array were found to be 30mm between the left and right columns, and 14-18mm between vertically adjacent elements. S-parameters from the

non-offset coil are shown in Figs. 2 and 3. Both reflection and coupling coefficients were successfully tuned and matched to below -20dB and -15dB, respectively. The non-offset coil has a more uniform B_1^+ excitation field and higher B_1^+ average (1.50μT) across a midsagittal slice of 30mm depth compared to the offset coil, which has a B_1^+ average of 1.09μT (Fig. 4). Fig. 5 shows a more uniformly distributed SAR map in the non-offset coil compared to the offset coil, however the max SAR is also higher (0.86W/kg vs 0.45W/kg).

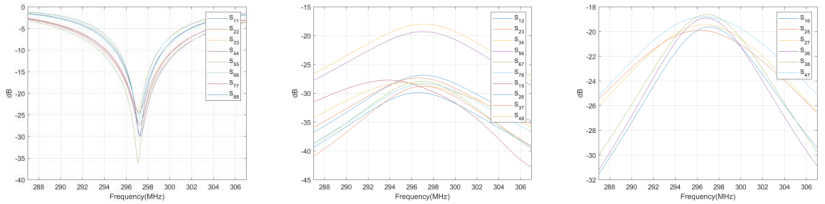

Fig. 2. S-parameters of non-offset coil, plotted for reflection coefficients (left), nearest-neighbor coupling (middle), and next-nearest neighbor coupling (right).

Discussion: Initial results from the non-offset coil simulations are promising and improve upon the offset design. The high SAR can be mitigated by increasing the distance between the coil and the subject.

	S1	S2	S3	S4	S5	S6	S7	S8
S1	-25							
S2	-30	-24						
S3	-27	-29	-24					
S4	-41	-29	-18	-29				
S5	-29	-20	-43	-48	-35			
S6	-20	-27	-19	-39	-19	-26		
S7	-40	-19	-27	-19	-30	-28	-27	
S8	-46	-40	-19	-29	-41	-26	-28	-30

Fig. 3. S-parameter matrix for non-offset array, in dB.

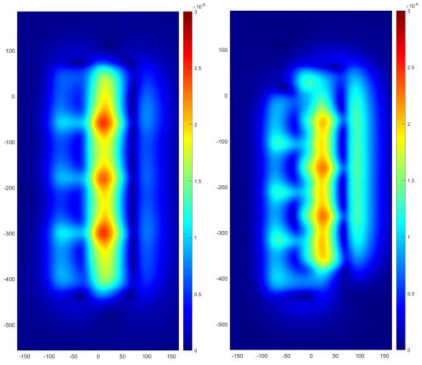

Fig. 4. B_1^+ maps of non-offset (left) and offset (right) arrays, scaled to a maximum of 3μT.

Conclusions: FDTD EM simulations of a prospective dual-column 8Tx array for thoracic-lumbar spinal imaging yield improved B_1^+ field distribution compared to an existing design with an offset between the right and left columns. Developing a 4Tx cervical-thoracic spine (neck) coil to the 8Tx array using channel splitters in future work would provide a better picture of whole-spine imaging.

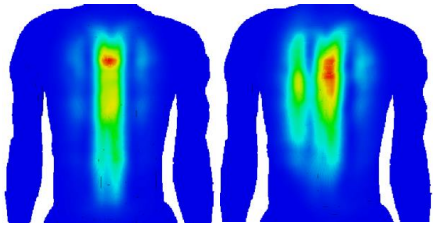

Fig. 5. SAR maps of non-offset (left) and offset (right) arrays.

References

[1] Williams et al. (2023). *Physics in Medicine and Biology*, **68**(2).
[2] Padormo et al. (2016). *NMR in Biomedicine*, **29**(9), 1145–1161.
[3] Kraff et al. (2009). *Invest. Radiol*, **44**(11), 734-740.

Developing AI based methods for glioma segmentation across novel clinical contexts

Gabriela Flores Lopez[1], Dr. Matthew K Townend[2,3], Dr. Hamied A Haroon[1,3]

[1]The University of Manchester, Oxford Road, Manchester, M13 9PL, UK
[2]King's College London, Strand, London, WC2R 2LS, UK
[3]AINOSTICS Limited, 3 Hardman Square, Spinningfields, Manchester, M3 3EB, UK

Introduction: Gliomas are some of the most common supratentorial tumours of the central nervous system (CNS), which are classified through growth rate into high-grade gliomas (HGGs) and low-grade gliomas (LGGs) [1]. Convolutional neural networks (CNNs) are used to segment glioma subregions in preoperative magnetic resonance imaging (MRI) scans. These accurately label oedema, tumour necrosis and tumour growths, which are useful for successful resection [2]. In this study, we applied pre-trained weights from our CNN model to novel datasets using transfer learning (TL) to reproduce clinically accurate segmentations (overall dice score above 0.78) across post-operative scans in HGGs via a modified nnUNet model.[2]

Methods: We used a modified baseline nnUNet model (MBL-nnUNet), an out-of-the-box segmentation tool for subregional tumour labelling [1][2]. We initially trained on the Brain Tumour Segmentation (BrATS) challenge 2020 dataset, reducing the total amount of epochs (iterations over total amount of data) to 100 from the original 1000. We applied TL across two additional cohorts: the Rio-Hortega University Hospital (RHUH-GBM) for HGGs [4] and the TCGA-LGG (TCGA-LGG) dataset for LGGs [5]. Each model had two configurations, 2D and 3D, where predictions were finetuned on a subset of the data: pre-finetuned models were termed 'Pre-MBL', whereas post-finetuned models were named 'Post-MBL'. Total training times for these models corresponded to 3.92 and 11.13 days, respectively.

Results:

1. **MBL-2D(RH) and MBL-3D(RH) performance before and after finetuning**

Glioma subregional predictions were assessed for the RHUH-GBM group, with an initial mean DSC of 0.489 for Pre-MBL2D(RH) and 0.491 for Pre-MBL3D(RH). Scans at three time points (pre-operative, post-operative and recurrence) were included for finetuning (n=8). We observed an increase in segmentation accuracy for overall mean DSC in both Post-MBL2D(RH) and Post-MBL3D(RH), with an overall accuracy of 0.783 and 0.795, respectively. Results for each subregional label with respect to ground truths (GTs) are reported in Table 1.

Mean DSC								
Model configuration			Pre-fine-tuning: PRE-MBL2D(RH), PRE-MBL3D(RH)			Post-fine-tuning POST-MBL2D(RH), POST-MBL3D(RH)		
	WT	ET	TC	**Mean**	WT	ET	TC	**Mean**
2D	0.439	0.433	0.596	**0.489**	0.854	0.686	0.763	**0.783**
3D	0.451	0.423	0.600	**0.491**	0.834	0.734	0.793	**0.795**

Table 1. MBL nnUNet accuracy before and after fine-tuning across the RHUH-GBM cohort. Results are presented through individual labels and overall accuracy as compared to ground truth (manual) segmentations*). WT = Whole Tumour, ET = Enhancing Tumour, TC= Tumour Core (necrosis).*

2. **Post-operative scans have analogous performance in Post-MBL2D(RH) and Post-MBL3D**

We assessed the performance in post-operative scans only for the RHUH dataset across finetuned models as compared to GTs. We found that neither performance on each subregional label nor overall DSC varied significantly across each model, as observed in Figure 1.

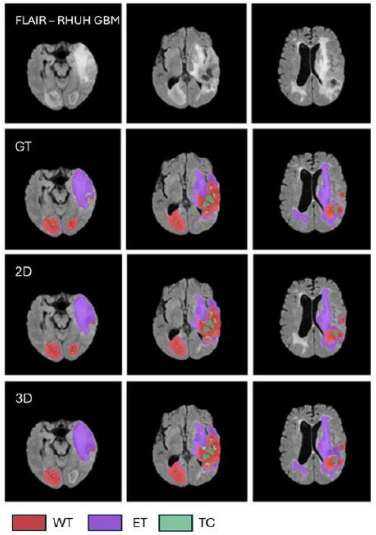

Figure 1. Post-MBL2D(RH) and Post-MBL3D(RH) performance in recurrence cases. Top row: RHUH post-operative FLAIR scan showing signal change due to a high-grade glioma. Second rows: GT segmentations across glioma subregions: WT, ET, and TC (colour-coded). Third and bottom rows: 2D and 3D predictions, respectively, after fine-tuning. (n=8)

Discussion: We aimed to generate accurate subregional glioma segmentations using weights from a MBL trained model using TL. We used this model to produce subregional segmentations (whole tumour, enhancing tumour, and tumour core) across two patient cohorts, RHUH-GBM (n=40) and TCGA-LGG (n=69). The most accurate segmentations were obtained from the Post-MBL3D(RH) model, though we did not observe a statistically significant drop in performance for the Post-MBL2D(RH) predictions. Further, the Post-MBL3D(RH) model sustained accurate predictions across post-operative and recurrence scans with structural differences from resection to those in the training set [6]. Nevertheless, we found that the model accuracy decreased in Post-MBL2D(LGG) compared to that of Post-MBL2D(RH), which could be attributed to differences in labelling for both tumour subtypes.

Conclusions: We aimed to show TL applied in subregional glioma segmentation across two novel clinical contexts for HGGs and LGGs. Our MBL nnUNet models produced subregional segmentations in a time-efficient manner by reducing the total number of epochs. This resulted in accurate subregional segmentations for the HGG group but was limited in the LGG group. Further research could elaborate on improving accuracy in regional segmentation of LGG by curating a more representative training cohort.

Acknowledgements: We thank AINOSTICS Limited for their support using their high-performance compute (HPC) cluster with high-spec GPU nodes.

References

[1] S. Bakas *et al.*, “Advancing The Cancer Genome Atlas glioma MRI collections with expert segmentation labels and radiomic features,” *Sci Data*, vol. 4, p. 170117, Sep. 2017, doi: 10.1038/sdata.2017.117.

[2] F. Isensee, P. F. Jaeger, S. A. A. Kohl, J. Petersen, and K. H. Maier-Hein, “nnU-Net: a self-configuring method for deep learning-based biomedical image segmentation,” *Nat Methods*, vol. 18, no. 2, pp. 203–211, Feb. 2021, doi: 10.1038/s41592-020-01008-z.

[3] F. Isensee, P. F. Jaeger, P. M. Full, P. Vollmuth, and K. H. Maier-Hein, “nnU-Net for Brain Tumor Segmentation.” arXiv, Nov. 02, 2020. Accessed: Apr. 08, 2024. [Online]. Available: http://arxiv.org/abs/2011.00848

[4] S. Cepeda *et al.*, “The Río Hortega University Hospital Glioblastoma dataset: A comprehensive collection of preoperative, early postoperative and recurrence MRI scans (RHUH-GBM),” *Data Brief*, vol. 50, p. 109617, Sep. 2023, doi: 10.1016/j.dib.2023.109617.

[5] “BRATS-TCGA-LGG,” The Cancer Imaging Archive (TCIA). Accessed: Apr. 03, 2024. [Online]. Available: https://www.cancerimagingarchive.net/analysis-result/brats-tcga-lgg/

[6] E. Cargnelutti, T. Ius, M. Skrap, and B. Tomasino, “What do we know about pre- and postoperative plasticity in patients with glioma? A review of neuroimaging and intraoperative mapping studies,” *Neuroimage Clin*, vol. 28, p. 102435, Sep. 2020, doi: 10.1016/j.nicl.2020.102435.

Developing an Open-Source Framework for the Simulation of MR Elastography Experiments

Mehmet N. YILDIRIM[1], Samuel Evans[2], Daniel Gallichan[1]
[1] CUBRIC / School of Engineering, Cardiff University, Cardiff, UK
[2] School of Engineering, Cardiff University, Cardiff, UK

Introduction: Magnetic Resonance Elastography (MRE) is a non-invasive quantitative medical imaging technique used to estimate tissue stiffness. The technique allows for the detailed assessment of tissue mechanical properties, providing valuable insights into liver disease, breast cancer, and neurological disorders such as Alzheimer's disease, multiple sclerosis, and traumatic brain injury [1]. Utilizing computational models and personalised simulations in MRE can offer valuable insights into the biomechanical properties of biological tissues in health and disease. Previous studies have shown that finite element (FE) modelling can be effectively utilized to develop and evaluate MRE, investigating the effects of material properties, excitation frequency, and boundary conditions on shear wave propagations [2, 3, 4]. In this work, we aim to develop an open-source approach for FE simulations of the tissue biomechanics that lead to the MRE contrast, allowing ourselves and others to test and compare different acquisition strategies as well as stiffness estimation techniques.

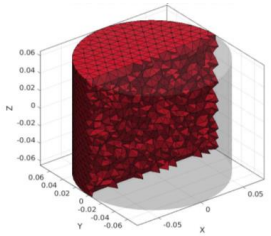

Fig. 1. Mesh view of 3D Cylindrical MRE phantom FE model.

Methods: For our initial simulation we investigated an elastic, homogeneous, nearly incompressible, and isotropic cylindrical model to create a simplified representation of tissue mechanics and to compare with real MRE data collected on a cylindrical phantom (CIRS Inc, VA, USA). The FE analysis for this study was conducted using the open-source package 'FEBio' [5], and using the GIBBON (Geometric Image-Based Bioengineering Network) toolbox in MATLAB to generate the mesh. In our FE analysis, we used tetrahedral (tet10) elements, which have 10-nodes and quadratic shape functions. The material properties of the phantom were characterized by a Young's modulus of 9kPa, a Poisson's ratio of 0.49 to ensure nearly incompressible behavior, and a density of 1000 kg/m³. Sinusoidal motions in the z-direction at 60.1 Hz with amplitude of 150 µm were applied to the nodes in the entire outer surface of the model to simulate the vibration used in MRE. The outer nodes were also fixed along X and Y, assuming the container to be rigid. A high-quality mesh is essential to achieve both high accuracy and computational efficiency in FE modelling. To determine the appropriate mesh resolution necessary for obtaining accurate results, we conducted a mesh sensitivity study.For the experimental part of the study, the phantom underwent MRE acquisitions on a 3T MR scanner (Siemens Healthineers, Erlangen, Germany). We utilized a Resoundant MRE system (Resoundant Inc., USA) that generated mechanical vibrations at a frequency of 60.1 Hz, synchronized with the MRE sequence. The phantom was positioned within the MR head coil, with the passive driver placed on its top surface to transmit mechanical vibrations produced by the pneumatic active driver.

Results: The displacement data show observable deformation patterns throughout the model. We plotted the resulting displacement values against different mesh sizes (Fig.2) to observe the effect of mesh refinement on the accuracy of the model. Our findings indicate that the mesh size converges at approximately 48,000 Solid Elements. At this convergence point, the displacement values stabilize, and further reductions in mesh size yield nearly negligible changes in the displacement values. The MRE wave images from both the FE simulation and experimental results at four phases of driving frequency, all conducted at 60.1 Hz, show good visual agreement in their depiction of the propagation of shear waves within the phantom (Fig.3).

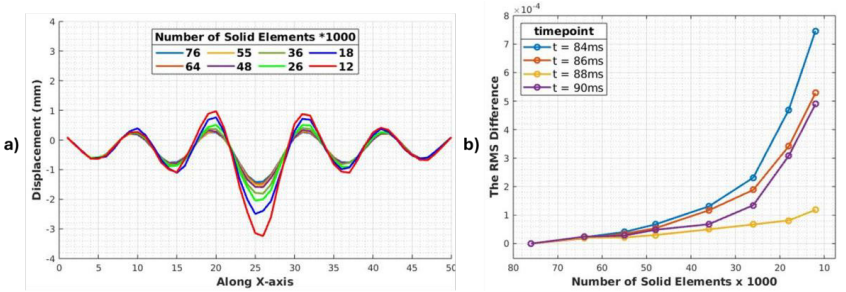

Fig. 2. Overview of mesh sensitivity study; **(a)** 1D Displacement profiles of simulated phantom for varying mesh sizes at timepoint *t* = 86ms . **(b)** The RMS difference (compared to reference mesh) of simulated displacement profiles each mesh.

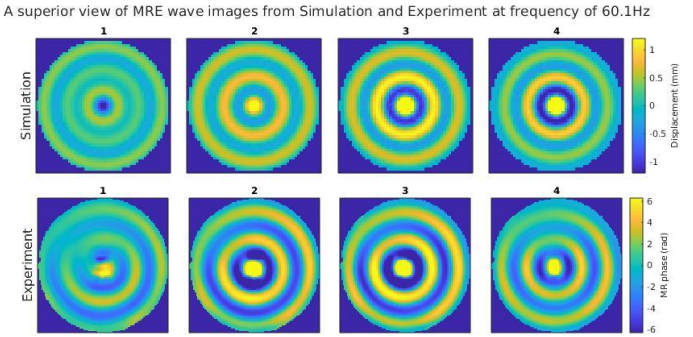

Fig. 3. Wave image comparison between experimental study and simulation results for four phases of driving frequency at 60.1Hz driving frequency.

Discussion: In this study, we examined the displacement data and frequency response of the MRE phantom under dynamic loading conditions using FEBio. Our mesh convergence analysis found that a mesh-size of ~48k elements should be sufficient for our simulations – and simulating 100 ms of transient behaviour took ~12 minutes on a 64-CPU compute node. The simulation model we have used so far is purely elastic and we would not expect this to accurately represent the viscoelastic behavior observed in biological tissues. The next step for our future work is to investigate how to incorporate realistic viscoelastic properties into our simulations.

Conclusions: Our preliminary results demonstrate the capabilities of open-source software implementations to simulate a simple MR elastography experiment in a cylindrical phantom. We aim to develop this approach to allow deeper investigation into the optimisation of brain MRE in human subjects.

Acknowledgements: Mehmet Nebi YILDIRIM's PhD study was funded by the Republic of Türkiye Ministry of National Education under the Study Abroad Scholarship Program.

References

[1] L. V. Hiscox *et al.*, *Phys. Med. Biol.*, vol. 61, no. 24, Art. no. 24, 2016, doi: 10.1088/0031-9155/61/24/R401.
[2] Q. Chen, S. I. Ringleb, A. Manduca, R. L. Ehman, and K.-N. An, *J. Biomech.*, vol. 38, no. 11, pp. 2198–2203, Nov. 2005, doi: 10.1016/j.jbiomech.2004.09.029.
[3] S. Tomita *et al.*, *J. Vis.*, vol. 21, no. 1, Art. no. 1, 2018, doi: 10.1007/s12650-017-0436-4.
[4] M. McGarry *et al.*, *Phys. Med. Biol.*, vol. 66, no. 5, p. 055029, Mar. 2021, doi: 10.1088/1361-6560/ab9a84.
[5] FEBio, 'FEBio Software Suite'. Accessed: Jun. 28, 2024. [Online]. Available: https://febio.org/

Validation of High Spatial Resolution ^{23}Na Imaging of the Skin.

Theodora Slater[1], Ben Prestwich[1], and Susan T Francis[1]
[1]Sir Peter Mansfield Imaging Centre, University of Nottingham, Nottingham, United Kingdom

Introduction: The storage of sodium in the skin has been shown to be a physiologically important regulatory mechanism for blood pressure, volume regulation, with an increase shown with age and hypertension [1,2], as well as in patients with renal [3,4] and cardiovascular disease [5]. The capability to perform robust sodium quantification in the skin *in vivo* will enable testing of treatments aimed at reducing sodium content in skin. However, the skin layer is thin, <2 mm, making imaging with standard coils difficult. Here we develop a dual tuned ^{1}H/^{23}Na coil to image both sodium and water to study the skin at high spatial resolution, and test this on a 'skin phantom' and in healthy subjects to study sodium quantification.

Methods: *Acquisition:* A dual tuned ^{1}H/^{23}Na surface coil was developed for high resolution imaging of the skin on a 3T Phillips Achieva scanner. Specific absorption rate (SAR) simulations and assessment of RF power deposition of the coil were performed to meet the safety requirements and assess the simulated sensitivity field. The surface coil was placed on a support with reference tubes of four sodium concentrations (15, 30, 45, 60 mmol/L) below. To establish the B_1 field of the surface coil, B_1 maps were collected on a uniform phantom of 50 mmol/L sodium using a 3D gradient echo (GRE) scheme of 1.5 × 1.5 x 10 mm^3 spatial resolution which collected images across a flip angle sweep (TE/TR = 2/100 ms, 0 – 140° in 10° steps, and 160 - 220 ° in 20° steps).

A 'skin phantom' was made comprising agar of approximately 3 mm thick and sodium concentration 50 mmol/L to mimic skin tissue, with 25 mmol/L sodium to mimic muscle, and a layer of lard of varied thickness at its minimum 3 mm to represent subcutaneous fat. ^{23}Na images were acquired on the skin phantom using a 3D GRE scheme of 1.5 × 1.5 x 10 mm^3 spatial resolution, and ^{1}H images were collected using a 3D T_1-weighted scheme at 0.18 × 0.18 x 2 mm^3.

In-vivo data was collected on the calf of six participants (age 20–28 years) using matched ^{23}Na and ^{1}H protocols to those used on the 'skin phantom', in addition a ^{1}H mDIXON scan was also collected to aid visualisation of the skin and vasculature. Skin phantom and *in vivo* ^{23}Na measures were also collected at spatial resolutions of 1 x 2.25 x 10 mm^3 and 0.75 x 3 x 10 mm^3 similar to that performed by Zhu et al. [6].

Analysis: The ^{23}Na images were B_1 corrected using both a sensitivity image and the B_1 map from the multiple flip angle data. Data was converted to total sodium concentration (TSC) in mmol/L using a regression line computed across the reference tube ^{23}Na concentrations.

Results: Figure 1 shows example ^{23}Na 'skin phantom' and *in vivo* images at each spatial resolution quantified using the B_1 mapping correction. Applying B_1 correction of the *in vivo* data led to skin sodium measures of 8-24 mmol/L across subjects from the 1.5 × 1.5 x 10 mm^3 spatial resolution data. Collecting ^{23}Na images at a higher in-plane resolution of 0.75 x 3 x 10 mm^3 increased the measured sodium to 17-35 mmol/L.

Discussion: This work has demonstrated that the 'skin phantom' is a useful tool to assess quantification of skin sodium, with B_1 mapping improving estimation. Further work will be performed to produce a phantom with thinner skin layers. The dual tuned ^{1}H/^{23}Na surface coil provides high sensitivity within a range of 10 mm from its surface allowing spatial resolution imaging of human skin, enabling better separation of the skin's ^{23}Na signal than the volume birdcage coil.

Conclusion: In future, segmentation of the ^{1}H images into tissue types will be used to correct for partial volume effects. These methods will be applied to study changes in sodium levels in the skin across age and ethnicity, and the effects of disease such as hypertension.

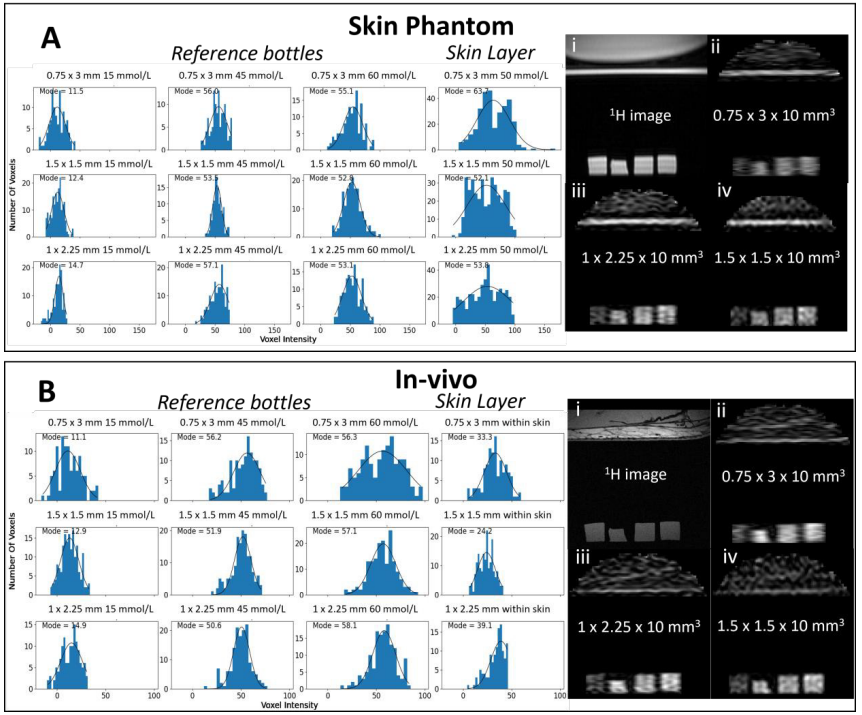

Figure 1: *(A) (i) 1H mDIXON image collected with the surface coil showing the skin phantom. Calibration of the reference tubes for ^{23}Na images in (ii), (iii) and (iv) and associated histograms of signals in the reference tubes. Note the 30 mmol/L tube has been ignored due to shrinkage. (B) In-vivo data from an example healthy subject showing (i) ^{1}H mDIXON image collected with the surface coil showing the skin layer and vasculature, (ii) ^{23}Na image uncorrected, (iii) ^{23}Na image following calibration using the reference tubes using simple sensitivity map, and (iv) ^{23}Na image following calibration using the reference tubes using B_1 map.*

References

[1] C. Kopp et al., "23Na magnetic resonance imaging of tissue sodium," Hypertension, vol. 59, no. 1, pp. 167–172, 2012.
[2] C. Ott et al., "Impact of renal denervation on tissue Na+ content in treatment-resistant hypertension," Clin. Res. Cardiol., vol. 107, no. 1, pp. 42–48, Jan. 2018.
[3] P. Schneider et al., "Skin sodium concentration correlates with left ventricular hypertrophy in CKD," J. Am. Soc. Nephrol., vol. 28, no. 6, pp. 1867–1876, Feb. 2017.
[4] A. Dahlmann et al., "Magnetic resonance-determined sodium removal from tissue stores in haemodialysis patients.," Kidney Int., vol. 87, no. 2, pp. 434–41, 2015.
[5] Jens Titze and Friedrich C. Luft. "Speculations on salt and the genesis of arterial hypertension". Kidney International, 91(6):1324–1335, 6 2017
[6] Jinxuan Zhu et al.,"Skin Sodium Concentration is Elevated with Aging but Relative Change Depends on Spatial Resolution of 23Na MRI". MR Imaging of X-Nuclei (23Na & Friends): From Controversies to Potential Clinical Applications, Part II, 2023.

A Standardized MRI Phantom for Dissolved Phase ^{129}Xe MRI.

Max Filkins[1,2], Arthur Harrison[1,3,4], Guilhem J. Collier[5], Graham Norquay[5], Jim M. Wild[5], Sean P. Rigby[2], Galina E. Pavlovskaya[1,3,4], Thomas Meersmann[1,3,4].
[1]Sir Peter Mansfield Imaging Centre, University of Nottingham, NG7 2RD, UK
[2]Department of Chemical and Environmental Engineering, University of Nottingham, NG7 2RD
[3]Translational Medical Science Unit, School of Medicine, University of Nottingham, NG7 2UH
[4]NIHR Nottingham Biomedical Research Centre, Nottingham University Hospitals
NHS Trust, Queen's Medical Centre, Derby Road, Nottingham NG7 2UH, UK
[5]POLARIS, Division of Clinical Medicine, School of Medicine and Population Health, Sheffield, UK

Introduction: Pulmonary MRI of hyperpolarized xenon-129 (hp^{129}Xe) dissolved in the lung parenchyma and vascular phase is gaining increasing attention for clinical assessment of gas exchange in multiple diseases. These conditions can involve thickening of barrier tissues due to fibrotic scarring or reduced capillary blood flow leading to diminished gas-blood exchange hence, the ratios between hp^{129}Xe signals arising from the lung membrane (M), the red blood cells (RBC), and the gas phase hold significant diagnostic value. However, comparing hp^{129}Xe signal ratios quantitatively across different studies poses significant challenges due to varied experimental conditions such as different field strengths, pulse sequence protocols and various, and specific the rf-coil design. Data from healthy volunteers does no not provide a good standard due to variabilities and the significant costs incurred due to the hp^{129}Xe gas contrast agent usage and associated regulatory requirements. A solution to this problem arises from materials science applications of hp^{129}Xe where xenon dissolved in materials such as polymers can display chemical shifts and hp^{129}Xe uptake dynamics that are similar to that typically found in human lungs in health and disease.

Methods: This work explores the generation of a dissolved phase ^{129}Xe MRI phantom standard that reproduces MR spectral profiles, with respect to chemical shift and signal uptake ratios. The identification of suitable phantom materials followed a two-step process. Firstly, polymer foams and oils were investigated for their dissolved phase ^{129}Xe chemical shift and uptake behaviour using a Bruker Avance III NMR spectrometer with a 9.4 Tesla vertical, clear-bore magnet (110.7 MHz ^{129}Xe frequency). A home-built hyperpolarizer was used for spin exchange optical pumping (SEOP) of a 5%:95% Xe:N2 gas mixture (26.4% ^{129}Xe natural abundance), producing a continuous flow of hp^{129}Xe with a spin polarization of P = 12 %.
In a second step, MR Images of suitable identified phantom materials were obtained with a clinical 1.5T whole body MRI scanner (GE HDX13) and a transmit/receive vest coil (Clinical MR Solutions, Wisconsin, USA) resonating at 17.66 MHz. A commercial hyperpolarizer (Polarean 9800) was used to fill Tedlar® bags with 1L concentrated hp^{129}Xe (92% isotopically enriched) with a hyperpolarization of P = 12 ±1 %. This MRI protocol is identical to the one used previously for a multi-site clinical study.

Results: At ambient temperatures, reticulated open cell polyurethane foam treated with olive oil as a fatty phase produce dissolved phase ^{129}Xe chemical shifts of 215 ppm and 196 ppm, respectively, that emulate typical RBC and TP signals (Fig 1A). During short timescales, the hp^{129}Xe uptake (Fig. 1B) into both the polymer and oil is governed by diffusion and follows a $\sqrt{t}$ dependence. The 2D EXSY NMR spectroscopy (Fig. 1C) indicates the major mode of gas exchange is from the gas phase directly into the oil and polymer phases and exchange between the two dissolved hp^{129}Xe phases is relatively small in comparison and will have little effect on the net build of both peaks.

Hp^{129}Xe MRI of dissolved phase phantom in 1.5T whole body scanner: The RBC/gas ratio difference between the various oil-free foams is much more pronounced than between the same foam with and without oil, as expected from polymer surface to gas volume ratio changed between foams and the hp^{129}Xe NMR spectroscopic data.

Power Pitch Session 2

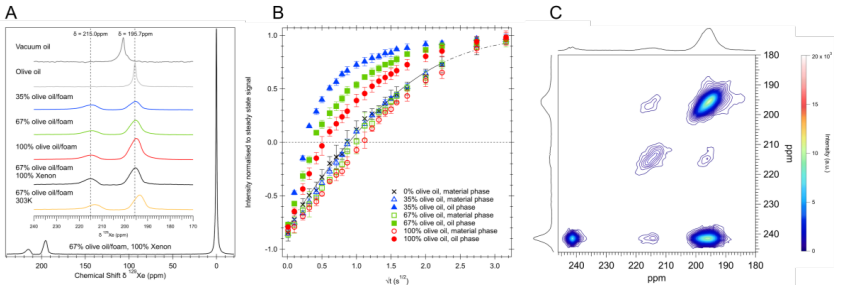

Figure 1. (A) Hp ^{129}Xe NMR spectra of oil and ZR45H-blue foams covered with oil at various mass percentages. **(B)** Hp^{129}Xe uptake in oil covered foam samples as a function of $\sqrt{\tau_{ex}}$ for various oil-foam mass percentages. Filled symbols (top three curves) show the uptake into the oil phase and open symbols (3 lowest curves) show the uptake into the polyurethane material. **(C)** Hp^{129}Xe 2D-EXSY NMR spectrum of the foam/oil system for $\tau_{ex} = 500ms$.

The highest RBC median value from the oil-free foams was measured with value of approx. 0.002 which is close to the 0.003-0.004 range observed in healthy volunteers. M/Gas ratios are as expected, strongly dependent on the quantity of oil and the median value for the 36% oil sample of ~0.00065 falls in range of what is expected for healthy volunteers. The M/RBC ratio of around 0.4 in the 36% oil sample is again very similar to that of human healthy volunteers and the 100% oil sample reflects quantitatively a M/RBC ratio reduction expected in severe fibrotic conditio

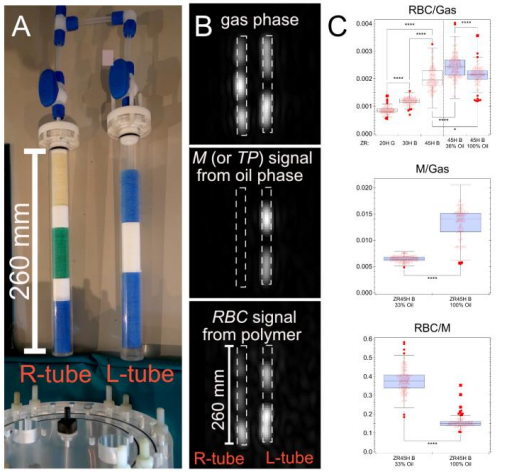

Figure 2. (A) Photograph of the hp^{129}Xe dissolved phase phantom loaded with various foams separated by white Teflon spacers. L-tube loaded with polyurethane foam containing 36% weight percent oil (bottom) and 100% oil (top) separated by spacer and free gas space at top. **(B)** The central slice of the 3D 1.5 T MRI of the three phases as indicated. **(C)** extracted boxplots of intensity ratios. RBC/M of 30% oil resembles that of healthy volunteers.

Discussion and conclusions: The current iteration of the developed phantom enables cost-effective training, easy setup, and rapid testing of experimental protocols without regulatory approval and governance. The devised system allows for gas handling protocols that match clinical protocols and reproduces signal ratios found in human lungs astonishingly well. Furthermore, the introduced concept shows a pathway for future development of a quantitative universal standard for dissolved phase pulmonary hp^{129}Xe MRI that will require materials with longer shelf lifetime as the oil-foam system and that would benefit from a more defined microstructure.

^{7}Li-MRI of the human brain following dietary supplementation with low-dose lithium

Mary A. Neal[1,2], Rebecca Strawbridge[3], Victoria C. Wing[2,4], David A. Cousins[1,2,4], Peter E. Thelwall[1,2]

[1]Translational and Clinical Research Institute, Newcastle University, Newcastle upon Tyne, UK
[2]Newcastle Magnetic Resonance Centre, Health Innovation Neighbourhood, Newcastle University, Newcastle upon Tyne, UK
[3]Department of Psychological Medicine, Institute of Psychiatry, Psychology & Neuroscience, King's College London, London, UK
[4]Cumbria, Northumberland, Tyne and Wear NHS Foundation Trust, UK

Introduction: Lithium carbonate, typically prescribed as a 400-1200 mg daily dose in adults, is the first line treatment for patients with bipolar disorder [1]. Lithium possesses acute antimanic and antidepressant properties, however its mechanism of action is incompletely defined. Recent studies suggest lithium also has neuroprotective effects [2], where trials have demonstrated that lithium ingested at both moderate [3] and low [4] doses decreased the rate of cognitive decline in Alzheimer's disease, but it is not clear how these findings relate to brain lithium concentration *in vivo*.

^{7}Li has a favourable magnetic resonance (MR) sensitivity at 29.4% that of proton (^{1}H), however, *in vivo* concentrations of ^{7}Li at prescribed therapeutic levels are many thousandths of the ^{1}H signal density in tissue, making detection by MR challenging. Nonetheless, 3D ^{7}Li-MR images of lithium distribution in the brain of patients taking therapeutic doses for treatment of bipolar disorder have recently been published [5]. In recognition of a growing research interest in the potential therapeutic utility of lithium at lower doses, we sought to determine whether this acquisition can be adapted to detect brain lithium from very low-dose lithium orotate dietary supplements.

Methods: Lithium orotate supplements (5 mg elemental lithium, ~2-7% of a typical therapeutic lithium dose) were taken daily by healthy adult male participants for up to 28 days. ^{7}Li-MR images were acquired on a clinical MRI scanner (Achieva 3T, Philips Medical Systems) interfaced to a dual-tuned ^{1}H/^{7}Li radiofrequency quadrature birdcage head coil (RAPID Biomedical) on two occasions: seven participants were scanned on days 14 and 28, one on days 0 (ie. pre-supplementation) and 14, and one on days 28 and 35 (ie. 1 week after supplementation cessation). A ^{1}H structural brain image was acquired using a 3D ^{1}H-TFE sequence with 2 mm isotropic resolution. A ^{7}Li image was then acquired using a one-dimensional balanced-steady state free precession (b-SSFP) acquisition sequence centred on the midbrain and oriented along the head-foot dimension (acquisition parameters: '2D b-FFE' with phase encoding then turned off, FOV = 600 mm, slice thickness = 37.5mm, acquisition resolution = 1x12x1 pixels, reconstructed resolution = 1x16x1 pixels, bandwidth = 500Hz/pixel, TE/TR = 1.5/10ms, flip angle = 40°, averages = 276480, duration = 46 mins 5s) (Fig. 1). Mean signal was determined from the four neighbouring highest signal datapoints. Noise measurements were made from four neighbouring voxels outside the head. Signal-to-noise ratio was measured as $(mean(signal)/SD(noise))\sqrt{2-(\pi/2)}$. The Wilcoxon signed-rank test was used to test the significance of paired SNR change between Days 14 and 28 and a two-tailed Mann-Whitney *U* Test was used to test the significance of difference between SNR measured at baseline and during supplementation. Data are presented as mean (±SD) throughout. Signal from a test object with physiologically representative ^{7}Li T_1, T_2 and coil loading [6] was used to quantify human brain lithium content.

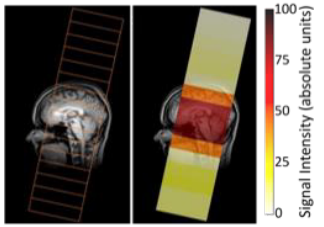

Fig. 1: Reconstructed voxel position and acquired ^{7}Li-MRI signal in one representative participant.

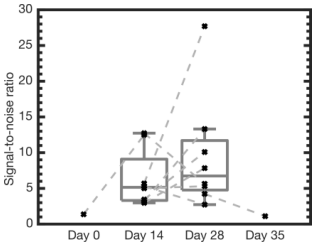

Fig. 2: SNR measured in each of the 9 participants on two MRI scan sessions.

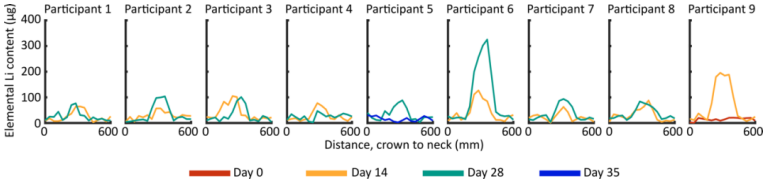

Fig. 3: Lithium content (ug) measured in each image slice on each of the two MRI scan sessions.

Results: Nine participants (9 male; mean age ± SD: 39 years ± 13 years) were recruited. No statistically significant change in SNR was measured between measurements on days 14 and 28 [$SNR_{day\ 14}$ = 5.5 (± 3.4) and $SNR_{day\ 28}$ = 10.4 (± 8.4), p=0.297] (Fig. 2). The mean *in vivo* elemental lithium content was 68 (± 48) µg per slice on Day 14, and 89 (± 70) µg on Day 28 (Fig. 3). There was absent signal before supplementation and seven days after supplementation cessation ($SNR_{day\ 0}$ = 1.4; $SNR_{day\ 35}$ = 1.1). These were significantly lower than the SNRs measured during supplementation, with complete separation between the two groups (U = 0, p = 0.013).

Discussion: The ability to directly and non-invasively quantify lithium content in its target organ holds potential utility as a research tool in a field where there is growing research interest in the therapeutic value of lower dose lithium. This study was able to detect very low brain lithium concentrations (in the range of ~10-100 uM) during lithium supplementation, with broadly constant concentrations between Days 14 and 28. Two individuals had notably higher ^{7}Li-signal intensities (~2-4×) compared to other study participants (Participants 6 and 9, Fig. 3), despite self-reporting good adherence to the dosage instructions. Future work will further explore these inter-individual differences in brain uptake, as well as the relative uptake and efficacy of different salt forms of lithium.

Conclusions: In this study we have demonstrated the ability to detect the very low brain ^{7}Li concentrations that arise from dietary supplementation with commercially available lithium orotate in healthy participants. This methodology affords the field with a novel approach to study lithium in its target organ, apposite for the study of low dose lithium administration in psychiatric and neurodegenerative disorders.

References:

1. Malhi, G.S., et al. Bipolar Disord., 2012. **14**: p. 1-21.
2. Rocha, N.K.R., et al. Front. Neurosci., 2020. **14**: p. e579984.
3. Matsunaga, S., et al. J. Alzheimers Dis., 2015. **48**(2): p. 403-410.
4. Nunes, M.A., T.A. Viel, and H.S. Buck. Curr. Alzheimer Res., 2013. **10**(1): p. 104-107.
5. Smith, F.E., et al. Mol. Psychiatr., 2018. **23**(11): p. 2184-2191.
6. Neal, M.A., et al. Journal of Affective Disorders, 2024. **360**: p. 139-145.

Power Pitch Session 2

Fitting for 7T Deuterium Metabolic Imaging (DMI)

Masha Novoselova[1], Jabrane Karkouri[1], Christopher T. Rodgers[1]
[1]Department of Clinical Neurosciences, University of Cambridge

Introduction: Deuterium metabolic imaging (DMI) is an MR technique designed to investigate human brain metabolism in vivo. Participants drink 0.75g/kg body weight of deuterated glucose (Glc) in solution. DMI enables non-invasive monitoring of Glc uptake and its subsequent metabolism. In the brain, signals are seen from semi-labelled water (HDO), glutamine/glutamate (Glx), lactate (Lac) and potentially lipids near the skull. These can be analysed quantitatively providing a radiation-free alternative/complement to ^{18}FDG-PET. This has potential applications in oncology and dementia. In a pilot study [1], we applied DMI in 6 healthy volunteers and a phantom. This abstract describes our work to develop a robust pipeline for analysis of 7T DMI data in readiness for planned clinical studies.

Methods: Data was acquired using a 7T Terra MRI (Siemens) and an 18-element ^{2}H/2-element ^{1}H dual-tuned receive array head coil (Virtumed LLC). The protocol was as follows. Baseline: Six healthy volunteers were instructed to fast for four hours prior to scanning. Baseline scans were performed to capture the natural abundance HDO signal as an internal reference before the consumption of the glucose tracer. The baseline scan included localizers, B_0 shimming, GRE structural imaging, and a 6.9mL resolution DMI scan (3D CSI, 16x16x8 matrix, 220x200x320mm^3 field of view, acquisition weighting with six averages at k=0, 250ms TR, 1ms hard pulse at Ernst angle (66°), 5kHz readout bandwidth, 4m59s scan time). Glucose Consumption: Subjects were moved out of the scanner and instructed to sit up to drink 0.75g/kg body weight (maximum 60g) of 6,6'-[$^2H_2$]-glucose dissolved in approximately 200mL of sterile water. DMI Time-Series: After consuming the glucose solution, subjects were repositioned in the scanner. B_0 shimming and structural imaging were repeated. Two DMI scans were conducted back-to-back to track any rapid deuterium uptake, followed by six additional DMI scans at 20-minute intervals.

Analysis: Spectra were processed using the OXSA Toolbox [2]. The first step involved combining the spectra using WSVD to improve the signal-to-noise ratio. Afterwards, PCA patch denoising was applied [3]. The denoised spectra were then analysed using AMARES [4], incorporating an updated prior knowledge file tailored to the deuterated species.

$$y_n = \sum_{k=1}^{K} a_k e^{j\phi_k} e^{(-d_k + j2\pi f_k)t_n} + e_n$$

AMARES is a time-domain fitting algorithm that models the measured MR signal, y_n, as a sum of exponentially damped sinusoids to fit N collected data points. Each kth sinusoid corresponds to a different metabolite peak in the spectrum once it undergoes a Fourier transform and has a specific amplitude, a_k, phase, ϕ_k, frequency, f_k, and damping factor, d_k. t_n is defined as the time from the application of the radiofrequency pulse to the collection of the last sampled data point and e_n is complex white gaussian noise.

Results & Discussion: Results shown are from a single example subject. For each voxel, a spectrum is generated (Fig1) and repeated over the time series. By extracting spectral properties such as amplitudes or phases, maps of deuterated glucose uptake and the production of downstream metabolites can be produced (Fig2). The fits, shown in red, generally agree with the data, but certain dropout regions in the amplitude maps deviate from expected trends in healthy volunteers. These regions revealed phase shifts creating visible boundaries, and a wave pattern in the baseline. Data was simulated to demonstrate how this phase shift can affect the resulting fit, as AMARES may mis-apportion one real signal into two peaks (Fig3). Unexpected lactate levels at the beginning of acquisition suggest erroneous fits, potentially due to digital filtering artefacts evidenced by an upward tail at the end of the free induction decays (FIDs). Residuals of the FIDs relative to AMARES fits showed non-random behaviour, particularly at the dataset's start. To address this, a spectrum using only the second half of the FID was plotted (Fig4), offering clearer insights. A phantom containing of D_2O, d-DMSO, and d-sodium fumarate was tested under the same conditions (Fig5). The higher signal-to-noise ratio revealed an oscillating pattern in the residuals, suggesting a long T_2 component possibly related to deuterium being a spin-1 nucleus, contributing to mis-fitting. This could also be attributed to the behaviour seen in the human data.

Conclusions: This study demonstrates the feasibility of applying the tailored time domain fitting algorithm, AMARES, to DMI data. Further understanding of the system and enhancements in the analysis pipeline are still required to minimize artefacts and leverage the advancements of using 7T MRI and optimized RF coils. Nonetheless, these have already yielded enhanced temporal and spatial resolutions. They hold significant potential for clinical and research applications, providing deeper insights into human brain metabolism and paving the way for future studies in both healthy and pathological conditions.

References

[1] Zhang M, Karkouri J, Atkinson D, Rodgers CT. Time-resolved deuterium metabolic imaging of the human brain at 7T. *Proc ISMRM* 2023. [2] Purvis LA, Clarke WT, Biasiolli L, Valkovič L, Robson MD, Rodgers CT. OXSA: an open-source magnetic resonance spectroscopy analysis toolbox in MATLAB. *PloS one*. 2017 Sep 22;12(9):e0185356. [3] M. Froeling, J. J. Prompers, D. W. J. Klomp, and T. A. van der Velden, PCA denoising and Wiener deconvolution of 31P 3D CSI data to enhance effective SNR and improve point spread function. *Magn. Reson. Med*. vol. 85. pp. 2992–3009. 2021. [4] Vanhamme, L., van den Boogaart, A., & Van Huffel, S. Improved method for accurate and efficient quantification of MRS data with use of prior knowledge. *Journal of Magnetic Resonance*, 129(1), 35-43. 1997.

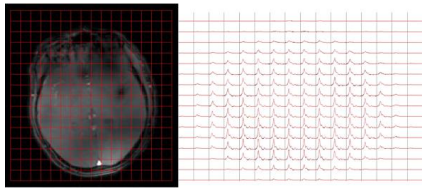

Fig1. Spectral grid map of a mid-transverse slice from a full 3D CSI dataset of a healthy brain at the final time point. The grid on the left overlays a localizer to demonstrate positioning.

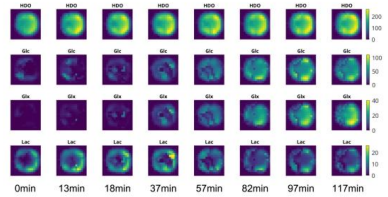

Fig2. Metabolite map over the time course of a mid-transverse slice from a full 3D CSI dataset of a healthy volunteer, showing signal dropouts predominantly in the brain's central region and in distinct patterns.

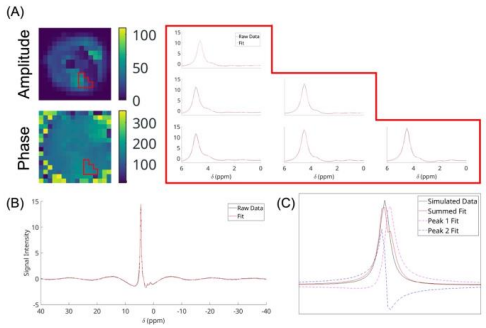

Fig3. (A) Boundary region showing signal dropout in a healthy volunteer at the 37-minute time point, depicted in both the phase and amplitude maps for the glucose peak. Voxels of interest along the boundary are outlined in red, with corresponding spectra plotted. (B) Full spectrum displayed for one of the voxels outlined in (A), revealing a discernible wave pattern in the baseline. (C) Simulated data illustrating misfit spectra resulting from phasing errors.

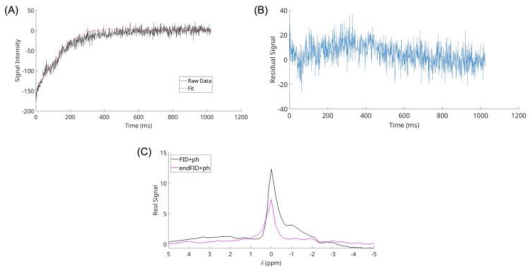

Fig4. (A) Free induction decay (FID) with AMARES model fit for an example voxel at the 37-minute time point in a healthy volunteer. (B) Residual plot showing non-random behaviour. (C) Spectrum plotted with the entire dataset in black (FID), and with only the latter half of the FID in magenta (endFID), both phase corrected.

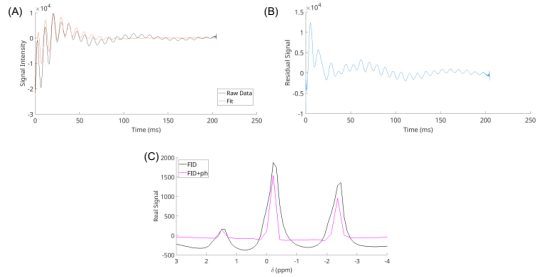

Fig5. (A) Free induction decay (FID) with AMARES model fit for an example voxel within a deuterium phantom. (B) Residual plot showing non-random behaviour. (C) Spectrum plotted with the entire dataset in black (FID), and with only the latter half of the FID in magenta (endFID), both phase corrected (+ph).

Measuring lipid turnover in human subjects using 2H magnetic resonance and heavy water loading

Daniel J. Cocking[1,2], Robin A. Damion[1,3,4], Matthew S. Brook[4,5,6], Dorothee P. Auer[1,3,4], Richard Bowtell[1,2,4]

[1]Sir Peter Mansfield Imaging Centre, University of Nottingham.
[2]School of Physics and Astronomy, University of Nottingham.
[3]Radiological Sciences, Division of Clinical Neuroscience, School of Medicine, University of Nottingham.
[4]NIHR Nottingham Biomedical Research Centre/Nottingham Clinical Research Facilities, Queen's Medical Centre.
[5]MRC-Versus Arthritis Centre for Musculoskeletal Ageing Research, University of Nottingham.
[6]School of Life Sciences, University of Nottingham.

Introduction

Heavy water (D_2O) loading over long periods has become a valuable technique for assessing fat turnover [1] and hepatic lipogenesis [2]. This involves measuring the incorporation of deuterium (^2H) from heavy water into the glycerol moiety and fatty acid chains of triglycerides during lipid formation. A typical approach requires invasive tissue sampling [1,] which restricts the range of tissue sites that can be sampled and causes patient discomfort. Here we evaluate whether ^2H MR in conjunction with D_2O loading could be used for non-invasive monitoring of lipid turnover in human subjects.

Methods

^2H signals were measured from the calf and abdomen in three healthy participants who underwent 28 days of heavy water loading. Scans were performed on a 3T scanner (Philips Achieva) equipped with ^2H surface coils (5 cm diameter for calf; 12 cm for abdomen). Measurements were made before loading, to characterise natural abundance (NA) signals, and then every ~14 days during/after loading for a further 8 sessions. Anatomical landmarks were used to position the coils over the same region for each scan (under the calf/adjacent to the right abdomen near the liver). ^1H gradient echo images were used for planning 3D-^2H-CSI measurements (parameters for calf/abdomen FOV:150x150x200/140x140x200 mm3; voxel size:15x15x20/20x20x20 mm3; BW:2000 Hz, TE:1.7 ms; Samples:64, Averages:36/48, T_{scan}:520/420 s). A TR of 50 or 70 ms was used to maximise the signal-to-noise ratio of the signal from fat whose T_1 is ~60 ms (c.f. ~200 ms for muscle water). Before loading started, subjects were scanned multiple times with inter-scan repositioning to allow

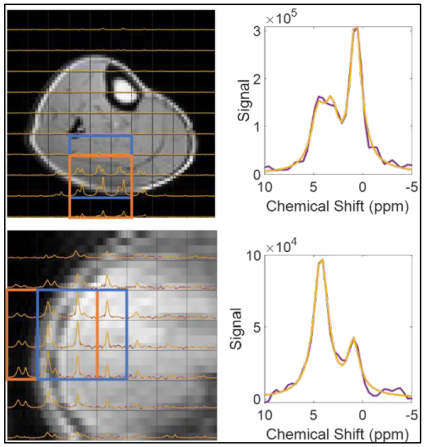

Figure 1. *3D CSI spectra plus fits in the calf and abdomen, overlaid on ^1H GE images. Data was acquired from Subject 1 at NA before loading (t=0 days); ROI for signal averaging for water (blue) and fat (orange), are shown.*

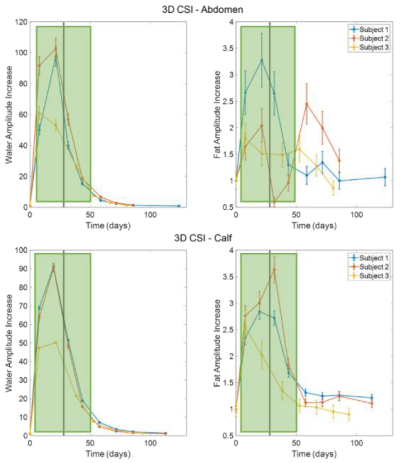

Figure 2. *The temporal variation of the averaged water/fat amplitudes (left/right) in the abdomen/calf (top/bottom). The black line indicates the end of the 28-day loading period. The green box indicates data acquired at t < 50 days. Error bars derived from the relative error measured from repeated experiments at NA.*

	Average Fat Enhancement from Natural Abundance Signal after 50 days of D_2O loading	
	Calf	Abdomen
Subject 1	1.26 ± 0.02 (P<0.01)*	1.13 ± 0.08 (P=0.09)
Subject 2	1.15 ± 0.03 (P=0.03)*	1.94 ± 0.31 (P=0.05)*
Subject 3	0.99 ± 0.04 (P=0.61)	1.25 ± 0.21 (P=0.18)

Table 1 . *Average and standard errors of the fat signal enhancement relative to NA. P-values for single-sided t-test for difference from NA are also reported.*

estimation of fractional signal variation due to positioning errors. OXSA-AMARES [3] was used to fit each voxel to a model incorporating water and fat peaks; in the calf, the water signal was modelled as a doublet (due to quadrupolar splitting) [4]. To produce single measures of signal enhancement with reduced sensitivity to FOV-positioning, we averaged fat and water signal amplitudes over regions-of-interest (ROI=3x3x3/3x5x3 voxels for the calf/abdomen) sited relative to the voxel with maximum water signal (i.e., over the centre of the surface coil). Examples of this are shown in Figure 1.

Results

A fat peak is seen in superficial voxels spanning subcutaneous fat close to the surface coil in the NA images in Figure 1, along with a water peak which appears over a wider spatial extent and is broadened by quadrupolar splitting in calf muscle. A robust fit to the fat signal could only be achieved at times >50 days, when the water signal had fallen to <10xNA. Figure 2 shows the temporal variation of the ROI-averaged fat and water signals. Although the fat signal shows significant early enhancement (t < 50 days) this tracks the water enhancement and is likely due to poor spectral fitting. The average fat signal enhancement at times > 50 days where fitting was robust is reported in Table 1.

Discussion

Fat signal was increased relative to NA in 5 of the 6 measurements and the increase reached statistical significance (P<0.05) in three measurements (Figure 3). These results provide encouraging evidence that ^2H MR can be used to detect the increased deuteration of subcutaneous fat resulting from lipid turn-over during long-term heavy water loading. The main experimental challenges were in quantifying ^2H signals from fat in the presence of large water signals and in reproducibly positioning the surface RF coils in repeated experiments. In future work higher field could be used to provide better spectral separation of fat and water signals and 3D-printed, individualised coil holders would allow more reproducible coil positioning.

References

1. Strawford, A., et al. Adipose tissue triglyceride turnover, de novo lipogenesis, and cell proliferation in humans measured with (H2O)-H-2. American Journal of Physiology-Endocrinology and Metabolism, 2004. 286(4): p. E577-E588.
2. Belew, G.D. and J.G. Jones, De novo lipogenesis in non-alcoholic fatty liver disease: Quantification with stable isotope tracers. European Journal of Clinical Investigation. 2022. 52(3):e13733.
3. Purvis, L. A. B., et al. OXSA: An open-source magnetic resonance spectroscopy analysis toolbox in MATLAB. PLOS ONE, 2017. 12(9), e0185356.
4. Gursan, A.,et al. Residual quadrupolar couplings observed in 7 Tesla deuterium MR spectra of skeletal muscle. Magnetic Resonance in Medicine, 2022. 87(3), 1165–1173. https://doi.org/10.1002/mrm.29053

Mapping the amplitude and phase of dissolved ^{129}Xe red blood cell signal oscillations with keyhole spectroscopic lung imaging

Jemima H Pilgrim-Morris[1], Guilhem J Collier[1,2], Mika Takigawa[1], Scarlett Strickland[3,4], Roger Thompson[1,4], Graham Norquay[1], Neil J Stewart[1,2], Jim M Wild[1,2]

[1]POLARIS, Section of Medical Imaging and Technologies, Division of Clinical Medicine, School of Medicine and Population Health, University of Sheffield, Sheffield, United Kingdom
[2]Insigneo Institute, University of Sheffield, Sheffield, United Kingdom
[3]Biomedical Research Centre, University of Sheffield, Sheffield, United Kingdom
[4]Sheffield Teaching Hospitals, Sheffield, United Kingdom

Introduction: The signal from hyperpolarised ^{129}Xe dissolved in the red blood cells (RBCs) is modulated by changes in the capillary blood volume over the cardiac cycle [1, 2]. These "oscillations" are sensitive to cardiopulmonary disease [3] and can be mapped regionally using a post-acquisition keyhole reconstruction [4, 5]. In this work, we employ a sliding window (SW) approach to reconstruct additional keyhole projections and estimate and correct for regional oscillation phase (ϕ). We apply this method to a small group of patients with chronic thromboembolic pulmonary hypertension (CTEPH), a disease with blood flow limitation due to vascular occlusion following pulmonary embolism.

Methods: RBC oscillation mapping was performed retrospectively in a cohort of 28 healthy volunteers and four CTEPH patients. ^{129}Xe gas transfer was measured with a 3D radial spectroscopic imaging sequence [6] on a 1.5T GE scanner using a ^{129}Xe transmit-receive vest coil and a 0.8–1L dose of hyperpolarised ^{129}Xe [7]. Eight healthy subjects underwent three additional scans to assess inter- and intra-exam repeatability. The whole-lung RBC oscillation amplitude (α_{k0}) was found from the mean peak-to-peak amplitude of the decay-corrected, filtered RBC signal from the centre of k-space over the first ~7s of the acquisition. Two keyhole [8] methods were used to perform oscillation mapping:

1. Two-Key [4]: the k_0 data were binned according to RBC signal amplitude (**Fig. 1A**) and images were reconstructed from the radial spokes in "low" and "high" bins (**Fig. 1B**). The oscillation amplitude ($\alpha_{2\text{-Key}}$) was found from the difference between the resulting "low" and "high" keyhole images, normalised by their mean.

2. SW: multiple keyhole reconstructions were performed, with the key projections stepped forward by one projection per reconstruction (**Fig. 1C**). The oscillation amplitude (α_{SW}) was calculated from the pixelwise difference between the minimum (S_{min}) and maximum (S_{max}) signal across the N keyhole images, normalised by the mean value. ϕ was estimated by converting the keyhole indices of S_{max} to phase relative to the whole-lung k_0 oscillation.

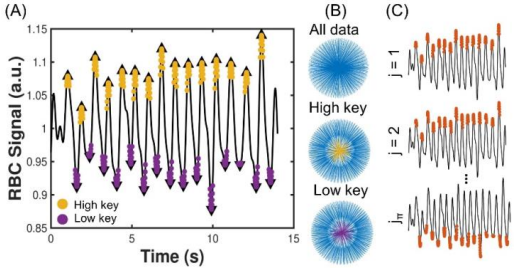

Fig. 1: (A) Radial projections chosen for the high and low keyholes. (B) 3D radial k-space: in keyhole reconstruction, the high-frequency data (blue) are included from all radial projections, but the low frequency data are only included for projections that have been selected for the key (yellow or purple). (C) The projections selected by the SW for the 1st, 2nd and ϕ = π keyhole reconstructions.

Results: Subject demographics and oscillation mapping results are shown in **Table 1**. RBC maps were successfully reconstructed for each phase of the SW, revealing regional variation in both oscillation phase and amplitude (**Fig. 2**). The $\alpha_{2\text{-Key}}$ maps exhibited areas of physiologically unrealistic negative amplitudes, which qualitatively correlated with regions of increased ϕ and became positive in the α_{SW} maps. The oscillation amplitude and phase maps were more heterogeneous (i.e. showed increased coefficient of variation, CV) for the CTEPH patients. α_{SW} was repeatable and had a lower 3-scan CV (0.07 ± 0.04) than α_{k0} (0.11 ± 0.04) or $\alpha_{2\text{-Key}}$ (0.16 ± 0.05).

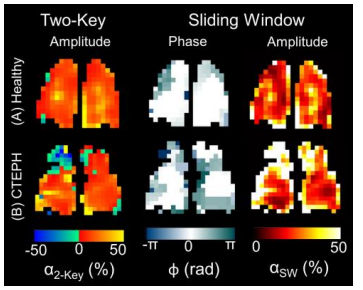

Figure 2: $\alpha_{2\text{-Key}}$, ϕ and α_{SW} maps for (A), a healthy participant and (B), a participant with CTEPH.

Discussion: Whereas previous work [4, 5] assumed a uniform ^{129}Xe RBC oscillation phase, here we implemented a SW to perform many keyhole reconstructions over one cardiac cycle to both adjust for, and estimate, oscillation phase. Regional phase differences may be caused by effects of the cardiac pulse wave, such as variations in blood flow velocity with vessel stiffness/compliance. Although mean α_{k0} for the CTEPH group was similar to that of the healthy group, the oscillation and phase maps revealed significant heterogeneity. This may imply a haemodynamic response to impedance to flow from vascular thrombi and/or microvascular damage. A limitation of our method is the requirement for high SNR RBC images and clear signal oscillations, which could limit its application in diseases with low RBC transfer.

Conclusions: Sliding window keyhole reconstruction of radial dissolved ^{129}Xe imaging reveals regional phase differences in the RBC oscillations which are not captured when performing Two-Key keyhole reconstruction. This regional phase information may reflect the hemodynamic effect of the cardiac pulse wave in the pulmonary microvasculature and shows potential sensitivity to disease.

Acknowledgements: Dr Laura Saunders, Discovery Medicine North (DiMeN) Doctoral Training Partnership and the MRC.

*Table 1: Subject demographics and α mapping results. Differences between the groups were assessed with Wilcoxon rank sum tests. * indicates a significant (<0.05) p-value.*

	Healthy	CTEPH	*p*-value
n (female)	28 (12)	4 (0)	-
Age (years)	38.8 ± 11.1	63.0 ± 7.3	0.0036*
α_{k0} (%)	15 (10-27)	15 ± 5	0.8047
$\alpha_{2-\text{Key}}$ (%)	14 ± 3	10 ± 3	0.0286*
α_{SW} (%)	29 ± 3	33 ± 4	0.0541
ϕ (rad)	0.27 ± 0.19	0.24 ± 0.13	0.8416
$CV_{2\text{-Key}}$	1.4 ± 0.3	2.9 ± 0.9	0.0001*
CV_{SW}	0.66 ± 0.06	0.76 ± 0.01	0.0039*
CV_{ϕ}	0.85 ± 0.05	0.92 ±0.03	0.0134*

References

[1] Venkatesh AK, Hong KS, Kubatina L, et al. Direct Observation of the Transport of ^{129}Xe from the Lung-Gas to the Tissue and the Blood. *in Proc. Intl. Soc. Mag. Reson. Med.,* 2001.
[2] Norquay G, Leung G, Stewart NJ, Wolber J, and Wild JM, ^{129}Xe chemical shift in human blood and pulmonary blood oxygenation measurement in humans using hyperpolarized ^{129}Xe NMR. *Magn. Reson. Med.*, 2017. **77**(4): p. 1399-1408.
[3] Wang ZY, Bier EA, Swaminathan A, et al., Diverse cardiopulmonary diseases are associated with distinct xenon magnetic resonance imaging signatures. *Eur. Resp. J.*, 2019. **54**(6).
[4] Niedbalski PJ, Bier EA, Wang Z, et al., Mapping cardiopulmonary dynamics within the microvasculature of the lungs using dissolved ^{129}Xe MRI. *J. Appl. Physiol.*, 2020. **129**(2): p. 218-229.
[5] Lu J, Alenezi F, Bier E, et al., Optimized quantitative mapping of cardiopulmonary oscillations using hyperpolarized 129Xe gas exchange MRI: Digital phantoms and clinical evaluation in CTEPH. *Magn. Reson. Med*, 2024. **91**(4): p. 1541-1555.
[6] Collier GJ, Eaden JA, Hughes PJC, et al., Dissolved Xe-129 lung MRI with four-echo 3D radial spectroscopic imaging: Quantification of regional gas transfer in idiopathic pulmonary fibrosis. *Magn. Reson. Med*, 2021. **85**(5): p. 2622-2633.
[7] Norquay G, Collier GJ, Rao M, Stewart NJ, and Wild JM, 129Xe-Rb Spin-Exchange Optical Pumping with High Photon Efficiency. *Phys. Rev. Lett.*, 2018. **121**(15): p. 153201.
[8] Lethmate R, Wajer FTAW, Crémillieux Y, van Ormondt D, and Graveron-Demilly D, Dynamic MR-Imaging with Radial Scanning, a Post-Acquisition Keyhole Approach. EURASIP Journal on Advances in Signal Processing, 2003. **2003**(5): p. 794878.

Using NORDIC with ^{23}Na MRI to study dynamic changes in tissue sodium concentration

Ben Prestwich[1], Rosemary Nicholas[1], Daniel Marsh[1] and Susan T Francis[1]
[1]Sir Peter Mansfield Imaging Centre, University of Nottingham, Nottingham, United Kingdom

Introduction

Sodium (^{23}Na) MRI has intrinsically low signal-to-noise-ratio (SNR) due to the low ^{23}Na ion concentration *in vivo* (15–30 mol/L muscle), short relaxation times, and the gyromagnetic ratio being ~ 4 x lower than for ^{1}H [1]. This results in the need for long scan times (~10–20 min) and large voxel sizes (e.g. 4 mm isotropic) compared to ^{1}H-MRI and means that any study of dynamic changes in ^{23}Na *in-vivo* is challenging. Recently, the NOise Reduction with DIstribution Corrected (NORDIC) PCA denoising method using local low rank principal component analysis was published and shown to provide impressive improvements in image SNR for neuroimaging data, e.g. for high spatial resolution Diffusion Tensor Imaging (DTI) [2] and temporal SNR for functional MRI [3] data. NORDIC enables higher spatial and temporal resolution data, particularly benefitting data in the thermal noise dominated regime. Here, we assess NORDIC denoising for non-proton ^{23}Na MRI data, with the goal of applying this to study dynamic ^{23}Na changes *in-vivo*, as an example the change in sodium in the muscle on exercise.

Methods

Phantom data has been collected for validation of measuring dynamic ^{23}Na changes, as well as the *in-vivo* in response to exercise:

Data Acquisition: All MRI data was collected on a 3T Philips Ingenia scanner, using a ^{23}Na birdcage leg coil (PulseTeq Ltd) to acquire ^{23}Na MRI scans, and the Q-body coil to collect ^{1}H measures. ^{23}Na MRI data were acquired using a 3D GRE short TR sequence (3x3x30mm^3, 10 slices, TE/TR=1.26/13ms, FA=46°) for a high sampling rate (4.4s per acquisition) For each scan a final noise image was collected with no RF and no gradients. For all acquisitions the 'SNR Maxima' and 'SNR clip factor' were set to 100 and 0.01 respectively to improve the data's dynamic range, both magnitude and phase data were saved.

Phantom validation: To assess the accuracy of quantifying the change in ^{23}Na concentration dynamically, data was collected of a 120 mm diameter cylindrical phantom, this was filled with an initial concentration of 20mmol/L. A 50ml 400mmol/L NaCl solution was added at a rate of 250ml/hr to the phantom using an MR compatible infusion pump. This increased the sodium concentration in the phantom to 30mmol/L in 12-minutes with a stirrer mounted in the phantom ensuring mixing of the sodium solution through the infusion period (Figure 1). During the infusion ^{23}Na MRI was continuous acquired. An second phantom experiment was performed, for this, the phantom consisted of a small bottle situated inside a larger container, and the ^{23}Na signal of the small bottle was changed dynamically by changing the shielding while ^{23}Na MRI was continuous acquired.

In-vivo data collection: ^{23}Na MRI of the calf muscle was collected in 5 volunteers whilst they performed plantar flexion using an MRI-compatible ergometer (Trispect, Ergospect, Innsbruck Austria), Figure 4. First ^{1}H mDIXON scans were acquired to image the calf. A 43-minute protocol was then performed during which baseline data was collected for 13 minutes, following by repeated plantar flexion exercise at 50% of maximum voluntary contraction for 3.5-minutes, followed by 30-minutes recovery.

Data analysis: Data analysis was carried out in MATLAB. NORDIC was performed on the MRI data. Linear regression of the reference bottles (10, 20, 30, 40 mmol/L) to convert voxel intensity to ^{23}Na concentration, mmol/L was performed and applied to the phantom/calf (correction performed both using an average image and dynamically). An ROI was placed in the phantom and in the gastrocnemius muscle in the calf and the mean and variance in each region was measured.

Results

Figure 2 shows the timecourse of the mean signal and spatial variance within the phantom during the infusion. Figure 3 shows the timecourse of the mean sodium concentration measured in the phantom during infusion when performing dynamic-by-dynamic sodium concentration calibration using the reference bottles. Note, the large variance for raw data, whilst applying NORDIC provides high R^2 and low root-mean-square-error, particularly using a running average (over 44s). Figure 4 shows the time course of the ^{23}Na signal in the small bottle. Figure 5 shows *in-vivo* raw and NORDIC corrected ^{23}Na MRI calf data collected before, during and after exercise. The time course over the gastrocnemius, during exercise (0:88- 5:52mins) and recovery (24:56-30:28 mins) and the high temporal resolution timecourse of the NORDIC data to study dynamically the sodium change in the muscle.

Discussion

This work demonstrates the NORDIC denoising gains for ^{23}Na MRI which is in the low SNR regime dominated by thermal noise. We validate on a phantom that it is possible to dynamically quantify sodium concentration by applying NORDIC denoising, and that this can be used to study *in vivo* the spatial and temporal changes in muscle sodium on exercise.

Conclusion

NORDIC can be used to correct low SNR ^{23}Na MRI data to study spatially localised sodium changes in muscle dynamically. This methodology could in future also be applied to ^{23}Na functional MRI brain studies.

References

1. Madelin, G., Lee, J. S., Regatte, R. R., & Jerschow, A. (2014). Sodium MRI: Methods and applications. In Progress in Nuclear Magnetic Resonance Spectroscopy (Vol. 79, pp. 14–47). Pergamon.
2. Moeller, S., Pisharady, P. K., Ramanna, S., Lenglet, C., Wu, X., Dowdle, L., Yacoub, E., Uğurbil, K., & Akçakaya, M. (2021). NOise reduction with DIstribution Corrected (NORDIC) PCA in dMRI with complex-valued parameter-free locally low-rank processing. NeuroImage, 226, 117539.
3. Vizioli, L., Moeller, S., Dowdle, L., Akçakaya, M., De Martino, F., Yacoub, E., & Uğurbil, K. (2021). Lowering the thermal noise barrier in functional brain mapping with magnetic resonance imaging. Nature Communications, 12(1), 5181.

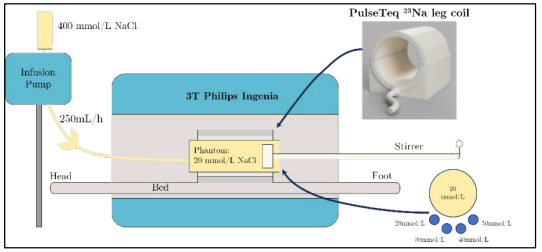

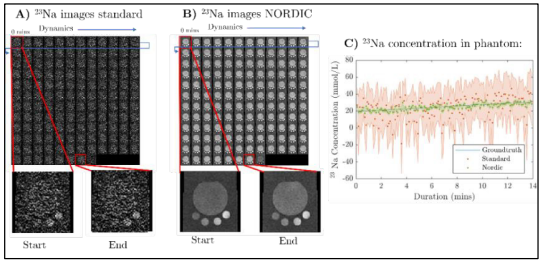

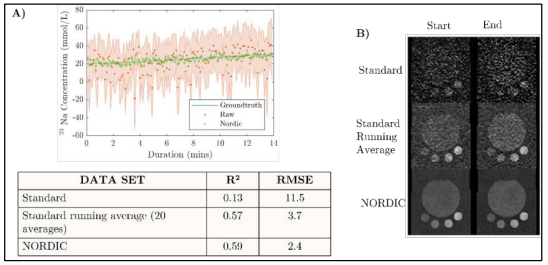

DATA SET	R^2	RMSE
Standard	0.13	11.5
Standard running average (20 averages)	0.57	3.7
NORDIC	0.59	2.4

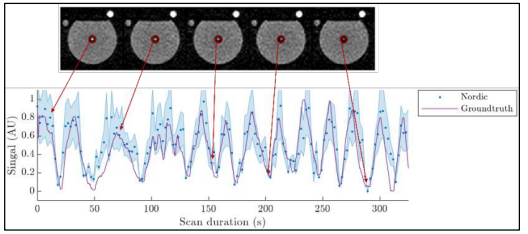

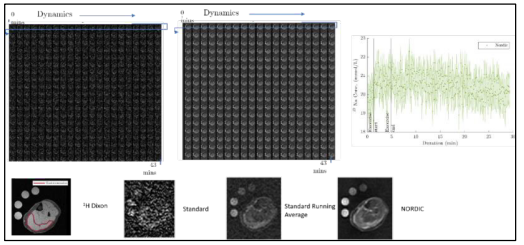

Figures

Figure 1: Experimental set-up to achieve a controlled change in sodium concentration in the phantom over a 14-minute duration by infusing 400 mmol/L saline solution into the phantom and stirring throughout to achieve a homogenous solution.

Figure 2: Images time series of the mean sodium concentration and spatial variance from within the phantom during infusion of sodium as the ^{23}Na concentration increases from 20 mmol/L to 30 mmol/L over 14 mins. ^{23}Na images collected every 4.4s shown for A) raw data before NORDIC and B) after NORDIC. Also shown are enlarged images at the start (nominal 20 mmol/L) and end (nominal 30 mmol/L) of infusion. C) Timeseries of the signal from the phantom and variance within the phantom for raw data and data after NORDIC correction using average bottle calibration.

Figure 3: A) Timecourse of the mean ^{23}Na concentration measured in the phantom during the infusion. This is the computed dynamic-by-dynamic 23Na concentration calibration using the reference bottles and applied to the phantom. Note, the raw data has large variance, which is reduced with applying a moving average. Using NORDIC dynamic-by-dynamic bottle calibration is possible with, the lowest variance for the moving average with NORDIC. See Table for R^2 and RMSE metrics. B) Example images at start and end of the infusion.

Figure 4: Timecourse of ^{23}Na signal in small bottle located at the centre of a large in a large phantom. The measured ^{23}Na signal is compared to the ground truth. The signal in the large compartment and reference tubes positioned above remained constant.

Figure 5: A) In-vivo raw running average timeseries of change in sodium in the gastrocnemius muscle in response to exercise. B) ^{1}H mDIXON image showing gastrocnemius ROI and 23Na images binned over exercise (0:88-5:52mins) and recovery (24:56-30:28mins) periods. C) NORDIC corrected high temporal resolution timeseries showing the change in peak sodium on exercise. B) Timeseries of raw ^{23}MRI calf images collected data before and C) after NORDIC.

Reliability and repeatability of total creatine measurements in multiple human brain regions using ^{1}H-MR spectroscopy

Jedd Pratt[1], James McStravick[1], Aneurin Kennerley[1], Craig Sale[1]

[1]Department of Sport and Exercise Sciences, Manchester Metropolitan University Institute of Sport, Manchester, United Kingdom

Introduction: Creatine (Cr) serves an important role in supporting brain energetics, particularly in metabolically demanding scenarios, such as sleep deprivation, mild traumatic brain injury, neurological disease, and ageing [1]. Although existing literature is scarce, emerging data suggest that increasing brain creatine concentrations may improve cognitive function during these periods [2]. As brain Cr dynamics gain further interest, proton magnetic resonance spectroscopy (^{1}H-MRS) will become increasingly used to quantify total creatine (tCr) concentrations. More consideration should be given, however, to the inherent sources of error in ^{1}H-MRS, and their effect on the reliability of repeated measurements, prior to experimental investigation. This need is driven by large margins of error (up to 20%) in repeated ^{1}H-MRS measurements of tCr reported to date [3-5]. Accordingly, we assessed the intra- and inter-session reliability and repeatability of ^{1}H-MRS for determining tCr concentrations in multiple brain regions (midbrain: MB; visual cortex: VC; frontal cortex FC).

Methods: Eighteen healthy adults aged between 20 and 32 years (mean age = 25 ± 3years; 50% female) were recruited [n=14 intra-session protocol; n=15 inter-session protocol (11 participants completed both)]. MR imaging and ^{1}H-MRS (utilising PRESS) were conducted on a Siemens MAGNETOM Vida at 3 Tesla (T) with a 20-channel head coil. For intra-session analyses, repeated measurements of the MB, VC and FC were taken without removing the participant from the scanner. For inter-session analyses, repeated measurements were taken from the same regions, but with a brief break between measurements where the participant was removed / repositioned on the scanner, new localisers and structural scans were taken, and voxels were repositioned. ^{1}H-MRS data were analysed using TARQUIN, using water unsuppressed data to quantify absolute tCr concentrations. Voxel fractions of cerebrospinal fluid (CSF), grey matter (GM) and white matter (WM) were calculated using segmentation. Statistical analyses included paired t-tests, minimum detectable change (MDC), Pearson's correlation coefficient (r), coefficient of variation (CV) and intra-class correlation coefficient (ICC). Bland-Altman plots allowed for a visual assessment of the data.

Results: 174 spectra were acquired, including 84 from intra-session analyses and 90 from inter-session analyses (example voxel positioning, spectra, residuals and model fit presented in Figure 1). Voxel fractions of CSF, GM and WM did not correlate with differences in repeated measures of tCr concentration, thus no corrections were performed. No significant differences were observed in tCr concentration between repeated intra- or inter-session measurements in any brain region (mean differences=0.1-1.2%). Depending on region, intra-session r values ranged between 0.909-0.985 (all $p<0.001$), and inter-session r values ranged between 0.836-0.858 (all $p<0.001$). No trends in measurement bias were shown for any region. For the MB, VC and FC, intra-session CVs were 1.7%, 0.8% and 2.1%, ICCs were 0.903 (95%CI=0.727-0.968), 0.979 (95%CI=0.935-0.993) and 0.921 (95%CI=0.772-0.974) (all $p<0.001$), and MDCs were 1.2%, 0.6% and 1.5%, while inter-session CVs were 2.7%, 1.7% and 2.7%, ICCs were 0.835 (95%CI=0.578-0.941), 0.854 (95%CI=0.619-0.948) and 0.847 (95%CI=0.603–0.946) (all $p<0.001$), and MDCs were 1.9%, 1.2% and 1.9%. Inter-regional differences of up to ~21% in tCr concentration were shown.

Conclusions: Absolute tCr concentrations can be reliably and repeatably determined using ^{1}H-MRS at 3T, when inherent sources of error are suitably managed. Differences in tCr concentration larger than 2% may be discernible from inherent ^{1}H-MRS measurement error, although this margin should be established in a centre-specific manner. Future studies are required to establish whether similar findings are observed when other analyses packages are used, and when other populations of interest (*e.g.,* people suffering from neurological disease or movement disorder) are examined.

References

[1] DG Candow, SC Forbes, SM Ostojic, et al. "Heads Up" for Creatine Supplementation and its Potential Applications for Brain Health and Function. *Sports Med*. 2023. **53**, 49-65.
[2] A Gordji-Nejad, A Matusch, S Kleedörfer, et al. Single dose creatine improves cognitive performance and induces changes in cerebral high energy phosphates during sleep deprivation. *Sci Rep*. 2024. **28**, 4937.
[3] I Marshall, J Wardlaw, J Cannon, et al. Reproducibility of metabolite peak areas in 1H MRS of brain. *Magn Reson Imaging*. 1996. **14**, 281-92.
[4] M Terpstra, I Cheong, T Lyu, et al. Test-retest reproducibility of neurochemical profiles with short-echo, single-voxel MR spectroscopy at 3T and 7T. *Magn Reson Med*. 2016. **76**, 1083-91.
[5] BS Li, H Wang, O Gonen. Metabolite ratios to assumed stable creatine level may confound the quantification of proton brain MR spectroscopy. *Magn Reson Imaging*. 2003. **21**, 923-8.

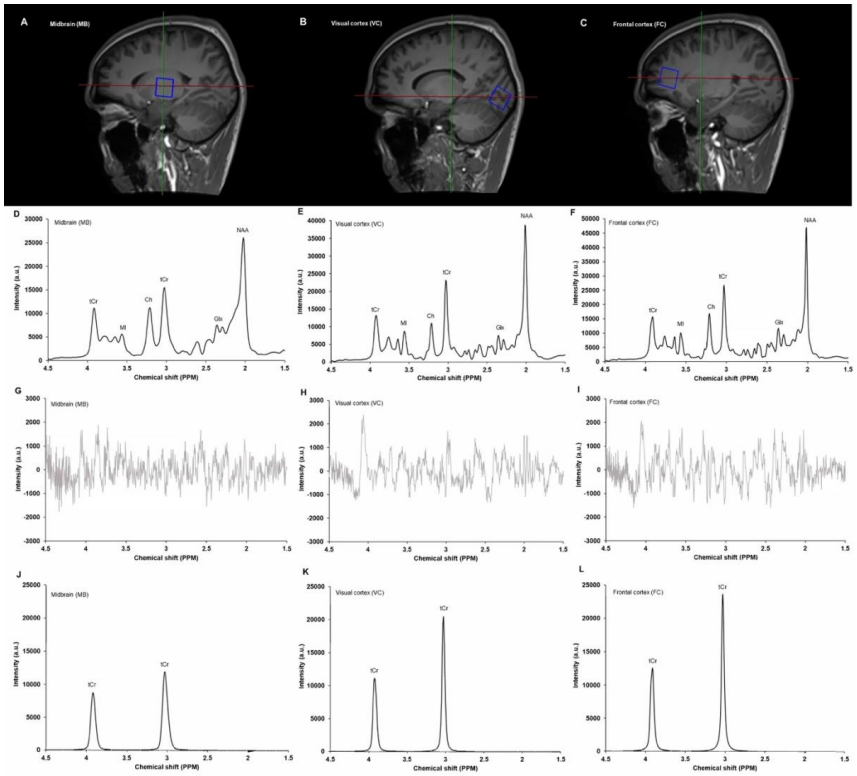

Fig 1. Example voxel positioning (A-C), spectra (D-F), residuals (G-I) and TARQUIN model fits for total creatine (J-L), in the midbrain (A, D, G, J), visual cortex (B, E, H, K) and frontal cortex (C, F, I, L). Metabolites shown include tCr = total creatine; MI = *myo*-inositol; Ch = choline; Glx = glutamate-glutamine complex; NAA = N-acetylaspartate

Evaluating the potential of PARAshift contrast agents to image biomarkers for acquired brain injury (ABI)

Sakaorna Jeyanathan[1], Peter Harvey[1], Melissa Trotman-Lucas[1], Valentina Di Pietro[2], Claire Gibson[1]
[1]University of Nottingham, School of Psychology, Nottingham, NG7 2RD
[2]University of Birmingham, Institute of Inflammation and Ageing, Mindelsohn Way, Edgbaston, Birmingham, B15 2TT

Introduction

Acquired brain injury (ABI), an umbrella term that encompasses stroke and traumatic brain injury (TBI) (1), can result in significant fatalities and disabilities. There is a need to increase our understanding of the pathophysiology of ABI, to aid more accurate and timely diagnosis. ABI initiates a pathophysiological cascade involving, but not limited to, excitotoxicity, axon degeneration and apoptotic cell death, resulting in cerebral acidosis. This, in turn, induces changes in temperature and pH (2,3), two physiological outputs which are potential biomarkers for ABI. This project will develop targeted PARAshift magnetic resonance imaging (MRI) contrast agents to image changes in pH and temperature during ABI. PARAshift agents incorporate paramagnetic metal ions that produce rapidly relaxing, highly shifted resonances that can directly be imaged (4). PARAshift contrast agents are intrinsically temperature sensitive, and we aim to modify the compound(s) to provide pH sensitivity. This approach will allow us to multichannel image temperature, pH, and anatomy, providing detailed visualisation of pathology.

Methods

Two pH-sensitive PARAshift compounds were designed and synthesised with varying lanthanides to determine which lanthanide provided optimal resonance frequency (figure 1). Here, a reporting tert-butyl resonance and an amide group were integrated to provide pH sensitivity. This was attached to the cyclen based macrocycle structure 1,4,7,10-tetraazacyclododecane-1,4,7-triacetic acid (DO3A). The varying lanthanide (III) ions were later complexed within the compound. A paramagnetic proton nuclear magnetic resonance spectroscopy (^{1}H NMR) was first conducted at pH 7 and temperature of 298 Kelvin (K). The compounds were later immersed in D_20 at varying pH's within a biologically relevant range (pH 5-8), and paramagnetic^{1}H NMRs were collected. Temperature paramagnetic ^{1}H NMRs were taken of compound B complexed with terbium (III), where the compound was immersed in D_20 and subjected to temperatures from 303K-315K. All ^{1}H NMRs were conducted using the Bruker NMR Spectrometer DRX- 500 MHz (11.7 T). The resonance was expected to shift to a region of the 1H NMR paramagnetic spectral window away from the standard region observed from 0–12 ppm.

Results

Compound A did not show a shift away for the standard region but there was a chemical shift in the desired region when compound B was complexed with terbium (III) and dysprosium (III) (figure 2). The compound presented in B complexed with terbium (III), exhibited a shift of -6 ppm (figure 2a) and when complexed with dysprosium (III), a shift of -20 ppm was observed (figure 2b). The terbium complex has also shown to shift in resonance when varying the temperature of the compound, exhibiting a shift of 0.13 ppm/K. However, a significant shift was not observed when altering the pH of the compound.

1

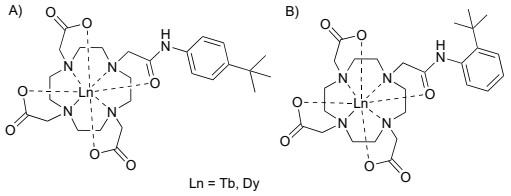

Figure 1 Compounds synthesised (A) and (B), each compound was complexed with terbium (III) (Tb) and dysprosium (III) (Dy)

2

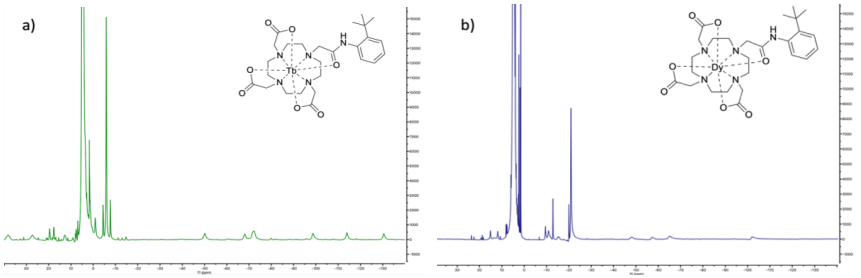

Figure 2 Paramagnetic ^{1}H NMRs of compound B complexed with terbium (III) (a) and dysprosium (III) (b). The compound was immersed in the solvent D_20. Both spectra were collated at pH 7 and 298K using the Bruker NMR Spectrometer DRX-500 MHz (11.7 T.)

Discussion

Compound B complexed with terbium (III) and dysprosium (III) at the metal centre are characteristic of a PARAshift contrast agent, with dysprosium (III) exhibiting a larger shift than terbium (III). The terbium (III) complex has also shown a distinct change in shift when varying the temperature. Both compounds may be utilised to provide independent and specific signals, in addition to the standard water signals observed in MRI. Although the shift is adequate, modifying the compound may promote a larger shift by, for example, reducing the distance between the proton reporter group and the metal centre. However, the compound does not show promise to alter in pH within the expected biological range (6-7.5). This highlights the need to modify the compound with an alternative pH moiety and/or adapt the molecular design to adjust the amide pK_a value. Complexation with other lanthanide (III) ions are ongoing and may provide improved properties.

Conclusion

Overall, we aim to optimise the aforementioned PARAshift agents to detect changes in pH/temperature. Once successful, we will test these compounds biologically using in-vitro/in-vivo models of ABI and pre-clinical MRI. This will allow us to track changes in progression of pathology and evaluate effectiveness of candidate therapeutic interventions.

Acknowledgements

Dr. Charlotte Gidman, Dr. Olivia Churchill, Xiwen Ma
Funding received from Medical Research Council (MRC).

References

1. Gilmore N, Katz DI, Kiran S. Acquired Brain Injury in Adults: A Review of Pathophysiology, Recovery, and Rehabilitation. Perspect ASHA Spec Interest Groups. 2021 Aug 20;6(4):714–27.
2. Tóth OM, Menyhárt Á, Frank R, Hantosi D, Farkas E, Bari F. Tissue acidosis associated with ischemic stroke to guide neuroprotective drug delivery. Vol. 9, Biology. MDPI AG; 2020. p. 1–15.
3. Clausen T, Khaldi A, Zauner A, Reinert M, Doppenberg E, Menzel M, et al. Cerebral acid–base homeostasis after severe traumatic brain injury. 2005.
4. Harvey P, Blamire AM, Wilson JI, Finney KLNA, Funk AM, Senanayake PK, et al. Moving the goal posts: Enhancing the sensitivity of PARASHIFT proton magnetic resonance imaging and spectroscopy. Chem Sci. 2013 Sep 30;4(11):4251–8.

Power Pitch Session 2

Preliminary Phase-Based EPT in Parkinson's Disease: Effects of Open-Ended Fringe Lines

Oriana V. Arsenov[1], Jierong Luo[1], George E.C. Thomas[2], Rimona S. Weil[2], Karin Shmueli[1]
[1]Medical Physics and Biomedical Engineering, University College London, London, UK
[2]Dementia Research Centre, Institute of Neurology, University College London, London, UK

Introduction: Parkinson's disease (PD) is one of the most prevalent progressive neurodegenerative disorder and is characterized by the aggregation of α-synuclein into structures called Lewy bodies [1]. Lewy bodies are mainly found in the substantia nigra (SN) pars compacta but can be present in other brain regions. Elevated levels of metal ions, particularly Ca^{2+}, are found in these structures [1,2], due to disruptions of calcium homeostasis. Changes in concentration of free iron ions, Fe^{2+}, released from ferritin, are also expected in SN [3].

MRI electrical properties tomography (MR-EPT) reconstructs the tissue electrical conductivity which, at high frequencies, is related to the tissue ion content. Hence, it could provide clinically useful information for PD. In this study, we used a multiple-echo 2D gradient-echo echo-planar imaging (ME-GRE-EPI) acquisition to investigate conductivity values in patients with Parkinsons's disease compared to healthy controls (HC).

Methods: MRI Acquisition: As part of an ongoing study of PD we acquired 2D ME-EPI brain images using a sequence with multi-echo capability [4] on a 3T Siemens Prisma, with a 64-channel head coil, with 1.3 mm isotropic resolution, matrix size=184x168x126, BW= 1812 Hz/Pixel, FA=90°, 3 TEs, TE1/ΔTE/TE5=14.80/24.53/63.86 ms and TR=4034 ms, with multiband 3 and GRAPPA 4 for 70 volumes. Here, we present results from 4 PD participants (M/F: 3/1, age: 63.7±7.6 years) and 6 healthy controls (HC) (M/F: 5/1, age: 72.2±3.6 years) acquired to date.

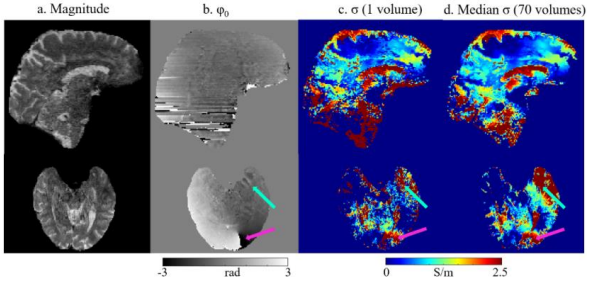

Fig. 1. Open-ended fringe lines (pink arrow) and aliasing artifact (green arrow) in φ_0 (b), create artifacts in the conductivity maps at each timepoint (c) and the median conductivity over all timepoints (d).

EPT pipeline: The phase offset at TE=0 (φ_0) was extrapolated from a non-linear fit [5] of the complex data over all echoes and unwrapped [6]. A mask was generated using FSL BET [7], refined by thresholding [8,9], and eroded by 1 voxel to reduce brain edge artifacts. Slice-to-slice inconsistencies in φ_0 were corrected by subtracting the median in each axial slice in the brain [10]. EPT on masked φ_0 maps, used the integral approach (differentiation and integral kernels: 17 and 39 voxels) with magnitude-weighted and segmentation-based edge preservation [11] using the echo-combined magnitude [12]. High quality structural conductivity maps (σ) were calculated by taking the median of positive values in each voxel of co-registered EPT reconstructions over all 70 timepoints.

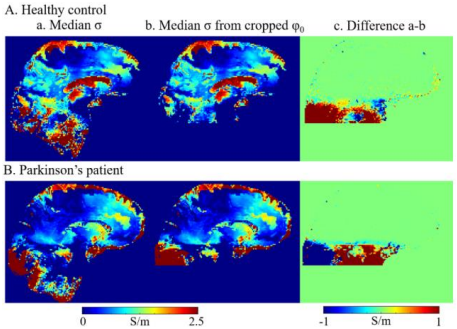

Fig. 2. Median conductivity maps reconstructed from the whole φ_0 (a) and cropped φ_0 (b) and the difference maps (c) in one healthy control (A) and one PD participant (B).

Results and Discussion: All phase data acquired so far suffers from open-ended fringe lines that propagate into the extrapolated φ_0 (pink arrow Fig. 1b), and from Moire interference of aliasing artifacts [13] (green arrow Fig. 1b). The open-ended fringe lines appear in the lower part of the brain, where slice-to-slice inconsistencies also appear more pronounced.

Therefore, we removed a lower section of the brain from φ_0 in every volume. The difference between median σ reconstructed from the full and cropped φ_0 (Fig. 2) shows that artifacts in σ propagate upwards towards the middle of the brain but did not affect the upper part of the brain. The width of this difference was consistent across subjects and similar to the 20-voxel radius of the integral kernel.

Conductivity distributions from the cropped φ_0 for each subject in cerebrospinal fluid (CSF), gray matter (GM), and white matter (WM) are displayed in Fig. 3 with negative conductivity values and those > 1.5 times the interquartile range above the third quartile [14] excluded. A t-test between PD and HC mean values showed no significant changes ($p > 0.05$) in σ in all three regions.

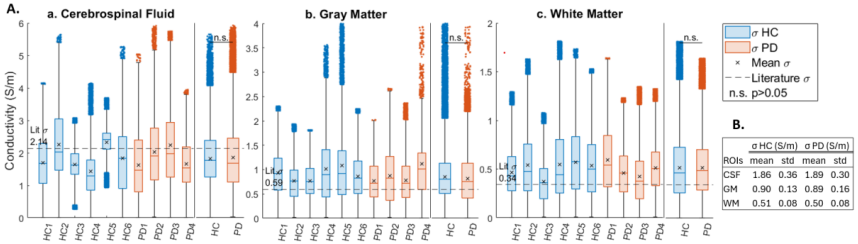

B.

	σ HC (S/m)		σ PD (S/m)	
ROIs	mean	std	mean	std
CSF	1.86	0.36	1.89	0.30
GM	0.90	0.13	0.89	0.16
WM	0.51	0.08	0.50	0.08

Fig. 3. σ distribution in each PD and HC together with distributions across subjects (A) and mean σ values ± standard deviations (B) in PD compared to HC participants. Literature value measured ex-vivo in healthy tissue [15] is indicated by the dashed line in each region of interest, CSF (a), GM (b), and WM (c). p-values showing no significant differences are displayed for each region.

Conclusions: Open-ended fringe lines, likely caused by imperfect complex coil combination, represent a challenge for EPT reconstruction. We removed the areas most affected by this artifact from the input φ_0 images to improve EPT reconstructions. In this small preliminary data set, reconstructed conductivities presented no significant differences in mean conductivities values in CSF, gray matter, and white matter, in Parkinson's disease compared to healthy controls. As more subjects continue to be acquired as part of this study, further work will include investigating the effect of higher-order shimming on open-ended fringe lines and evaluating conductivity changes in gray matter sub-regions to better understand conductivity changes in Parkinson's disease.

References

[1] Zaichick, Sofia V., et al. Disease models & mechanisms 10.5 (2017): 519-535.
[2] Moons, Rani, et al. Scientific reports 10.1 (2020): 16293.
[3]. Zeng, Weiqi, et al. Cellular and Molecular Neurobiology 44.1 (2024): 26.
[4] CMRR. Multi-Band Accelerated EPI Pulse Sequences. https://www.cmrr.umn.edu/multiband/ (2022).
[5] Liu, Tian, et al. *Magnetic resonance in medicine* 69.2 (2013): 467-476.
[6] Karsa, Anita, et al. *IEEE transactions on medical imaging* 38.6 (2018): 1347-1357.
[7] Smith, Stephen M. *Human brain mapping* 17.3 (2002): 143-155.
[8] Karsa, Anita et al. *Magnetic Resonance in Medicine* 84.6 (2020): 3206-3222.
[9] Kiersnowski, Oliver C., et al. *BIC- ISMRM PG Symposium* (2023).
[10] Arsenov, Oriana V., et al. *ISMRM* (2024).
[11] Karsa, Anita, et al. *ISMRM* (2021).
[12] Poser, Benedikt A., et al. *Neuroimage* 45.4 (2009): 1162-1172.
[13] Stadler, Alfred, et al. *European radiology* 17 (2007): 1242-1255.
[14] Rousseeuw, Peter J., et al. *Journal of the American Statistical association* 88.424 (1993): 1273-1283.
[15] Gabriel, Sami, et al. *Physics in medicine & biology* 41.11 (1996): 2271.

Optimising EPT to Assess Brain Conductivity in Sickle Cell Anaemia at 1.5T

Philippa Sha[1], Jierong Luo[1], Oriana Arsenov[1], Mitchel Lee[1], Fenella Kirkham[2], Karin Shmueli[1]
[1] *Department of Medical Physics and Biomedical Engineering, University College London, London, United Kingdom.*
[2] *Imaging and Biophysics, Departmental Neurosciences, Institute of Child Health, London, United Kingdom.*

Introduction: Sickle cell anaemia (SCA) is a genetic blood disorder that causes haemoglobin to polymerize and red blood cells to become sickle-shaped. SCA is known to affect normal neurocognition, and poses serious risks such as haemorrhagic or ischaemic stroke [1]. This study aims to assess, for the first time, the effect of SCA on brain tissue electrical conductivity (at ~64 MHz). MR Electrical Properties Tomography (EPT) is a non-invasive technique for calculating high-frequency tissue electrical conductivity (σ), an intrinsic property determined by the concentration and mobility of ions [2]. Phase-based EPT derives σ from the MR transceive phase (φ_0), using the integral form of the truncated Helmholtz equation [3]. Here, a pipeline for performing phase-based EPT was optimised for complex data originally acquired for quantitative susceptibility mapping at 1.5T [4].

Methods

EPT was optimised in a representative sample of 10 Tanzanian children, 5 with SCA and 5 healthy controls (HCs), aged 12.4 ± 4.1 years, 7/3 male/female, from a total study cohort of 163 children with SCA and 47 HCs, aged 12.6 ± 3.9 years.

MRI acquisition: T2*-weighted multi-echo 3D GRE and T1-weighted MPRAGE were acquired at 1.5T (Phillips, Achieva) using either an 8-channel or birdcage RF coil. 3D-GRE sequence parameters were: 5 echoes, TE_1 = 4.28 ms, ΔTE = 4.94 ms, TR = 27.4 ms, resolution = 1.458 x 1.45 8 x 1.5 mm^3, bandwidth = 287 Hz/pixel, FA = 15˚.

EPT: An existing EPT pipeline [5] was optimised as follows. To account for poorer SNR at 1.5T compared to 3T, MP-PCA denoising [6] was applied to the raw complex images. iField correction [7] was applied to remove echo-to-echo linear phase inconsistencies [8]. Complex images were unwrapped using SEGUE [9]. φ_0 was estimated by extrapolation and unwrapped again using SEGUE. A binary mask was generated from the raw magnitude image at TE2 using FSL-BET [10]. Quantitative conductivity maps (QCMs) were reconstructed using 3D quadratic fitting with both magnitude- and segmentation-based weighting (*MagSeg*), for greater edge preservation and noise reduction [5].

Kernel size optimisation: The radius for both the differential (k_{diff}) and integral kernels (k_{int}) was varied, as described in [5], using a conductivity phantom (1mm isotropic resolution, simulated at 128MHz, Sim4Life [11]). Mean absolute error (MAE) and error in the CSF were computed between the resulting conductivity maps and the ground truth.

Segmentation optimisation: For segmentation of grey matter (GM), white matter (WM) and cerebrospinal fluid (CSF), we compared: SPM [12] on the 2nd echo GRE magnitude image (as this was the only echo that provided consistent segmentation), SPM on the co-registered T1-weighted (T1w) image, and FSL-FAST [13] on the same T1w image.

Magnitude weighting optimisation: We compared magnitude echoes 2 and 5 (TE2/5), and the combined-echo magnitude [14]. The value of the δ parameter used for magnitude weighting was varied between 0.15–0.65. We also implemented a new method of varying δ automatically depending on phase noise levels [15].

Results and Discussion

Denoising: Figure 1 shows that, in general, applying MP-PCA denoising resulted in more detailed conductivity maps with greater contrast.

Kernel size: Optimal radii were chosen to be k_{diff} = 15 mm and k_{int} = 25 mm, as these achieved minimum error while avoiding over-smoothing in the reconstructed image.

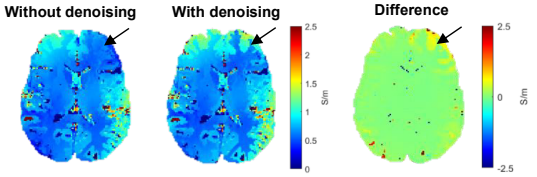

Fig. 1: *Conductivity maps in an axial slice of a representative HC subject reconstructed without/with MP-PCA denoising. MP-PCA denoising increased GM-WM contrast in some regions (indicated by black arrow).*

Segmentation method: Figure 2 shows that, as expected, segmentations using the T1w image provide better contrast between tissue types, especially at GM-WM boundaries. FSL-FAST provided greater detail and a significant increase (of 0.44 S/m) in median CSF conductivity values compared to SPM.

Magnitude method: There was very little visual difference in conductivity maps between using different magnitude-weighting inputs, with combined-echo magnitude providing slightly better GM-WM contrast. For selection of δ, our method of automatically varying δ was optimal in reducing noise.

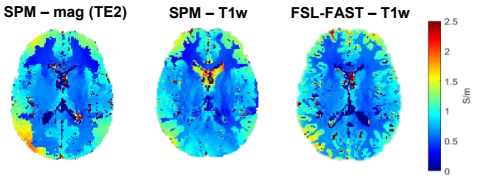

Fig. 2: *Conductivity maps in an axial slice of a representative HC subject using different segmentation methods for EPT segmentation weighting.*

Preliminary conductivity results in SCA vs HCs: The results of applying the optimised pipeline in the 10 subjects are shown in Figure 3. Although there were no statistically significant differences between groups, these preliminary results suggest that children with SCA exhibit greater conductivity compared to healthy controls in both GM and WM, but not in CSF.

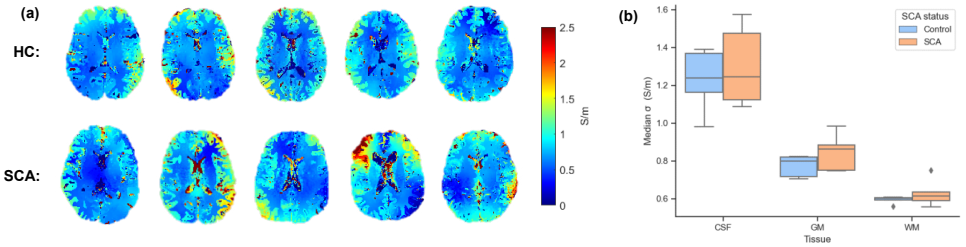

Fig. 3(a): *Conductivity maps generated using the optimised EPT pipeline.* ***Fig. 3(b):*** *Median conductivity values for each tissue type, segmented using FSL-FAST on T1w images.*

Conclusion: Here, we optimised a phase-based EPT pipeline to investigate the effect of SCA on brain tissue conductivity, in Tanzanian children at 1.5T. Denoising and field correction were implemented. Optimal reconstruction parameters were found to be: k_{diff} = 15 mm, k_{int} = 25 mm, FSL-FAST segmentation on the T1w image, and combined-echo magnitude input with automatically varying δ. This pipeline consistently produced high-quality conductivity maps and will now allow investigation of conductivities in the full cohort.

References:

[1] Farooq, S. et al. Neurologic Complications of Sickle Cell Disease. Curr Neurol Neurosci Rep. 2019; 19(4):17.
[2] Katscher, U. Electrical Properties Mapping. Quantitative MRI. 2020; 807-817.
[3] Katscher, U. et al. Electric properties tomography: Biochemical, physical and technical background, evaluation and clinical applications. NMR Biomed. 2017; 30(8):e3729.
[4] Lee, M. et al. Improved QSM pipeline to investigate the effect of sickle cell anaemia on brain magnetic susceptibility in Tanzanian children at 1.5 Tesla. Proc. Ann Meeting ISMRM 2024; 4828.
[5] Karsa, A. et al. New approaches for simultaneous noise suppression and edge preservation to achieve accurate quantitative conductivity mapping in noisy images. Proc. Ann. Meeting ISMRM 2021; 3774.
[6] Doniza, L. et al. MP-PCA image denoising technique for high resolution quantitative susceptibility mapping (QSM) of the human brain in vivo. Proc. Ann. Meeting ISMRM 2023; 2948.
[7] De Rochefort, L. et al. Quantitative susceptibility map reconstruction from MR phase data using bayesian regularization: Validation and application to brain imaging. Magn Reson Med. 2010; 63:194–206.
[8] Spincemaille, P. et al. Correction of residual echo-to-echo phase inconsistencies in readout phase corrected multi-echo gradient echo for quantitative susceptibility mapping. ISMRM 4th International Workshop on MRI Phase Contrast & Quantitative Susceptibility Mapping. 2016; 46.
[9] Karsa, A. et al. SEGUE: A Speedy rEgion-Growing Algorithm for Unwrapping Estimated Phase. IEEE Trans Med Imag. 2019; 38(6):1347-1357.
[10] Smith, S.M. Fast robust automated brain extraction. Human Brain Mapping. 2002; 17(3):143-155.
[11] Meerbothe, T.G. et al. A database for MR-based electrical properties tomography with in silico brain data – ADEPT. Magn Reson Med. 2023; 91(3):1190-1199.
[12] Ashburner, J. et al. Spm12 manual. Wellcome Trust Centre for Neuroimag. 2014; 2464.
[13] Zhang, Y. et al. Segmentation of brain MR images through a hidden Markov random field model and the expectation-maximization algorithm. IEEE Trans Med Imag. 2001; 20(1):45-57.
[14] Poser, B.A. et al. Investigating the benefits of multi-echo EPI for fMRI at 7T. NeuroImage. 2009; 45(4):1162-1172.
[15] Luo, J. et al. An automatically optimised Gaussian weighting function width for magnitude-weighted phase-based electrical properties tomography (EPT). Proc. Ann. Meeting ISMRM 2024; 137.

Comparing Novel Functional Electrical Properties Tomography (fEPT) with Simultaneous BOLD fMRI using Multi-Echo Echo-Planar Imaging

Jierong Luo[1], Oriana Arsenov[1], Jannette Nassar[1], Patrick Fuchs[1], and Karin Shmueli[1]
[1]Department of Medical Physics & Biomedical Engineering, University College London, London, UK

Introduction: Phase-based electrical properties tomography (EPT) estimates tissue electrical conductivities from MR transceive phase (φ_0) via the Helmholtz equation [1]. Recently, EPT has shown the potential to detect brain functional activations using the general linear model (GLM) approach [2], but the underlying biophysiological mechanisms remain unclear [3-8]. Using conventional EPI-based BOLD fMRI as a reference, the few existing functional EPT (fEPT) studies gave inconsistent results and often required sequences additional to EPI to measure conductivity changes [3-7]. However, these separate sequences and acquisitions may introduce bias and variation, respectively, to the comparison between fMRI and fEPT. A recently developed high-resolution multi-echo (ME) gradient-echo EPI approach [9] has enabled simultaneous fEPT and fMRI [8], allowing for comparison between fEPT and fMRI without sequence-introduced bias or inter-scan variation. Therefore, here we compared the image quality and results of fEPT with simultaneous BOLD fMRI in 4 healthy volunteers.

Methods: Four healthy volunteers (HVs) were scanned using a high-resolution ME GRE-EPI sequence [9] at 3T, with a visual stimulus paradigm of an 8 Hz flickering checkerboard alternated with a white screen in 15.6 s blocks for 70 volumes. T_1w images were acquired using a 1-mm isotropic MPRAGE sequence. Within each volume, the magnitude echo images were combined for optimal BOLD contrast [10], and the complex data were used to calculate φ_0, as described previously [8]. To minimise noise and boundary artefacts in EPT [1], the φ_0 gradient was first estimated by weighted polynomial fitting, and the conductivity was then calculated via the surface integral of the φ_0 gradient with magnitude and segmentation weighting [11]. To avoid introducing any BOLD fMRI weighting from the magnitude signal into the fEPT analysis, the weights for fitting and the tissue segmentations [12] were derived from the temporally constant mean echo-combined [10] magnitude images over all 70 volumes. To investigate how this magnitude image used for EPT reconstruction may affect the functional analysis, the EPT time series were also reconstructed using standard T_1w structural MPRAGE image inputs for magnitude and segmentation weighting and then analysed identically.

Functional analysis was performed for the echo-combined magnitude and EPT time series using SPM12 [13]. To avoid any bias introduced by preprocessing [14], no filtering or smoothing was applied to the time series prior to the functional analysis. For fEPT, voxels with non-physiological negative conductivities were excluded during smoothing and model estimation. We performed functional analysis using GLM, with the signal response modelled by the canonical hemodynamic response function without derivatives [2]. A t-test was used to detect statistically significant voxel-wise activations at p<0.001 without family-wise error correction [15]. As a control for spurious activations, ME GRE-EPI data were also acquired in one HV without a visual stimulus and processed identically.

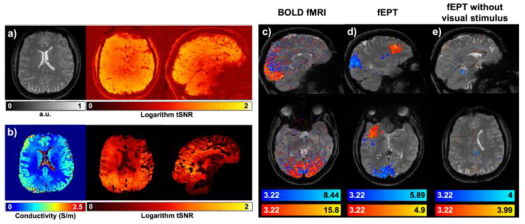

Fig. 1. Comparison of whole-brain BOLD fMRI and fEPT in HV1. Echo-combined magnitude (a) and EPT (b) images, and the corresponding tSNR maps (logarithmic scale). Maximum intensity projections of T-statistics (p<0.001) showing positive (red) and negative (blue) functional activations in BOLD fMRI (c), fEPT (d) and fEPT without visual stimulus (e) displayed on the mean echo-combined magnitude image over all 70 volumes.

Results and Discussion: Fig. 1 compares whole-brain fMRI and fEPT in a representative subject. The highest magnitude tSNR is found at the posterior brain edges, reflecting the RF coil sensitivity distribution. In contrast, the EPTs showed a more inhomogeneous tSNR distribution with the lowest tSNR found in CSF perhaps due to highly variable reconstructed CSF conductivity values. The EPT tSNR was very low in the cerebellum likely due to residual slice-to-slice phase inconsistencies [9,16].

In BOLD fMRI (Fig. 1c, Fig. 2a-c), large clusters of positively activated voxels are found in the primary visual cortex for all subjects. However, the activations found in fEPT (Fig. 1d, Fig. 2d-f) are much weaker, and we observed both positive [6] and negative activations [5] with large inter-subject variation of their location and the size (Fig. 2). Nevertheless, in the absence of a visual stimulus (Fig. 1e), we found only very few scattered activated voxels in fEPT, suggesting that activated fEPT clusters (Fig. 1d, Fig. 2d-f) are not due to type 1 error. Inter-subject variation was also observed in fEPT reconstructed using T_1w magnitude inputs, with fewer and weaker activations.

Conclusions: We characterised and compared the image quality and activations of fEPT with simultaneous BOLD fMRI. We found a distinctive tSNR distribution for fEPT. Our results show that fEPT is noisier and shows larger inter-subject variation than BOLD fMRI. Future studies are required to optimise fEPT and investigate the physiological mechanism underlying the observed activations.

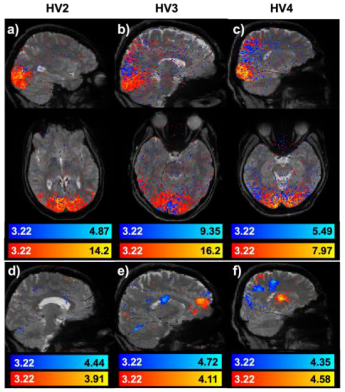

Fig. 2. Positive (red) and negative (blue) functional activations in BOLD fMRI (a-c) and fEPT (d-f) in HV2 (a,d), HV3 (b,e) and HV4 (c,f). Maximum intensity projections of T-statistics (p<0.001) are displayed on the the mean echo-combined magnitude image over all 70 volumes.

References

[1] U. Katscher and C. A.T. van den Berg. electric properties tomography: biochemical, physical and technical background, evaluation and clinical applications. NMR Biomed. 2017; 30(8): e3729.
[2] K. J. Friston, et al. Statistical parametric maps in functional imaging: a general linear approach. Hum. Brain Mapp. 1995; 2(4): 189-210.
[3] M. Helle and U. Katscher. Electrical properties tomography based functional magnetic resonance imaging (EPT-fMRI). Proc. Ann. Meeting ISMRM 2019; 3759.
[4] R. Schmidt. Electrical conductivity as a potential mean to decouple the hemodynamic response from fMRI. Proc. Ann. Meeting ISMRM 2019; 3777.
[5] K. J. Jung, et al. Investigation of electrical conductivity changes during functional activity of the brain via phase-based MR-EPT: preliminary observation. Proc. Ann. Meeting ISMRM 2023; 0922.
[6] G. H. Jahng, et al. High-frequency conductivity signal changes measured with functional MREPT during visual stimulation. Proc. Ann. Meeting ISMRM 2023; 0923.
[7] C. D. Rae, et al. Functional conductivity imaging: quantitative mapping of brain activity. Proc. Ann. Meeting ISMRM 2024; 1293.
[8] J. Luo, et al. Preliminary whole-brain functional electrical properties tomography using gradient-echo echo-planar imaging. Proc. Ann. Meeting ISMRM 2024; 3681.
[9] O. C. Kiersnowski, et al. Rapid high resolution integrated structural and functional susceptibility and conductivity mapping in the human brain. Proc. Ann. Meeting ISMRM 2024; 188.
[10] B. A. Poser, et al. BOLD contrast sensitivity enhancement and artifact reduction with multiecho EPI: parallel-acquired inhomogeneity-desensitized fMRI. Magn Reson Med 2006; 55: 1227–1235.
[11] A. Karsa and K. Shmueli. New approaches for simultaneous noise suppression and edge preservation to achieve accurate quantitative conductivity mapping in noisy images. Proc Ann Meeting ISMRM 2021; 3774.
[12] J. Ashburner J and K. Friston. Unified segmentation. NeuroImage 2005; 26: 839-851.
[13] J. Ashburner, et al. SPM12 Manual. Wellcome Trust Centre for Neuroimaging, London, 2021.
[14] S. Mandija et al. The first MR electrical properties tomography (MR-EPT) reconstruction challenge: preliminary results of simulated data. Proc Ann Meeting ISMRM 2024; 182.
[15] K. J. Friston, et al. Analysis of functional MRI time-series. Hum Brain Mapp. 1994; 1(2): 153-171.
[16] O. V. Arsenov, et al. Artifact reduction for rapid phase-based EPT in the human brain in vivo using a multi-echo 2D EPI sequence. Proc Ann Meeting ISMRM 2024; 3675.

Accelerated T2 mapping for clinical applications: a comparison with conventional methods in the NIST/ISMRM system phantom.

Jack J. Allen[1], Joely Smith[2], Stephen Wastling[3], Marzena Arridge[3], Anastasia Papadaki[3], Laura Mancini[3], Iulius Dragonu[4], Tom Hilbert[5], John Thornton[3], Tarek Yousry[3], David L. Thomas[3], Matthew Grech-Sollars[1].

[1]Department of Computer Science, University College London, London, United Kingdom.
[2]Department of Imaging, Imperial College Healthcare NHS Trust, London, United Kingdom.
[3]Neuroradiological Academic Unit, UCL Queen Square Institute of Neurology, London, United Kingdom.
[4]Research and Collaborations GB&I, Siemens Healthcare Ltd, Camberley, United Kingdom.
[5]Advanced Clinical Imaging Technology, Siemens Healthineers International AG, Lausanne, Switzerland.

Introduction: Quantitative MRI methods, such as T2 mapping, can increase assessment objectivity in comparison to conventional qualitative imaging and have promise in clinical applications. Conventional Multi-Echo Spin-Echo (MESE) [1] T2 mapping scan durations are often too long for clinical use. Dual-Echo Turbo Spin-Echo (DE-TSE) [2] reduces the total acquisition time by acquiring images at only 2 Echo Times (TEs) but compromises accuracy and precision. GRAPPATINI [3] accelerates MESE via Generalized Autocalibrating Partially Parallel Acquisition (GRAPPA) [4] and Model-based Accelerated RelaxomeTry by Iterative Nonlinear Inversion (MARTINI) [5]. The performance of rapid T2 mapping methods must be characterised before clinical use. In this study, we compared T2 mapping measurements from DE-TSE, MESE, and GRAPPATINI in a multi-compartment phantom.

Methods: T2 measurements were made using DE-TSE, MESE, and GRAPPATINI, scanning a traceable NIST/ISMRM system phantom (serial number 130-102) [1] 10 times across 5 sessions (twice in each session). The NIST/ISMRM phantom contains vials with $MnCl_2$ solutions of different concentrations, and therefore different T2 values. Phantom temperature was measured before and after each session. General scan parameters: 3T MAGNETOM Prisma^{Fit} scanner (Siemens Healthineers AG, Germany), 32-channel head coil, reconstructed voxel size 0.4x0.4x3.0mm, field of view 230x216mm, matrix size 512x480, GRAPPA acceleration factor 2, sagittal slices centred on the array of T2 samples, slice distance factor 0%. Sequence-specific parameters: DE-TSE: TE1/TE2 30ms/119ms, 44 slices, Repetition Time (TR) 7600ms, Acquisition Time (TA) 4min 12s (5.7s/slice), phase resolution 60%; 1 spinal coil element in addition to the head coil; MESE: 7 TEs (min:incr:max) [24:24:168]ms, 20 slices, TR 3530ms, TA 9min 14s (27.7s/slice), phase resolution 60%; GRAPPATINI: 16 TEs (min:incr:max) [11.6:11.6:185.6]ms, 44 slices, TR 4240ms, TA 6min 57s (9.5s/slice), phase resolution 100%.

Voxel-wise DE-TSE and MESE T2 maps were derived from magnitude T2-weighted images, using an image ratio calculation for DE-TSE [2] and Auto-Regression on Linear Operations (ARLO) fitting [1] for MESE. The first echo time was omitted from the MESE fits to mitigate imperfect spin-echo refocusing [4]. The GRAPPATINI sequence is a Siemens research application and provides on-scanner T2 maps using an iterative, model-based reconstruction [3, 6]. Central-slice Regions-of-Interest (ROIs) were selected for 6 T2 vials, with 22°C manufacturer reference T2 values: 392.5ms, 277.0ms, 181.5ms, 92.3ms, 65.7ms, and 45.9ms. Measured T2s were corrected to 22°C using the mean phantom temperature for the session and a linear model derived from manufacturer T2 values for temperature range (min:incr:max) [16:2:26]°C. Corrected T2 mean and Standard Deviation (SD) was calculated for each ROI and compared with the 22°C reference values. All fitting and analysis was performed in MATLAB (R2024a, MathWorks, USA).

Results: Phantom temperature distribution across all scans (mean±SD): 23.2°C±0.5°C. Coefficient of Variation (CV) range across all 6 vials: DE-TSE: 2.5%-4.4%; MESE: 1.6%-3.2%; GRAPPATINI: 1.5%-3.4%. Figure 1 shows the relative T2 deviation from the reference value for each of the 6 vials, after correcting the T2s to 22°C. Relative Bland-Altman analysis (mean, 95% Limits of Agreement (LoA)): DE-TSE 28.9%, LoA 23.1%, 34.8%; MESE -0.5%, LoA -6.9%, 5.8%; GRAPPATINI -2.8%, LoA -12.0%, 6.4%.

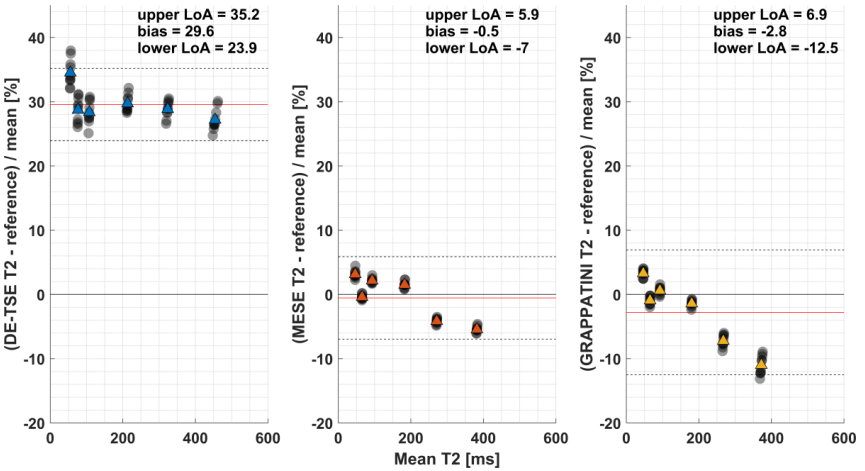

Fig. 1. Relative deviation of the measured T2 values from the manufacturer reference T2 values, after correction to 22°C, showing the mean bias and Limits of Agreement (LoA). The Bland-Altman analysis was performed using the mean T2 values for each vial in each scan (grey circles). The mean for each of the 6 vials is plotted for visualisation purposes (triangles).

Discussion: Temperature-corrected multi-session measurements were used to compare conventional T2 mapping techniques (DE-TSE and 7-TE MESE) with the iterative model-based GRAPPATINI method. GRAPPATINI and MESE both showed good accuracy and precision, but GRAPPATINI was ~3x faster per imaging slice (MESE 9min 14s, 27.7s/slice; GRAPPATINI 6min 57s, 9.5s/slice). DE-TSE was faster (DE-TSE 4min 12s, 5.7s/slice) but considerably overestimated T2. Previous work has demonstrated initial examples of GRAPPATINI in the brain [6] but further studies are required, such as evaluations at higher spatial resolutions and comparisons with resolution-matched conventional methods to explore how phantom results translate to *in vivo* maps.

Conclusions: GRAPPATINI demonstrates potential as a precise and accurate clinical tool for fast T2 mapping. Additional research is needed to assess the methods *in vivo*, which we are exploring for quantitative brain imaging.

Acknowledgements: This study was supported by researchers at the National Institute for Health and Care Research University College London Hospitals Biomedical Research Centre. Siemens Healthineers provided support and the GRAPPATINI research application sequence through a research agreement. Tom Hilbert and Iulius Dragonu are employed by Siemens Healthineers.

References

[1] B. K. Statton, J. Smith, M. E. Finnegan, G. Koerzdoerfer, R. A. Quest, M. Grech-Sollars, *Magnetic Resonance in Medicine* **2022**, *87*, 1446.
[2] G. P. Winston, S. B. Vos, J. L. Burdett, M. J. Cardoso, S. Ourselin, J. S. Duncan, *Epilepsia* **2017**, *58*, 1645.
[3] T. Hilbert, T. J. Sumpf, E. Weiland, J. Frahm, J.-P. Thiran, R. Meuli, T. Kober, G. Krueger, *Journal of Magnetic Resonance Imaging* **2018**, *48*, 359.
[4] M. A. Griswold, P. M. Jakob, R. M. Heidemann, M. Nittka, V. Jellus, J. Wang, B. Kiefer, A. Haase, *Magn. Reson. Med.* **2002**, *47*, 1202.
[5] T. J. Sumpf, M. Uecker, S. Boretius, J. Frahm, *Journal of Magnetic Resonance Imaging* **2011**, *34*, 420.
[6] N. Gruenebach, M. A. Abello Mercado, N. F. Grauhan, A. Sanner, A. Kronfeld, S. Groppa, V. I. Schoeffling, T. Hilbert, M. A. Brockmann, A. E. Othman, *Heliyon* **2023**, *9*, e15064.

Power Pitch Session 2

Investigating The Impact Of Denoising Methods On Dti Estimates

Joshua Mawuli Ametepe[1], James Gholam[1], Leandro Beltrachini[2], Mara Cercignani[1], and Derek Kenton Jones[1]
[1]School of Psychology, Cardiff University, Cardiff, United Kingdom, [2]School of Physics and Astronomy, Cardiff University, Cardiff, United Kingdom

INTRODUCTION

Diffusion Tensor Imaging (DTI) probes tissue microstructure [1] but suffers from reduced signal-to-noise ratio (SNR) due to signal attenuation in diffusion-weighted images. This impacts the estimation of DTI parameters like fractional anisotropy (FA) and the tensor orientation [2]. Many denoising methods aim to improve SNR, but their impact on FA, tensor orientation, and other DTI estimates is not fully explored [3]. A major challenge is the lack of ground truth images for comparison. This study creates ground truth data to evaluate the effectiveness of various denoising algorithms.

METHODS

We designed digital phantoms as ground truth for comparisons. This study focuses on one phantom made of five bars representing 'fibres' (4 voxels thick) crossing at the center of each slice in a 101x101x101 volume. The bars in each slice have a fixed FA, which varies between slices, and the background FA is set to 0. Each voxel has a mean diffusivity of 0.0007 mm²/s [2,4].

For denoising methods like Patch2Self [5] and MPPCA [6] which need multiple diffusion-weighted images, we created a b0 image and simulated DWI datasets with 6, 15, 30, and 60 gradient directions using isotropically distributed gradient orientations from a bipolar electrostatic repulsion model [7,8].

For crossing fibres, we used a multi-tensor approach where the diffusion-weighted signal is a weighted sum of signals from multiple tensors[9-11].

$$S = \sum_1^N \frac{1}{N} S_0 e^{-b(gD_n g^T)},$$

Where, N is the total number of crossing fibres, D_n is the diffusion tensor associated with a particular fibre, S is the diffusion weighted signal, S_0 is the b0 signal, g is the gradient orientation and b is the b-value, which was set to 1000 s/mm² for all images. Rician noise was simulated in the images with an SNR or 5 in the b0 image [4,12] .

This study tested five denoising methods: DDM2 [13], Patch2Self [5], MPPCA [6], non-local means denoising [14] and total variation denoising [15,16]. MPPCA and Patch2Self implementations from Dipy[17], non-local means from Advanced Normalization Tools (ANTs) [18], and total variation from Scikit-image toolbox [19] were used.

Each method denoised the datasets, and diffusion tensors were computed to obtain FA and principal fibre orientations. The DDM2 model rescales images to a range of 0 to 1, so we used inverse min-max scaling based on an online repository. This scaling might be inconsistent across volumes, and we have contacted the authors for clarification.

We also found that DiPy's Patch2Self does not denoise b0 images with a b value below the set threshold, even when the option to denoise b0 is true. To address this, we set the b0 threshold to 0 and changed the b value of the b0 image to 0.1. We have contacted a DiPy developer for advice, as this might affect our results.

RESULTS

Figure 1 shows the denoised output the various denoising methods for one gradient orientation in the 60 direction dataset. For four selected FA values in the ground truth (1,0.7,0.4,0.1), the mean absolute error in the predicted FA is displayed in Figure 2 as a probability density function. Figure 3 shows the absolute value of the dot product error in fibre orientations for these selected FA values.

DISCUSSION

Our results show that errors decrease with higher FA values or more DWI volumes. While some models recover lost detail effectively, this does not always translate to improved FA and fiber orientation.

CONCLUSION

Our work is a preliminary study on the impact of denoising methods on DTI estimates. Further work will explore different kinds of phantoms and resolution in the case of crossing fibres.

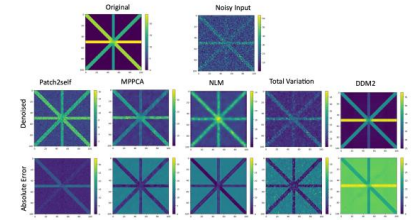

Figure 1 A visual comparison of the results of one gradient orientation in a 60 direction dataset

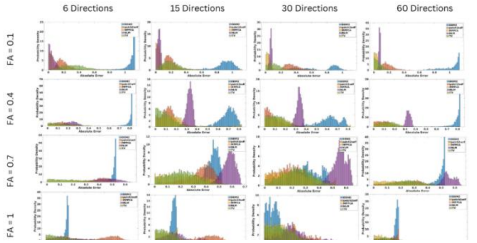

Figure 2 The absolute error between the FA of the denoised images and the ground truth for various FA values and number of gradient directions presented as probability density functions.

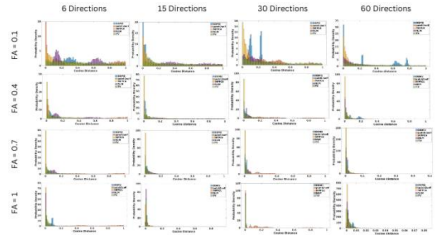

Figure 3 The cosine distance (1 minus the absolute value of the dot product) between the FA of the denoised images and the ground truth for various FA values and number of gradient directions presented as probability density functions

REFERENCES

1. Kubicki M, Westin C-F, Maier SE, et al. Diffusion tensor imaging and its application to neuropsychiatric disorders. *Harvard review of psychiatry*. 2002;10(6):324-336.
2. Pierpaoli C, Basser PJ. Toward a quantitative assessment of diffusion anisotropy. *Magnetic Resonance in Medicine*. 1996-12-01 1996;36(6):893-906. doi:10.1002/mrm.1910360612
3. Manzano Patron JP, Moeller S, Andersson JL, Ugurbil K, Yacoub E, Sotiropoulos SN. Denoising Diffusion MRI: Considerations and implications for analysis. *Imaging Neuroscience*. 2024;2:1-29.
4. Jones DK, Basser PJ. "Squashing peanuts and smashing pumpkins": how noise distorts diffusion-weighted MR data. *Magnetic Resonance in Medicine: An Official Journal of the International Society for Magnetic Resonance in Medicine*. 2004;52(5):979-993.
5. Fadnavis S, Batson J, Garyfallidis E. Patch2Self: Denoising Diffusion MRI with Self-Supervised Learning. *Advances in Neural Information Processing Systems*. 2020;33:16293-16303.
6. Veraart J, Novikov DS, Christiaens D, Ades-Aron B, Sijbers J, Fieremans E. Denoising of diffusion MRI using random matrix theory. *Neuroimage*. 2016;142:394-406.
7. Jones DK, Horsfield MA, Simmons A. Optimal strategies for measuring diffusion in anisotropic systems by magnetic resonance imaging. *Magnetic Resonance in Medicine: An Official Journal of the International Society for Magnetic Resonance in Medicine*. 1999;42(3):515-525.
8. Papadakis NG, Murrills CD, Hall LD, Huang CL-H, Carpenter TA. Minimal gradient encoding for robust estimation of diffusion anisotropy☆. *Magnetic resonance imaging*. 2000;18(6):671-679.
9. Seunarine KK, Alexander DC. Multiple fibers: beyond the diffusion tensor. *Diffusion Mri*. Elsevier; 2014:105-123.
10. Dell'Acqua F, Rizzo G, Scifo P, et al. A deconvolution approach based on multi-tensor model to solve fiber crossing in diffusion-MRI. IEEE; 2006:1415-1418.
11. Filatova OG, Van Vliet LJ, Schouten AC, Kwakkel G, Van der Helm FC, Vos FM. Comparison of multi-tensor diffusion models' performance for white matter integrity estimation in chronic stroke. *Frontiers in neuroscience*. 2018;12:247.
12. Gudbjartsson H, Patz S. The Rician distribution of noisy MRI data. *Magnetic resonance in medicine*. 1995;34(6):910-914.
13. Xiang T, Yurt M, Syed AB, Setsompop K, Chaudhari A. DDM $^ 2$: Self-Supervised Diffusion MRI Denoising with Generative Diffusion Models. *arXiv preprint arXiv:230203018*. 2023;
14. Manjón JV, Carbonell-Caballero J, Lull JJ, García-Martí G, Martí-Bonmatí L, Robles M. MRI denoising using non-local means. *Medical image analysis*. 2008;12(4):514-523.
15. Vogel CR, Oman ME. Iterative methods for total variation denoising. *SIAM Journal on Scientific Computing*. 1996;17(1):227-238.
16. Selesnick I. Total variation denoising (an MM algorithm). *NYU Polytechnic School of Engineering Lecture Notes*. 2012;32
17. Garyfallidis E, Brett M, Amirbekian B, et al. Dipy, a library for the analysis of diffusion MRI data. *Frontiers in neuroinformatics*. 2014;8:8.
18. Avants BB, Tustison N, Song G. Advanced normalization tools (ANTS). *Insight j*. 2009;2(365):1-35.
19. Van der Walt S, Schönberger JL, Nunez-Iglesias J, et al. scikit-image: image processing in Python. *PeerJ*. 2014;2:e453.

Current UK perspectives on the challenges for clinical translation of quantitative MR imaging biomarkers.

Julia E. Markus[1], Penny L. Hubbard Cristinacce*[2], Harpreet Hyare[1,3], and Po-Wah So[4]
[1] Centre for Medical Imaging, Division of Medicine, University College London, London, W1W 7TY, UK
[2] Quantitative Biomedical Imaging Laboratory, The University of Manchester, M13 9PT, UK
[3] Department of Brain Repair and Rehabilitation, UCL Institute of Neurology, London, WC1N 3BG, UK
[4] Department of Neuroimaging, Institute of Psychiatry, King's College London, London, SE5 9NU, UK
*Presenting author

Introduction An interactive session at the British & Irish Chapter (BIC)-ISMRM Annual Meeting 2022 Clinical Translation Workshop "Steps on the Path to Clinical Translation" asked attendees to address 7 areas pertinent to improving clinical translation for quantitative MR (qMR) imaging biomarkers (IBs). The conclusions/ further questions that resulted from discussions were developed into a survey. We aimed to investigate the UK-based MRI community's perspectives on major obstacles in clinically translating qMR IBs, and what actions could be useful to address them.

Methods A REDCap project was used to derive a web-based e-survey and a QR/quick access link distributed as an open invitation. The survey, open for 5 weeks, was made available during the 2022 BIC-ISMRM Annual Meeting and subsequently distributed via communication emails/newsletters to the BIC-ISMRM, MR-PHYSICS, British Society of Neuroradiologists (BSNR) and various institutional emailing lists. The survey was made of 40 questions covering 7 topics, see [1] and Table 1. Descriptive statistics were drawn from multiple choice (MCQ), Likert and agree/disagree questions, and a thematic analysis with a deductive approach [1] was performed on free text questions to identify themes across topics. Basic occupational demographic questions allowed us to monitor MRI community representation.

Results & Discussion We received 69 responses with completion varying from 27.7–100%. Responses were received from imaging scientists (research (64%) and clinical (18%)), clinicians (10%), others (8%). Three significant themes emerged from thematic analysis across all free text questions.

Consensus The need to build consensus and resources dedicated to improving the standardisation of certain aspects of IB development: (i) terminology, (ii) decision making and (iii) validation (Q 1B, 1Bii, 3B, 3D, 4E, 5C, and 5D). Views were frequently expressed on: (i) the format for sharing consensus, (ii) what consensus building should target, (iii) the lack of multi-disciplinary guidelines, (iv) standardisation of terminology, and (v) the need for action groups and (vi) for publications on how to define the pathway. Figure 1 shows that respondents agree with the need to improve consensus.

Key Area Questions		Survey questions	
What will and won't work in a clinical workflow?	1A	Is an imaging biomarker useful if it doesn't give a YES/NO answer to aid diagnosis?	Yes/no
	1Ai	Additional comments.	Free text
	1B	How can we standardise the language we use to aid clinical translation	Free text
	1Bi	Should effort be made to develop a consensus paper to standardize terminology to aid clinical translation?	Yes/no
	1Bii	Additional comments.	Free text
	1C	Quantitative MR parameter maps often need to be created away from the scanner console. What is the maximum amount of time after acquisition, if an imaging biomarker is to be integrated into the clinical workflow?	MCQ
	1D	Other comments.	Free text
How big of an improvement justifies a change in clinical practice?	2A	In regards to sensitivity and specificity, what percentage of change is significant enough to change practice?	MCQ
	2Ai	How should this be defined?	Free text
	2B	Who should be involved in the decision to change practice?	MCQ
	2Bi	Additional comments.	Free text
	2C	Should change in clinical practice be for all patients or selected cohorts?	MCQ
	2Ci	Additional comments.	Free text
	2D	Other comments.	Free text
How can we improve validation of an imaging biomarker?	3A	Does "validation" mean something different to a physicist and a clinician? How much do you agree with the following statements?	
	3Ai	Validation is knowing an imaging biomarker's repeatability and reproducibility	Likert
	3Aii	Validation is knowing the accuracy and precision of the measurement	Likert
	3Aiii	Validation is making a clinician happy to use your imaging biomarker	Likert
	3Aiii	Validation is knowing how well we can measure an imaging biomarker	Likert
	3B	At what point do you consider something validated?	Free text
	3C	How do we incentivize transparency and reproducibility? How much do you agree with the following statement?	
	3Ci	Funders need to mandate sharing of code	Likert
	3Cii	Funders need to mandate sharing of data	Likert
	3Ciii	Publishers need to mandate sharing of code	Likert
	3Civ	Institutions need to provide knowledge support for code sharing	Liker
	3Cv	Institutions need to provide knowledge support for data sharing	Likert
	3D	Other comments.	Free text
How do we standardise data acquisition and analysis more effectively?	4A	It is known that vendors will find a method less attractive if a method requires a phantom, so when should we use a phantom	Free text
	4B	Should we use phantoms to standardize data acquisition for every sequence?	Yes/no
	4Bi	Additional comments.	Free text
	4C	Do you agree with a goal-orientated approach to quality?	Yes/no
	4D	Should we standardize, harmonise or optimize pulse sequences in multi-center studies?	MCQ
	4E	Other comments.	Free text
How do we share data, code, and good practice more effectively?	5A	At what point should we be sharing code?	MCQ
	5B	At what point should we be sharing data?	MCQ
	5C	How do we balance the need for the subject's privacy against the value of sharing data?	Free text
	5D	Techniques generally require buy-in from scanner manufacturers to become part of their product in order to change clinical practice. How do we balance the need for researchers to protect the IP to allow this to happen, against the value of sharing code and data publicly?	Free text
	5E	Other comments.	Free text
How can we improve quality management of qMR imaging biomarkers?	6A	Does a Quality Management System (QMS) exist in your place of work?	Yes/no
	6Ai	Do you use it?	Yes/no
	6B	How do we incentivise the use of a QMS?	Free text
	6C	Other comments.	Free text
How can we engage with end users to support clinical translation?	7A	As an early career researcher, what's the best way to contact clinicians?	Free text
	7B	How do we integrate our MR development with PACs systems?	Free text
	7C	How do we find out if a patient group can tolerate the imaging method?	Free text
	7D	Other comments.	Free text

Table 1. Outline the survey questions and detail the question type.

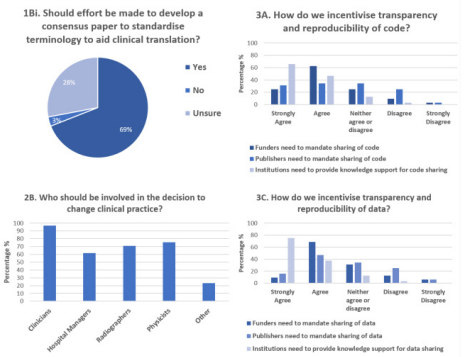

Fig. 1. Consensus building: Answers to Q1Bi, 2B, 3A and 3C.

Context dependency The theme of context dependency was frequently raised across all topics: (i) phantoms, (ii) terminology, (iii) decision making and (iv) endpoints (Q 1Ai, 1D, 2Ai, 2Bi, 4Bi and 7B). Views were expressed strongly regarding the uniqueness of each clinical situation when integrating IBs into the clinical workflow. The nature of this integration raised variability in views, but most frequently, that the context should be developed based on the IBs themselves, closely followed by the clinical question, availability, and cost.

Expectations of the IB (Product Profile) When considering the product profile [7] (Q1Ai, 1D, 2Ai, 2Bi, 2Ci and 7A), opinions strongly favoured qMR IBs supplementing, rather than replacing existing pathways. Many considered that a specific endpoint of an IB in clinical practice would have a staged approach, although this varied when considering IBs across patient groups or along a treatment process. For example, in question 2Ci, many stated that the ideal situation would be to target clinical translation of an IB for a single situation/patient group initially and then, following subsequent phased research/ development, transfer the IB to other patient pathways. Respondents often stated conversations required increased input from a larger breadth of stakeholders and networks, such as vendors and national/international societies involved in qMR. A clear product profile can aid the research design and end translation of a medical test [8], but more input from the MRI community would be required to establish clear product profiles for individual qMR IBs.

Our survey demonstrates that, according to a national cohort of the MRI community in the UK, there remain unmet needs and challenges in improving the pathway to clinical translation of qMRI IBs. Published consensus often addresses the context dependency by a siloed approach, but our results suggest that a more standardised, but adaptive approach, would allow a common ground that could have larger benefit. A move to a more standardised consensus was observed in recommendations for Arterial Spin Labelling (ASL), where a more structured and holistic approach was developed in [3] than in [4]. Recent consensus building has developed guidance for a range of IBs in broader contexts [5,6], nevertheless consensus methodology is highly variable, and more work is needed to establish the more standardised, but adaptive, approach that was suggested by the survey results.

Conclusion We plan to build on this study by providing a forum for continued action and "widening the conversation". We hope to develop a multifaceted and successful approach to addressing the many, and diverse, needs and challenges in translating qMR IBs into the clinic.

References [1] [1] P. L. Hubbard Cristinacce, et al. *MRM.* **90**, (3) 1130-1136 (2023). [2] Michelle E. Kiger & Lara Varpio (2020), Medical Teacher, 42:8, 846-854, DOI: 10.1080/0142159X.2020.1755030. [3] Nery F, Buchanan CE, Harteveld AA, Odudu A, Bane O, Cox EF, et al. Magn Reson Mater Physics, Biol Med 2020;33:141–61. https://doi.org/10.1007/s10334-019-00800-z. [4] Alsop DC, Detre JA, Golay X, Günther M, Hendrikse J, Hernandez-Garcia L, et al. Magn Reson Med 2015;73:102–6. https://doi.org/10.1002/mrm.25197. [5] deSouza, N.M., Achten, E., Alberich-Bayarri, A. et al. Insights Imaging 10, 87 (2019). https://doi.org/10.1186/s13244-019-0764-0. [6] O'Connor JP, Aboagye EO, Adams JE, Aerts HJ. et al. Nat Rev Clin Oncol. 2017 Mar;14(3):169-186. doi: 10.1038/nrclinonc.2016.162. [7] Cocco P, Ayaz-Shah A, Messenger MP, West RM, Shinkins B. BMC Med. 2020 May 11;18(1):119. doi: 10.1186/s12916-020-01582-1. [8] Terry RF, Plasència A, Reeder JC. Health Res Policy Syst. 2019 Dec 12;17(1):97. doi: 10.1186/s12961-019-0507-1.

Bayesian parameter estimation and non-linear least squares fitting for the multi-compartment analysis of T_2 in breast cancer

1. Kangwa A. Nkonde, MSc, k.a.nkonde2@newcastle.ac.uk
1. Sai Man Cheung, PhD, gabe.cheung@newcastle.ac.uk
2. Nicholas Senn, PhD, nicholas.senn2@abdn.ac.uk
3. Ehab Husain, PhD, ehab.husain@nhs.scot
4.Yazan Masannat, MD, yazan.masannat1@nhs.net
1. Jiabao He, PhD, jiabao.he@newcastle.ac.uk

1. Newcastle Magnetic Resonance Centre, Translational and Clinical Research Institute, Faculty of Medical Sciences, Newcastle University
2. Institute of Medical Sciences, School of Medicine, Medical Sciences and Nutrition, University of Aberdeen
3. Pathology Department, Aberdeen Royal Infirmary
4. Breast Unit, Broomfield Hospital, Mid and South Essex NHS Trust

Introduction: Transverse relaxation time (T_2) of breast tumours is affected by the local structural and biochemical micro-environment and is indicative of associated disease processes [1]. The single-compartment model, although commonly adopted for mathematical simplicity and computational speed, does not capture the complexity of biological tissue, demanding multi-compartment (MC) approaches[2]. The non-linear least squares (NLLS) and Bayesian parameter estimation (BPE) algorithms have been applied to estimate parameters in MC models in parts of human body outside the breast [3]. NLLS allows the estimation of T_2 based on minimising the sum of squares of errors, suffering from potential overfitting and consequent misinterpretation. BPE has been introduced using the constraints imposed by neighbouring voxels [4]. We therefore set out to examine the NLLS and BPE algorithms for quantitative T_2 maps acquired on a clinical scanner from breast tumour specimens.

Methods: Twenty tumour specimens freshly excised from female patients with breast cancer (invasive ductal carcinoma, 10/10 grade II/III) were placed in 10% buffered formalin solution immediately after surgery (Figure 1). The study was approved by the North-West – Greater Manchester East Research Ethics Committee (Identifier: 16/NW/0221), and signed written informed consent was obtained from all participants prior to the study.

Acquisition: Five repeated quantitative T_2 images were acquired from each specimen on a clinical 3T MRI scanner (Achieva TX, Philips Healthcare, Best, Netherlands), using multishot gradient and spin echo (GRASE) sequence, with 24 echo times (TE) from 13 ms to 312 ms at an echo spacing of 13 ms, FOV of 141 × 141 mm^2 and image resolution of 2.2 × 2.2 x 2.2 mm mm^2.

Analysis: Voxel-wise two-compartment analysis was performed in MATLAB (R2021a, MathWorks, Natick, USA) using NLLS based on Levenberg-Marquardt algorithm and BPE based on a flat prior. The fitting was performed over the regions-of-interest (ROIs) encompassing the whole tumour, to compute the short and long T_2 components (T_{2S} and T_{2L}) and the restricted water fractions (f) in a two-compartment model. T_{2S} and T_{2L} components characterise the intra- and extracellular water compartments, respectively [5], with f representing the signal ratio in the two compartments [6]. The mean of each parameter was calculated within the ROI for each specimen across acquisitions.

Statistics: Statistical analysis was performed in SPSS statistical software (IBM SPSS Statistics, Version 27.0, Armonk, USA) . Within-subject coefficients of variations (%wCV) of the BPE and NLLS of the two-compartment parameters were calculated [7], and Wilcoxon tests performed to compare the variations in parameters between the two methods. The correlations of f, T_{2S} and T_{2L} between BPE and NLLS were performed using Spearman's correlation test [8]. A p-value < 0.05 was considered statistically significant.

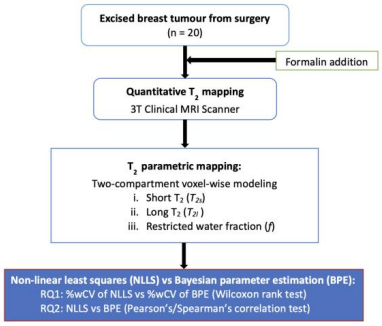

Figure 1. Study design.

Results: There was a significant difference between the %wCV of $T_{2L,\,NLLS}$ (1.27%) and $T_{2L,\,BPE}$ (2.11%), p = 0.019 (Figure 2.a). There were no significant differences between $T_{2S,\,NLLS}$ (3.60%) and $T_{2S,\,BPE}$ (3.90%), p = 0.083, and between $f_{,NLLS}$ (10.18%) and $f_{,\,BPE}$ (6.51%), p = 0.498 (Figure 2.a). There were significant positive correlations between f_{BPE} and f_{NLLS} (r = 0.795, p < 0.001, Figure 2.b), $T_{2L,\,BPE}$ and $T_{2L,\,NLLS}$ (ρ = 0.529, p < 0.018, Figure 2.c), and $T_{2S,\,BPE}$ and $T_{2S,\,NLLS}$ (r = 0.484, p < 0.031, Figure 2.d).

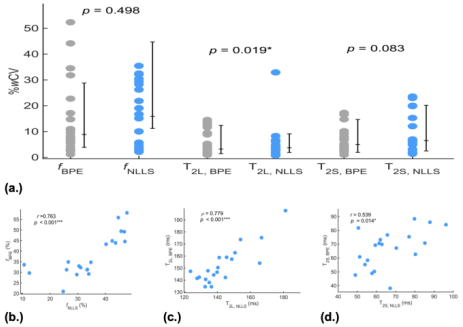

Figure 2. Model stability comparison and correlation of Bayesian parameter estimation methods (BPE) and Non-linear least squares (NLLS) methods.

Discussion: The two-compartment model may offer more refined representation of cellular structure within breast tumours than single-compartment model. All values of %wCV were less than 10%, except for the water fraction from NLLS. There were significant correlations between the parameters from BPE and NLLS.

Conclusion: Bayesian and least squares methods show promise for analysing two-compartment breast cancer models, potentially providing more refined estimates of the underlying biological process.

References

1. Kiselev VG, Novikov DS. Transverse NMR relaxation in biological tissues. *Neuroimage*. 2018.
2. Ababneh Z, Beloeil H, Berde CB, Gambarota G, Maier SE, Mulkern R V. Biexponential parameterisation of diffusion and T2 relaxation decay curves in a rat muscle edema model: decay curve components and water compartments. *Magn Reson Med*. 2005.
3. Kumar D, Nguyen TD, Gauthier SA, Raj A. Bayesian algorithm using spatial priors for multiexponential T2 relaxometry from multiecho spin echo MRI. *Magn Reson Med*. 2012.

4. Bretthorst GL, Hutton WC, Garbow JR, Ackerman JJH. Exponential Parameter Estimation (in NMR) Using Bayesian Probability Theory. *Magn Reson Med*. 2005.
5. McSweeney MB, Small WC, Goldstein JH, Sewell CW, Powell RW. Nuclear magnetic resonance (NMR) relaxation characteristics of human breast tissue. *Magn Reson Imaging*. 1982.
6. Sabouri S, Chang SD, Savdie R, et al. Luminal Water Imaging: A New MR Imaging T2 Mapping Technique for Prostate Cancer Diagnosis. *Radiol*. 2017.
7. Barnhart HX, Barboriak DP. Applications of the Repeatability of Quantitative Imaging Biomarkers: A Review of Statistical Analysis of Repeat Data Sets. *Transl Oncol*. 2009.
8. Barnhart HX, Haber MJ, Lin LI, Lin L. An Overview On Assessing Agreement With Continuous Measurement. *J Biopharm Stat*. 2007.

Estimation of Apparent diffusion coefficients of the three major metabolites measured in the human brain at 3 T

Z. Javed[1], G. Collier[1,2], N. Hoggard[1], J.M. Wild[1,2]
[1]Section of Medical Imaging and Technologies, Faculty of Health, University of Sheffield, Sheffield, UK
[2]INSIGNEO institute, University of Sheffield, Sheffield, UK

Introduction: Diffusion-weighted proton magnetic resonance spectroscopy (DW-MRS) offers the ability to assess the physiological micro-environments of metabolites in the human brain [1], which can be indicative of various neurological conditions. In this work a DW-STEAM sequence was implemented at 3T and the diffusion characteristics of neuronal and glial metabolites N-acetylaspartate (NAA), Choline (Cho) and Creatine (Cr) were analysed in phantoms and healthy human brains.

Methods: The vendor sequence, stimulated echo acquisition mode (STEAM) [2], was modified to diffusion weighted sequence (DW-STEAM) by applying paired diffusion gradients (represented by white pulses in Fig. 1.a) in each of the x, y and z directions. Conventional radio frequency (RF) 90° pulses were applied along with slice select gradients (represented by vertical grey lines). A crusher gradient (represented by diagonal grey lines) was applied in the read direction (G_y) only to minimise unwanted coherences. The b-value measures the degree of diffusion weighting applied, thereby indicating the amplitude (G), time of applied gradients (δ) and duration between the paired gradients (Δ).

$$\mathbf{b}=\gamma^2 G_1^2[\delta^2\left(\Delta-\frac{\delta}{3}\right)+\zeta^3/\mathbf{30}-\delta\zeta^2/\mathbf{6}]$$

where (γ) is the gyromagnetic ratio and (ζ) is the gradient slope duration.

The apparent diffusion coefficient was calculated as;

$$ADC=\frac{ln\,[S_m\,(b_2)/S_m\,(b_1)]}{b_2-b_1}$$

where $S_m\,(b_2)$is the maximum peak intensity for each metabolite, m from the spectrum acquired with b-value b_2. $S_m\,(b_1)$ is the maximum peak intensity for each metabolite, m from the spectra with b-value b_1.

All MR experiments were performed using a GE 3T Signa PET/MR scanner. A 24 cm inner diameter eight channel birdcage volume coil was used as a transmitter and receiver. The sequence was first tested using the BRAINO phantom [3] containing the required metabolites at concentrations mimicking the human brain. For in-vivo testing, three healthy volunteers were scanned using the modified DW-STEAM sequence. Anatomical T1-weighted (T1w) images were initially acquired using a FLAIR sequence to position the MRS voxel and the acquisition parameters were kept as follows; repetition time (TR):1500ms, effective echo time (TEeff): 35ms, field of view (FOV): 24 x 24 (mm), voxel: 20x 20x20 $(mm)^3$, number of averages (NA): 8, number of coils (Nc):8, mixing time (TM):13.7ms, spectral width (sw)=5000 Hz, total acquisition time: 2min 12sec. The following diffusion weighting conditions were used: b= [378.2,968.2,1512.8,6671.7,9455.3] s/cm^2 with diffusion gradients applied in three orthogonal directions [5,5,5] mT/m, [8,8,8] mT/m, [10,10,10] mT/m, [21,21,21] mT/m, [25,25,25] mT/m in the VOI coordinate system.

Results: The phantom results produced high diffusivities for all three metabolites due to the absence of cellular barriers and metabolic activity in the homogeneous phantom. The DW-STEAM sequence was tested on three healthy volunteers. Fig. 1.b shows the plot of the logarithm of the mean metabolite intensities versus the b-values. Additionally, the ADC values for every single metabolite are also displayed in units of cm^2/s. The ADC values obtained are in agreement with literature [4]. Good quality spectra were obtained for all participants and one representative spectrum is presented

in Fig. 1.c where the metabolites identified include the following: NAA at 2.0 ppm, Cr at 3.0 ppm, Cho at 3.2 ppm.

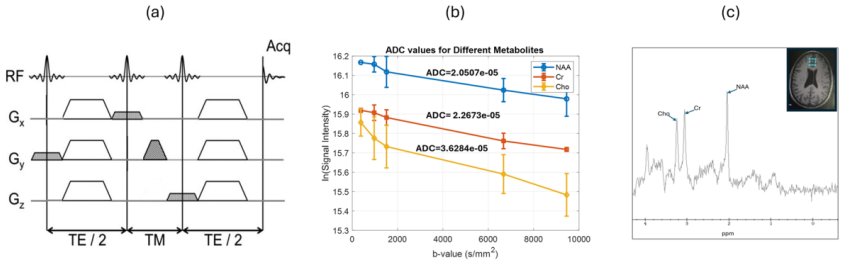

Fig. 1. (a) The DW-STEAM pulse sequence, (b) Data represent logarithm of the mean metabolite intensities ± standard error versus b-values. The calculated ADC values for each metabolite are also indicated, (c) Example of an MR spectrum acquired at the lowest value of b=378.2 for a healthy volunteer. The voxel position in the prefrontal cortex region is shown in the inset.

Discussion: The estimation of diffusion coefficients for the three major metabolites—N-acetylaspartate (NAA), creatine (Cr), and choline (Cho)—in the human brain at 3T provides critical insights into the microstructural and functional characteristics of neural tissue. Diffusion-weighted spectroscopy allows for a non-invasive investigation of the diffusivity of these metabolites, reflecting their movement within the extracellular and intracellular spaces. Our findings indicate that NAA, predominantly located in neurons, exhibits a more restricted diffusion profile when compared to Cr and Cho, which are associated with energy metabolism and cell membrane turnover, respectively. This differentiation is crucial for enhancing our understanding of normal brain physiology and can serve as a baseline for detecting pathological changes. For instance, alterations in the diffusion properties of these metabolites might indicate early signs of neurodegenerative diseases, such as Alzheimer's disease, or the presence of brain tumors [5]. Thus, the ability to accurately measure and interpret the diffusion coefficients of NAA, Cr, and Cho represents a significant advancement in the field of neuroimaging, offering potential for improved diagnosis and monitoring of various neurological conditions.

Conclusions: The results demonstrate distinct diffusion characteristics for NAA, Cr, and Cho, contributing to a more nuanced understanding of metabolic processes in the brain. This preliminary study validates that diffusion weighted spectroscopy holds potential for enhancing diagnostic precision and monitoring the progression of neurological disorders through non-invasive means.

Acknowledgements: This work is funded by the Imaging and Engineering for Health research theme of NIHR Sheffield Biomedical Research Centre (BRC).

References

[1] Ligneul C, Najac C, Döring A, et al. Magn Reson Med. 91: 860-885(2024).
[2] Ruschke S, Kienberger H, Baum T, et al. Magn Reson Med. 75(1): 32-41(2016).
[3] Schirmer, T. and Auer, D.P. NMR Biomed. 13: 28-36(2000).
[4] S Posse, C A Cuenod, and D Le Bihan. Radiology. 188:3, 719-725(1993).
[5] De Marco R, Ronen I, Branzoli F, et al. Brain Behav Immun. 99:256-265(2022).

Towards phase contrast MRI of stratified multiphase flows: a probe for rheology under combined shear and extension

Richard Hodgkinson[1], Steven Reynolds[2]
[1]Department of Materials Science and Engineering, University of Sheffield, Sheffield.
[2]Preclinical MRI Facility, Faculty of Heath, University of Sheffield, Sheffield.

Introduction: A fluid packet may be strained via shearing or extension, and rheology studies a fluid's stress response to such strains. Behaviour can be very different under extensional vs. shear flow for complex fluids, making it critical to understand for situations such as polymer processing. Since changes to underlying microstructure generate rheological responses, it is a cross-coupling factor in kinematically mixed flows, flows with simultaneous shear and extension. Until now there was no method to directly and simultaneously probe specific stress responses of fluids under combined deformation: changes in full-field data such as velocity/flow pattern[1] and birefringence[2-4] could potentially be attributed to either extensional[5], shear[6], or time dependant rheology[7]. A previous study by us developed an optical PIV (particle image velocimetry) two-phase flow technique, using an immiscible Newtonian oil acting as a shear stress sensor above a non-Newtonian aqueous phase[8], allowing measurement of shear rheology under simultaneous combination of shear and extensional deformation. However, optical techniques limit the variety of materials which may be accessed. Flow velocimetry by Phase-Contrast (PC) MRI can examine a wider range of fluids, e.g. opaque suspensions, and chemically resolve these. The aim of this project is to establish a MRI method for measuring velocity profiles for two contacting, stratified, flowing immiscible fluids, one Newtonian, the other non-Newtonian. Here we outline the preliminary develops undertaken in realising this.

Methods: For development purposes phantoms carrying separate flowing fluids were placed side by side. MRI velocimetry was performed using a horizontal bore Bruker 7T, 70/30, MRI scanner running Paravision 7.0. Custom pulled glass phantoms (axisymmetric taper in/tapered out constriction from 26 mm to 4 mm over a length of 100 mm) provided proof of concept extensional flow velocity profiles for PDMS silicone oil/water, Figure 1, which was imaged using a standard FLOWMAP sequence. This sequence was adapted to provide interleaved chemical shift selective velocity maps, with non-spatially selective rf-pulse (PW 7.0 ms, BW 600 Hz, FA 90°) alternately applied at the glycerol/water resonances (-1.5 ppm wrt water, 0.0 ppm) or silicone oil (-4.55 ppm). Alternating with these frequencies, a slice selective excitation pulse was applied (1.16 mm slice thickness; PW 14.0 ms, BW 300 Hz, FA 30°) and signal acquired at -4.55 or -1.5 ppm. Three flow direction were encoded up to 50 cm/s; TE/TR 13.1/500 ms, FOV 32x32 mm, Matrix 128x128. Data was post-processed using Matlab.

Results and Discussion: Proof of principle velocity map images have been measured for the pulled glass phantom tubes, successfully resolving the velocity profiles for the two fluids at the narrowest point of the tubes, see Figure 1. The polydimethylsiloxane (PDMS) oil has the advantage of a simple

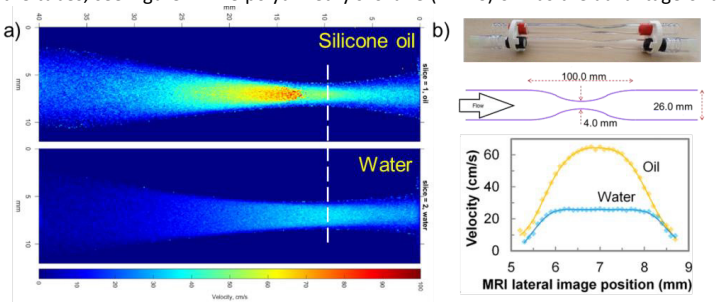

Figure 1: Velocity map images from the twin tapered phantom containing silicone oil alongside water. The in-plane velocity profile at the location indicated by the white dashed line is shown, b.

NMR spectrum, see Figure 2, with a well-defined methylated silicone peak 4-5 ppm downfield from water. At &T the glycerol peak in water/glycerol mixture is sufficiently well separated upfield (~3.3 ppm) for selective excitation without excessively long pulse duration, Figure 2.

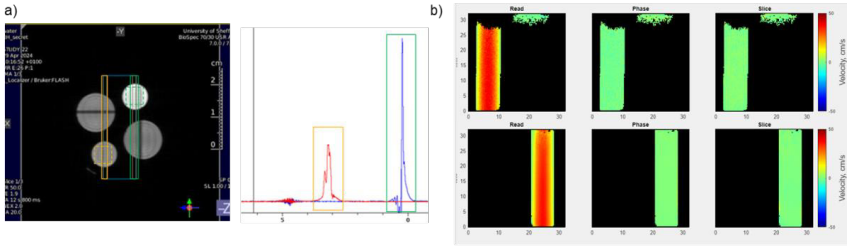

Figure 2: Straight tube (dia. 12 mm) phantoms were used as a simple benchmark with PDMS silicone oil/application representative 18% water: 82% glycerol solution. Two water filled vials (dia. 8 m) were included for static fluid checks a) left, localiser image showing slice locations (solid box) and PRESS voxels (dashed box) for water/glycerol (orange) and silicone oil (green).; right PRESS spectra. b) FLOWMAP images for water/glycerol (top) and silicone oil (bottom).

Future steps and challenges: Work is ongoing to develop the flow cell rig with a stable flow of two immiscible fluids, where the interface between these passes through the centre of a tapered constriction, see Figure 3. Development comprises:

1. Two-piece dissimilar surface flow cell phantom to control fluid wetting profile (a)
2. MR compatible flow level control/sensor in flow splitter tank (b) and peristaltic pumps (c)
3. MR compatible low-cost cameras for remote experiment monitoring
4. Packaging of system in MR-compatible sled and setup procedure development
5. Investigate the observation of linear velocity field in static fluid for short TE
6. Add SPIRAL readout to imaging sequence

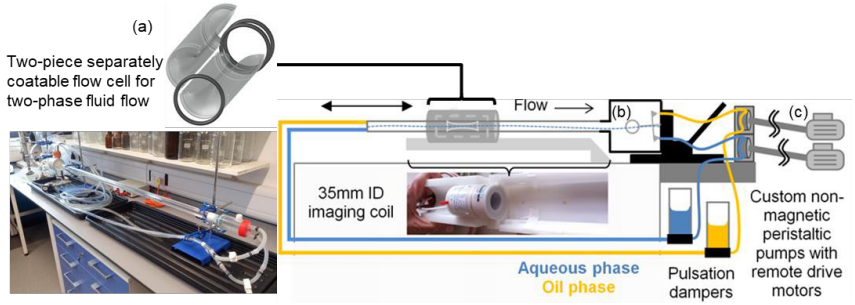

Figure 3: Develop of MR-compatible two-phase flow cell rig

References

1. Alves, M. A., *et al.*, *Journal of Rheology* (2008) **52** (6), 1347
2. Lee, K., *et al.*, *Journal of Rheology* (2001) **45** (6), 1261
3. Liu, Q., *et al.*, *Rheologica Acta* (2022) **61** (2), 139
4. Olley, P., *et al.*, *Plastics, Rubber and Composites* (2021) **50** (1), 18
5. Haward, S. J., *et al.*, *Physical Review Letters* (2012) **109** (12), 128301
6. Trebbin, M., *et al.*, *Proceedings of the National Academy of Sciences* (2013) **110** (17), 6706
7. Varchanis, S., *et al.*, *Journal of Non-Newtonian Fluid Mechanics* (2022) **300**, 104698
8. Hodgkinson, R., *et al.*, *Journal of Rheology* (2022) **66** (4), 79.

Magnetic Resonance Imaging (MRI) as a tool to characterize viscoelastic behaviours of syrup free vegan soft candies

Pelin Pocan[1], Jim Hall[1], Rob Morris[1]
[1]Department of Physics & Mathematics, School of Science &Technology, Nottingham Trent University, Nottingham, United Kingdom

Introduction: Gelatin, which is frequently used as a gelling agent in soft candies, is not preferred by a certain segment of the society who have preferred a vegan diet, due to its animal origin. At this point, agar-agar obtained from the cell wall of red algae constitutes a very suitable alternative to gelatin [1]. Apart from vegan concerns, the use of sweeteners such as sugar alcohols is gaining importance in the confectionery industry, as the demand for low calorie products is increasing. Another concern about confectionery products is the use of corn syrup, which is frequently used to increase shelf life, increase stability, prevent crystallization and reduce cost. Within the scope of this study, the production potential of agar-agar-based vegan candies in the presence of different sugars and concentrations, without corn syrup, will be investigated and these samples were characterized through MRI experiments. For this purpose, agar-agar-based, syrup free vegan soft candies containing different types of sugars (sucrose, glucose, fructose) and sweeteners (erythritol) at different concentrations (20,30,40,50,60%) were formulated. Since these different types of sugars and sweeteners have distinct viscosities, their viscosity changes were tried to be detected through T_1 (spin-lattice) relaxation time constants obtained through Magnetic Resonance Imaging (MRI). The main objective of this study is to explore the power of MRI to monitor the viscosity changes of vegan soft candies containing different type of sugar and sweeteners and trying making correlations between their viscosities and T_1 relaxation times obtained through Magnetic Resonance Imaging (MRI)

Methods: Agar based vegan soft candies were prepared by considering previous method [1]. 2% (w/v) of agar–agar was dispersed in distilled water, heated up to 50 °C, and properly mixed during this process. Afterward, different powdered sugars (sucrose (SUC), erythritol (ERT), glucose (GLU) or fructose (FRU)) at fixed concentrations (20%,30%,40%,50% and 60%) were added to agar–agar dispersion. This final solution again heated up to 95 °C using magnetic stirrer. After reaching this temperature (95 °C), mixtures were poured into molds and waited at room temperature for 24 h. This process is done and processed separately for all types of sugars.

For the viscosity measurements, Brookfield DV-II + Pro Viscometer (Brookfield Laboratories, INC, USA) was used to determine the viscosities of the agar solutions containing different types of sugars at different concentrations.

For the MRI experiments, 1.5 Tesla clinical MR Scanner (Siemens, Germany) was utilized. Longitudinal T_1 relaxation times were measured by using IR (Inversion Recovery) sequence with TR (repetition time) of 16000 ms and TE (echo time) of 72 ms.

Mono-exponential fitting was conducted on the relaxation curves by using MATLAB.

Results: T2 Weighted images of sucrose containing samples can be seen below (Fig.1) Results of the viscosities (Fig 2) and T_1 relaxation times (Fig.3) obtained through MRI experiments were also shown in below. It was found that, there is a strong, inverse correlation between mono-exponential T_1 relaxation times and viscosities of the samples ($r = -0.59$, $p<0.05$).

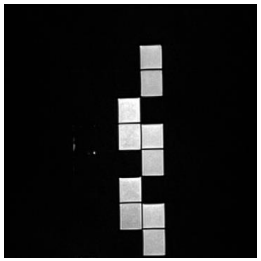

Fig. 1. Representative T_2 weighted Image of sucrose containing agar based vegan soft candies at different concentrations (20%,30%,40%,50% and 60%)

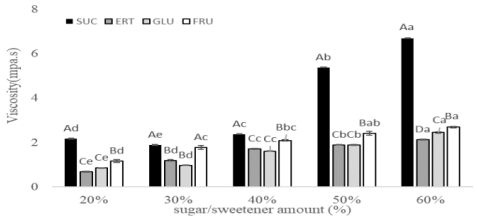

Fig. 2. Viscosities of vegan candies containing different type of sugars (SUC, GLU, FRU and ERT) at different concentrations (20%,30%,40%,50% and 60%)

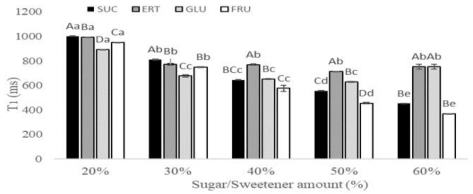

Fig. 3. T_1 relaxation times of vegan candies containing different type of sugars (SUC, GLU, FRU, ERT) at different concentrations (20%,30%,40%,50% 60%)

Discussion: In previous studies different NMR techniques such as Fast Field Cycling (FFC) NMR [2] and Time Domain (TD) NMR [3] were utilized to characterise the soft candies. To best our knowledge, it is the first study that examines the viscoelastic behaviour of soft candies through MRI technique.

Conclusions: It was concluded that T_1 relaxation times obtained through MRI could be utilized as a fingerprint to monitor viscosity changes of syrup free, agar based vegan soft candies containing different type of sugars at different concentrations.

Acknowledgements: Pelin Pocan has received financial support from The Scientific and Technological Research Council of Türkiye (TUBITAK) 2219-International Postdoctoral Research Fellowship Program.

References

[1] Pocan P., Erunsal S.C. *Eur. Food Res.Technol.* (2024). [2] Pocan P., Ilhan E.; et al. *J. Food Eng.*, **294**,110422 (2021). [3] Pocan P.; Ilhan E.,Oztop MH. *Magn. Reson. Chem.*, **57**, 661-673 (2019).

A pipeline for quantitative histological analysis to validate microstructure imaging through diffusion MRI

Elise Gwyther[1], Andrada Ianus[2], Beat Jucker[3], Rui V. Simoes[4], Rafael N. Henriques[2], Tania Carvalho[2], Noam Shemesh[2] ,Derek Jones[1,5], Chantal Tax[1,6], Marco Palombo[1,5]

[1]Cardiff University Brain Research Imaging Centre (CUBRIC), School of Psychology, Cardiff University, Cardiff, United Kingdom; [2]Champalimaud Research, Champalimaud Centre for the Unknown, Lisbon, Portugal; [3]Glaxosmithkline, Pennsylvania, United States; [4]Institute for Research & Innovation in Health (i3S), University of Porto, Porto, Portugal; [5]School of Computer Science and Informatics, Cardiff University, Cardiff, United Kingdom; [6]University Medical Center Utrecht, Utrecht, Netherlands

Introduction

Histology is a recognized gold standard characterization of brain microstructure, essential to validate estimates of microstructural characteristics derived from diffusion-weighted MRI (DW-MRI). However, due to the challenging comparison between imaging modalities with different resolutions and contrasts, qualitative comparisons are often used, neglecting precious information obtainable from histology. In this work, we present an automatic histological analysis pipeline which measures quantitative microstructural features of brain tissue from histological images and reconstructs histological parameter maps for a whole brain slice at the DW-MRI resolution.

Methods

Ex-vivo DW-MRI scans of 7 mouse brains (1 healthy control, 3 with induced GL261 cell line gliomas and 3 with induced CT2A cell line gliomas) were acquired with a PGSE-EPI sequence: TR/TE=3000/20ms, 4 shots, in-plane resolution = 0.1x0.1mm^2; more details in[1]. The SANDI[2] model was fitted to these scans, producing parameter maps for f_{sphere}, f_{stick}, R_{sphere}, f_{ball}, D_{ball}, D_{stick}, as described in[1]. After scanning, each mouse brain was formalin-fixed, paraffin-embedded, sectioned at 4 µm from striatum to caudal hippocampus, and stained with hematoxylin and eosin (H&E)(**Fig.1**). H&E stains nuclei a dark purple and all other tissue a shade of pink. The nuclei were the histological feature selected for analysis, as they were robustly distinguishable from other tissue components. Nuclei and soma morphology are strongly correlated[3], so measurements of nuclei size from histology were related to SANDI estimates of soma radius, R_{sphere}, according to [4]:

$$R_{sphere}(Histology) = \left(\frac{< R^5 >}{< R^3 >}\right)^{\frac{1}{2}} \qquad (1)$$

Where $< R^3 >$ and $< R^5 >$ are the third and fifth moments of the distribution of nuclei radii. The histological analysis pipeline was implemented using *.groovy* scripts in the software QuPath[5]. For each image, the pixel size in µm, and the image height Y and width X in number of pixels were retrieved. To match the MRI resolution, the tile dimension t in number of pixels was calculated by dividing 100µm by the pixel size in µm. Two sets were defined:

$$A = \left[0, \frac{X}{t}\right] \cap \mathbb{Z}, \qquad B = \left[0, \frac{Y}{t}\right] \cap \mathbb{Z}$$

The cartesian product: $tA \times tB = \{(ta, tb) |\ a \in A \text{ and } b \in B\}$ generated a list of coordinates which were used to assign square tiles with area 100µm^2 to locations in the image. The StarDist[6] deep learning model *he_heavy_augment.pb*, which utilizes a U-net architecture to detect nuclei in H&E brightfield images, was applied in each tile. This created a detection object for each nucleus containing an outline of the nuclei, its area in µm^2, and other data. The list of detection objects was exported. The histological parameter map was reconstructed in Python using the nuclei radius in each tile and Eq.1. **Fig.1** shows the analysis steps. The histology slides were matched to DW-MRI slices manually using the tumor and brain shapes as guide. Tumor regions of interest (ROIs) were manually segmented (**Fig.2**). Linear regression analysis was used to examine the relationship between R_{sphere}(SANDI) and R_{sphere}(histology) in the ROIs.

Results

Fig.2c shows a histological parameter map of R_{sphere}(histology). **Fig.2e** shows mean R_{sphere} (histology) against R_{sphere} (SANDI) in tumor ROIs with a linear regression line (slope=0.259, intercept=4.37,

Power Pitch Session 2

Pearson correlation coefficient= 0.789, p value= 0.01).

Discussion and Conclusion

Despite the different slice thickness between MRI and histology, a significant positive linear relationship between the R_{sphere} from SANDI and histology in tumor ROIs was found, which validates the sensitivity of the SANDI model to soma radius. The linear regression line intercept is explained by the lower bound on DW-MRI estimates of soma radius[7]. The slope value can be explained by the cell volume increasing linearly with nuclei volume. The analysis pipeline can work with other DW-MRI methods (e.g., different voxel size and microstructure model) and alternative histological stains which highlight different features of the tissue, with minimal adaptations, e.g. using a different pretrained deep learning model for the segmentation[8][9] . Here we have introduced a histological analysis pipeline which quantitatively analyzed histological images of brain tissue and generated MRI compatible parameter maps. This demonstrates how histology can be used to validate tissue microstructure estimates from DW-MRI models.

Figures

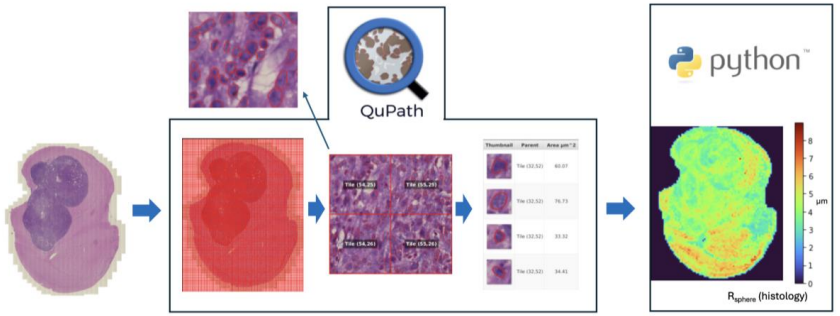

Fig. 1: The quantitative histological analysis pipeline. Red squares show the individual tiles applied to the image. Red outlines show the detection objects (nuclei). The detection object data was exported from QuPath and used to reconstruct the histological parameter map for R_{sphere}(Histology) in Python

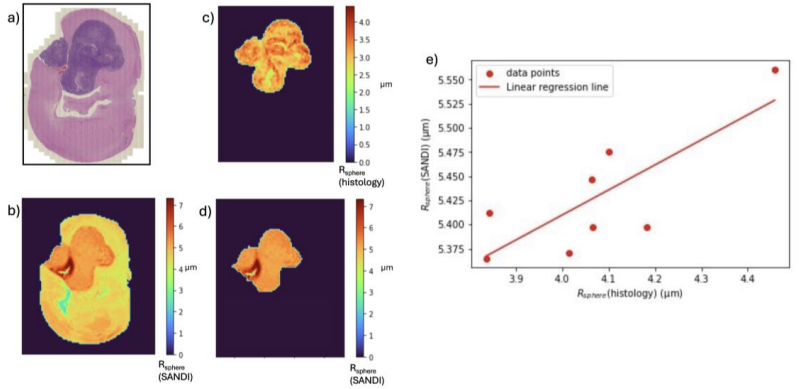

Fig. 2: a) H&E stained histological image; b) R_{sphere}(SANDI) parameter map for the DW-MRI slice corresponding to histology slice in a); c) R_{sphere}(Histology) parameter map for the segmented tumor ROI; d) R_{sphere}(SANDI); e) Graph showing the mean R_{sphere} value in the tumor ROI for the SANDI and histology parameter maps: each datapoint is associated with a single DW-MRI/histology slice.

References

[1] Ianus A. et al. ISMRM 2023

[2] Palombo, M., Andrada Ianus, Guerreri, M., Nunes, D., Alexander, D.C., Shemesh, N. and Zhang, H. (2020). SANDI: A compartment-based model for non-invasive apparent soma and neurite imaging by diffusion MRI. *NeuroImage*, 215, pp.116835–116835.

[3] Wu, Y., Pegoraro, A.F., Weitz, D.A., Janmey, P. and Sun, S.X. (2022). The correlation between cell and nucleus size is explained by an eukaryotic cell growth model. *PLOS Computational Biology*, 18(2), p.e1009400.

[4] Olesen, J.L., Østergaard, L., Shemesh, N. and Jespersen, S.N. (2022). Diffusion time dependence, power-law scaling, and exchange in gray matter. *NeuroImage*, 251(06), pp.118976–118976.

[5] Bankhead, P. et al. QuPath: Open source software for digital pathology image analysis**.** *Scientific Reports* (2017)

[6] Uwe Schmidt, Martin Weigert, Coleman Broaddus, and Gene Myers. Cell Detection with Star-convex Polygons. *International Conference on Medical Image Computing and Computer-Assisted Intervention (MICCAI)*, Granada, Spain, September 2018.

[7]Afzali, Maryam, et al. “SPHERIOUSLY? The Challenges of Estimating Sphere Radius Non-Invasively in the Human Brain from Diffusion MRI.” *NeuroImage*, vol. 237, 1 Aug. 2021, pp. 118183–118183

[8]Ahmed, A.A., Abouzid, M. and Kaczmarek, E. (2022). Deep Learning Approaches in Histopathology. *Cancers*, 14(21), p.5264.

[9]Kaczmarzyk, J.R., O’Callaghan, A., Inglis, F., Gat, S., Kurc, T., Gupta, R., Bremer, E., Bankhead, P. and Saltz, J.H. (2024). Open and reusable deep learning for pathology with WSInfer and QuPath. *npj Precision Oncology*, 8(1), pp.1–5.

Power Pitch Session 3

Prediction of progressive disease in treated high grade glioma using DSC-derived oxygen extraction fraction and microvasculature biomarkers

Tamadur A. Alsulami[1], Catarina Pinto[2], João Ramos[3], Laura Mancini[3], Xavier Golay[1], Sotirios Bisdas[3], David L. Thomas[1]

[1]UCL Queen Square Institute of Neurology, University College London, London, United Kingdom
[2] Neuroradiology Department,Centro Hospitalar Universitário Santo António, Porto, Portugal.
[3]Lysholm Department of Neuroradiology, The National Hospital for Neurology and Neurosurgery, London, United Kingdom.

Introduction: Distinguishing progressive disease (PD) from pseudo-progression (PsP) following chemoradiotherapy of high-grade glioma (HGG) has been challenging using conventional MRI [1,2]. Dynamic susceptibility contrast (DSC) MRI could provide an insight into neovascularisation and the tumour microvasculature [3,4], which potentially could aid early detection of PD. Therefore, the aim of this work was to assess the added value of DSC-derived microvascular and oxygen metabolism biomarkers, compared to the conventional perfusion parameters, to predict progression in treated HGG.

Methods: This retrospective data analysis was performed under local ethical approval permitting analysis of images acquired for clinical management at University College London Hospitals (UCLH). Patients with histopathologically proven HGG, who developed new or enlarging enhancing lesions after completing standard-of-care concurrent chemoradiotherapy (CCRT) with temozolomide, were consecutively identified. Subjects were scanned between 2017 and 2021 using a 3T Prisma (Siemens Healthineers, Germany) and 3T Achieva (Philips Healthcare, Netherlands). In addition to the well-established rCBV and rCBF analysis using two different software packages (Cercare (Cercare Medical, Aarhus, Denmark) and NordicICE (NordicNeuroLab, Bergen, Norway)), oxygen extraction fraction (OEF), relative cerebral metabolic rate of oxygen ($rCMRO_2$), and capillary transit-time heterogeneity (CTH) were also obtained from the Cercare software. Enhancing lesions were segmented manually on 3D post-contrast T1-weighted images co-registered to the raw DSC time course images by two experienced neuroradiologists. To obtain the normalised relative values of rCBV and rCBF (from both software) and $rCMRO_2$, tumour ROI values were normalised to the contralateral normal appearing white matter in the post-contrast images. Differences in DSC-biomarkers between PD and PsP groups were assessed using the Mann-Whitney U test. The ability of these parameters to differentiate PD from PsP was assessed by receiver operating characteristic (ROC) curves. Logistic regression was carried out to investigate whether the combination of two or more parameters could enhance the diagnostic accuracy of the discrimination.

Results: Thirty patients with HGG were included. Based on clinical-radiological criteria, 19 were classified as PD, whilst 11 as PsP (see Table 1). Progressing lesions exhibited significantly lower OEF, with a median of 11% [interquartile range (IQR): [5, 35]] compared to that in PsP group (median 46% [IQR: [15, 77]]), (p= 0.01, Table 2 and Figure 1). However, the differences in CTH and normalised $rCMRO_2$, $rCBV_{Cercare}$, $rCBV_{NodicICE,}$ $rCBF_{Cercare}$, $rCBF_{NodicICE}$ between these groups were not statistically significant (Table 2). Moreover, OEF yielded the highest AUC, sensitivity and specificity (0.73, 0.72 and 0.67, respectively (Table 2). Combining normalised rCBV and $rCMRO_2$ measurements with OEF improved AUC and senstivity to 0.82 and 0.83, respectively (Table 2 and Figure 2).

Discussion: In this study, PD of post-treatment HGG was associated with significantly lower OEF than in the PsP group, consistent with a previous study in glioblastoma (GBM) [5], a type of HGG. Although it is known that GBMs typically show severe hypoxia, interestingly, both low- and high grade of glioma and peritumoral brain tissue also present with hypoxia [6], and hypoxia-inducible factors are found to be overexpressed [7]. In PsP, to compensate for CBF reduction and to maintain neuronal function and cellular integrity following the onset of cerebral ischemia, OEF typically increases [8]. The difference in rCBV and rCBF between the two groups was statistically insignificant, which was a consistent finding for both analytical software packages and can be explained by the fact that hypoxia occurs independently of perfusion [9], and tumor oxygenation cannot be inferred from the degree of angiogenesis (i.e. CBV) or CBF solely [10]. The reduction in OEF in PD was accompanied by an insignificant elevation of $rCMRO_2$ compared to the PsP group (Table 2). This can be explained by the theory of the negative correlation between $CMRO_2$ and OEF. In extensive angiogenesis and chaotic microvasculature topology, oxygen extraction tends to be less efficient [10]. It is anticipated that abnormal capillary bed morphology and shunts associated with neovascularisation could lead to an elevated CTH [11,12]. However, Park et el. [5] observed elevated CTH values in PsP compared to that in recurrence, whilst this did not reach a significance level in the current study, which is conceivably because of the smaller sample size and the heterogeneity in genetics and histological information.

Power Pitch Session 3

Conclusions: This work showed that OEF has the potential to discriminate between groups of PD and PsP, at early post chemoradiation stage of HGG. The combination of OEF, $rCMRO_2$ and rCBV could lead to a further improvement in diagnostic accuracy.

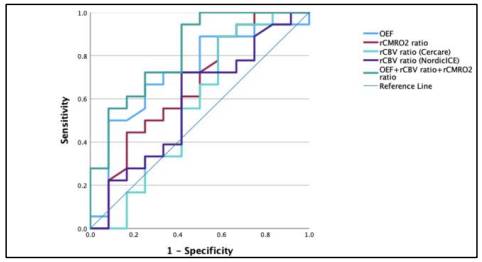

Fig. 2. Receiver operating characteristic (ROC) curves of DSC derived OEF and normalised $rCMRO_2$ and rCBV and their combination. Area under curves (AUC) [95%CI] are in Table 2.

Table 1. Characteristics of studied cohort. WHO: world health organisation; CCRT: concurrent chemoradiotherapy.

	All Patients n=30	Progression Group n=19	Pseudo-progression Group n=11
Median age (range) *years*	58.5 (32–79)	58.7 (32 –79.8)	56.8 (39.9–72)
Initial WHO diagnosis			
IV	19	14	5
III	11	5	6
Histology			
glioblastoma	19	14	5
astrocytoma	10	4	6
oligodendroglioma	1	1	0
Isocitrate dehydrogenase (*IDH*) mutation status			
wild-type	17	13	4
mutant	11	5	6
NA	2	1	1
1p/19q status of *IDH* mutant glioma			
retained	10	4	6
co-deleted	1	1	0
O6-methylguanine-DNA methyltransferase *(MGMT)* promoter methylation status			
unmethylated	9	7	2
methylated	17	9	8
NA	4	3	1
Integrated WHO diagnosis			
IV	17	13	4
III	11	5	6
NA	2	1	1
Median time interval between CCRT end and imaging (range) *months*	2.8 (0–6.8)	2.3 (1–5.3)	3.1 (0-6.8)

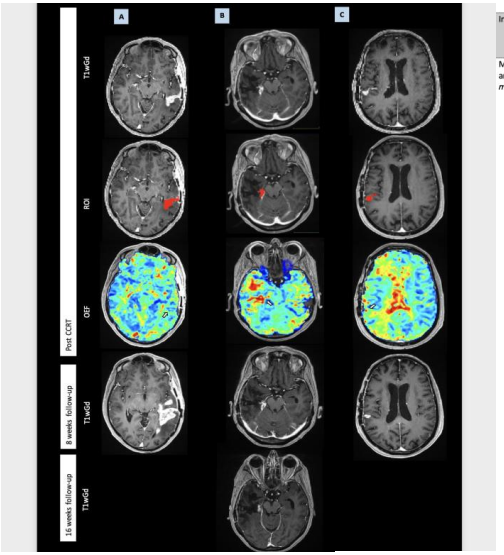

Fig. 1. A. True progression example. An enlarging enhancing lesion in the left temporal region, with relatively low OEF post CCRT. Follow-up MRI showed a marked interval progression in the extent and degree of nodular enhancement. **B,C.** Pseudo-progression examples. **B.** Enhancing lesion in the right temporal lobe , with elevated OEF post CCRT. The lesion seems to resolve in two subsequent follow-up exams. **C.** A peripherally enhancing nodule in the supramarginal gyrus of the right parietal lobe showed an area of somewhat elevated OEF and the lesion does appear to have decrease in size in follow-up.

Table 2. Differences in DSC-derived biomarkers between progression and pseudo-progression in high grade glioma, and corresponding diagnostic accuracy metrics. IQR: interquartile range. AUC: area under curve; CI: confidence interval; *: statistically significant.

DSC-biomarker	Quantitative Differences			Diagnostic Accuracy		
	Progression n = 19	Pseudo-progression n = 11	*p*-value	Sensitivity	Specificity	AUC [95% CI]
	median [IQR]	median [IQR]				
OEF [%]	11.0 [5.0, 35.0]	46.0 [15.0, 77.0]	0.01*	0.72	0.67	0.73 [0.53, 0.91]
normalised $rCMRO_2$	1.32 [0.90, 1.62]	1.05 [0.40, 1.40]	0.14	0.61	0.59	0.66 [0.45, 0.87]
CTH [*seconds*]	6.2 [4.37, 7.56]	6.5 [5.21, 12.82]	0.66	0.60	0.50	0.56 [0.32, 0.77]
normalised rCBV Cercare	1.41 [1.10, 1.71]	1.30 [0.65, 1.70]	0.34	0.67	0.50	0.60 [0.43, 0.85]
normalised rCBV NordicICE	1.48 [1.03, 1.84]	1.25 [0.83, 1.81]	0.20	0.72	0.60	0.65[0.38, 0.82]
normalised rCBF Cercare	1.08 [0.5, 2.46]	1.09 [0.18, 2.44]	0.78	0.60	0.50	0.52 [0.34, 0.80]
normalised rCBF NordicICE	1.27 [0.53, 3.15]	1.30 [0.29, 9.0]	0.64	0.63	0.50	0.58 [0.36, 0.80]
OEF+rCBV+$rCMRO_2$				0.83	0.60	0.82 [0.66, 0.97]

References

[1] Mullins ME, Barest GD, Schaefer PW, Hochberg FH, Gonzalez RG, Lev MH. Radiation necrosis versus glioma recurrence: conventional MR imaging clues to diagnosis. *AJNR Am J Neuroradiol*. 2005;26(8):1967-1972.

[2] Stockham AL, Tievsky AL, Koyfman SA, et al. Conventional MRI does not reliably distinguish radiation necrosis from tumor recurrence after stereotactic radiosurgery. *J Neurooncol*. 2012;109(1):149-158.

[3] Hansen MB, Tietze A, Kalpathy-Cramer J, et al. Reliable estimation of microvascular flow patterns in patients with disrupted blood-brain barrier using dynamic susceptibility contrast MRI. *J Magn Reson Imaging*. 2017;46(2):537-549. doi:10.1002/jmri.25549

[4] Kickingereder P, Brugnara G, Hansen MB, et al. Noninvasive Characterization of Tumor Angiogenesis and Oxygenation in Bevacizumab-treated Recurrent Glioblastoma by Using Dynamic Susceptibility MRI: Secondary Analysis of the European Organization for Research and Treatment of Cancer 26101 Trial. *Radiology*. 2020;297(1):164-175. doi:10.1148/radiol.2020200978

[5] Park JE, Kim HS, Kim N, et al. Prediction of pseudoprogression in post-treatment glioblastoma using dynamic susceptibility contrast-derived oxygenation and microvascular transit time heterogeneity measures. *Eur Radiol*. Published online October 18, 2023. doi:10.1007/s00330-023-10324-9

[6] Collingridge DR, Piepmeier JM, Rockwell S, Knisely JP. Polarographic measurements of oxygen tension in human glioma and surrounding peritumoural brain tissue. *Radiother Oncol*. 1999;53(2):127-131. doi:10.1016/s0167-8140(99)00121-8

[7] Zagzag D, Zhong H, Scalzitti JM, Laughner E, Simons JW, Semenza GL. Expression of hypoxia-inducible factor 1alpha in brain tumors: association with angiogenesis, invasion, and progression. *Cancer*. 2000;88(11):2606-2618.

[8] Fan AP, Khalil AA, Fiebach JB, et al. Elevated brain oxygen extraction fraction measured by MRI susceptibility relates to perfusion status in acute ischemic stroke. *J Cereb Blood Flow Metab*. 2020;40(3):539-551. doi:10.1177/0271678X19827944

[9] Bruehlmeier M, Roelcke U, Schubiger PA, Ametamey SM. Assessment of hypoxia and perfusion in human brain tumors using PET with 18F-fluoromisonidazole and 15O-H2O. *J Nucl Med*. 2004;45(11):1851-1859.

[10] Bonekamp D, Mouridsen K, Radbruch A, et al. Assessment of tumor oxygenation and its impact on treatment response in bevacizumab-treated recurrent glioblastoma. *J Cereb Blood Flow Metab*. 2017;37(2):485-494. doi:10.1177/0271678X16630322

[11] Ostergaard L, Tietze A, Nielsen T, et al. The relationship between tumor blood flow, angiogenesis, tumor hypoxia, and aerobic glycolysis. *Cancer Res*. 2013;73(18):5618-5624. doi:10.1158/0008-5472.CAN-13-0964

[12] Stadlbauer A, Mouridsen K, Doerfler A, et al. Recurrence of glioblastoma is associated with elevated microvascular transit time heterogeneity and increased hypoxia. *J Cereb Blood Flow Metab*. 2018;38(3):422-432. doi:10.1177/0271678X17694905

Power Pitch Session 3

Automatic Segmentation of Pediatric Brain Tumours using Diffusion-weighted MRI: Downstream Performance in a Diagnostic Classifier

Daniel Griffiths-King[1], Timothy Mulvany[1], Andrew Peet[2,3], John Apps[2,3], Jan Novak[1]
[1]Aston Institute of Health and Neurodevelopment, Aston University, Birmingham, United Kingdom
[2]Department of Oncology, Birmingham Childrens Hospital, Birmingham, United Kingdom
[3] Institute of Cancer and Genomic Sciences, University of Birmingham, Birmingham, United Kingdom

Introduction: Segmentation of pathological tissue on MRI is crucial for analysing imaging biomarkers from brain tumours, such as extracting the apparent diffusion coefficient (ADC) from diffusion-weighted MRI (DWI) to provide insights into the tumour microenvironment and classify tumour types.

Manual segmentation by expert neuroradiologists is costly, time-consuming, and prone to inter- and intra-rater disagreement [1], making it unsuitable for clinical implementation. Automated deep-learning approaches offer a promising alternative, demonstrating reasonable performance in adult datasets [2] and recent translation into pediatrics [3]. These automated approaches are typically evaluated by comparing predicted segmentations against expert-drawn 'ground truth' segmentations. However, in clinical scenarios where models are applied to unseen data, ground truth comparisons are not possible, highlighting the importance of determining when segmentation performance is sufficient for the downstream tasks that utilise these tumour masks.

This study employed an automated tumour segmentation model using DWI in pediatric brain tumour patients. We evaluated the model's performance on two downstream tasks: extracting ADC radiomic features and classifying tumour diagnosis using these features.

Methods: *Dataset*: Pediatric brain tumour patients (n=107, Table 1) were recruited from the Birmingham Children's Hospital for the UK Children's Cancer and Leukaemia Group Functional Imaging (CCLG-FIG) Database Study. DWI was acquired clinically before surgical intervention or adjuvant therapy.

Image Preprocessing: Apparent diffusion coefficient (ADC) maps were calculated from diffusion signals with B-values of 0 and 1000 s/mm². ADC maps were resampled to 1mm isotropic and intensity-normalised. Ground-truth ROIs were manually drawn on B0 volumes, excluding oedema and large cystic regions.

Automated Segmentation Model: Automated segmentation used Deepmedic (ver.0.8.4) [4], a multi-scale 3D CNN with 11 layers. The model was trained using transfer learning and fine-tuning, with post-processing applied (an approach developed within the lab). Final segmentation masks were generated through 4-fold cross-validation, with modest performance on test data, assessed using Dice score, comparing overlap of automated and ground truth ROIs (mean $Dice_{test}$=.485, median $Dice_{test}$=.567).

ADC Feature Extraction: Using ground truth (GT) and automated segmentation (Autoseg) ROIs, 19 first-order radiomic features were extracted using PyRadiomics [5], describing ADC values within the ROI for each participant.

Analysis: ADC radiomic feature sets were evaluated using intraclass correlation coefficient (ICC) to estimate consistency between the two segmentation approaches. For the diagnostic cohort (n=70, including MB, PA, and EP), ADC feature sets were included in a random forest classifier to predict diagnostic category, using default parameters. Diagnostic accuracy was estimated with leave-one-out cross validation (LOO-CV) for each segmentation approach. Feature importance was estimated using the mean decrease in the Gini index.

Results: The consistency in ADC radiomic features between the GT and Autoseg ROIs was generally poor (mean ICC=.405, median ICC=.405, range=.155-.741), with only seven features achieving an ICC of 0.5 or above. Despite this, the random forest classifier performed well with both GT (Acc.=88.6%, 95% CI [78.7-94.9]) and Autoseg (Acc.=81.2%, 95% CI [69.9-89.6]) features. Limiting the feature set to those with ICC > 0.5 decreased accuracy for the GT model (Acc.=87.1%, 95% CI [77.0-94.0]) but increased it for the Autoseg model (Acc.=85.5%, 95% CI [75.0-92.8]). The top five important features for classification in the best GT model were the 10th Percentile, RMS, Median, Mean, and Min. When the model was trained on GT features but tested on Autoseg features, performance dropped significantly (Acc.=60.9%, 95% CI [48.4-72.4]).

Table 1. Demographic characteristics of the cohort

	Full Cohort	*Diagnostic Classifier Cohort*
N	*N=107*	*N=70*
Sex (M:F)	*54:53*	*32:38*
Age (yrs; Mean(Range))	*6.9 (0.0-16.3)*	*7.0 (0.3-16.3)*
Diagnoses (n)	*25 distinct diagnostic classifications*	*Medulloblastoma (MB, n=27)* *Pilocytic Astrocytoma (PA, n=31)* *Ependymoma (EP, n=12)*

Discussion: The results show that even with modest automated segmentation accuracy, diagnostic classifiers built using radiomic features maintain high accuracy. Our previous work found that systematic dilation/erosion of manually drawn tumour masks biased DWI-derived radiomic features but had little impact on diagnostic classification, especially with feature selection prioritizing feature robustness [6]. The current results echo this in a real-world scenario: while segmentation errors affected DWI radiomic feature extraction, the diagnostic classifier's performance remained robust. However, these results are specific to this downstream task and cohort. It is unclear if they would generalise to hold-out test data, where automatic segmentation performance might decrease due to differences between training and hold-out datasets.

Conclusions: In the context of a clinical DWI biomarker pipeline, we showed that even a modestly performing segmentation algorithm can generate clinically useful ROIs. These perform adequately for the purposes of downstream diagnostic classification in pediatric brain tumours, which could further benefit clinical implementation.

Acknowledgements: Thanks to the Birmingham Children's Hospital Brain Tumour Research Group for their support; researchers, clinicians, and families of the CCLG-FIG study; and "Help Harry Help Others" for funding TM.

References

[1] Zhang, L., et al., *J Advances in Neural Information Processing Systems*, 2020. **33**, 15750-15762 (2020).
[2] Ghosh, A. and S. Thakur. *12th International Conference on Cloud Computing, Data Science & Engineering*. (2022).
[3] Vossough, A., et al., *American Journal of Neuroradiology,* (2024).
[4] Kamnitsas, K., et al. *Brainlesion: Glioma, Multiple Sclerosis, Stroke and Traumatic Brain Injuries: Second International Workshop, BrainLes,* (2016).
[5] van Griethuysen, J.J.M., et al., *Cancer Res,* **77**(21): e104-e107 (2017).
[6] Mulvany, T., et al., *ISMRM British Irish Chapter Postgraduate researcher Symposium*. (2024).

Power Pitch Session 3

Automatic Segmentation of Pediatric Brain Tumours using Diffusion-weighted MRI: Transfer Learning and Multi-input Ensembling Approaches

Daniel Griffiths-King[1], Timothy Mulvany[1], Heather Rose[2], Andrew Peet[3,4], John Apps[3,4], Jan Novak[1]
[1]Aston Institute of Health and Neurodevelopment, Aston University, Birmingham, United Kingdom
[2]College of Engineering and Physical Sci., Aston University, Birmingham, United Kingdom
[3]Department of Oncology, Birmingham Childrens Hospital, Birmingham, United Kingdom
[4]Institute of Cancer and Genomic Sciences, University of Birmingham, Birmingham, United Kingdom

Introduction: Diffusion-weighted MRI (DWI) is valuable for neuroradiological assessment of pediatric brain tumours, providing insights into tumour microenvironment and enabling diagnostic classification [1]. Extracting biomarkers like apparent diffusion coefficient (ADC) requires tumour delineation using regions of interest (ROIs), but manually-drawn ROIs are time-consuming, require expert input, and are subject to inter-/intra-rater variability [2], making them impractical for clinical implementation.

Automated segmentation approaches using deep learning have successfully extracted tumour masks from conventional MRI (T1w, T2w, T2-FLAIR) [3] with accuracy improving when including DWI [4]. However, additional modalities require more resources for processing and inter-modality coregistration, which is challenging in presence of pathology/artefacts [5] and may not be appropriate due to differing sensitivity to tissue types of each modality. By exclusively using DWI images, this study presents a deep-learning model for automated segmentation of pediatric brain tumours from DWI.

Methods: Data from 107 pediatric brain tumor patients (across ~25 tumour types) recruited from Birmingham Children's Hospital to the UK Children's Cancer and Leukaemia Group – Functional Imaging Group (CCLG-FIG) database were used. DWI was acquired during standard care before surgical intervention and/or adjuvant therapy. B0 and B1000 images were extracted from DWI, and parametric ADC maps calculated. B0/B1000 images were corrected for bias field and Gibbs artifact, resampled to 1mm isotropic, and intensity-normalised. ROIs were manually-drawn on B0 volumes using 3D Slicer, with additional modalities reviewed to ensure tumour inclusion and exclusion of oedema and macro-cystic regions. ROIs were iteratively refined by TM and reviewed by JN & DGK until consensus.

Automated segmentation was performed using the Deepmedic package [6], a CNN with 11 layers, including normal- and low-resolution pathways, and three fully-connected layers. A model was trained for each image set (B0/B1000/ADC), generating three probabilistic tumour segmentations. Two models were created, a baseline model trained only on the current cohort data, and a segmentation model, pretrained on open-access T2w MRI data of pediatric brain tumours (n=99) [7], and utilising transfer learning. For the transfer learning, the final three fully-connected layers were retrained, with the remaining layers frozen. Fine-tuning used a smaller learning rate, unfreezing and retraining all layers. Probabilistic segmentations of each image set were post-processed through erosion and dilation using a 3x3 all-ones kernel, producing binary segmentations. Three runs of transfer-learning and fine tuning were run, one for each DWI image (B0/B1000/ADC). Ensembling segmentations from all models (B0/B1000/ADC) was tested using four schemas: i) weighted voting, ii) binary voting, iii) union mask, and iv) intersect mask.
All models were evaluated using 4-fold cross-validation (CV). Post-processing decisions were based on performance on training data, and final results reported for test data folds. Spatial-overlap between segmentations and ground truth ROIs was assessed using cohort average Dice scores (Dice = 2TP / (2TP + FP + FN), where Dice = 1 indicates perfect overlap).

Results: *Model Training*: Model training, across the three DWI images (B0/B1000/ADC), was most successful when using a transfer learning plus fine tuning approach— the models performed better on predicting cases in the training data. Optimal probability thresholds and erosion/dilation steps varied between images. Among ensembling schemas, weighted (probability) voting ($Dice_{train}$=.947) was selected as optimal for training, having outperformed binary voting ($Dice_{train}$=.944), intersection mask ($Dice_{train}$=.904), and union mask ($Dice_{train}$=.814). *Model Testing:* On test data, the fine-tuned ADC model with post-processing performed best ($Dice_{test}$=.485), with substantial improvement in the median Dice score compared to other models ($Dice_{test}$=.567). Only the post-processed ADC model and the ensemble outperformed the baseline model (table 1).

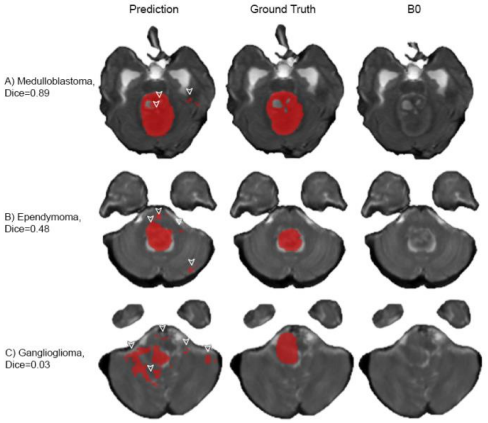

Fig. 1. Examples of tumour masks for individual cases with high (A) to low (C) segmentation performance, based upon Dice score. Arrows indicate areas of prediction error.

Table 1. Performance of best performing models for each modality and for the ensemble (across both train and test cohorts, over all folds).

Modality	Performance			
	$Dice_{train}$	$Dice_{test}$		
	Mean	Mean	SD	Median
Baseline	.976	**.397**	**.276**	**.358**
B0	.830	**.372**	**.286**	**.365**
B1000	.936	**.353**	**.289**	**.310**
ADC	.940	**.485**	**.296**	**.567**
Ensemble[a]	.947	**.459**	**.299**	**.488**

N.B. [a]Weighted voting

Discussion: ADC maps outperformed other DWI images and an ensemble that included the ADC map, despite high performance on training for all models. This supports studies highlighting the sensitivity of ADC metrics to tumour tissue. As the ensemble did not outperform the ADC model, this suggests that inclusion of B0/B1000 volumes may be redundant in such a model. While, the best model's DICE score was still lower than the 2023 BraTS-PEDs Challenge winning score (0.80 for tumour core using typical MR modalities). this study demonstrated that transfer learning and fine-tuning, even with a different imaging modality (T2w vs. DWI), improves segmentation performance versus a comparable baseline model.

Conclusions: Fast, reproducible, accurate and modality appropriate ROIS are vital in the development of advanced radiological assessment in paediatric brain tumours. Here we present deep learning model, with cross-modality transfer learning for DWI based ROI generation.

Acknowledgements: Thanks to the Birmingham Children's Hospital Brain Tumour Research Group for their support; researchers, clinicians, and families of the CCLG-FIG study; and "Help Harry Help Others" for funding TM.

References

[1] Novak, J., et. al., Scientific Reports, 11(1): p. 2987. (2021).
[2] Zhang, L., et al., *J Advances in Neural Information Processing Systems*. **33**, 15750-15762 (2020).
[3] Ghosh, A. & S. Thakur. *12th International Conf. on Cloud Computing, Data Science & Engineering.* (2022).
[4] Khorasani, A., et al. Physical and Engineering Sciences in Medicine **45(3):** p. 925-934. (2022).
[5] Crum, W.R., et. al., J. of Neuroscience Methods, **216(1):** p. 62-77. (2013).
[6] Kamnitsas, K., et al. *Brainlesion: Glioma, Multiple Sclerosis, Stroke and Traumatic Brain Injuries* (2016).
[7] Kazerooni, A. F., et al. *arXiv preprint*. (2023).

Enhancing subtle cortical lesion detection and tissue characterization via multi-dimensional MRI modelling and optimization

Eirini Messaritaki[1], Kadir Şimşek[1], Charlie Air-Rossiter[1], Derek K. Jones[1], Marco Palombo[1]
Cardiff University Brain Research Imaging Centre (CUBRIC), Cardiff University, UK

Introduction: The limited ability of conventional MRI to detect cortical lesions is problematic for patients suffering from conditions such as focal cortical dysplasia (FCD). Multi-dimensional MRI allows simultaneous quantification of multiple properties sensitive to tissue microstructure but requires long acquisitions [1].
We use Monte-Carlo simulations to optimize relaxation-diffusion MRI and enhance detection of cortical lesions. We use FCD as an example pathology that is challenging to image [2]. We simulate the multi-dimensional MRI signal for healthy neurons [3], and for dysmorphic neurons and balloon cells that comprise the pathology of type-II FCD [2,4,5]. We use the simulation results to predict characteristics of the pathological tissue from MRI images of a FCD-IIb patient, paving the way for the use of MRI scanners as non-invasive microscopes.
Methods: We downloaded digital reconstructions (swc files) of neurons from the frontal, motor and temporal cortices from https://neuromorpho.org [6]. We used some unchanged to represent healthy neurons. We adapted others (enlarging the soma and trimming the dendrites in the Trees Toolbox [7]) to resemble balloon cells or dysmorphic neurons. We generated meshes representing their boundaries using the Blender software [8].
We performed Monte-Carlo simulations using a modified version of Disimpy [9] with the added capability to simulate the combined relaxation-diffusion MRI signal accounting for surface relaxivity and T_2 effects.
The phase accumulated by spin *j* moving inside a neuron under a diffusion-sensitising gradient $\boldsymbol{g}(t)$ after one echo time (TE=Kδt) is [10]: $\phi_j = \gamma \int_0^{TE} a(\tau)\boldsymbol{g}(\tau)\cdot\boldsymbol{r}_j(\tau)d\tau$, with $a\left(t<\frac{TE}{2}\right)=+1$, $a\left(t\geq\frac{TE}{2}\right)=-1$. The T_2–magnetization decay is governed by the bulk and the non-uniform magnetization at the boundary of the domain [11,12]. Thus, the magnetization of spin *j* at echo time (TE) is: $M^j = \prod_{k=1}^{K} e^{-\frac{\delta t}{T_{2,i}}}\left(1-\psi^j P(k)\right)$, where $P(k)=1$ if the spin hits the boundary and 0 if not, and $\psi^j = \frac{2}{3}\rho_2\frac{\delta s}{D_0}$ (δs=step length in time δt, D_0=diffusivity, ρ_2=membrane surface relaxivity). The normalized signal of *N* spins at TE is: $S_{norm} = \frac{\sum_{j=1}^{N} M^j e^{-i\phi}}{\sum_{j=1}^{N} M^j}$.
We placed 10^6 spins inside each simulated neuronal substrate. We simulated a PGSE sequence with 12 b-values (0, 500, 1200, 2400, and 3000 to 10,000s/mm^2 in increments of 1000) and 128 isotropically-distributed gradient directions for 2 diffusion timings (Δ/δ=45/15ms, Δ/δ=25/9ms), 7 TEs (64, 70, 80, 90, 100, 110, 120ms) and surface relaxivity of 10^{-7}m/s. We ran simulations for healthy neurons, balloon cells and dysmorphic neurons. For each {b-value, Δ/δ, TE} set, we averaged the signal over the 128 gradient directions and normalized over the b0 signal.
To identify acquisition parameters that maximally differentiate between healthy and FCD tissue, we calculated signal differences $S_{healthy} - S_{pathol}$, and fractional signal differences $(S_{healthy} - S_{pathol})/S_{healthy}$. Healthy voxels comprised 22% extracellular space and 78% healthy neurons. We simulated 2 pathology cases, both with 27% extracellular space [13]: a) 40% dysmorphic neurons, 33% healthy neurons (FCD-IIa), b) 20% balloon cells, 20% dysmorphic neurons, 33% healthy neurons (FCD-IIb) [5].
To derive characteristics of the pathological tissue, we used data collected from a 36-year-old FCD-IIb patient (b=0, 200, 500, 1200, 2400, 6000s/mm^2, 13/20/20/60/61/61 directions respectively, Δ/δ=24/7ms, TE=59ms). We ran simulations for healthy neurons, balloon cells and dysmorphic neurons for those parameters. We created a bank of sample signals for different volume fractions of healthy neurons (F_h), balloon cells (F_b), dysmorphic neurons (F_d) and extracellular space (F_e), with the extracellular space signal analytically calculated. For each lesion voxel in the patient data we calculated the discrepancy score between the measured signal S_m in that voxel and each sample signal S_s in the bank: $\Delta S(F_h,F_b,F_d,F_e) = \sqrt{\sum_{b-val}|S_m^b - S_s^b(F_h,F_b,F_d,F_e)|^2}$. The values of F_h, F_b, F_d and F_e resulting in the lowest value for ΔS in each voxel were deemed to represent the values closest to the ground truth.
Results: Fig. 1 shows our balloon-cell and dysmorphic-neuron models. They faithfully capture the characteristics of those pathological neurons seen via histology [4].
The normalized direction-averaged signal was higher for healthy neurons than for pathological ones, across b-values and TEs (Fig. 2). The absolute and fractional signal differences between the healthy and pathological voxels are shown in Fig. 3. Fig. 4 shows the optimal values of F_h, F_b, F_d and F_e for the lesion voxels.
Discussion: Signal differences peaked at b=2000s/mm^2 for both PGSE schemes, allowing differentiation between healthy and FCD tissue in the clinic. Fractional signal differences peaked at b=6000s/mm^2 and above and were larger for FCD-IIb voxels than FCD-IIa voxels, offering a way to non-invasively distinguish between the two types of pathology. Our analysis identified the presence balloon cells in the patient data, confirming the FCD-IIb diagnosis.
Conclusions: Advanced MRI acquisitions offer hope for the detection and differentiation of cortical pathologies.

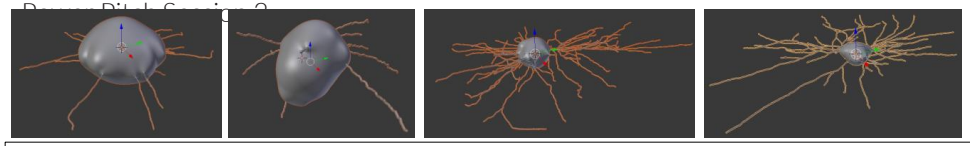

Fig. 1. Models representing balloon cells as seen in histology images from vimentin-stained cortical sections (2 left-most) and dysmorphic neurons as seen in histology images from Golgi-stained cortical sections (2 right-most). [4]

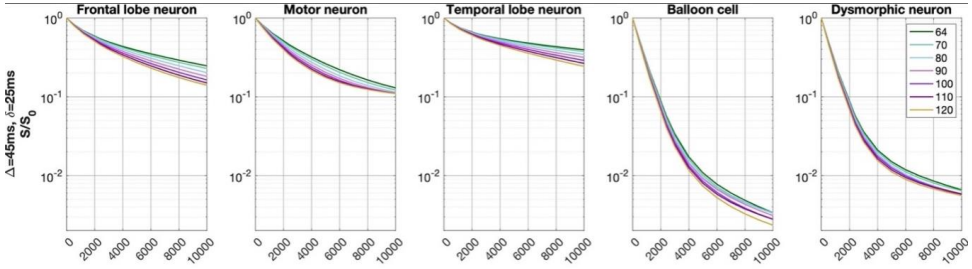

Fig. 2. Normalized direction-averaged signal vs b-value for the 5 neurons simulated, for a PGSE scheme with Δ/δ=45/15ms. Each line represents a TE as listed in the legend (64 – 120ms).

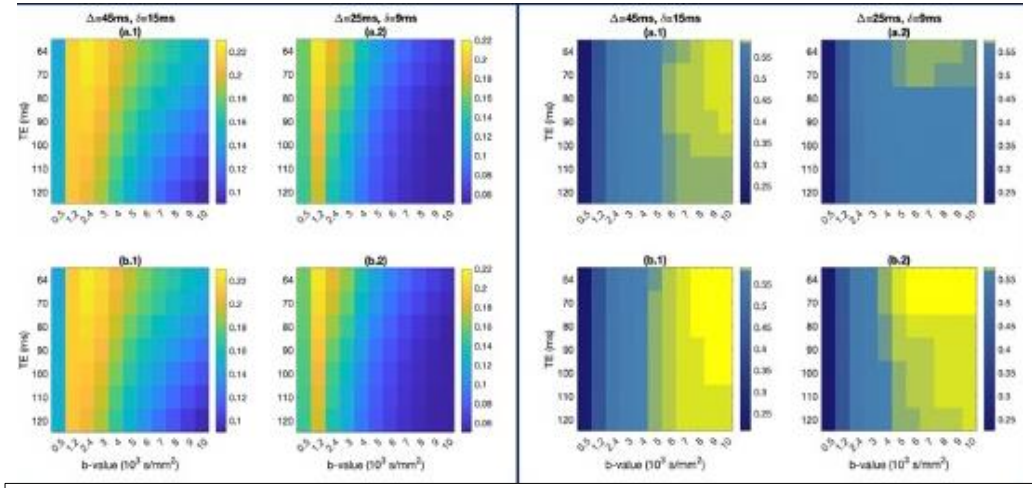

Fig. 3. Signal diff. (L), fractional signal diff. (R) in pathology v. healthy tissue across b-values & TEs. (a): FCD-IIa,(b): FCD-IIb.

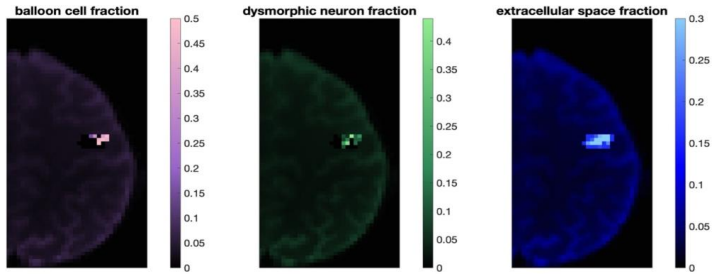

Fig. 4. Volume fractions that minimize the difference between actual and simulated signal in the patient data. The left panel indicates the presence of balloon cells, consistent with the FCD-IIb diagnosis of the patient. The right panel indicates an elevated extracellular space fraction, consistent with FCD pathology.

References: [1]Afzali et al., Magn Reson Med. 2022; 88:2043. [2]Aslan et al., EJRNM 2019; 50:15. [3]Palombo et al., NeuroImage 2020, 215:116835. [4]Rossini et al., Brain 2021; 144(1):251. [5]Aronica & Muhlebner, Handbook of Clinical Neurology 2018; 145:193. [6]Akram et al., Sci. Data 2018; 5:180006. [7]Cuntz et al., PLoS Comput Biol 2010; 6:e1000877. [8]www.blender.org. [9]Kerkelä et al., J. Open Source Softw. 2020; 5:2527. [10]Hall & Alexander, IEEE TMI 2009; 28:1354. [11]Mao-jin et al., J. Cent. South. Univ. 2014; 21:1091. [12]Benavides et al., Comput. Geosci. 2017; 106:200. [13]Zamecnik et al., Eur.J.Neurosci. 2012; 36.

Shining Light on Degeneracies and Uncertainties in the NEXI and SANDIX Models with µGUIDE

Maëliss Jallais[1,2], Marco Palombo[1,2], Ileana Jelescu[3,4], Quentin Uhl[3,4]

[1]Cardiff University Brain Research Imaging Centre (CUBRIC), Cardiff University, Cardiff, United Kingdom; [2]School of Computer Science and Informatics, Cardiff University, Cardiff, United Kingdom; [3]Department of Radiology, CHUV, Lausanne, Switzerland; [4]UNIL, Lausanne, Switzerland

Introduction: NEXI[1]/SMEX[2] and SANDIX[2] are recent gray matter (GM) microstructure models that focus on estimating exchange time, with SANDIX also considering soma fraction and radius. While these models aim to represent the underlying GM microstructure, their complexity makes the estimation of the model parameters challenging. For a given model, the choice of acquisition protocol is crucial, as it allows to tune the sensitivity to specific tissue parameters. However, rich protocol acquisitions are unsuited for patients due to very long scan time, as opposed to preclinical acquisitions. In clinical settings, where the protocol is less extensive, it becomes necessary to characterize its suitability for estimating microstructure parameters of a given model. Bayesian inference methods, such as µGUIDE [3], aim to estimate full posterior distributions, which allow to quantify the quality of the fitting and highlight degeneracies. This work aims at studying the fitting quality of NEXI and SANDIX, given two acquisition protocols used in literature, using µGUIDE. We investigate the impact on the fitting of both the acquisition protocol and the noise.

Methods: Model definitions: NEXI [1] is a two-compartment model with four parameters: exchange time between neurites and extra-cellular space t_{ex}, intra/extra-neurite diffusivities D_i/D_e, and neurite signal fraction f. SANDIX [2] adds a third compartment of impermeable spheres to model soma, with soma signal fraction f_s and radius r_s, making it more challenging to fit.

Protocols: We considered two Pulsed Gradient Spin Echo protocols: an extensive ex-vivo acquisition protocol, similar to the one used to introduce SANDIX [2], and the NEXI 3T Connectom protocol [4], feasible for in-vivo human acquisitions.

Simulated data: Synthetic signals were generated using both models and both protocols, with random parameter combinations sampled on biological feasible ranges. Rician noise levels sampled from the clinical data were added to the signals, with a median signal-to-noise ratio of 50, to mimic real data acquisitions. 10^6 synthetic signals were used for training µGUIDE.

Clinical data: Four healthy volunteers were scanned (2 of whom rescanned on a different day). An MPRAGE was acquired for anatomical reference (1mm isotropic resolution). Diffusion-weighted images were acquired on a 3T Siemens Connectom system using a PGSE EPI sequence with combinations of b-values=[1,2.5,4,6,7.5]ms/µm² with [13,25,25,32,65] directions respectively, and Δ=[20,29,39,49]ms; δ=9ms, and 15 b=0 images per Δ at 1.8mm isotropic resolution, TE/TR=76/3700ms. Total scan time 45'.

Processing: Multi-shell multi-diffusion time data was preprocessed jointly; steps included MP-PCA magnitude denoising [5], Gibbs ringing correction [6], distortion and eddy current correction [7]. The cortical ribbon was segmented on the MPRAGE image using FastSurfer [8] and projected onto the diffusion native space using linear registration [9]. Parametric maps were estimated using non-linear least squares (NLS) and µGUIDE. We extracted three measures from the estimated posterior distributions: maximum-a-posteriori; ambiguity and uncertainty [3], which quantify the variance of the posterior distribution, hence the confidence in the estimates.

Results: Fig.1 presents the fitting results of the NEXI model on both protocols, considering noise-free and noisy signals. The extensive protocol allows to remove almost all degeneracies and substantially reduce the uncertainty of the estimates, but is heavily impacted by noise, as the signal for high b-values is mostly lost. The fitting quality of the Connectom protocol is more robust to noise, as it relies on smaller b-values. However, even when considering a noise-free scenario, this protocol shows bias and variance in the parameter estimates. Similar trends are obtained using the SANDIX model.
Fig. 2 compares the estimations obtained on the cortical ribbons of all the participants using µGUIDE and NLS for both models. For µGUIDE, only the estimates with uncertainty and ambiguity inferior to 50% were kept (more than 98% for De and f, and 68% for t_{ex}). Differences between µGUIDE and NLS may be attributed to the more limited precision of NLS, or to the prior distributions not sufficiently adapted to the range of expected values in the tissue. In particular, the peak t_{ex}<3ms is unreliable given Δ>20ms and δ=9ms, and could be due to CSF contamination. The shoulder around 25-30ms is likely more robust; the peak t_{ex}>125ms could represent voxels with substantial WM partial volume.

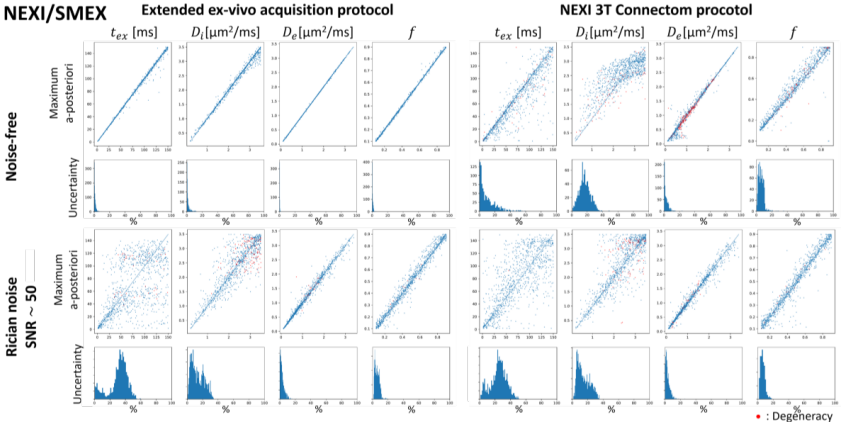

Fig. 1. Fitting results of the NEXI model using µGUIDE, on simulations generated following the extensive ex-vivo acquisition protocol, and on the NEXI 3T Connectom protocol.

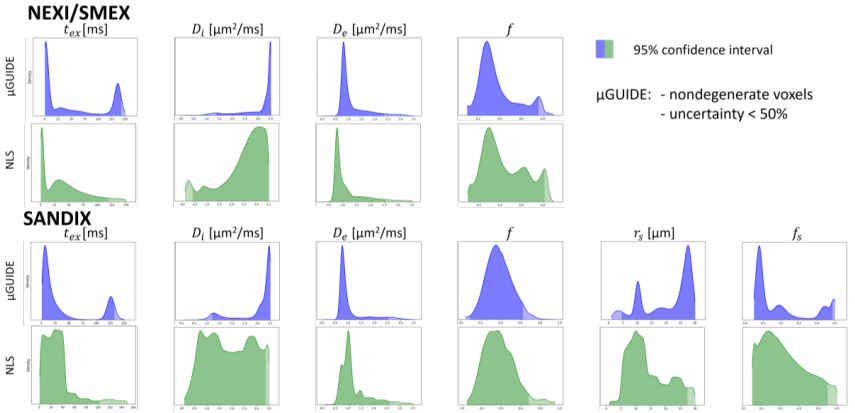

Fig. 2. Histograms of the NEXI and SANDIX estimates from µGUIDE and Non-linear Least Square.

Discussion: Our results reveal that each protocol exhibits unique strengths. The extended protocol allows for the estimation of exchange time in a noise-free scenario, while the Connectom protocol demonstrates robustness to noise.

Conclusion: The estimation of exchange time using the two investigated models in a clinical setting proves to be challenging.

Acknowledgements: MJ and MP are supported by UKRI Future Leaders Fellowship (MR/T020296/2).

References:[1]Jelescu et al., *NeuroImage* 2022; [2]Olesen et al., *NeuroImage* 2022; [3]Jallais et al., *arXiv* 2024; [4]Uhl et al., *Imaging Neuroscience* 2024; [5]Veerart et al., *NeuroImage* 2016; [6]Kellner et al., *MRM* 2016; [7]Andersson et al., *NeuroImage* 2016; [8]Henschel et al., *NeuroImage* 2020;[9] Avants et al., *Insight j*, 2009.

Power Pitch Session 3

Simulation-based inference in diffusion MRI: From uncertainty mapping to probabilistic tractography

J.P. Manzano Patron[1], Michael Deistler[2], Cornelius Schroeder[2], Theodore Kypraios[3], Pedro Gonçalves[2,4], Jakob H. Macke[2], Stamatios N Sotiropoulos[1]

[1]Sir Peter Mansfield Imaging Centre, University of Nottingham, UK, [2]Machine Learning in Science, Excellence Cluster Machine Learning, University of Tübingen & Tübingen AI Center, Germany, [3]School of Mathematical Sciences, University of Nottingham, UK, [4]VIB-Neuroelectronics Research Flanders (NERF), Belgium

Introduction: Uncertainty quantification in diffusion MRI (dMRI) provides a principled way of assessing confidence in the results [1], quantifying noise effects [2] and aiding experimental design [3]. Furthermore, uncertainty mapping for estimated fibre orientations provides the basis for white matter (WM) probabilistic tractography, generally done via bootstrapping [4] or Bayesian inference (MCMC) [5]. Simulation-based inference (SBI) [6] has emerged as a data-driven alternative that allows likelihood-free and amortized inference, thereby enabling a dramatic speed-up of inference on large datasets, while at the same time making it possible to tackle complex models. SBI is based on first training an artificial neural network (ANN) on simulated data to learn posterior distributions for unseen data (i.e., to amortise inference), avoiding repeated likelihood evaluations or expensive MCMC sampling. Recent studies have successfully explored the application of SBI into dMRI microstructural models [7,8,9]. Here, we extend these by exploring performance of SBI for mapping uncertainty of fibre orientation models and using it in probabilistic tractography of brain WM.

Methods: We developed an SBI framework for fitting the Ball&Sticks model [2] (N=2 crossing fibres). As shown in Fig. 1, SBI trains a Neural Posterior Estimator (NPE) [10,11] using synthetic data and learns the mapping between observations and the joint posterior distribution of the model parameters given the data. NPE can then be applied to estimate parameters and quantify their uncertainty on new unseen observations. We implemented and evaluated two different approaches: 1) *SBI_joint*: a single NPE on both single- and crossing-fibre examples. 2) *SBI_classifier*: Similar to [9,12], using the dMRI signal as input, a classifier first performs model selection and selects which of two NPEs trained independently (for N=1 and N=2, respectively) is employed. Both SBI approaches were trained with the default implementations in [13], with 6M and 1M samples, respectively. For the classifier, we implemented a Multi-Layer Perceptron (4 hidden layers of 256, 128, 64, 32 units, respectively, dropout and ReLu activation functions, SoftMax output, Cross-Entropy Loss, Adam optimization). We compared SBI against MCMC (with a sparsifying ARD prior on the volume fractions to enable online model selection [2]). We also assessed their ability to perform landmark-based probabilistic tractography [14] using data from a single-shell acquisition (50 directions, b=2000 s/mm^2) [15].

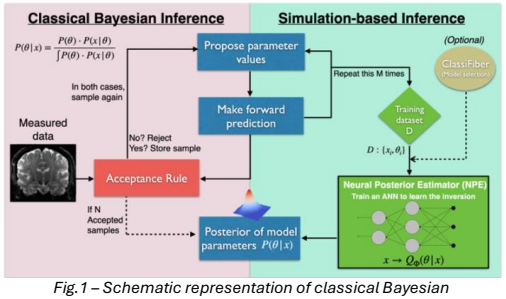

Fig.1 – Schematic representation of classical Bayesian inference (e.g., MCMC) and Simulation-based frameworks.

Results and discussion: Fig. 2 shows a comparison of the estimates obtained from MCMC vs SBI, both in terms of mean estimates and their precision. Regarding the number of fibres predicted per voxel, both *SBI_classifier* and *SBI_joint* return similar patterns and rates of crossings to MCMC (~47%, 59%, and 51%, respectively). High agreement was also found in mean estimates maps for scalar parameters (such as volume fractions, Fig. 2A), as well as for mean 3D fibre orientation estimates (Fig. 2B). Similarly, similar patterns in the uncertainty of the estimated fibre orientations (Fig. 2c) were reproduced, with the SBI approaches returning slightly higher uncertainty (broader posterior) in some WM areas. Differences with MCMC are slightly larger in *SBI_joint* than in *SBI_classifier*, potentially reflective of the more explicit model selection used in SBI_classifier and the MCMC.

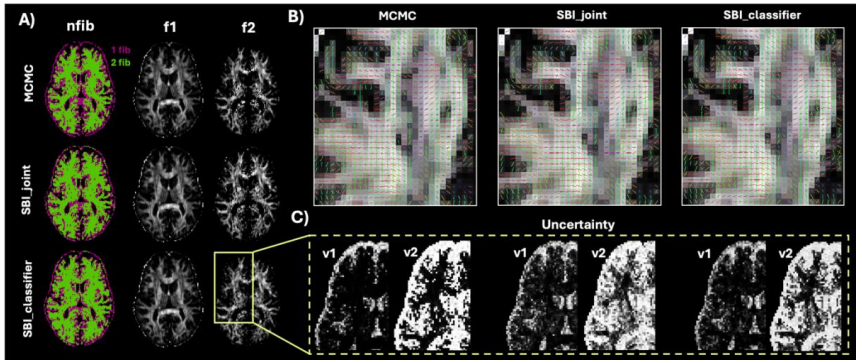

Fig.2 – Comparison between the different methods in estimating A) the number of fibres per voxel and mean of the volume fraction posterior, B) mean of orientation posteriors (crossings in SLFs area), and C) uncertainty of fibre orientation posteriors (high uncertainty – bright, low uncertainty – dark).

We subsequently explored whether these small differences have an effect in probabilistic tractography. We used the fibre orientations and their uncertainties estimated by each method to reconstruct major white matter bundles. Fig. 3A shows the relevant comparison and the UKBiobank average tract atlas [13] as a reference. All methods were able to reconstruct all the bundle tracts successfully. Some false positives were observed (see arrows in Fig. 3A), but correlations against the UKB average atlas across tracts were reasonable and within the expected range [13]. Interestingly, SBI approaches achieved a better performance compared to MCMC (Fig. 3B). SBI estimates increased agreement in WM tractography reconstructions for the dataset employed here, against reconstructions obtained from better quality data, averaged across 1000 subjects.

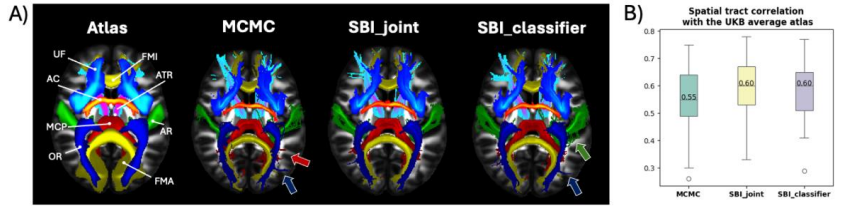

Fig. 3 – A) Maximum Intensity Projections (MIPs) of tracts reconstructed by the different methods. The UK Biobank atlas (average of 1000 subjects) is shown as reference. B) Spatial tract correlation with the UKB average atlas.

Conclusion: Our results demonstrate the feasibility of using SBI for identifying and estimating fibre orientation in dMRI models, mapping calibrated uncertainty and use it subsequently for probabilistic tractography. SBI returned similar levels of accuracy and precision to MCMC with ARD priors. With orders-of-magnitude speedups in inference and greater flexibility in handling likelihood-free scenarios, our results highlight the potential SBI has in quantitative dMRI and modelling.

Acknowledgements: JP and SS are supported by an ERC Consolidator Grant (101000969), MD, CS and JHM by the German Research Foundation (DFG) through Germany's Excellence Strategy (EXC-Number 2064/1, PN 390727645) and SFB1233 (PN 276693517), the German Federal Ministry of Education and Research (Tübingen AI Center, FKZ: 01IS18039) the Carl Zeiss Foundation and the Else Kröner Fresenius Stiftung (Project ClinbrAIn).

References

[1]. Jones DK. Determining and visualizing uncertainty in estimates of fiber orientation from diffusion tensor MRI. *Magnet Reson Med*, 2003. 49(1):7–12

[2]. Behrens TEJ, Woolrich MW, Jenkinson M, Johansen-Berg H, Nunes RG, et al. Characterization and propagation of uncertainty in diffusion-weighted MR imaging. *Magnet Reson Med*, 2003. 50(5):1077–88

[3]. Alexander DC. A general framework for experiment design in diffusion MRI and its application in measuring direct tissue-microstructure features. *Magnet Reson Med*, 2008. 60(2):439–48

[4]. Jones, DK. Tractography gone wild: probabilistic fibre tracking using the wild bootstrap with diffusion tensor MRI. IEEE transactions on medical imaging, 2008. Vol. 27, no.9, p. 1268-1274

[5]. Behrens TEJ, Berg HJ, Jbabdi S, Rushworth MFS, Woolrich MW. Probabilistic diffusion tractography with multiple fibre orientations: What can we gain? *Neuroimage*, 2007, vol. 34, no 1, p. 144-155

[6]. Cranmer K, Brehmer J, Louppe G. The frontier of simulation-based inference. *Proc National Acad Sci*. 2020. 117(48):30055–62

[7]. Manzano-Patron JP, Kypraios T, Sotiropoulos, SN. Amortised inference in diffusion MRI biophysical models using artificial neural networks and simulation-based frameworks. *Proc. Intl. Soc. Mag. Reson. Med. 30*, 2022

[8]. Jallais M, Palombo M. **μ**GUIDE: a framework for microstructure imaging via generalized uncertainty-driven inference using deep learning. arXiv:2312.17293 [physics], 2024

[9]. Karimi HS, Pal A, Ning L., Rathi Y. Likelihood-free posterior estimation and uncertainty quantification for diffusion MRI models. *Imaging Neuroscience*, 2024. 2 1–22. Doi: https://doi.org/10.1162/imag_a_00088

[10]. Papamakarios G, Murray I. Fast ε-free inference of simulation models with bayesian conditional density estimation. *Advances in neural information processing systems*. 2016;29

[11]. Greenberg D, Nonnenmache M, Macke J. Automatic posterior transformation for likelihood-free inference. *International Conference on Machine Learning*, 2019.

[12]. Schröder, C, Macke, JH. Simultaneous identification of models and parameters of scientific simulators. arXiv:2305.15174 [cs], 2024.

[13]. Tejero-Cantero A, Boelts J, Deistler M, Lueckmann J-M, Durkan C, et al. sbi: A toolkit for simulation-based inference. *J Open Source Softw*, 2020. 5(52):2505

[14]. Warrington S, Bryant KL, Khrapitchev AA, Sallet J, Charquero-Ballester M, et al. XTRACT - Standardised protocols for automated tractography in the human and macaque brain. *Neuroimage 2020*. 217:116923

Power Pitch Session 3

[15]. Manzano-Patron JP, Moeller S, Andersson JLR, Ugurbil K, Yacoub E, Sotiropoulos SN. Denoising Diffusion MRI: Considerations and implications for analysis. *Imaging Neuroscience*, 2024. https://doi.org/10.1162/imag_a_00060.

Power Pitch Session 3

Comparing Deep Learning and Patch-based Denoising of Diffusion MRI

Francesco D'Antonio[1], Shaun Warrington[1], Jose Pedro Manzano Patron[1], Jaemin Shin[2], Tim Sprenger[2], Paul S. Morgan[1], Stamatios N. Sotiropoulos[1]

[1]Sir Peter Mansfield Imaging Centre, Mental Health and Clinical Neurosciences, School of Medicine, University of Nottingham, Nottingham, United Kingdom
[2]GE HealthCare

Introduction: The trade-off between resolution, noise and scan time typically governs acquisition choices for MRI and particularly for noise-prone modalities, such as diffusion MRI (dMRI). Patch-based denoising approaches, such as MPPCA [1] and NORDIC [2], offer better middle-ground solutions, allowing higher resolution and/or SNR/CNR per scan time in SNR-starved acquisitions [3]. Novel denoising methods have been recently proposed using deep learning [4,5,6], but comprehensive evaluation of their performance for dMRI analysis is lacking. Previous work has suggested that the way and the domain (magnitude/complex) into which denoising is applied can have significant implications for subsequent analysis, affecting noise-induced variance [7], bias and true resolution in different ways [3]. In this work, we compare magnitude and complex patch-based approaches (|MPPCA|, MPPCA* [1] and NORDIC* [2]) with GE HealthCare's AIR™ Recon DL (ARDL) [4] (convolutional neural-network-based) denoising to understand their effects on SNR/CNR and noise-floor. We use an HCP-style dataset at 1.25mm isotropic resolution and up to b=3000 s/mm² [8,9] to demonstrate how denoising affects dMRI performance in a wide-bore 3T scanner.

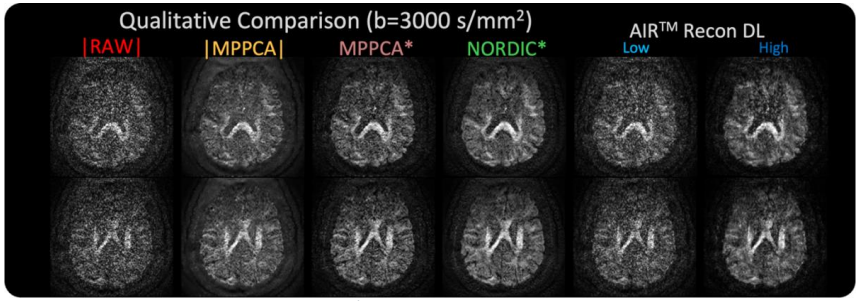

Figure 1: Qualitative comparison of two b=3000 s/mm² volumes. From left to right: magnitude raw data, magnitude MPPCA denoising, complex MPPCA denoising, complex NORDIC denoising, ARDL (complex) on low and high settings.

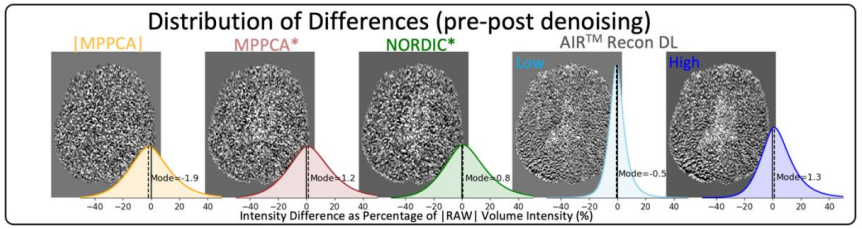

Figure 2: Distribution of differences (raw minus denoised data). Higher intensities in the ventricles and positive mode of distributions for complex MPPCA, NORDIC and high ARDL indicate noise floor suppression.

Methods: DMRI data was acquired using an HCP-style sequence [8,9] (1.25mm isotropic, 46 volumes/shell, two shells: b=1500, 3000 s/mm², MB=4, TE=88.7ms, TR=4.8s, Homodyne Reconstruction [10]) on a GE HealthCare 3T Premier scanner (MR29.2). We developed an offline reconstruction pipeline to retain complex data for denoising [11]. ARDL, which operates in the complex domain on 2D slices, was applied with low and high denoising weighting on the same data, using retrospective reconstruction on the scanner. Data was acquired using a 160x160 matrix. ARDL requires a 256x256 input matrix; therefore, k-space was resampled during reconstruction and then down-sampled using spline interpolation [12,13]. Magnitude and complex domain MPPCA (|MPPCA|, MPPCA*), as well as NORDIC* were applied. Post-denoising, data preprocessing and distortion correction were carried out using an in-house pipeline [14] and FSL-eddy [15]. SNR and CNR metrics were obtained using FSL-eddyQC [16]. To account for noise spatial non-stationarities, noise distributions were estimated from inside the brain (rather than background) using maximally attenuated CSF signal from the ventricles [17]. Noise-floor induced signal rectification was assessed by examining the signal attenuation parallel to principal fibre directions in highly anisotropic voxels [17].

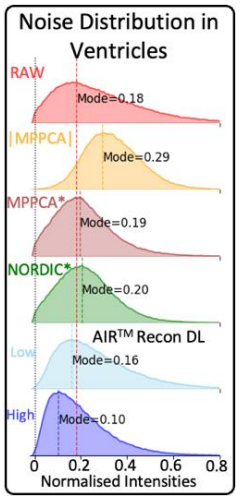

Figure 3: Noise distribution in ventricles highlighting noise floor suppression in complex denoising.

Results and Discussion: Fig. 1 shows a qualitative comparison of b = 3000 s/mm² raw magnitude data along with magnitude images obtained using the various denoising approaches. Fig. 2 shows the distribution of differences (raw minus denoised data) both visually and graphically. The positive mean difference distributions in complex MPPCA, NORDIC and High ARDL are indicative of noise-floor suppression [3]. Suppression of the noise floor is further highlighted in Fig. 3, where the distribution of noise inside the brain is plotted. Additionally, Fig. 4 shows signal attenuation in the corpus callosum, highlighting signal rectification caused by noise-floor suppression. Fig. 5 highlights SNR and CNR gains for denoising methods. It is important to point out that ARDL performs 2D denoising on individual slices, while MPPCA and NORDIC consider all volumes simultaneously and perform 4D denoising.

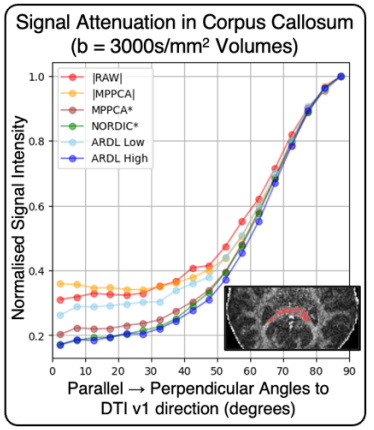

Figure 4: Average signal attenuation in the Corpus Callosum. Noise floor suppression in complex denoising leads to higher dynamic range.

Conclusion: We found significant gains in dMRI data quality from a wide-bore scanner when denoising in the complex domain, both for reducing noise-induced variance and bias. Complex-domain denoising using deep learning (high ARDL) had the most suppression of noise-floor and performed comparably to MPPCA for SNR and CNR gains. NORDIC* denoising had the highest gain in SNR and CNR, with comparable signal rectification to high ARDL.

Acknowledgements: FD is supported by a studentship funded by GE HealthCare and the University of Nottingham. SW, JPMP and SNS are supported by an ERC Consolidator Grant (101000969). We would like to also thank Gavin Houston and Suchandrima Banerjee from GE HealthCare for useful discussions.

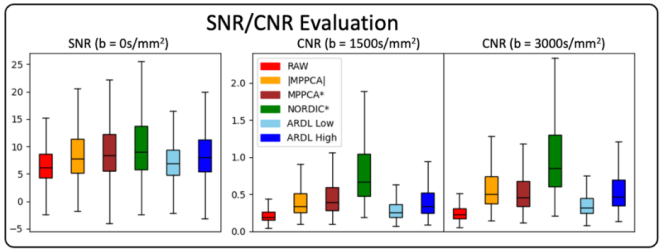

Figure 5: Comparison of magnitude raw and denoised data. MPPCA and NORDIC perform 4D denoising whereas ARDL performs 3D denoising.

References:
[1] Veraart, J., Novikov, D. S., Christiaens, D., Ades-Aron, B., Sijbers, J., & Fieremans, E. (2016). Denoising of diffusion MRI using random matrix theory. Neuroimage, 142, 394-406.

[2] Moeller, S., Pisharady, P. K., Ramanna, S., Lenglet, C., Wu, X., Dowdle, L., ... & Akçakaya, M. (2021). NOise reduction with DIstribution Corrected (NORDIC) PCA in dMRI with complex-valued parameter-free locally low-rank processing. Neuroimage, 226, 117539.

[3] Manzano Patron, J. P., Moeller, S., Andersson, J. L., Ugurbil, K., Yacoub, E., & Sotiropoulos, S. N. (2024). Denoising Diffusion MRI: Considerations and implications for analysis. Imaging Neuroscience, 2, 1-29.

[4] Lebel, R. M. (2020). Performance characterization of a novel deep learning-based MR image reconstruction pipeline. arXiv preprint arXiv:2008.06559.

[5] Zhang, K., Zuo, W., Chen, Y., Meng, D., & Zhang, L. (2017). Beyond a gaussian denoiser: Residual learning of deep cnn for image denoising. IEEE transactions on image processing, 26(7), 3142-3155.

[6] Sadikov, A., Pan, X., Choi, H., Cai, L. T., & Mukherjee, P. (2024). Generative AI for Rapid Diffusion MRI with Improved Image Quality, Reliability and Generalizability. Imaging Neuroscience.

[7] Choi, K. S., Figee, M., Lebel, R. M., Fung, M., Banerjee, S., Mayberg, H. S., & Shin, J. (2022). Evaluation of the efficacy of a Deep Learning-based Reconstruction in the Connectomic Deep Brain Stimulation. Abstract presented at the International Society for Magnetic Resonance in Medicine (ISMRM) Annual Meeting, Abstract #3375.

[8] Sotiropoulos, S. N., Jbabdi, S., Xu, J., Andersson, J. L., Moeller, S., Auerbach, E. J., ... & Wu-Minn Hcp Consortium. (2013). Advances in diffusion MRI acquisition and processing in the Human Connectome Project. Neuroimage, 80, 125-143.

[9] Uğurbil, K., Xu, J., Auerbach, E. J., Moeller, S., Vu, A. T., Duarte-Carvajalino, J. M., ... & WU-Minn HCP Consortium. (2013). Pushing spatial and temporal resolution for functional and diffusion MRI in the Human Connectome Project. Neuroimage, 80, 80-104.

[10] Pauly, J. (2005). Partial k-space reconstruction. http://ee-classes.usc.edu/ ee591/library/Pauly-PartialKspace.pdf. Accessed June 2nd, 2024.

[11] D'Antonio, F., Warrington, S., Morgan, P. S., Sotiropoulos, S. N. (2024) End-to-end Complex Reconstruction and Denoising Pipeline for GE Diffusion MRI Acquisitions. British and Irish Chapter of ISMRM Annual meeting, Abstract Submission

[12] Jenkinson, M., Bannister, P., Brady, M., & Smith, S. (2002). Improved optimization for the robust and accurate linear registration and motion correction of brain images. Neuroimage, 17(2), 825-841.

[13] Jenkinson, M., & Smith, S. (2001). A global optimisation method for robust affine registration of brain images. Medical image analysis, 5(2), 143-156.

[14] Ali-Reza Mohammadi-Nejad, Stefan Pszczolkowski, Dorothee Auer, Stamatios Sotiropoulos. Multi-modal neuroimaging pipelines for data preprocessing. Zenodo. http://doi.org/10.5281/zenodo.3624973

[15] Andersson, J. L., & Sotiropoulos, S. N. (2016). An integrated approach to correction for off-resonance effects and subject movement in diffusion MR imaging. Neuroimage, 125, 1063-1078.

[16] Bastiani, M., Cottaar, M., Fitzgibbon, S. P., Suri, S., Alfaro-Almagro, F., Sotiropoulos, S. N., ... & Andersson, J. L. (2019). Automated quality control for within and between studies diffusion MRI data using a non-parametric framework for movement and distortion correction. Neuroimage, 184, 801-812.

[17] Sotiropoulos, S. N., Moeller, S., Jbabdi, S., Xu, J., Andersson, J. L., Auerbach, E. J., ... & Lenglet, C. (2013). Effects of image reconstruction on fiber orientation mapping from multichannel diffusion MRI: reducing the noise floor using SENSE. Magnetic resonance in medicine, 70(6), 1682-1689.

Power Pitch Session 3

Power Pitch Session 3

End-to-end Complex Reconstruction and Denoising Pipeline for GE Diffusion MRI Acquisitions

Francesco D'Antonio[1], Shaun Warrington[1], Paul S. Morgan[1], Stamatios N. Sotiropoulos[1]

[1]Sir Peter Mansfield Imaging Centre, Mental Health and Clinical Neurosciences, School of Medicine, University of Nottingham, Nottingham, United Kingdom

Introduction: The use of complex MRI data has seen a resurgence over the last few years due to their application in the training of convolutional neural networks (CNN) and their improved denoising outcomes compared to magnitude data [1,2]. CNNs trained on complex data show superior reconstruction to magnitude-trained CNNs in terms of normalised RMS and SNR [1,3,4]. Additionally, denoising complex diffusion data improves SNR, CNR and reduces noise-floor effects compared to denoising magnitude data [2]. Reconstructing complex data in diffusion MRI acquisitions is not available as standard from many scanner manufacturers, making magnitude denoising and training the only widely available option. In this work we developed a scalable offline reconstruction pipeline for diffusion acquisitions on GE HealthCare scanners which uses raw data from individual coil elements and returns both complex and magnitude data. The pipeline has built-in capabilities for dMRI denoising, using MPPCA [5,6] and NORDIC [7] algorithms, as well as options to modify the reconstruction steps. We tested the equivalence of the offline and scanner reconstructions in the magnitude domain.

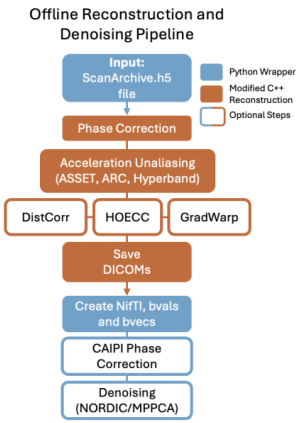

***Figure 1**: Offline reconstruction and denoising pipeline workflow. Python wrapper steps are in blue, C++ reconstruction in orange and steps which can be optionally included are unfilled.*

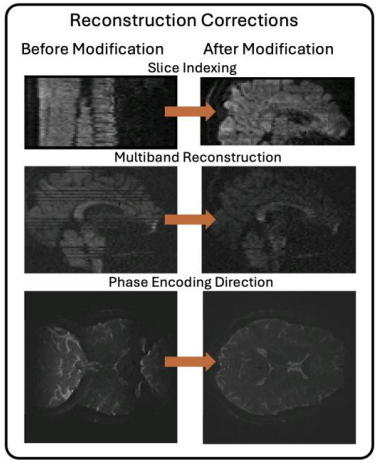

***Figure 2:** Examples of corrections performed by the pipeline (right) with respect to the C++ Orchestra SDK (left): correct slice indexing (top), multiband reconstruction (middle) and phase encoding direction (bottom).*

Methods: We developed an end-to-end python pipeline for complex reconstruction by building upon the C++ Orchestra SDK available through GE HealthCare's WeConnect website. The pipeline takes as input ScanArchive.h5 files and outputs DICOMs and denoised NIfTI files (either magnitude or complex). Compared to default Orchestra, our workflow allows: i) Proper reconstruction of multiband acquisitions; ii) Proper indexing of dMRI volumes and slices for all combinations of in-plane and out-of-plane accelerations; iii) Accounting for phase encoding direction and creation of bvals and bvecs files; iv) Optional flags to modify the reconstruction (such as gradient non-linearity correction, high-order eddy current correction, complex/homodyne reconstruction, see Fig. 1). Figure 2 highlights examples of how the proposed pipeline addresses challenges faced by the default Orchestra SDK. Reconstruction of diffusion MRI data is supported for both in-plane and out-of-plane accelerations. Data using SENSE-like acceleration [8] (ASSET factors 1 and 2), GRAPPA-like acceleration [9] (ARC factors 1 and 2), multiband (MB) [10,11] (1 and 4), and partial Fourier (using the Homodyne method [12]), were acquired and reconstructed offline, using the developed reconstruction pipeline, and on the scanner. To validate the pipeline, scanner and offline reconstructions were compared by analysing the difference in the magnitude domain. Image noise (captured as the distribution of diffusion-weighted, maximally attenuated CSF signal in the ventricles) was analysed for Homodyne reconstructions to explore proximity to a Rician distribution. The phase maps for zero-filled partial Fourier and full Fourier acquisitions were reconstructed using checkerboard and CAIPIRINHA [13] corrections.

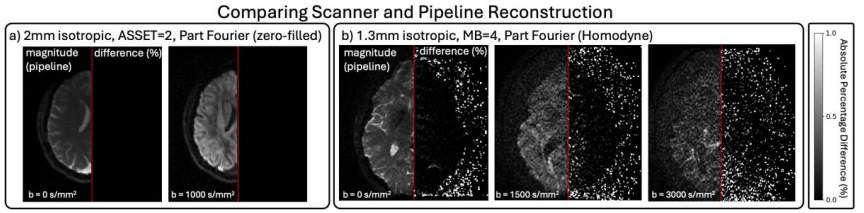

***Figure 3:** Magnitude percentage differences between pipeline and scanner reconstruction. a) 2mm isotropic, ASSET=2, zero-filled reconstruction. b) 1.3mm isotropic, MB=4, Homodyne reconstruction.*

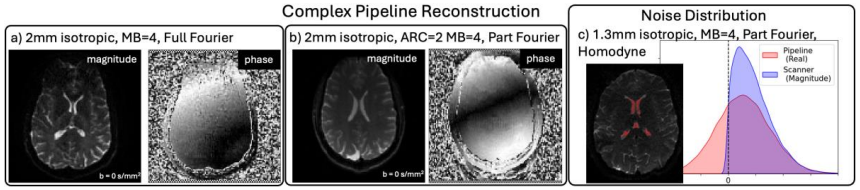

***Figure 4:** Examples of complex reconstruction. a) Phase from 2mm isotropic MB=4 data. b) Phase from 2mm isotropic MB=4 ARC=2 data. c) 1.3 mm MB=4 homodyne reconstruction showing gaussian noise in the ventricles.*

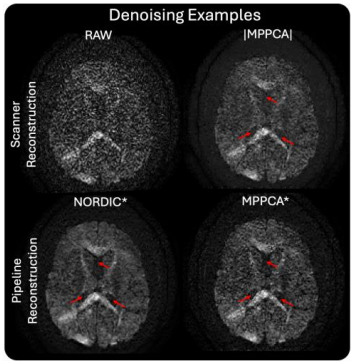

***Figure 5:** Denoising examples using 1.3mm iso, MB=4, b=3000s/mm². Top: scanner recon with magnitude denoising. Bottom: complex denoising from pipeline recon showing superior noise floor suppression (red arrows).*

Results and Discussion: Scanner and pipeline magnitude reconstruction gave almost identical results, as highlighted in Figure 3, validating the offline reconstruction. Examples of reconstructing phase are shown in Figure 4a and 4b. Figure 4c shows the noise distribution of Homodyne reconstructed data, validating that the pipeline provides a non-skewed Gaussian distribution, as expected (since homodyne reconstruction rotates and retains complex information into the real channel). Figure 5 showcases examples of denoising complex data, enabled by the pipeline reconstruction, highlighting the suppression of the noise-floor when compared to the magnitude alternative (red arrows). The pipeline is open-source and available upon request to users with a GE Research Code Sharing License (RCSL).

Conclusion: Complex reconstruction of diffusion acquisitions on GE HealthCare scanners is now publicly available through the developed pipeline. We validated the pipeline by comparing scanner and pipeline magnitude reconstruction, showing minimal differences and supporting several in-plane and out-of-plane accelerations, as well as denoising options.

Acknowledgements: FD is supported by a studentship funded by GE HealthCare and the University of Nottingham. SW and SNS are supported by an ERC Consolidator Grant (101000969). Thank you to colleagues from GE HealthCare Jaemin Shin, Tim Sprenger, Gavin Houston and Suchandrima Banerjee for their advice and support.

References

[1] Cole, E., Cheng, J., Pauly, J., & Vasanawala, S. (2021). Analysis of deep complex-valued convolutional neural networks for MRI reconstruction and phase-focused applications. *Magnetic Resonance in Medicine*, 86(2), 1093-1109.

[2] Manzano Patron, J. P., Moeller, S., Andersson, J. L., Ugurbil, K., Yacoub, E., & Sotiropoulos, S. N. (2024). Denoising Diffusion MRI: Considerations and implications for analysis. *Imaging Neuroscience*, 2, 1-29.

[3] Eo, T., Jun, Y., Kim, T., Jang, J., Lee, H. J., & Hwang, D. (2018). KIKI-net: cross-domain convolutional neural networks for reconstructing undersampled magnetic resonance images. Magnetic resonance in medicine, 80(5), 2188-2201.

[4] Zhu, B., Liu, J. Z., Cauley, S. F., Rosen, B. R., & Rosen, M. S. (2018). Image reconstruction by domain-transform manifold learning. Nature, 555(7697), 487-492.

[5] Veraart, J., Novikov, D. S., Christiaens, D., Ades-Aron, B., Sijbers, J., & Fieremans, E. (2016). Denoising of diffusion MRI using random matrix theory. *Neuroimage*, 142, 394-406.

[6] Cordero-Grande, L., Christiaens, D., Hutter, J., Price, A. N., & Hajnal, J. V. (2019). Complex diffusion-weighted image estimation via matrix recovery under general noise models. *Neuroimage*, *200*, 391-404.

[7] Moeller, S., Pisharady, P. K., Ramanna, S., Lenglet, C., Wu, X., Dowdle, L., ... & Akçakaya, M. (2021). NOise reduction with DIstribution Corrected (NORDIC) PCA in dMRI with complex-valued parameter-free locally low-rank processing. Neuroimage, 226, 117539.

[8] Pruessmann, K. P., Weiger, M., Scheidegger, M. B., & Boesiger, P. (1999). SENSE: sensitivity encoding for fast MRI. Magnetic Resonance in Medicine, 42(5), 952-962.

[9] Griswold, M. A., Jakob, P. M., Heidemann, R. M., Nittka, M., Jellus, V., Wang, J., ... & Haase, A. (2002). Generalized autocalibrating partially parallel acquisitions (GRAPPA). Magnetic Resonance in Medicine, 47(6), 1202-1210.

[10] Weaver, J. B. (1988). Simultaneous multislice acquisition of MR images. Magnetic resonance in medicine, 8(3), 275-284.

[11] Larkman, D. J., Hajnal, J. V., Herlihy, A. H., Coutts, G. A., Young, I. R., & Ehnholm, G. (2001). Use of multicoil arrays for separation of signal from multiple slices simultaneously excited. Journal of Magnetic Resonance Imaging, 13(2), 313-317.

[12] Pauly, J. (2005). Partial k-space reconstruction. http://ee-classes.usc.edu/ ee591/library/Pauly-PartialKspace.pdf. Accessed June 2nd, 2024.

[13] Breuer, F. A., Blaimer, M., Heidemann, R. M., Mueller, M. F., Griswold, M. A., & Jakob, P. M. (2005). Controlled aliasing in parallel imaging results in higher acceleration (CAIPIRINHA) for multi-slice imaging. *Magnetic Resonance in Medicine*, 53(3), 684-691.

Towards quantifying Gray Matter "micro-connectivity": the measurable impact of dendritic spines on metabolite diffusion

Kadir Şimşek[1,2] and Marco Palombo[1,2] - [1]Cardiff University Brain Research Imaging Centre (CUBRIC), School of Psychology, Cardiff University, Cardiff, United Kingdom; [2]School of Computer Science and Informatics, Cardiff University, Cardiff, United Kingdom

Introduction: The brain gray matter (GM) exhibits highly heterogeneous and complex microstructures, that can be probed by diffusion-weighted MRS (dMRS) in-vivo[1–4]. Several works have already investigated the effect of cell body size/density[5,6]; cell processes branching[6–8], undulation[9], beading[10] and orientation dispersion[7,11] on dMRS measurements.

However, only a few works[12,13] have investigated the potential effects of secondary structures like dendritic spines. Dendritic spines play a crucial role in synapse development and plasticity in both healthy and pathological conditions[14–16]. But it is still unclear what the impact of dendritic spine is on metabolites dMRS signal and whether we can measure it in typical human acquisitions. Here we aim to answer these questions by investigating the impact of dendritic spines density on dMRS measurements using numerical simulations.

Methods:

Spiny Dendritic Segments: Skeletons for ten spiny branches were built on MATLAB R2022a (MathWorks) involving functions from the Trees-Toolbox[17] and then surface meshed using Python Blender API v2.79. The geometric properties of the substrates are documented in **Fig.1**. Notably, any of these features can be changed arbitrarily, but here we focused on spine density, σ, and purposely varied only that. Moreover, to investigate the impact of undulation and beading in addition to spine, we also added undulation and beading with period [0-8] and amplitude [0-3]µm, respectively.

Diffusion Simulations & Data Analysis: All diffusion Monte-Carlo simulations were performed using DisimPy[18] with periodic boundary conditions. The number of spins 10^6 and time steps 2000 were determined by the Monte-Carlo[19,20]; intra-branch diffusivity was 0.35µm^2/ms (typical value for N-acetyl-aspartate, NAA[21]). We simulated 15 different pulsed gradient schemes with combinations of 8 gradients separations(Δ= [10, 25, 35, 55, 85, 160, 235, 310] ms), two gradients (δ= [3, 15] ms), 128 directions and b-values up to 25ms/µm^2.

To characterize the hindering/restricting effect of spines on metabolites diffusion, we used a modified astro-sticks model (mAS)[4,22,23]. This model is based on randomly-oriented sticks with effective intra-stick axial diffusivity $D_{eff}(D_{intra}, K_{intra}, b) = D_{intra}(1 - K_{intra}D_{intra}bcos^2\theta)$, where θ is the angle between the branch direction and the diffusion gradient direction, D_{intra} is the metabolite intra-stick apparent axial diffusivity, K_{intra} is the metabolite intra-stick apparent axial kurtosis, accommodating non-Gaussian diffusion due to spines hindering/restriction[22,23]. The numerical integration yields the corresponding powder-averaged signal[13,24,25]: $S/S_0 = \int_0^1 e^{-bD_{eff}cos^2\theta} d(cos\theta)$

Results: **Fig.2** reports the sensitivity analysis for spine detection for ideal and realistic acquisitions. **Fig.3** shows the impact of undulation and beading.

Discussion & Conclusion: For changes in σ from the typical value 1µm^{-1} observed in pathologies like essential tremor (~-25%)[14] and autism (~+50%)[15], D_{intra} & K_{intra} from the mAS model show measurable changes for the ideal acquisition at t_d=9ms. For the pulse scheme used in clinical human studies[13,24], only changes in D_{intra} remains measurable, while changes in K_{intra} requires SNR>100 to be measurable.

Noteworthy, undulations and beading overall lead to further decreasing D_{intra} and increasing K_{intra} up to ~+-10% for realistic values of beading amplitude (1-2µm) and undulation period (0-4).

This study suggests that metabolite diffusion as measured by dMRS can be sensitive to spine density σ and that D_{intra} & K_{intra} from the mAS model can be promising imaging markers of GM 'micro-connectivity' in healthy and diseased brain.

Acknowledgements: This work, KS and MP are supported by UKRI Future Leaders Fellowship (MR/T020296/2).

References: 1. Novikov DS, et al. MRM, 2018 2. Ronen I, et al. eMagRes, 2015 3. Palombo M, et al. Neuroimage, 2018 5. Palombo M, et al. Neuroimage, 2020 6. Ianus A, et al. Neuroimage, 2021 7. Vincent M, et al. Neuroimage, 2020 8. Palombo M, et al. PNAS, 2016 9. Brabec J, et al. NMR Biomed. 2020 10. Budde MD, et al. PNAS, 2010 11. Lundell H, et al. Neuroimage, 2021 12. Palombo M, et al. Neuroimage, 2018 13. Palombo M, et al. ISMRM, 2020 14. Louis ED, et al. Brain, 2014 15. Hutsler JJ, et al. Brain Res, 2010 16. Perez-Cruz C, et al. Journal of Neuroscience, 2011 17. Cuntz H, et al. PLoS Comput Biol. 2010 18. Kerkelä L, et al. J Open Source Softw. 2020 19. Hall MG, et al. IEEE Trans Med Imaging, 2009 20. Rafael-Patino J, et al. Front Neuroinform, 2020 21. Palombo M, et al. MRM, 2017 22. Sukstanskii AL, et al. J. Magn. Reason, 2008 23. Yablonskiy DA, et al. NMR Biomed, 2010 24. Simsek K, et al. ESMRMB, 2023 25. Palombo M, et al. Neuroimage, 2018

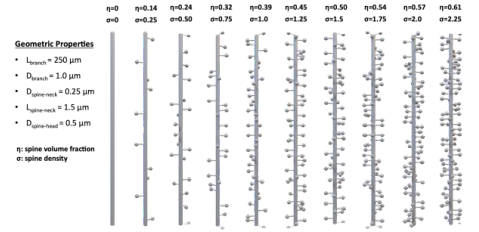

Figure 3: Illustration of spiny dendritic segments. The geometric properties are reported in the figure.

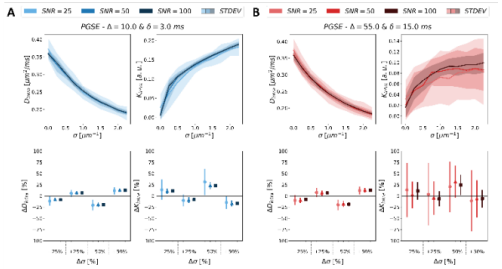

*Figure 2: Spine sensitivity analysis: A hundred diffusion signals with different signal-to-noise (SNR) levels were generated. The mean D_{intra} & K_{intra} and their corresponding standard deviations are shown as a function of σ in the figure (**A**: ideal gradient scheme; **B**: clinically feasible gradient scheme). At the bottom of each panel, the change in intra-stick diffusivities and kurtosis, D_{intra} & K_{intra}, are presented with correspind error for typical changes [±25%, ±50%] in σ=1μm^{-1} due to pathology*[14–16]

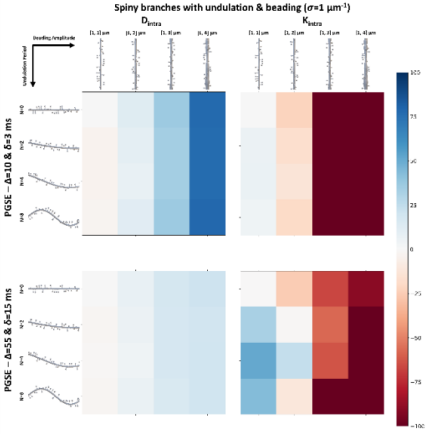

Figure 1: The changes in D_{intra} & K_{intra} with respect to the case of no undulation and beading for σ=1μm^{-1}, obtained from undulated and beaded spiny branch simulation estimates. D_{intra} & K_{intra} percentage differences are shown for ideal (top) and clinically feasible (bottom) pulse schemes.

Diffusion in dendritic spines: impact on permeative exchange estimation with time-dependent diffusion-weighted MRI

Kadir Şimşek[1,2] and Marco Palombo[1,2] - [1]Cardiff University Brain Research Imaging Centre (CUBRIC), School of Psychology, Cardiff University, Cardiff, United Kingdom; [2]School of Computer Science and Informatics, Cardiff University, Cardiff, United Kingdom

Introduction: Time-dependent diffusion-weighted MRI (dMRI) can probe exchange in complex biological tissues[1–4]. While it is expected that different exchange mechanisms contribute to the time-dependent signal[5,6], measurements are often primarily interpreted in terms of transcytolemmal water exchange. The Neurite Exchange Imaging (NEXI)[3] and the Standard Model with Exchange (SMEX)[2] are two recent examples of model-based approaches to estimate exchange in brain tissue. Both NEXI and SMEX assumes that the only exchange mechanism leading to the measured time-dependent dMRI signal is permeative exchange between intra and extra-neurite compartments.

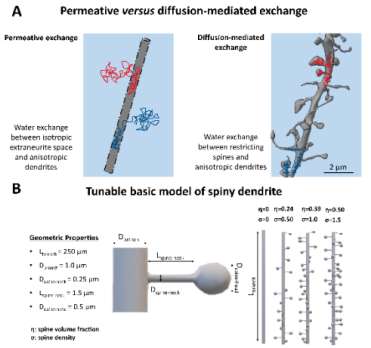

*Fig.1: **A**. Permeative exchange & diffusion-mediated exchange with no permeation, due to the presence of spines. **B**. The tunable basic model of spiny dendrites we developed to control spine morphology and density.*

The aim of this work is to underscore the importance of considering diffusion-mediated exchange when interpreting model-based estimates of exchange in complex microstructures such as the brain Gray Matter (GM). We hypothesize that water diffusing within spiny dendrites in the GM, without crossing the cell membrane, can originate a time-dependent signature which is indistinguishable from permeative exchange (**Fig.1A**); and use Monte-Carlo simulations with a basic model of spiny dendrite (**Fig.1B**) to validate it and evaluate the impact of different spine densities on NEXI/SMEX estimates.

Methods: ***Spiny Dendritic Meshes:*** Skeletons of spiny dendritic branches for two sets of substrates were built on MathWorks MATLAB 2022a involving functions from the Trees-Toolbox[7] and then surface meshed using Python Blender API v2.79. Set I: ten spiny branches (σ=[0, 2.25] μm^{-1}) for investigating the exchange effect of diffusion in spines without undulation and/or beading. Set II: 16 spiny branches (σ=1μm^{-1}): 4 undulation periods (N_{period}=[0, 2, 4, 8]) x 4 beading amplitudes (A_{bead}=[0, 1, 2, 3] μm).

Diffusion Simulations & Data Analysis: DisimPy[8] was employed in all simulations. The number of spins 10^6 and time steps 2000 were determined by the Monte-Carlo convergence[9,10]. Five different pulsed gradient schemes, combinations of three gradient separations (Δ= [10, 25, 35] ms) and two gradient durations (δ= [3, 15] ms) were used with 128 directions and diffusion-weighting b up to 7ms/μm^2. Periodic boundary conditions were used for intra-branch diffusion simulations with diffusivities 2μm^2/ms (typical value for intra-neurite water[2,11]).

For a fair comparison with NEXI/SMEX biophysical modelling, we simulated the total signal S_{total} arising from a dMRI voxel as the weighted sum of intra and extra-neurite signals, $S_{neurite}$ and $S_{Gaussian}$, respectively: $S_{total} = 0.7S_{neurite} + 0.3S_{Gaussian}$. $S_{neurite}$ is derived from our simulation in spiny dendrites at different spine densities and/or undulations, while $S_{Gaussian}$ is mono-exponential decay with diffusivity of 1 μm^2/ms (**Fig.3,4**). We assumed 70% intra-neurite signal fraction. S_{total} was fitted using NEXI model[3] to estimate the exchange time (t_{ex}) for all simulated conditions.

Results: **Fig.2A** illustrates exemplary spiny branches featuring only undulation and only beading the exchange and presents the modelled diffusion signal from a dMRI voxel for a fair comparison with NEXI/SMEX biophysical models. **Fig.2B** reports t_{ex} estimations as a function of σ while Fig.2**C** presents

estimated t_{ex} as a function of undulation period when there is no membrane permeability. **Fig.3** illustrates **simulated** diffusion signals of spiny dendritic branches in the case of only beading.

Discussion & Conclusion: The estimated t_{ex} values (3-60 ms) for spine densities typically observed in healthy cortical GM (0.5–1.5 µm^{-1}) are in very good agreement with both in-vivo and ex-vivo estimates from rat GM[2,3] and human[12].

The time-dependent signal from diffusion within impermeable spiny dendrites is indistinguishable from permeative exchange. Our findings can contribute to a more insightful interpretation of exchange estimates using dMRI, underscoring the importance of cautioning when inferring exchange estimates as indicators of membrane permeability only.

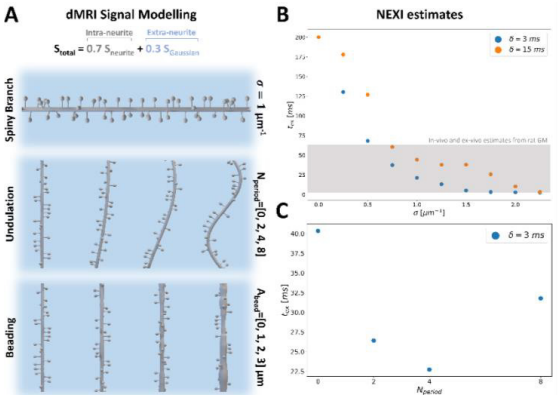

*Fig.2: (**A**) Modelling the total signal arising from a dMRI voxel as the weighted sum of intra and extra-neurite signals, $S_{neurite}$ (our simulations) and $S_{Gaussian}$ (mono-exponential decay with diffusivity of 1 µm²/ms), respectively. In the bottom, exemplary spiny branches for undulation only and beading only cases. (**B**) the estimates of exchange time are reported as a function of spine density for both narrow and fat pulse cases. (**C**) The estimated t_{ex} times for the case of only undulated spiny branches are shown as a function of undulation period for short pulse condition.*

Finally, we acknowledge that the simulated spiny dendrites are oversimplified. Other microstructural features, such us undulations and beading could also confound the interpretation of exchange mechanisms. Indeed, adding undulations lead to shorter exchange times when estimated with NEXI for realistic undulation periods 0-4 (Fig.2). In contrast, Fig.3 shows that beading leads to a different time-dependence of the direction-averaged signal, indicating more restriction to the diffusion, as previously reported[13].

Future work will investigate whether it is possible to disentangle permeative from diffusion-mediated exchange, and how sensitive and specific our measurements can be to spine-induced diffusion-mediated exchange (e.g. with respect to undulations and beading).

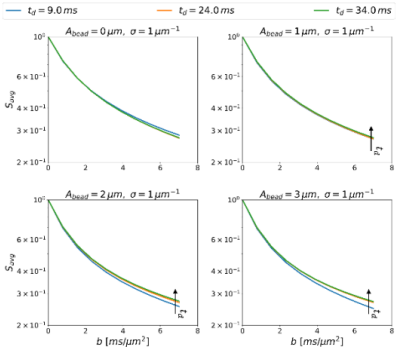

Fig. 3: Simulated diffusion signals of beaded substrates do not indicate intra-compartmental (i.e., from spines to dendritic branch) exchange due to increasing signal amplitudes with increasing diffusion time. This outcome highlights beading is only introduce a restriction to the molecular diffusion as reported in the literature[13].

Acknowledgements: This work, KS and MP are supported by UKRI Future Leaders Fellowship (MR/T020296/2).

References: 1. Kärger J. et al. Ann Phys, 1971 2. Olesen JL, et al. Neuroimage, 2022 3. Jelescu IO, et al. Neuroimage, 2022 4. Lasič S, et al. MRM, 2011 5. Khateri M, NMR Biomed, 2022 6. Bai R, et al. Neuroimage, 2020 7. Cuntz H, et al. PLoS Comput Biol. 2010 9. Hall MG, et al. IEEE Trans Med Imaging, 2009 10. Rafael-Patino J, et al. Front Neuroinform, 2020 11. Palombo M, et al. Neuroimage, 2019 12. Uhl Q, arxiv, 2023 13. Budde MD, et al. PNAS, 2010

Subjective craving and brain response to drug-related cues in former drug addicts: An fMRI study

Elza A. Othman[1], Nor A.A Mohd Nawawi[1], Fairuz Mohd Nasir[1], Kamarul A. Abdullah[1], Aini I. Abd Hamid[2], Wan M.A. Wan Mohd Yunus[3], Ahmad N. Yusoff[4], Mazlyfarina Mohamad[4], Hamzaini Abd Hamid[5], Nor S. Abdul Wahab[5], Mohammad F.I.L Abdullah[6], Mohd N. Baharudin[7], Vincent P. Giampietro[8]

[1]School of Medical Imaging, Faculty of Health Sciences, Universiti Sultan Zainal Abidin, Terengganu, Malaysia
[2]Department of Neurosciences, School of Medical Sciences, Universiti Sains Malaysia, Kelantan, Malaysia
[3]Department of Psychology, School of Human Resource Development and Psychology, Faculty of Social Sciences and Humanities, Universiti Teknologi Malaysia, Johor, Malaysia
[4]Center for Diagnostic, Therapeutic and Investigative Studies, Faculty of Health Science, Universiti Kebangsaan Malaysia, Kuala Lumpur, Malaysia
[5]Radiology Department, UKM Children Specialist Hospital, Kuala Lumpur, Malaysia
[6]Department of Community Health, Advanced Medical and Dental Institute, Universiti Sains Malaysia, Pulau Pinang, Malaysia
[7]Department of Social Administration and Justice, Faculty of Arts and Social Science, Universiti Malaya, Kuala Lumpur
[8]Institute of Psychiatry, Psychology & Neuroscience, King's College London, London, United Kingdom

Introduction: Drug addiction has emerged as a pervasive global issue affecting individuals, families, and societies across the world. From affluent nations to developing countries, the prevalence of drug addiction continues to rise, posing significant burdens to public health and socioeconomic stability [1]. In an effort to curb drug addiction, authorities have established various rehabilitation programmes to help cease cravings among drug addicts [2]. Despite these efforts, the relapse rate continues to skyrocket. A plausible assumption derived from the current literature is that rehabilitation programmes may not have been effective in reducing neural activity in brain areas associated with the reward pathway [3-4]. As such, it was hypothesised that exposure to drug-related cues may evoke neural activation in brain areas associated with drug cravings in former drug addicts (FDAs) after completing rehabilitation programmes, thus leading to relapse. To test the hypothesis, this study was performed to examine the brain activity of FDAs towards drug-related cues and its relationship to the level of subjective craving.

Methods: A cross-sectional study was conducted involving 20 FDAs (mean abstinence period of 6.20 ± 3.79 years) and 23 gender-matched healthy controls (HCs). Participants were recruited for the study via purposive sampling. The FDAs were individuals who had completed the community-based rehabilitation programmes operated under the National Anti-Drug Agency (NADA). All participants performed a 16-minute functional MRI (fMRI) experimental task inside a 2.89 Tesla Siemens Skyra MRI system, where they viewed a series of drug-related cues interleaved with baseline images presented in a block-design paradigm. The drug-related cues were obtained from the Methamphetamine and Opioid Cue Database (MOCD) [5]. Participants' subjective drug craving scores were acquired using a visual analogue scale (VAS) before and immediately after the fMRI scans. The fMRI data were pre-processed and analysed in Statistical Parametric Mapping (SPM12). Individual data were analysed using fixed-effect analysis (FFX) to obtain individual brain activation maps. Random-effect analysis (RFX) was later performed to generate within-group (one-sample t-test) and between-group (two-sample t-test) brain activation maps. The number of activated voxels (NOV) was correlated with the level of subjective craving scores using a Spearman rank correlation analysis. The statistical significance level was set at P < .05.

Results: Whole-brain analysis showed significant (P_{FWE} < .05) activity in brain regions associated with visuospatial attention and visual processing in both groups when participants viewed the drug-related

cues. These regions were the inferior occipital gyrus (IOG), middle occipital gyrus (MOG), occipital pole (OCP), calcarine cortex (Calc), inferior temporal gyrus (ITG), occipital fusiform gyrus (OFuG), fusiform gyrus (FuG), and thalamus proper. However, a direct comparison through a two-sample t-test did not reveal any brain areas significantly differentially activated between groups at a stringent threshold of $P_{FWE} < 0.05$. Figure 1 illustrates the brain activation pattern in the FDA group and the HC group during the fMRI task (drug > baseline). Additionally, the Spearman rank correlation analysis revealed no significant correlation between brain activation and craving scores in both groups.

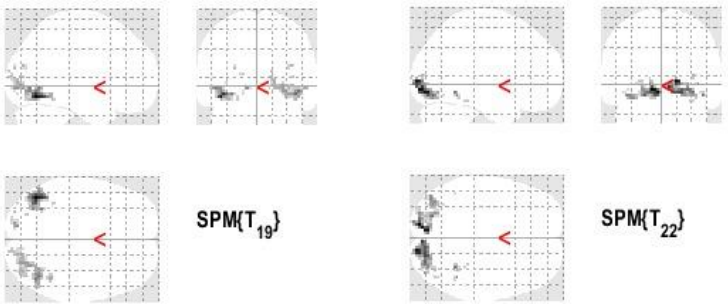

Fig. 1. Whole-brain analysis demonstrates significantly activated brain areas ($P_{FWE} < .05$) for the FDA group (*left panel*) and the HC group (*right panel*) during the visual fMRI task (drug > baseline).

Discussion: Both FDAs and HCs showed a significant increase in brain activities in areas associated with visuospatial attention and visual processing when viewing drug-related cues. A detailed inspection of these brain areas indicates that they were not directly involved in drug cravings. This finding suggests that the increased activations were due to participants' actively viewing the visual drug-related cues during the fMRI experiment and were not due to heightened levels of craving. Additionally, the non-significant fMRI results between the FDAs and HCs indicate that the brains of the FDAs were not significantly evoked by the drug-related cues, suggesting that the FDAs may have recovered from drug addiction. This is further supported by the non-significant correlation between the NOV and subjective craving score.

Conclusions: This study provides new evidence that the brains of FDAs do not show significant responses to drug-related cues, implying that they may not be affected by visual drug-related cues upon completing rehabilitation programmes. This finding contradicts current evidence that increased activations in FDAs lead to relapse. Future works are warranted to address factors that may contribute to this discrepancy.

Acknowledgements: The authors thank the Ministry of Higher Education (MOHE) for providing funding support for this Fundamental Research Grant Scheme project (FRGS/1/2022/SKK06/UNISZA/02/2).

References

[1] A.K. Schlag. Percentages of problem drug use and their implications for policy making: A review of the literature. Drug Sci. Policy Law 2020; 6, 1-9.
[2] N.A.A. Mohd Nawawi, E. Othman, F. Mohd Nasir, et al. Drug addictions in Malaysia: a mini-review on drug types, rehabilitation centers and therapeutic programs. J. Ethn. Subst. Abuse 2014; 8, 1-13.
[3] F. Devoto, L. Zapparoli, G. Spinelli, et al. How the harm of drugs and their availability affect brain reactions to drug cues: a meta-analysis of 64 neuroimaging activation studies. Trans. Psychiatry 2020; 10, 429.
[4] H. Zeng, D. Su, P. Wang, et al. the action representation elicited by different types of drug-related cues in heroin-abstinent individuals. Front. Behav. Neurosci. 2018; 12, 123.
[5] H. Ekhtiari, R. Kuplicki, A, Pruthi, et al. Methamphetamine and opioid cue database (MOCD): development and validation. Drug Alcohol Depend. 2020; 209,107941.

Fast (<100ms TR) 3T fMRI unravels the dynamics of visual perception: investigation of travelling waves in binocular rivalry.

Rowan Huxley[1], Oliver Mundell[2], Aneurin J Kennerley[2], Elisa Zamboni[1]
[1]School of Psychology, Faculty of Science, University of Nottingham, Nottingham, UK
[2]Institute of Sport, Department of Sport and Exercise Sciences, Manchester Metropolitan University, Manchester, UK

Introduction: Understanding the mechanisms of visual dominance and suppression in the human brain is crucial for insights into various neurological and psychiatric conditions. When different visual stimuli are presented to each eye, the brain does not merge them into a single image, but instead experiences binocular rivalry, where conscious perception alternates between the two stimuli [1]. The dynamic changes in perceptual alternations during binocular rivalry have potential as biomarkers for disorders such as schizophrenia [2], autism [3], and ADHD [4]. Additionally, in strabismus (eye misalignment), one eye becomes dominant and suppresses the input from the weaker eye, which can lead to reduced neural representation and function in the affected eye over time [5,6]. A deeper understanding of these cognitive processes and neural mechanisms can aid in early diagnosis and monitoring of disease progression and offer insights into how visual competition affects conditions like strabismus and amblyopia. Previous research suggests that these perceptual changes may manifest as travelling waves across the visual field [7]. In this process, the suppressed image initially appears in one location and then gradually becomes dominant. Typically, these changes are triggered by abrupt contrast shifts between the images [8]. This study employs fast (<100ms TR) functional MRI at 3T t detect phase shifts in response onset across different parts of the visual field (Fig.2), aiming to characterise visual stimuli properties involved in binocular rivalry and perceptual dominance fluctuations. Understanding these mechanisms can unravel how to the brain processes conflicting sensory information and resolves perceptual ambiguities.

Methods: Data acquisition was performed on a Siemens 3T MAGNETOM Vida system using a 64-channel head/neck coil at the Institute of Sport, following approval by the Science and Engineering ethics review board at Manchester Metropolitan University. Functional scans used a T2* gradient-recalled-echo pulse sequence (TR/TE=100/23ms, FA=15, pF=6/8, bandwidth=1520 Hz/px, FOV=188mm, effective inplane resolution = 2 x 2 mm, 10mm slice thickness). A retinotopic map (GE-EPI:52 slices, 2.5mm iso, TR/TE=1000/30ms) was acquired to identify the grey matter voxels that corresponded, retinotopically, to the stimulus annulus presented in the main experiment. Whole-brain T1-weighted structural images (0.8mm isotropic) were acquired using standard MP2RAGE.
Paradigm: Rival stimuli comprised radial annulus patterns with varying radial and angular cycles to create one concentric grating and one radial grating, each covering 9 degrees of visual angle. The stimuli were presented at the same location on the screen, but distinct colours allowed each grating to be seen by only one eye through red-cyan anaglyph glasses (Fig.1). Trials began with the concentric grating shown for 30ms, followed by the radial grating, which ensured that the radial grating became the conscious percept. After 480ms, the contrast in a small region of the concentric grating at the annulus's top was abruptly increased for 75ms. This pulse typically initiated a perceptual travelling wave, causing the concentric grating to emerge into consciousness while the radial grating was suppressed. Participants pressed a key when the traveling wave reached a marked area at the bottom of the annulus, after which the stimuli were removed, and a blank screen was shown for 9s before the next trial.
Data analysis: Retinotopic mapping data identified the V1 region representing the stimulus annulus (Fig.3A). Main experimental session data were pre-processed (head motion correction, slice timing correction, high pass filtering). The average timecourse for each voxel within the V1 region was extracted and fitted to a sinusoidal function to estimate phase and amplitude, which corresponded to the time-to-peak and response amplitude of the fMRI response to the travelling wave stimuli.

Results: Using the eccentricity map, the V1 voxels representing the stimulus annulus were identified (Fig.3A). The polar angle map pinpointed the top region where the contrast change triggered the

travelling wave (Fig.3A). The average timecourse for voxels in this region during trials showed a slight delay in time-to-peak (Fig,3B, C), with an onset time variance of 2.7s ±0.6s, consistent with Lee et al. (2005)[9].

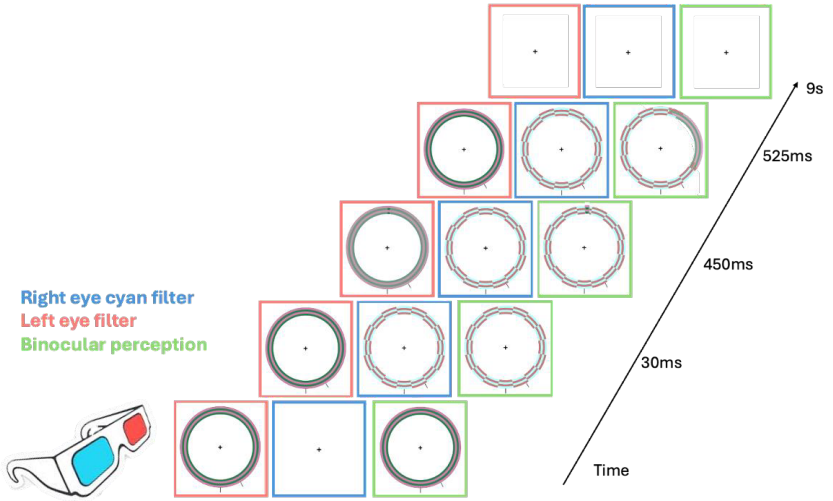

Fig. 1. Experimental Design. Low contrast, concentric grating and high contrast radial grating are presented while participants wear red-cyan anaglyph glasses to ensure that only one stimulus is processed by one eye. The third column (green) gives a representation of what the participant perceives at each trial. The concentric grating is suppressed following presentation of the radial grating, the change in contrast at the top of the concentric grating generates a change in dominance/suppression. This results in a travelling wave spreading along the annulus. Participants press a key when the wave reaches the black nonius at the bottom of the annulus.

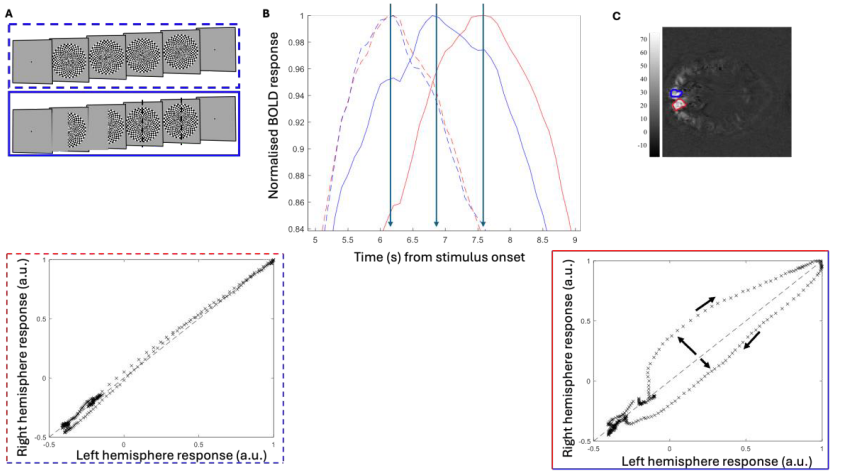

Fig. 2. (A) Experimental design: dashed line trials where left and right hemispheres are stimulated simultaneously (flickering checkerboard; 2s ON, 26s OFF). Solid line trials where the left hemisphere (right hemifield) is stimulated 1000ms before the right hemisphere. **(B)** Mean response to stimulation of the right (blue) and left (red) visual hemifield. Dashed lines for both hemifield stimulated simultaneously. When the hemifields are stimulated 1000ms apart, there is a clear delay in the peak response, further affected by the stimulation of the left hemifield. Bottom: Lissajous plots for the zero- (left), and the 1000ms delay condition (right). **(C)** Activation map and ROIs used for data in (B).

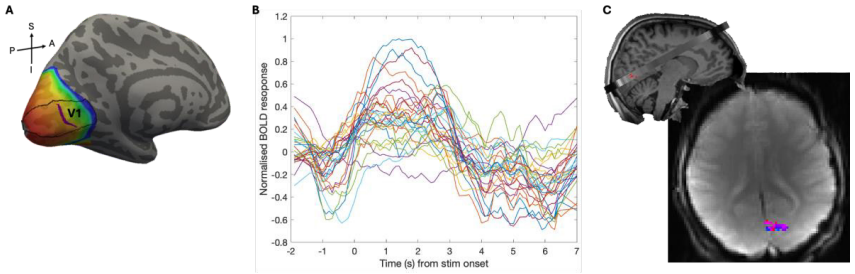

Fig. 3. (A) Surface representation of V1 mapping overlaid onto eccentricity map. The region in purple shows the retinotopic presentation of the annulus used in the main experiment. **(B)** Example of average timecourses of grey matter voxels included in the ROI. These show a shift in time their maximum amplitude, suggestive that the delay in travelling wave can be measured via fast fMRI. **(C)** heatmap showing distribution of estimated phase (i.e., time delay) for each grey matter voxel within the ROI during trials that elicited a change in dominance (travelling wave).

Discussion: This study explores perceptual dominance and suppression states in the form of travelling waves during binocular rivalry, providing insights into visual awareness processes. Fast fMRI enables measurements of onset changes across V1's cortical surface during the travelling wave experience.

This understanding of binocular rivalry mechanisms can enhance our grasp of how the brain resolves visual discrepancies and prioritises stimuli, which is crucial for diagnosing and treating conditions like amblyopia and other sensory integration disorders [6]. Additionally, abnormalities in binocular rivalry could indicate early signs of neurological disorders, such as Alzheimer's and schizophrenia [2]. This research thus holds potentials for advancing diagnostic methods and developing treatments for these conditions.

Acknowledgements: EZ/AJK acknowledge provision of MR scanning time and development from the Manchester Metropolitan University. RH/EZ acknowledge Prof McGraw (UoN) and Dr Schluppeck for discussions on experimental design.

References

[1] Blake (1989) A neural theory of binocular rivalry. Psychological Review, 96(1), 145-167
[2] Ye et al. (2019) Slower and less variable binocular rivalry rates in patients with Bipolar Disorder, OCD, Makor Depression, and Schizophrenia. Front Neurosci, 13:514
[3] Skerwetat et al. (2022) Visual consciousness dynamics in adults with and without autism. Scientific Reports, 12, 4376.
[4] Amador-Campos et al. (2013) Assessing Attention deficit by Binocular Rivalry. Journal of Attention Disorders, 19(12), 1064-1073.
[5] Levi (2006) Visual processing in amblyopia: human studies. Strabismus, 14(1), 11-19
[6] Baker & Meese (2007) Binocular contrast interactions: dichoptic masking is not a single process. Vision Research, 47(23), 3096-3104
[7] Wilson et al. (2001) Dynamics of travelling waves in visual perception. Nature, 412, 907
[8] Naber et al. (2009) Suppression wave dynamics: visual field anisotropies and inducer strength. Vision Research, 49, 1805-1813
[9] Lee et al. (2005) Travelling waves of activity in primary visual cortex during binocular rivalry. Nat Neurosci, 8(1), 22-23

A Bio-engineered BOLD Alternative for High-Resolution Brain Function Mapping

Elizabeth Jane Fear[1,2], Antonella Antonelli[1], Passant Abdalla[1], Simon Benedict Duckett[2], Mauro Magnani[1], and Aneurin James Kennerley[2,3]

1. Department of Biomolecular Sciences, University of Urbino Carlo Bo, Urbino, Italy
2. Centre for Hyperpolarisation in Magnetic Resonance (CHyM), Chemistry, University of York, York, United Kingdom
3. Sport and Exercise Science, Institute of Science, Manchester Metropolitan University, Manchester, United Kingdom

Introduction: We have developed a next-generation, safe, personalised iron-based contrast agent (CA) for enhancing cerebral blood volume (CBV) weighted functional MRI (fMRI). Our novel method encapsulates superparamagnetic iron oxide nanoparticles (SPIONs) in red blood cells (RBCs), to overcome rapid removal by the reticuloendothelial system (RES) and improves the stability of the CA in blood circulation. Here we present preclinical validation using human Ferucarbotran®-loaded RBCs for mapping brain function based on cerebral blood volume (CBV) changes in a rat model using 7T fMRI. Our method mirrors the contrast of free SPIONs in preclinical fMRI, offering functional sensitivity at cortical laminar resolutions, giving an advantage over routine Blood Oxygenation Level Dependent (BOLD) measures. Our approach provides a non-BOLD alternative for high-resolution brain function mapping, promoting further development for long-term assessments in animal and human models.

Methods: *Contrast Agent Preparation*: Ferucarbotran® (Meito Sangyo) was encapsulated into human RBCs (using 11.2 mg Fe/ml of 70% haematocrit loaded solution) using a patented hypotonic dialysis method (Fig 1 A).[1][2] The T_1 longitudinal relaxation time of the Ferucarbotran®-loaded-RBCs at 44% haematocrit were measured at 9.4T (Avance-400 NMR, Bruker) to determine iron concentration. Transmission Electron Microscopy (TEM) was used to confirm entrapment of the SPION within the RBCs and to evaluate morphological changes. 1.5 ml of human Ferucarbotran®-loaded-RBCs at 44% haematocrit were used for injection into non-recovery rat models.

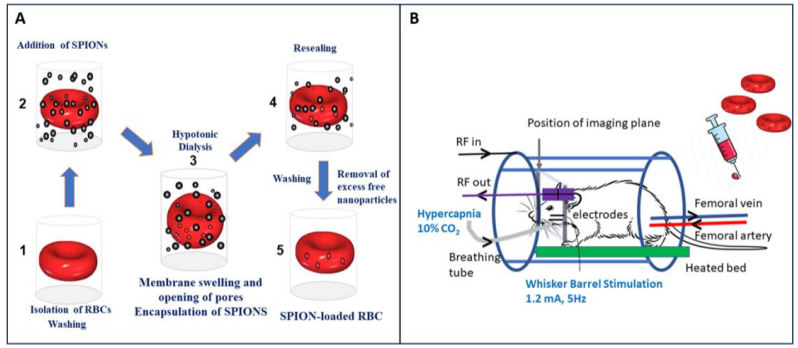

Figure 1. Encapsulation methods and fMRI experimental set up (**A**) Schematic representation of the SPIONs loading into RBCs by hypotonic dialysis and isotonic resealing. (**B**) Preclinical fMRI set up showing the positioning of the imaging plane, RF volume transmit coil, RF head receiver coil, femoral artery and veins cannulated to monitor blood pressure and infuse the CA, breathing tube for ventilation and delivery of medical air/CO_2 for hypercapnia respiratory challenge and the positioning of the electrodes for electrical whisker stimulation.

Imaging: Pre-clinical MRI measurements were made at 7 Tesla (Bruker BioSpec 70/30, 310mm bore). Urethane anaesthetized rats were artificially ventilated and cannulated for monitoring arterial blood pressure and intravenous infusion (Fig 2 B). BOLD and IRON fMRI data were acquired in the coronal plane with a GE-EPI readout (TR/TE=1000/12ms, 64*64, FOV=30mm, slice thickness=2mm, FA 90°).

BOLD fMRI (pre-CA injection) signal changes to whisker stimulation (16s, 1.2mA, 5Hz) and respiratory challenge (increased end-tidal $FiCO_2$<10%) were acquired.[3] Following BOLD fMRI measurements, injection of the encapsulated cells (1.5 ml) was completed in 0.5 ml stages and Structural GE images (256*256, FOV 30mm, 9 slices, 1 mm thick) were captured for assessment of baseline blood volume fraction[4] to aid quantification of CBV-fMRI measures. Hypercapnia and whisker stimulation were repeated, and IRON fMRI measurements were acquired. Percentage changes in CBV were calculated using both the pre-CA (BOLD) and post-CA (IRON)-injection measurements.

Results: TEM confirmed the presence of a homogeneous distribution of iron oxide within the RBCs with no cell morphological changes. NMR confirmed Ferucarbotran® concentration encapsulated in the RBCs as 11.27 ± 2.79 mM of Fe. fMRI data were obtained following injection of 1.5 ml of Ferucarbotran®-loaded-RBCs to i) estimate baseline blood volume fractions in rat brain and ii) validate CBV weighting of fMRI signals (Fig 2A). CBV response is maximal in layer-IV of the cortex, unlike BOLD signals localized to superficial cortical layers (Fig 2B). We observed peak CBV responses of 37.1 ± 12.8% to respiratory challenge and 9.4 ± 1.3% to whisker pad stimulation.

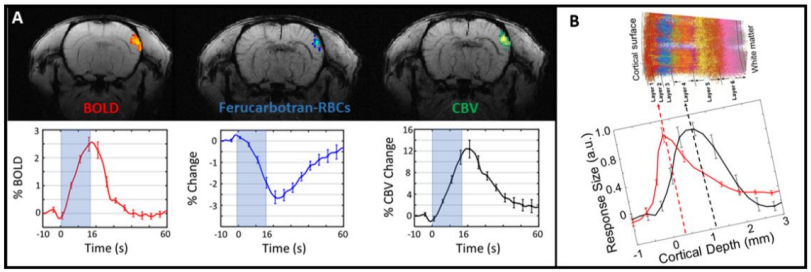

Figure 2. fMRI measures in response to somatosensory whisker stimulation (16s, 1.2mA, 5 Hz). **(A)** Representative signal maps overlaid on GE structural scans. EPI time series (TR/TE = 1000/12ms) of positive BOLD signal (red), negative signal with iron (blue) after injection of Ferucarbotran®-loaded RBCs and calculated percentage CBV change. **(B)** Cortical depth profiles showing BOLD signal (red) weighted to the surface of the cortex due to large draining veins and CBV signal (black) found much deeper in layer IV of the cortex.

Discussions/Conclusions: Here we introduce an innovative BOLD replacement for safe, personalised iron-based contrast agent (CA) empowered functional Magnetic Resonance Imaging (fMRI). Utilising advanced red blood cell (RBC) encapsulation technology, we developed a biocompatible super-paramagnetic CA. This CA was validated using fMRI in a preclinical rat model, demonstrating its capability to map cerebral blood volume (CBV) in response to respiratory challenge and somatosensory stimulation. This approach provides a non-BOLD alternative for high-resolution, layer-specific mapping of brain function. Future longitudinal validation will find application in measuring CBV as a biomarker for brain disorders including stroke and neurodegenerative diseases.

References:

[1] Antonelli A, Magnani M. SPIO nanoparticles and magnetic erythrocytes as contrast agents for biomedical and diagnostic applications. *Journal of Magnetism and Magnetic Materials.* 2022;541.

[2] Antonelli A, Pacifico S, Sfara C, Tamma M, Magnani M. Ferucarbotran-loaded red blood cells as long circulating MRI contrast agents: first in vivo results in mice. *Nanomedicine.* 2018;13(7):675-687

[3] Huber L, Poser BA, Kaas AL, et al. Validating layer-specific VASO across species. *Neuroimage.* 2021;237

[4] Tropres I, Grimault S, Vaeth A, et al. Vessel size imaging. *Magnetic Resonance in Medicine.* 2001;45(3):397-408

Acknowledgements: PON BIO-D Development of diagnostic biomarkers for precision medicine and personalized therapy. Project Code: ARS01_00876 (CUP B32F20000270005) and Royal Society International Exchange Scheme Grant.

fQSM versus fMRI: A Comparative Analysis of Activations in Veins

Jannette Nassar[1], Oliver C. Kiersnowski[1], Patrick Fuchs[1], Karin Shmueli[1]

[1] *Department of Medical Physics and Biomedical Engineering, University College London, London, United Kingdom*

Introduction: Functional quantitative susceptibility mapping (fQSM) detects blood oxygenation changes related to neuronal activation "upstream" of the magnitude signal, offering a complementary perspective to conventional fMRI. FQSM reveals the blood susceptibility changes that underlie conventional Blood Oxygenation Level Dependent (BOLD) activation: fQSM is based on a linear dependence of susceptibility on blood oxygenation, unlike the non-linear dependence of conventional BOLD fMRI based on the signal magnitude [3, 4]. Therefore, fQSM may improve the localization of neuronal activity [1, 2], and detect less activation in large draining veins [4]. Hence, here, we aimed to investigate whether fQSM is less affected by signals arising in venous vessels than fMRI.

Methods: Image acquisition: We acquired 70 multi-echo 2D GRE EPI volumes in 7 healthy volunteers, age 27.7 ± 3.8, using a 3T Siemens-Prisma system with a 64-channel head coil, with 1.3 mm isotropic resolution; GRAPPA=4; MB=3; partial Fourier 6/8; TE=14.8, 39.33, 68.86 ms; TR=4034 ms; TA = 6 min 15 s [5]. To maximize the BOLD signal, we employed a standard visual stimulation paradigm, with a conventional block design. The stimulation consisted of a (black and white) checkerboard flickering at 8Hz in 15.6 s blocks alternating with rest blocks of 15.6 s.

Data processing steps included the generation of brain masks using FSL BET [6] on the second echo magnitude images, followed by single-voxel erosion. For magnitude-based fMRI, multi-echo magnitude images were combined using T_2^*-weighted echo summation [7]. QSMs were calculated for each volume by: non-linear fitting of the complex data [8]; Laplacian phase unwrapping [9]; intra- and inter-slice background field removal with 2D+3D V-SHARP[18,19]; and dipole inversion using non-linear total variation regularisation (FANSI, $\alpha = 2x10^{-4}$) [11].

Functional Analysis: We used SPM12 [12, 13] for fMRI and fQSM analysis [14]. Spatial pre-processing involved (1) rigid-body realignment of the echo-combined magnitude images to the first image in the time-series to correct for motion. The resulting transformations were then applied to the corresponding absolute susceptibility maps. (2) Spatial smoothing with a 4-mm FWHM Gaussian kernel to enhance SNR and statistical power [15]. A general-linear model (GLM) was reconstructed with a regressor for the visual stimuli. Significant activations were identified by thresholding t-score maps to create fMRI and fQSM activation maps using a threshold of $p<0.05$ with Family Wise Error (FWE) correction and no restriction on minimum cluster size.

A mask to highlight highly paramagnetic venous vessels was computed by thresholding at the 99th percentile of the susceptibility distribution. An axial maximum intensity projection (MIP) of the venous vessel mask is shown in Figure 1c. The number of activated voxels detected by fQSM and fMRI were compared, specifically focusing on those within the venous vessel regions. We calculated the percentage of venous vessel voxels that were activated in fQSM v. fMRI.

Results & Discussion: As shown in Fig. 2a, fMRI generally shows higher brain activation than fQSM, and there is significant variability in the number of activated voxels among the volunteers for both methods. Figs 1f, g and 2b show that there were fewer activated voxels in the venous vessels region and a lower percentage of activated venous voxels with fQSM compared to fMRI in all subjects. This suggests that fQSM activations are less contaminated by venous voxels. A major limitation of this study is the creation of the venous mask by thresholding the QSM distribution which clearly includes non-vascular strongly paramagnetic structures (Fig 1c). Future work will involve more sophisticated vessel masking [16, 17, 18].

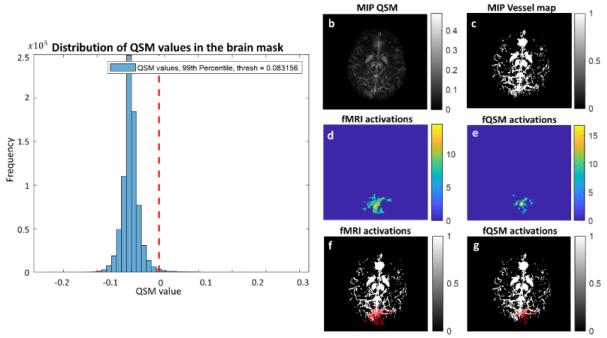

Figure 1. (a). Distribution of QSM values in the brain mask, showing the 99th percentile threshold used to compute the venous vessel mask, in one volunteer. MIPs of the QSM map and the vein mask are shown in (b) and (c) respectively, and MIPs of the fMRI and fQSM activations in (d) and (e) respectively. The MIP of the fMRI and fQSM activations overlaid on a MIP of the vein mask are shown in (f) and (g), respectively.

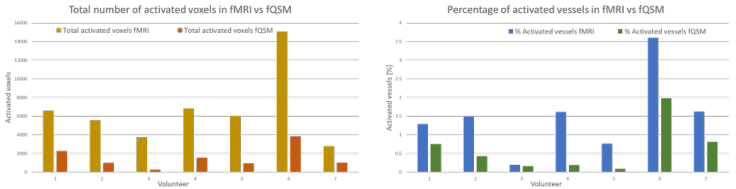

Figure 2. (a). Number of activated voxels in fMRI vs fQSM in all seven volunteers, (b) Percentage of activated vessels in fMRI vs fQSM.

Conclusions: In this first study to employ multi-echo fQSM, in all seven volunteers, fQSM had fewer activated voxels in veins than conventional fMRI, indicating that fQSM is more localized and less contaminated by activations in large veins.

References:

[1] V. Jain, O. Abdulmalik, K. J. Propert, and F. W. Wehrli, "Investigating the magnetic susceptibility properties of fresh human blood for noninvasive oxygen saturation quantification," *Magnetic Resonance in Medicine*, vol. 68, no. 3, pp. 863–867, 2012, doi: 10.1002/mrm.23282.

[2] P. S. Özbay *et al.*, "Probing neuronal activation by functional quantitative susceptibility mapping under a visual paradigm: A group level comparison with BOLD fMRI and PET," *Neuroimage*, vol. 137, pp. 52–60, Aug. 2016, doi: 10.1016/j.neuroimage.2016.05.013.

[3] D. Z. Balla *et al.*, "Functional quantitative susceptibility mapping (fQSM)," *Neuroimage*, vol. 100, pp. 112–124, Oct. 2014, doi: 10.1016/j.neuroimage.2014.06.011.

[4] S, Straub, "Functional quantitative susceptibility mapping for layer specific activation, Program Number: 3127," *ISMRM 2024*.

[5] Kiersnowski O C, et al., "Rapid high resolution integrated structural and functional susceptibility and conductivity mapping in the human brain," *Proc. Ann. Meeting ISMRM 2024, Abstract 188.*, 2024.

[6] S. M. Smith, "Fast robust automated brain extraction," *Hum Brain Mapp*, vol. 17, no. 3, pp. 143–155, Nov. 2002, doi: 10.1002/hbm.10062.

[7] B. A. Poser, M. J. Versluis, J. M. Hoogduin, and D. G. Norris, "BOLD contrast sensitivity enhancement and artifact reduction with multiecho EPI: Parallel-acquired inhomogeneity-desensitized fMRI," *Magnetic Resonance in Medicine*, vol. 55, no. 6, pp. 1227–1235, 2006, doi: 10.1002/mrm.20900.

[8] T. Liu, C. Wisnieff, M. Lou, W. Chen, P. Spincemaille, and Y. Wang, "Nonlinear formulation of the magnetic field to source relationship for robust quantitative susceptibility mapping," *Magnetic resonance in medicine*, 2013, doi: 10.1002/mrm.24272.

[9] M. A. Schofield and Y. Zhu, "Fast phase unwrapping algorithm for interferometric applications," *Opt Lett*, vol. 28, no. 14, pp. 1194–1196, Jul. 2003, doi: 10.1364/ol.28.001194.

[10] W. Li, B. Wu, and C. Liu, "Quantitative susceptibility mapping of human brain reflects spatial variation in tissue composition," *NeuroImage*, vol. 55, no. 4, pp. 1645–1656, Apr. 2011, doi: 10.1016/j.neuroimage.2010.11.088.

[11] "Fast nonlinear susceptibility inversion with variational regularization - Milovic - 2018 - Magnetic Resonance in Medicine - Wiley Online Library." Accessed: Nov. 07, 2022. [Online]. Available: https://onlinelibrary.wiley.com/doi/10.1002/mrm.27073

[12] K. J. Friston, A. P. Holmes, K. J. Worsley, J.-P. Poline, C. D. Frith, and R. S. J. Frackowiak, "Statistical parametric maps in functional imaging: A general linear approach," *Human Brain Mapping*, vol. 2, no. 4, pp. 189–210, 1994, doi: 10.1002/hbm.460020402.

[13] J. Ashburner, "SPM: A history," *NeuroImage*, vol. 62, no. 2, pp. 791–800, Aug. 2012, doi: 10.1016/j.neuroimage.2011.10.025.

[14] J. Nassar and et al, "Optimising Functional Quantitative Susceptibility Mapping (fQSM): The Effect of Multiband Acceleration and Absolute vs. Signed QSM," *Proc. Ann. Meeting ISMRM 2024, Abstract 3415*.

[15] M. K. Chung, "Gaussian kernel smoothing." arXiv, Nov. 29, 2021. doi: 10.48550/arXiv.2007.09539.

[16] "Gap-free segmentation of vascular networks with automatic image processing pipeline - ScienceDirect." Available: https://www.sciencedirect.com/science/article/pii/S0010482517300173?via%3Dihub

[17] "Optimization of quantitative susceptibility mapping for regional estimation of oxygen extraction fraction in the brain - McFadden - 2021 - Magnetic Resonance in Medicine - Wiley Online Library." Available: https://onlinelibrary.wiley.com/doi/10.1002/mrm.28789

[18] A. P. Fan *et al.*, "Quantitative oxygenation venography from MRI phase," *Magnetic Resonance in Medicine*, vol. 72, no. 1, pp. 149–159, 2014, doi: 10.1002/mrm.24918.

Assessing somatotopic organisation of focal hand dystonia using 7T fMRI

[1]Michael Asghar, [1]Daisie Pakenham, [1]Lauren Gascoyne, [1]Denis Schluppeck, [2]Rosa Sanchez-Panchuelo, [3]George O'Neill, [4]Miles Humberstone, [1]Paul Glover and [1]Susan Francis.
[1]Sir Peter Mansfield Imaging Centre, University of Nottingham, [2]University Hospitals Birmingham NHSFT, [3]Wellcome Centre for Human Neuroimaging UCL, [4]Nottingham Trust University Hospitals.

Introduction: Focal Hand Dystonia (FHD) is a movement disorder that affects the hand. Treatment is with BoNT-A(Botox)[1], which is injected into the nerve to allow temporary relief from cramp. It is not understood how this affects sensorimotor maps. Here, we use 7T fMRI to investigate whether 1) there are any differences in cortical maps between healthy controls (HC) and FHD patients, and 2) there are any differences in the cortical response in FHD patients between ~30 days (BTX, peak effect) and ~100 days (NoBTX, minimal effect) after BoNT-A[2].

Methods: 6 FHDs (ages:54(11.2), mean(std)) and 6 age-matched HCs underwent a behavioural session and 7T fMRI. *Behavioural tasks:* Temporal discrimination, amplitude thresholding on both hands, spatial acuity grating orientation task (GOT) on the affected hand using domes with different spatial frequencies. Reproducibility of behavioural tasks was tested on a separate cohort of 10 HCs.
fMRI: a) Travelling wave (TW) somatosensory digit mapping (Both hands, D1-D5, 4s/digit, 20s/cycle, 8 cycles, 1 pair of forward/reverse, 1.25x1.25x1.25mm^3 voxels, 48 slices, TR2s); b) Cued digit tapping motortopy task separately on dominant (HC) and affected (FHD) hand (parameters as TW, participants wore an accelerometer glove to confirm digit movements);
Analysis: fMRI data were distortion corrected (FSL-TOPUP). Structural data were segmented in Freesurfer and used for registration and flat maps. Fourier and pRF analysis of the somatosensory and motortopy data was performed producing maps of digit-phase maps and pRF size respectively. Digit-phase maps were compared to a template somatosensory probabilistic atlas [3] with central tendency (CT) (1=perfect overlap between subject and atlas digits) and Figure of Merit (FoM) scores (finds the digit specificity from the CT overlap matrices) calculated for these.

Results: *Behavioural:* FHDs had raised spatial acuity thresholds (Mean HC (std): 1.87 (0.19), Mean BTX (std): 2.96 (0.93), Mean NoBTX (std): 3 (0.88); one-way ANOVA $p<0.05$), but no other differences between groups. Reproducibility coefficient of variation (CoV) was similar to previous literature [4]. *fMRI:* (i) Digit Mapping: TW sensorimotor maps showed no visual abnormalities in FHD (PA) compared to HCs. Somatosensory and motor maps showed strong overlap (DICE) in all groups and when compared to the probabilistic atlas central tendency (CT) values were close to 1. For the non-dominant hand, the PA NoBTX group had better digit representation to the atlas compared to the non-dominant hand of the HCs, as measured by the FoM. The HC FoM values are in-line with the leave-one-out validation values performed on the probabilistic atlas. (ii) pRF size: In all groups, the pRF sizes followed typical trends: increase from D1-D4, and smaller for D5, with larger pRF sizes in Brodmann areas (BA) 1 and 2 compared to 3a and 3b [5]. Motor task pRF sizes were larger than for the somatosensory task. Non-dominant hands showed larger pRF sizes compared to the dominant hand for BTX and HV groups. For the dominant hand, there were no differences in pRF size between HCs, BTX and NoBTX groups for the somatosensory and motor task. For the non-dominant hand, BTX had larger pRF sizes than HV ($p<0.05$, ANOVA), and BTX had larger pRF sizes than NoBTX group ($p<0.05$, ANOVA).

Discussion: Raised spatial acuity in FHD was consistent with literature [6]. Lack of blurring in the digit maps between groups and visits indicated that digit organisation was preserved in this group of FHD patients compared to HCs, with the BoNT-A treatment having little effect on this metric. Both FHD and HC participants fit well to the probabilistic atlas, as supported by normal somatotopy seen at individual level in FHDs. When looking at D1-D4 pRF size trends were similar across all groups, D5 being smaller. Motor pRF sizes were larger than somatosensory pRFs, which is supported in the literature [7]. In the dominant hand, there was no difference in pRF size between any groups (HC, PA BTX, PA NoBTX); consistent with normal TW somatotopy seen. It is of interest that in the non-dominant hand, BTX

Power Pitch Session 3

exhibited larger pRF sizes than HCs and NoBTX groups. This suggests that the pRF analysis captures an increase in pRF size which occurs alongside treatment.

Conclusion: There was no large-scale blurring of digit somatotopy in FHDs, at a participant level or when compared to a probabilistic atlas. pRF mapping indicated there were no differences between HCs, PA BTX and PA NoBTX groups in the dominant hand. The non-dominant hand showed changes in digit representation and pRF size.

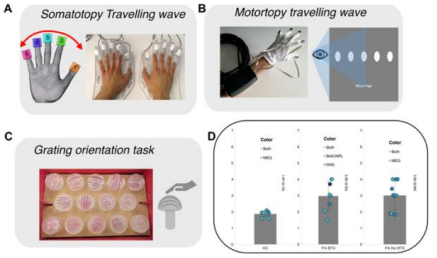

Figure 1: A) Experimental setup for somatosensory task; B) Setup for the motor tapping task, shown with accelerometer glove; C) Spatial acuity grating orientation task (GOT); D) Results for GOT showing patients (PA) have larger thresholds than controls (HC).

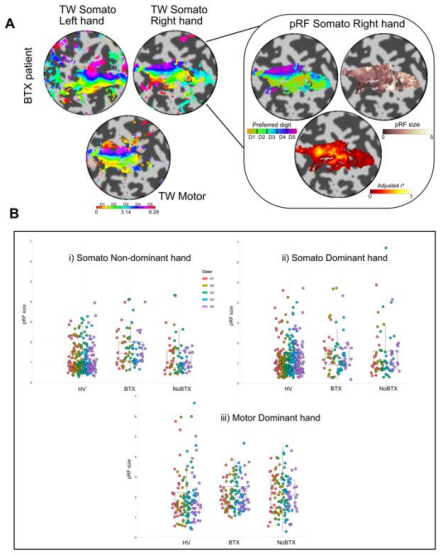

Figure 2: A) Travelling wave somato and motor maps for an example BTX patient, and somatosensory pRF map for the dominant (right) hand. B) pRF sizes are shown for somatosensory i) non-dominant, ii) dominant, and iii) motor tasks.

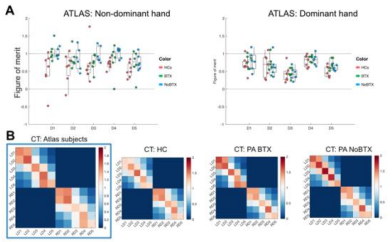

Figure 3: A) Figure of merit (FoM) plots shown for all controls (HC) and patients (PA). The FoM is a metric of how well each digit is represented when comparing overlap with the probabilistic atlas. B) Central tendency (CT) matrices for each group – comparing each subject digit to the probabilistic atlas digit. The blue boxed matrix shows the central tendency calculated from a leave one-out validation procedure from a healthy subject included in the probabilistic atlas.

References

[1] The Dystonia Society, "Focal Hand Dystonia." Accessed: Jul. 20, 2008. [Online]. Available: http://www.dystonia.org.uk/index.p hp/professional-research/types-of-dystonia/focal-hand-dystonia

[2] L. G. Cohen, M. Hallett, B. D. Geller, and F. Hochberg, "Treatment of focal dystonias of the hand with botulinum toxin injections.," *J Neurol Neurosurg Psychiatry*, vol. 52, no. 3, pp. 355–63, 1989, doi: 10.1136/jnnp.52.3.355.

[3] G. C. O'Neill *et al.*, "A probabilistic atlas of finger dominance in the primary somatosensory cortex," *Neuroimage*, vol. 217, Aug. 2020, doi: 10.1016/j.neuroimage.2020.116880.

[4] M. Mikkelsen, J. He, M. Tommerdahl, R. A. E. Edden, S. H. Mostofsky, and N. A. J. Puts, "Reproducibility of flutter-range vibrotactile detection and discrimination thresholds," *Sci Rep*, vol. 10, no. 1, Dec. 2020, doi: 10.1038/s41598-020-63208-z.

[5] M. Asghar, R. Sanchez-Panchuelo, D. Schluppeck, and S. Francis, "Two-Dimensional Population Receptive Field Mapping of Human Primary Somatosensory Cortex," *Brain Topogr*, vol. 36, no. 6, pp. 816–834, Nov. 2023, doi: 10.1007/s10548-023-01000-8.

[6] F. M. Molloy, T. D. Carr, K. E. Zeuner, J. M. Dambrosia, and M. Hallett, "Abnormalities of spatial discrimination in focal and generalized dystonia," *Brain*, vol. 126, no. 10, pp. 2175–2182, 2003, doi: 10.1093/brain/awg219.

[7] W. Schellekens, N. Petridou, and N. F. Ramsey, "Detailed somatotopy in primary motor and somatosensory cortex revealed by Gaussian population receptive fields," *Neuroimage*, vol. 179, no. May, pp. 337–347, 2018, doi: 10.1016/j.neuroimage.2018.06.062.

[8] M. Nevrlý, P. Hluštík, P. Hok, P. Otruba, Z. Tüdös, and P. Kaňovský, "Changes in sensorimotor network activation after botulinum toxin type A injections in patients with cervical dystonia: a functional MRI study," *Exp Brain Res*, vol. 236, no. 10, pp. 2627–2637, Oct. 2018, doi: 10.1007/s00221-018-5322-3.

fMRI reveals pain-like responses in a patient with pain insensitivity due to rare genetic mutation of FAAH-out gene.

Michael Asghar[1], Francis McGlone[3], David Finn[6], Duncan Hodkinson[1], Warren Moore[2], Oleg Favorov[4], Devjit Srivastava[5], Susan Francis[1], Andrew Marshall[2].
[1]SPMIC University of Nottingham, [2]University of Liverpool, [3]Liverpool John Moores University, [4]University of North Carolina at Chapel Hill, [5]Department of Anaesthesia, Raigmore Hospital, Inverness, [6]University of Galway.

Introduction: MRI provides a tool to study complex brain changes. Here, a case study is presented of a unique pain free subject (PFS) with congenital insensitivity to pain, lack of anxiety, and faster wound healing, who had co-inheritance of a microdeletion in a pseudogene FAAH-OUT and FAAH polymorphism, leading to enhanced endocannabinoid signaling[1]. Quantitative sensory testing revealed hyposensitivity to noxious thermal and mechanical stimuli. ***Aim:*** To understand how these genetic and perceptual alterations were expressed in the brain, PFS underwent 3T and 7T MRI measures of their responses to sensory and pain stimuli.
Methods: PFS underwent 3T and 7T MRI on the same day. Heat pain threshold was at a ceiling level for the MEDOC PATHWAY system (50°C). ***3T MRI***: fMRI: 1) Heat pain task on the thenar (MEDOC, 23s ON, 8s OFF2 runs; 2) C-tactile (CT) brushing task (6 scans, 2 runs at 0.3cms^{-1}, 3cm^{-1}, 30cms^{-1} brush stroking velocity applied to the hairy skin of the hand dorsum (fMRI acquisitions: 2x2x2.5mm, 48 slices, TR1s, 5mins). 1mm isotropic structural MPRAGE and T_1 mapping data was also collected. ***7T MRI***: fMRI: 1) Heat pain task on the thenar (2 runs, as above 5mins), and 2) Travelling wave (TW) digit mapping (Left hand, D1-D5 4s ON, 12 repeats per scan, 1 pair of forward and reverse (fMRI acquisition 1.25x1.25x1.25mm, 34 slices, TR2s). rs-fMRI, PSIR and MRS (ACC, OCC, Insula). ***Analysis***: fMRI data were distortion corrected (FSL-TOPUP) and corrected for thermal (NORDIC [2]) and physiological (RETROICOR[3]) noise. Structural data were segmented in Freesurfer and used for registration and flat maps. 3T and 7T heat pain data were analysed with a GLM in SPM12, producing maps of heat pain response. Heat pain maps were moved to flattened space to assess the alignment with nociresponsive Brodmann area 3a[4]. PFS's heat pain responses were compared to a neurological pain signature pattern map (NPS); this process finds the dot product of the NPS and the input heat pain response[5]. The NPS in PFS was compared to a group of healthy subjects (n=7, 2 female, age=29.9(5.1) (Mean, (STD)) collected with the same experimental setup and scan protocol. C-tactile (CT) data were analysed in SPM12, producing activation maps for each stroking velocity. Fourier and pRF analysis of the digit mapping data was performed, producing digit-phase coherence maps, and measures of pRF size. Digit maps were compared to a template somatosensory probabilistic atlas[6].
Results: The heat pain fMRI response at both 3T and 7T in PFS was typical (Fig1), with heat pain regions (primary & secondary somatosensory cortex (S1, S2), insula, anterior cingulate (ACC), thalamus, amygdala, middle frontal gyrus) activated in fMRI [4]. NPS scores for PFS were within the normal range as compared to healthy subjects. Nociresponsive 3a was activated by heat pain. Digit mapping showed a typical somatotopic arrangement in S1 (Fig2). When compared to the probabilistic atlas, central tendency values were close to 1. Behaviourally, PFS showed a typical inverted U-shaped velocity preference to CT targeted brushing. The brushing task activated typical regions implicated in this form of touch[7]. 3cms-1 produced the weakest response compared to the other velocities.
Discussion: PFS shows typical responses to heat pain stimulation, including activation of S1, S2, Cingulate, OFC, Amygdala and Insula, all implicated in a pain connectome. There were no differences in NPS scores of PFS compared to healthy subjects, reinforcing PFS's normal cortical, as opposed to behavioural, heatpain responses. Digit maps of PFS do not show any strong deviations or abnormalities and follow the typical somatotopy of D1-D5 as validated against a probabilistic atlas. CT responses do not show strong preference for the 3cms^{-1} condition; there is no evidence of preferential DPINS (dorsal posterior insula) activation with CT targeted touch.

Power Pitch Session 3

Conclusion: PFS displays typical cortical responses to heat pain stimulation, in contrast to perceptual hypoalgesia. Although the neurobiological basis for the insensitivity to pain remains enigmatic, deeper understanding of FAAH-based analgesia could open new opportunities for the treatment of pain.

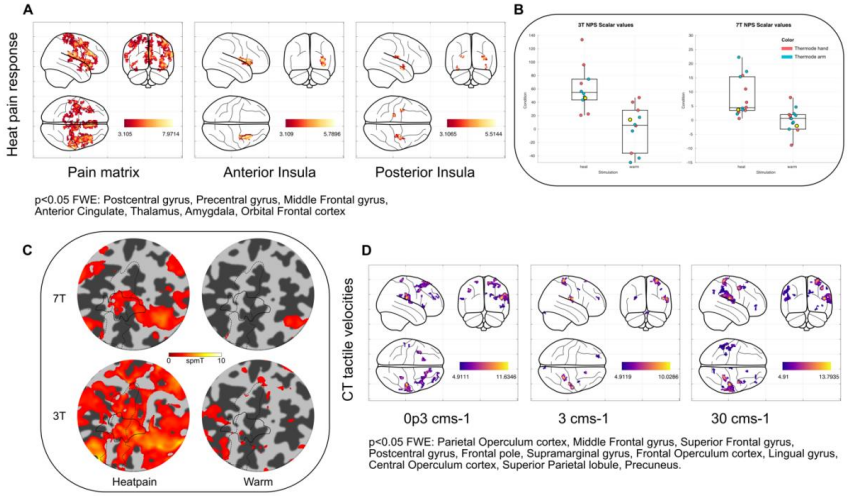

Figure 1: A: Heat pain response of PFS in typical pain regions, with insula regions highlighted. B: Neurological pain signature dot products (from combining template pattern map with heat pain contrast maps from SPM12), for PFS (yellow), and healthy subjects for heat pain task at 3T and 7T. Red = thermode on hand, Blue = thermode on inside of forearm. C: Heat pain response in native space, on a flattened patch of corte overlaid are the digit map outline, and Brodmann area 3a from the Freesurfer segmentation. D: CT Tactile velocity maps at 3 velocities of brush stroking.

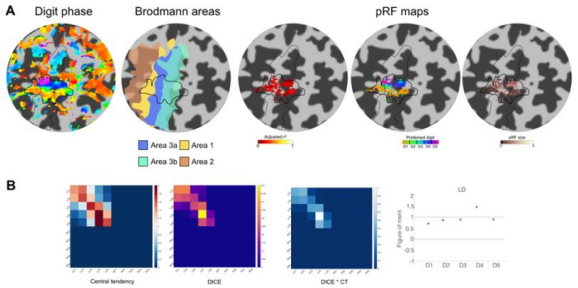

Figure 2: A: Digit mapping in native space, on a flattened patch of cortex. Overlaid are the digit map outline, and Brodmann area 3a from the Freesurfer segmentation. B: Comparison of digit map with the probabilistic atlas. Central tendency shows how well the subject's digits match with the atlas. 1 = perfect overlap. Figure of Merit (bottom right) penalises poor representation and degeneracy, by operating on the CT values.

[1] A. M. Habib *et al.*, "Microdeletion in a FAAH pseudogene identified in a patient with high anandamide concentrations and pain insensitivity," *Br J Anaesth*, vol. 123, no. 2, pp. e249–e253, Aug. 2019, doi: 10.1016/j.bja.2019.02.019.

[2] L. Vizioli *et al.*, "Lowering the thermal noise barrier in functional brain mapping with magnetic resonance imaging," *Nat Commun*, vol. 12, no. 1, Dec. 2021, doi: 10.1038/s41467-021-25431-8.

[3] G. H. Glover, T.-Q. Li, and D. Ress, "Image-Based Method for Retrospective Correction of Physiological Motion Effects in fMRI: RETROICOR," *Magn Reson Med*, vol. 167, no. December 1999, pp. 162–167, 2000, [Online]. Available: http://web.mit.edu/swg/ImagingPubs/Motion Correction/Glover.retrocor.2000.pdf

[4] R. M. S. Panchuelo, S. Eldeghaidy, A. Marshall, F. McGlone, S. T. Francis, and O. Favorov, "A nociresponsive specific area of human somatosensory cortex within BA3a: BA3c?," *Neuroimage*, vol. 221, p. 117187, 2020, doi: https://doi.org/10.1016/j.neuroimage.2020.117187.

[5] T. D. Wager, L. Y. Atlas, M. A. Lindquist, M. Roy, C.-W. Woo, and E. Kross, "An fMRI-Based Neurologic Signature of Physical Pain," *New England Journal of Medicine*, vol. 368, no. 15, pp. 1388–1397, Apr. 2013, doi: 10.1056/nejmoa1204471.

[6] G. C. O'Neill *et al.*, "A probabilistic atlas of finger dominance in the primary somatosensory cortex," *Neuroimage*, vol. 217, Aug. 2020, doi: 10.1016/j.neuroimage.2020.116880.

[7] H. W. Olausson *et al.*, "Unmyelinated tactile afferents have opposite effects on insular and somatosensory cortical processing," *Neurosci Lett*, vol. 436, no. 2, pp. 128–132, May 2008, doi: 10.1016/j.neulet.2008.03.015.

Abnormal Resting State Network Connectivity in Sickle Cell Anaemia

Mitchel Lee[1], Fenella Kirkham[2], Karin Shmueli[1]

[1]Medical Physics and Biomedical Engineering, University College London, London, UK

[2]Developmental Neurosciences, Institute of Child Health, University College London, London, UK

Introduction: Sickle cell anaemia (SCA) is a severe genetic blood disorder resulting from inheritance of two abnormal sickle beta-globin genes [1]. SCA causes deoxygenated haemoglobin to become rigid and polymerised, resulting in vaso-occlusion and haemolytic anaemia. Secondary complications are widespread, including in the brain, with a large burden of cognitive issues and chronic pain.

Independent component analysis (ICA) is a popular framework for investigating the properties of large-scale resting state networks in the brain, with abnormal connectivity being observed in several networks of the brain across various diseases and physiological states [2]. Spatially constrained ICA is a technique that can combine data-driven network discovery with established knowledge of functional brain organisation to robustly estimate brain networks [3].

Previous work investigating resting state brain function in SCA is inconclusive, with studies finding both increases and decreases in connectivity between various regions/networks, using a wide range of analysis techniques [4-6]. Here, we aim to investigate network-scale functional connectivity changes in SCA using spatially constrained ICA.

Methods: 36 SCA patients (aged 8-64 years, mean age 23 years, 15 male) and 16 healthy controls (HCs, aged 10-64 years, mean age 18 years, 12 male), recruited for the Prevention of Morbidity in Sickle Cell Anaemia (POMS) study [7], were imaged at 3T with a 6.2 minute single-echo EPI resting state scan with parameters: TR = 1.24s, TE = 26ms, 2.5 x 2.5 x 3 mm resolution, matrix 80 x 80 x 40, and a T1 weighted structural MPRAGE image with 1mm isotropic resolution.

Functional and structural data were pre-processed with a standard pipeline including geometric distortion correction, slice timing correction, outlier detection, direct segmentation and MNI-space normalization, 8mm FWHM Gaussian smoothing, and denoising, all implemented in the CONN toolbox [8]. Subject-level networks were obtained from the pre-processed functional data using a spatially constrained ICA method (MOO-ICAR [3]) implemented in the GIFT toolbox [9]. MOO-ICAR jointly optimises for the spatial independence of components (ICs) and for the spatial similarity to a chosen network template, to obtain subject-level ICs. Group-level components were obtained by taking the mean of each component across all patients and HCs. Using a template by Allen et al. [10], 28 ICs were estimated, corresponding to sensorimotor (6 ICs), basal ganglia (1 IC), auditory (1 IC), visual (6 ICs),

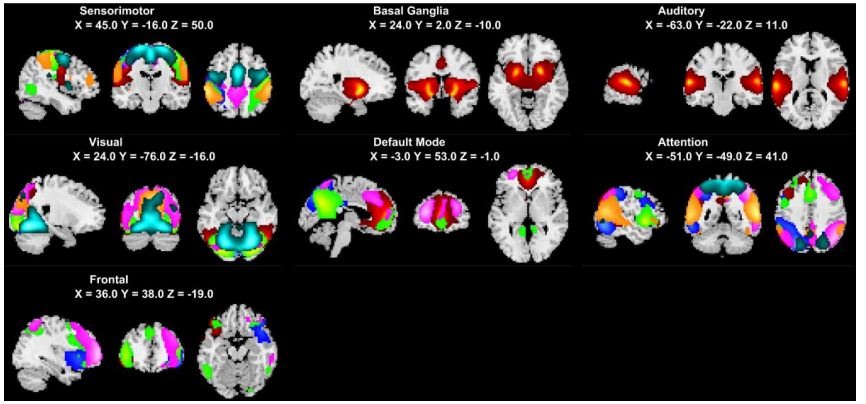

Figure 1: Maps of the group-level resting state networks estimated using ICA. For each network, the constituent ICA components are shown in different colours. MNI coordinates of peak activation are shown for each network.

default mode (5 ICs), attention (6 ICs) and frontal (4 ICs) networks. The estimated group-level ICs were imported into CONN as ROIs, and functional connectivity estimates between each pair of ICs were calculated as the Fisher-transformed bivariate correlation coefficient. Differences in connectivity between SCA patients and controls were assessed at the cluster (groups of network-network connections) level, applying the Functional Network Connectivity [11] approach to the pre-defined networks of ICs, with a joint significance threshold of $p < 0.05$ on individual connections and false discovery rate corrected p-FDR < 0.05 on clusters. Age and sex effects were regressed out of all comparisons as confounds of no interest.

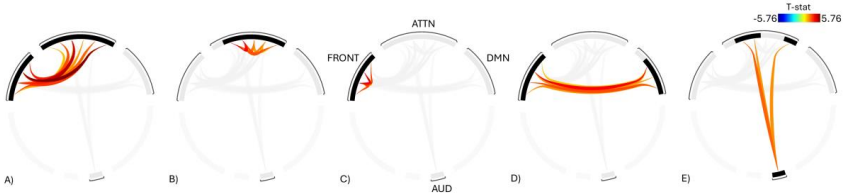

Figure 2: *Connectome rings showing 5 clusters of significantly increased network connectivity in SCA. Networks are labelled on the central ring: FRONT – frontal network, ATTN – attention network, DMN – default mode network, AUD – auditory network. For each cluster, significant component-to-component connections are highlighted based on significance.*

Results: The group-level resting state networks extracted by ICA are shown in Figure 1. Figure 2 shows the results of the comparison between SCA and control network connectivity. Five clusters of significantly increased connectivity in SCA were identified. Increased connectivity was observed between the frontal and attention networks (cluster A), within the attention network (cluster B) and within the frontal network (cluster C). Increased connectivity was also found between the default mode and frontal networks (cluster D), and between the auditory and attention networks (cluster E).

Discussion: The direction of changes in functional connectivity can be difficult to interpret, particularly in chronic conditions such as SCA, where it has been suggested that increases may represent a compensatory mechanism to preserve brain function [4]. Decreased structural connectivity, reflecting disruption to white matter pathways, has been observed in a previous study [12] that included subjects from this work among others. Increased functional connectivity in the context of white matter integrity loss has been theorised to be a consequence of reduced functional segregation of the brain [13], with more diffuse activation in the resting state. Future work will consider clinical associations with these observed connectivity changes, particularly measures of pain burden and cognition, to further improve our understanding of functional network disruption in SCA.

Conclusions: We used independent component analysis to investigate changes to network level resting-state functional connectivity measures in a cohort of sickle cell anaemia patients, finding increased connectivity compared to controls within and between several resting state networks.

References

[1] Kato GJ, Piel FB, Reid CD, et al. *Nat Rev Dis Primers*. 2018;4:18010.
[2] Lee MH, Smyser CD, Shimony JS. *AJNR Am J Neuroradiol*. 2013;34(10):1866-1872.
[3] Du Y, Fu Z, Sui J, et al. *Neuroimage Clin*. 2020;28:102375
[4] Colombatti R, Lucchetta M, Montanaro M, et al. *PLoS One*. 2016;11(6):e0157090.
[5] Zempsky WT, Stevens MC, Santanelli JP, Gaynor AM, Khadka S. *Clin J Pain*. 2017;33(12):1060-1070.
[6] Fields ME, Mirro AE, Guilliams KP, et al. *Ann Neurol*. 2020;88(5):995-1008.
[7] Howard J, Slee AE, Skene S, et al. *Trials*. 2018;19(1):55.
[8] Whitfield-Gabrieli S, Nieto-Castanon A. *Brain Connect*. 2012;2(3):125-41.
[9] Calhoun VD, Adali T, Pearlson GD, Pekar JJ. *Hum Brain Mapp*. 2001;14(3):140-151.
[10] Allen EA, Erhardt EB, Damaraju E, et al. *Front Syst Neurosci*. 2011;5:2.
[11] Jafri MJ, Pearlson GD, Stevens M, Calhoun VD. *Neuroimage*. 2008;39(4):1666-1681.
[12] Clayden JD, Stotesbury H, Kawadler JM, et al. *Blood Adv*. 2023;7(11):2297-2308.
[13] Hawellek DJ, Hipp JF, Lewis CM, et al. *Proc Natl Acad Sci U S A*. 2011;108(47):19066-19071.

Real-time quantification of brain metabolism during neuronal stimulation in healthy volunteers using hyperpolarised [1-^{13}C] pyruvate MRI.

Sébastien Serres[1,2], James T. Grist[3,4,5], Robin A. Damion[6,7,8], Jan A. Paul[6], Sheila Hirst[6,7,8], Sarah Wolfe[6], Peter G. Morris[6], Dorothee P. Auer[6,7,8]

[1]School of Life Sciences, University of Nottingham, Nottingham, UK
[2]The David Greenfield Human Physiology Unit, University of Nottingham, Nottingham, UK
[3]Department of Physiology, Anatomy, and Genetics, University of Oxford, Oxford, UK
[4]Oxford Centre for Clinical Magnetic Resonance Research, University of Oxford, Oxford, UK
[5]Department of Radiology, Oxford University Hospitals, Oxford, UK
[6]Sir Peter Mansfield Imaging Centre, University of Nottingham, Nottingham, UK
[7]Mental Health and Clinical Neuroscience, School of Medicine, University of Nottingham, Nottingham, UK
[8]NIHR Nottingham Biomedical Research Centre/Nottingham Clinical Research Facilities, Queen's Medical Centre, Nottingham, UK

Introduction: The development of hyperpolarised-^{13}C MRI (HP-^{13}C MRI) had enabled the real-time imaging of cellular metabolism in the brain by following the conversion of HP-[1-^{13}C] pyruvate into [1-^{13}C] lactate and [^{13}C] bicarbonate (1). Two recent studies have used either ^{13}C-MR spectroscopy (2) or ^{13}C spectral spatial imaging (Uthayakumar et al 2024 ISMRM) to assess brain metabolic changes during functional activation and have shown contradictory results on how pyruvate is metabolised in the brain during neuronal activation. The aim of this study was to re-evaluate the metabolism of HP-[1-^{13}C] pyruvate in the brain using a visual stimulation and a highly sensitive ^{13}C spectral-spatial imaging sequence to accurately measure brain metabolism response to neuronal activity.

Methods: Three age- and BMI-matched healthy young subjects (2 males and 1 female, aged 19 to 29 years) were each injected twice with HP-[1-^{13}C] pyruvate (0.43 ml/kg over 15 seconds) on two separate days. Stimulus and control HP-^{13}C MR scans were performed at 3T using a modified 3D echoplanar sequence with B_1 and B_0 map correction and flip angles set to 5° for pyruvate, 15° for lactate, and 60° for bicarbonate, with an isotropic resolution of 4.5 cm³ (Grist et al., 2024, under review). During the stimulus scan, participants viewed an 8 Hz flashing checkerboard, while no stimulus was applied during the control scan. A minimum of two days separated the two HP-^{13}C scans, and 3D T_1-weighted images were acquired at 3T for anatomical co-registration. On a separate day, arterial spin labelling (ASL)-MRI was performed at 3T with and without the same visual stimulus to measure cerebral blood flow (CBF).

For image analysis, anatomical T_1-weighted images were aligned in the Montreal Neurological Institute (MNI) space for cortical atlas parcellations, and regions of interest (ROIs) were extracted for the whole cortex, including the visual cortex. MNI ROIs were used to calculate signal intensities in the visual and non-visual cortices of ^{13}C-pyruvate, ^{13}C-lactate, and ^{13}C-bicarbonate images. Signal intensities in the visual cortex were normalised to the rest of the cortex, and lactate/pyruvate and bicarbonate/pyruvate signal ratios in the visual cortex were obtained for both stimulus and control scans. A similar approach was used to analyse ASL-MRI, with FSL used to calculate CBF maps (3). All data are presented as mean ± SEM. Statistical analysis was conducted using a paired t-test to compare data between stimulus and control groups, and an unpaired t-test was used to identify differences between visual and non-visual cortices.

Results: An increase in basal CBF in the visual cortex was observed during stimulus (~20%), confirming increased metabolic demand in response to visual stimuli. Dynamic acquisition of HP-[1-^{13}C] pyruvate MR images of the whole brain revealed ^{13}C labelling of lactate and bicarbonate, catalysed by cytosolic lactate dehydrogenase and mitochondrial pyruvate dehydrogenase, respectively, with a much-improved signal-to-noise ratio than previously (Fig 1) (1). There was a trend towards an increase in the bicarbonate/pyruvate ratio in the visual cortex after stimulation, but this was not statistically significant (p=0.109, N=3, Fig 2). No significant change in the lactate/pyruvate ratio was found

between stimulation and control scans in the visual cortex, with only one individual showing a response to the task. The bicarbonate/lactate ratios were consistently higher in the visual cortex compared to the rest of the cortex, although this change was not significant (p=0.15, N=3, Fig 3).

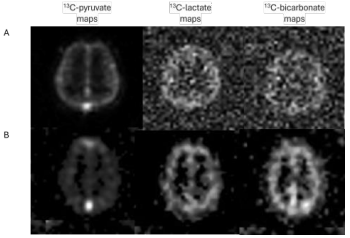

Fig 1: *^{13}C-metabolite maps show a higher SNR when using our modified ^{13}C spectral-spatial imaging scan (B) vs a standard method (A).*

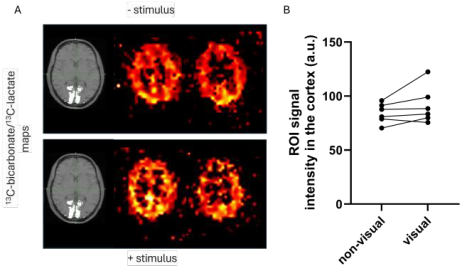

Fig 3: *(A) T_1-weighted images with MNI ROIs and ^{13}C-bicarbonate/ ^{13}C-lactate maps with or without stimulus. (B) Graph showing changes in ROI signal in both visual cortex and the rest of the cortex (non-visual).*

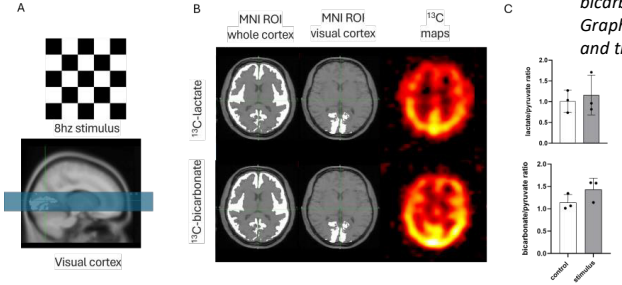

Fig 2: *(A) Experimental design. (B) T_1-weighted images with MNI ROIs and ^{13}C-metabolite maps. (C) Graphs showing lactate/pyruvate and bicarbonate/pyruvate ratios in the visual cortex in both control and stimulus conditions, respectively.*

Discussion: Pyruvate dehydrogenase flux (indicated by ^{13}C-bicarbonate labelling) was consistently higher compared to lactate dehydrogenase flux (indicated by ^{13}C-lactate labelling) in the visual cortex compared to the rest of the cortex. We therefore hypothesise that visual cortical regions possess a higher oxidative metabolism than in the rest of the brain. However, we also cannot exclude that there may be a residual stimulation of the visual cortex regions even without stimulus (2). Notably, ^{13}C-bicarbonate signal increased with visual stimulation while ^{13}C-lactate did not, as demonstrated by improved ^{13}C spectral-spatial imaging. This finding suggests that neuronal activation associated with visual stimulus is supported by oxidative metabolism, as shown previously (2, 4). Further repeats are warranted to reach statistical significance (effect size=1.3, N=8 with a power of 95%).

Conclusion: The metabolism of HP-[1-^{13}C] pyruvate during visual stimulation appears to be supported by oxidative metabolism, but further investigations are needed to explore the mechanisms behind this signal change. This finding has implications for future clinical studies, as brain metabolism tends to rely more on non-oxidative pathways with aging and in disease.

Acknowledgements: This work was supported by a Life Cycle charity award.

References

1. J. T. Grist *et al.*, Quantifying normal human brain metabolism using hyperpolarized [1-(13)C]pyruvate and magnetic resonance imaging. *Neuroimage* **189**, 171-179 (2019).
2. M. Zaidi *et al.*, Functional activation of pyruvate dehydrogenase in human brain using hyperpolarized [1-(13) C]pyruvate. *Magn Reson Med* **91**, 1822-1833 (2024).
3. M. Sarmiento Soto *et al.*, STAT3-mediated astrocyte reactivity associated with brain metastasis contributes to neurovascular dysfunction. *Cancer Res* 10.1158/0008-5472.CAN-20-2251 (2020).
4. N. Chhina *et al.*, Measurement of human tricarboxylic acid cycle rates during visual activation by (13)C magnetic resonance spectroscopy. *J Neurosci Res* **66**, 737-746 (2001).

Structural Connectivity Differences In White Matter Tracts Of NGF Carriers with Pain Insensitivity

Arnas Tamasauskas[1], Irene Perini[2], India Morrison[2], Andrew Marshall[1]
[1] University of Liverpool, [2] Linköping University

Introduction: The research of pain and nociceptive reactions of people with Nerve Growth Factor (NGF) mutations has revealed congenitally reduced density of C-nociceptor afferent fibres in the peripheral nerve system, but the impact of these gene mutations on whole brain connectivity has not yet been explored.

Methods: This study utilised Diffusion Tensor Imaging (DTI) and T1-weighted scans of a group of 11 R221W heterozygous carriers, who have impaired pain and temperature perception, and 11 gender-, age-, and education-matched healthy controls. DTI scans were acquired using single phase encoding. For preprocessing, Synb0, was utilised to synthesize reverse phase encoding from T1 scans. Whole-brain Voxel-based Tract-Based Spatial Statistics (TBSS) and Fixel-based group comparison analyses were performed to examine different metrics of white-matter structure and integrity. Significance thresholding ($p<0.05$) was applied to Fixel FD, FC and FDC metrics, which were then registered to a John Hopkins University (JHU) ICBM-DTI-81 white-matter labels atlas using FSL Linear Image Registration Tool. Additionally, these tracts were converted to Voxels and used for Region of Interest (ROI) specified Probabilistic Second-order Integration over Fibre Orientation Distributions (iFOD2).

Results: TBSS analysis showed no significant differences between the R221W carrier group and healthy controls in fractional anisotropy (FA), mean diffusivity (MD), and Radial Diffusivity (RD). Fixel-based group comparison between R221W carriers and healthy controls showed significant microstructural fibre density (FD), and fibre density and cross-section metric (FDC) reductions in specific white matter tracts in midbrain and pons ($p < 0.05$) (Figure 1), but no significant differences in fibre cross-section (FC). JHU atlas-based White-matter investigations provided specificity in identifying tracts with significantly reduced FD and FDC of R221W carrier group as compared to healthy controls. These affected tracts were: the middle cerebellar peduncle, corticospinal tract, medial lemniscus, and inferior and superior cerebellar peduncles. Some minimal but significant ($p<0.005$) FD and FDC differences were seen in: corona radiata, as well as slight FD differences in external capsule, and slight FDC differences in internal capsule and uncinate fasciculus. Voxel-based iFOD2 analysis supported significant difference findings in FD and FDC populations in the midbrain, pons, cerebellum, and parts of temporal and occipital cortices. ($p < 0.05$) (Figure 2).

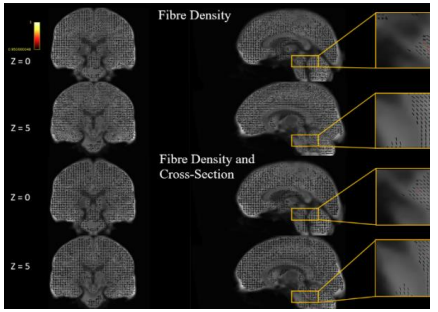

Figure 1: *Fixel Fibre Density, and Fibre Density and Cross-Section Significant Tracts*

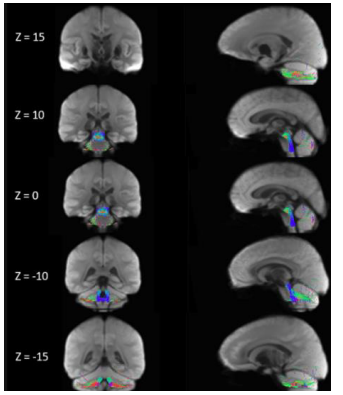

Figure 2: *Significant Fixel Fibre Density tracts represented through Probabilistic Second-order Integration over Fibre Orientation Distributions*

Discussion: While Voxel-based statistics did not indicate any significant structural white matter differences, Fixel-based FD and FDC findings suggest reduced intra-axonal volume in the spinothalamic and corticothalamic tracts of R221W carriers. This would indicate that the reduction of C-nociceptor afferent nerve density of R221W carriers is not constrained to the periphery, but is also present in parts of the brain. Particularly, brainstem pathways to the cerebellum and deep brain structures appear to have the most fibre density and cross-section reduction. However, the differences are not constrained to the brainstem as some differences are present in tracts located in occipital and temporal lobes. Fixel-based analyses provided a more detailed investigation of fibre orientations than TBSS, but iFOD2 provided additional support for significant difference findings in fibre density and cross-section when converted to voxel-based metrics.

Conclusion: Carriers of genetic mutations that reduce NGF may result not only in reduced density of C-nociceptor afferent fibres in the peripheral nerve system, but also in structural integrity of white matter tracts. These results contribute to the understanding of how the spinocortical tracts and the cerebellum are implicated in pain networks. Further ROI TBSS, Fixel-based and Voxel-based analyses are needed to investigate the differences in intra-axonal volume and crossing-fibres of specific brain regions.

References

1. Perini, I., Ceko, M., Cerliani, L., van Ettinger-Veenstra, H., Minde, J., & Morrison, I. (2020). Mutation carriers with reduced C-afferent density reveal cortical dynamics of pain–action relationship during acute pain. *Cerebral Cortex*, *30*(9), 4858-4870.
2. Schilling, K. G., Blaber, J., Hansen, C., Cai, L., Rogers, B., Anderson, A. W., ... & Landman, B. A. (2020). Distortion correction of diffusion weighted MRI without reverse phase-encoding scans or field-maps. *PLoS One*, *15*(7), e0236418.
3. Schilling, K. G., Blaber, J., Huo, Y., Newton, A., Hansen, C., Nath, V., ... & Landman, B. A. (2019). Synthesized b0 for diffusion distortion correction (Synb0-DisCo). *Magnetic resonance imaging*, *64*, 62-70.
4. Smith, S. M., Jenkinson, M., Johansen-Berg, H., Rueckert, D., Nichols, T. E., Mackay, C. E., ... & Behrens, T. E. (2006). Tract-based spatial statistics: voxelwise analysis of multi-subject diffusion data. Neuroimage, 31(4), 1487-1505.
5. Raffelt, D. A., Tournier, J. D., Smith, R. E., Vaughan, D. N., Jackson, G., Ridgway, G. R., & Connelly, A. (2017). Investigating white matter fibre density and morphology using fixel-based analysis. *Neuroimage*, *144*, 58-73.
6. Mori, S., Wakana, S., Van Zijl, P. C., & Nagae-Poetscher, L. M. (2005). *MRI atlas of human white matter*. Elsevier.
7. Tournier, J. Donald, Fernando Calamante, and Alan Connelly. "Improved probabilistic streamlines tractography by 2nd order integration over fibre orientation distributions." *Proceedings of the international society for magnetic resonance in medicine*. Vol. 1670. John Wiley & Sons, Inc, New Jersey, 2010.

Analytical and deep-learning models predict distinct alterations in brain structure-function relation in psychosis patients

Qing Cai[1,2], Vanessa Hyde[1], Hannah Thomas[1], Carolyn McNabb[1], Pedro Luque Laguna[1], Krish D. Singh[1], Derek K. Jones[1], Eirini Messaritaki[1]
[1]Cardiff University Brain Research Imaging Centre, Cardiff, UK. [2]Tiangong University, Tianjin, China.

Introduction: Diffusion MRI (dMRI) allows mapping of the white-matter tracts of the human brain and of their characteristics (myelination, axonal diameter, etc.) which underlie brain functional connectivity (FC). FC can be measured with milli-second precision via magnetoencephalography (MEG). Here we use two models, one analytical and one based on deep-learning, to predict MEG-measured FC (mFC) from structural connectivity (SC) for healthy participants (HPs) and psychosis patients. We investigate how the brain structure-function relationship is affected by psychosis, employing a participant-specific analysis.

Methods: *Data*: Data were collected from 101 HPs (18–35 years, 54 female) and 5 psychosis patients (18–35 years, 3 female). dMRI data were acquired on a 3T Connectom scanner (300mT/m) with a single-shot spin-echo EPI sequence in A>P and P>A phase-encoding directions [1]. A>P data comprised 6 shells: 200/500/1200/2400/4000/6000s/mm^2 with 20/20/30/61/61/61 gradient directions respectively, and 13 images at b=0s/mm^2. P>A data comprised 30 gradient directions at 1200s/mm^2 and 3 images at b=0s/mm^2. T1-weighted images were acquired with a MPRAGE sequence. McDESPOT data [2] were acquired with a T1-weighted 3D SPGR sequence, a SPGR-IR sequence and a SSFP sequence. Ten-minute MEG resting-state data were acquired on a 275-channel CTF radial gradiometer system at 1200Hz.
Preprocessing: dMRI data were corrected for thermal noise, signal drift, susceptibility distortions, motion and eddy-current distortions, gradient non-uniformity and Gibbs ringing [3,4]. Anatomically-constrained tractography was performed [4,5] with 20 million streamlines. T1-weighted images were parcellated, using FreeSurfer [6,7], into the 84 regions of the Desikan-Killiany atlas [8]. McDESPOT data were motion-corrected and a 3-compartment model [2] was fitted to derive pools representing myelin water, intra/extra-cellular water and cerebrospinal fluid. MEG data were down-sampled to 600 Hz, filtered with a 1Hz high-pass and a 150Hz low-pass filter and segmented into 2-s epochs [9,10]. Epochs exhibiting large head movements or other artefacts were rejected from further analysis. Data were source-localized using Fieldtrip with a LCMV beamformer [11,12].
Connectivity: SC matrices were constructed with the Desikan-Killiany atlas areas as nodes and the white-matter tracts joining them as edges [13]. Five SC matrices were derived for each HP and patient, each with a different microstructural metric as edge weight: number of streamlines connecting the brain areas (NS), tract mean fractional anisotropy (FA), inverse mean radial diffusivity (iRD), mean myelin water fraction (MWF) and mean restricted signal fraction (FRt). FC matrices were derived from MEG data [10] with the Desikan-Killiany atlas areas as nodes and correlations of the Hilbert envelope of the beamformer time-series as edges. Four FC matrices were constructed for each HP and patient, one for each frequency band of the MEG data (delta: 1–4Hz, theta: 4–8Hz, alpha: 8–13Hz, beta: 13–30Hz).
FC prediction: Two methods were used to predict the mFC from the SC: a) an analytical model that combines the shortest-path-length (SPL) and search-information (SI) communication mechanisms [14] and b) a deep-learning model based on a Graph Multi-Head Attention Autoencoder that captures complex relationships in connectivity data. For the analytical model (SPL-SI), the data of each HP and patient were passed through it. The deep-learning model was trained on the HP connectivity matrices and tested using 5-fold cross-validation; patient connectivity matrices were then passed through the HP-trained model to predict the patient FC.
Statistics: For each FC-predicting model, correlations were calculated between predicted FC and mFC for each HP and patient, in each frequency band, for each microstructural metric. The distributions of correlations of HPs were compared to those of patients with 2-sample t-tests. p-values were corrected for multiple comparisons.

Results: Both models gave very good predictions of the mFC for HPs (boxplots, Fig. 2,3) across frequency bands and microstructural metrics. They predicted the alpha- and beta-band FC better than the delta- and theta-band FC. Myelin-weighted SC matrices provided better predictions than NS-weighted ones (p<0.004). The SPL-SI algorithm (Fig. 2) predicted the delta-band FC in patients more accurately than in HPs (p<10^{-12} across edge weights); the opposite was true in the alpha and beta bands (alpha:p<0.007 for FA and iRD; beta:p<0.004 for FA, iRD, MWF and FRt). The deep-learning model predicted FC in HPs more accurately than in patients across frequency bands and microstructural metrics (p<10^{-15}; Fig. 3).

Discussion: The SPL-SI model better represents communication between brain areas in the delta band for psychosis patients than HPs; the opposite is true for the alpha and beta bands. The deep-learning model distinguishes HPs from psychosis patients, providing a way to classify participants based on the brain structure-function relation. Our work provides additional multi-faceted evidence on the existence of aberrant FC in psychosis [15].

References: [1] Koller et al., NeuroImage, 2021, 225:117406. [2] Deoni et al., Magn. Reson. Med., 2013, 70:147. [3] Jenkinson et al., NeuroImage, 2012, 68:782. [4] Tournier et al., NeuroImage, 2019, 202:116137. [5] Smith et al., NeuroImage, 2015, 26:1558. [6]

Dale et al., NeuroImage, 1999, 9:179. [7] Fischl, Cereb. Cortex, 2004, 14:11. [8] Desikan et al., NeuroImage, 2006, 31:968. [9] Messaritaki et al., NeuroImage, 2017, 159:302. [10] Koelewijn et al., eLife, 2019. [11] Oostenveld et al., Computat. Intel. Neurosc., 2011. [12] Nolte, Phys. Med. Biol., 2003, 48:3637. [13] Messaritaki et al., Netw. Neurosci., 2021, 5. [14] Goñi et al., PNAS, 2014, 111:833. [15] Sun et al., Hum. Brain Mapp, 2017, 38:2008.

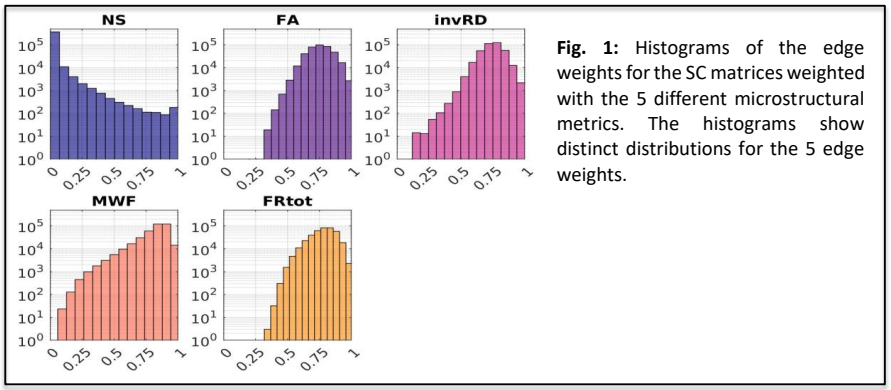

Fig. 1: Histograms of the edge weights for the SC matrices weighted with the 5 different microstructural metrics. The histograms show distinct distributions for the 5 edge weights.

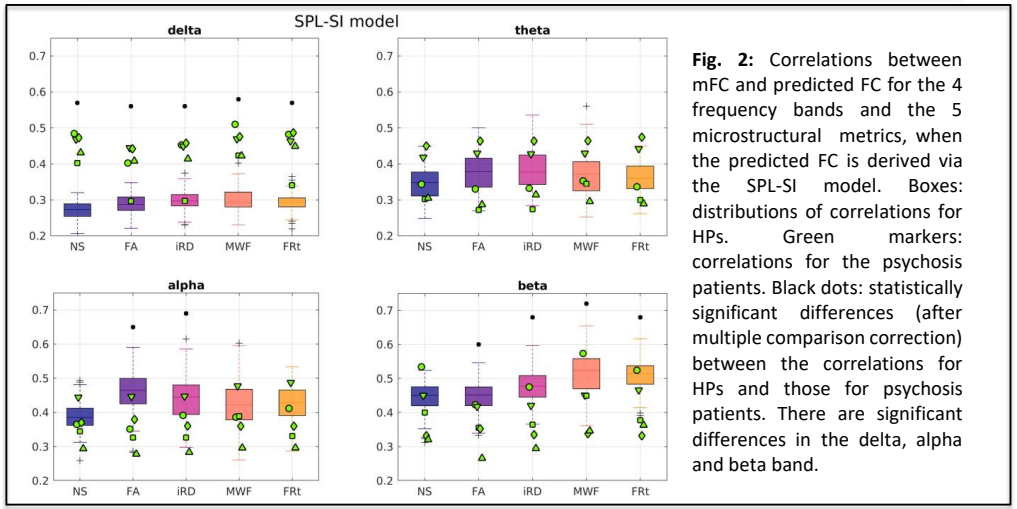

Fig. 2: Correlations between mFC and predicted FC for the 4 frequency bands and the 5 microstructural metrics, when the predicted FC is derived via the SPL-SI model. Boxes: distributions of correlations for HPs. Green markers: correlations for the psychosis patients. Black dots: statistically significant differences (after multiple comparison correction) between the correlations for HPs and those for psychosis patients. There are significant differences in the delta, alpha and beta band.

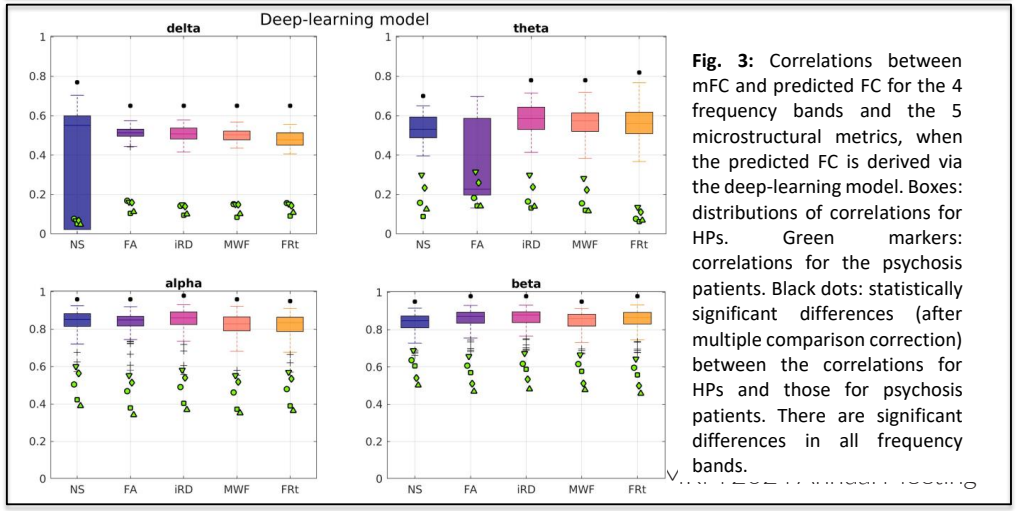

Fig. 3: Correlations between mFC and predicted FC for the 4 frequency bands and the 5 microstructural metrics, when the predicted FC is derived via the deep-learning model. Boxes: distributions of correlations for HPs. Green markers: correlations for the psychosis patients. Black dots: statistically significant differences (after multiple comparison correction) between the correlations for HPs and those for psychosis patients. There are significant differences in all frequency bands.

Altered cognitive and neurovascular profiling in Long Covid

O.Mundell[1] F. Zambolin[1] E.Zamboni[2] N. Bakerly[3] S.Ramjut[3] J.McPhee[1] A.Kennerley[1]

[1]Manchester Metropolitan University, 99 Oxford Rd, Manchester M1 7EL

[2]University of Nottingham, University Park Campus, University Park, Nottingham, NG7 2RD

[3] Salford Royal Hospital Stott Lane Salford M6 8HD

Introduction: Despite the acute phase of the SARS-CoV-2 pandemic subsiding, Long Covid (LC) remains a significant challenge, affecting an estimated 10-30% of non-hospitalized and 50-70% of hospitalized COVID-19 cases in the UK [1,2,3,4]. LC is characterized by symptoms such as fatigue, anxiety, depression, and attentional deficits, which suggest underlying neurobiological changes impacting higher processing regions like the prefrontal cortex. Additionally, approximately 80,000 individuals in the UK are currently unable to work due to LC-related symptoms [5]. This study aims to investigate the neural correlates of LC through comprehensive cognitive tasks and multiparametric imaging techniques.

Methods: Fifteen participants diagnosed with Long Covid (LC) and fifteen healthy controls participated in this study. Each participant underwent functional magnetic resonance imaging (fMRI) using a BOLD-sensitive EPI sequence on a 3T Siemens MAGNETOM Vida MRI System, using a 64-channel head/neck coil. The imaging parameters included a repetition time (TR) of 1000 ms, an echo time (TE) of 23 ms, 3.0mm slice thickness 192mm FoV, bandwidth of 1834Hz/px, and a flip angle of 70 degrees. The Eriksen Flanker task, programmed with PsychoPy [6], was presented on an MRI-compatible LCD screen (Nordic Neuro Lab). Briefly, the Eriksen Flanker task involves the presentation of a central target stimulus flanked by adjacent distractors. The feature of the target (e.g., orientation) can either be congruent or incongruent with that of the distractors. Congruency here is randomised and participants responded by pressing the left or right keys of an MRI-compatible mouse to indicate the direction of the centrally presented target (fig 1). Inter-stimulus interval in our study was randomised to between 8-12 seconds. Each session lasted 10 minutes. Data analysis was performed using FMRIB Software Library (FSL) [7] with preprocessing and generalized linear modelling to investigate BOLD signal changes associated with task performance across groups.

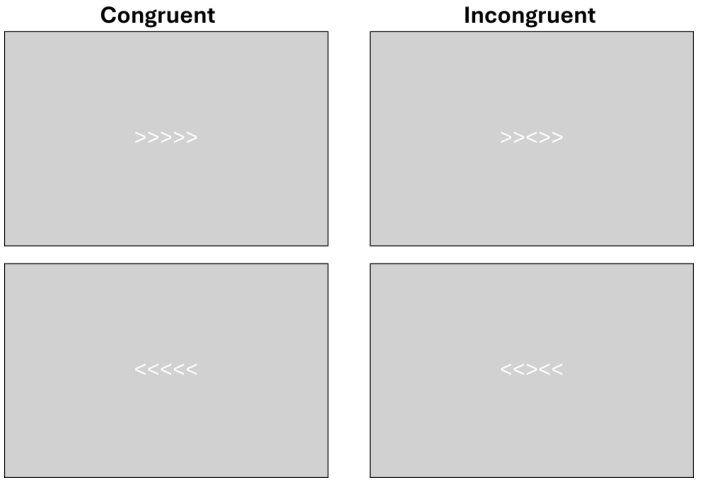

Fig.1. Representation of flanker stimuli shown in the Eriksen Flanker task experimental paradigm showing both congruent and incongruent conditions.

Results: This study investigates neural activation patterns during the Eriksen Flanker task using fMRI in individuals with Long Covid (LC) and healthy controls. Preliminary data in a healthy cohort (fig 2) shows that reliable responses across visual, attentional, and sensory-motor networks to the overall flanker task can be detected with our scanning parameters.

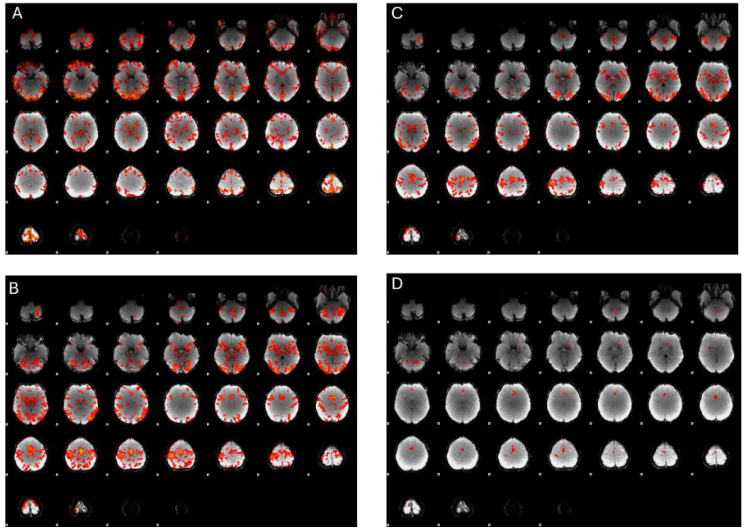

Fig.2. Activation maps showing significant (p<0.05) clusters in response to different flanker conditions. **(A)** BOLD response to eyes-open resting state condition. **(B)** BOLD signal in response to incongruent and **(C)** congruent flanker tasks. **(D)** Activation map showing significant clusters for incongruent vs congruent contrast. Cluster Z score range: 3.1-11.6.

These results enable exploration of brain regions involved in processing congruent/incongruent stimuli, as well as understanding how congruency level affects the motor response, both in terms of action planning and executing. By implementing a group-level analysis and leveraging the contrast between the two groups (LC vs healthy volunteers), differences in activation/inhibition patterns of relevant networks and brain regions such as the default mode network (DMN) and the dorsolateral prefrontal cortex will be examined. These data will be further enriched by integrating, in a multimodal and multiparametric fashion with blood-based assays measurements to establish participants thrombogenic profile.

Discussion: This study will provide vital insight into the understanding of the pathophysiological factors driving LC progression and will be further augmented by assessing the type and severity of LC symptoms in according the modified C19YRS scale [8]. As such, we work towards delineating putative subgroups of people living with LC as well as better informing the interplay between microbial infection and long-term health complications generally. These findings can ultimately lead towards better clinical trial and therapeutic intervention design for conditions that place considerable socioeconomic burden on global healthcare systems. Future investigations could expand upon the current study by incorporating assessments of physical fatigue through standardized testing protocols; exploring vascular space occupancy alongside assessments of neurovascular function and neurometabolic performance. Additionally, correlations with blood assays to investigate inflammatory markers and haemostatic profiles in LC participants compared to controls, could provide further insights into the neurobiological mechanisms underlying cognitive impairments and their association with systemic inflammation. These multidimensional approaches aim to advance our understanding of the complex pathophysiology of LC and inform targeted interventions for improved clinical management.

References

1. Al-Aly, Z., Bowe, B. and Xie, Y. (2022) “Long COVID after breakthrough SARS-CoV-2 infection,” *Nature medicine*. Springer Science and Business Media LLC, 28(7), pp. 1461–1467.

2. Ayoubkhani, D. *et al.* (2022) “Risk of Long Covid in people infected with SARS-CoV-2 after two doses of a COVID-19 vaccine: community-based, matched cohort study,” *bioRxiv*. doi: 10.1101/2022.02.23.22271388.

3. Ceban, F. *et al.* (2022) “Fatigue and cognitive impairment in Post-COVID-19 Syndrome: A systematic review and meta-analysis,” *Brain, behavior, and immunity*. Elsevier BV, 101, pp. 93–135.

4. Bull-Otterson, L. *et al.* (2022) “Post–COVID conditions among adult COVID-19 survivors aged 18–64 and ≥65 years — United States, march 2020–November 2021,” *MMWR. Morbidity and mortality weekly report*. Centers for Disease Control MMWR Office, 71(21), pp. 713–717.

5. Reuschke, D. and Houston, D. (2023) “The impact of Long COVID on the UK workforce,” *Applied economics letters*. Informa UK Limited, 30(18), pp. 2510–2514.

6. Peirce, J. W., Gray, J. R., Simpson, S., MacAskill, M. R., Höchenberger, R., Sogo, H., Kastman, E., Lindeløv, J. (2019). PsychoPy2: experiments in behavior made easy. Behavior Research Methods. 10.3758/s13428-018-01193-y

7. M. Jenkinson, C.F. Beckmann, T.E. Behrens, M.W. Woolrich, S.M. Smith. FSL. NeuroImage, 62:782-90, 2012

8. Sivan M, Preston N, Parkin A, Makower S, Gee J, Ross D, Tarrant R, Davison J, Halpin S, O'Connor RJ, Horton M. The modified COVID-19 Yorkshire Rehabilitation Scale (C19-YRSm) patient-reported outcome measure for Long Covid or Post-COVID-19 syndrome. J Med Virol. 2022 Sep;94(9):4253-4264. doi: 10.1002/jmv.27878. Epub 2022 Jun 1. PMID: 35603810; PMCID: PMC9348420.

Ghostbusting: Body motion correction at standing position in 0.5 T Upright scanner

Laura Bortolotti, Katherine Sewart, Eleanor Church, Olivier Mougin, Paul Glower, Richard Bowtell, Penny Gowland;

Affiliation: SPMIC, University of Nottingham (UK)

Introduction: Open MRI scanners enhance patient comfort and enable the study of physiology in natural postures. Unlike conventional supine MRI, which tends to restrict motion, the upright position in open MRI imposes fewer constraints on body movement. However, upright body MRI poses several challenges, including increased bulk-body motion, respiratory motion, and internal organ movement. Here, early results on retrospective motion correction (RMC) of shoulder MRI are presented.

Methods: The optical tracking camera was cross calibrated to the scanner reference frame [2]. Three subjects were scanned using a Multislice Fast Spin Echo sequence (FOV = 390 x 300 mm, 1.4 x 1 mm/px, TE = 116 ms, TR = 4104 ms) while standing facing the scanner coil, leaning against padding with the shoulder at the isocentre. The volunteers were instructed to keep their shoulder still, which was also secured to the torso with a sling to reduce involuntary rotator cuff movements (Figure 1.a). This configuration prevents the markers from being occluded during motion [3] and allows translation movements by stepping to the side, but it unconstrained other movements (e.g. respiration, being restless). K-space image data were then retrospectively motion corrected (RMC) for translations only using motion tracking data and the Python nufft function included in the sigpy library [4].

Results: Application of the RMC technique successfully restored the anatomical details sharpness. This is clearly visible in the shoulder joints. Overall, the motion related artefacts were ameliorated (Figure 1, b). Comparing the free-motion image with the motion corrected image, the details of the shoulder structure were restored, and effect of motion reduced. However, the presence of artefacts in the phase encoding direction confounds the motion corrected results and prevents a direct comparison with the ground truth image (rest).

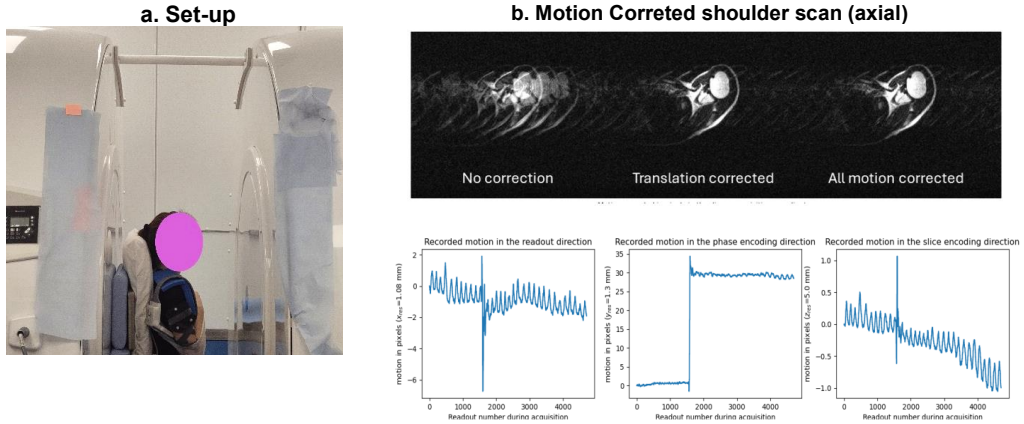

Figure1: (a) MoCo set-up. The figure shows the patient sandwiched between the open MRI scanner coils to make the shoulder clearly visible to the VDUO optical camera. (b) results for one subject for (approximately) pure translation along z. Residual artefacts on the image are due to an interaction between phase-encoding and system instability. Data show the translations along z axes in the scanner reference frame (on different scales in each case).

Discussion: The resulted corrected images display several residual artefacts. The predominant one is

by phase-encoding ghosting. Residual motion artefacts would be due to rotations, residual respiratory motion happening in the 1.5 min of the scan (leading on shoulder movements, torso expansion, oscillations) and voluntary body motion (restless). The unconstrained body motion prevents the use of the respiratory gating tool previously implemented [4].

Conclusions: Shoulder MRI in a standing position was successfully retrospectively motion corrected by tracking the rigid body motion of the shoulder whilst it was rigidly coupled with the torso. Reproducibility of the results over subjects was proved. Future work will focus on incorporating rotations, field inhomogeneities and gradient nonlinearities into the Motion Correction technique.

References

Reference: [1] Zaitsev M et. al.(2015) "Motion artifacts in MRI: A complex problem with many partial solutions"; **[2]** Bortolotti et all (2023), "Optical camera calibration to implement various marker-based motion correction techniques in open geometry 0.5 T upright scanner"; **[3]** Bortolotti et all "Evaluation of body motion at various patient position in a 0.5 T Upright scanner";[4] Ong et al "SigPy: A Python Package for High Performance Iterative Reconstruction"; **[5]** Bortolotti et all "Effect of respiratory motion on gated torso MRI in an upright 0.5 T scanner with seated and standing subjects".

Measuring Quantitative Cortico-Medullary Gradients in Ex-Vivo Renal Tissue

Alexander J Daniel[1] and Susan T Francis[1]

[1]Sir Peter Mansfield Imaging Centre, University of Nottingham, Nottingham, United Kingdom

Introduction: Key to the analysis of renal MRI studies is the reporting of quantitative measures in the cortex and medulla. This is often performed using manual regions-of-interest (ROI) which are difficult to define. The Twelve Layer Concentric Object (TLCO) method was proposed by Pruijm *et. al*[1] as an alternative to ROI analysis when studying blood oxygenation level dependent (BOLD) R_2^* renal maps. TLCO uses two user-delineated boundaries to generate twelve equidistant layers between the renal pelvis and surface, the average R_2^* in each layer is calculated, from which $R_2^*{}_{outer}$, $R_2^*{}_{inner}$, and $R_2^*{}_{slope}$, representing cortex, medulla and cortico-medullary difference is computed. The TLCO software requires a single slice, coronal oblique acquisition. However, a recent renal BOLD consensus survey[2], highlighted that the need for oblique coronal images for TLCO was not always the preferred acquisition. This and the limitation of TLCO being a single slice analysis method motivated this work on 3DQLayers, a 3D quantitative-depth-based method for multiparametric data. We use 3DQLayers to study kidneys declined for transplant imaged ex-vivo and compare to manual ROIs.

Methods: Data was acquired using the ADMIRE protocol[3] with data collected on 15 ex-vivo kidneys that were retrieved, but later declined for transplant. These kidneys were then scanned using a multiparametric MRI protocol on a 3T Philips Achieva scanner.

The process of generating layers is outlined in more detail in Daniel *et al*[4]. Briefly, a binary mask generated automatically from whole-kidney structural images is converted from a voxel-representation (Fig. 1a) to a smooth surface-mesh-representation (Fig. 1b), the distance from the centre of each voxel in the mask to the surface of the mesh is then calculated producing a depth map (Fig. 1c). As the tissue adjacent to the renal pelvis is not representative of the medulla, it is excluded from layer-based-analysis. This is achieved by automatically segmenting the pelvis then calculating the distance from each voxel to the surface of the pelvis as above (Fig. 1d). Voxels closer than a specified threshold, here 5mm, are excluded from the depth map (Fig. 1e). Finally, a layer image is generated by quantising the depth map to a desired layer thickness (Fig. 1f), here 0.5mm.

The layers can be applied to any quantitative map by resampling the layer image to the same space as the quantitative map. Voxel-wise measures within each layer are calculated. Measurements of quantitative parameters in the outer and inner layers can be produced as in Pruijm *et al*[1]. Finally, a measure similar to $R_2^*{}_{slope}$ is calculated by performing a linear regression between a voxels quantitative value and depth, (Fig. 1g). Unlike TLCO, the slope here is fully quantitative as they are calculated based on depth rather than layer numbers of arbitrary thickness.

3DQLayers was applied to T_1, T_2, T_2^*, ADC and Magnetisation Transfer Ratio (MTR) maps to determine the median of the outer 20% and inner 45% of layers, these were compared to the median of the cortex and medulla generated from tissue ROI labels. These ROI labels were produced from a T_1-weighted anatomical using a Gaussian mixture model followed by manual correction. The slope of each parameter for the central layers was also calculated and compared to the cortical-medullary ratio. The Pearsons correlation coefficient was used to assess the strength of the relationship between layer-based measurements and tissue-based measurements.

Results: Figure 2 shows depth profiles from a representative kidney. Figure 3 shows the relationship between layer-based measurements and tissue-based measurements. A significant correlation between outer layers and the cortex, and inner layers and the medulla was shown across all mapping techniques. A significant correlation between cortico-medullary ratio and layer gradient was shown for T_1, T_2, T_2^* and MTR mapping.

Discussion: The ADC acquisition of the ADMIRE protocol is relatively low SNR due to small amount of diffusion in cold, ex-vivo tissue; this underlies why no significant correlation was observed between cortico-medullary ratio and the layers gradient. 3DQLayers calculates gradients as a function of depth of the tissue, this allows for a more principled comparison of large and small kidneys. If normalisation for kidney size is desired, gradients could be normalised by total kidney volume rather than the radius of the slice imaged as in TLCO.

Conclusions: 3DQLayers has been used to measure renal cortico-medullary gradients in ex-vivo tissue across quantitative MRI measures and shown to have a significant correlation with tissue ROI based techniques. 3DQLayers could be used to decrease user variability in analysis and increase the rate at which large datasets can be analysed by minimising the need for manual masking. This technique is readily applicable to in-vivo renal multiparametric MRI data, and will be applied to the UK-wide Application of Functional Renal MRI to improve assessment of chronic kidney disease (AFiRM) study.

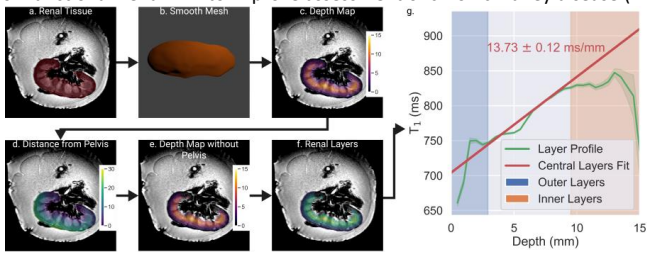

Figure 1: An outline of the pipeline for layer-based analysis of ex-vivo renal MRI data. Here layers are shown at 2.5mm thickness for illustrative purposes, data was processed with 0.5mm thick layers.

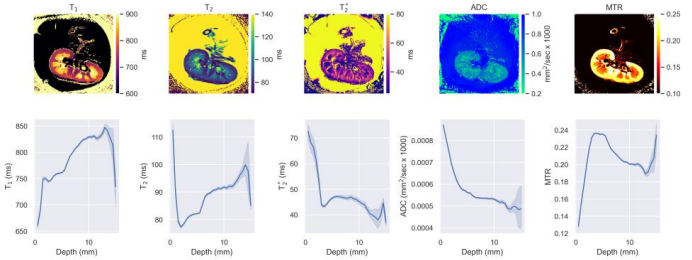

Figure 2: Example quantitative maps and associated depth profiles. Uncertainty shading shows the 95% confidence interval of each layer.

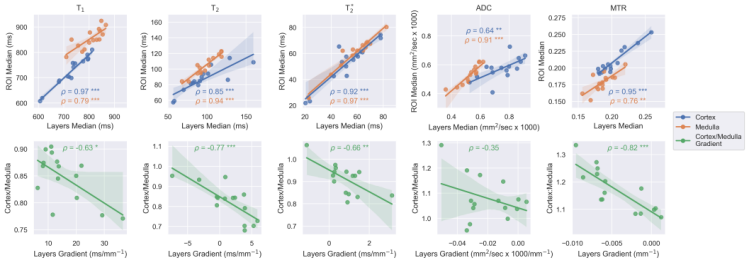

*Figure 3: Agreement between tissue label-based analysis methods and layer-based analysis methods and the Pearsons correlation coefficient. p-value of * < 0.05, ** < 0.01 and *** < 0.001.*

Acknowledgements: This work is funded by Kidney Research UK Grant KS_RP_002_20210111

References

1. Li LP, Milani B, Pruijm M, et al. Renal BOLD MRI in patients with chronic kidney disease: comparison of the semi-automated twelve layer concentric objects (TLCO) and manual ROI methods. *Magn Reson Mater Phys Biol Med*. 2020;33(1):113-120. doi:10.1007/s10334-019-00808-5
2. Bane O, Mendichovszky IA, Milani B, et al. Consensus-based technical recommendations for clinical translation of renal BOLD MRI. *Magn Reson Mater Phys Biol Med*. 2020;33(1):199-215. doi:10.1007/s10334-019-00802-x
3. Daniel AJ, Fawaz S, Charles P, et al. Development of an MR Imaging Protocol for Ex-Vivo Assessment of Deceased Donor Human Kidneys. In: *Proc. Intl. Soc. Mag. Reson. Med. 32*. Toronto; 2023:3805.
4. Daniel AJ, Francis ST. Volumetric Layer Based Analysis for Quantitative Renal MRI. In: *Proc. Intl. Soc. Mag. Reson. Med. 33*. Singapore; 2024:2748.

3D Kidney Segmentation using Transformers on DIXON-MRI

Authors: Ajo Joseph Thomas[1], Kywe Kywe Soe[1], Kanishka Sharma[2], Joao Dos Santos Periquito[1], Bashair Al-Hummiany[3], David Shelley[3], Andrew Forbes Brown[4], Jonathan Fulford[4], Angela Shore[4], Nicolas Grenier[5], Maria F. Gomez[6], Kim Gooding[4], Steven P Sourbron[1].
[1]University of Sheffield, Sheffield UK, [2]Antaros Medical AB, Mölndal Sweden, [3]University of Leeds, Leeds UK, [4]University of Exeter, Exeter UK, [5]University of Bordeaux, Bordeaux France, [6]Lund University Diabetes Centre, Malmö, Sweden.

Introduction: Transformers such as UNETR are a novel class of deep learning architectures for medical image segmentation [1]. Our first results have shown that transformers provide promising results on single opposed-phase MRI but also indicated substantial mismatch with ground truths [2]. Combining the 4 individual Dixon MRI series (in/out-phase, fat & water) could maximize yield in AI outputs. **Aim:** To determine the optimal series of images for 3D kidney segmentation on DIXON-MRI with Transformers & compare AI segmentation outputs between the overall 15 possible models. **Methods:** ***Study Subjects*** - This study used 80 consecutive baseline MRI studies from the ongoing multi-centre iBEAt study on diabetic kidney disease [3]. ***Data Acquisition*** - MRI were acquired on 3T Siemens and centralized in an XNAT database. Post-contrast DIXON scans were acquired using data preparation scripts. Ground truths (GT) were defined by a nephrologist (>3 years' experience). ***Model Training*** - UNETR in MONAI (monai.io) was trained and validated over 25,000 iterations using 72 cases and tested in 8 new cases. These were performed (x15 possible arrangements) using the 4 individual DIXON-MRI. ***Data Analysis*** - DICE scores were used to select the optimal model and statistical analysis including paired t-test and F-test with significant differences defined at $p<0.05$. **Results:** Figure 1 and figure 3 show the distributions of all 3 metrics in more detail and figure 2 illustrates the result of 3 individual cases. The optimal model (mean ± sd DICE score 98 ± 1%) used 3 DIXON series (in/out-phase + water). It was more accurate than the in-phase model (DICE 83 ± 14%, $p=0.014$), but not significantly different from the out-phase model (DICE 95 ± 7%, $p=0.21$). On average, the volume error of the optimal model (-0.35%) was not significantly different from the in-phase (-12.2%, $p=0.20$) or the out-phase model (-7.15, $p=0.55$). However, volumes of the optimal model (SD 1.72%) were significantly more precise than the in-phase (SD 24.6%, $p<0.001$) and the out-phase model (SD 11.8%, $p=0.04$). Errors in kidney compactness were not significantly different between optimal (-2.3% ± 6.5%) and in-phase (1.7% ± 4.8%, $p=0.08$) or out-phase (-1.2% ± 3.4%, $p=0.73$) models. **Discussion:** Most accurate results are obtained with 3 DIXON channels, in contrast to findings in a recent study using CNNs, which found best performance on DIXON in-phase alone (DICE 90.2% ± 3.4% [4]). Multiple channels are beneficial, however, not statistically significant on this small test dataset. **Conclusion:** Transformers with multi-channel DIXON images (in/out-phase + water) are optimal and substantially more precise than solutions using only a single in- or opposed-phase image.

References

[1] Hatamizadeh, A. et al. (2022) 'UNETR: Transformers for 3D Medical Image Segmentation', in 2022 IEEE/CVF WACV. 2022 IEEE/CVF WACV, Waikoloa, HI, USA: IEEE, pp. 1748–1758.
[2] Sharma, K. et al. (2024) '3D Kidney Segmentation in MRI using Transformers', in. ISMRM 2024, Singapore.
[3] Gooding, K.M. et al. (2020) 'Prognostic imaging biomarkers for diabetic kidney disease (iBEAt): study protocol', BMC Nephrology, 21(1), p. 242.
[4] Inoue, K. et al. (2023) 'The utility of automatic segmentation of kidney MRI in chronic kidney disease using a 3D convolutional neural network', Scientific Reports, 13(1), p. 17361.

Acknowledgements:
This project has received funding from the Innovative Medicines Initiative 2 Joint Undertaking under grant agreement no. 115974. Healthy Lifespan Institute (HELSI), University of Sheffield. EPSRC.

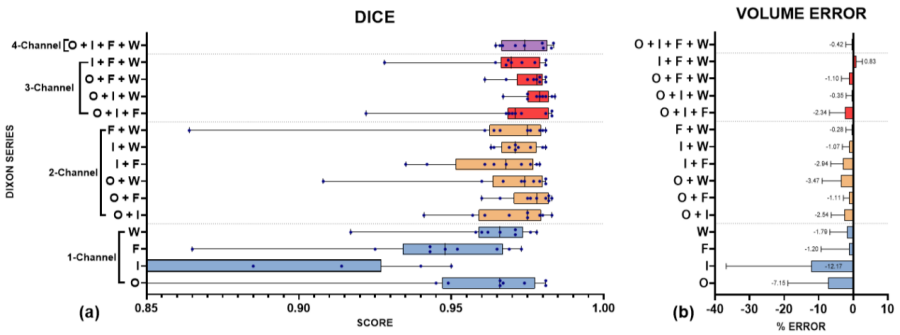

Fig. 1. O = opposed-phase, I = in-phase, F = fat, W = water. **(a)** DICE scores for test case evaluations in all 15 UNETR output models. The figure has a truncated x-axis for clarity. **(b)** Box plots showing the relative volume errors as a clinical endpoint for all 15 models.

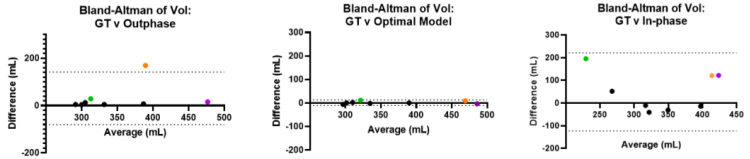

Fig. 2. Bland-Altman showing volume against difference for GT v 3 models. Outliers are highlighted: case 3 (orange), case 4 (purple), case 5 (green).

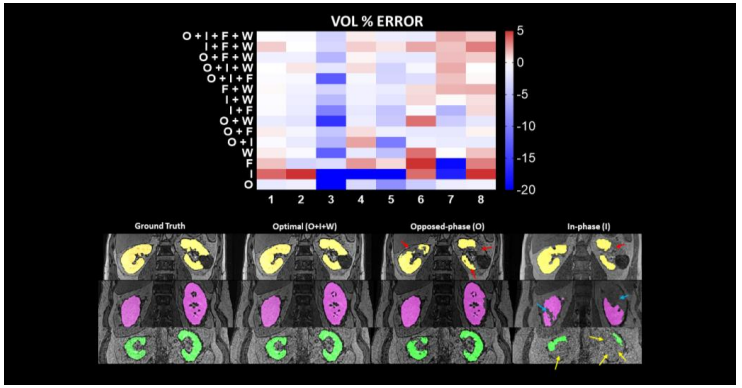

Fig. 3. Comparison of kidney mask outputs between Ground truth (GT) and 3 models. Heatmap shows volume % errors for each test case. Case 3 (yellow) shows significant mask underestimations (red arrows) by opposed-phase and in-phase models. Similarly, in case 4 (purple with blue arrows) and case 5 (green with yellow arrows) by in-phase (I).

Measurement of *in vivo* T_2^* of inhaled perfluoropropane gas and its dependence on lung microstructure.

Dominic Harrison[1,2], Mary Neal[1,2], Pete Thelwall[1,2]
[1]Newcastle Magnetic Resonance Centre, Newcastle University, Newcastle upon Tyne; [2]Translational and Clinical Research Institute, Newcastle University, Newcastle upon Tyne

Introduction: Pulmonary T_2^* measurements are sensitive to lung microstructure due to their dependency on magnetic susceptibility differences at boundaries between air and tissue at the mesoscopic level. These cause localized field gradients, where signal from MR-detectable nuclei within these gradients experience rapid de-phasing and thus exhibit a short transverse relaxation rate (T_2^*)[1]. Therefore, pulmonary T_2^* measurements are sensitive to structural changes associated with lung physiology (e.g., depth of inspiration) or pathophysiology (i.e., structural change associated with disease) and may allow for early detection of diseases such as emphysema, cystic fibrosis, and chronic bronchitis. Our research focuses on ^{19}F-MRI of inhaled perfluoropropane (PFP) to assess lung ventilation properties, and the assessment of lung microstructural influences on relaxation properties of this MR-visible gas. Previous T_2^* measurements of inhaled PFP have either lacked spatial information[2] or high confidence[3], and our experience with T_2^* mapping highlighted challenges due to low confidence in measured T_2^* from ^{19}F-MRI data with relatively low SNR. Therefore, we employed image selected *in vivo* spectroscopy (ISIS)[4] to acquire spatially-localised T_2^* measurements with high SNR. A slice selective 1D-ISIS sequence was used for spatial localisation of signal from PFP, accommodating its rapid in vivo T_1 relaxation (T_1 ~ 12.4 ms)[5]. These spectroscopic data show the sensitivity of inhaled PFP's T_2^* to microanatomical change at different inhalation depths in healthy volunteers, as well as provide an accurate localized T_2^* measurement for validation of ^{19}F-MRI T_2^* mapping.

Methods: Scans were performed on a Philips Achieva 3T using a Rapid ^{19}F transmit/receive chest birdcage coil. Spectra were acquired into 64 datapoints over an 8 kHz bandwidth, 50 mm slice thickness and NSA = 124, with a total acquisition time of 5s. The healthy volunteer was recruited under local research ethical approval and instructed to inhale a 79% PFP/ 21% O_2 gas mixture. Three deep inhalations were performed prior to initial scanning for sufficient wash in of the fluorocarbon gas. The first scanning session involved four consecutive 1D-ISIS scans acquired from the peripheral 5cm of the right lung (Figure 1) at maximum inhalation, maximum expiration, under free breathing, and at tidal volume. The second scanning session acquired two 1D-ISIS scans within a single breath hold at max inhalation, located at the lung periphery and main airways respectively (Figure 1). T_2^* was calculated by fitting a decaying exponential function (Equation 1, where S_o is initial signal, t is the sample time and C is noise) to the ISIS time domain data.

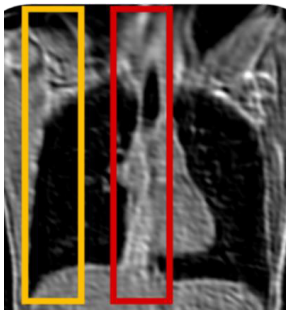

Figure 1 Central slice of a ^{1}H-MRI survey scan of our healthy volunteer at maximum inspiration, showing ^{19}F-MR ISIS slab locations in regions of lung periphery (yellow) and major airways (red).

$$S(t) = S_o e^{-t/T_2^*} + C$$

Results: Average SNR was 122.2 ± 57.2 (SD). The T_2^* of inhaled PFP in the peripheral region of the right lung was 1.9 ± 0.3 ms (95% CI) at maximum inhalation and free breathing, 1.7 ± 0.3 ms at minimum inhalation and 1.8± 0.1 ms at tidal volume inhalation. The T_2^* of the inhaled PFP in regions

predominantly containing central airways was 2.3 ± 0.3 ms at max inhalation and 2.0 ± 0.3 at the lung periphery in scan session 2. Figure 2 shows all ISIS scan time domain data and exponential fits.

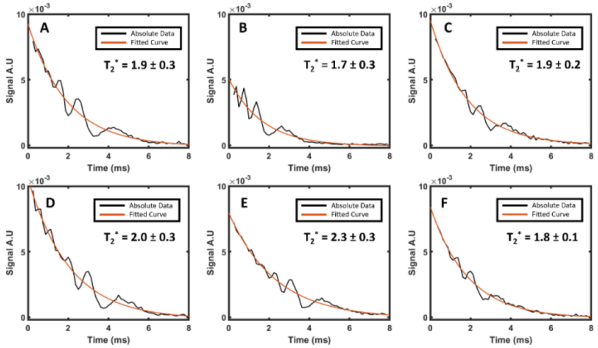

Figure 2 Plotted signal decays and fitted curves for: A) maximum inhalation localized at the lung periphery, B) minimum inhalation localized at the lung periphery, C) tidal volume inhalation localized at the lung periphery, D) repeated max inhalation localized at the lung periphery, E) max inhalation localized at the major airways, and F) free breathing localized at the lung periphery.

Discussion: The observed change in PFP's T_2^* over the respiratory cycle reflects a sensitivity to change in pulmonary physiology and microstructure. Measurements of T_2^* of lung periphery at max inhalation show close agreement from each scanning session, demonstrating repeatability in our protocol for an identical slice selection and breath hold regime. Measured T_2^* across the major airways was shorter than anticipated, likely caused by the large volume of interest (VOI) spanning multiple generations of the tracheobronchial tree, reducing the mean T_2^*. This limitation arises from our decision to employ slice selective ISIS due to the short T_1 relaxation of *in vivo* PFP. However, calculated SNR shows sufficient signal to further reduce VOI slice thickness, potentially mitigating the reduction of mean T_2^*. These data provide the ability to discriminate physiological/structural pulmonary change in a measurement with high SNR and narrow confidence intervals, and therefore could highlight PFP ^{19}F-MRI's potential for early detection of microstructural alterations arising from lung disease.

Conclusion: Our data demonstrate that spatially localised ^{19}F-MRS measurements can be used to measure the T_2^* of inhaled PFP, and that T_2^* is sensitive to change in lung microstructure at different inhalation depths and to regional differences in lung structure. Measurement of the T_2^* of inhaled PFP has potential to report on microstructural changes due to lung pathology and may allow for early detection of lung diseases. This technique will also contribute to the development of our ^{19}F-MRI T_2^* mapping by providing accurate localized measurements for which to validate our T_2^* maps.

References

1. Wild, J.M., et al., *MRI of the lung (1/3): methods.* Insights into Imaging, 2012. **3**(4): p. 345-353.
2. Neal, M.A., et al., *Dynamic susceptibility contrast 19 F-MRI of inhaled perfluoropropane: a novel approach to combined pulmonary ventilation and perfusion imaging.* Magnetic Resonance in Medicine, 2020. **83**(2): p. 452-461.
3. Maunder, A., et al., *MR properties of 19F C3F8 gas in the lungs of healthy volunteers: and apparent diffusion coefficient at 1.5T and at 3T.* Magnetic Resonance in Medicine, 2021. **85**(3): p. 1561-1570.
4. Ordidge, R.J., A. Connelly, and J.A.B. Lohman, *Image-selected in Vivo spectroscopy (ISIS). A new technique for spatially selective nmr spectroscopy.* Journal of Magnetic Resonance (1969), 1986. **66**(2): p. 283-294.
5. Couch, M.J., et al., *Pulmonary ultrashort echo time 19F MR imaging with inhaled fluorinated gas mixtures in healthy volunteers: feasibility.* Radiology, 2013. **269**(3): p. 903-9.

Monitoring diabetic kidney disease progression with DTI and tractography

Joao Periquito[1], Kanishka Sharma[1], Kywe Soe[1], Bashair Alhummiany[3], Jonathan Fulford[2], David Shelley[3], Kim Gooding[2], Angela Shore[2], Michael Mansfield[4], Maria Gomez[5], Steven Sourbron[1]

[1]The University of Sheffield, Sheffield, UK
[2]The University of Exeter Medical School, Exeter, UK
[3]The University of Leeds, Leeds, UK
[4]Leeds Teaching Hospitals NHS Trust, Leeds, UK
[5]The University of Lund, Sweden.

Introduction: Progression of diabetic kidney disease (DKD) is currently monitored with clinical markers eGFR (estimated glomerular filtration rate) and UACR (urine albumin-creatinine ratio). Unfortunately these only respond in advanced stages of the disease, when the management options for reducing the rate of decline are more limited. A wide array of novel blood- and urine biomarkers have been proposed to pick up disease progression earlier, but these have so far failed to deliver in patients [1]. Previous studies have shown that diffusion tensor imaging (DTI) and tractography may act as early indicator of DKD, correlate with pathological measures of fibrosis and predict the decline of kidney function in chronic kidney disease [2-7]. The aim of this study was to identify DTI biomarkers that may be sensitive to changes over a relatively short 2-year time frame in early stage DKD.

Methods: Data acquisition: Thirteen type 2 diabetic patients with eGFR greater or equal to 30 mL/min/1.73m^2 were scanned two times during a two-year period on MAGNETOM Prisma 3T MRI (Siemens Healthcare GmbH, Erlangen, Germany) using the MRI protocol of the iBEAt study [8]: free-breathing single-shot EPI readout (TE=70ms, TR=5100ms, GRAPPA=2, 30 slices) with a pulsed-gradient spin-echo (PGSE), consisting of two diffusion-weighting shells (number of directions) of b = 100 s/mm^2 (24 directions), 600 s/mm^2 (122 directions) with 3 non-diffusion-weighted volumes (~ 0 s/mm^2). All patients arrived fasted (>8hrs) and were provided with standardized meal and fluid prior to the MRI scan. Image processing: Images were processed using DIPY open-source python library, in two different ways: (1) Using *reconst.dti* function library from DIPY: mean diffusivity (MD), fraction anisotropy (FA), axial diffusivity (AD), radial diffusivity (RD), sphericity, planarity and linearity were calculated from the DWI images. (2) Tractography: fibres were reconstructed using a deterministic (*deterministic maximum direction getter*) and a probabilistic fibre tracking (*probabilistic direction getter*) algorithm from DIPY *tracking* function library. A minimum FA threshold of 0.10 and a maximum turning angle of 55° between two adjacent voxels were used. Fibre lengths were extracted from the two tracking methods. Image analysis: Whole kidney ROIs were placed over the left and right kidney for baseline and follow-up scans. For each of the 9 parameters 20 metrics were extracted: mean, standard-deviation, median, minimum, maximum, percentiles (2.5%, 5%, 10%, 25%, 75%, 90%, 95% and 97.5%), inter-quartile range, range, 90% range, coefficient of variation, heterogeneity, kurtosis, and skewness, leading to a total of 180 biomarkers to be evaluated. A pairwise t-test was performed to identify the biomarkers that change between baseline and follow-up. For biomarkers with p<0.05, errors in individual measurements were estimated from a prior repeatability study in healthy volunteers, and applied to determine whether the changes in individuals are consistent with measurement uncertainty.

Results: Figure 2 shows the relative mean change for each of the 180 biomarkers along with its 95% confidence interval; the cohen-d coefficient that reflects effect size for each biomarker; and the p-value of the pairwise t-test. 46 biomarkers showed a significant change over the 2 years, with mean changes that reach over ½ of a standard deviation and cohen-d effect sizes up to 0.6. **Figure 3** displays the top 25 significant biomarkers ranked by the mean change, along with their uncertainty estimates. The figure highlights individual changes that are consistent with real tissue progression.

Discussion: The results suggest that DTI picks up microstructural changes over 2 years, a potentially significant finding considering clinical changes in this population of relatively early stage DKD are expected to be small. Tensor shape biomarkers *planarity* and *sphericity* accounted for 7 of the 10 most

substantial changes, and 5 biomarkers related to MD appear in the top 25. The largest significant change in tractography markers is associated to the deterministic model – heterogeneity of the fiber length distribution. Considering the small sample size and the large number of biomarkers screened, these findings should be treated as hypotheses that are to be validated in the larger population. Data collection for this larger study is underway and more conclusive testing of these hypotheses is expected in the course of 2024.

Conclusions: DTI biomarkers show strong changes in early-stage diabetic kidney disease over 2 years, a time frame where clinical biomarkers are typically stable. This indicates that DTI picks up subclinical changes in renal microstructure, a finding that may have significant implications for clinical practice if confirmed in the larger population.

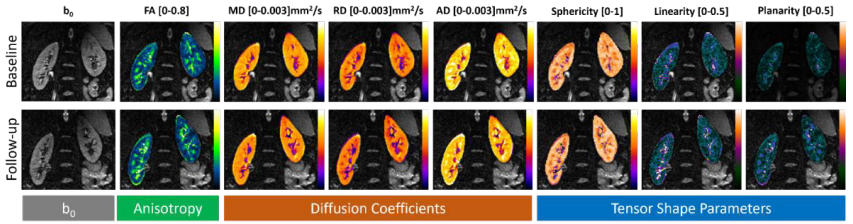

Figure 1: Calculated DTI maps. b_0 image was used as the background for all the calculated DTI maps: FA, directionality, MD, AD, RD, sphericity, planarity, and linearity. Top row DTI maps calculated from baseline visit; bottom row DTI maps from follow-up visit

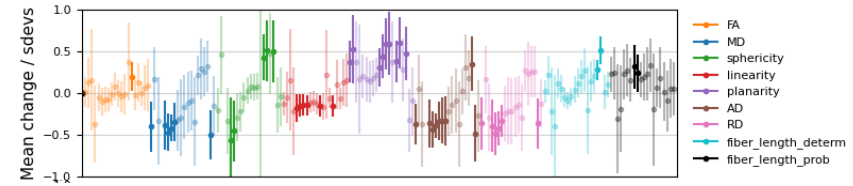

Figure 2: Relative changes from baseline to follow-up scan. Planarity and AD seems to have the largest number (nine) of significant biomarkers, where the least (one) is FA. A cut-off of p-value < 0.05 was used.

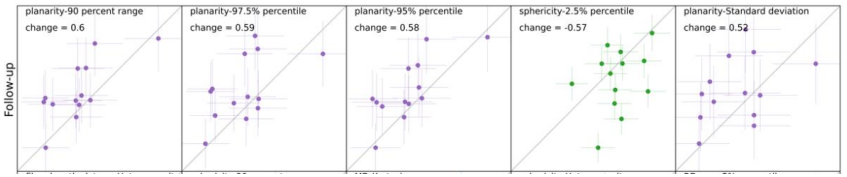

Figure 3: Scatter plot (baseline vs follow-up) of the top 5 significant biomarkers with the largest relative mean change. Tensor shape sphericity and planarity has 7 out of the top 10. MD related biomarkers appear 5 times in the top 25. Only one tractography biomarker (associated with the determinist algorithm) appears in the top 25 – fiber length heterogeneity.

References: [1] - Heinzel, Andreas, et al. Diabetes care 41.9 (2018): 1947-1954 ; [2] - Caroli, Anna, et al. Nephrology Dialysis Transplantation 33.suppl_2 (2018): ii29-ii40 ; [3] - Lu, Lan, et al. American journal of nephrology 34.5 (2011): 476-482; [4] - Inoue, Tsutomu, et al. Journal of the American Society of Nephrology: JASN 22.8 (2011): 1429; [5] - Hueper, Katja et al. European radiology vol. 21,11 (2011): 2427-33. doi:10.1007/s00330-011-2189-0; [6] - Delgado, Jorge, et al. Pediatric Radiology 49 (2019): 175-186; [7] - Berchtold, Lena, et al. Kidney international 101.4 (2022): 804-813; [8] - Gooding, Kim M et al. BMC nephrology vol. 21,1 242. 29 Jun. 2020, doi:10.1186/s12882-020-01901-x

Lipid composition during neoadjuvant chemotherapy of breast cancer through chemical shift-encoded imaging

Sai Man Cheung[1,2], Kwok Shing Chan[2,3], Nicholas Senn[2], Ravi Sharma[4], Trevor McGoldrick[4], Tanja Gagliardi[2,5], Ehab Husain[6], Yazan Masannat[7], Jiabao He[1,2]
[1]Newcastle Magnetic Resonance Centre, Translational and Clinical Research Institute, Faculty of Medical Sciences, Newcastle University
[2]Institute of Medical Sciences, University of Aberdeen
[3]Massachusetts General Hospital, Boston, United States of America
[4]Department of Oncology, Aberdeen Royal Infirmary
[5]Radiology Department, Royal Marsden Hospital, London
[6]Pathology Department, Aberdeen Royal Infirmary
[7]Breast Unit, Broomfield Hospital, Mid and South Essex NHS Foundation Trust

Introduction: Breast cancer is the most common cancer among women, with age-adjusted annual incidence of 205 per 100,000 [1]. An imbalance of monounsaturated, polyunsaturated and saturated fatty acids (MUFA, PUFA, SFA) has been shown in the peri-tumoural adipose tissue adjacent to breast tumour [2]. Novel chemical shift-encoded imaging (CSEI) provides a rapid mapping of lipid composition in the breast, and may serve response monitoring of neoadjuvant chemotherapy (NACT) for stratified treatment. We therefore hypothesise that there might be a difference in lipid composition in the peri-tumoural region and the whole breast between good and poor responders after one cycle of NACT.

Methods: Seventeen patients (age 46 – 58 years) with invasive ductal carcinoma participated in the longitudinal study to undertake MRI scan at Baseline and after Cycle 1. Patients with a tumour size larger than 2 cm on mammography and have not had hormonal therapy prior to chemotherapy were eligible. Miller-Payne system was used to assess pathological complete response for good responder [3]. The study was approved by the London Research Ethics Committee (ID: 17/LO/1777), and written informed consents were obtained from all the participants (Figure 1).

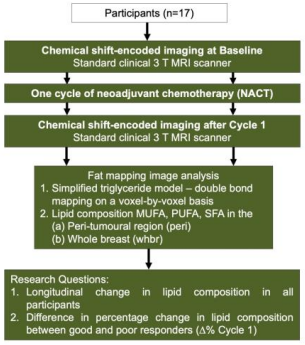

Figure 1. Study design.

Lipid Composition Mapping All images were acquired on a 3 T whole-body clinical MRI scanner (Achieva TX, Philips Healthcare, Best, Netherlands). Lipid composition images were acquired from the diseased breast in all participants using a 2D CSEI sequence [4,5] with 48 echoes, initial echo time of 1.14 ms, echo spacing of 1.14 ms, repetition time of 60 ms, reconstruction matrix of 96 × 96, reconstruction pixel size of 2.5 × 2.5 mm^2 and slice thickness of 5.0 mm.

Data Processing Image analysis was conducted in MATLAB (R2020a, MathWorks Inc., Natick, MA, USA). The maps of the number of double bonds in triglycerides were computed from raw data, before subsequent calculation of quantitative maps of MUFA, PUFA and SFA as a fraction of the total amount of lipids [4,5]. The boundary of tumour was delineated on the first echo of lipid composition images, with reference to anatomical and diffusion weighted images. The peri-tumoural region was defined as a growth of 15 mm (6 voxels) concentric ring surrounding the tumour boundary. The whole breast was defined to contain only adipose and fibroglandular tissue, and excluding the tumour. Adipose voxels with lipid signal over 60% of total signal were extracted from lipid composition maps. The mean lipid composition from the regions-of-interest was subsequently computed for each lipid constituent. Percentage change in lipid composition was calculated as: [Cycle 1 – Baseline] / Baseline × 100%.

Statistical Analysis All statistical analysis was performed in the *R* software (v3.6.3, *R* Foundation for Statistical Computing, Vienna, Austria). Wilcoxon signed rank paired tests were performed for comparison of lipid composition in the peri-tumoural region and the whole breast between Baseline

and Cycle 1. Wilcoxon rank sum tests were performed for comparison of percentage change in lipid composition between good and poor responders. Statistical significant finding was determined by $p < 0.05$.

Results: The histopathological findings of the patient cohort are shown in Table 1.

Tumour histology	Patients (n=17)
Tumour Size (cm)	3.4 ± 1.1
Nottingham Prognostic Index (NPI)	5.3 ± 1.2
Histology grade	
II	1
III	16
Lymphovascular invasion	6
Lymph node involvement	11
Molecular subtypes	
Luminal A	0
Luminal B-HER2 negative	5
Luminal B-HER2 positive	4
Triple Negative	8

HER2 – human epidermal growth factor receptor 2.

Table 1. Patient demographics.

Baseline and Cycle 1 In the peri-tumoural region, there was no significant difference at borderline in MUFA (p=0.055) at Cycle 1 compared to Baseline. There was no significant difference (p=0.073) in PUFA between Baseline and Cycle 1. There was no significant difference at borderline in SFA (p=0.055) at Cycle 1 compared to Baseline (Figure 2). In the whole breast, there was no significant difference in lipid composition between Baseline and Cycle 1 (Figure 2).

Good and Poor Responders There was no significant difference in percentage change in lipid composition in the peri-tumoural region and the whole breast between good and poor responders after one cycle of NACT (Figure 3).

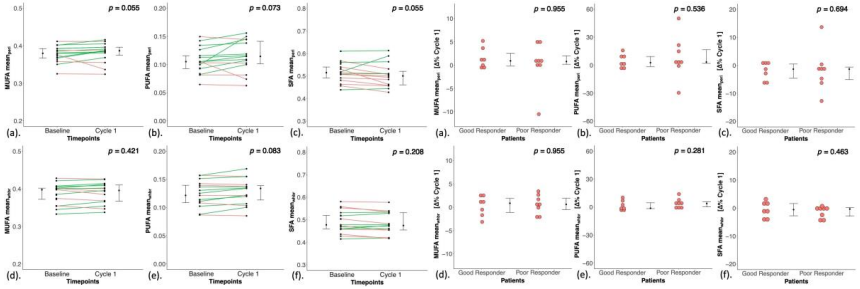

Figure 2. Longitudinal change in lipid composition. **Figure 3.** Difference in lipid composition.

Discussion: There was no significant difference at borderline in MUFA, PUFA and SFA after the first treatment cycle, showing a complete treatment induced lipid normalisation might not occur at an early phase of NACT. However, the insignificant difference at borderline might show a difference in response in a larger cohort, even though it did not reach the statistical threshold to be significant as a primary force in this study. There was no significant difference in the percentage change in lipid composition between good and poor responders, however the cohort size is small and further studies are warranted to unravel lipid regulation during tumour regression and subsequent treatment induced normalisation in patients with breast cancer undergoing NACT.

Conclusions: There was no significant difference in percentage change in lipid composition in the breast between good and poor responders after one cycle of neoadjuvant chemotherapy, and peri-tumoural lipid composition might not be early predictive marker of pathological complete response.

Acknowledgements: The authors would like to thank Dr Matthew Clemence (Philips Healthcare Clinical Science, UK) for clinical scientist support. The project was funded by Friends of Aberdeen and North Centre for Haematology, Oncology and Radiotherapy (ANCHOR), NHS Grampian Endowment Research Fund and Tenovus Scotland.

References:

[1] Smittenaar CR, Petersen KA, Stewart K, Moitt N. *Br J Cancer.* **115**, 1147-1155 (2016).
[2] Chan KS, Cheung SM, Senn N, *et al. BMC Cancer*. **22**, 285 (2022).
[3] Ogston KN, Miller ID, Payne S, *et al. Breast.* **12**, 320-327 (2003).
[4] Bydder M, Girard O, Hamilton G. *Magn Reson Imaging*. **29**, 1041-1046 (2011).
[5] Peterson P, Månsson S. *Magn Reson Med.* **69**, 688-697 (2013).

Investigating live human sperm metabolism during hyperactivation and the acrosome reaction using ^{13}C-NMR

Evie Gruszyk[1], Allan Pacey[2], Steven Reynolds[1]
[1]School of Medicine and Population Health, Faculty of Heath, University of Sheffield, Sheffield.
[2]School of Medical Sciences, Faculty of Biology, Medicine and Health, University of Manchester, Manchester

Introduction: In addition to capacitation, hyperactivation and the acrosome reaction are key events that must occur for successful fertilization[1]. It remains unclear what the energy demands for these events are and the role of glycolysis or oxidative phosphorylation in supplying ATP to drive this. ^{13}C-NMR can identify multiple simultaneous biochemical pathways utilised by live sperm using isotopically labelled substrates[2]. In this study, we investigated live human sperm energy metabolism during hyperactivation and the acrosome reaction.

Methodology: Washed sperm (n=11) were incubated with $^{13}C_u$-glucose at 37°C for eight-hours and the metabolic conversion by sperm measured by ^{13}C-NMR. First, capacitation was initiated by Human Serum Albumin and bicarbonate for 4 hours and subsequently stimulated for either hyperactivation (8 mM caffeine) or the acrosome reaction (10 µM progesterone, 5 µM Prostaglandin E1 and 30 mM ammonium chloride). Hyperactivation was determined using CASA (Compute Aided Sperm Analysis) and the acrosome reaction using fluorescent staining, Pisum sativum agglutinin. Lactate and bicarbonate NMR integrals were normalised by vital sperm concentration, see Figure 1. Statistical analysis used the Wilcoxon test and date is presented as mean ± SEM.

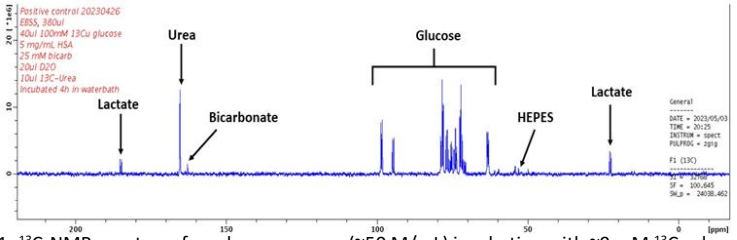

Figure 1: ^{13}C-NMR spectrum from human sperm (~50 M/mL) incubation with ~9 mM $^{13}C_6$-glucose. Spectra were acquired at 9.4T with a $^{13}C\{^1H\}$ inverse-gated pulse sequence (SW = 239 ppm, NA = 4096, AQ = 0.5 s, D1 = 2 s, TD = 24036, FA = 16°). The spectra were processed using a 5 Hz exponential line broadening. The urea signal (δ = 165.5 ppm) was used as a reference.

Results: Hyperactivation (n=11, 0.1±0.1% to 28.1±5.9%, p<0.001) and the acrosome reaction (n=11, 6.04 ± 1.4% to 9.7 ± 1.1%, p=0.017) were significantly induced in human sperm. There was significantly more lactate produced during hyperactivation (Arbitrary units (a.u.): $1.3\pm0.1\times10^7$ to $1.9\pm0.2\times10^7$, p<0.001) and the acrosome reaction (a.u.: $9.8\pm0.8\times10^6$ to $1.2\pm0.1\times10^7$, p<0.001). Significantly, less bicarbonate was produced during the acrosome reaction (a.u.: $3.1\pm0.5\times10^5$ to $1.6\pm0.2\times10^5$, p=0.03) in human sperm, however there were no differences in bicarbonate production during hyperactivation.

Conclusions: The increased lactate production during hyperactivation and the acrosome reaction suggests glycolysis dependency for these processes without a reliance on oxidative phosphorylation. The bicarbonate production measured during hyperactivation suggests oxidative phosphorylation is occurring at a background level.

References

1. Alasmari, W., Barratt, C. L. R., Publicover, S. J., Whalley, K. M., Foster, E., Kay, V., Da Silva, S. M. & Oxenham, S. K. 2013a. Human Reproduction, 28, 866-876.
2. Reynolds S, Calvert SJ, Walters SJ, Paley MN, Pacey AA. Reprod. Fertil. 2022, 3(2), 77–89.

Power Pitch Session 4

Using Magnetisation Transfer Ratio, T1 and T2 to monitor the in-vitro gastric digestion of chicken and plant-based chicken analogues

May Alotaibi [1,2], Olivier Mougin[3], Molly Muleya[1], Andrew Salter[1], Penny Gowland[3], Sally Eldeghaidy [1,3] and Caroline Hoad [3, 4]

[1]Division of Food, Nutrition & Dietetics, School of Biosciences, University of Nottingham, LE12 5RD, UK; [2]Clinical Nutrition Program, Department of Health Sciences, College of Health and Rehabilitation Sciences, Princess Nourah Bint Abdulrahman University, Riyadh, Kingdom of Saudi Arabia; [3]Sir Peter Mansfield Imaging Centre, School of Physics and Astronomy, University of Nottingham, Nottingham NG7 2RD, UK; [4] NIHR Nottingham Biomedical Research Centre (BRC), Nottingham University Hospitals NHS Trust and University of Nottingham, Nottingham, UK.

Introduction:

Monitoring the breakdown of food during gastrointestinal digestion is critical for understanding how the structure of food influences nutrient bioavailability and bioaccessibility. Magnetic Resonance Imaging (MRI) allows for the non-destructive and spatially resolved assessment of alterations in the multi-scale structural characteristics of food[1]. In-vitro digestion models are commonly used, however it remains challenging to validate these models with in-vivo observations, and MRI techniques provides a great tool to narrow this gap. This study aims to compare chicken and plant-based chicken analogues in terms of their hydrolysis and digestibility by using relaxation time (T1&T2) and Magnetization Transfer (MT) measurements in samples during gastric phases of static digestion model.

Methods:

In-vitro digestion was performed following the INFOGEST harmonised static in-vitro digestion model[2] for soups without dilution and enzymes at baseline, and then 1h, 1:30h and 2h in the gastric phase. Protein sources from chicken (breast and thigh) and two commercial plant-based chicken analogues (P-C1 [soy protein, 63%], P-C2 [wheat protein, pea protein]) were assessed as part of a soup meal. All soups were designed to match for calories and content of protein, fat, carbohydrates. T1, T2 and Chemical Exchange Saturation Transfer (CEST) were measured using 3T *Philips* Ingenia MRI scanner using a 3D FFE multi-shot sequence with 18 slices (5mm slice thickness), Flip Angle 5°, Compressed Sense 6, FOV 300 x 300 mm^2 and in-plane resolution 0.93 x 0.93 mm^2. MT amplitude was obtained by fitting the CEST spectrum (22 frequencies) using a Lorentzian lineshape. Regions of interest in the different samples were drawn at the bottom of the tubes using MIPAV[3] The calculations and processing were carried out using MATLAB R2022a (MT amplitude) and C (T1 and T2). The statistical differences were calculated using Two-way ANOVA analysis followed by a Tukey test ($p < 0.05$) Using GraphPad Prism 10.

Results:

MT amplitude was significantly higher at the baseline in the undiluted soup prior to digestion when compared to the later timepoints for all samples ($P<0.0001$), where digestion process decreased the MT, Figure 1. There was a significant effect of digestion time between 1hour and 1:30 hour in breast, thigh and P-C1 with ($P<0.0001$). However, there were no significant differences of MT between the samples. There was a significant increase in T1- and T2-values for the samples in the digestion model compared to baseline soup ($P<0.0001$), except T2-values for P-C2 sample. T1-values demonstrated a significant difference between the animal-based chicken (breast and thigh) compared to plant-based chicken ($P<0.001$). T2-value was higher for thigh samples compared to other samples ($P<0.01$). However, the T1 and T2-values did not vary during the digestion time, see Tables 1.

Discussion:

The higher MT amplitude of breast and thigh at 1hour could be attributed to the muscle content, in which the MT give a higher value in the muscle compared to the other organs[4]. However, P-C1 (soy protein) does not contain muscle and has a higher MT value. This could be explained by the higher fibrous structure of soy protein which is similar to or slightly superior to the fibrous structure of chicken breast[5]. In terms of T1& T2, the increase of T1&T2 values in the samples compared to the baseline could be due to the high dilution factors used in the experiment. This was considered as a limitation of the study and will be further investigated with a semi-dynamic model. Similarly, change in T1 could be taken into account for a more accurate quantification of the MT pool size.

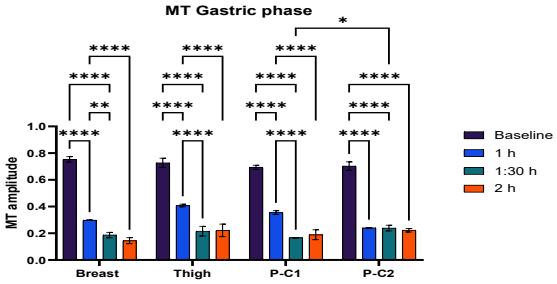

Figure 1. MT amplitude of chicken and plant-based chicken soup samples by different digestion time. Error bars represent SD, and the asterisks on bars indicate to differences, determined with the two-way ANOVA test ($p < 0.05$). (****): ($P \leq 0.0001$); (***): ($P \leq 0.001$); (**): ($P \leq 0.01$); (*) :($P \leq 0.05$).

Table 1: T1&T2-values of chicken and plant-based chicken soup samples by different digestion time. Data are presented as mean ± standard deviation (SD) of two replicates

	T1			T2		
Samples	Baseline	1h	2h	Baseline	1h	2h
Breast	2.18±0.03	3.12±0.19	3.10±0.16	0.15±0.003	0.34±0.07	0.31±0.05
Thigh	1.73±0.06	3.08±0.13	3.04±0.14	0.32±0.01	0.52±0.04	0.41±0.03
P-C1	1.05±0.06	2.73±0.06	2.65±0.07	0.15±0.05	0.38±0.03	0.29±0.02
P-C2	1.17±0.03	2.53±0.09	2.34±0.01	0.25±0.05	0.28±0.01	0.25±0.005

Conclusion:

MT, T2 and T1 can be applied to monitoring the in-vitro gastric digestion of chicken and chicken analogues. These finding will be extended to monitoring dynamic in-vivo digestion of chicken and chicken analogues as well as semi-dynamic in-vitro digestion models. This will be a guide for further studies to monitor the digestibility of different types of protein both in-vitro and in-vivo.

References: [1] Benders, S. et al., 2019. *Physical sciences reviews*, *4*(10), p.20180177. [2] Brodkorb, André, et al., 2019. Nature protocols 14.4: 991-1014. [3] McAuliffe MJ. et al., 2001. Ieee computer-based medical systems (CBMS), 381-386. [4] Boss, A et al., 2006. *Journal of Magnetic Resonance Imaging*, *24*(5), pp.1183-1187. [5] Chiang, J.H. et al., 2019. *Food Structure*, *19*, p.100102.

Co-ingestion of whey protein enhances liver glycogen repletion following ingestion of combined glucose and fructose in trained cyclists

Sophie Hannon[1], James McStravick[1], Libby Henthorn[1], Fiona Smith[1], Nathan Hodson[1], Gabriella Rossetti[1], James Morton[2], Aneurin J Kennerley[1], Mark Hearris[1]

[1]Institute of Sport, Department of Sports & Exercise Science, Manchester Metropolitan University, Manchester.

[2]Research Institute for Sport and Exercise Sciences, Liverpool John Moores University, Liverpool.

Introduction: Carbohydrates (CHO) are crucial for energy production during prolonged endurance activities (1). Despite this, storage of CHO within the liver (~120g) and muscle (~500g) as glycogen is relatively limited and can become significantly depleted following prolonged exercise (2). Rapid glycogen replenishment represents a priority when performance must be restored within a limited timeframe (e.g., <24 hours). While post-exercise CHO consumption is vital for restoring glycogen, combining it with dietary protein may enhance liver glycogen repletion. This study uses non-invasive ^{13}C magnetic resonance spectroscopy (MRS) to assess skeletal muscle and liver glycogen concentrations during a 5-hour post-exercise recovery period in response to four nutritional interventions. This research aims to provide nutritionists, metabolism researchers and athletes with practical refueling recommendations.

Methods: Trials were conducted at the Institute of Sport (Manchester, UK) following approval from Manchester Metropolitan University Research Ethics Committee in accordance with the Declaration of Helsinki. Ten endurance trained cyclists (mean ± SD: age 30 ± 8 years, body mass 77.8 ± 6.5 kg, height 181.4 ± 4.8 cm, VO_{2max} 57.5 ± 5.7 ml $kg^{-1}min^{-1}$, peak power output [PPO] 384 ± 31 W) performed glycogen depleting exercise followed by five hours of recovery. During the recovery period, participants ingested 60 $g.h^{-1}$ CHO from either maltodextrin (M), fructose (F), maltodextrin + fructose (M&F) or maltodextrin + fructose + protein (Pro; 30 g whey protein consumed at 0 and 180 minutes). ^{1}H Magnetic Resonance Imaging (MRI; and ^{13}C spectroscopic data were acquired immediately post-depletion (t=0 minutes), at two hours (t=120 minutes) and at five hours (t=300 minutes) to establish liver volume and glycogen concentrations within the liver and the thigh muscle. Data were acquired on a Siemens MAGNETON Vida 3T MR system (70cm bore, preinstalled XQ 45/200 gradients, XA31 software - Siemens Healthcare GmbH, Erlangen, Germany). For whole liver volume assessment Spine 32 and Body 18 1H array coils were used. 3D Slicer using an artificial intelligence-based segmentation tool (Totalsegmentator) was used to extract liver volume (V_L). MRS utilised a dual-channel $^{1}H/^{13}C$ transmit-receive flexible surface coil (01365; Rapid Biomedical GmbH, Rimpar, Germany) positioned over the liver or thigh muscle. Following standard 1H localisation, manual frequency, power, and 3D shimming (MGE field mapping) achieved a 1H water peak FWHM of 19.9 ± 1.0 Hz. FID-based acquisition was implemented (TR 200 ms; NA 4096; FA 90°; bandwidth (BW) 16000 Hz; acquisition duration 128 ms; spectral points 2048). ^{13}C spectral data were analysed offline in MATLAB 2024a (The MathWorks, Natick) using software routines developed in-house. Following 5Hz line broadening, spectra were manually phased (0 & 1st order correction). Spectra were windowed around the C-1 glycogen doublet (~100ppm) and fitted, using nonlinear least squares with a Levenberg–Marquardt algorithm, to appropriate Gaussian/Lorentzian functions and a quadratic polynomial for the baseline (Figure 1). Fitting parameters were used to isolate the signal contribution from glycogen. The area under the curve was extracted and normalised to a small 50mM phantom acetate standard (secured on the opposite coil surface). Total liver glycogen content (LGC) was calculated using: $LGC(g) = \frac{162(g.M^{-1})}{1000} . V_L . [Glyc]$.

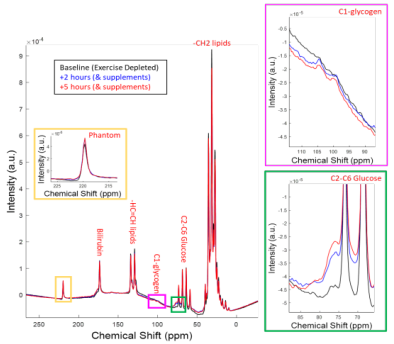

Figure 1. Example ^{13}C spectra.

Results: The changes in liver and muscle glycogen (%) post-exercise over a 5-hour recovery period are illustrated in Figure 2. The highest mean (± SEM) percentage change in liver glycogen at 5 hours was observed in the Pro trial, with an increase of 67.3 ± 11.6%. This represents a 53.4% increase over trial M, which showed the lowest percentage change of glycogen resynthesis among the carbohydrate (CHO) trials. Notably, the glycogen repletion rate in the Pro trial between 2 to 5 hours post-exercise was markedly higher (59%) compared to the initial 2 hours, where resynthesis was considerably slower at 8.3 ± 7.9%. After the 5 hrs of recovery the F and M&F trials saw comparable glycogen resynthesis levels (45.4 ± 8.5 and 46.6 ± 9.9 %, respectively). Regarding muscle glycogen resynthesis, the M trial exhibited the highest percentage rise, with a 68.5 ± 16.4% increase after 5 hours of recovery. In contrast, the F trial resulted in the smallest percentage change among the CHO trials, with a 25.6 ± 11.9% change. Similar to liver glycogen resynthesis, F and M&F trials saw similar changes in glycogen resynthesis (25.6 ± 11.9 and 27.8 ± 11.2 %).

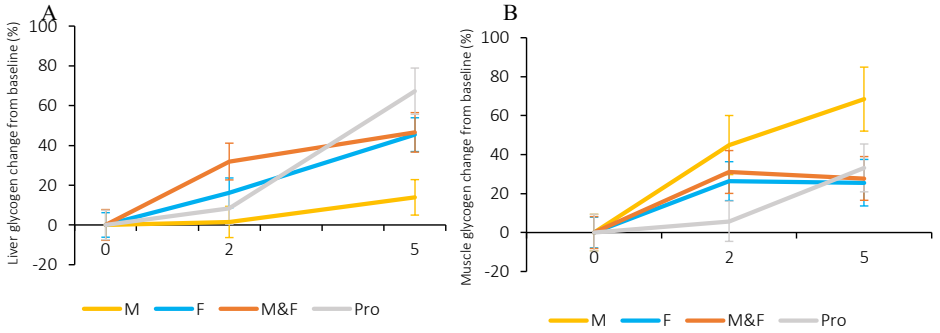

Fig. 3. Percentage change in glycogen from t=0 to t=300 minutes for (A) liver and (B) thigh muscle.

Conclusion: In conclusion, these data support the hypothesis that co-ingestion of protein (30 g at 0 and 180 mins) with CHO (60 $g.h^{-1}$) further enhances liver glycogen repletion beyond CHO alone during a 5-hour recovery period in endurance trained male cyclists. In contrast within the muscle, it was observed that maltodextrin (60 $g.h^{-1}$) produced the greatest increase in muscle glycogen resynthesis.

References: 1. Jeukendrup AE. Carbohydrate intake during exercise and performance. *Nutrition*. 2004;20(7-8). doi:10.1016/j.nut.2004.04.017, **2.** Gonzalez JT, Fuchs CJ, Betts JA, van Loon LJC. Liver glycogen metabolism during and after prolonged endurance-type exercise. *American Journal of Physiology - Endocrinology and Metabolism*. 2016;311(3). doi:10.1152/ajpendo.00232.2016

Power Pitch Session 4

Multi-organ quantitative abdominal MRI in paediatric patients with Cystic Fibrosis

Chris R Bradley[1,2], Alexander Yule[2], Nayan Dey[2], Christabella Ng[2], Naaventhan Palaniyappan[2], Zachary Peggs[1,2], Jonathan Brooke[2], Neele Dellschaft[1,2], Luca Marciani[1,2], Robin Spiller[2], Guruprasad Aithal[2], Caroline Hoad[1,2], Penny Gowland[1,2], Ian Hall[2], Alan Smyth[2], Susan T Francis[1] and Andrew Prayle[2]
[1]Sir Peter Mansfield Imaging Centre, University of Nottingham, Nottingham, United Kingdom
[2]NIHR Biomedical Research Centre, Nottingham Univ. Hospital NHS Trust and Univ. Nottingham, Nottingham, UK.

Introduction: Cystic fibrosis (CF) is a multi-system, life-limiting autosomal recessive genetic disorder which causes mucus to build-up in certain organs, such as the lungs, liver, pancreas, and intestines. Cystic Fibrosis Transmembrane Regulator (CFTR) Modulator therapies target multiple organ systems, and modulators have maximal benefit when commenced in early childhood. There is a need for multisystem assessment of beneficial as well as potential adverse effects of modulators in children. *Aim:* To apply multi-organ MRI (the GIFT protocol) designed to be tolerable for children aged 6 to 11 years to quantify measures of lung, liver, spleen, pancreas and gut function for future study of CFTR therapies. This abstract presents results on the abdominal (liver, pancreas and spleen) measures.

Methods:

Study protocol: Eight children with CF (aged 9±2 years) and 3 healthy volunteers (HV) (aged 9±3 years) were recruited (https://clinicaltrials.gov/study/NCT05699148). The study day consisted of a fasted gut MRI (small bowel water content and gut motility) [1] followed by abdominal (liver, pancreas and spleen) MRI acquired in 20-minutes. Subjects then had a set breakfast, with a gut and lung scan (lung UTE and PREFUL) collected at 240-minutes after breakfast, followed by a second set meal and a gut scan 300-minutes post breakfast (Fig. 1).

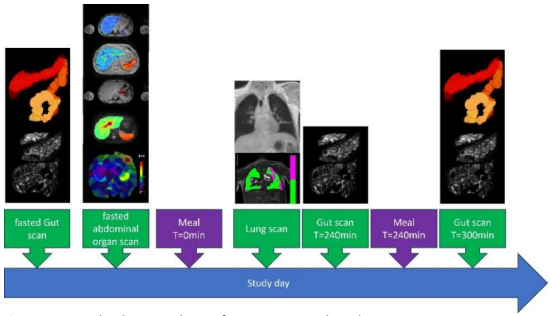

Figure 1: Study day timeline of GIFT protocol and representative images collected for the gut, abdomen (liver, pancreas, spleen), and lung.

All scans were acquired on a Philips 3T Ingenia scanner using a 16-channel anterior coil with paediatric coil holder. Children undertook the scan protocol without sedation. Abdominal MRI measures collected included a breath hold mDIXON-Quant sequence to assess organ volume and fat fraction, and a fat suppressed respiratory triggered spin-echo echo-planar-imaging (SE-EPI) inversion recovery technique with 15 inversion times (100-1500ms, ascend/descend acquisition) to assess organ tissue T_1 in ~3 minutes (3x3x8mm^3 voxel size, 9 axial slices). A breath hold multi-echo (mFFE) sequence was used to collect T_2* data (10s,12 echoes, TE1=2.35ms, ΔTE=2.35ms,3x3x8mm^3,9 axial slices), and T_2 data were collected using a respiratory triggered GraSE sequence with 30 echoes (TE1=5.6ms,ΔTE=5.6ms,3x3x8mm^3, 9 axial slices). Phase contrast MRI (PC-MRI) assessed blood flow through the superior mesenteric artery (SMA), hepatic artery (HA) and portal vein (PV) (velocity encoding: 140, 100 and 50cm/s respectively,1x1x6mm^3) to monitor for CF related liver disease and portal hypertension [2]. Liver MR elastography (MRE) was collected using a QIBA recommended SE-EPI sequence with 4 axial slices, 4 phase offsets and 60Hz vibration frequency [3].

Data Analysis: mDIXON fat fraction (FF), T_2 and T_2*, and MRE stiffness maps were scanner computed. T_1 data were fit voxel-wise to compute T_1 maps (MATLAB). A manual ROI was drawn of the liver, spleen and pancreas from the mDIXON images and used to compute organ volume. This ROI was then used to interrogate the quantitative maps with histogram analysis performed to compute the mode of a fitted gaussian. PC-MRI data was analysed in Philips Q-flow software to compute flow, mean velocity and mean cross sectional area.

Results: Liver tissue T_1, T_2, T_2*, stiffness, FF and volume were comparable between children with CF and HVs, Fig. 2, but note outlier values in 1 CF child who was independently being reviewed for CF-related liver disease. For the pancreas, there was a trend for higher FF in CF (CF=6.3(78)%, HV=0.9(2)%, p=0.09), with 3 CF children having partial or complete replacement by fat tissue, Fig. 3A. There was also a significant increase in pancreas T_1 (CF=1166(494)ms, HV=736(228)ms, p<0.004) and T_2 (CF=111±32ms HV=59.9±5.9ms, p<0.002). There was also a trend for an increase in spleen tissue T_1 in CF (CF=1418±40ms, HV=1381±24ms, p=0.05), Fig. 3B. There was no difference in SMA or PV flow but a significant increase in hepatic artery velocity in CF (CF=13.1±6.4cm/s, HV=8.2±1.5cm/s, p<0.04) Fig. 4.

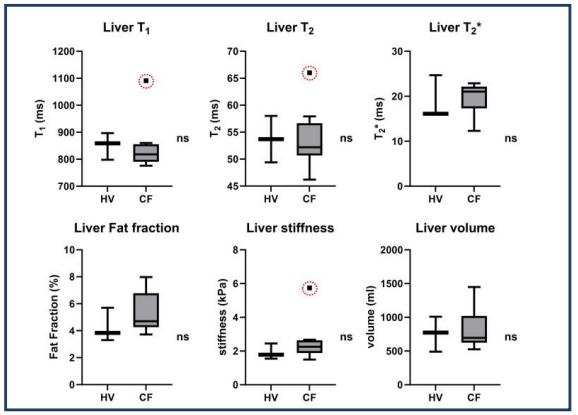

Figure 2: Liver tissue T_1, T_2, T_2*, FF, MRE stiffness, and volume in HV and CF. Outlier with high T_1, T_2, and MRE stiffness, this child had CF-related liver disease.

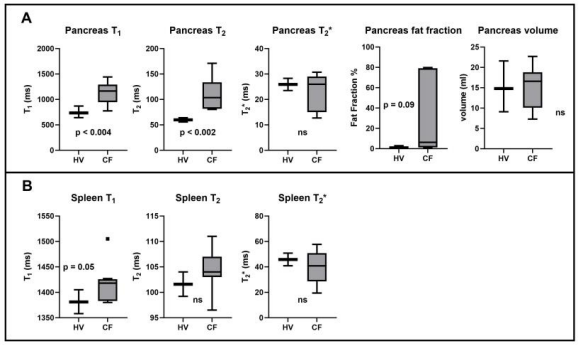

Figure 3: A) Pancreas in CF compared to HV has a significant increase in T_1 (CF 1166(494)ms, HV 736(228)ms, p<0.004) and T_2 (CF 111±32ms HV 59.9±5.9ms, p<0.002), and a trend for increased FF (CF = 6.3(78)%, HV = 0.9(2)%, p = 0.09). B) Spleen shows a trend for an increase in spleen tissue T_1 in CF (CF 1418±40ms, HV 1381±24ms, p=0.05).

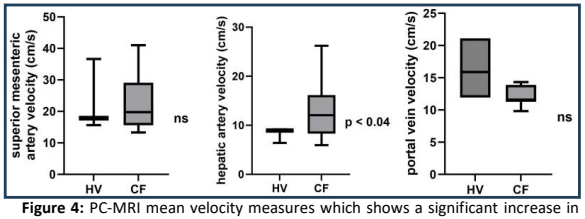

Figure 4: PC-MRI mean velocity measures which shows a significant increase in the hepatic artery in CF (CF 13.1±6.4cm/s, HV 8.2±1.5cm/s, p<0.04), but no difference in the SMA or portal vein.

Discussion: We have demonstrated the feasibility of acquiring a multiorgan multiparametric quantitative MRI protocol in children. Differences in liver, pancreas and spleen MRI measures in CF compared to HVs were seen in the spleen and pancreas, alongside liver changes in a CF child later diagnosed with liver disease. HV T_1 measures agree with literature paediatric values [4], and we plan to collect more HV data.

Conclusion: Following this baseline feasibility, we are now studying the effect of CFTR therapy on lung, gut, liver, pancreas and spleen function by scanning these children with CF 12-months after commencement of Kaftrio.

References:

1) Dellschaft NS, Ng C, Hoad C, et al. Journal of Cystic Fibrosis 21:502–505. (2022).
2) Palaniyappan N, Cox E, Bradley C, et al. J Hepatol 65(6):1131-1139. (2016).
3) Quantitative Imaging Biomarkers Alliance (2017) QIBA Profile: Magnetic Resonance Elastography of the Liver. 1–65 (2019).
4) Gilligan LA, Dillman JR, Tkach JA, et al. Pediatr Radiol 49:1018–1024. (2019).

Power Pitch Session 4

Novel MRI contrast agents and image analysis for studying kidney pathophysiology.

Georgia L. Aspinall[1], Susan Francis[2], Derek Irvine[3], Geoffrey Rivers[3], Peter Harvey[1,4]
[1]School of Chemistry, University of Nottingham, Nottingham, NG7 2RD
[2]Sir Peter Mansfield Imaging Centre, School of Physics and Astronomy, University of Nottingham, Nottingham, NG7 2QX
[3]Centre for Additive Manufacturing, University of Nottingham, Nottingham, NG8 1BB
[4]Sir Peter Mansfield Imaging Centre, School of Medicine, University of Nottingham, Nottingham, NG7 2UH

Introduction:

Accurate quantification of nephron number is central to assessing overall kidney function as a deficit in nephron number has been linked to increased risk of cardiovascular and renal disease in adults.[1] Current clinical methods of assessing kidney function are highly invasive and often miss the early stages of renal disease preventing the use of any early intervention which may slow or halt progression. Contrast enhanced magnetic resonance imaging (MRI) has shown potential as a non-destructive method of counting individual nephrons in an intact kidney.[2]

Gadolinium(III) based contrast agents have long since been the gold standard for use in MRI, however rising concerns of nephrogenic systemic fibrosis in patients with reduced kidney function have prompted a search for alternatives.[3] The salen ligand has been effectively researched in the world of catalysis for decades.[4] Its simple synthesis and affinity for transition metal complexation make it a promising candidate for a range of new contrast agents capable of increasing T_1 relaxation rates.

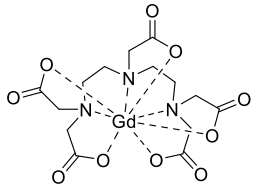

Gd-DTPA

Molecular Weight: 590.7 $gmol^{-1}$
✘ Not cell permeable
✘ Nephrogenic systemic fibrosis
✓ Best metal for MRI contrast
✓ Can use relatively low doses

Mn-salen

Molecular Weight: 356.7 $gmol^{-1}$
✓ More likely to permeate into cells
✓ Mn is biologically abundant
✘ Less unpaired electrons
✘ Higher concentrations needed

Figure 1 Comparison between the advantages and disadvantages of current clinical contrast agent gadopentetic acid (Gd-DTPA) in comparison to Mn-salen, one of the proposed new complexes for MRI.

Methods:

Salen compounds were made following literature procedures and characterised through standard techniques. Relaxation parameters were measured in phantoms at varying concentration on a 7 T Bruker MR scanner. T_1 and T_2 calculations were conducted using ImageJ and corresponding R_1 and R_2 maps produced. Relaxivity values were calculated from graphs of relaxation rate against concentration. To test relaxation properties of the complexes in tissue, 4mM solutions of Mn-salen and 2mM Gd-DTPA were made in degassed PBS. Formalin fixed tissue (kidney and brain) was soaked in degassed PBS for a week to remove any traces of formalin and baseline scans of the tissue were obtained. The tissue was then soaked in each solution for 7 days and rescanned with the same parameters to observe the change in tissue relaxation rate. Upon completion of this process, tissue was sliced, and atmospheric-pressure matrix assisted laser absorption ionisation spectrometry (AP-MALDI) was performed to confirm that the metal had remained complexed throughout the tissue.

Results:

A library of transition metal salen complexes have been synthesised, including complexes with ligand modifications to increase solubility and resulting cell uptake of the complexes. Manganese, iron, chromium and copper complexes were all shown to increase relaxation rate with increasing concentration but less so than Gd-DTPA. In the tissue however, Mn-salen has shown promise as an *ex vivo* stain in kidney tissue effectively enhancing T_1 and T_2 relaxation rate while simultaneously increasing contrast between differing tissue regions. In comparison, Gd-DTPA enhanced relaxation rates across the whole kidney, reducing the contrast between differing regions.

Discussion:

Transition metals have fewer unpaired electrons than gadolinium so were expected to be less efficient contrast agents. With regard to the tissue staining however, the vast difference in the relaxation rate ability could be due to the molecules size and lipophilicity. Gd-DTPA with a molecular weight of 546 is not able to enter cells whereas a much smaller, planar Mn-salen with a molecular weight of 357 would be much better suited for this. From the obtained results, it appears that Mn-salen may favour uptake in some tissues more than others, leading to the drastic difference in contrast between tissue types.

Conclusions:

Mn-salen is a planar molecule with a low molecular weight that has shown great promise as an MRI active tissue stain in comparison to clinically used Gd-DTPA. While it has been confirmed using spectroscopic techniques that the Mn-salen complex remained complexed throughout the tissue, further studies to confirm whether it has permeated through cell membranes are needed.

Acknowledgements:

Funding was provided by the EPSRC as part of the Advanced Medical Imaging Doctoral Training Program in collaboration with The University of Queensland.

References

[1] B. M. Brenner and D. L. Garcia, *Am J Hypertens*, 1988, **1**, 335–347.
[2] M. J. DeFreitas, C. P. Katsoufis, J. C. Infante, M. L. Granda, C. L. Abitbol and A. Fornoni, *Pediatr. Nephrol.*, 2021, **36**, 517–525.
[3] R. Kaewlai and H. Abujudeh, *Am. J. Roentgenol.*, 2012, **199**, W17–W23.
[4] P. G. Cozzi, *Chem. Soc. Rev.*, 2004, **33**, 410–421.

Power Pitch Session 4

Visualisation of tablet dissolution in the human stomach using magnetic resonance imaging and manganese as a marker

Tejal Akbar1, Pavel Gershkovich2, Konstantinos Stamatopoulos3, Penny A. Gowland4, Snow Stolnik2, James Butler3 and Luca Marciani1*

1 Nottingham Digestive Diseases Centre and National Institute for Health Research (NIHR) Nottingham Biomedical Research Centre, Nottingham University Hospitals NHS Trust and University of Nottingham, Nottingham NG7 2UH, UK

2 School of Pharmacy, University of Nottingham, Nottingham NG7 2RD, UK

3 Drug Product Development, GSK R&D, Ware, Hertfordshire SG12 0GX, UK

4 Sir Peter Mansfield Imaging Centre, School of Physics and Astronomy, University of Nottingham, Nottingham NG7 2QX, UK

Introduction

The addition of a contrast agent into a drug dosage form significantly enhances its visibility when imaging it the gastro intestinal (GI) tract using magnetic resonance imaging (MRI) [1]. The contrast agent assists to discriminate the system from water, food materials and gas present in the complex GI environment. In recent years, contrast agents including gadolinium-chelates, magnetite, pineapple and hibiscus tea have been attempted, not only in imaging the dosage form, but also imaging its disintegration and dispersion in both the fasted and fed stomach. It is well known that rate limiting step to absorption of drugs from the GI tract to the systemic circulation is dissolution [2]. This area has not been actively investigated due to limitations posed by contrast agents. This study uses the paramagnetic substance of manganese gluconate added to a tablet to image its dissolution in the fed stomach.

Methods

A. Tablet development

Tablets were manufactured using a Riva Piccola rotary press equipped with round, bevelled edge flat faced 15 mm punch and die sets. Each 750 mg tablet included 18.75 mg of manganese gluconate (Sigma-Aldrich) and commonly used excipients for producing direct compression tablets. Pharmacopeial tests such as uniformity of mass, friability and disintegration time were used to evaluate the success of the tablet formulation.

B. Experimental design

Ten healthy human volunteers were asked to drink 300 mL of a nutrient drink (428 kCals) to induce a fed state after a ten hour overnight fast. After five minutes, one tablet and 240 ml of water were administered to the participant. MRI scans were then acquired serially for one-hour post-administration.

Results

Figures 1B and 2B show the typical appearance of the tablet in the stomach of one participant four minutes post-dosing. The tablet size and shape observed in the images is representative of the physical shape of the tablet; a bevelled edge tablet of approximately 15 mm in diameter is observed as shown in inset Figure 1E.

A bright ‘halo’ effect can also be observed around the surface of the tablet, consistent with T1 shortening of the bulk water surrounding the tablet due to dissolution of the manganese contrast agent in the stomach. No significant mixing of the stomach contents occurred during the imaging period, and the ‘halo’ remained largely around the tablet. With time, the tablets showed increased erosion, which was inferred by observing a decrease in tablet size and change in shape. The brightening of the signal from the meal contents around the tablet was also clearly seen to increase in size as the study progressed. This phenomenon was observed consistently in all subjects in the T1-weighted imaging sequences.

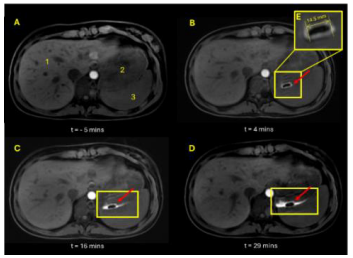

Figure 1: Axial, 3D LAVA MRI images of abdomen. Image A shows image after administration of nutritional drink and prior to tablet administration. Image B, C, D show tablet at time points 4, 16 and 29 minutes, respectively, post tablet administration with inset E showing an enlarged image of tablet. Anatomical landmarks indicated in image A, liver(1), stomach(2), spleen(3).

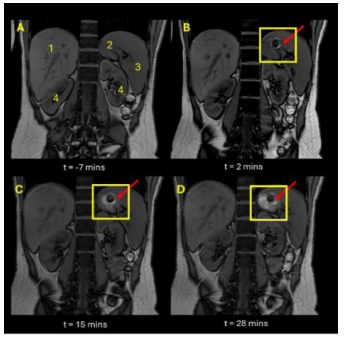

Figure 2: Coronal, T1-weighted Dual Echo MRI images of abdomen. Image A shows image after administration of nutritional drink and prior to tablet administration. Image B, C, D show participant at time points 2, 15 and 28 minutes respectively post tablet administration. Anatomical landmarks indicated in image A, liver (1), stomach(2), spleen(3), kidneys(4).

Discussion and Conclusion

This is, to the best of our knowledge the first study to use MRI to image tablet dissolution in the fed stomach using the addition of manganese gluconate as a contrast agent. A bright ‘halo’ effect is observed around the surface of the tablet, consistent with T1 shortening of the bulk water surrounding the tablet. This positive contrast enhancement or shortening of the T1 signal is observed only when the manganese from the tablet dissolves into water. The lack of mixing of the meal was a contributing factor in making the ‘halo’ visible over a prolonged time.

The use of manganese ions for this application has not previously been used for dissolution imaging of tablets using MRI. Typically, for an oral formulation, dissolution of the drug must occur as the first step in ensuring an efficacious dose is delivered. Expanding knowledge of dispersion and dissolution using manganese gluconate has the potential for improved understanding of disintegration and dissolution and may inform *in silico* modelling and potentially lead to better *in vitro* and *in vivo* agreement.

References

1. Giovagnoni, A., A. Fabbri, and F. Maccioni, *Oral contrast agents in MRI of the gastrointestinal tract*. Abdominal Radiology, 2002. **27**(4): p. 367.
2. Hörter, D. and J. Dressman, *Influence of physicochemical properties on dissolution of drugs in the gastrointestinal tract*. Advanced drug delivery reviews, 2001. **46**(1-3): p. 75-87.

Power Pitch Session 4

Diffusion-Weighted Imaging in Intraoperative MRI: A Comparison between Echo Planar and Turbo Spin-Echo Techniques

James C Thorpe[1], Stefanie C Thust[1,2,3,4], Claire H M Gillon[1], Selene Rowe[1], Charlotte E Swain[1], Donald C MacArthur[1,2], Simon P Howarth[1], Shivaram Avula[5], Paul S Morgan[1,2,3], Rob A Dineen[1,2,3]

[1]Nottingham University Hospitals, Nottingham, UK

[2]School of Medicine, University of Nottingham, UK

[3]NIHR Nottingham Biomedical Research Centre, Nottingham, UK

[4]Department of Brain Rehabilitation and Repair, UCL Institute of Neurology, Queen Square, London, UK

[5]Radiology, Alder Hey Children's Hospital NHS Foundation Trust, Liverpool UK

Introduction: In intraoperative MRI (IoMRI) guided brain tumour surgery, Diffusion Weighted Imaging (DWI) is routinely used in the detection of acute cerebral ischaemia and the identification of purulent infection (1-3). Conventionally echo planar imaging DWI (EPI-DWI) is used; however, it is susceptible to distortion and signal pile-up artefacts that affect image quality (4,5). This is a particular issue in the IoMRI setting in which intracranial air is introduced during surgery. An alternative technique with minimal spatial distortion and signal pile-up artefact is Turbo Spin Echo DWI (TSE-DWI) (6,7). This study sought to compare via single and multisequence assessment EPI-DWI and TSE-DWI in the IoMRI setting to determine whether there is a radiological preference for either sequence.

Methods: Thirty-four consecutive patients (22 female) aged 2-61 years (24 under 18) were scanned with EPI- and TSE-DWI as part of standard IoMRI scanning protocol while undergoing IoMRI during surgical resection of intracranial tumours. A neuroradiologist blinded to sequence type performed a single sequence assessment of spatial distortion and image artefact. Images were scored on distortion and artefact, around and remote to the resection cavity, and visibility and confidence of abnormality detection. Two further neuroradiologists performed a multisequence radiological assessment with access to all other imaging from each case. The DWI images were directly compared with radiologists scoring which they preferred with respect to anatomy, abnormality, artefact, and overall preference. The multisequence assessment also asked two further questions. Firstly, "Does one DWI sequence display clinically important information that is not visible in the other sequence that aids your assessment?" Secondly, "Does one sequence display artefacts/misleading information that is not present in the other sequence that hinders your assessment?"

Results For the blinded single sequence assessment the TSE-DWI was scored equal to or superior to the EPI-DWI for every criterion for every case ($p<0.001$ for each question using Wilcoxon Signed Ranks Test). In the multisequence assessment both radiologists independently expressed (with a near complete interrater agreement of $\kappa_W = 0.94$) a preference for TSE-DWI over EPI-DWI on viewing brain anatomy, abnormalities and artefacts with TSE-DWI preferred overall for intraoperative assessments. Both radiologists reported instances (n = 7 / 12) in which there was clinically important information visible in the TSE-DWI that was not visible in the EPI-DWI, with one radiologist reporting one instance of the opposite. Both radiologists also reported instances (n = 4 / 19) of EPI-DWI featuring artefacts that hindered their assessment in a way that was not seen in TSE-DWI, with one instance of the TSE-DWI having uniquely misleading information. An example of an occasion in which the EPI-DWI featured a large signal pile-up artefact that obscured the view of a cerebellar infarct that was otherwise visible in the TSE-DWI is shown (for b=1000 images and ADC maps) in Figure 1.

Discussion: Overall, the results showed that for IoMRI, TSE-DWI had consistently superior image quality to EPI-DWI over a broad range of criteria according to both the blinded scoring and direct comparisons. However, the TSE-DWI had a significantly longer acquisition time (approximately 3.5 times longer than EPI-DWI), even when scan coverage was minimised for the TSE-DWI. This is not ideal in an intraoperative setting where it is desirable to acquire images as quickly as possible to allow the operation to continue and reduce time under anaesthetic.

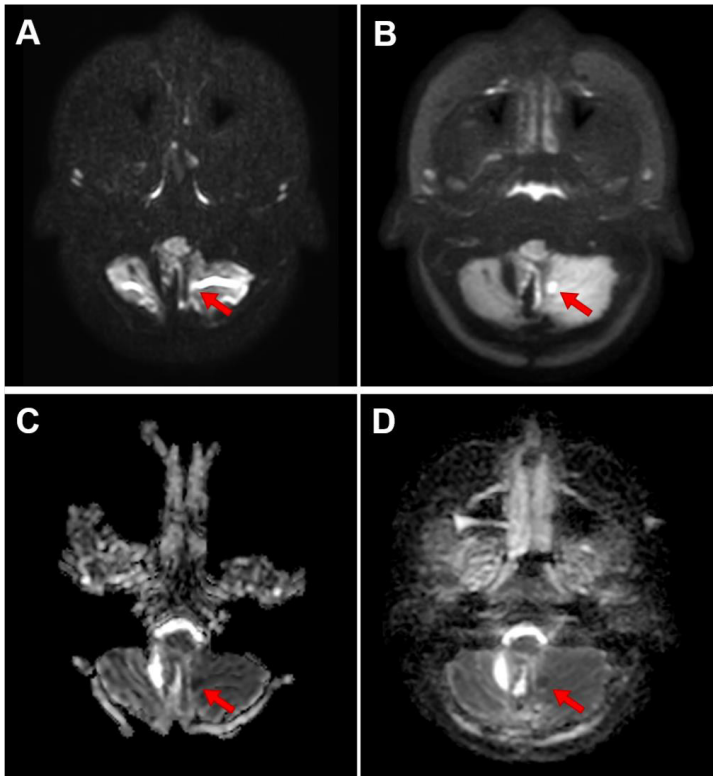

Fig. 1. b=1000 (A, B) and ADC (C, D) images for EPI-DWI (A, C) and TSE-DWI (B, D) featuring cerebellar infarct indicated by red arrow

Conclusions: Overall, both single sequence and multisequence assessments favoured the TSE-DWI over EPI-DWI for IoMRI, although the TSE-DWI was significantly longer.

Acknowledgements: Thanks to Children with Cancer UK, Nottingham Hospitals Charity, and the University of Nottingham CARO for their support in funding of the IoMRI facility used in this analysis.

References

[1] Dineen RA, Avula S, Peet AC, Morana G, Warmuth-Metz M. Anatomical and Biological Imaging of Pediatric Brain Tumor. Brain and Spinal Tumors of Childhood. 2020:61-92.
[2] Kono K, Inoue Y, Nakayama K, Shakudo M, Morino M, Ohata K, et al. The role of diffusion-weighted imaging in patients with brain tumors. American journal of neuroradiology. 2001;22(6):1081-8.
[3] Fanning NF, Laffan EE, Shroff MM. Serial diffusion-weighted MRI correlates with clinical course and treatment response in children with intracranial pus collections. Pediatric radiology. 2006;36:26-37.
[4] Koh D-M, Collins DJ. Diffusion-weighted MRI in the body: applications and challenges in oncology. American Journal of Roentgenology. 2007;188(6):1622-35.
[5] Voglis S, Hiller A, Hofer A-S, et al. Failure of diffusion-weighted imaging in intraoperative 3 Tesla MRI to identify hyperacute strokes during glioma surgery. Scientific Reports. 2021;11(1):16137.
[6] Panyarak W, Chikui T, et al. Image quality and ADC assessment in turbo spin-echo and Echo-Planar diffusion-weighted MR imaging of tumors of the head and neck. Academic radiology. 2019;26(10):e305-e16.
[7] Andersson JL, Skare S, Ashburner J. How to correct susceptibility distortions in spin-echo echo-planar images: application to diffusion tensor imaging. Neuroimage. 2003;20(2):870-88.

Power Pitch Session 4

Application of Magnetic Resonance Imaging and Spectroscopy Methods to Identify Fat Malabsorption in the Colon

Introduction

Fat malabsorption is one of the most prevalent malabsorption conditions [1]. Fat digestion and absorption is complex; in fat malabsorption conditions, undigested fat progresses through the small bowel and reaches the colon where, in health, fat is not generally found. Unabsorbed fat is associated with symptoms including diarrhoea, loose-oily stools (steatorrhea), and discomfort [1].

Fat malabsorption has been diagnosed using invasive, poorly tolerated or unreliable techniques as such there is a demand for new, non-invasive methods [2]. Magnetic Resonance Imaging (MRI) and Spectroscopy (MRS) are non-invasive techniques that can be used to image or detect fat. MRI has previously been used to visualise and quantify fat in the liver [3]. Currently it has not been demonstrated whether MRI can be used to visualise and/or quantify fat in the colon.

Orlistat (Alli®, GSK) is a weight loss drug aimed at people with obesity [4]. It is a lipase inhibitor that prevents the breakdown of fat and therefore can be used to mimic fat malabsorption in healthy participants [4].

Aims and Hypothesis

This study hypothesised that MRI could be used to visualise fat in the colon.
The aim was to induce fat malabsorption in healthy volunteers and assess whether fat could be detected in the colon using MRI.

Methods

This was a two-way cross over study using placebo or 120mg of Orlistat with a 7-day wash out period. N=7 participants consumed 50ml of Calogen® Energy Dense Supplement (Nutricia) containing 25g fat and their allocated treatment with both lunch and dinner the day before their study day. Participants arrived fasted at the MRI centre for a breakfast meal containing 22g fat and their allocated treatment followed by a lunch meal containing 21.1g fat and their allocated treatment. An MRI scan was conducted 2 hours after the lunch meal. Participants completed a 7-day Bristol stool score for (3 days before the scan day, the scan day, and 3 days after) for both arms.

Participants were scanned on a 3T Ingenia Widebore scanner (Philips, Best, The Netherlands) using a range of sequences including mDIXON [5]. 3D Dual Echo FFE mDIXON images were taken coronally, with 2 stacks and 30mm overlap in HF direction. 111 (reconstructed 1.8mm) slices were collected within each stack acquired as an 18s breath hold. Fat-only images were used to identify high fat areas of chyme in the colon, if any. Water-only images were used to confirm whether suspected high fat areas of chyme were fat or artefact. For additional sequences the field of view (FOV) was centred over suspected high fat areas of the chyme.

MRS (multi-echo, single voxel, STEAM spectroscopy (10x10x10mm)) was carried out on regions of interest where fat was identified or in the ascending colon and sigmoid colon if no obvious fat regions were observed.

Results

Study procedures were acceptable to participants and the orlistat fat malabsorption model worked well. MRI showed large areas of fat in the chyme in the descending and sigmoid colon or smaller scattered regions of fat. Large volumes of fat filled the entire lumen of the colon, colon walls were visible against the fat within the colon and the visceral fat surrounding the colon (Figure 1).

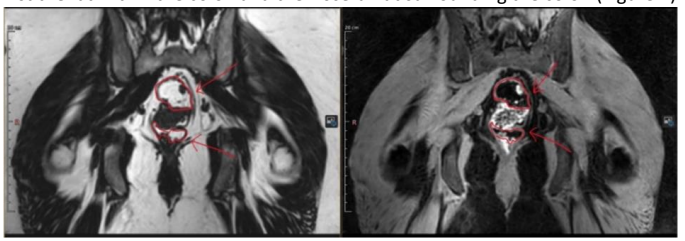

Fig 1 Fat-only image (left) and water-only image (right) of large volumes of fat in the sigmoid colon.

Smaller high fat areas of chyme were detected throughout the colon. These high fat areas of chyme appeared more mixed in the chyme and did not fill the width of the lumen (Figure 2).

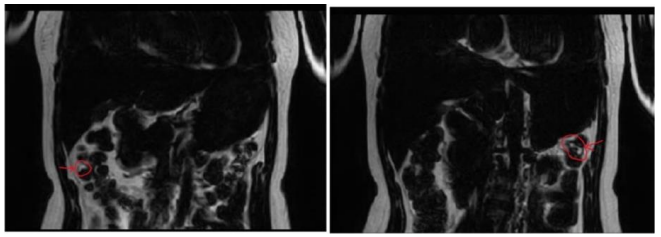

Fig 2 Fat- only images showing smaller, more dispersed high fat areas of chyme in the ascending colon (left) and descending colon (right).

Discussion and Conclusions

This study is ongoing and preliminary data have been presented. MRI could visualise fat in the colon using an orlistat model of fat malabsorption. Methods to quantify the volume of fat in the colon are currently being explored. The relationship between the volume of high fat areas of chyme and gastrointestinal symptoms is yet to be assessed. MRI could be used as an alternative technique to assess patients for fat malabsorption conditions.

References

1. Zuvarox, T. and C. Belletieri, *Malabsorption Syndromes*. 2022: StatPearls Publishing, Treasure Island (FL).
2. Nikaki, K.M.D.M. and G.L.M.D.M. Gupte, *Assessment of intestinal malabsorption.* Baillière's best practice & research. Clinical gastroenterology, 2016. **30**(2): p. 225-235.
3. Reeder, S.B. and C.B. Sirlin, *Quantification of Liver Fat with Magnetic Resonance Imaging.* Magnetic Resonance Imaging Clinics of North America, 2010. **18**(3): p. 337-357.
4. Heck, A.M., J.A. Yanovski, and K.A. Calis, *Orlistat, a new lipase inhibitor for the management of obesity.* Pharmacotherapy, 2000. **20**(3): p. 270-9.
5. Eggers, H., et al., *Dual-echo Dixon imaging with flexible choice of echo times.* Magn Reson Med, 2011. **65**(1): p. 96-107.

Optimisation of Gradient Echo Protocols for Quantitative Assessment of Pulmonary Ventilation and Perfusion at 3 T

Zachary J.T. Peggs[1], Penny A. Gowland[1], Susan T. Francis[1]
[1]Sir Peter Mansfield Imaging Centre, School of Physics & Astronomy, University of Nottingham, UK

Introduction: Several emerging non-contrast proton (^{1}H) MRI techniques make use of dynamic imaging to generate maps of pulmonary ventilation (V) and perfusion (Q). Recent studies have shown that spoiled gradient echo sequences (SPGR, T1-FFE, FLASH) can be used to measure these signals. Such 2D SPGR sequences can measure both ventilation and perfusion information simultaneously in the lung. Ventilation metrics are calculated from the local proton density variations in the lung parenchyma during respiration, while the time-of-flight effect provides signal from which to estimate perfusion. As the clinical availability of 3 T MRI continues to expand, optimisation of these dynamic imaging protocols is required to maximise the functional sensitivity and patient tolerability.
Generally low flip angles of 3-5° close to the Ernst angle are used, given the relatively long T_1 of lung parenchyma (~1000 ms at 3 T) [1]. However, a low flip angle reduces the contrast between the lung tissue and the pulmonary vasculature. This is potentially problematic for eliminating perfusion signals from parenchyma ventilation analysis, as well as for the assessment of perfusion signals. In addition, the optimum number of dynamic images required to determine the V/Q parametric maps remains unknown.
The aim of this work was to assess in healthy individuals the effect of flip angle and length of dynamic image series on the quantification of V/Q parameter maps from free-breathing proton MRI at 3T. VOxel-wise Lung VEntilation (VOLVE) analysis was performed to quantify V/Q correlation values [2].

Methods: 5 healthy volunteers were recruited to undergo ^{1}H lung MRI on a 3 T Philips Ingenia scanner. Images were acquired during free-breathing using a 2D fast field echo (FFE) sequence (TR/TE=1.9/0.57ms, 4.37 images/second) at a range of flip angles (α: 3°, 5°, 7°,10°, 12°, 14° and 18°). A single coronal slice placed approximately 1 cm posterior to the heart was imaged, with 512 images collected in 117s for a given scan. Three repeats of the scan was collected for each flip angle.
VOLVE analysis [2] was performed in MATLAB (R2022b) for each flip angle dataset. All images were registered to a mid-ventilation image using a demons-based registration. The thoracic cavity was segmented for each image series via seeded region growing to generate a whole lung mask. The whole-lung masks for each flip angle were split into parenchyma and vessel masks via adaptive thresholding with manual corrections if needed.
The mean signal, S_{Avg}, was computed voxel-wise for each flip angle. The VOLVE ventilation correlation coefficient (CC_V) and perfusion correlation coefficient (CC_Q) were computed by comparing the registered parenchyma timeseries values to a lung-diaphragm navigator signal, and an aorta or major pulmonary vessel-based cardiac signal time course, respectively [2]. For the α=18° data, the VOLVE fitting routine was repeated for each dataset with varying numbers of dynamic images included, ranging from 2-256 images (retrospective temporal under sampling). The median of each ventilation parameter map (XCC_V, Lag_V, $Grad_V$) was computed for each dynamic series length. Convergence of the parameters was defined as the point at which the root mean square deviation over a 5 image sliding window did not change by more than 5%.

Results: Fig. 1 shows a trend for S_{Avg} and CC_V to decrease in the parenchyma with increasing flip angle ($r = -0.99$, $p = 0.003$). Conversely, CC_Q increases with increasing flip angle, until reaching a plateau at ~10°-14°. Fig. 2 shows the number of images required for convergence of Lag_V was greater than for XCC_V or $Grad_V$.

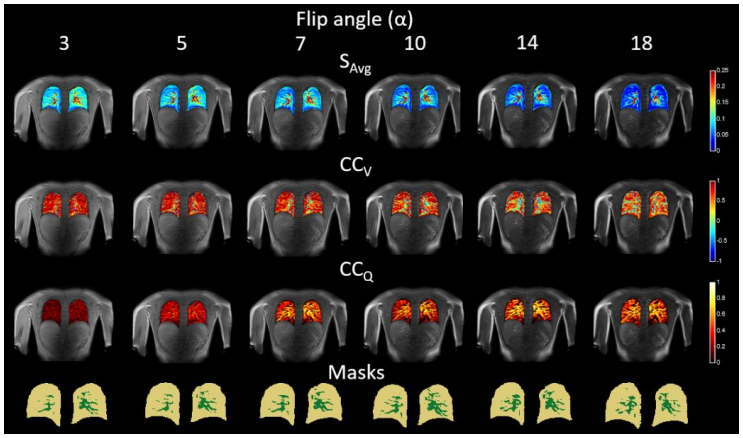

Fig. 1. Example maps of S_{Avg}, CC_V and CC_Q in a healthy volunteer (age 24, female) across flip angle (α), and associated parenchyma (yellow) and vessel masks (green). On increasing the flip angle, S_{Avg} and CC_V tend to decrease, while CC_Q increases.

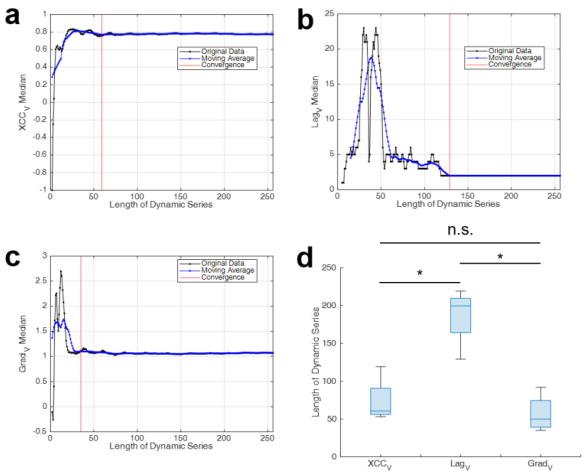

Fig. 2. Example convergence plots for ventilation metrics in a healthy volunteer (age 24, female) shown for **a)** XCC_V, **b)** Lag_V and **c)** $Grad_V$. **d)** shows the number of images required for convergence for all five participants. Significant differences in the length of required scan (Wilcoxon rank-sum) are indicated with asterisks (*).

Discussion: While low flip angles close to the Ernst angle for the parenchyma elicit a strong CC_V, this results in a lower CC_Q. To trade-off the estimation of both parenchyma V and Q signals, a flip angle higher than the Ernst of α=7-12° may be appropriate. In addition, the delay/phase information (Lag_V) requires increased sampling of the respiratory cycle compared to correlation/gradient metrics.

Conclusion: The need for a trade-off between obtaining a strong ventilation signal whilst not suppressing the parenchyma perfusion signal is demonstrated. Further work is required to verify these results in lung disease in which the parenchyma T_1 may increase, and where the convergence may be impacted by a reduction in SNR due to altered alveolar susceptibility profiles.

References

[1] Gai *et al.* Journal of Magnetic Resonance Imaging, 45: 1097-1104 (2017)
[2] Peggs *et al.* Journal of Magnetic Resonance Imaging (2024)

ICA-enabled oxygen-enhanced MRI (OE-MRI) correlates with pulmonary function tests in cystic fibrosis

Sarah H. Needleman[1], Mina Kim[1], Jamie R. McClelland[1], Marta Tibiletti[2], Christopher Short[3,4,5], Thomas Semple[3,4], Jane C. Davies[3,4,5], Geoff J. M. Parker[1,2]
[1]Centre for Medical Image Computing, Department of Medical Physics & Biomedical Engineering, University College London, [2]Bioxydyn Limited, [3]National Heart & Lung Institute, Imperial College London, [4]Royal Brompton Hospital, Guy's & St Thomas' Trust, [5]European CF Society Lung Clearance Index Core Facility

Introduction: Dynamic oxygen-enhanced MRI (OE-MRI) uses inhaled oxygen to provide contrast to indicate regional lung function. T_2^*-sensitive dual-echo dynamic lung OE-MRI acquisitions have recently been demonstrated at 3T [1] and 1.5T [2]. However, the presence of artefacts, confounding signals, and poor lung tissue SNR makes the analysis of dynamic lung OE-MRI challenging. Application of independent component analysis (ICA) to dynamic lung OE-MRI can enable the separation of the lung's oxygen-enhancement response from confounding signals [3]. Here we apply ICA to dual-echo dynamic OE-MRI in cystic fibrosis (CF) and examine the correlation between dynamic OE-MRI, the lung clearance index and spirometry.

Methods: 11 CF patients (median age 26 years, range 8-46) were recruited. Subjects underwent pulmonary function testing (PFT) using multiple breath N_2 washout to obtain the lung clearance index ($LCI_{2.5}$), and spirometry to obtain FEV1 %predicted (FEV1%p) and FVC %predicted (FVC%p). Subjects were imaged using a free-breathing dynamic 2D multi-slice dual-echo RF-spoiled gradient echo OE-MRI acquisition at 1.5T [2]. Subjects inhaled: medical air (1.5 minutes), 100% oxygen (3.5 minutes), and medical air (4 minutes). The dynamic MRI series were registered using NiftyReg [3,4]; a 3x3x3 median filter was applied to each echo [5].
R_2^* and S_0 were extracted from the dual-echo data within a cardiac mask consisting of cardiac tissue, lung tissue, and major blood vessels. In a spoiled gradient echo acquisition, S_0 is influenced by proton density and R_1. ICA was applied to extract the oxygen-enhancement response of R_2^* and S_0 from confounds using a previously developed analysis pipeline [3]. The pipeline was adapted for application to R_2^* and S_0 and a single oxygen-inhalation period by considering 2-72 ICA components. The ICA-extracted ΔR_2^* was calculated as the difference between 100% oxygen-inhalation (average over 180-215 dynamics) and air-inhalation (average over 10-50 dynamics); the percentage signal enhancement of the ICA-extracted S_0, $PSES_0$, was calculated as the percentage difference between 100% oxygen-inhalation and air-inhalation. The ICA-extracted ΔR_2^* and $PSES_0$ were thresholded within the lung to evaluate the ventilated volume fraction (VVF) and ventilated with oxygen uptake volume fraction (VUVF), respectively [2]. The median lung ΔR_2^* and $PSES_0$, and the VVF and VUVF values, were compared with the PFT measures using Pearson's correlation; $p < 0.05$ was considered significant.

Results: ΔR_2^*, VVF, and VUVF exhibited significant correlations with $LCI_{2.5}$ and FEV1%p, with ΔR_2^* and VVF correlations generally being stronger (Table 1). $PSES_0$ did not exhibit any significant correlations. Maps of ΔR_2^*, $PSES_0$, VVF, and VUVF are presented in Figure 1.

	$LCI_{2.5}$	FEV1%p	FVC%p
ΔR_2^* (ms^{-1})	-0.93 **$p < 0.001$**	0.94 **$p < 0.001$**	0.80 **$p = 0.003$**
$PSES_0$	-0.42 $p = 0.20$	0.26 $p = 0.44$	0.08 $p = 0.81$
VVF	-0.91 **$p < 0.001$**	0.90 **$p < 0.001$**	0.77 **$p = 0.006$**
VUVF	-0.73 **$p = 0.01$**	0.65 **$p = 0.03$**	0.50 $p = 0.12$

Table 1: Pearson's correlation of the ICA-extracted OE-MRI measures with PFTs.

Discussion: $LCI_{2.5}$ is of interest as a global marker of CF disease severity, particularly for early disease [6]. OE-MRI biomarkers provide regional measures of lung function, of relevance to heterogeneous presentations of CF. The OE-MRI measures of ΔR_2^* and VVF exhibited significant correlations with $LCI_{2.5}$, FEV1%p, and FVC%p suggesting they share a common basis in gas ventilation information, concordant with literature understanding of the source of the ΔR_2^* signal [3,7]. $PSES_0$ and VUVF demonstrated a substantially weaker relationship with $LCI_{2.5}$, FEV1%p, and FVC%p which we speculate is due to the additional influence of gas uptake dynamics to these MRI signals [3]. Overall the OE-MRI method shows good sensitivity to CF.

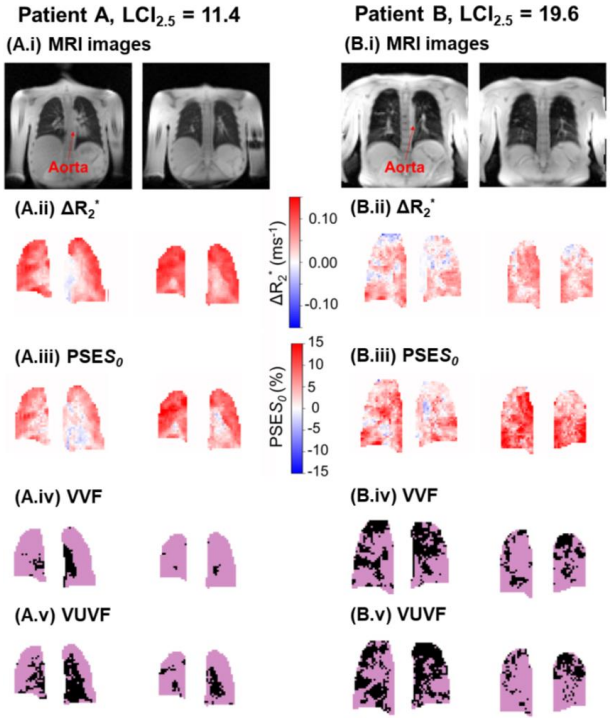

Figure 1: (i) MRI images, and maps of ICA-extracted (ii) ΔR_2^*, (iii) $PSES_0$, (iv) VVF, and (v) VUVF. Two coronal slices from two CF patients are shown: (A) 19 years, $LCI_{2.5}$ = 11.4, FEV1p% = 96, FVCp% = 112, and (B) 46 years, $LCI_{2.5}$ = 19.6, FEV1p% = 51, FVCp% = 58. Pink indicates lung voxels classed as functioning in VVF and VUVF maps; black indicates lung voxels classed as non-functioning. The lung appeared heterogeneous in ΔR_2^* and $PSES_0$ for subject (B). Subject (B) demonstrated a greater lung fraction classed as non-functioning in the VVF and VUVF maps compared to subject (A).

Conclusions: ΔR_2^*, VVF, and VUVF, extracted from dual-echo gradient echo dynamic OE-MRI using ICA, demonstrated good correlation with lung clearance index in cystic fibrosis, suggesting a potential sensitivity to disease severity.

Acknowledgements: This work is supported by the EPSRC-funded UCL Centre for Doctoral Training in Medical Imaging (EP/L016478/1), by the CRUK NCITA award C1519/A28682, by Innovate UK award 104629, by Cystic Fibrosis Foundation, grant number 0208A120, and by the NIHR Imperial Biomedical Research Centre. JM acknowledges funding from CRUK via the Network Accelerator Award Grant (A21993) to the ART-NET consortium and WEISS (203145/Z/16/Z).

References:

[1] Kim M, et al. Feasibility of dynamic T_2*-based oxygen-enhanced lung MRI at 3T. *Magn Reson Med*. 2024;91:972-986. doi:10.1002/mrm.29914. [2] Tibiletti M, et al. Double-echo Oxygen Enhanced MRI at 1.5 T correlates with clinical lung function in CF patients. In: *Proc. Intl. Soc. Mag. Reson. Med. 32*.;2023:1399. doi:10.3389/fninf.2014.00044.4. [3] Needleman SH, et al. Independent component analysis (ICA) applied to dynamic oxygen-enhanced MRI (OE-MRI) for robust functional lung imaging at 3 T. *Magn Reson Med*. 2024;91:955-971. doi:10.1002/mrm.29912. [4] Modat M, et al. Fast free-form deformation using graphics processing units. *Comput Methods Programs Biomed*. 2010;98(3):278-284. doi:10.1016/j.cmpb.2009.09.002. [5] van der Walt S, et al. scikit-image: image processing in Python. *PeerJ*. 2014;2:e453. doi:10.7717/peerj.453. [6] Davies JC, et al. Lung clearance index in CF: a sensitive marker of lung disease severity. *Thorax*. 2008;63(2):96 LP - 97. doi:10.1136/thx.2007.082768. [7] Pracht ED, et al. Oxygen-enhanced proton imaging of the human lung using T2*. *Magn Reson Med*. 2005;53(5):1193-1196. doi:10.1002/mrm.20448.

Power Pitch Session 4

How do b-Values in Diffusion-Weighted Imaging Affect Measures of Skeletal Muscle Architecture and Diffusivity?

Zhenkai Zhao[1,2,*], Fiona Elizabeth Smith[3], Emma Hodson-Tole[1,2]
[1]Department of Life Sciences, Manchester Metropolitan University, Manchester, United Kingdom
[2]Manchester Institute of Sport, Manchester Metropolitan University, Manchester, United Kingdom
[3]Wolfson Active Ageing Imaging Laboratory, Manchester Institute of Sport, Department of Sport and Exercise Science, Faculty of Science and Engineering, Manchester Metropolitan University, Manchester, United Kingdom
[*]**Corresponding author**
Zhenkai Zhao
z.zhao@mmu.ac.uk

Introduction: The b-value parameter in DWI acquisition protocols can be manipulated to optimize image quality and sensitivity to microstructure characteristics. Informed determination of b-values is essential for enhancing the diagnostic and research capabilities of DWI in assessing skeletal muscle health and pathology [1, 2]. In the literature a wide range of b-values (10-1000s/mm^2) have been used to study skeletal muscles [3, 4]. However, there is a scarcity of systematic, objective assessments of the effects of different b-values on measures of skeletal muscle architecture. Therefore, this study aims to systematically investigate how different b-values affect the quantification of fascicle characteristics in lower leg skeletal muscles, thereby providing insights that could refine DWI protocols for muscle studies.

Methods: Six healthy adults (3 males and 3 females, aged 24-46 years) were recruited for the study. DWIs were acquired on a 3T MRI scanner (Siemens MAGNETOM Vida) using six different b-values, ranging from 10 to 500 s/mm². The medial gastrocnemius (MG), tibialis anterior (TA), and lateral gastrocnemius (LG) muscles were examined. Spin echo, echo-planar imaging (SE-EPI) was used for DWI acquisition, with a slice thickness of 5 mm, and 60 slices collected for each muscle. Key diffusion parameters such as fractional anisotropy (FA) and mean diffusivity (MD), along with muscle architectural factors including fascicle curvature, pennation angle (PA), and fascicle length (FL), were analyzed across different b-values.

Results: Greater FA and MD values were associated with lower b-values, particularly for b-values below 100 s/mm² for all muscles studied. MD values ranged from 4-8 mm²/s at b = 10 s/mm² compared to 1.3-1.5 mm²/s at b = 500 s/mm². Within participants, fascicle curvatures were greater at lower b-values, increasing from 8.5 m^{-1} at b = 500 s/mm² to 15 m^{-1} at b = 10 s/mm². PA increased from 20° at b = 500 s/mm² to over 35° at b = 10 s/mm². In MG muscle, PA did not vary significantly across b-values, but differed between b = 100 s/mm^2 and b = 500 s/mm^2 for LG and TA muscle. Similar variations were observed for curvature measurements. Fascicle lengths were shorter at lower b-values for the three muscles (46.3 mm at b = 500 s/mm^2 and 20.3 mm at b = 10 s/mm^2 for MG muscle). Additionally, extremely short fascicles were captured for b-values lower than 50 s/mm^2 under the same stopping criteria. As depicted in Fig.1C, fewer fascicles were captured for b = 10 s/mm^2 and FLs were shorter compared to Fig. 1B with b = 500 s/mm^2. Although by using softer stopping criteria, longer and larger numbers of fascicles can be captured, the resulting fascicles presented unrealistic PA and curvature values. Overall, median FL, PA, curvature, and diffusivity values were consistent when b-values exceeded 100 s/mm².

Discussion: B-values less than 100 s/mm² significantly influenced the number of fascicles detected and the features measured, in particular the fascicle length. The intravoxel incoherent motion (IVIM) effects for b-values lower than 100 s/mm^2 likely influenced the fascicle tract number and architectural values measured, as the perfusion effects contribute more than the diffusion effects at lower b-values. While the very low b-values have been used to explore specific muscle characteristics, such as motor unit territory, it is clear they are not suitable for architectural measures.

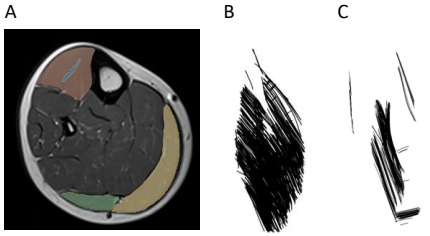

Fig.1. (A) Description of segmentation for three muscles, MG, LG, and TA, including segmentation for aponeurosis inside TA. (B) Fascicles captured from tractography techniques for b = 500 s/mm^2. (C) Fascicles captured from tractography techniques for b = 10 s/mm^2.

Conclusions: The variation of b-values can lead to differences in both architectural and diffusivity measurements of the lower leg muscles. The specific change in variance differs between the muscles studied and the range of b-values selected. These findings suggest that unlike lower b-values, higher b-values (greater than 100 s/mm²) can provide consistent architectural and diffusion parameters. Considering both the image quality acquired and data accuracy, b-values equal to and higher than 250 s/mm^2 are recommended for DWI/DTI scanning of lower leg muscles.

References

1. Xie, S., et al., *How does B-value affect HARDI reconstruction using clinical diffusion MRI data?* PloS one, 2015. **10**: p. e0120773.
2. Cha, S.Y., E. Kim, and S.Y. Park, *Why Is a b-value Range of 1500-2000 s/mm(2) Optimal for Evaluating Prostatic Index Lesions on Synthetic Diffusion-Weighted Imaging?* Korean J Radiol, 2021. **22**(6): p. 922-930.
3. Froeling, M., et al., *DTI of human skeletal muscle: the effects of diffusion encoding parameters, signal-to-noise ratio and T2 on tensor indices and fiber tracts.* NMR Biomed, 2013. **26**(11): p. 1339-52.
4. Whittaker, R.G., et al., *Functional magnetic resonance imaging of human motor unit fasciculation in amyotrophic lateral sclerosis.* Annals of Neurology, 2019. **85**(3): p. 455-459.

Power Pitch Session 4

Quadrupolar Splittings in the Forearm and Lower Leg after Deuterium Oxide Loading

Robin Damion[1,2,3], Daniel Cocking[3,4], Matthew Brook[2,5,6] Dorothee Auer[1,2,3], and Richard Bowtell[2,3,4]
[1]Mental Health and Clinical Neuroscience, School of Medicine, University of Nottingham, UK.
[2]NIHR Nottingham Biomedical Research Centre/Nottingham Clinical Research Facilities, Queen's Medical Centre, UK.
[3]Sir Peter Mansfield Imaging Centre, University of Nottingham, UK.
[4]School of Physics and Astronomy, University of Nottingham, UK.
[5]MRC-Versus Arthritis Centre for Musculoskeletal Ageing Research, University of Nottingham, UK
[6]School of Life Sciences, University of Nottingham, UK

Introduction: Partially ordered biological tissues can be studied via the deuterium (^{2}H) magnetic resonance of water because the quadrupolar interaction produces a frequency doublet whose splitting is sensitive to the effect of ordering on the time-averaged direction of the local electric field gradient with respect to the B_0-direction [1,2]. The low natural abundance of deuterium (0.015%) means that performing ^{2}H MR measurements in vivo can be challenging, even at high field [3]. Additionally, tissues typically contain multiple water compartments and spectra are complicated by the superposition of ordered (anisotropic) and disordered (isotropic) signal components. Here, these issues were investigated by measuring the angular dependence of the ^{2}H quadrupolar splittings from the lower leg and forearm muscles in healthy human participants who had ingested D_2O to enrich their deuterium levels to ~100x natural abundance. Comparisons to measurements employing double-quantum filtering (DQF) were also made.

Methods: Deuterium spectroscopy and chemical shift imaging (CSI) were performed on the lower leg and forearm in three human volunteers, using in-house-built ^{2}H coils resonating at 19.6 MHz, interfaced to a Philips Achieva 3T scanner. A 16 cm diameter saddle coil was used for the lower leg, and a 15 cm diameter Helmholtz coil was used for the forearm.

Deuterium 3D CSI images were acquired with resolution 10x10x10 mm^3, TR/TE=500/6.2 ms, sampling bandwidth 750 Hz, 256 samples, 2 averages. Images were acquired in each subject with the lower leg parallel to the B_0-direction and with the forearm at 10 angles (~0 – 90°) to B_0.

DQF deuterium spectra were acquired from a 2-cm axial slice of the lower leg or forearm, using hard pulses in combination with outer-volume saturation. Spectra were obtained via an anti-phase DQF sequence [4] whereby the quadrupole-doublet peaks acquire a relative phase of 180°. DQF spectra were acquired for a range of values of the creation time, $1 \leq \tau \leq 36$ ms, with TR/TE=1000/0.58 ms, sampling bandwidth 3000 Hz, 1024 samples, 56 averages.

Deuterium 2D CSI data were also acquired from a single 2-cm axial slice, using outer-volume suppression. CSI data were acquired for the pulse-acquire sequence, and using the anti-phase DQF sequence (DQF-CSI) with $\tau = 5$ ms. The in-plane resolution was 10x10 mm^2, TR/TE=1000/2 ms, 256 samples, bandwidth 750 Hz, 4 averages (CSI), 8 averages (DQF-CSI).

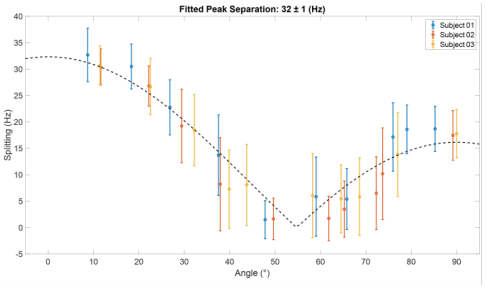

Figure 1. *Averaged quadrupolar splittings from forearms oriented at different angles ϑ to the B_0-direction. The dotted line is a fit to the function $f_q|3\cos\theta^2 - 1|/2$.*

Results: Spectra from CSI data of the forearm, oriented at different angles, θ, to the B_0-direction were analysed to obtain the quadrupolar splittings. Figure 1 shows the averaged splitting frequencies plotted against angle, for three participants. An average splitting value of $f_q = 32 \pm 1$ Hz was obtained from a fit to the expected angular-dependence.

Figure 2 shows DQF spectra from forearms oriented approximately parallel to the B_0-direction, plotted as a function of creation time, τ, displaying the build-up and decay of the double-quantum coherence amplitude.

Figure 3 shows a comparison of 2D CSI and DQF-CSI data for the lower leg, highlighting spectra in individual voxels in the tibialis anterior and soleus.

Discussion: The residual quadrupolar splitting of the deuterated water spectrum provides evidence of some local ordering of the tissue, and has been previously observed in muscle, tendon, cartilage, and nerves [3—6]. The observed splittings in the muscles of the forearm, as seen in Figure 1, exhibit an angular dependence that is consistent with a quadrupolar interaction. The measured value of f_q is similar to previous 7T measurements in the lower leg [3] and with values found from fitting to the DQF spectra (Figure 2).

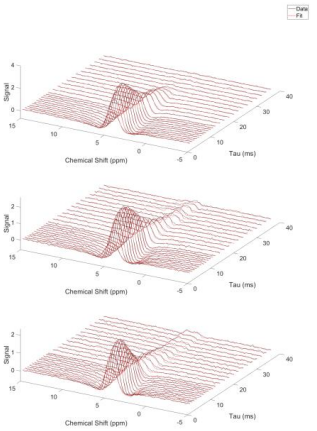

Figure 2. *DQF spectra from forearms parallel to the B_0-direction, plotted against creation time τ.*

The anti-phase DQF sequence produces spectra whose peaks have opposite phases. Consequently, signals with zero or very small splittings will vanish or be very small, and this provides a way of displaying only signals with non-zero splittings. These signals are shown in Figure 2, which roughly follow the form $Ae^{-2\tau/T_2}\sin 2\pi f_q \tau$. The utility of the DQF sequence is illustrated in Figure 3, where standard spectra with isotropic peaks in addition to a doublet (tibialis anterior), or no clear doublet (soleus) provide non-vanishing DQF spectra of varying amplitude.

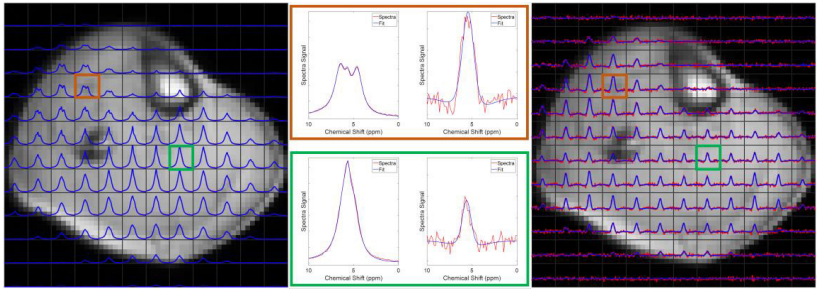

Figure 3. *CSI (left) and DQF-CSI (right) data from the lower leg. Spectra are highlighted from muscles of the anterior tibialis (red) and soleus (green).*

Conclusions: Quadrupolar splittings in the lower leg are most prominent in the region of the tibialis anterior. This is because the fibres of this muscle align closely with the B_0-direction, but could also indicate a more ordered environment in which the water resides. In the forearm, splittings are more homogeneous. The DQF sequence is useful in isolating the anisotropic signals from isotropic.

References

[1] Seelig J. *Q. Rev. Biophys*. 1977; **10**(3): 353 – 418.
[2] Eliav U, Navon G. *eMagRes.* 2016; **5**(1). DOI: 10.1002/9780470034590.emrstm1448
[3] Gursan A, Froeling M, Hendriks AD, *et al. Magn. Reson. Med*. 2022; **87**: 1165 – 1173.
[4] Sharf Y, Eliav U, Shinar H, Navon G. *J. Magn. Reson.* 1995; **B107**: 60 – 67.
[5] Perea W, Cannella M, Yang J, *et al. Magn. Reson. Med*. 2007; **57**: 990 – 999.
[6] Eliav U, Wehli FW, Navon G. *Magn. Reson. Med*. 2020; **84**(2): 535 – 541.

Power Pitch Session 4

Optimized bone imaging protocol via IR-ZTE with long-T2 suppression

Diana Catargiu[1], Tobias C. Wood[1]

[1]Department of Neuroimaging, Institute of Psychiatry, Psychology and Neuroscience, King's College London

Introduction: Bone imaging using MRI is gaining traction due to its ability to produce clinically useful images without the need for additional ionizing CT scans [1]. Techniques such as Ultrashort Echo Time (UTE) or Zero Echo Time (ZTE) are preferred to effectively capture the rapidly decaying signal in bone [2][3][4]. In this study we use Inversion Recovery Zero Echo Time (IR-ZTE) combined with physics-based subspace reconstruction to visualize cortical bone [3]. We compare bone sharpness across two bandwidth settings, evaluating the trade-offs involved in achieving better quality bone images.

Methods: A healthy volunteer was scanned in a 3T magnet equipped with a 48 channel head coil (GE Premier). We acquired two scans, with the following sequence parameters: (a) readout bandwidth ±31.5kHz, 250 spokes per segment, 256mm FOV, 0.8 mm voxel size, flip angle 2°, 2.83ms TR, 5ms Inversion Time, 7min 38s scan time (b) readout bandwidth ±50.0kHz, 400 spokes per segment, 256mm FOV, 0.8 mm voxel size, flip angle 1.6°, 1.87ms TR, 5ms Inversion Time, 7min 42s scan time. The trajectory within a segment was a generalized spiral [5] with golden means rotation between each segment to produce an overall incoherent trajectory [6]. Low-resolution segments were acquired with the gradients ramped down by a factor of 8 to fill the dead-time gap [7].

Sensitivity maps were calculated from a calibration ASSET (Array Spatial Sensitivity Encoding Technique) scan [8], acquired at low spatial resolution with readout bandwidth ±31.5kHz, 128 spokes per segment, 256mm FOV, 0.8 mm voxel size, flip angle 2°, 30s scan time.

The data was reconstructed with the RIESLING toolbox [9]. To construct the required subspace basis vectors, the evolution of 128 samples from 6 simulated tissue types (CSF, Grey Matter, White Matter, Blood, Fat and Bone) with T1 ranges of 3.80-4.80, 1.20-1.70, 0.80-1.10, 1.30-1.80, 0.30-0.50, 0.20-0.50, was simulated using a simulation framework for segmented, magnetization-prepared sequences using homogenized Bloch equations and an eigenanalysis to find the steady state [10]. Finally, a Singular Value Decomposition was taken. We reconstructed the data using a least squares algorithm with 4 maximum iterations.

Results: Figure 1 shows slices at time-point T=80, chosen to maximize positive bone contrast while minimizing the signal from soft tissues. In both scans, the cortical bone is clearly visible. The scan acquired at 31.5 kHz appears less noisy, with better suppression of grey matter and background noise. However, fat has not been entirely suppressed and off-resonance effects are noticeable. The fat-bone separation is more accurate at 50.0 kHz; blurring is reduced, leading to a clearer distinction between the tissues.

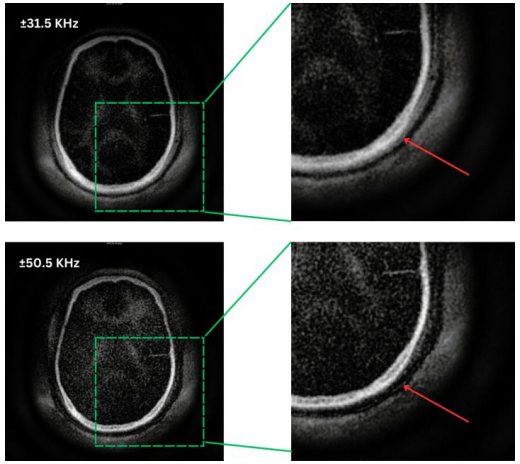

Fig. 1. IR-ZTE Bone scans at ±31.5kHz and ±50.0kHz bandwidth with highlighted bone/fat separation

Discussion: Lower bandwidth improves the signal-to-noise ratio (SNR) due to increased averaging of noise per sample point [11]. Higher SNR results in better image quality for tissues with longer T2 relaxation times, where the signal persists for longer. However, blurring can result for tissues either with short T2 (due to decay of the signal before acquiring high spatial frequencies) or large chemical shift (due to accrual of phase by the end of the of the readout). This is particularly problematic for bone and fat respectively. Hence, we need to consider a trade-off between a higher SNR, less blurring, and sufficient bone signal for better bone visualisation.

Conclusions: The images demonstrate that using a higher bandwidth can improve fat-bone separation and reduce off-resonance effects, resulting in clearer and more accurate imaging of bone structures. However, the trade-off involves increased noise and potential SNR reduction. To address these issues and further enhance image quality, we are currently employing a Total Generalized Variation (TGV) regularized reconstruction technique, which we expect to improve the image quality by reducing noise.

References

[1] F. Wiesinger and M.-L. Ho, 'Zero-TE MRI: principles and applications in the head and neck', BJR, p. 20220059, Jun. 2022, doi: 10.1259/bjr.20220059.
[2] F. Wiesinger et al., 'Zero TE-based pseudo-CT image conversion in the head and its application in PET/MR attenuation correction and MR-guided radiation therapy planning', Magnetic Resonance in Medicine, vol. 80, no. 4, pp. 1440–1451, Oct. 2018, doi: 10.1002/mrm.27134.
[3] M. Weiger et al., 'ZTE imaging with long-T2 suppression', NMR Biomed., vol. 28, no. 2, pp. 247–254, Feb. 2015, doi: 10.1002/nbm.3246.
[4] M. Weiger and K. P. Pruessmann, 'Short-T2 MRI: Principles and recent advances', Progress in Nuclear Magnetic Resonance Spectroscopy, vol. 114–115, pp. 237–270, Oct. 2019, doi: 10.1016/j.pnmrs.2019.07.001.
[5] S. Ramachandran, TC. Wood, G. Zhang, and M. Lustig, 'Arc-ZTE: Incoherent k-space sampling in time using continuously-slewed gradients for flexible, dynamic, quiet Zero TE MRI' *Conference abstract, ISMRM 2024*
[6] R. W. Chan, E. A. Ramsay, C. H. Cunningham, and D. B. Plewes, 'Temporal stability of adaptive 3D radial MRI using multidimensional golden means', Magn. Reson. Med., vol. 61, no. 2, pp. 354–363, Feb. 2009, doi: 10.1002/mrm.21837.
[7] Y. Wu et al., 'Water- and fat-suppressed proton projection MRI (WASPI) of rat femur bone', Magnetic Resonance in Medicine, vol. 57, no. 3, pp. 554–567, Mar. 2007, doi: 10.1002/mrm.21174.
[8] K.F. King, 'ASSET – Parallel Imaging on the GE Scanner' GE Healthcare instruction document
[9] T. Wood, E. Ljungberg, and F. Wiesinger, 'Radial Interstices Enable Speedy Low-volume Imaging', JOSS, vol. 6, no. 66, p. 3500, Oct. 2021, doi: 10.21105/joss.03500.
[10] S. J. Malik, R. P. A. G. Teixeira, D. J. West, T. C. Wood, and J. V. Hajnal, 'Steady-state imaging with inhomogeneous magnetization transfer contrast using multiband radiofrequency pulses', Magnetic Resonance in Medicine, Sep. 2019, doi: 10.1002/mrm.27984.
[11] D. Wang, R. K. Robison, Z. Li, J. G. Pipe, 'High SNR rapid T1-weighted MPRAGE using spiral imaging with long readouts and improved deblurring', Magnetic Resonance in Medicine, March 2023, doi: 10.1002/mrm.29492

Imaging choroid plexus diffusion characteristics using FLAIR-IVIM DW-MRI

Authors - Charith Perera[1], Shereen Nizari[1], Ian Harrison[1], Mark F Lythgoe[1], David L Thomas[2], Jack A Wells[1]

Introduction – The blood-cerebrospinal fluid barrier (BCSFB) at the choroid plexus (CP) plays a critical role in CNS homeostasis. Invasive and ex-vivo studies of the aged brain have revealed marked changes to BCSFB morphology and function, which may seed downstream neurodegenerative events[1-2]. Thus, the development of translatable, non-invasive tools for investigating BCSFB microstructure may be valuable to improve understanding of the BCSFB's role in age-related neurodegenerative disease. Previous attempts of using diffusion weighted (DW)-MRI to investigate CP microstructure are likely confounded by substantial partial volume (PV) contributions from CSF[3-5]. To overcome this, we investigated the feasibility of using a fluid-attenuated inversion recovery (FLAIR) intravoxel-incoherent motion (IVIM[6]) DW-MRI to more reliably and non-invasively assess CP diffusion behaviour, whilst attenuating PV from surrounding CSF, in the mouse brain. In a pilot study, we probe differences in diffusion outputs obtained from the brain cortex to novel measures localised to the CP and determine the inter-subject variability. We then applied this methodology to investigate differences in diffusion characteristics between healthy adult mice and aged mice, with an aim of detecting microstructural alterations in a non-invasive, translatable manner.

Methods – In a pilot cohort, MR imaging (Bruker 9.4T) was conducted in the anaesthetised mouse brain (C57BL/6, n= 7 (5 subjects, 2 rescanned, ~30 weeks, male). Data from this cohort was used to optimise the analytical pipeline, prior to application in the ageing study.

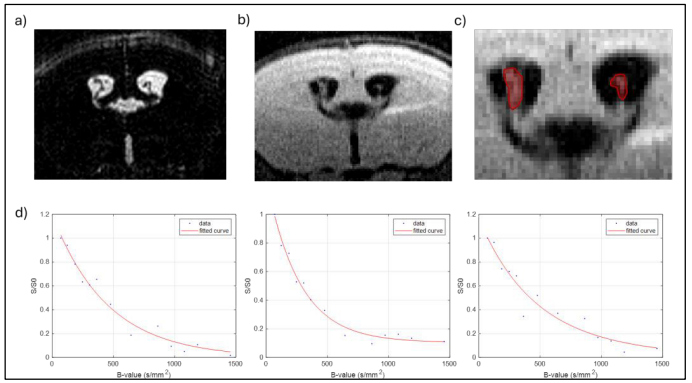

Fig 1 – FLAIR-IVIM data and analysis for example pilot subject: a) Example slice from 3D T2-weighted structural image to pinpoint choroid plexus (CP) tissue (dark), within ventricular CSF (bright). **b)** B0 image (B = 71 s/mm^2). **c)** ROI selection for analysis of CP (red) from B0 FLAIR-IVIM image, guided by T2-weighted structural scan (a). **d)** Example biexponential modelling of acquired voxel-wise, noise-corrected [B, S/S0] data (3 example CP voxels).

Initially, 3D T2-weighted structural scans (ultra-long TE = 176 ms), were used to determine CP location within the lateral ventricular compartment (Fig 1a). IVIM data was acquired using the *remmi toolbox*[7] fast spin echo (FSE) sequence (TR/TE = 6000/36 ms; 15×15 mm^2 FOV; 120×120 matrix; 0.35 mm slice thickness; 10 averages; A-P direction; 13 arrayed b-values (71-1454 s/mm^2); partial-FT (1.0,1.5) (Fig 1b). Prior to the DW module, a FLAIR pulse was applied to suppress CSF. This pulse utilised a subject-wise inversion time (IR-TI), calculated separately from DW images with matched parameters to those used for FLAIR-IVIM, but with varying TIs to determine the TI at which CSF is effectively suppressed.

Subsequently, FLAIR-IVIM data underwent voxel-wise noise correction, as described previously[8], and were subject to ROI analysis; a conservative region was drawn to include CP signal within the ventricles, using the prior structural scan for reference (Fig 1a,c). For CP voxels, noise-corrected voxel-wise signal values were used to fit biexponential models for the extraction of diffusion parameters: diffusion coefficient (D), and the intravascular fraction (F) (Fig 1d)[6]. Separately. cortical signals were averaged, and mean signal values were used for fitting cortical diffusion outputs. Voxel-wise maps were also generated across the brain to visualise differences in D and F.

For the ageing study, an identical imaging protocol was applied in aged C57BL/6JRj mice (n = 12, 24-months, male), and strain-matched adults (n = 10, 6-months, male).

Results & Discussion – FLAIR-IVIM pilot datasets revealed that compared to the cortex, the CP had a significantly higher D value [8.0 x 10^{-4} LV vs 5.9 x 10^{-4} cortex, p<0.01], as well as displaying a significant, 9-fold higher intravascular fraction, F [0.51 LV vs 0.06 cortex, p<0.0001] (Fig 2), in line with the much higher perfusion rate observed at the CP previously[9-10]. The pooled CP average biexponential fitting R^2 was 0.85 across the pilot cohort. The mean extracted D and F values had coefficient of variance values of 12% and 11% respectively, indicating relatively low inter-subject measurement variability. Previous human CP ADC measures have yielded values 2-3 times higher, likely due to confounding CSF PV contributions[3-5].

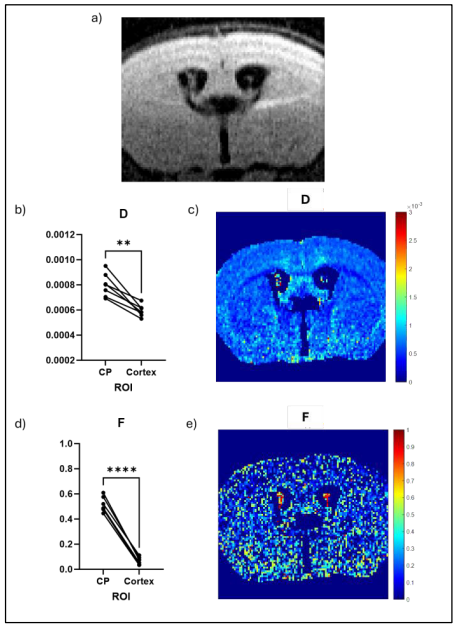

Fig 2 – FLAIR-IVIM pilot cohort results. a) B0 image (B = 71 s/mm^2), representative subject (n = 1). Paired comparison of diffusion outputs from CP and cortex: **b)** diffusion coefficient (D), and **d)** perfusion fraction (F). From example subject (a), voxel-wise D and F maps are shown to highlight regional difference in diffusion outputs **(c, e).**

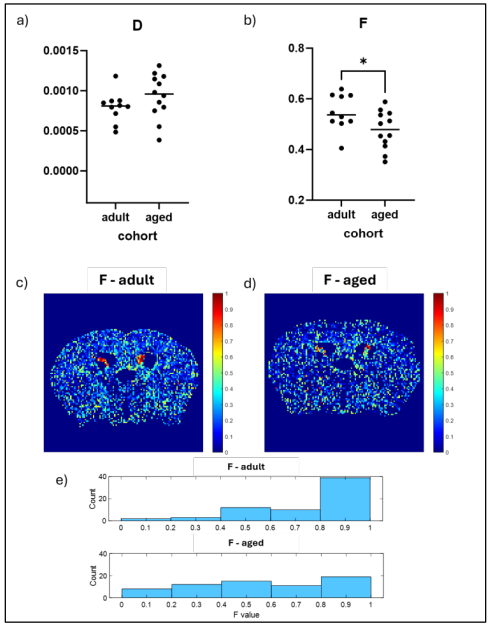

Fig 3 – FLAIR-IVIM ageing study results. Diffusion outputs (D) comparison between adult and aged subjects (n = 12, Welch's t-test), alongside mean: **a)** diffusion coefficient, and **b)** intravascular fraction. Example voxel wise maps for intravascular fraction, F, for **c)** adult, and **d)** aged subjects (representative n = 1 each). **e)** From these same subjects, histograms of the F values are shown for adult (66 CP voxels) vs aged (65 CP voxels).

In the ageing study, adult and aged mice exhibited similar D values [adult 7.9 x 10^{-4} vs aged 9.3 x 10^{-4}, p = 0.18] (Fig 3a). However, aged mice displayed a significantly lower intravascular fraction compared to adult mice (F = [0.55 adult, vs 0.48 aged], p = 0.03)] (Fig 3b-e). This is in-line with post-mortem human measures where normal aging accompanied significant decreases in CP microvessel density[11], as well as decreased CP perfusion in aged mice[9]. This is likely exacerbated in neurodegenerative pathology, and so highlights the potential for F to serve as a valuable, early biomarker of age-related neurodegenerative processes.

Conclusion – By attenuating CSF signal, FLAIR-IVIM can non-invasively inform on the microstructural and vascular characteristics of the CP, providing outputs that are distinct to the brain cortex, without major CSF PV confounding contributions. Studying diffusion outputs, e.g. F, in the contexts of health and disease may provide a potential biomarker for neurodegenerative processes, as well as deepening our understanding of CP structural/functional changes involved in pathophysiology.

References – 1. Balusu S, Brkic M, Libert C, Vandenbroucke RE. The choroid plexus-cerebrospinal fluid interface in Alzheimer's disease: more than just a barrier. Neural Regen Res. 2016 Apr;11(4):534-7. **2.** Serot JM, Foliguet B, Béné MC, Faure GC. Choroid plexus and ageing in rats: a morphometric and ultrastructural study. Eur J Neurosci. 2001 Sep;14(5):794-8. **3.** Alisch, J. S., Egan, J. M., & Bouhrara, M. (2022). Frontiers in Endocrinology, 13, 984929. **4.** Alicioglu, B., Yilmaz, G., Tosun, O., & Bulakbasi, N. (2017). The neuroradiology journal, 30(5), 490–495. **5.** Grech-Sollars, M., et al. (2015). NMR in Biomedicine, 28(4), 468-485. **6.** Le Bihan, D. (2019). Neuroimage, 187, 56-67. **7. Remmi toolbox** https://remmi-toolbox.github.io/ **8.** Gudbjartsson H, Patz S. The Rician distribution of noisy MRI data. Magn Reson Med. 1995 Dec;34(6):910-4. **9.** Evans, P. G., et al. Nature communications, 11(1), 2081. **10.** Faraci, F. M., et al (1988). Circulation research, 63(2), 373-379. **11.** Thore CR, Anstrom JA, Moody DM, Challa VR, Marion MC, Brown WR. Morphometric analysis of arteriolar tortuosity in human cerebral white matter of preterm, young, and aged subjects. J Neuropathol Exp Neurol. 2007 May;66(5):337-45.

Affiliations - 1. UCL Centre for Advanced Biomedical Imaging, University College London, UK. **2.** Neuroradiological Academic Unit, Department of Brain Repair and Rehabilitation, UCL Queen Square Institute of Neurology, UK

Towards accurate, reproducible PDFF quantification in the liver using a 3D dual-echo Dixon body composition sequence

Yifei Jin[1], Markus Henningsson[1], Carolina Fernandes[1]
[1]Perspectum, Oxford, United Kingdom

Introduction: Water-fat separation using 3D dual-echo Dixon is provided by all major MRI vendors. However, in quantitative analysis, the signal fat fraction (SFF) from scanner-derived water and fat images is biased compared to proton density fat fraction (PDFF), which is a biomarker for diseases such as metabolic dysfunction-associated steatohepatitis [1]. The large flip angle (α~10°) and short repetition time (TR~4-8 msec) optimised for fast acquisition will lead to a T1-biased SFF [2]. The different echo times (TE) and fat models used by vendors also introduce vendor-specific biases [3]. Here, we propose a correction method targeting these two biases, achieving more accurate and reproducible fat quantification in the liver across different vendors and field strengths.

Theory: The T1-bias is corrected using a term calculated from α, TR, water T1 ($T1_{water}$) and fat T1 ($T1_{fat}$)[4]. The vendor-specific bias was then corrected using a simulation-based technique. The signal was simulated for the full PDFF range (0-100%) using the liver fat model [5], then SFF reconstruction was performed with the derived vendor-specific fat model and algorithm. By locating the closest simulated SFF to the acquired SFF, the corresponding PDFF for the simulated SFF was obtained.

Experiments: To evaluate the T1-bias correction performance, 15 volunteers were scanned on 1.5T GE scanners at multiple sites using the 3D dual-echo spoiled gradient echo (Lava-Flex) sequence: $TE_{1,2}$ = (2.08, 4.17) msec, TR = [6.03–6.10] msec, α = 5° and 15°. For each volunteer, the two datasets acquired with different α were T1-bias corrected and their $SFF_{T1corrected}$ were compared.

To evaluate the Dixon-derived PDFF reproducibility using the full proposed correction, data were acquired on multiple vendors. In addition to the 15 1.5T GE datasets with α = 15°, 10 and 7 volunteers were scanned on 1.5T Siemens and 3T Siemens respectively, using the dual-echo spoiled gradient echo Dixon (VIBE-Dixon) sequence. On 1.5T Siemens: $TE_{1,2}$ = (2.08, 4.17) msec, TR = [6.80–7.36] msec and α = 15° were used. On 3T Siemens: $TE_{1,2}$ = (1.23, 2.46) msec, TR = 3.92 msec and α = 9° were used. 2D LiverMultiScan IDEAL (LMS IDEAL) was acquired for each volunteer to obtain liver PDFF [5]. MOLLI T1 and Dixon T2* were acquired for each volunteer, and the median liver $T1_{water}$ was extracted from the MOLLI T1 data, using as inputs PDFF and T2* [6]. The T1-bias and vendor-specific correction was performed as shown in Fig. 1 and the result was compared to the LMS IDEAL PDFF.

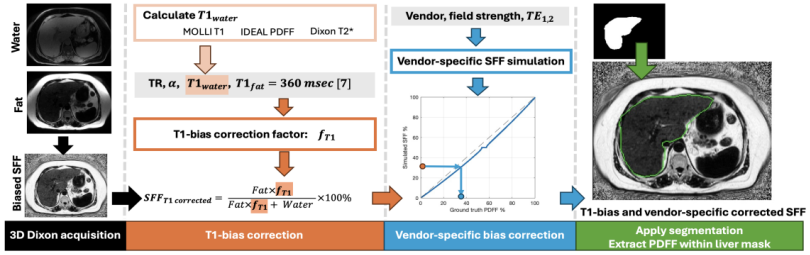

Fig. 1. Schematics of the proposed correction (from left to right). The $SFF_{T1corrected}$ was first obtained with correction factor $f_{T1} = \frac{T1W_{water}}{T1W_{water}}$, where T1-weighting of fat or water component signal is $T1W_{comp} = \frac{(1-e^{-TR/T1comp})\sin\alpha}{1-e^{-TR/T1comp}\cos\alpha}$. TR, α, calculated $T1_{water}$ and literature $T1_{fat}$ value [7] were used to compute f_{T1}. The $SFF_{T1corrected}$ was matched to the simulated SFF to find PDFF. Median liver PDFF was then extracted within the segmented liver mask.

Results: With T1-bias correction, the data acquired using different α (Fig. 2A) were corrected towards a similar $SFF_{T1corrected}$ (Fig. 2B). The values are still biased relative to PDFF due to vendor-specific biases, which can be simulated as shown in Fig. 2. With the full proposed correction, the 95% limits of agreement (LoA) of approximately ± 3% and 0.5% mean bias is achieved across vendors and field strengths (Fig. 3). It meets the QIBA requirement for subject-level liver PDFF measurement precision, indicating good agreement with LMS IDEAL PDFF [8]. Fig. 4 shows an example of the SFF map before and after each step of correction and LMS IDEAL PDFF.

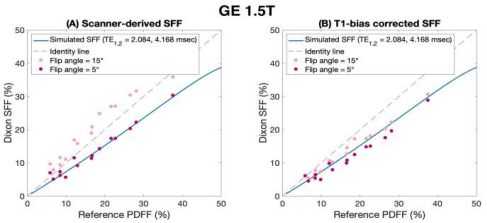

Fig. 2. Median Liver Dixon SFF is plotted against LMS IDEAL PDFF for each volunteer for scanner-derived SFF (A), and $SFF_{T1corrected}$ (B). The simulation SFF result is plotted against ground truth PDFF.

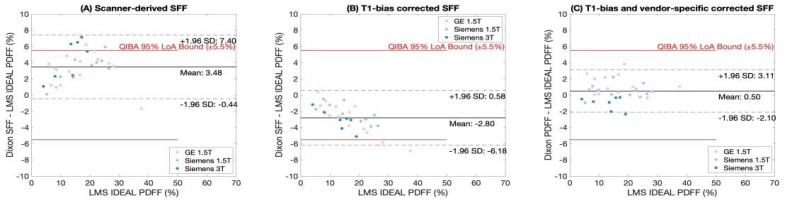

Fig. 3. Bland-Altman plots of Dixon SFF using LMS IDEAL PDFF as reference, for scanner-derived SFF (A), T1-bias corrected SFF (B) and T1-bias and vendor-specific corrected SFF (C). Data acquired on different vendors and field strengths are plotted with different colours, and the QIBA subject-level liver PDFF measurement precision requirements for 95% LoA [8] are also shown.

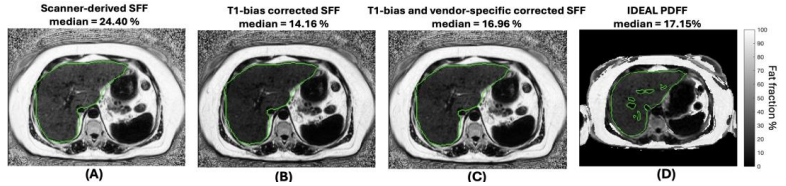

Fig. 4. Fat fraction map of the scanner-derived Dixon SFF (A), T1-bias corrected SFF (B), T1-bias and vendor-specific corrected SFF (C) and IDEAL PDFF (D). The liver segmentation mask is indicated in green, and the median value within the segmentation mask is shown above each figure.

Limitations: A bias between the $SFF_{T1corrected}$ obtained from different flip angle datasets is visible in Fig. 2B, indicating incomplete removal of the T1 bias, which could be related to the inaccurate effective flip angle due to B1 field inhomogeneity. Bias due to noise and T2* was not considered in this work.

Conclusions: We proposed a bias correction approach to achieve more accurate and reproducible fat quantification in the liver using commercialised 3D dual-echo Dixon sequences on different vendors and field strengths, including 32 volunteers on 1.5T GE, 1.5T Siemens and 3T Siemens scanners at 9 sites. Corrected liver SFF shows good agreement with LMS IDEAL PDFF.

References: **[1]** T Yokoo, M Bydder, G Hamilton, et al. *Radiology.* 251(1):67-76 (2009). **[2]** CY Liu, CA McKenzie, H Yu, JH Brittain and SB Redder *Magn Reson Med.* 58(2), 354-64 (2007). **[3]** D Hernando, ZP Liang and P Kellman *Magn Reson Med.* 64(3), 811-822 (2010). **[4]** WT Triplett, C Baligand, SC Forbes, et al. *Magn Reson Med.*72(1):8-19. (2014). **[5]** A Triay Bagur, et al. *Magn Reson Med*. 82(1), 460-475 (2019). **[6]** FE Mozes, EM Tunnicliffe, A Moolla, et al. *NMR Biomed.* 32(2):e4030. (2019). **[7]** Garnov N, Linder N, Schaudinn A, et al. *NMR Biomed.*27(9):1123-1128. (2014). **[8]** QIBA Proton Density Fat Fraction Biomarker Committee, 2023. Quantitative Imaging Biomarkers Alliance, December 2023. Available at: https://qibawiki.rsna.org/index.php/Profiles